UNIVERSITY OF BIRMINGHAM

COMMERCIAL DEVELOPMENT AND APPLICATIONS OF PROTON TRANSFER REACTION-MASS SPECTROMETRY

by

Renaud Roger Antoine Dassonville, Dipl.-Eng., M.Eng.

A thesis submitted to the University of Birmingham for the degree of

DOCTOR OF PHILOSOPHY

Molecular Physics Group

School of Physics and Astronomy

University of Birmingham, UK

March 2022

Abstract

Proton Transfer Reaction-Mass Spectrometry (PTR-MS) has been in use since the 1990s for real-time measurement of trace volatile organic compounds (VOCs) from parts per million by volume down to sub-parts per billion by volume in a wide range of applications such as environmental monitoring, health, homeland security and food sciences.

The work presented in this thesis deals with new developments and applications of PTR-MS and has different interconnected themes. The first is hardware development; principally the testing and characterisation of new radio frequency (RF) ion-funnels within the PTR reactor designed to improve ion transmission and thus sensitivity of detection for trace compounds. The desire to characterise better the effect of RF fields on analyte ions in the reactor led to a fundamental study in which the proportion of analyte product ions was determined as a function of the reduced electric field strength, first without the application of RF fields. This was to compare their behaviours when subject to RF fields. An unexpected and previously unreported shift in these product ion distributions was discovered, depending upon how the reduced electric field, E/n, was created.

A second theme is the creation of a methodology for, and production of, a mass spectral library for individual VOCs analysed by PTR-MS. This was to assist in the development and testing of a new software algorithm for compound identification and quantification of complex VOC mixtures when no pre-separation technique such as gas chromatography (GC) is used.

The third theme is the application of both these hardware and software developments in the practical analysis of VOCs, not just in ambient air but also in water, where a portable water sampler has also been developed, so that impurities in water could be determined with high specificity and sensitivity in real-time. This has been used in tandem not only with PTR-MS,

but also with two more conventional portable electron impact mass spectrometers (EI-MS). One of these analysers was taken to Mainz, Germany, as part of a secondment, to investigate the possibility of using the instrument instead of the more expensive and complicated PTR-MS for determination of a parameter of interest to atmospheric chemists: ‘the total OH reactivity' of the atmosphere.

The work in this thesis was conducted as part of a Marie Skłodowska-Curie Actions Innovative Training Network (ITN): Ion-Molecule Processes for Analytical Chemical Technologies (IMPACT). This European ITN programme was named through the European Commission’s HORIZON 2020 Programme. The work was directly influenced by the desire to improve analytical tools available to a commercial analytical instrument manufacturer, Kore Technology Ltd, at whose premises most of the work took place.

Dedication

* Dedicated to my aunt Blanche, Doctor in Philosophy, who dedicated her whole life to others.

* Dédié à ma tante Blanche, docteur en philosophie, qui consacra sa vie aux autres.

* Gewidmet meiner Tante Blanche, Doktor in Philosophie, die ihr gesamtes Leben andern Menschen widmete.

Acknowledgments

This project would not have been possible without a remarkable level of support and guidance. The people to thank are numerous.

First of all, I would like to make a special mention to my industrial supervisor, Fraser Reich, of Kore Technology Ltd, who, as well as listening to and understanding each of my reflections or concerns in this project, suggested directions to give a coherence to my various ideas. He helped me to evaluate my different proposals within the project, and to determine which might have the likeliest chance of success. He has been the first and main person to help me in each step of my new life in the United Kingdom. He always made an effort to explain cultural differences to me and to work through them with me. He made me feel welcome right from the beginning and also believed in my ideas, helping me to do justice to them.

Secondly, I would like to thank my academic supervisor Prof. Chris Mayhew of the University of Birmingham (UoB) for his academic support. Prof. Mayhew's book 'Proton Transfer Reaction Mass Spectrometry, Principles and Applications' has been a huge source of inspiration to me, increasing my theoretical physics knowledge and my understanding of ion chemistry. Sometimes, we think we know enough already and are competent to tackle a subject. Prof Mayhew has challenged me many times and in many ways and helped me appreciate the importance of positive criticism.

Most work has been conducted at Kore, an instrument company providing an ideal work context to brainstorm ideas and to implement them quickly: assembling a few pipes, valves, or electronic boards from scratch to test an idea. My direct contact with the commercial business of the company has helped me understand the importance of having innovations and developments that can be implemented in practice and make economic sense.

At Kore, I would like to thank Clive Corlett for all of his brilliant engineering ideas, technical knowledge and drawings – the basis of any hardware development. Steve Mullock for his innovative software development and theoretical knowledge in physics; indispensable in giving direction to any instrumental development. Caroline Lamont Smith for her support in the water analysis development, and Danny Blenkhorn, a former student of the UoB Molecular Physics Group and now Kore employee, for helpful discussions and guidance on all things PTR. Finally, to Dave Martin for organising the logistics around my project as efficiently as possible.

This project has been punctuated by visits to the Molecular Physics Group of the UoB, led by Prof Mayhew, which offered very welcoming conditions to work, discussions and exchange of ideas about different aspects of my project. I thank its members, including David Olivenza León, a fellow member of the same 'IMPACT' ITN.

This PhD project has been part of the Innovative Training Network (ITN) 'Ion-Molecule Processes for Analytical Chemical Technologies' (IMPACT) which involved 10 Early Stage Researchers from different countries; each one of us located in a different country from our birth. All the ITN meetings have been productive and offered the chance to meet and share not just our scientific projects, but also to meet with one another, find support and have a sense of community. I am fully aware of this privilege and I am thankful to all my IMPACT colleagues who have made it a memorable experience.

I conducted my first secondment at the Max Planck Institute for Chemistry of Mainz with the ORSUM group led by Prof. Jonathan Williams. They all welcomed me as a member of the group and it was a great experience to work with my IMPACT colleague Nijing Wang as well as practising science in German. This specific experience confirmed my instinct to seek work in the future at the interface between Analytical Chemistry and Environmental Sciences.

I then conducted my second secondment at the J. Heyrovský Institute of Physical Chemistry of Prague, collaborating with my other IMPACT colleague, Michal Lacko and his supervisor Patrik Španěl, as well as Dr Anatolii Spesyvyi. They introduced me to the selected ion flow-drift tube-mass spectrometry (SIFDT-MS) instrument. The gain in ion chemistry knowledge I received from this exchange was crucial for the fundamental research side of my project.

I also gratefully acknowledge the financial support of the European Union (IMPACT-ITN project) through Marie Skłodowska-Curie Actions (Grant Agreement Number 674911).

My early studies in France taught me that it is in times of hardship that we recognise the people who really care about us, and that sometimes it is important for us to make temporary sacrifices so that we can ensure a future that we wish for. The last words therefore are for my parents, family and friends who believed in me and have supported me.

TABLE OF CONTENTS

List of figures

List of tables

List of abbreviations ***(in alphabetical order)***

124TCB	1,2,4-trichlorobenzene
BTEX	Benzene-Toluene-Ethylbenzene-Xylenes
CE	Charge Exchange
CI	Chemical Ionisation
CP	Confinement Power
DC	Direct Current
E	DC Electric field
EI	Electron Ionisation
EI-(ToF)-MS	Electron Impact/Ionisation-(Time of Flight)-Mass Spectrometer
EPA	Environmental Protection Agency
ESR	Early Stage Researcher
eV	Electron Volt
FFR	Field Free Region
FWHM	Full Width Half Maximum (resolution)
GC-MS	Gas Chromatography-Mass Spectrometry
GD	Glow discharge
HC/HC13BD	Hexachloro-1,3-butadiene
IE	Ionisation Energy
IMS	Ion mobility spectrometry
Inter	Intermediate electrode
ITN	Innovative Training Network
Kore	Kore Technology Limited
LG	Linear Gradient
MCP	Microchannel Plate
MSV	Mass Spectrometer Vacuum
nBB	n-butylbenzene
OHR	OH Reactivity

P	Pressure
PA	Proton Affinity
PAH	Polynuclear Aromatic Hydrocarbon
PCB	Printed Circuit Board
PID	Product Ion Distribution
PRE	Primary Reaction Energy
PTR	Proton Transfer Reaction
PTR-(ToF)-MS	Proton Transfer Reaction-(Time of Flight)-Mass Spectrometer
Quad	Quadrupole
RF	Radio Frequency
RSD	Relative Standard Deviation
SCI-(ToF)-MS	Soft Chemical Ionisation-(Time of Flight)-Mass Spectrometry
SD	Source Drift/Standard Deviation (specified for each section)
SG	Split Gradient
SEM	Secondary Electron Multiplier
SGR	Split Gradient Reactor
SIFDT-MS	Selected Ion Flow Drift Tube-Mass Spectrometry
SIFT	Selected Ion Flow Tube
SRE	Secondary Reaction Energy
STP	Standard Temperature and Pressure (273.15 K and 1013 25 hPa)
sVOC	Semi Volatile Organic Compound
T	Temperature
Td	Townsend (unit)
TDC	Time-To-Digital converter
TEP	Triethylphosphate
ToF	Time of Flight
UoB	University of Birmingham
VOC	Volatile Organic Compound

CHAPTER 1: INTRODUCTION

1.1 The context of this research programme

The PhD programme was registered with the School of Physics and Astronomy of the University of Birmingham in the Molecular Physics group supervised by Prof. Chris Mayhew. It was part of a European Union Innovative Training Network (ITN) programme, in which each member had the status of an Early Stage Researcher (ESR) [1]. The ESR position of the author involved location in an industrial setting, namely Kore Technology Ltd in Ely, Cambridgeshire, under the supervision of Dr. Fraser Reich.

1.1.1 The 'IMPACT' ITN

The ITN programme was named ‘IMPACT’ (Ion-Molecule Processes for Analytical Chemical Technologies). The purpose of the ITN was to understand better the ion-molecule interactions which take place in the gas phase in various analytical technologies using 'soft ionisation' as a means of charging and detecting molecules for chemical analysis. As well as studying fundamental processes, these analytical tools have practical applications in areas such as health, environmental science and homeland security. There were ten ESRs in the programme, but only two were located in industrial situations; the rest were in academic institutions [1]. As part of the network, ESRs were encouraged to spend time in each other's laboratories, collaborating on projects that were of joint interest to the ITN. For the project presented in this thesis, this meant time was spent in Mainz and Prague. For more details about the ITN, please see the appendices A.1 (Figure A.1.1) and A.2 (Table A.2.1).

1.1.2 Kore Technology Ltd

Kore is a UK-based commercial analytical instrument company specialising in the design and build of instruments based on time-of-flight mass spectrometers (ToF-MS). In 2003 Kore built the first instrument that combined the benefits of a ToF-MS with proton transfer reaction ionisation (PTR). They have gone on to develop soft chemical ionisation instrumentation, and different embodiments form part of the current instrument offerings from the company [2]. Naturally, ongoing instrument development is desirable (a) to meet ever-changing requirements by users, and (b) to remain competitive in a commercial marketplace.

1.1.3 The intersectoral nature of the research programme

This researcher came to the PhD programme with a bachelor equivalence in Chemistry, two master's degrees in environmental sciences and a long-standing interest in environmental Chemistry. Environmental chemists have many urgent questions that they wish to answer, yet it is the physicists who often develop the tools that might be used to answer such questions. This research is therefore intersectoral: it is based on mass spectrometric techniques (hence the contract at Kore), using so-called 'soft' ion-molecule interactions (hence the registration at the UoB's Molecular Physics Group), and this work is also integrated into the wider 'IMPACT' network, through interaction and collaboration with other ESRs in the network in various fields of science.

1.2 Motivation and areas of research in this project

Understanding the effects of biogenic and anthropogenic compounds released into the Earth's atmosphere is of greater importance than ever. There is overwhelming consensus within the global scientific community that climate change is driven by human industrial activity [3].

Fortunately, there is growing awareness among the public and an increasing willingness to adopt 'eco-friendly' technologies and processes [4-6].

Compounds that are emitted as part of an existing chemical process and which are now identified as harmful to the environment can be addressed through so-called 'green chemistry', which seeks to reduce or eliminate the use or generation of hazardous substances involved in that chemical product or process. This is also known as 'sustainable chemistry' [7].

If the reason for an environmental issue is an unintended consequence or accident (such as leakage or spillage) from an otherwise managed chemical process, remediation will be required. The aim is then to remove or contain toxic or hazardous material from sites left in the open or improperly managed. This includes manufacturing facilities, processing plants, landfills and mining sites [8, 9]. However, in relation to volatile organic compounds (VOCs), before one can discuss action to reduce harmful levels in air, water or soils, one has to be able to measure and track changes in concentrations and distributions of these chemical compounds. Real-time monitoring schemes for well-known pollutants such as NOx, SOx etc. are well-developed. Monitoring of heavy metals in water is also commonplace, but there is less legislation and thus less motivation to identify and quantify VOCs, and particularly the huge range of those of anthropogenic (industrial) origin.

Current methods for identifying and quantifying VOCs in ambient air have been based on a 'static' trap tube method, in which a tube filled with sorbent material is placed within a monitoring station and left for some days during which it absorbs VOCs from the atmosphere. Following collection, the tube is sent to a laboratory and typically analysed by Gas Chromatography-Mass Spectrometry (GC-MS) [10]. The method has sensitivity and specificity, but extremely poor time resolution. By contrast, soft chemical ionisation using mass spectrometry (SCI-MS) with no GC pre-separation offers real-time measurement of VOCs.

This, in combination with transportability, offers the possibility of fast surveying for monitoring and tracking down polluters.

This thesis addresses some aspects of the ion-molecule physics of these new instrumental methods, as well as application developments aimed at real-time VOC measurements of ambient air (and indeed water sources). Necessary developments include:

1) Increasing the detection sensitivity such that sufficient statistics can be obtained in the mass spectral data in real-time (e.g. sampling every second).
2) Improving the field-portability of the measurement technique. There is little point developing a real-time method if the equipment cannot be taken easily to the place where VOCs are varying in concentration in real-time.
3) Addressing the considerable challenge of how to identify with a high level of confidence the signature of an individual VOC among a potential forest of other mass spectral signatures, when there is no pre-separation stage such as a GC.
4) Extending the detection of VOCs in ambient air to the detection of VOCs in water in the environment: rivers, treated water supplies etc.

1.2.1 Instrumental methods

1.2.1.1 Soft chemical ionisation mass spectrometry (SCI-MS)

At the heart of this research programme is the mass spectrometry-based analytical technique known as soft chemical ionisation. This technique uses chemical ionisation, either by proton transfer reaction or charge exchange (CE) from a reagent ion to an analyte molecule in a collision reactor, as a means to impart a charge to the analyte molecule so that it can subsequently be measured in a mass spectrometer. Proton transfer reaction-mass spectrometry (PTR-MS) is thus a sub-set of SCI-MS, though the two terms are often used interchangeably

(but inappropriately). The rate of renewal of the contents of the reactor is ~ 10 Hz, and thus changes in sample gas composition can be sampled at 100 ms resolution (though the ToF spectrometer cycles at much higher rates of up to 50 kHz).

Ionisation of the analytes of interest takes place in a reactor (collision cell) at 1-2 millibar pressure, where the number of collisions is high enough (~ 2,000 in Kore's instruments) to create a viscous flow where an analyte molecule is extremely likely to collide with a reagent ion. Reagent ions in this case means typically H_3O^+, O_2^+ or NO^+. In proton transfer, it is thermodynamically favourable for a proton to be transferred from the protonated water ion (known as 'hydronium', the simplest oxonium ion) to the analyte molecule of interest, provided that the proton affinity (PA) of the analyte is greater than that of water at 691 kJ/mol. For charge exchange of an electron, if the recombination energy of the reagent ion is greater than the ionisation energy (IE) of the analyte, then electron transfer is thermodynamically allowed. However, unlike proton transfer for which exothermicity is the only requirement for an efficient ion-molecule reaction, for charge transfer exothermicity is a necessary but not sufficient requirement for a facile process [11, 12]. A table in appendix A.3 (Table A.3.1 [13]) provides values of the IEs and PAs of important atomic and molecular species. The compounds are ranked according to increasing proton affinities.

1.2.1.2 Electron Impact-Mass Spectrometry (EI-MS)

As well as soft chemical ionisation methods, Kore produces compact instruments based on the more conventional electron impact methods. Data acquired using 70 eV electron ionisation are the basis for the NIST mass spectral database of compounds; a widely consulted library with more than 350,000 EI spectra as of the 2020 release [14]. Apart from some robust molecules, EI at 70 eV often results in significant fragmentation, such that often little or even none of the

parent molecular ion is produced. This can therefore be described as a 'hard' ionisation compared to 'soft' ionisation in SCI-MS, since deliberate attempts are made in SCI-MS to minimise the amount of molecular fragmentation that occurs as a result of the ionisation process. Nevertheless, the EI method is in widespread use and has an important place, particularly in GC-MS methods.

1.2.2 Harnessing analytical developments for environmental applications

The research has sought to use insights from ion-molecule physics for the development of analytical tools in the service of environmental chemistry. It involves the understanding of the surrounding world through the study of biogenic and anthropogenic chemicals and their behaviours in air, water, soils and sediments, leading to different sub-branches of this area [8]: atmospheric chemistry, aquatic chemistry and soil chemistry. The interconnections between the fields involved are presented in Figure 1.1 [15-17].

With respect to measurement of any chemical in the environment, it is always a question of quantity. This was understood many centuries ago, and is the root of pollution study and toxicology: “All things are poison, and nothing is without poison, the dosage alone makes it so a thing is not a poison” [18].

Accordingly, in this research, as well as attempting to improve the instrumental methods discussed in the previous section 1.2.1, attention has been paid into how they can be applied in practice, and not just in the laboratory either. In the case of the instrumental methods under discussion this has involved:

1) Maximising the range of compounds that can be analysed (with reference to compounds of interest to environmental chemists)
2) Improving the detection sensitivity for those compounds

3) Improving the identification of those compounds within a complex matrix

4) Extending the sample matrix that can be analysed to include water

5) Making it possible to transport and operate the equipment in the field.

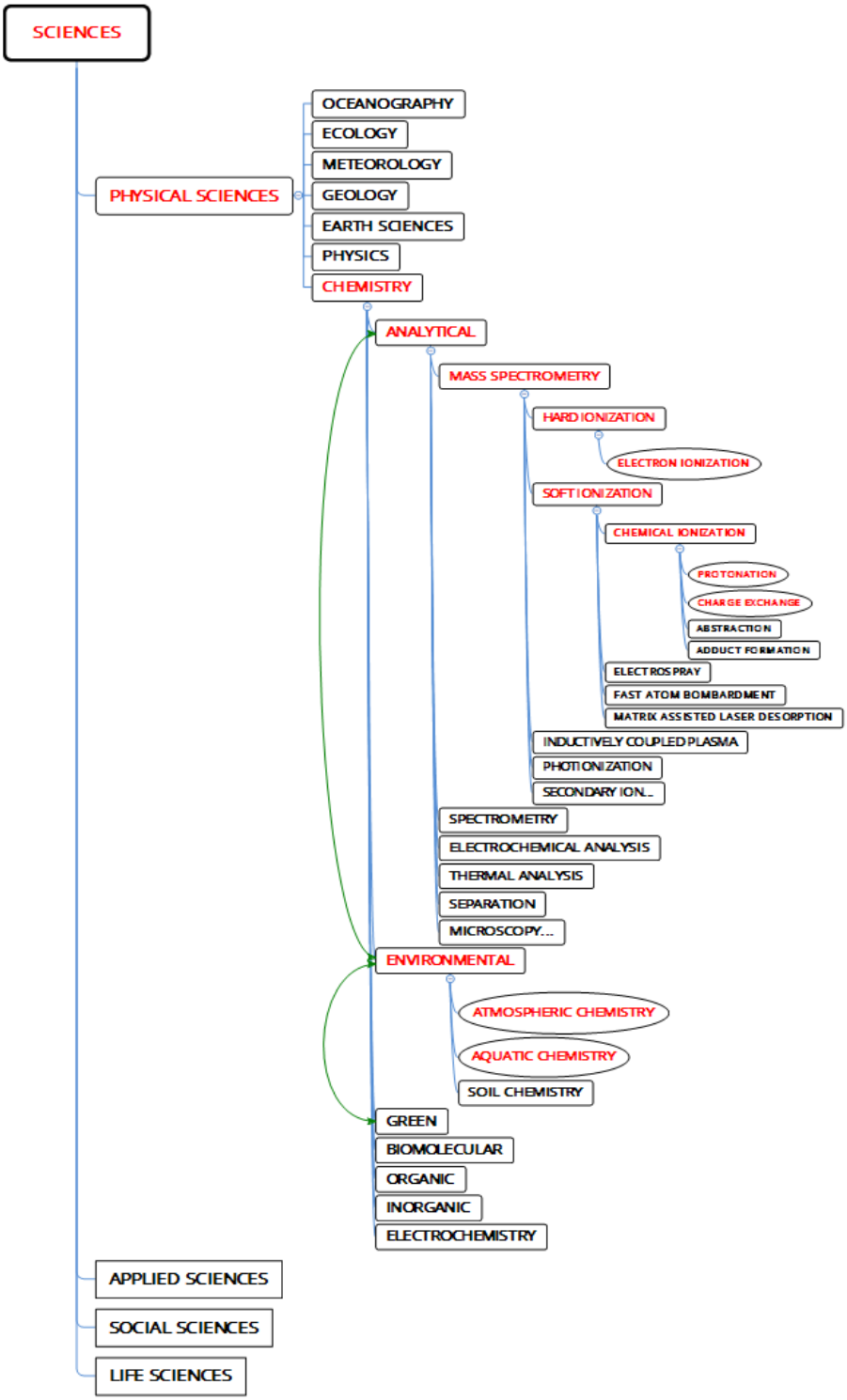

Figure 1.1: Interconnections between scientific fields

1.3 Chapter overviews

Chapter 2 is principally a review of the PTR method and its embodiment in the Kore instrumentation. After discussing the ionisation source and the 'drift' region immediately following, it introduces the mode of operation that was in use prior to the incorporation of the RF funnel in the reactor, and was used for much of the data collection in chapter 5, namely what is termed the 'DC mode' of operation. The 'RF mode' is then introduced. The two ionisation mechanisms employed in the thesis are then introduced as well as a discussion on relevant kinetics and ion energetics. The theory of effective potentials in RF fields is reviewed as this is drawn upon extensively when discussing the results of the ion-funnel developments presented in chapter 3. Detail is then given on the kinetic energy in the centre of mass of a colliding system, as this theory was also applied to data that are discussed in chapter 5. A brief description is given of the ion transfer optics that follow the reactor, followed by a description of the principles of the reflectron time-of-flight spectrometer and the means of data collection, namely a micro channel plate detector and a time-to-digital converter system. The last part of this chapter is a description of the electron impact mass spectrometer technique used in the thesis, with a brief outline of the two separate instruments used.

Chapter 3 deals with developments made to the RF funnel and reports on how effective those developments were in improving their analytical performances. The original motivation for incorporating an RF ion-funnel into the PTR reactor is discussed, and the first implementation by Kore is reviewed. After this, a description is given of the modifications made in this project to evolve the ion-funnel to enhance the ion transmission, resulting in various new funnels that have been tested. Using benzene as the test analyte, data are given on the performance of the funnels with regard to sensitivity improvements. Analysis of the results is given according to consideration of effective potentials within the reactor as derived from RF

ion-funnel theory in chapter 2. The ability of the different ion-funnels to transmit analyte ions without excessive fragmentation is then explored, and further data are shown from other analytes such as toluene, ethylbenzene and xylene to explore this effect. Data showing changes in the product ion distributions of the analytes studied is presented to demonstrate the interaction of the axial DC electric field (driving ions forward through the reactor) with the radial RF field (funnelling ions into the centre of the reactor).

Chapter 4 discusses a modification made to the PTR reactor in which two separate electric fields were created. When the RF field is applied in the PTR reactor, the DC electric field required for optimum performance of the reactor has to be reduced significantly, resulting in a much lower field strength in the first half of the reactor where there is no funnel. The effect of applying two separate DC electric fields (hence a 'split field'), is explored in this chapter in an attempt to minimise space charge losses of ions in the first part of the reactor by increasing the DC electric field to more typical levels, while preserving the lower DC field required for optimum funnel performance. The effects of the split gradient of potentials on the product ion distributions of two probe molecules are reported, and once again concepts from the RF field theory are used to explain the data.

Chapter 5 is concerned with the reporting of the reduced electric field parameter E/n, which is quoted routinely in all literature on studies using PTR-MS to state the optimum conditions for measuring different analytes. In an effort to understand better the effect of the RF field on the parameter E/n, three molecules were first studied in the DC mode without any applied RF. The aim was to characterise fully their product ion distributions as a function of E/n, so that when applying the RF an effective E/n inside the funnel could be deduced from the measured product ion distributions. However, it was discovered that, if different settings of electric field, temperature and pressure are used to achieve the same calculated E/n, the product

ion distributions are not the same. This chapter reports this phenomenon in detail for the first time. Partial success was achieved at reconciling the shifts in the distributions at different temperatures for the same E/n, but the chapter acknowledges that understanding the effects of pressure requires further work.

Chapter 6 tackles the topic of identifying and quantifying individual VOC compounds in a complex mixture when no pre-separation is employed. The chapter gives some background on a new software method developed at Kore, and which required the production of a mass spectral library comprising the product ion distributions of each compound in the U.S. Environmental Protection Agency (E.P.A.) Method TO-14; a 39-mixture of halocarbons identified as harmful to human health. The chapter discusses how the work in this thesis to develop the mass spectral library was used to test and refine the method for subsequent commercial use.

Chapter 7 reports on developments made in this project of a portable water sampling unit designed to extract any VOCs from water for subsequent analysis in a mass spectrometer. The motivation for coupling this to a portable mass spectrometer is discussed, along with preliminary results from a prototype water sampler coupled to such a spectrometer. However, much of the work in the chapter was conducted using a second, better engineered iteration of the water sampler coupled to a PTR-ToF-MS to extend the analysis matrix from ambient air to water. Water samples 'spiked' with benzene, toluene, ethylbenzene and xylene (BTEX) were used to assess the performance of the water sampler, and the software discussed in chapter 6 was used to analyse the data. Various commercially available water products were also analysed, from drinking water to water produced for use in steam irons.

Chapter 8 is a relatively short chapter to report on a secondment made as part of the ITN scheme, in which a portable electron impact mass spectrometer was taken to the Max Planck

Institute in Mainz to discover if the instrument could be used as a substitute for a much more expensive PTR-MS. The latter instrument is used in a technique to determine the 'OH reactivity' of ambient air, and the utility of determining this reactivity is explained in the chapter. The small spectrometer fell short of the hoped-for performance that would release the more expensive instrument for other work, and the challenges encountered are discussed.

Chapter 9 draws conclusions made from the work undertaken in the thesis and consider how certain topics could be explored further.

CHAPTER 2: MASS SPECTROMETRIC INSTRUMENTAL METHODS AND IONISATION MECHANISMS

2.1 Introduction

This chapter describes the two types of instruments directly involved in this PhD project as well as their respective ionisation processes and forms the basis for the results presented later with regards to instrumental details and chemical ionisation (proton transfer and charge exchange) and electron impact ionisation processes.

The proton transfer reaction-time of flight-mass spectrometer (PTR-ToF-MS) section describes the specific case of one research instrument used in this work involving a discussion of proton transfer and charge exchange processes, whereas the electron impact ionisation-time of flight-mass spectrometer (EI-ToF-MS) section considers both transportable and portable instruments designed and manufactured by Kore, namely the 'INFORMS' and the 'MS-200' instruments, respectively.

2.2 PTR-ToF-MS

A general sketch of the PTR-ToF-MS used in this thesis is presented in Figure 2.1, being reproduced for convenience in appendix A.4 (Figure A.4.1). The main sections of the instrument are discussed individually, starting from the ion source through to signal detection.

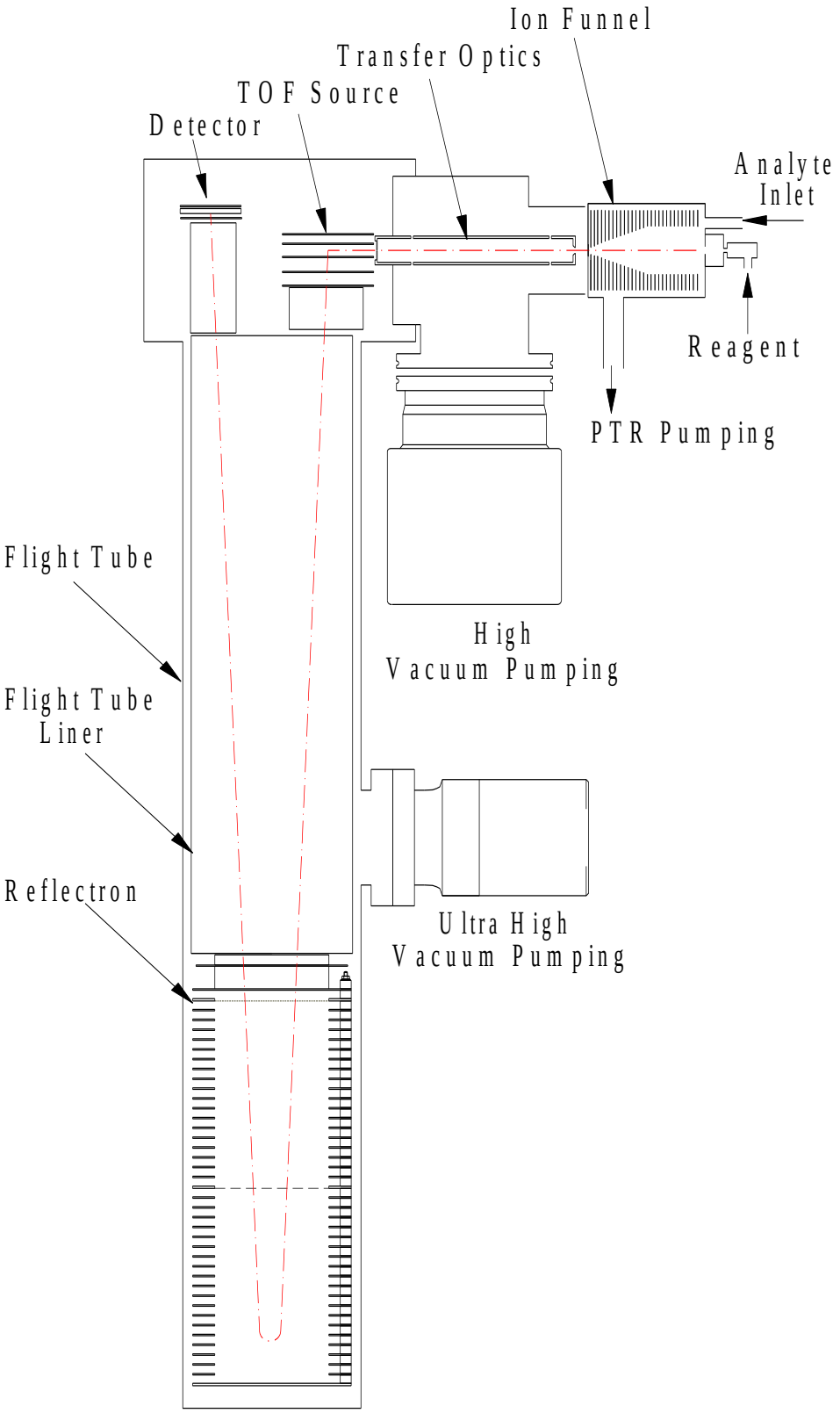

Figure 2.1: Schematic representation of the PTR-ToF-MS used at Kore for this PhD work

2.2.1 Ion source

The ‘reagent ions’ are generated in a hollow cathode glow discharge through the application of a sufficiently strong electric field between two electrodes, the cathode and an anode as presented in Figure 2.2:

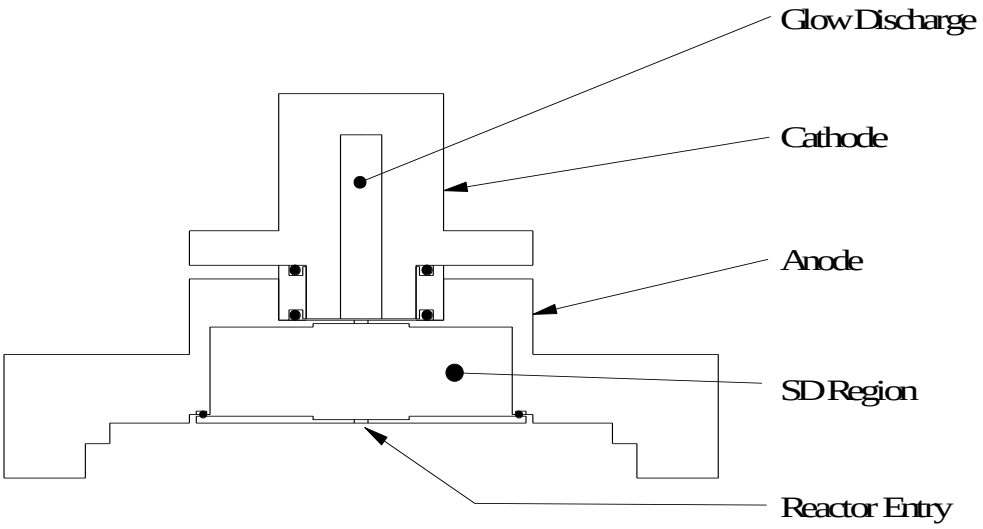

Figure 2.2: Cross-sectional drawing of the cylindrical ion source and source drift (SD) region of PTR-ToF-MS

Details of the Source Drift (SD) region are presented in the next section.

If the electrical potential between both electrodes is equal to or greater than the breakdown voltage V_B (which is a function of the product of the pressure p inside the hollow cathode and the distance d between both electrodes [19]), a self-sustaining plasma is formed.

Paschen’s Law, which is graphically represented for different gases in Figure 2.3 [20], provides the breakdown voltage (V_B) as a function of the product of the gas pressure (p) and gap distance (d) in the hollow cathode. At Kore, the bore of the hollow cathode is 0.4 cm in diameter and the pressure inside is raised to 1.50-2.25 torr initially. This results in a pd value of 0.8/0.9 torr·cm, meaning that a voltage difference of approximately 400 volts will be sufficient to cause a voltage breakdown and start the plasma discharge.

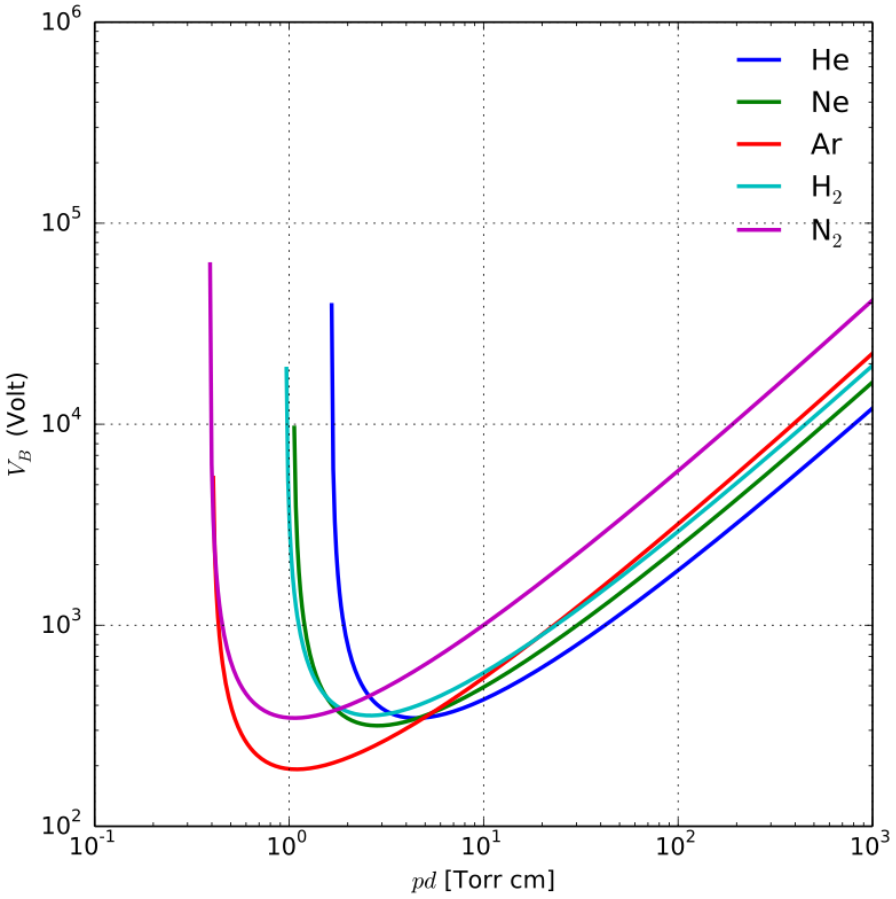

Figure 2.3: Paschen curves for common gases in a glow discharge hollow cathode [20]

The supply voltage is able to apply a maximum of 800 volts between the anode and cathode, to ensure that the discharge can be started under these conditions. When the ion source is fed with water vapour the electrical discharge results in a number of ions shown in the equations E 2.1-E 2.5:

$$e^- + H_2O \rightarrow H_2O^+ + 2e^- \quad \text{E 2.1}$$

$$e^- + H_2O \rightarrow H^+ + OH + 2e^- \quad \text{E 2.2}$$

$$e^- + H_2O \rightarrow H_2^+ + O + 2e^- \quad \text{E 2.3}$$

$$e^- + H_2O \rightarrow OH^+ + H + 2e^- \quad \text{E 2.4}$$

$$e^- + H_2O \rightarrow O^+ + H_2 + 2e^- \quad \text{E 2.5}$$

All of which react with water, resulting in H_2O^+ or H_3O^+ as shown in the equations E 2.6-E 2.11 [21]:

$$H_2O^+ + H_2O \rightarrow H_3O^+ + HO \quad (k = 1.8 \times 10^{-9}\ cm^3/s) \qquad \text{E 2.6}$$

$$HO^+ + H_2O \rightarrow H_2O^+ + HO \quad (k = 1.8 \times 10^{-9}\ cm^3/s) \qquad \text{E 2.7}$$

$$O^+ + H_2O \rightarrow H_2O^+ + O \quad (k = 2.6 \times 10^{-9}\ cm^3/s) \qquad \text{E 2.8}$$

$$H_2^+ + H_2O \rightarrow H_3O^+ + H \quad (k = 3.4 \times 10^{-9}\ cm^3/s) \qquad \text{E 2.9}$$

$$H_2^+ + H_2O \rightarrow H_2O^+ + H_2 \quad (k = 3.7 \times 10^{-9}\ cm^3/s) \qquad \text{E 2.10}$$

$$H^+ + H_2O \rightarrow H_2O^+ + H \quad (k = 8.2 \times 10^{-9}\ cm^3/s) \qquad \text{E 2.11}$$

H_2O^+ then rapidly reacts with a water molecule, cf. E 2.12 [21]:

$$H_2O^+ + H_2O \rightarrow H_3O^+ + HO \quad (k = 1.8 \times 10^{-9}\ cm^3/s) \qquad \text{E 2.12}$$

where k is the rate coefficient at 300 K.

The rate coefficients of the equations E 2.6-E 2.11 are within experimental error the same as the collision-limiting rates [21], which results in H_3O^+ rapidly becoming the main terminal ion. Typically 97 % of the ions leaving the hollow cathode are $H_3O^+ \cdot (H_2O)_n$ (n = 0, 1, 2 ,3,…), the other 3 % are reagent ions that either cannot (NO^+) or have not had time to react with water (O_2^+).

The reagent ions are accelerated to the lowest potential, the anode, which then pass through the anode aperture creating the ion beam [22].

2.2.2 Source drift region

The aim of the source drift (SD) region, shown in detail in Figure 2.2, is to purify the ion beam as much as possible by dissociating the protonated water clusters to H_3O^+, so that predominantly H_3O^+ enters the drift tube. However, association in the drift tube results in protonated water clusters, the intensities of which are determined by the reduced electric field and the humidity in the drift tube.

The SD region comprises the anode aperture (1 mm diameter), and an electrode 10 mm away, named the SD exit electrode, held at approximately 200 volts more negative than the anode. A few millimetres downstream from the SD exit electrode is the reactor entry electrode, which, as the name implies is at the entry voltage of the reactor and is approximately 20 volts more negative than the SD exit voltage. These latter two electrodes have apertures 2 mm in diameter.

When the analyte entering the drift tube is air, back-diffusion of oxygen and nitrogen into the hollow cathode region occurs leading to other reagent ions, such as N_2^+ and O_2^+.

N_2^+ is rapidly removed, charge exchanging with H_2O, cf. E 2.13 [21]:

$$N_2^+ + H_2O \rightarrow H_2O^+ + N_2 \qquad (k = 2.8 \times 10^{-9}\ cm^3/s) \qquad \text{E 2.13}$$

H_2O^+ reacts with H_2O to produce the terminal ion H_3O^+ according to E 2.12.

Any O_2^+ that is created cannot charge exchange with water molecules in the hollow cathode and SD regions as its recombination energy is less than the ionisation energy of water (IE (H_2O) = 12.61 eV [23]). However, once it associates with water to form $O_2^+ \cdot H_2O$, it can react with water via an exchange process: $O_2^+ \cdot H_2O + H_2O \rightarrow H_3O^+ \cdot OH + O_2$. Dissociation of $H_3O^+ \cdot OH$ leads to $H_3O^+ + OH$.

NO^+ is formed in the hollow cathode through the following reaction E 2.14 [21]:

$$N^+ + O_2 \rightarrow NO^+ + O \qquad (k = 2.6 \times 10^{-10}\ cm^3/s) \qquad \text{E 2.14}$$

As with O_2^+, NO^+ cannot charge exchange with H_2O owing to its low recombination energy. Association of three waters to form $NO^+ \cdot (H_2O)_3$ is required before a switching reaction can occur with water: $NO \cdot (H_2O)_3^+ \rightarrow H_3O^+ \cdot H_2O + HNO_2$. Complete deionisation of O_2^+ and NO^+ to $H_3O^+ \cdot OH$ and $H_3O^+ \cdot H_2O$, respectively, does not occur owing to insufficient reaction time and low pressures in the hollow cathode region, which results in a small concentration of O_2^+ and NO^+ entering the drift tube. Altogether NO^+ and O_2^+ make up about 3 % of the total reagent ion signal, which often can be neglected owing to the much more dominant signal associated with H_3O^+ when using water vapour as the reagent neutral in the glow discharge.

2.2.3 Reactor / Drift tube – Technical aspect

The reactor is the section after the SD region and is the location where the reagent ions react with neutral analytes mixed into a selected carrier gas. The reactor of the research PTR-ToF-MS is composed of 29 stainless-steel ring-shaped electrodes each having a thickness of 0.2 mm and separated from each other by 3.2 mm, with the first electrode after the SD region being defined as number 1. The first half of the reactor (up to the 14th plate) is made of identical 40 mm inner diameter-electrodes whereas the second half (from the 14th plate) contains the funnel and is comprised of electrodes with a decreasing orifice until the last plate, which has an orifice of 6 mm diameter. The exit plate contains a 400 μm aperture and marks the end of the reactor. This is illustrated in Figure 2.4.

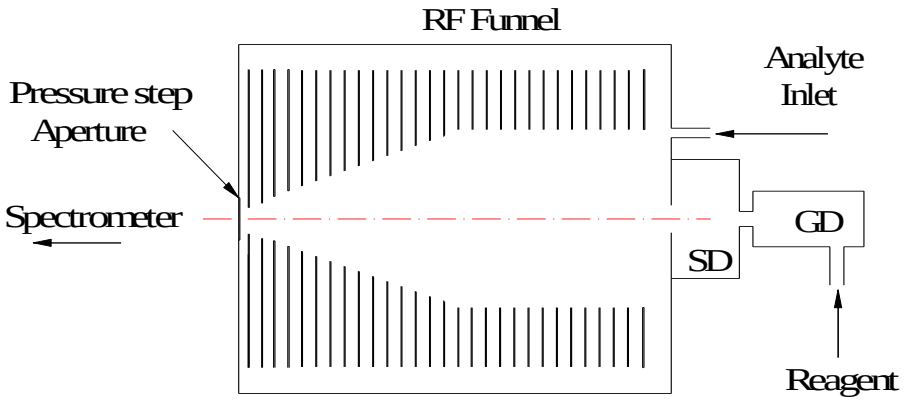

Figure 2.4: Schematic of the funnel-shaped reactor cell inside the Kore PTR-ToF-MS GD, SD and RF respectively stand for Glow Discharge, Source Drift and Radio Frequency

Electrodes 1 to 27 form a single stack whereas the 28th and 29th electrodes are permanently mounted onto the base flange at the end of the reactor. From the 1st to the 26th electrode, each electrode is electrically connected through a series of resistors each of resistance 1 MΩ leading to a total resistance of 25 MΩ. As well as resistors between plates, the second half of the reactor has capacitors of ~ 100 nF between each consecutive even pair and each consecutive odd pair of electrodes, except for the 1st even pair (12th and 14th plates) where this value does not exceed ~ 30 pF (ideally 10 pF). However, the number of ions passing the reactor exit aperture highly depends on the mode used between the Direct Current (DC) mode and the Radio Frequency (RF) mode.

2.2.3.1 Direct current (DC) mode

In DC mode, a linear voltage gradient only is applied across the reactor as shown in Figure 2.5.

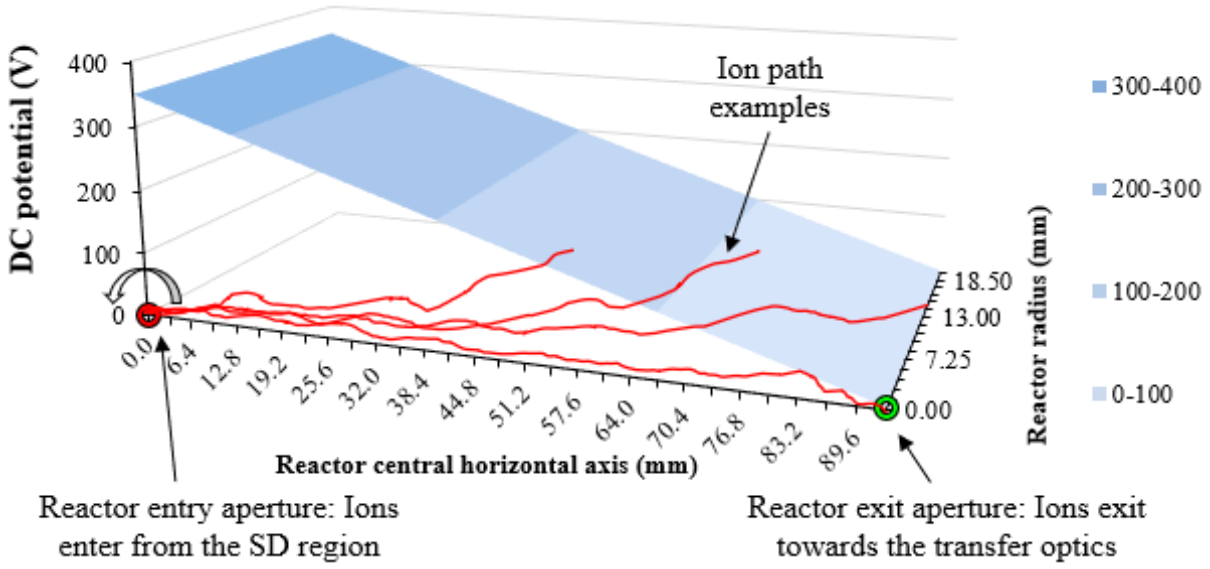

Figure 2.5: DC field applied inside the PTR-ToF-MS reactor in DC mode
DC and SD respectively stand for Direct Current and Source Drift
The rounded arrow implies circular symmetry in the reactor

The generated DC electric field is then expressed by equation E 2.15:

$$E = \frac{V_D}{l_D} = \frac{V_{Entry} - V_{Exit}}{l_D} \qquad \text{E 2.15}$$

where V_D is the potential difference across the reactor and l_D the length of the reactor.

However, the parameter that is almost universally reported in PTR-MS literature as the key operational parameter is the reduced electric field, E/n, defined in the equation E 2.16 (where n is the total molecular number density) being directly determined from the Ideal Gas Law [24]):

$$\frac{E}{n} = \frac{V_D k_B T}{l_D P} \qquad \text{E 2.16}$$

where k_B is the Boltzmann constant, T is the reactor's temperature and P is the reactor's pressure.

E/n provides a measure for the average collisional energy between an ion and the neutral buffer gas within the reactor. In SI units, E/n is given as $V \cdot m^2$ but this is usually converted to Townsend (Td), where 1 Td = 10^{-21} $V \cdot m^2$. E/n, the temperature and pressure are generally kept constant whilst V_D is changed.

As shown in Figure 2.5, typical settings in DC mode with the research instrument are 350 V for reactor entry, 4 V for reactor exit, with the reactor operating at a pressure of 1 mbar and at room temperature (23.6 °C). Knowing the reactor has a length of 93 mm, the value of E/n for these conditions is equal to 152 Td. It is commonly stated in the literature that 120-150 Td is the typical range for operating a reactor [25], however, in this thesis, a wider range was explored.

2.2.3.2 Radio frequency (RF) mode

Ion-funnels using RF fields were reported in the literature as a means to increase the transmission of ions at relatively high pressures [26]. In seeking to improve the sensitivity of the existing PTR-ToF-MS, Kore decided to incorporate an ion-funnel within the existing reactor, since the typical operating pressures of 1-2 mbar are similar to those reported in the literature for the operation of ion-funnels.

The first PTR-ToF-MS ion-funnel designed by Kore was delivered to Leicester University in 2013. This device worked well, with impressive increases in analyte detection by factors of 20-50 [9]. With these improvements, the researchers at Leicester used the funnel in their applications but made no attempts to explore more fundamental properties of the funnel.

The RF mode is the effect of a radio frequency electric field applied in the second half of the reactors studied in this project, on top of the DC electric field previously described, where the inner diameter of the electrodes continuously decreases until the exit of the reactor. Radio frequency potentials of opposite polarity are applied on adjacent electrodes in order to create the RF field, characterised by a frequency and an amplitude. The superposition of both DC and RF potentials applied across the reactor on the ion trajectories is represented in Figure 2.6. In RF mode, the DC electric field is lower with 100 V at the reactor entry. As the voltage gradient is not linear anymore across the reactor, E/n cannot be used anymore to define the collisional energy, at least in the second half of the reactor. That is why the entry voltage, or the DC electric field, is provided.

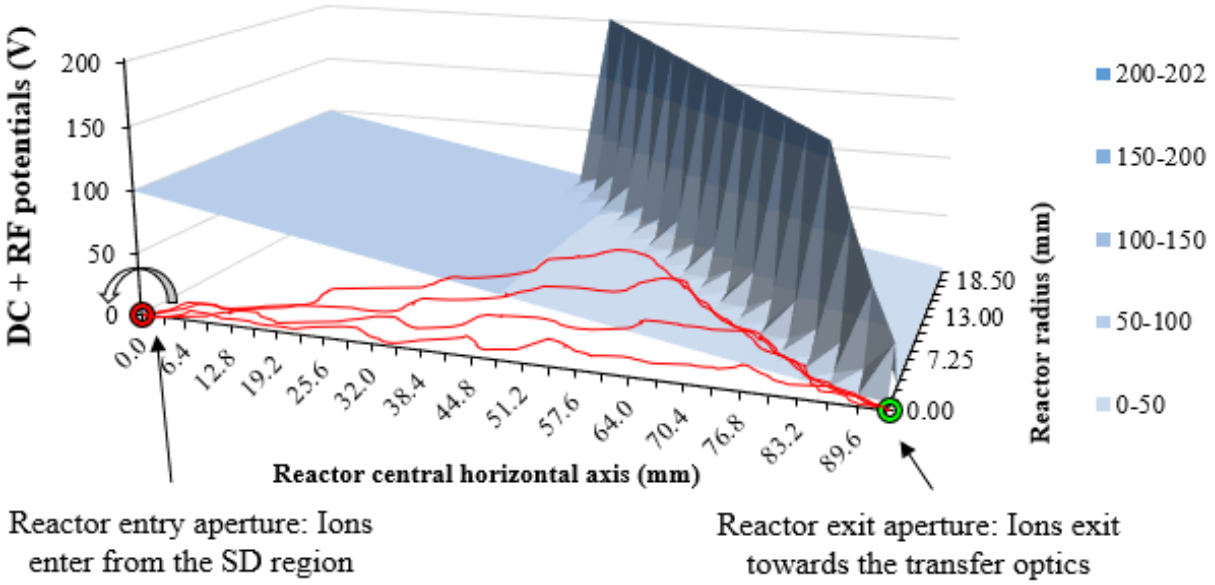

Figure 2.6: DC and RF fields applied inside the PTR-ToF-MS reactor in RF mode
DC, RF and SD respectively stand for Direct Current, Radio Frequency and Source Drift
The rounded arrow implies circular symmetry in the reactor

2.2.4 Reactor / Drift tube – Thermodynamics

2.2.4.1 Proton transfer (PT)

Proton transfer is the reaction occurring when a proton is transferred from a reagent ion to a neutral species [27-29]. In typical PTR reactions, where water is used as reagent neutral, the hydronium ions can transfer protons to a neutral analyte, M, when its proton affinity (PA) is greater than that of water (i.e. > 691 kJ/mol) In this case the reaction is exothermic and thermodynamically possible following the equation E 2.17 [27, 28, 30]:

$$H_3O^+ + M \rightarrow H_2O + MH^+ \qquad \text{E 2.17}$$

Inside the reactor, protonated water clusters can exist, with their concentrations being dependent on the value of E/n and the humidity within the drift tube. $H_3O^+ \cdot (H_2O)_n$ (n = 1, 2 and 3) can react with M via proton transfer providing that PA(M) is greater than that of the $(H_2O)_{n+1}$ following the equation E 2.18:

$$(H_2O)_n H_3O^+ + M \rightarrow (H_2O)_{n+1} + MH^+ \qquad \text{E 2.18}$$

However, even if these protonated water cluster reactions can occur, they become less pronounced with increasing E/n. Indeed, protonated water clusters are hydrogen bonded assemblies where hydrogen bonds presents a strength around 30 kJ/mol [31]. What is more, the more massive the water cluster is, the higher its PA is [32] and the less likely it is to transfer a proton to an analyte. Values of the PAs of the water monomer and the water dimer are 691 [23, 33] and 808 kJ/mol [33], respectively.

Contrary to electron ionisation (EI), chemical ionisation (CI) uses reactive collisions between reagent ions and the neutral analyte to achieve its ionisation via a bimolecular process such as proton transfer. Case by case it is possible to know if a reagent ion can protonate a given analyte through the notion of gas phase basicity (GB) or PA [34].

If a molecule, M, is considered and is protonated in the gas phase following E 2.19:

$$M_g + H_g^+ \rightarrow MH_g^+ \qquad \text{E 2.19}$$

the tendency of M to accept a proton is then quantitatively described by the two above-named terms presented in the equations E 2.20 and E 2.21 [34]:

$$GB_{(M)} = -\Delta G_r^o \qquad \text{E 2.20}$$

where $-\Delta G_r°$ is the negative free energy change for the proton transfer and the superscript ° refers to the standard state (different from the STP conditions as already mentioned) and:

$$PA_{(M)} = -\Delta H_r^o \qquad \text{E 2.21}$$

where $-\Delta H_r°$ is the negative enthalpy change for the proton transfer.
The parameters G and S (entropy) are linked as follows in E 2.22 [34, 35]:

$$\Delta G^o = \Delta H^o - T\Delta S^o \qquad \text{E 2.22}$$

where T is the absolute temperature and ΔS^o is the entropy difference between reactants and products in the protonation reaction at standard conditions of pressure and temperature.

After combination, E 2.20, E 2.21 and E 2.22 give E 2.23 [34, 35]:

$$PA_{(M)} = GB_{(M)} - T\Delta S^{o} \qquad \text{E 2.23}$$

Furthermore, in equilibrium, the following reaction in E 2.24 is valid [34, 35]:

$$H_3O^+ + M \rightleftharpoons H_2O + MH^+ \qquad \text{E 2.24}$$

whose equilibrium constant K_{eq} is given as follows through E 2.25 [34, 35]:

$$K_{eq} = \frac{[MH^+][H_2O]}{[H_3O^+][M]} \qquad \text{E 2.25}$$

where the square brackets around each species denote the concentration.

ΔG^o is related to K_{eq} through the following equation E 2.26 [34, 35]:

$$-\Delta G^{o} = RT \ln K_{eq} \qquad \text{E 2.26}$$

where R is the ideal gas constant.

Combination of E 2.20, E 2.25 and E 2.26 gives new equations for GB and PA (E 2.27 and E 2.28 [34, 35]):

$$GB_{(M)} = RT\ln\left(\frac{[MH^+][H_2O]}{[H_3O^+][M]}\right) \qquad \text{E 2.27}$$

$$PA_{(M)} = RT\ln\left(\frac{[MH^+][H_2O]}{[H_3O^+][M]}\right) - T\Delta S^{o} \qquad \text{E 2.28}$$

Knowing that the entropy term $T\Delta S^o$ is usually relatively small (25-40 kJ/mol), E 2.28 becomes E 2.29 when this last term becomes negligible compared to $GB_{(M)}$ [34]:

$$PA_{(M)} \approx GB_{(M)} = RTln(\frac{[MH^+][H_2O]}{[H_3O^+][M]}) \quad \text{E 2.29}$$

The reaction rate coefficient can be determined starting from E 2.24 where the formation of MH^+ can be defined by the following second-order differential equation E 2.30 [36]:

$$-\frac{d([H_3O^+])}{dt} = \frac{d([MH^+])}{dt} = k[H_3O^+][M] \quad \text{E 2.30}$$

Assuming that [M] >> $[H_3O^+]$, meaning only a negligible proportion of the analyte is protonated, [M] can be considered constant [36]. Hence E 2.30 becomes a pseudo first order differential equation that can be easily solved to produce E 2.31:

$$\ln\left([H_3O^+]_t\right) = -k[M]t + C \quad \text{E 2.31}$$

where t is the cell reaction time and C is a constant of integration that can be determined through the initial conditions in E 2.32, i.e. at t = 0, there is a specific concentration of hydronium:

$$[H_3O^+]_{t=0} = [H_3O^+]_o \quad \text{E 2.32}$$

Inserting E 2.32 into E 2.31 gives E 2.33:

$$C = \ln\left([H_3O^+]_o\right) \quad \text{E 2.33}$$

Inserting E 2.33 into E 2.31 gives, after rearrangement, E 2.34 [36]:

$$\mathbf{\left[H_3O^+\right]_t = \left[H_3O^+\right]_o e^{-k[M]t}} \qquad \text{E 2.34}$$

Considering the 2nd and 3rd terms of E 2.30, and inserting E 2.34 into the 3rd one, give E 2.35:

$$\frac{d([MH^+])}{dt} = k[M]\left[H_3O^+\right]_o \mathbf{e^{-k[M]t}} \qquad \text{E 2.35}$$

The integration of E 2.35 gives E 2.36:

$$\left[MH^+\right]_t = k[M]\left[H_3O^+\right]_o \frac{\mathbf{e^{-k[M]t}}}{-k[M]} + D \qquad \text{E 2.36}$$

where D is a constant that can be determined through the initial conditions in E 2.37, i.e. at t = 0, there is no protonated analyte:

$$\left[MH^+\right]_{t=0} = 0 \qquad \text{E 2.37}$$

Inserting E 2.37 into E 2.36 gives E 2.38:

$$D = \left[H_3O^+\right]_o \qquad \text{E 2.38}$$

Inserting E 2.38 into E 2.36 gives, after rearrangement, E 2.39:

$$\mathbf{\left[MH^+\right]_t = \left[H_3O^+\right]_o (1-e^{-k[M]t})} \qquad \text{E 2.39}$$

Given that k[M]t < 1, a Taylor expansion gives E 2.40.

$$\left[MH^+\right]_t = [H_3O^+](1 - (1 + (-k[M]t))) \qquad \text{E 2.40}$$

E 2.40, after rearrangement, gives E 2.41:

$$\mathbf{k = \frac{\left[MH^+\right]}{[H_3O^+][M]t}} \qquad \text{E 2.41}$$

Biomolecular rate coefficients are macroscopic and statistical in nature involving an average of a large number of ions to give a sense to this notion [37].

2.2.4.2 Charge exchange

Charge exchange (CE) is the reaction occurring when an ionic charge is transferred from an ion to neutral species. In PTR-MS, O_2^+ is often used as a reagent ion for CE. To achieve high O_2^+ reagent ion densities, O_2 replaces H_2O in the ion source. Another reagent ion that is sometimes used in PTR-MS for CE is NO^+, which is generated through a series of ion-molecule reactions in the ion source when air is introduced into the discharge [27, 28, 38]. For CE to be exothermic (E 2.42 and E 2.43), the ionisation energy (IE) of the neutral M must be less than the recombination energy of the reagent ion. Namely for reactions with O_2^+ or NO^+ to be exothermic, IE(M) needs to be < 12.1 eV or < 9.3 eV, respectively. Given the low recombination energy of NO^+, CE is limited. However, hydride transfer is an often observed reaction pathway with NO^+.

$$O_2^{+\bullet} + M \rightarrow O_2 + M^{+\bullet} \qquad \text{E 2.42}$$

$$NO^{+\bullet} + M \rightarrow NO + M^{+\bullet} \qquad \text{E 2.43}$$

where '•' indicates a single valence electron due to an odd total number of electrons. Given the limited use of NO^+ in CE, the work presented in this thesis used O_2^+ as the reagent ion for CE reactions.

2.2.5. Reactor / Drift tube – Kinetics and energetics

In any chemical ionisation process occurring in the PTR-MS reactor, there are ions and neutrals involving different kinetics.

2.2.5.1 Mean ion drift velocity – v_D

Regarding ions, their reaction time t_D (meaning the average time a reagent ion takes to travel across the reactor) can be defined by the equation E 2.44:

$$t_D = \frac{l_D}{v_D} \qquad \text{E 2.44}$$

where l_D is the length of the reactor and v_D the mean drift velocity of the ions within the reactor. The notion of mean free path (λ), which is the average distance an ion can travel between two consecutive collisions, can be now introduced as follows in E 2.45 [39]:

$$\lambda = \frac{k_B T_D}{\sqrt{2}\pi P_D {d_m}^2} \qquad \text{E 2.45}$$

where d_m is the diameter of the considered ion.

For example, an ion of 200 mass units presents a λ of 10^{-5} m at 1.33 x 10^{-3} mbar and 450 m at 1.33 x 10^{-9} mbar [40].

Considering a nitrogen flow for a usual set of PTR conditions with T_D at 23.6 °C = 296.75 K and P_D at 1.3 mbar = 1.3 x 10^2 Pa and that a nitrogen molecule presents a diameter of 3.7 Å (1 Å = 10^{-10} m), $\lambda(N_2)$ = 5.2 x 10^{-5} m = 52 μm. At this point two distinct situations can be considered: if $\lambda < l_D$ the ions move in the viscous flow regime whereas if $\lambda > l_D$ they move in the molecular flow regime. As 5.2 x 10^{-3} cm < 9.36 cm, the nitrogen flow behaves like a viscous flow. That is why it is crucial to consider the collisions that the ions undergo to determine their drift velocity.

When the residence time t_D is not available, the ion mean drift velocity v_D can be described for sufficiently low electric fields through the following equation E 2.46 [41]:

$$\mathbf{v_D = KE} \qquad \text{E 2.46}$$

where K is the ion mobility of a given ion through a specified neutral gas. This parameter is a function of the mass and the structure of both chemical entities, pressure and temperature. E still represents the DC electric field applied across the reactor. Often K is converted to a reduced ion mobility, K_o to allow for differences in pressures and temperatures between different studies. This corresponds to its value at STP, and is given in E 2.47 [41]:

$$K = K_o \frac{T_D P^o}{P_D T^o} \qquad \text{E 2.47}$$

Inserting E 2.47 into E 2.46 then E 2.46 into E 2.44, it is possible to calculate t_D using ion mobility values from either experiments or literature through E 2.48 [41]:

$$t_D = \frac{l_D}{KE} = \frac{l_D}{K_o \frac{T_D P^o}{P_D T^o} E} \qquad \text{E 2.48}$$

Considering, for E = 37.4 V/cm, a reduced ion mobility of H_3O^+ in N_2 of 2.26 cm²/(V·s) (calculated from an experiment run during this thesis), a drift temperature T_D = 23.6 °C = 296.75 K and a drift pressure P_D = 1.3 mbar = 0.977 Torr, the drift time $t_D(H_3O^+ \text{ in } N_2)$ = 1.30 x 10^{-4} s = 130 μs and where $v_D(H_3O^+ \text{ in } N_2)$ = 7.15·10^4 cm/s = 715 m/s.

2.2.5.2 Mean DC kinetic energy – $E_{k,DC}$

Using the mean ion drift velocity, it is possible to calculate the mean kinetic energy of an ion in the laboratory frame of reference through the equation E 2.49:

$$E_{k,DC} = \frac{1}{2} m_i v_D^2 \qquad \text{E 2.49}$$

with m_i the mass of the considered ion.

It is important to mention that the mean DC kinetic energy must be calculated through E 2.49. Indeed, the conservation of energy, expressed through E 2.50 between the DC electric potential energy and the mean kinetic energy is valid in vacuum or at least in molecular flow.

$$E_{el,DC} = zeV_D = \frac{1}{2} m_i v_D^2 = E_{k,DC} \qquad \text{E 2.50}$$

where z is the number of charge of the ion, e the elementary charge and V_D the difference of potentials inside the reactor.

There is a high density of ions in the reactor and the repulsion due to space charge pushes the ions outwards such that they can be lost of the side walls of the reactor. If the ion residence time is short because the drift velocity in the electric field is high, the effects of space charge are reduced. However, as the kinetic energy increases with increasing ion velocity, more energetic collisions result, which lead to a greater chance of fragmentation.

2.2.5.3 Effective potential of the RF electric field – V^*

Tolmachev and colleagues have worked extensively to describe mathematically the effective potential V* (or pseudo-potential) locally created by the RF field and these derivations are reproduced in equation E 2.51 [42-46]:

$$V^*(r,z) = \frac{ze \mid E_{RF}(r,z) \mid^2}{4m\omega^2} = \frac{ze \mid E_{RF}(r,z) \mid^2}{4m(2\pi\nu)^2} \qquad \text{E 2.51}$$

where z is the number of charge of the ion, e the elementary charge, $E_{RF}(r,z)$ the absolute value of the local amplitude of the RF electric field, r and z the radial and axial cylindrical coordinates respectively of the ion, ω the angular frequency and ν the frequency.

The effective potential can be analytically studied through the equations E 2.52-E 2.54 [43, 45]:

$$\begin{aligned} V^*(r,z) &= V_{trap}\left(I_1^2\left(\frac{r}{\delta}\right)\cos^2\left(\frac{z}{\delta}\right) + I_0^2\left(\frac{r}{\delta}\right)\sin^2\left(\frac{z}{\delta}\right)\right) \\ &= V_{trap}\left(I_1^2\left(\frac{\pi r}{d}\right)\cos^2\left(\frac{\pi z}{d}\right) + I_0^2\left(\frac{\pi r}{d}\right)\sin^2\left(\frac{\pi z}{d}\right)\right) \end{aligned} \qquad \text{E 2.52}$$

$$V_{trap} = \frac{V_{max}}{I_0^2\left(\frac{\rho}{\delta}\right)} = \frac{V_{max}}{I_0^2\left(\frac{\rho\pi}{d}\right)} \qquad \text{E 2.53}$$

$$V_{max} = \frac{z_i e {V_{RF}}^2}{4m\omega^2\delta^2} = \frac{z_i e \left(\frac{V_{PP}}{2}\right)^2}{4m(2\pi\nu)^2 \left(\frac{d}{\pi}\right)^2} \quad \text{E 2.54}$$

where V_{trap} is the axial effective potential well depth, V_{max} is the maximum value of the effective potential at $r = \rho$ (maximum radius for a given z) and $z = d(i + ½)$ with $i = 0, 1,\ldots$ (on the walls of the reactor at the level of each electrode), I_0 and I_1 are zero and first order modified Bessel functions, V_{RF} is the RF voltage amplitude and is equal to half of the peak-to-peak value: $V_{RF} = V_{PP}/2$, d is the spacing between adjacent electrodes and $\delta = d/\pi$. [43, 45].

E 2.53 and E 2.54 can be simplified using the following approximation for the modified Bessel functions in E 2.55 [45]:

$$I_0(x) \approx I_1(x) \approx \frac{e^x}{\sqrt{2\pi x}} \quad \text{for } x \gg 1 \quad \text{E 2.55}$$

V_{trap} can now be expressed through E 2.56:

$$V_{trap} = V_{max} 2\pi^2 \left(\frac{\rho}{d}\right) e^{-2\pi\rho/d} \quad \text{for } r \gg \delta \quad \text{E 2.56}$$

and $V^*(r)$ through E 2.57 after rearrangement:

$$V^*(r) = \frac{z_i e \left(\frac{V_{PP}}{2}\right)^2}{16m(\nu d)^2} \left(\frac{\rho}{r}\right) e^{2\pi(r-\rho)/d} \quad \text{for } r \gg \delta \quad \text{E 2.57}$$

Notice that the condition $r >> \delta = d/\pi$ means $r >> d$. The notion of 'much greater than' being subjective and the highest r/d ratio being met in this study being 6.25, and also in order to be

able to model the effective potential, the condition ρ > r > d is considered enough to apply the approximations in equations E 2.56-E 2.57 (and consequently the condition x > 1 in E 2.55) [43]. As a few critical parameters have been described, it would be pertinent to display examples to visualise them.

When the condition r > d is not satisfied, as in Figure 2.7 [45], the equation E 2.52 is used to model V^* involving cosine and sine in the expression.

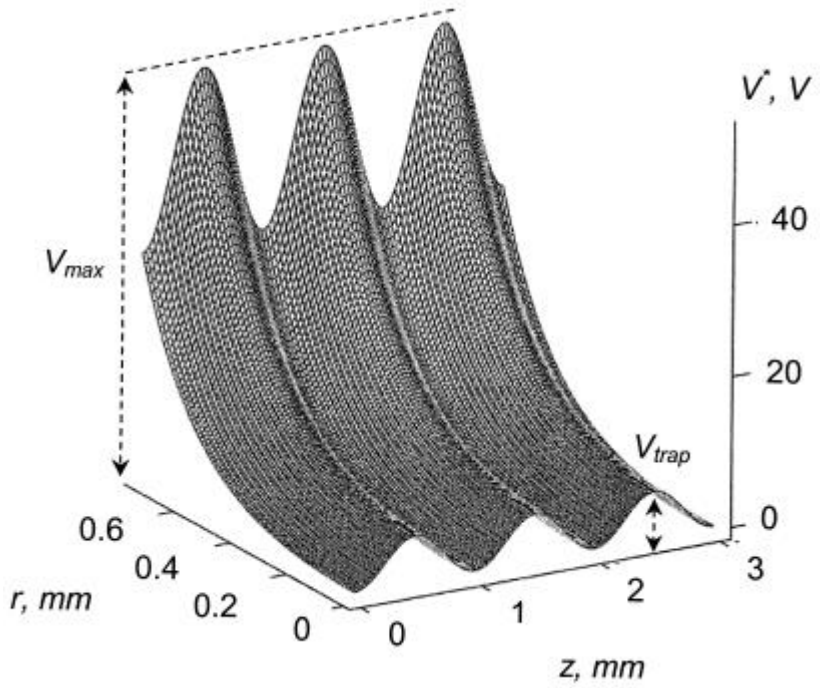

Figure 2.7: Modelling of V^* for r < d only when RF electric field is applied in the PTR-ToF-MS reactor [45]

That is why the 'shape' of the effective potential surface as a function of z is sinusoidal. V_{max} is the maximum V^* for a given z (when r = ρ) and V_{trap} is the minimal V^* for a given z both at the level of an electrode. On the axis V^* fluctuates between V_{trap} and 0 V through the equation E 2.58 [45]:

$$V^*(r=0,z) = V_{trap}\sin^2\left(\frac{z}{\delta}\right) = V_{trap}\sin^2\left(\frac{\pi z}{d}\right) \qquad \text{E 2.58}$$

V_{trap} is for an ion, the lowest potential to override across the reactor. That is why it is essential to have a sufficiently good effective confining field to 'push' the ions towards the centre.

Figure 2.8 [45] shows that the greater r is (meaning more away of the centre), the 'less sinusoidal' the evolution of V^* is across the reactor (as a function of z for a given r).

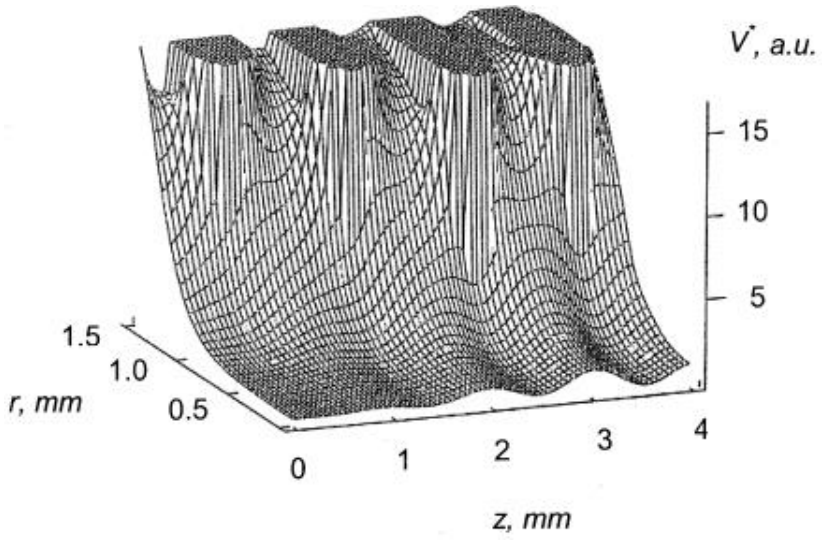

Figure 2.8: Modelling of V* for r < d and r > d when RF electric field is applied in the PTR-ToF-MS reactor [45]

As expressed earlier, the condition r > d (= 1 mm) seems 'reasonable' considering Figure 2.8. For r < d, the evolution of V* for a given r is 'rather' sinusoidal whereas for r > 1, it becomes more 'random'. Figure 2.8 also proves that V_{trap} evolves as a function of ρ.

What the parameters and examples show so far is that, as soon as a RF field is applied, an effective potential is created everywhere in the 'RF area'. That includes a maximum along the reactor walls and a minimum along the central axis varying between 0 V and V_{trap}. Independently of the chemistry, the aim of an ion-funnel, is to confine the ions as much as possible towards the central axis presenting at the same time the lowest axial effective potential well depth.

Throughout this thesis, V^* is calculated only for z values matching the position of an electrode (when $z = d(i + ½)$ with $i = 0, 1,\ldots$ with $V^*(0,0) = 0$ V) (except along the centre axis, i.e. when r is nil). However, both Figure 2.7 and Figure 2.8 show positive values of V^* between 2 adjacent electrodes but when z does not match the position of an electrode, the values of the amplitude and frequency of the RF field require further calculations. That is why the whole plots of V* are deliberately presented here as 'smoothed' between the z coordinates of the electrodes only.

It is crucial to realise all the effective potential expressions above disregard the collisional damping due to the buffer gas becoming non-negligible in viscous flow and defined by the coefficient γ in E 2.59 [47-49]:

$$\gamma = \frac{\omega^2\tau^2}{1 + \omega^2\tau^2} = \frac{(2\pi\nu)^2 \left(\frac{m_i K}{e}\right)^2}{1 + (2\pi\nu)^2 \left(\frac{m_i K}{e}\right)^2} \qquad \text{E 2.59}$$

where τ is the ion velocity relaxation time. γ varies between 0 and 1 and characterises the effect of the collisional damping and consequently the alteration of the RF field. In all the experimental conditions of this project, any effective potential value must be multiplied by γ.

2.2.5.4 Effective RF electric field – E^*

Once the collisional damping is considered, reducing the effective potentials, the effective RF electric field E^* can be obtained as the gradient of effective potentials V^* through E 2.60 [45, 50]:

$$E^*(r,z) = -\nabla V^*(r,z) = -\left(\frac{\partial V^*(r,z)}{\partial r}, \frac{\partial V^*(r,z)}{\partial z}\right) \quad \text{E 2.60}$$

where ∇ is the Nabla operator. From E 2.60 two specific cases were studied in this project.

Firstly, when r = 0, E^* is the axial effective field along the central axis and is the only axial effective field studied, due to the calculations' complexity between electrodes and because the central axis presents the lowest axial effective field, which is called in this report the 'effective trapping field, E_{trap}' and which is described in E 2.61 [45]:

$$E^*(0,z) = E_{trap} = -\nabla V^*(0,z) = \frac{\partial}{\partial z}\left(-V_{trap}\sin^2\left(\frac{\pi z}{d}\right)\right) = \frac{-V_{trap}\pi}{d}\sin\left(\frac{2\pi z}{d}\right) \quad \text{E 2.61}$$

Without considering extra energy in the system, the necessary condition for an ion to be effectively dragged across the reactor is described as follows in E 2.62 [45]:

$$E_z = E_{DC} > E_{trap} = \frac{V_{trap}}{\delta} = \frac{\pi V_{trap}}{d} \quad \text{E 2.62}$$

E_{DC} needs to be greater than E_{trap}. That is why, in certain cases, it is necessary to operate a DC electric field above a certain limit. However, this impacts the energy of the system. Within this thesis, the difference between both electric fields E_z and E_{trap} is called the 'overriding field, E_{over}', i.e. the DC electric field that drags the ions across the reactor once E_{trap} was considered.

Secondly, for a given z, E^* is the radial effective field being the component of E^* that pushes the ions towards the centre of the reactor. Therefore, $E^*(r)$ is called the effective confining field [46] whose absolute value is expressed in E 2.63:

$$\left|\, E^*(r) \,\right| = \nabla V^*(r) = \frac{\partial}{\partial r}\left(V^*(r)\right) = \frac{\partial}{\partial r}\left(\frac{z_i e\left(\frac{V_{PP}}{2}\right)^2}{16m(\nu d)^2}\left(\frac{\rho}{r}\right) e^{2\pi(r-\rho)/d}\right) = \left(\frac{2\pi}{d} - \frac{1}{r}\right)V^*(r) \qquad \text{E 2.63}$$

where V*(r) was determined in E 2.57.

2.2.5.5 Maximum current – i_{max}

Considering E_z, it can lead to another useful relationship to estimate the maximum current i_{max} transmitted through the funnel ion guide as expressed in E 2.64 [43, 45]:

$$i_{max} = \pi\varepsilon_o\tau\rho E_z\left(\frac{ze}{m_i}\right)^2\frac{{V_{RF}}^2}{\omega^2\delta^3} = \pi\varepsilon_o\tau\rho E_{DC}\left(\frac{ze}{m_i}\right)^2\frac{\left(\frac{V_{PP}}{2}\right)^2}{(2\pi\nu)^2\left(\frac{d}{\pi}\right)^3} \qquad \text{E 2.64}$$

where ε_o is the dielectric constant. It is noticeable to mention i_{max} is inversely proportional to d^3, indicating the importance of attempting to minimising the electrode spacing in the ion-funnel.

2.2.5.6 Mean RF electric and kinetic energies – $E_{el,RF}$ and $E_{k,RF}$

In terms of energetics, the ions under the influence of the RF field receive extra energy on top of that imparted by the mean DC kinetic energy equal to a) the mean RF electric energy (obtained by multiplying V* as expressed in E 2.51 by the elementary charge e) which, by conservation of energy, is equal to b) the mean kinetic energy due to the RF-induced ion motion added. Both a) and b) are defined in E 2.65 [46]:

$$E_{el,RF} = eV^* = \frac{ze^2 \mid E_{RF}(r,z) \mid^2}{4m(2\pi\nu)^2} = \frac{1}{2}m < v_{RF}^2 > = E_{k,RF} \qquad \text{E 2.65}$$

where v_{RF} is the instantaneous velocity of the RF oscillation of the ion. The values of V^* and v_{RF} in E 2.65 are mean averages and consequently independent of r and z. Under PTR reactor pressure ranges, E_{RF} must consider the collisional damping through γ as follows in E 2.66 [48, 51]:

$$E_{RF}(P) = \gamma E_{RF}(vacuum) \qquad \text{E 2.66}$$

where E_{RF}(vacuum) is defined in E 2.67 [52]:

$$E_{RF}(vacuum) = \omega \sqrt{\frac{2mdE_{DC}\sin(\alpha)}{e}} \qquad \text{E 2.67}$$

where α represents the angle of the ion-funnel inner diameter gradient.

Combining E 2.65, E 2.66 and E 2.67, $E_{k,RF}$ is simplified in E 2.68 [52]:

$$E_{k,RF} = \gamma^2 \frac{zed}{2} E_{DC}\sin(\alpha) \qquad \text{E 2.68}$$

2.2.5.7 Kinetic energy in the centre of mass of the colliding system – E_k(CM)

The kinetic energies presented previously are in the laboratory frame of reference, which is not directly relevant to collisions. The mean collision energy can be obtained from the centre of mass frame collision energy, whose basics of ion kinetics were obtained using SIFT-MS

instruments (Selected Ion Flow Tube-Mass Spectrometry) where reactions strictly occur at room temperature (matching the temperature of the reactor) [53].

Contrary to SIFT-MS, the ions in PTR-MS reactors are affected by an electric field which increases their effective translational temperature, i.e. $T_{ion} > T_D$. This fact is a consequence of the selective heating of the ions by the electric field [54].

It is now useful to describe the total mean ion kinetic energy $E_k(i)$ which was derived by Wannier [55, 56] as follows in the equation E 2.69:

$$E_k(i) = \frac{3}{2}k_B T_D + \frac{1}{2}m_i {v_D}^2 + \frac{1}{2}m_c {v_D}^2 \qquad \text{E 2.69}$$

The terms on the right-hand side of E 2.69 are, respectively (from left to right), the thermal contribution to the kinetic energy of the ion, the kinetic energy of the ion traveling across the reactor at v_D and the term deriving from the collisions between the ions and the neutral carrier gas (of mass m_c) which provides an additional velocity contribution [57].
E 2.69 can be rearranged as follows in the equation E 2.70:

$$E_k(i) = \left(\frac{{v_D}^2}{2}\right)(m_i + m_c) + \frac{3}{2}k_B T_D \qquad \text{E 2.70}$$

E 2.70 refers to the ion kinetic energy in the laboratory frame of reference. To study the impact of $E_k(i)$ on the outcome of an ion-molecule reaction, it is necessary to work with the collision energy in the centre of mass frame, i.e. the kinetic energy relative to the colliding species. The centre of mass (CM) frame of reference makes the observer travel along with the centre of mass resulting in a fixed nil total momentum [57, 58]. This property makes the CM frame independent of experimental geometry, allowing comparisons between collisions realised under

different types of experiments. The kinetic energy relative to the centre-of-mass of the colliding system $E_k(CM)$, available for the reaction process, is presented in the equation E 2.71 [57]:

$$E_k(CM) = \frac{1}{2}\left(\frac{m_n m_i}{m_n+m_i}\right)(v_i^2+v_n^2) \qquad \text{E 2.71}$$

where v_i and v_n are respectively the velocities of the ion and the neutral involved in the colliding system. Notice the neutral involved in this reaction can be either a non-reactive entity of the carrier gas or an analyte entity [57]. The ratio $\frac{m_n m_i}{m_n+m_i}$ then refers to the mass of the colliding system which is called the reduced mass $\mu(CM)$ and is derived from the equation E 2.72:

$$\frac{1}{\mu(CM)} = \frac{1}{m_i} + \frac{1}{m_n} \qquad \text{E 2.72}$$

In E 2.71, i.e. still in the context of the colliding system, the new expression of the kinetic energy of the ion and the thermal kinetic energy of the colliding system can be respectively specified in E 2.73 and E 2.74 [57]:

$$E_k(i) = \frac{1}{2} m_i v_i^2 \qquad \text{E 2.73}$$

$$\frac{3}{2} k_B T_D = \frac{1}{2} m_n v_n^2 \qquad \text{E 2.74}$$

Equalizing E 2.69 and E 2.73, v_i is deduced and v_n is deduced from E 2.74. Inserting these both new expressions into E 2.71, $E_k(CM)$ becomes after rearrangement the final expression in equation E 2.75 [59]:

$$\mathbf{E_k(CM) = \frac{m_n}{m_n+m_i}\left(\frac{v_D^2}{2}\right)(m_i+m_c) + \frac{3}{2}k_B T_D} \qquad \text{E 2.75}$$

Consider, for example, the collisions between H_3O^+ and neutral benzene. They have respective masses of 3.16 x 10^{-26} (m_i) and 1.31 x 10^{-25} kg (m_n and m_c). The value of v_D of 715 m/s previously calculated together with T_D = 296.75 K makes E_k(CM) equal to 2.22 x 10^{-20} J = 0.139 eV, which is about 3.6 times greater than the thermal kinetic energy at the same temperature. This difference shows clearly the extra energy that the electric field provides to the system in PTR-MS. To express this difference of energy (and remembering that through the effect of the electric field $T_{ion} > T_D$) E 2.75 can be expressed as follows in the equation E 2.76 [59]:

$$E_k(CM) = \frac{3}{2}k_B T_{coll} \qquad \text{E 2.76}$$

where T_{coll} is the temperature of the collision between the ion and the neutral reactant within the carrier gas. Equalizing E 2.75 and E 2.76, T_{coll} becomes as follows in the equation E 2.77:

$$T_{coll} = T_D + \frac{m_n(m_i+m_c)}{m_n+m_i}\frac{v_D^2}{3k_B} \qquad \text{E 2.77}$$

T_{coll} varies with the neutral compound. In the case where the neutral reactant is the carrier gas (i.e. $m_n = m_c$ as with the previous example of neutral nitrogen), which represents most of the collisions within the reactor, T_{coll} becomes the effective temperature T_{eff} [59] and E 2.77 is simplified as follows in the equation E 2.78:

$$T_{eff} = T_D + m_n \frac{v_D^2}{3k_B} \qquad \text{E 2.78}$$

It is noticeable that once the different masses involved in the system are known, the last unknown is v_D, which cannot be easily obtained with commercial PTR-MS systems, but can be calculated. However certain research instruments like a selected ion flow-drift tube-mass spectrometer (SIFDT-MS) are able for a given system (m_n, m_i and m_c) to experimentally determine v_D making it possible through E 2.46-E 2.48 to determine the absolute ion mobility of a selected ion. Then, reducing this mobility to the conditions of a given PTR-MS, v_D can theoretically be calculated. This experiment was undertaken at the J. Heyrovský Institute of Physical Chemistry of the Czech Academy of Sciences in Prague, CZ during a secondment.

2.2.6 Transfer optics

After leaving the reactor exit aperture, the ions enter the transfer lens section. There is a drop in pressure of approximately 4 orders of magnitude due to the turbo molecular pumping of this section. At a pressure of 7 x 10^{-5}-1 x 10^{-4} mbar, the ions are in the molecular flow regime and so it is possible to use conventional electrostatic ion optics to focus the beam. Indeed, the mean free path of nitrogen molecules at 297 K and $1 \cdot 10^{-4}$ mbar is ~ 67 cm. This distance is far greater that the dimensions of the transfer optics, whose length is ~ 15 cm. The first function of the transfer lens, shown in Figure 2.9, is to collect ions emerging from the reactor exit aperture.

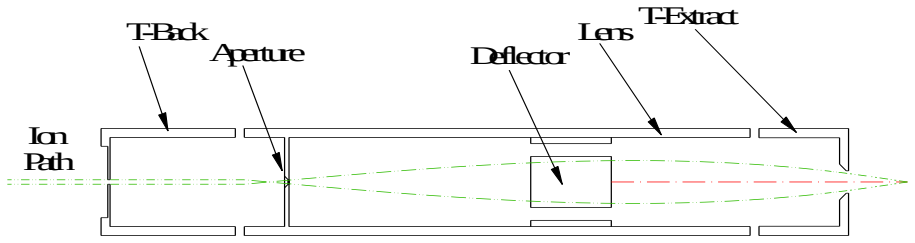

Figure 2.9: Transfer optics of a typical Kore PTR-ToF-MS with ion flow from right to left – T stand for Transfer

With the reactor exit set between 3.5 and 4.5 V, the T-Extract voltage was set between -6 and -11 V, providing a weak electric field over a distance of 5 mm intended to prevent fragmentation of larger ions as they are extracted. The T-lens electrode was usually set between -100 and -115 V and is thus an accelerating lens. The second lensing action between T-lens and T-back is a decelerating lens, and the ions leave a slit in T-back and are injected into the ToF source with the kinetic energy set by the potential of the reactor exit electrode, namely ~ 4 eV.

The transfer optics also provide an intermediate region for the ions, after the relatively high pressure of the reactor and before the high vacuum of the spectrometer. Configuration and setting are made such that a parallel ion beam is ready for injection into the ToF source.

2.2.7 Time of flight mass spectrometer

The ion beam exiting the transfer optics finally enters the Time of Flight (ToF) spectrometer where the ions are discriminated as a function of their masses. Its use is currently preferred to that of a quadrupole (bandpass filter) because the ToF system has the ability to record a full mass spectrum with a greater mass resolution than a quadrupole, which needs to scan the selected mass range one mass unit by one at a designated scan rate.

The pressure in the spectrometer is usually kept between 2 x 10^{-7} and 5 x 10^{-7} mbar, partly to increase the mean free path yet again (by another 3 orders of magnitude to 670 m considering the same room temperature), and also because the ion detector operates with least background noise at pressures lower than 1 x 10^{-6} mbar.

The ToF-Spectrometer comprises three main parts:

- ToF source – extracts a “packet” of ions out of the ion beam toward the flight tube.
- Flight tube including reflectron – allows ions of the same m/z but different energies to be focused in time at the detector.

- Detector including Time to Digital Converter (TDC) – counts and records the ions.

2.2.7.1 ToF source

The ToF source comprises 4 electrodes, as shown in Figure 2.10.

(a) The 'back' of the ToF source (at ground potential)

(b) The Extract electrode (gridded)

(c) The Intermediate electrode

(d) The final accelerating electrode, name 'field-free', also gridded

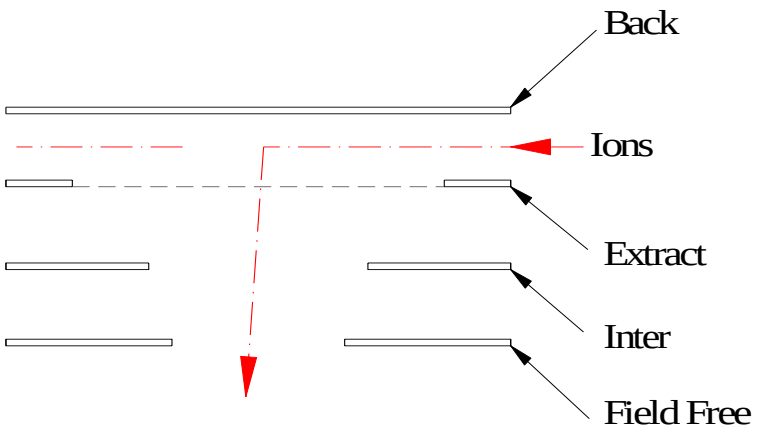

Figure 2.10: ToF source inside the time of flight (ToF) mass analyser of a typical PTR-ToF-MS

The function of the ToF source is to create a short pulse of ions for each 'ToF cycle' and extract them orthogonally from the continuous ion beam entering the ToF source. Orthogonal extraction increases the mass resolution and dynamic range achievable compared to a 'straight-through' geometry, and is commonly used in ToF-MS systems.

When the ToF source is not pulsing, the extract electrode is held at ground potential, and with no electric field between Back and Extract, ions simply pass through the source. A

Faraday cup is positioned on the opposite side of the source to the entrance to allow measurement of the ion current.

When pulsed, the Extract electrode is set to ~ -400 V within a few nanoseconds and is held there typically for 3 microseconds to extract the ions in the ToF source at that time. The Intermediate electrode is a weak focusing electrode that is usually set at ~ -1000 V, but is adjustable. The final accelerating electrode is set at the flight potential of -2 keV. From this point onwards (until the reflectron), the ions travel in a field-free region, hence the name of this final electrode. The forward momentum of the ions entering the ToF source (~ 4 eV) results in a small deviation by approximately 2.5 degrees from the orthogonal direction.

2.2.7.2 Flight tube (including reflectron)

Once the ions have been extracted and have passed the final accelerating electrode, they enter the field free region (FFR), i.e. a region where there are no potential differences and consequently where the acceleration/deceleration of the ions is nil. In this section, the ions begin to separate as a function of their masses, i.e. of their time of flight, which means the time an ion takes to "fly" from the pulse location to the detector. This can be defined, starting from the conservation of the energy of an ion, by the following equation in E 2.79:

$$E_k(\text{ion}) = E_{elec,p}(\text{ion}) \qquad \text{E 2.79}$$

where E_k, and $E_{elec,p}$ are respectively the kinetic and the electric potential energies of an ion. E 2.79 can be developed as follows in E 2.80 [60, 61]:

$$\frac{1}{2} m_i v_i^2 = qV = zeV \qquad \text{E 2.80}$$

where m_i and v_i are respectively the mass and the velocity of the ion in the FFR, q the electric charge of the ion (in Coulomb), V the difference of potentials between the pulse location and the entry of the FFR, z the charge number of the ion and e the elementary-charge constant (1 e = 1.6022 x 10^{-19} C). Isolating v_i, E 2.80 gives E 2.81 [60, 61]:

$$v_i = \sqrt{\frac{2zeV}{m_i}} = \frac{l_{FFR}}{t_{FFR}} \qquad \text{E 2.81}$$

where l_{FFR} is the length of the FFR and t_{FFR} the time taken by the ion to travel through the FFR. Isolating t_{FFR}, E 2.81 gives E 2.82 [60, 61]:

$$t_{FFR} = \sqrt{\frac{m_i l_{FFR}^2}{2zeV}} \qquad \text{E 2.82}$$

E 2.82 shows t_{FFR}, and consequently the ToF, of an ion is proportional to the square root of its mass.

Reflectron analyser basics

A brief description is now presented concerning the reflectron analyser in the research PTR instrument used throughout this thesis. The analyser comprises a set of 25 circular electrodes connected with 1 MΩ resistors. The entrance electrode is gridded and held at the same potential as the 'field-free' liner (-2 kV), but thereafter there is a gradual increase in potential through to

the Reflect electrode which is held at -30 V. Halfway down the stack of electrodes is a gridded Retard electrode whose potential can be adjusted. In practice, this electrode potential is adjusted to optimise the mass peak shape and resolution. In this configuration, the ToF is redefined as follows in E 2.83:

$$ToF = t_{acc,1} + t_{FFR,1} + t_{dece} + t_{acc,2} + t_{FFR,2} \qquad \text{E 2.83}$$

where $t_{acc,1}$, $t_{FFR,1}$, t_{dece}, $t_{acc,2}$ and $t_{FFR,2}$ are respectively the times taken by the ion to accelerate through the extraction potential gradient, travel through the FFR, decelerate through the reflectron, accelerate back out of the reflectron through the FFR again until the detector. If the energy of the ions leaving the reflectron of 1.97 keV was considered sufficiently close to the 2 keV of the extraction potential gradient, the accelerations and decelerations phases could be considered as similar as well as the two FFR travel times, which would give E 2.84:

$$ToF \approx 3t_{acc,1} + t_{FFR,1} = 3t_{acc,1} + \sqrt{\frac{2m_i l^2}{zeV}} \qquad \text{E 2.84}$$

For a given flight tube length, the reflectron improves the mass resolution by an order of magnitude compared to a classical linear ToF-MS [60]. Notice the hyperbolic trajectory of the ions (having a forward momentum) flying towards the detector are directed, through the flight tube, by two pairs of deflectors.

In the hypothetical case of ions perfectly on axis and having 2 keV flight energy exactly and with no energy spread, the spread of recorded flight times would be zero and the resulting mass peak would be a line. However, since the ion beam has a width in space along the axis perpendicular to the ToF source electrodes, it is in the nature of the ion extraction process to

produce ions at the final accelerating electrode with a significant energy spread. During the extract pulse, a 400 V potential gradient is applied between the grounded backplate and the extract electrode. During this acceleration phase, ions closer to the back plate will acquire more energy than those closer to the extraction electrode.

One of the aims of the transfer lens optics is to inject a parallel beam into the ToF source to minimise the spatial spread within the ToF source. The beam diameter can be reduced upstream by reducing the size of the transfer lens aperture. This allows for greater time and thus mass resolution for a given size of spectrometer, but at the expense of sensitivity.

The reflectron is the means to minimise the effect of this energy spread on the time (and mass) resolution in the spectrum. Ions of the same m/z but with different energies are brought to a time focus at the surface of the detector. This is achieved by allowing ions with higher energies to penetrate deeper into the reflectron before they are reflected back out. In practice, the reflect and retard potentials are adjusted for the best time focus at the detector, and thus the optimum mass resolution.

The mass range of the reflectron analyser is in theory unlimited. In practice it is limited by (a) the ability to produce intact heavy ions in the gas phase (and thus the success of techniques such as MALDI – Matrix-Assisted Laser Desorption/Ionisation – in enabling ionisation and preservation of large biomolecules), and (b) the ability to convert such ions to electrons at the detector. The mass range of interest in most PTR experiments is limited to < 1000 m/z, and in practice the cycle time of the ToF experiment is adjusted to allow the heaviest expected mass of interest to arrive in that ToF cycle to avoid ‘wrap around’ into the next cycle. This results in cycle times of 25 to 75 microseconds and thus repetition rates of 40 kHz to 13.3 kHz.

2.2.7.3 Detector (including time-to-digital converter)

A dual micro channel plate detector (DMCP) is used in the research PTR instrument to create the electron amplification process, i.e. works as a secondary electron multiplier (SEM), which is based on the high probability the impact of ions on a solid surface leads to emissions of electrons, called secondary electrons, which under an accelerating potential strike further surfaces releasing yet more electrons until sufficient amplification has been achieved to enable an output current to be measured [37]. The DMCP was composed of a million 10 µm channels separated by 12 µm to each other providing an active circular area with a diameter of 25 mm. The gain of single plate is 10^3-10^4 which is lower than other SEMs, that is why 2 plates are sandwiched together to provide gains of 10^6-10^7. To make the cascade effect possible, the channels need to have a certain angle compared to the surface of the front plate with an opposite inclination of the channels of the 2nd plate as presented in Figure 2.11 (adapted from [62]):

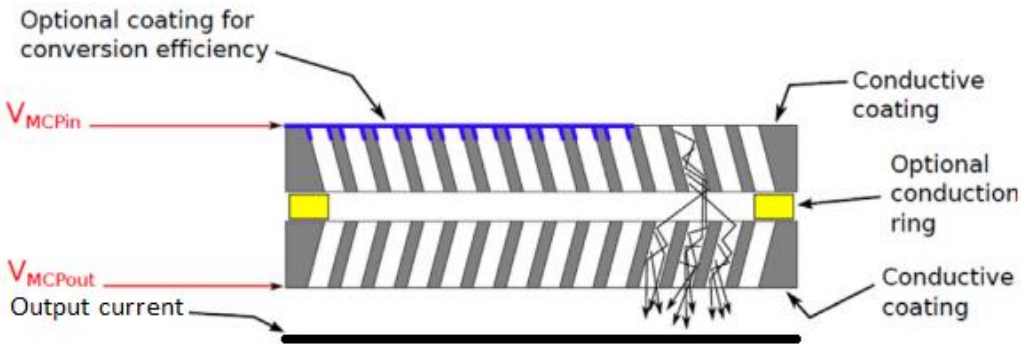

Figure 2.11: Dual microchannel plate (MCP) detector in Chevron configuration (adapted from [62])

This configuration is called Chevron plate and provides gains of 10^6-10^7 contributing to the performance of the detector, described through its gain G defined as follows in E 2.85 [63]:

$$G = \delta^n \qquad \text{E 2.85}$$

where δ (dimensionless like G) is the number of secondary electrons and n the number of amplification stages. δ is an increasing function of the voltage applied across the detector.

Once the ions are recorded by the MCP they are converted into numerical data through a time-to-digital converter (TDC) whose process is presented in Figure 2.12 (adapted from [64]):

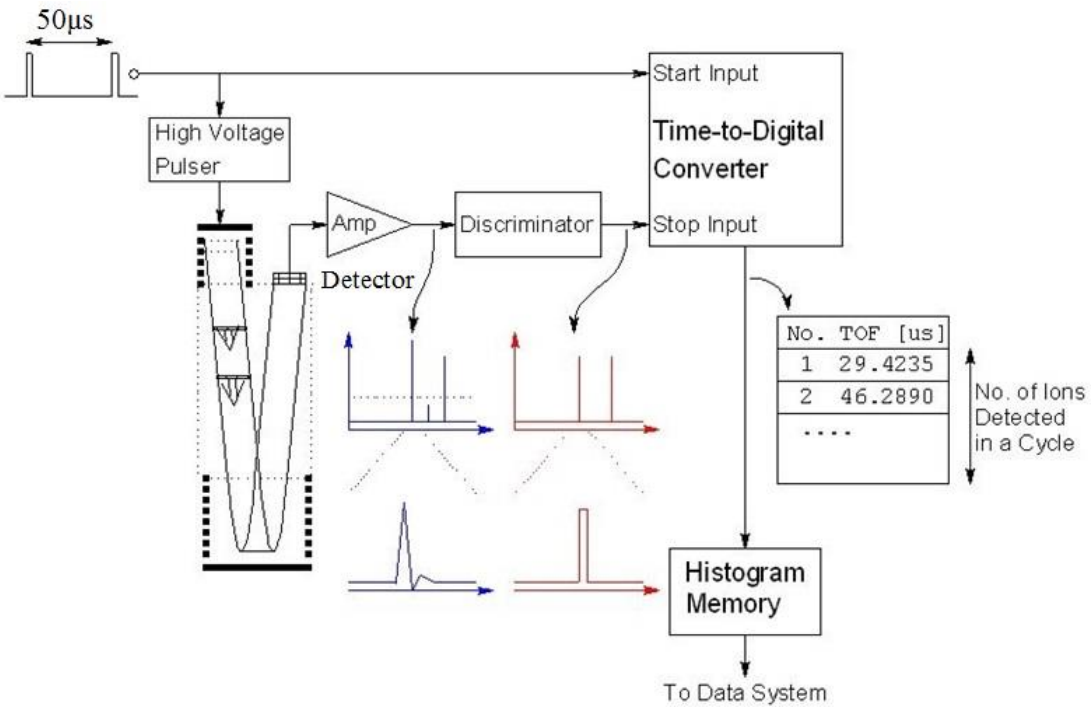

Figure 2.12: Time-to-digital converter (TDC) for signal treatment of ions flying inside a PTR flight tube (adapted from [64])

Each ion striking the detector generates a pulse of electrons at the rear of the detector which is then amplified and passed through a comparator so that only signals of a certain threshold are passed through to the TDC which, comparing to the starting point of the general pulse (from the pulser), provides a ToF (generally in µs) of each counted ion and the resulting list is stored in the histogram memory to finally present a spectrum of the intensity of ions as a function of their ToF [65]. The software then converts the times of flight to masses according to equation E 2.84. Further details about detectors and TDC are given within the appendix A.5.

2.3 EI-ToF-MS

Two EI-ToF-MS were involved in this project. A general sketch of each of them, the 'INFORMS' and the 'MS-200' instruments, are respectively presented in Figure 2.13 and Figure 2.14. Both instruments are then presented in further detail.

Figure 2.13 shows that, after electron ionisation in the ionisation chamber between neutral species and the electron beam, the ion beam is focused through transfer optics and passed into a ToF source, out of which a pulse of ions is injected into the ToF tube where a reflectron directs the ions, being mass discriminated, towards the detector where the signal is amplified and converted into a detectable signal. The high vacuum of the mass spectrometer is ensured by a turbomolecular pump.

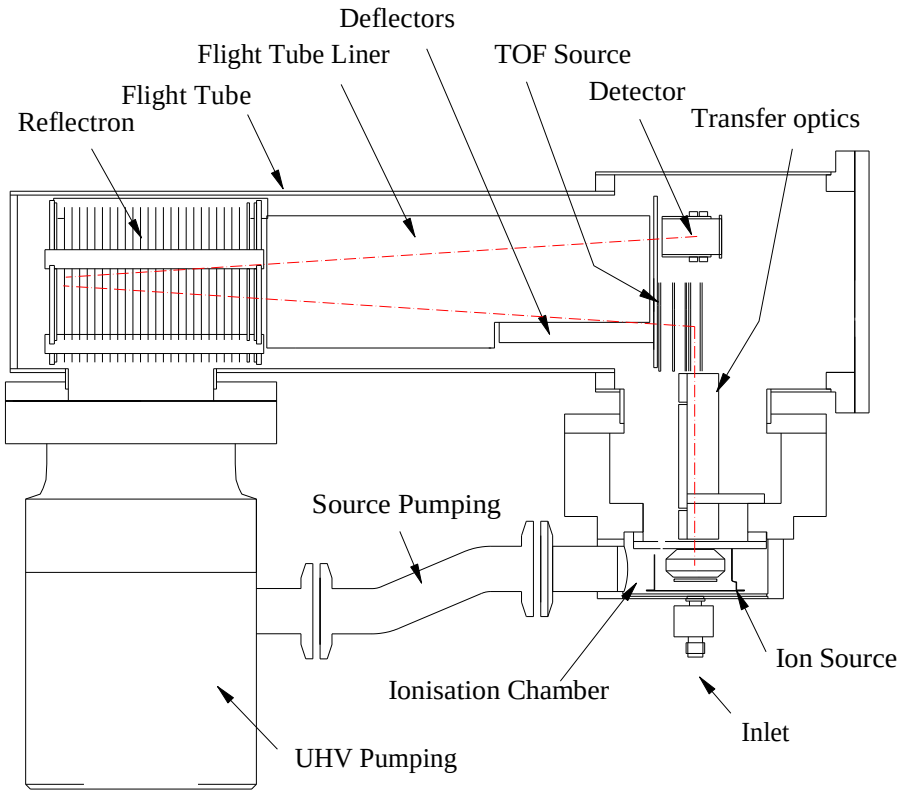

Figure 2.13: INFORMS, transportable EI-ToF-MS from Kore – General assembly schematic

Figure 2.14 shows that the sample introduction method is quite different in this instrument. The atmospheric pressure analyte gas passes through a silicone membrane into an intermediate chamber held at a pressure of < 5 mbar by a peristaltic pump. From this chamber the gas permeates through a second membrane and into the vacuum of the mass spectrometer. This is therefore called a 'dual membrane inlet system' (whose function is explained shortly). Ionisation occurs in the same pressure zone as the mass spectrometer. The MS-200 therefore does not have transfer optics as has been described previously for the other instruments.

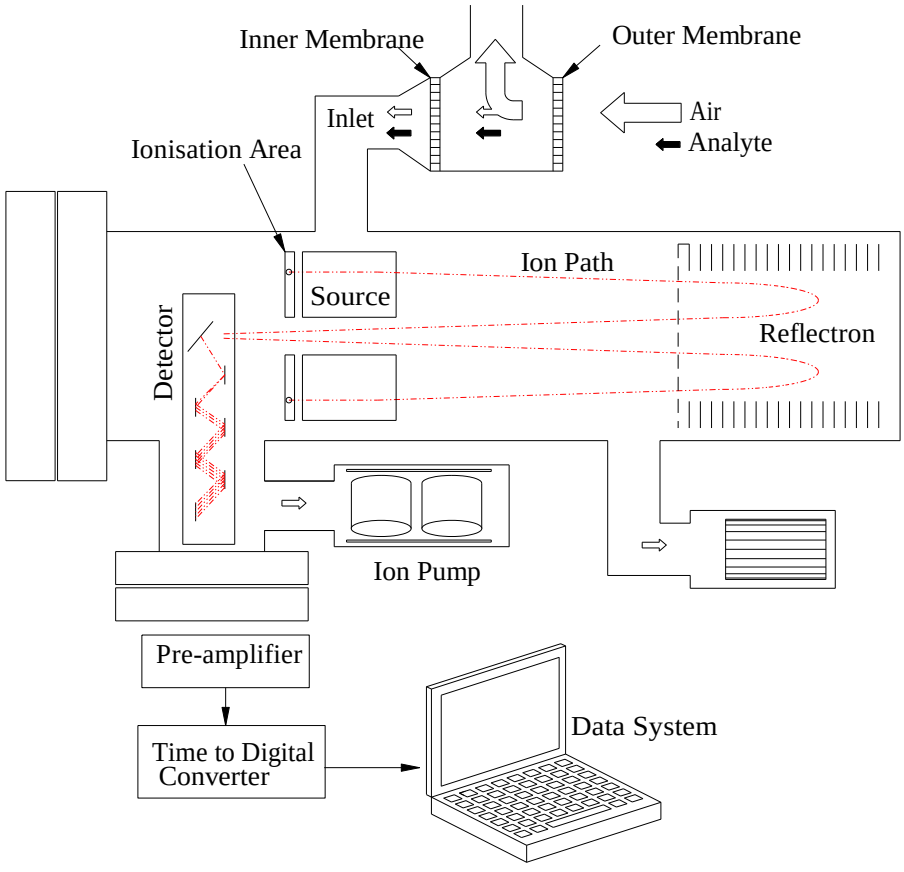

Figure 2.14: MS-200, portable EI-ToF-MS from Kore – General assembly schematic

2.3.1 Ionisation source – Technical details

Compared to a PTR instrument, the ionisation source is an electron-emitting hot filament (thermionic emitter). A schematic of a typical ion source arrangement is shown in Figure 2.15 [66], a filament is used as an electron source. It is a resistively heated metal wire, generally made of tungsten or yttria-coated iridium or rhenium which, reaching 2000 °C, produces electrons by thermionic emission. These primary electrons are then attracted towards the reaction chamber through a difference of potentials applied between the filament and the entry of the reaction chamber/ ion volume. In the centre of the reaction chamber, this electron beam then ionises neutral species due to several tens of electron·volts carried by each electron. The electrons are then collected in an electron trap. To minimise ions scattering, a low positive voltage is applied to the repeller electrode to push the ions away towards the mass analyser [66, 67].

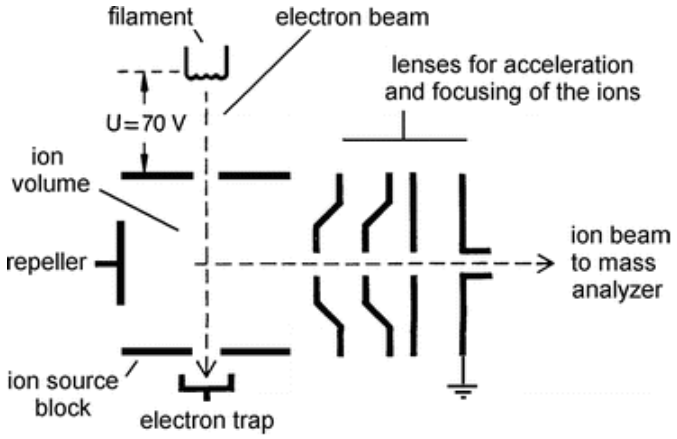

Figure 2.15: Schematic layout of a typical EI-MS ion source [66]

Compared to the PTR used during this project, the instruments involving electron ionisation both employed pre-concentration by means of a silicone membrane. INFORMS, the transportable EI-ToF-MS, uses a single silicone membrane, whereas the MS-200, the portable

EI-ToF-MS, uses a double membrane to pre-concentrate the sample. This configuration requires an intermediate vacuum regime between the two membranes, as presented in Figure 2.16 [68], and this is achieved in the MS-200 using a small peristaltic pump. The main spectrometer chamber is sealed and pumped only by a small ion pump so that the instrument is truly portable – there are no turbo molecular or backing pumps.

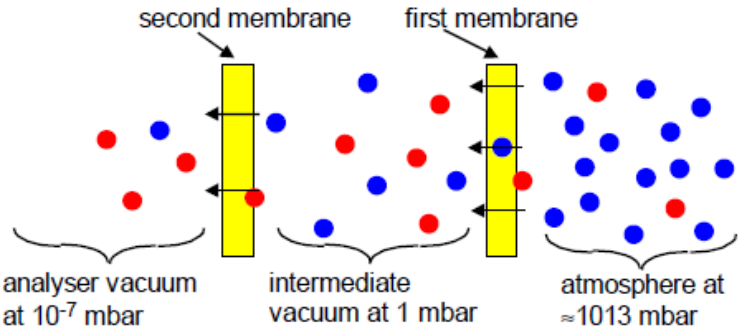

Figure 2.16: Double membranes configuration of the MS-200, the portable EI-ToF-MS from Kore [68]

2.3.2 Ion source – Electron ionisation

Although this is called electron ionisation (EI), it has formerly been termed electron impact ionisation or electron impact [69]. EI is the process occurring when an electron, with an energy of several tens of electron·volts, impacts on a neutral molecule, transferring energy to the neutral. Some of that energy is absorbed as internal energy, but the impacting 70 eV electron has far more energy than the ionisation energy of any molecule, resulting in ejection of an electron from the neutral and the production of a positive parent molecule [69, 70]:

$$M + e^- = M^{+\bullet} + 2e^- \qquad \text{E 2.86}$$

where M is the neutral species. Consequently, an even number of electrons within M results in the production of a radical cation (i.e. odd-electron molecule) [71].

The IE is the minimum amount of energy an atom or molecule must absorb in its electronic or rovibronic ground states to form an ion, which is also in its ground state after ejection of an electron [72].

Reaction through E 2.86 leading to a singly charged ion is the main electron ionisation process. However, depending on the analyte (M) and on the energy of the primary electron (accumulated after its emission of the filament), doubly and even triply charged ions can be observed as follows in E 2.87 and E 2.88 [69, 70]:

$$M + e^- = M^{2+} + 3e^- \qquad \text{E 2.87}$$

$$M + e^- = M^{3+\bullet} + 4e^- \qquad \text{E 2.88}$$

In rare cases, the neutral species can be a radical, leading to an even-electron ion as follows in E 2.89 [69]:

$$M^\bullet + e^- = M^+ + 2e^- \qquad \text{E 2.89}$$

Electron-neutral interactions do not necessarily lead to ionisation but in certain cases to excited neutrals (A*) that can then collide with ground state species (M) following two processes, Penning ionisation and associative ionisation (known as the Hornbeck-Molnar process) respectively following E 2.90 and E 2.91 [69]:

$$A^* + M = A + M^{+\bullet} + e^- \qquad \text{E 2.90}$$

$$A^* + M = AM^{+\bullet} + e^- \qquad \text{E 2.91}$$

Removal of an electron can occur at a σ-bond (single bond), π-bond (double bond) or lone electron pair (valence electrons not shared in a covalent bond with another atom). However, there are locations more favourable for electron ionisation than others. Anything contributing to the stabilization of the charge such as delocalization or hyperconjugation are favourable sites. Various factors affect the ability to remove an electron: lone electron pairs, π-bonds, and an increasing number of atoms in the molecule all reduce the barrier for removal. Therefore, the highest range of IE is found by the noble gas atoms, the most stable elements, then by diatomic molecules and then decreasing values are observed with increasing number of atoms for a given class of compounds such as hydrocarbons [72].

Most molecules have IEs in the 7-15 eV range. Impact by an electron with an amount of energy equal to the IE of the neutral does not guarantee ionisation because the ionisation efficiency will be low. Increasing the energy of the electron increases the probability of ionisation and even if every species has its own ionisation efficiency curve, they all present the same trend in ionisation cross section of the analyte versus electron energy presenting a maximum around 70 eV. Such an energy level presents the advantages to ionise any neutral species and to assure better reproducibility of spectra through a plateau of ionisation efficiency making small variations of electron energy negligible as shown in Figure 2.17 (adapted from [73]):

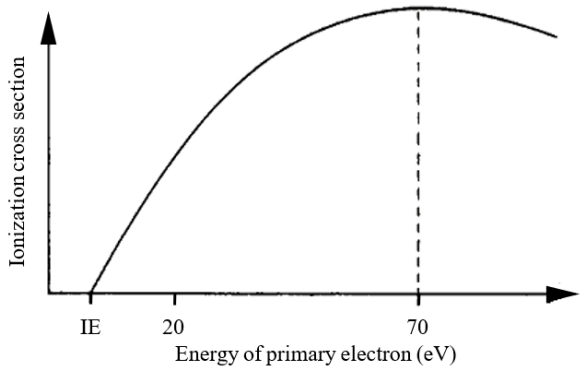

Figure 2.17: Generalized ionisation efficiency curve for Electron Ionisation (adapted from [73])

However, EI with energies less than 70 eV can be useful for reducing the extent of fragmentation of molecules, and values of 12-15 eV are often used. However, owing to the reduction in ionisation cross-section at lower electron energies, this approach is a compromise between a greater yield of higher mass ions and sensitivity [74]. Notice, in terms of kinetics, the ions follow the same rules as those presented for the ions resulting from a soft ionisation.

2.3.3 Transfer optics

Regarding INFORMS, the transfer optics is similar to that of the PTR-ToF-MS but at a smaller scale. However, regarding the MS-200, the ion source is within the spectrometer housing and there are no transfer optics, which results in a lower mass resolution but makes the design compact such that the whole instrument fits in a small suitcase and weighs 22 kg.

2.3.4 Time of flight mass spectrometer

2.3.4.1 ToF source and flight tube (including reflectron)

The pulser unit, the flight tube and the reflectron processes of both EI instruments are like those of the PTR instrument. In both EI-ToF-MS instruments, the design is at a smaller scale. However, regarding the MS-200, the mass spectrometer, as explained, incorporates the ionisation area as well.

2.3.4.2 Detector

Compared to the research PTR, both INFORMS and MS-200 instruments detect ions through a discrete dynode detector as shown in Figure 2.18 [75]:

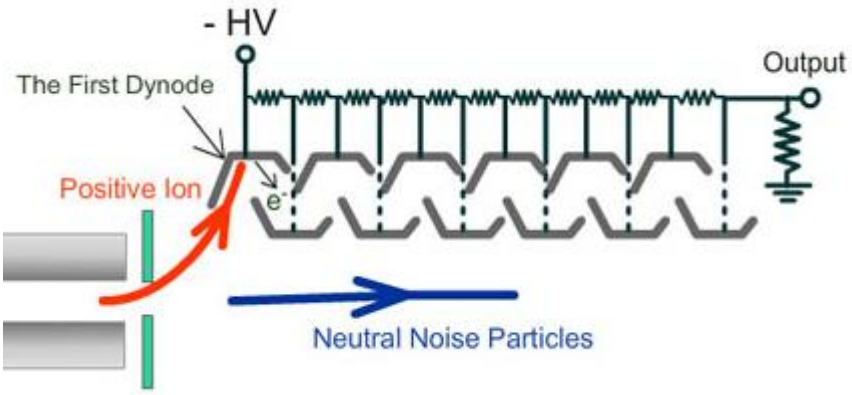

Figure 2.18: Discrete dynode detector schematic used for both transportable EI-ToF-MS from Kore [75]
HV stands for high voltage

This detector consists of a series of electrodes, called dynodes, across which appropriate voltages are applied using a high voltage power supply and a potential divider to create the cascade process [76]. The detector built in both EI instruments has 25 dynodes, so that 100 V between adjacent electrodes produces 2.5 kV across the entire detector. The first electrode has the highest negative potential, which then continuously increases (becoming less negative) across the chain until the last one, where ground potential is applied. This way, any electron emitted from the impact of an ion on the first electrode (consequently called the conversion dynode) is accelerated to the second electrode (as attracted to the higher positive potential). Each dynode must be coated with a material that has a secondary coefficient greater than 1, such as a thin aluminium oxide surface coating. The advantage of the discrete dynode detectors, compared to a MCP, is their stability in air being consequently much less affected by water molecules. The gain is defined through the same way than for a MCP in equation E 2.85 and can lead to amplification factor up to 10^7-10^8 [76].

CHAPTER 3: DEVELOPMENT AND IMPLEMENTATION OF NEW ION-FUNNELS INTO A PTR REACTOR

3.1 Introduction and initial concepts

Since their appearance in the literature in the mid-1990s, the function of the PTR reactor (also known as the 'drift tube' or 'collision cell') has been to ionise analyte molecules for subsequent detection in the mass spectrometer [77, 78]. An example of a typical early reactor that was designed by Kore for their early SCI-ToF-MS instruments is schematically represented in Figure 3.1. This was comprised of a series of electrodes spaced, 3 mm apart, each with a 40 mm orifice size and connected by an in-vacuo resistor stack to create a linear electric field. A vacuum pump at the base of the reactor is used to maintain a gas flow through the reactor from the analyte input to the exit aperture.

The 'Glow Discharge' (GD) is a hollow cathode ionisation source. The 'Source Drift' (SD) is a region where ions produced by the discharge undergo further reactions with water molecules to produce the H_3O^+ 'terminal ion'; the reagent ion that is the desired product for proton transfer.

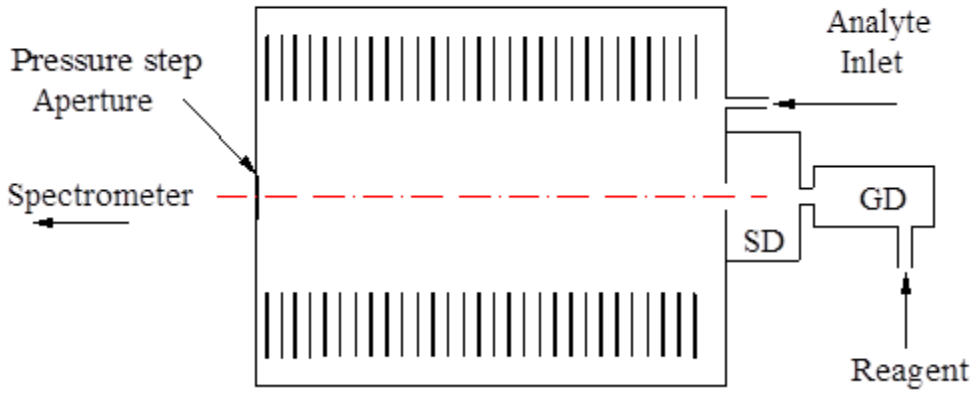

Figure 3.1: Schematic of the first SCI-ToF-MS reactor designed by Kore
GD and SD respectively stand for Glow Discharge and Source Drift.

The combination of the electric field (E in V/cm) and the viscous flow of buffer gas channels ions and neutral molecules to the exit orifice of the reactor. At the operational pressure

(~ 1-2 mbar), viscous flow occurs and conventional electrostatic ion optic methods are not applicable. At these pressures in the reactor, ions undergo ~ 2,000 collisions with the neutral gas during their transit across the Kore reactor, and thus, provided there is an excess of the reagent ions, the conversion of the analyte molecule to an ion is all but guaranteed (subject to suitable ion energetics). The parameter E/n, where n is the neutral number density in the reactor, is usually quoted as that determines the average ion-neutral collision energy within the reactor, and it is a parameter that is used widely in the literature in chemical ionisation techniques [79, 80]. However, it became clear from measurements made by Kore at the start and end of this reactor that a considerable proportion of the ions (> 95 %) in the first reactor were being lost, presumably due to space charge effects repelling ions to the electrode walls [81].

Ion-funnels using RF (Radio Frequency) fields[1] have been reported in the literature as a means to increase the transmission of ions at relatively high pressures [26]. In seeking to improve the sensitivity of the existing PTR-ToF-MS, Kore decided to incorporate an ion-funnel within the existing reactor, since the typical operating pressures of 1-2 mbar are similar to those reported in the literature for these other ion-funnels [82, 83]. The first ion-funnel designed by Kore, schematically shown in Figure 3.2, was delivered to Leicester University in 2013 and had a series of progressively reducing orifice diameters in the second half of the electrode stack within the reactor. These electrodes were also connected by two capacitor stacks connecting alternate plates on top of the resistor stack to permit the creation of RF fields as presented in Figure 3.2.

[1] The use of the RF (electric) field is always in addition to the DC electric field and its use represents the **RF mode** whereas the use of the DC electric field only is the **DC mode**. It will be assumed that talking about the RF mode, the collisional damping is considered.

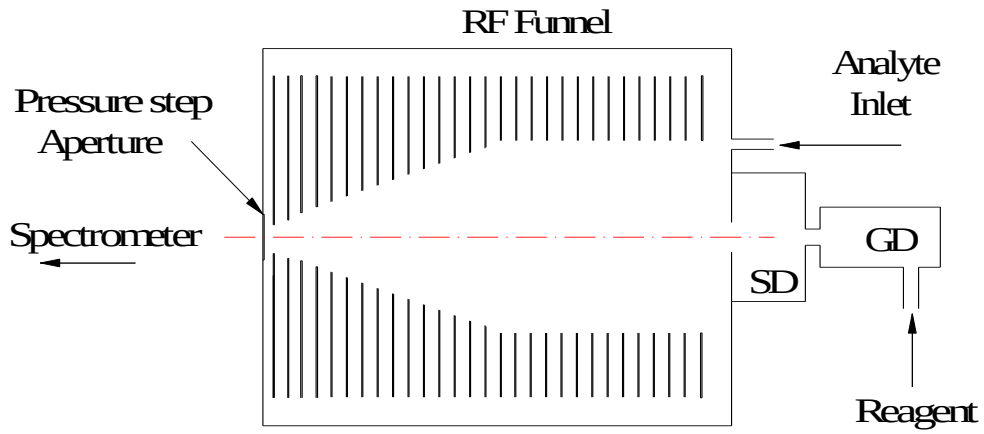

Figure 3.2: Schematic of the first RF funnel designed by Kore within a SCI-ToF-MS reactor GD, SD and RF respectively stand for Glow Discharge, Source Drift and Radio Frequency

The first RF funnel device from Kore worked well enough, with, as mentioned previously, remarkable increases in analyte detection by factors of 20-50 [77]. After such success, the Leicester researchers applied this technology to their applications, but no attempts to improve the performance nor to understand the properties of the funnel were made. By the 2010s, the ion-funnels were well integrated in commercially available PTR-MS instruments [77, 84, 85]. Ion-funnels are now used in other analytical techniques to reduce ion transmission losses at these relatively high pressures; for example, electrospray ionisation (ESI) techniques [42, 43].

However, there is always a desire to improve upon the performance of early designs, partly as demanded by environmental applications and (it will be admitted) as a result of commercial competition. This research programme has been tasked with exploring possible evolutions of the RF funnel design to increase sensitivity yet further.

3.2 New ion-funnels – Evolution of concept

An interesting aspect of this challenge has been to remain aware of commercial aspects of instrumental development i.e., to what extent can improvements be made with minimal

materials and engineering design costs. Thus, the first challenge was to consider what changes could be made that did not entail new RF drive electronics, nor a complete re-design of the reactor cell.

The inspiration for the first round of developments came from some simple geometric considerations of the funnel design and a simple ‘mental model’ of how the RF acts to re-direct ions away from the electrodes and back into the funnel. The last few plates of the ion-funnel have been found to be critical, and so in a second phase the last section of the funnel has been re-designed to create what is referred to as a separate 'micro-funnel'.

Four evolutions of the ion-funnel (Marks II to V) have been developed and tested in this project so far. A simple schematic is given in Figure 3.3 to show the evolution from Mark I to Mark V.

For the first PTR reactor (parallel electrodes and no funnel), there was always an intuition that space charge did not drive ions into the electrode walls until the second half of the reactor. Ion modelling using the SIMION program by Kore in 2012/2013 also pointed to this conclusion. SIMION was designed for ion modelling at high vacuum, and modelling ion trajectories in this viscous flow regime, and with significant space charge effects, is not straightforward; the results are far less reliable than the high vacuum case with molecular flow and no space charge. Therefore, the Mark I reactor has a funnel in the second half only. The transmission gains with Mark I confirmed the intuition and modelling. The Mark I funnel design was conservative in that it preserved the large inner diameters of the first half of the reactor. The question would be to know if the inner diameter of that first half could be reduced significantly without losing ions to space charge effects even before they had entered the funnel. The motivation for this was to create a lower angle inside the ion-funnel, i.e. a lower funnel inner-diameter gradient. From a simple geometric consideration, ions having a direction of

travel on axis meet the RF field at a lower angle of incidence, such that a greater proportion of the ions that change direction as a result of encountering the field are directed towards the centre of the funnel or towards the exit aperture.

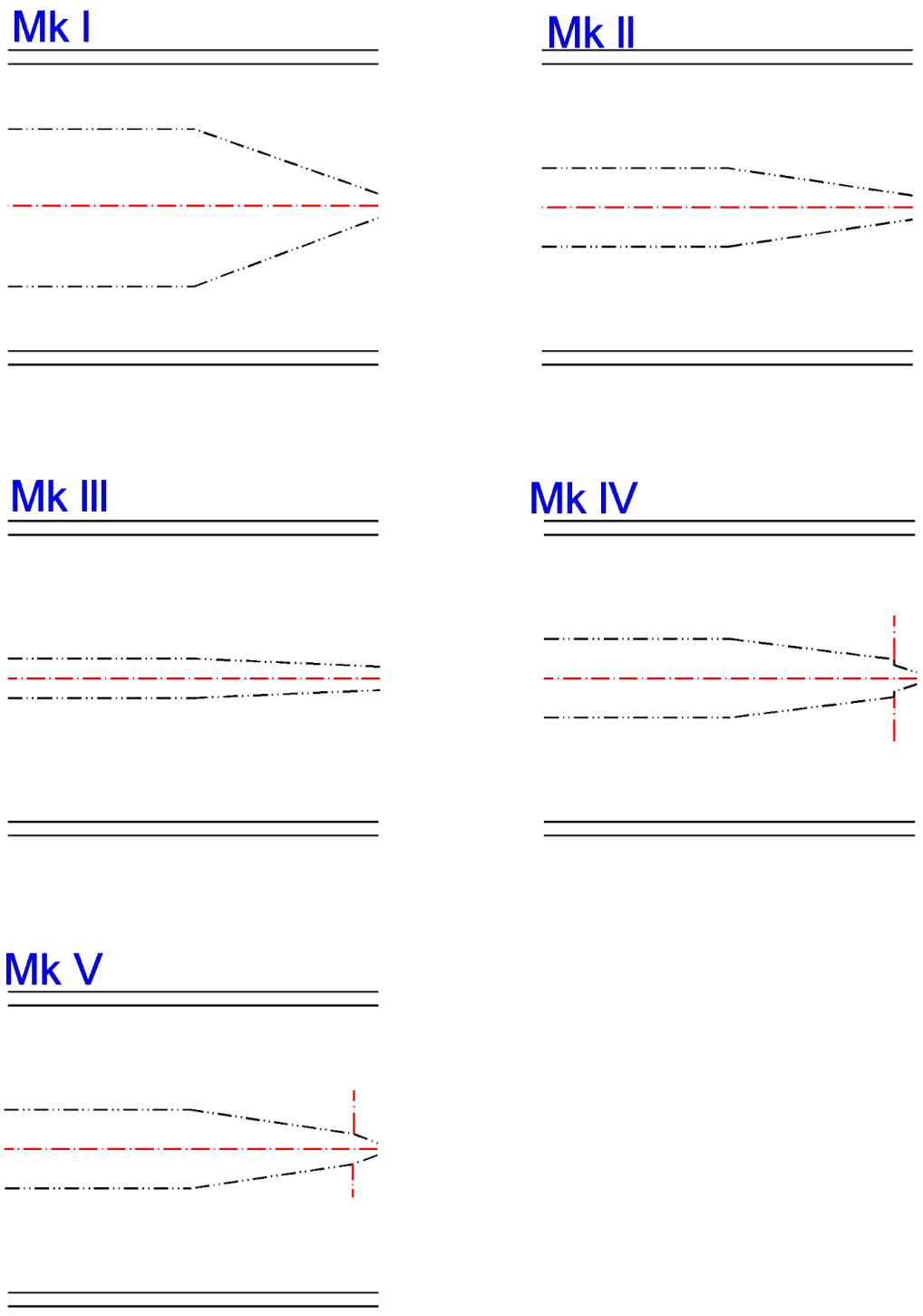

Figure 3.3: Simplified schematics of the Marks I-V PTR ion-funnels designed by Kore

The Mark II electrode stack thus had a first section (no funnel) with a reduction in inner diameter by a factor of two, consequently reducing the inner diameter gradient in the second section. To use the existing RF drive electronics with little or no modification, it was necessary to preserve the capacitance of the funnel electrodes. This was achieved by the simple expedient of preserving the area of each circularly symmetric electrode in the RF section. Since the Mark II funnel electrodes would otherwise have a much greater area than each equivalent electrode in Mark I, the electrodes were designed with cut-outs to keep the areas identical as shown in Figure 3.4.

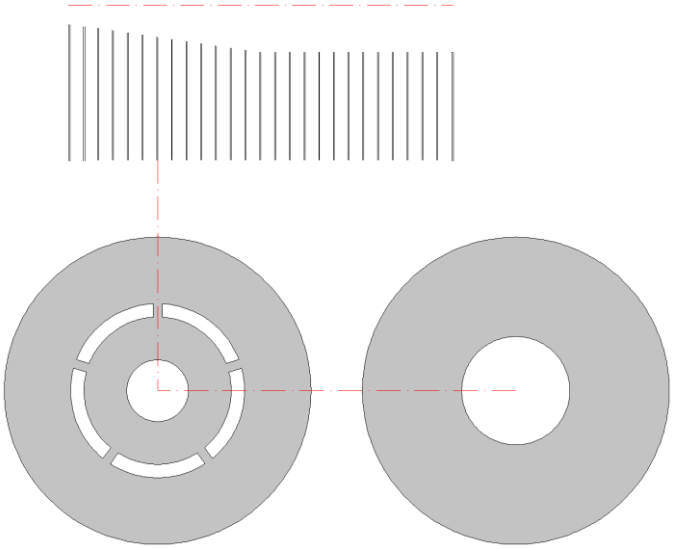

Figure 3.4: Presentation of the principle of electrodes surface preservation within the ion-funnels, independently of the inner diameter

The RF amplifier required minimal re-tuning for resonance, and the strategy of preserving electrode areas was justified. Encouraged by these gains, it was logical to continue, and so Mark III had the inner diameter of the first section reduced by another factor of two, resulting in an even shallower funnel inner-diameter gradient. Once again, new electrodes for the funnel were created that had the preserved area of equivalent electrodes from Mark I.

Mark I to Mark III funnels all have a feature where the last two electrodes of the RF funnel are physically separate from the rest of the electrode stack, and furthermore the last electrode can have its RF amplitude varied independently of the other electrodes in the funnel. Whereas the optimum amplitude was ~ 200 volts peak-to-peak for the rest of the funnel (at a frequency of ~ 700-720 kHz), the optimum RF amplitude for this last electrode for best

transmission of ions to the exit was approximately half of the other funnel electrodes. The tuning of this last plate is sensitive, and it became even clearer than before that this last section of the funnel was very critical. This is unsurprising, since it is likely that at this point all ions must pass through the RF field. Consequently, for the next evolution in the funnel, the last two electrodes of the old funnel were replaced each by three new electrodes, more closely packed, and with a smaller exit from this funnel as shown in Figure 3.5. The RF drive electronics have been modified to provide not only the standard RF amplitudes for most of the RF funnel electrodes, but also two separate RF amplitudes to this 'micro-funnel' where the distance between consecutive electrodes has been reduced. Mark IV was created using a modified version of Mark II according to some new ion modelling by Dr Steve Mullock at Kore, but with this extra micro-funnel in the end section. Because of the ease with which the electrode stack can be removed as a stand-alone unit, Mark V came about by simply experimenting with placing the original Mark II electrode stack on top of the new micro-funnel.

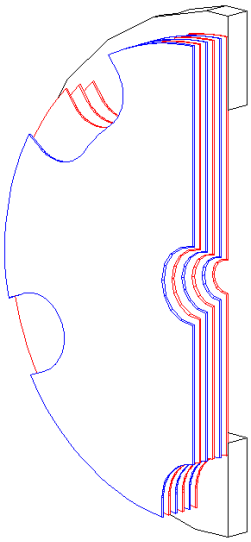

Figure 3.5: micro-funnel used in Marks IV and V ion-funnels

3.3 First measurements for enhanced sensitivity

3.3.1 Probe molecule – Benzene

The molecule of the ion-funnel study is benzene (whose structure is presented in Figure 3.6), key details of which and associated important ions are reported in Table 3.1 [86, 87].

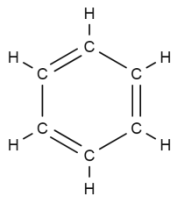

Figure 3.6: Structure of benzene

Table 3.1: Properties of benzene resulting in its protonation and charge exchange inside the PTR reactor [86, 87]

Formula	Benzene			Intensity (%)
Gas phase ion energetics data				
C_6H_6	Proton affinity	759	kJ/mol	N/A
	Ionisation energy	9.24	eV	N/A
Charge exchange				
$C_6H_6^+$	Average molecular weight	78.112060	g/mol or u	N/A
	Isotopic mass at m/z 78 (C_6H_6)	78.046950	g/mol or u	100
	Isotopic mass at m/z 79 ($^{13}CC_5H_6$)	79.050310	g/mol or u	6.6
Proton transfer				
$C_6H_7^+$	Average molecular weight	79.120000	g/mol or u	N/A
	Isotopic mass at m/z 79 (C_6H_7)	79.054775	g/mol or u	100
	Isotopic mass at m/z 80 ($^{13}CC_5H_7$)	80.058130	g/mol or u	6.6

This molecule was selected for the following reasons:

- Benzene has a proton affinity greater than that of water but less than the water dimer, so only protonation by H_3O^+ is possible energetically.
- Following proton transfer resulting in $C_6H_7^+$ or charge transfer resulting in $C_6H_6^+$, the product ion is very stable, and hence will be the dominant product ion species. Indeed, the Kekulé structure presented in Figure 3.6 shows alternating single and double carbon-carbon bonds. However, the more realistic interpretation of these bonds is the relocation of the π electrons between the six carbon atoms. That is why benzene is sometimes presented with a circle inside its structure.

  The consequence of its strength is that in most cases, the fragmentation of benzene can be neglected, and the parent molecule only can be considered, which simplifies the study.

Table 3.1 also shows an ionisation energy lower than the recombination energy of O_2^+, namely 12.62 eV, meaning benzene can undergo charge exchange with O_2^+ (or any reagent ion whose recombination energy is greater than the ionisation energy of benzene). Although a low level of charge exchange is observed, under typical conditions of operation the protonated molecule remains predominant. Nevertheless, to be rigorous, m/z 78 has also been monitored to subtract its isotope contribution at m/z 79 and 80 as presented in Figure 3.7:

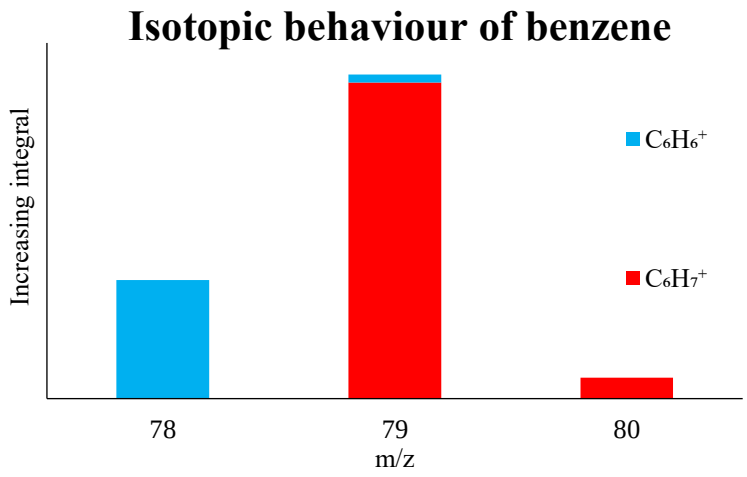

Figure 3.7: Isotopic distribution of both benzene parent molecules at m/z 78-80 making possible to subtract any signal coming from the charge-exchanged benzene to that of the protonated benzene

All the ions studied in these measurements are presented in Table 3.2. In order to characterise the mixed ionisation mode (proton transfer from H_3O^+ and N_2H^+ compared to charge exchange from NO^+ and O_2^+) and the softness of the ionisation ($H_3O^+/H_3O{\cdot}H_2O^+$ ratio) as a function of the ion-funnel, the main reagent ions have also been studied. The ions presenting a proportion of 2 % or more in at least one reactor generation have been considered.

Table 3.2: Ions studied within the ion-funnels experiments for enhanced sensitivity involving benzene

Group	Name	Code	Formula	Nominal mass x / m/z
Reagent ions	Hydronium/ Protonated water	N/A	H_3O^+	19
	Protonated nitrogen	N/A	N_2H^+	29
	Nitrogen oxide	N/A	NO^+	30
	Oxygen	N/A	O_2^+	32
	Protonated water dimer	NA	$H_3O^+ \cdot H_2O$	37
Benzene ions	Butyl fragment 1	$(M\text{-}C_2H_4)^+$	$C_4H_2^+$	50
	Butyl fragment 2	$(M\text{-}C_2H_3)^+$	$C_4H_3^+$	51
	Protonated benzene – H_2	$(MH\text{-}H_2)^+$	$C_6H_5^+$	77
	Charge-exchanged benzene	M^+	$C_6H_6^+$	78
	Protonated benzene	MH^+	$C_6H_7^+$	79

3.3.2 Experimental conditions

Sensitivity was chosen as a key parameter to compare the performance of the different funnels. Accordingly, some experimental conditions were fixed, while some instrument tuning parameters were adjusted to optimise sensitivity. Below is a summary of the chemical and acquisition parameters:

- Analyte: 100 ppbv of benzene diluting a standard bottle solution of 1 ppmv of benzene in dry nitrogen with a standard bottle of dry nitrogen.
- Mass species monitored: Mass 79, protonated benzene, $C_6H_7^+$ and its ^{13}C isotope on one carbon, mass 80, $C_5{}^{13}CH_7^+$ (~ 6.6 % of the intensity of mass 79).
- Reagent ion used: H_3O^+ for proton transfer
- Frequency of ToF: 20 kHz (50 µs ToF cycles)
- Data acquisition time: 10 s

The reactors parameters are listed in the Table 3.3:

Table 3.3: Reactors parameters during the ion-funnels experiments related to sensitivity enhancement involving benzene

Reactor generation	**Parameters <u>independent</u> of the reactor generation and the mode**					
All	**T**			**Water vapour flow in the ion source**		
	ºC			**sccm**		
	23.6			< 0.1		
	Parameters <u>dependent</u> of the reactor generation and the mode					
	DC mode			**RF mode**		
	P	**E**	**E/n**	**P**	**E**	**E/n**
	mbar	**V/cm**	**Td**	**mbar**	**V/cm**	**Td**
I	1.40	42.5	124	1.40	7.06	21
II	1.70	42.5	102	1.50	12.5	34
III	1.60	31.8	81	1.60	17.8	46
IV	1.60	37.2	95	1.20	14.6	50
V	1.60	37.2	95	1.50	12.5	34
	RF Ion-funnel tunings					
	$P_{26\text{-}28}$			**P_{29}**		
	V_{PP}	**ν**		**V_{PP}**	**ν**	
	V	**kHz**		**V**	**kHz**	
I	210	745		105	745	
II	215	745		131.5	745	
III	219	750		106.5	750	
	$P_{26\text{-}27}$		**P_{28s}**		**P_{29s}**	
	V_{PP}	**ν**	**V_{PP}**	**ν**	**V_{PP}**	**ν**
	V	**kHz**	**V**	**kHz**	**V**	**kHz**
IV	208	708	63	708	31	708
V	208	708	64	708	32	708

Throughout this thesis, the electrodes in the funnels are referred to by their number in the electrode stack. Thus, P_1 is the first electrode in the stack and P_{28} is the 28th plate in the stack. Notice that for the specific case of the micro-funnel, the electrodes are names P_{28s} and P_{29s} as they are composed of a group of three plates each.

The value of E/n that is reported when using the RF mode is only a value that applies to the first section of the reactor. There is no single, unique value of E/n in the second section with the funnel. For funnels I to III, once the RF circuit was tuned for resonance, the amplitude of

the RF was fixed, but the amplitude on P_{29} could be adjusted to optimise sensitivity. For funnels IV and V, it was possible to change the RF amplitude on both P_{28s} and P_{29s}.

3.3.3 Results and discussions

3.3.3.1 Sensitivity – DC mode – m/z 79 only

Figure 3.8 represents the sensitivity for m/z 79 only as a function of the ion-funnel in DC mode.

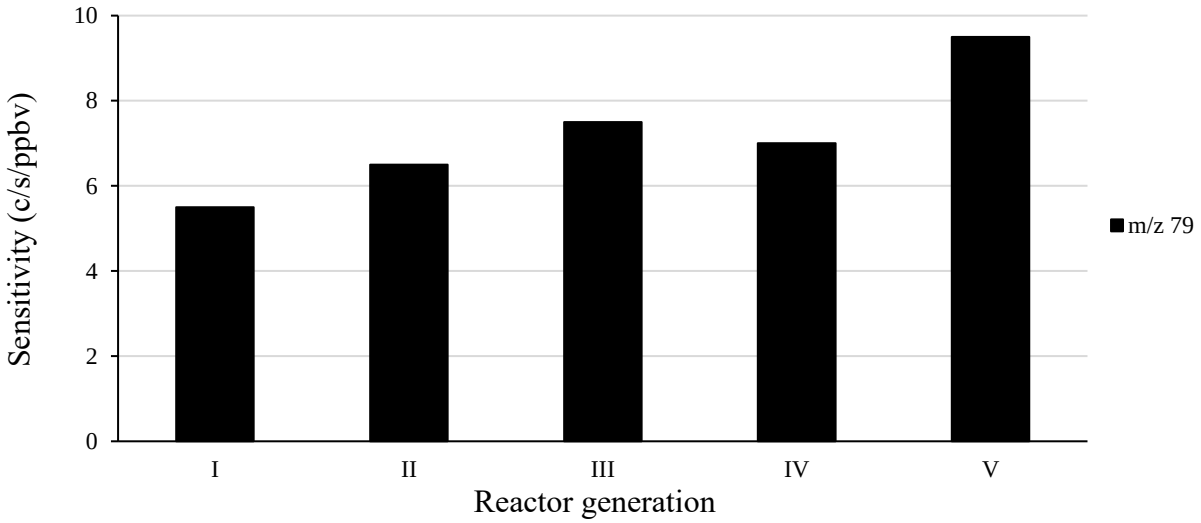

Figure 3.8: Sensitivity for protonated benzene in nitrogen as a function of the PTR ion-funnel in DC mode

Except for Mark IV, there is a continuous increase of signal from Marks I to V. These experiments highlight the fact geometrical considerations of the ion-funnel already impact the sensitivity of the instrument in DC mode.

3.3.3.2 Sensitivity – RF mode

Figure 3.9 and Figure 3.10 respectively represent the sensitivity of the instrument for the main benzene ions and the count rate of the main reagent ions when analysing benzene.

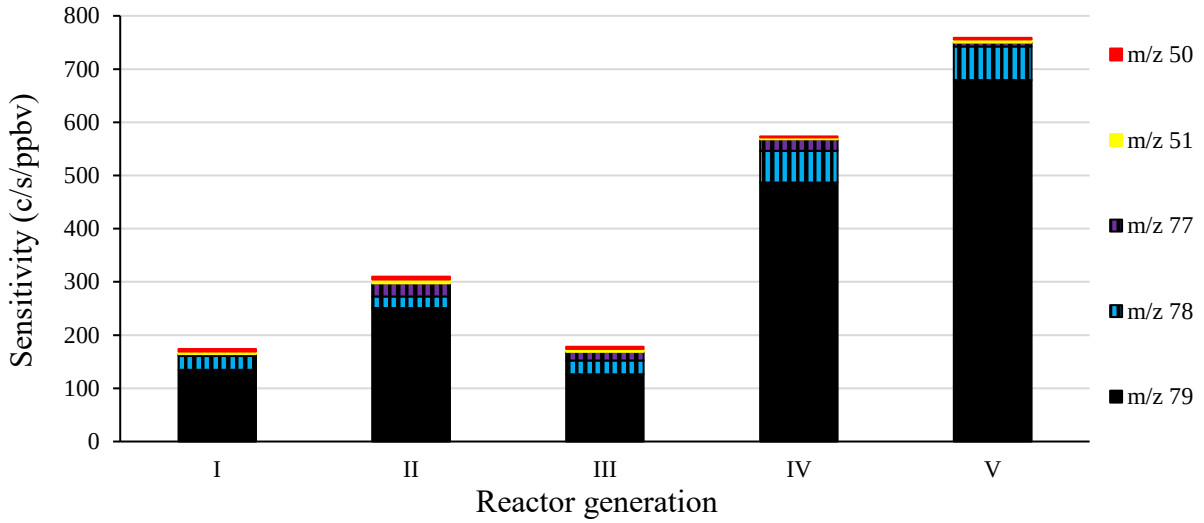

Figure 3.9: Sensitivity for the main benzene ions as a function of the PTR ion-funnel in RF mode

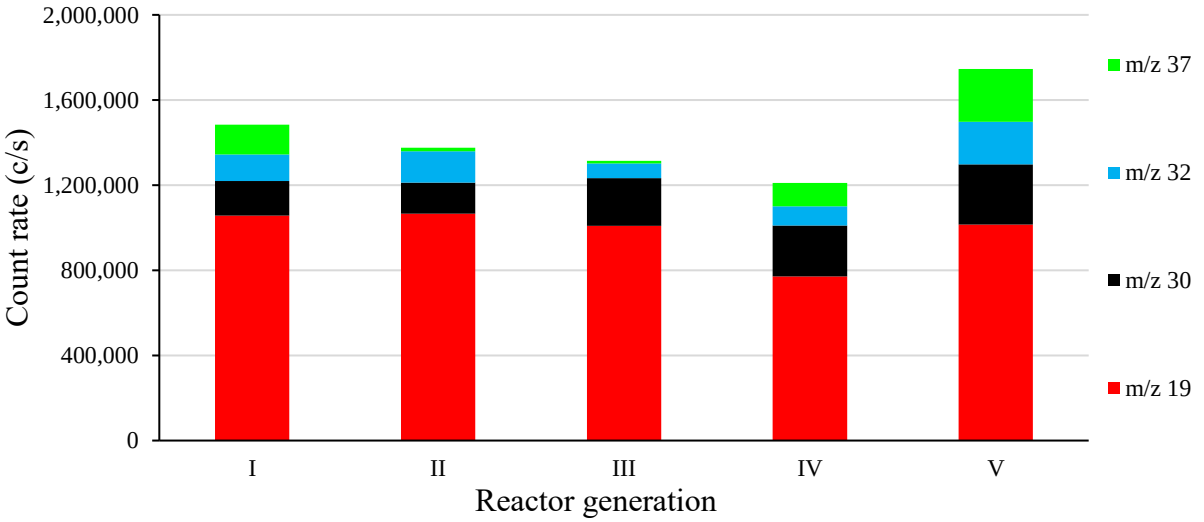

Figure 3.10: Count rate for the main reagent ions (analysing benzene) as a function of the PTR ion-funnel in RF mode

In Figure 3.9, the evolution from Marks I to V gives an enhancement factor greater than 6. In Figure 3.10, the N_2H^+ signal (at m/z 29) is not displayed. Its intensity could not be determined because (a) the main peak was saturated and (b) the isotopic peak at m/z 30 was masked by an intense NO^+ signal and at m/z 31 mostly by $^{15}NO^+$ signal. Although the intensity of N_2H^+ is not known and N_2 has a proton affinity of 493.8 kJ/mol [88] (making N_2H^+ a potential proton donor to benzene and water) the role of protonated nitrogen could be ignored if produced after the

drift tube. It is also noticeable that in any generation, the RF mode provides a mixed mode ionisation through non-negligible O_2^+ and NO^+ signals (respectively at m/z 32 and 30).

Within each plot in Figure 3.11 and Figure 3.12 is shown, respectively for the DC and RF modes, for m/z 79 only, typical, reproducible performance, compared to the maximum that was obtained in Figure 3.8 and Figure 3.9.

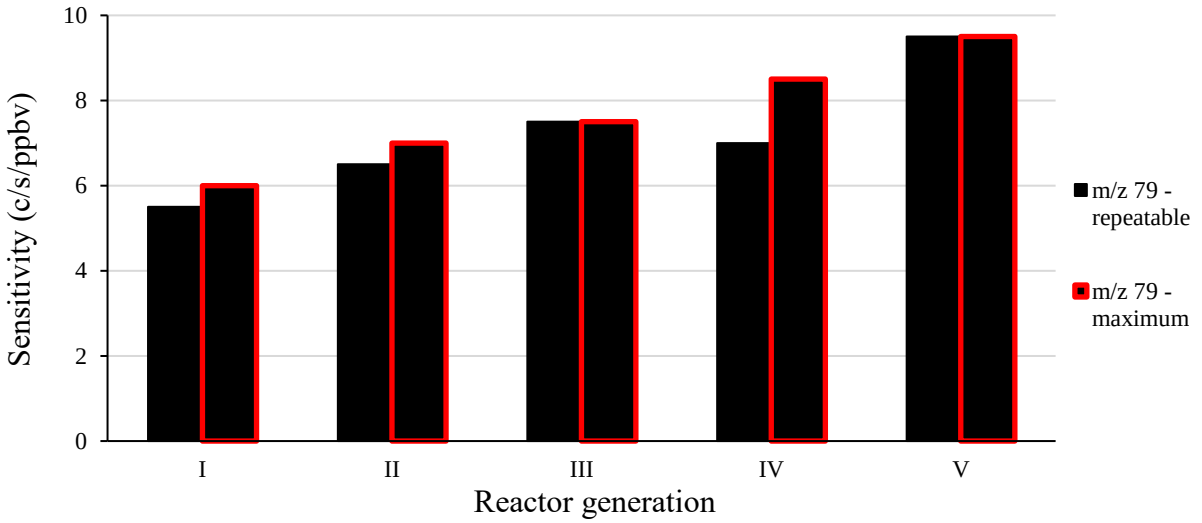

Figure 3.11: Maximum and reproducible sensitivities for protonated benzene as a function of the PTR ion-funnel in DC mode

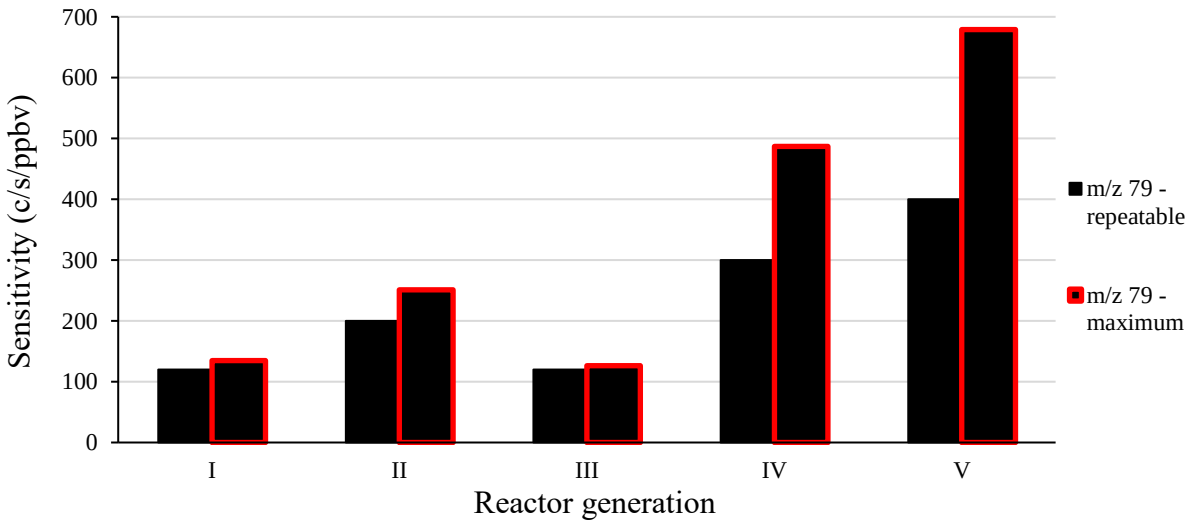

Figure 3.12: Maximum and reproducible sensitivities for protonated benzene as a function of the PTR ion-funnel in RF mode

In order to meet the instrument specification, the PTR fitted with a Mark I funnel was required to achieve a sensitivity in DC and RF modes in the respective ranges of 5 c/s/ppbv, i.e. 5000 c/s/ppmv and 100 c/s/ppbv.

3.3.3.3 Effective potential – V^*

The effective potentials, described in the subsection 2.2.5.3 of chapter 2, were determined to make possible the calculation of effective fields through the same way that DC potentials provide data for DC electric fields in the reactors. The ions being dragged as a viscous flow through the reactors, the collisional damping inside the RF section, represented by γ, needed to be considered.

The different experimental conditions for each ion-funnel resulted in different values of γ (calculated through the equation E 2.59 and considering a rounded value of the ion mobility of protonated benzene in nitrogen of 2 $cm^2/(V \cdot s)$ [89]) as shown in Table 3.4.

Table 3.4: γ(protonated benzene in nitrogen) as a function of the PTR ion-funnel in RF mode

Reactor generation	**I**	**II**	**III**	**IV**	**V**
γ(protonated benzene in N_2)	0.27	0.24	0.22	0.31	0.22

Figure 3.13-Figure 3.17 represent the effective potential V^* (considering γ through the equation 2.56) for protonated benzene in nitrogen within respectively Marks I-V ion-funnels.

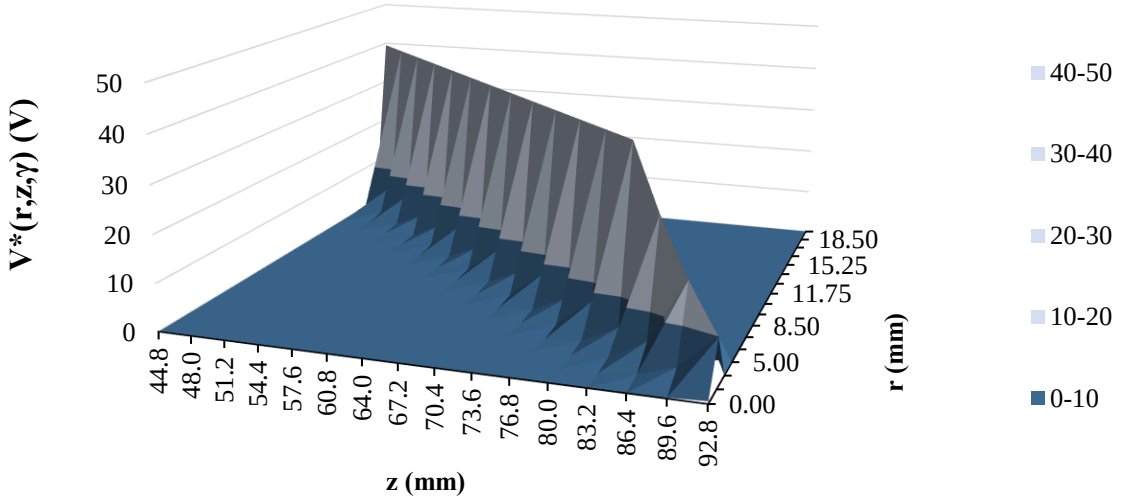

Figure 3.13: Effective potential applied to protonated benzene in nitrogen within Mark I PTR ion-funnel under RF field

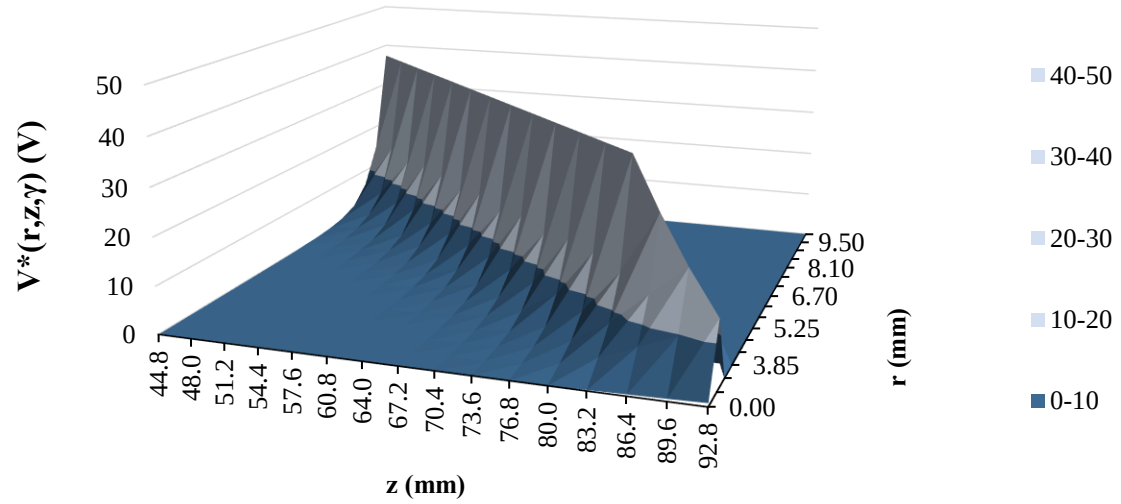

Figure 3.14: Effective potential applied to protonated benzene in nitrogen within Mark II PTR ion-funnel under RF field

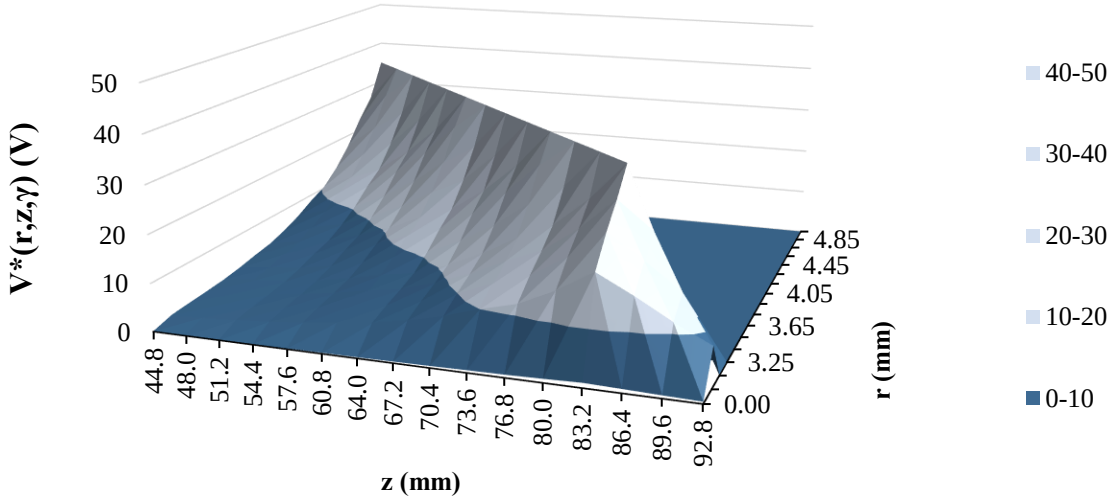

Figure 3.15: Effective potential applied to protonated benzene in nitrogen within Mark III PTR ion-funnel under RF field

For Marks IV and V ion-funnels, the micro-funnel is introduced for the last plates, i.e. from 86.4 mm (section at a different scale than the rest of the ion-funnel for the purpose of details study).

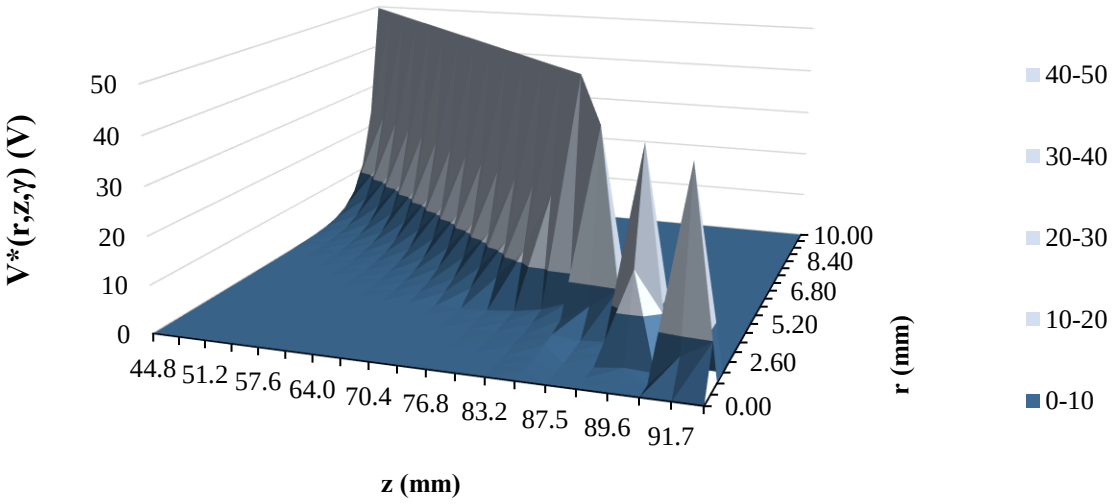

Figure 3.16: Effective potential applied to protonated benzene in nitrogen within Mark IV PTR ion-funnel under RF field

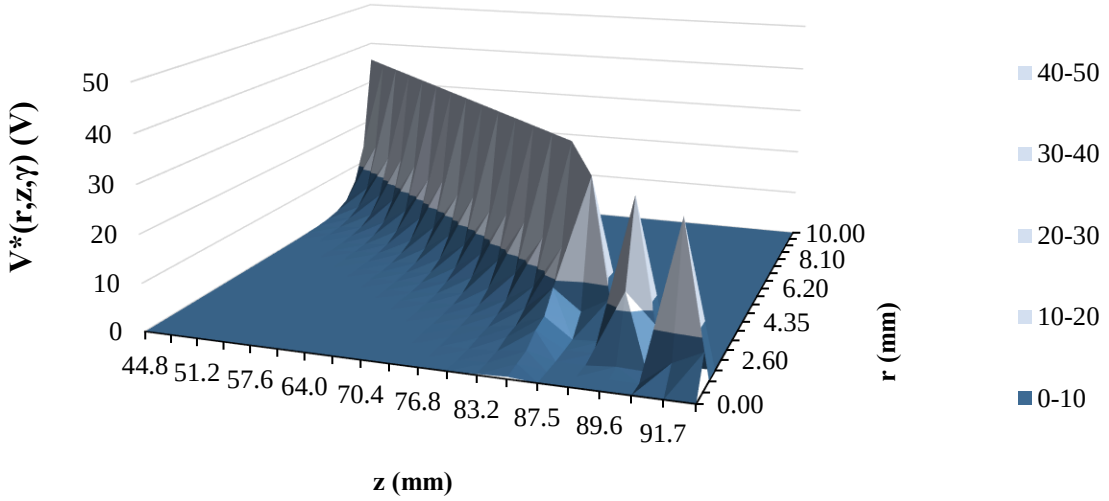

Figure 3.17: Effective potential applied to protonated benzene in nitrogen within Mark V PTR ion-funnel under RF field

Notice that for plots in Figure 3.13 to Figure 3.17 there is no attempt to represent the more realistic transition of potentials between the electrodes. Using the example of Mark III, Figure 3.18 represents a 'more realistic' representation of the values of V^* than Figure 3.15 where it is now possible to notice the periodical oscillation of V_{trap} along the centre (i.e. at r = 0 mm).

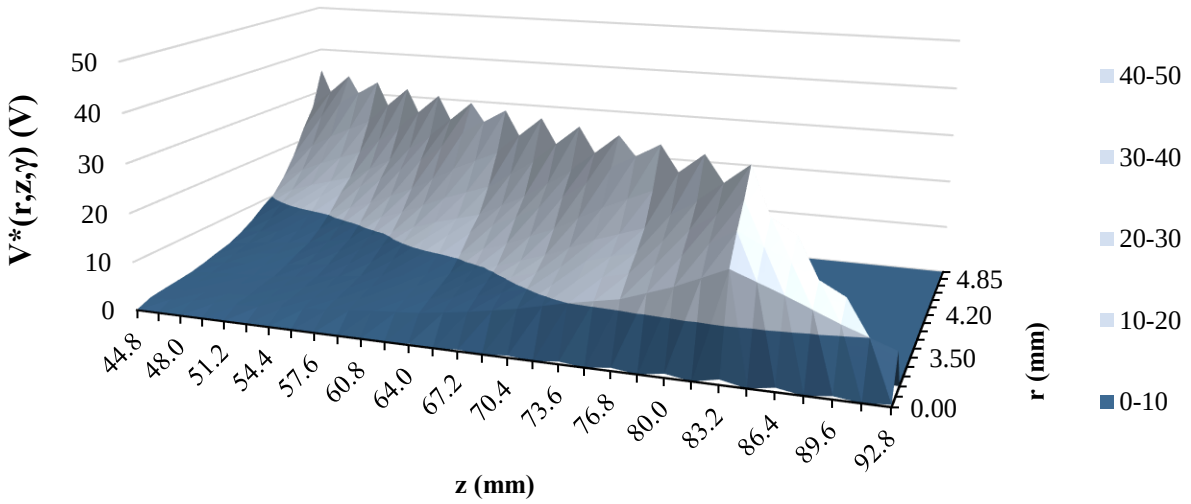

Figure 3.18: 'More realistic' effective potential evolution applied to protonated benzene in nitrogen within Mark III PTR ion-funnel under RF field

V^* increased from Mark I to Mark III. However, the last millimetres underwent a reduction of effective potential, where, for Marks IV and V, the micro-funnel enhanced the effective potential.

3.3.3.4 Confining effective field

As explained in the calculations of chapter 2, E^* is the derivate of V^*. As the function of the confining effective field is to direct the ions towards the centre of the reactor it was logical to consider the derivate of V* as a function of the radius r, as detailed in the equation E 2.63. Figure 3.19-Figure 3.23 represent the absolute value of the confining effective field E^* (considering γ) for protonated benzene in nitrogen within respectively Marks I-V ion-funnels.

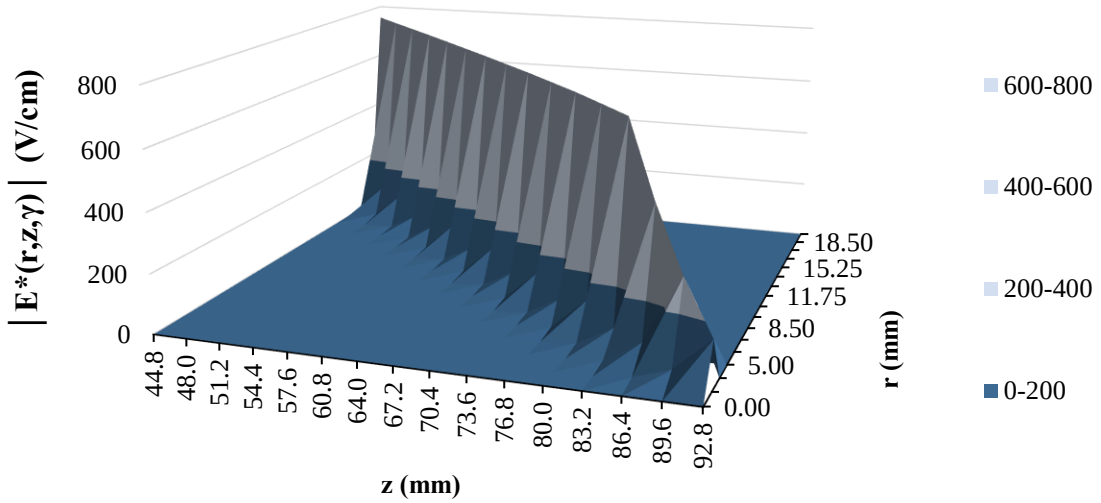

Figure 3.19: Absolute value of the effective confining field applied to protonated benzene in nitrogen within Mark I PTR ion-funnel under RF field

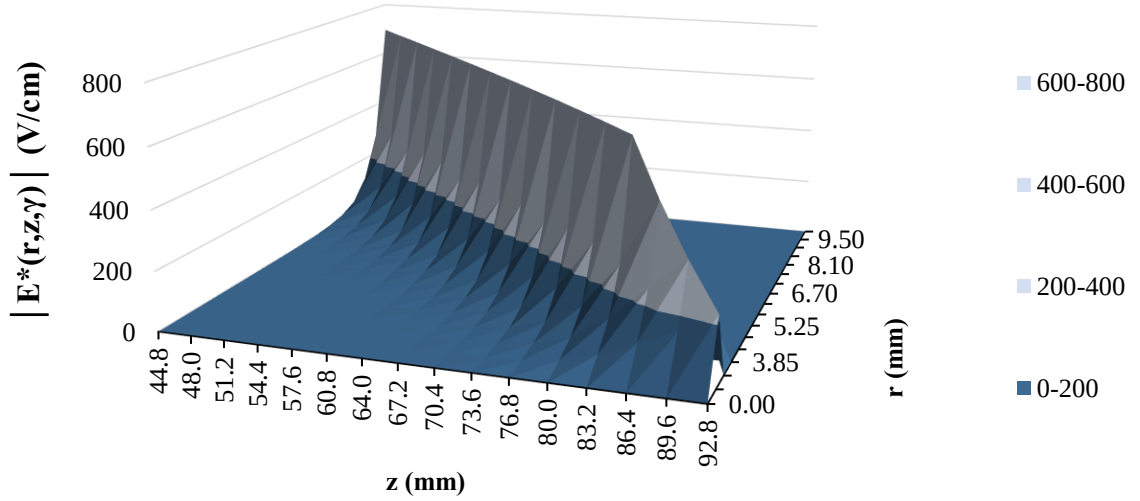

Figure 3.20: Absolute value of the effective confining field applied to protonated benzene in nitrogen within Mark II PTR ion-funnel under RF field

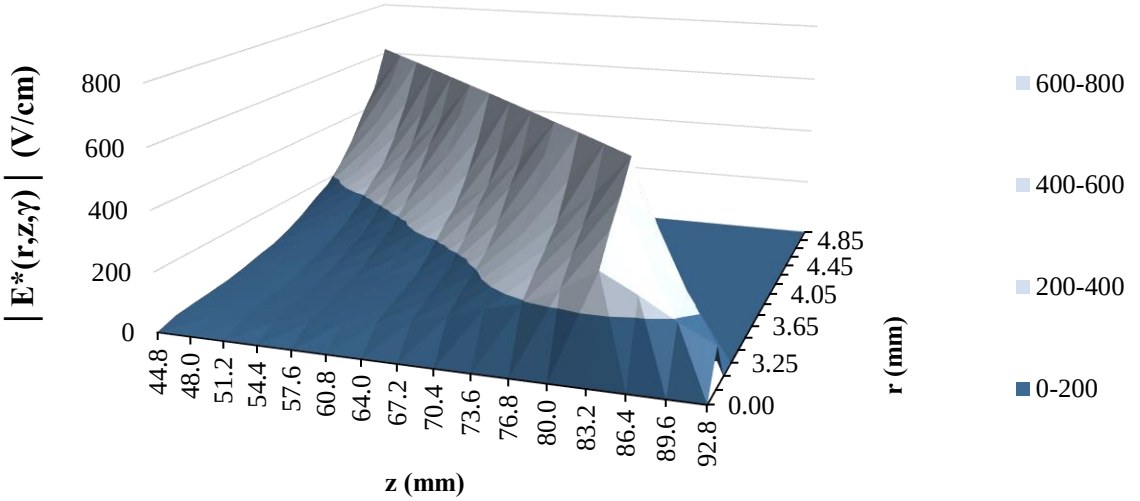

Figure 3.21: Absolute value of the effective confining field applied to protonated benzene in nitrogen within Mark III PTR ion-funnel under RF field

In the above plots for the Marks I to III reactors, the data points for the values of E* on the z-axis are equidistant, because the electrodes throughout the reactor are all equidistant. However, in the plots for Marks IV and V which follow, the electrodes in the micro-funnel are closer together and thus, for the purpose of clarity, the data points for E* on the z axis are stretched out in the micro-funnel section, where data point separation changed from 3.2 mm to 1.05 mm.

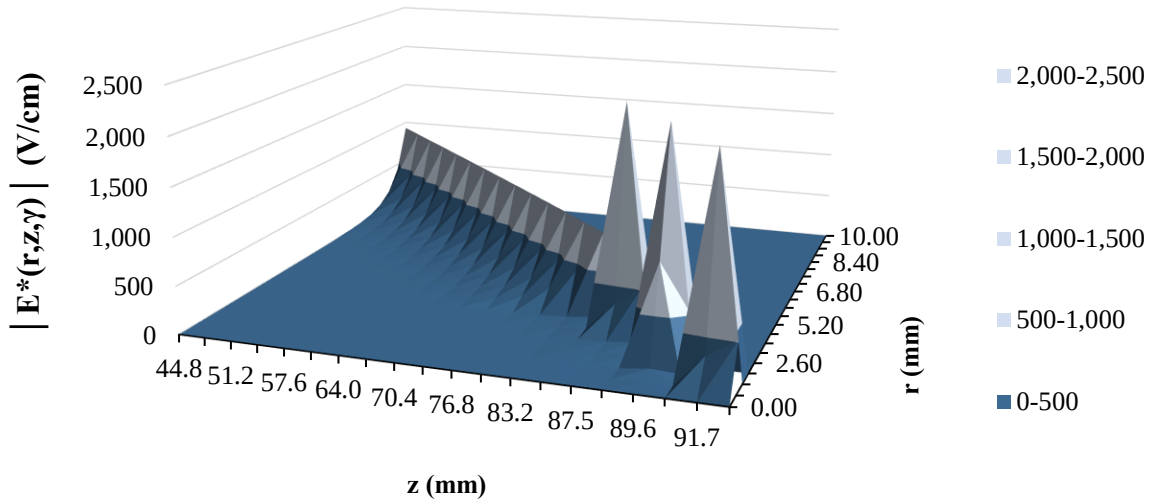

Figure 3.22: Absolute value of the effective confining field applied to protonated benzene in nitrogen within Mark IV PTR ion-funnel under RF field

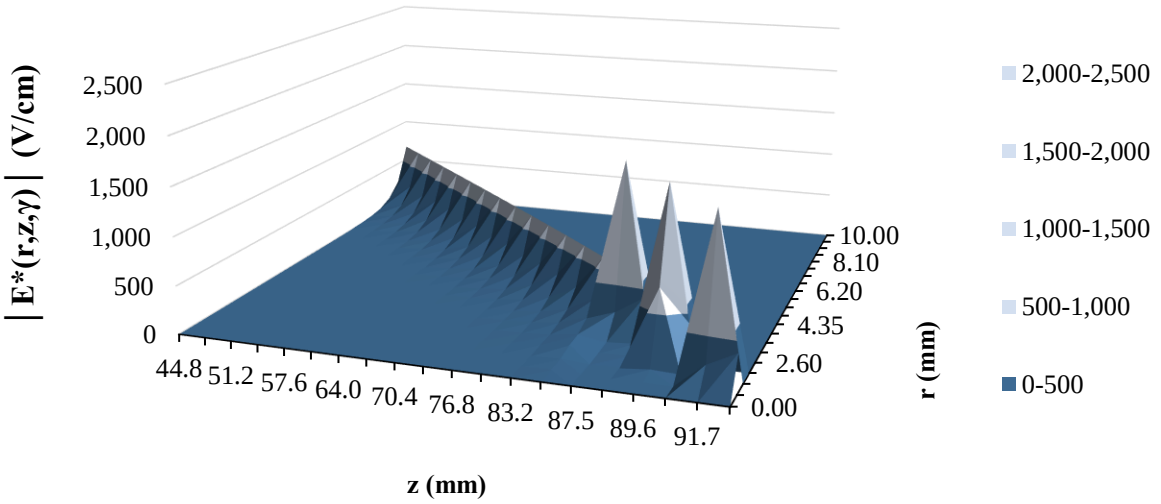

Figure 3.23: Absolute value of the effective confining field applied to protonated benzene in nitrogen within Mark V PTR ion-funnel under RF field

Despite the increasing $|E^*|$ values from Mark I to Mark III, Marks IV and V clearly present the greatest confining effective fields through the micro-funnel introduced in the last millimetres of the reactor. Another idea of the improvement can be obtained by analysing the difference of effective potential between the centre and the wall of an electrode for each z coordinate as presented in Figure 3.24:

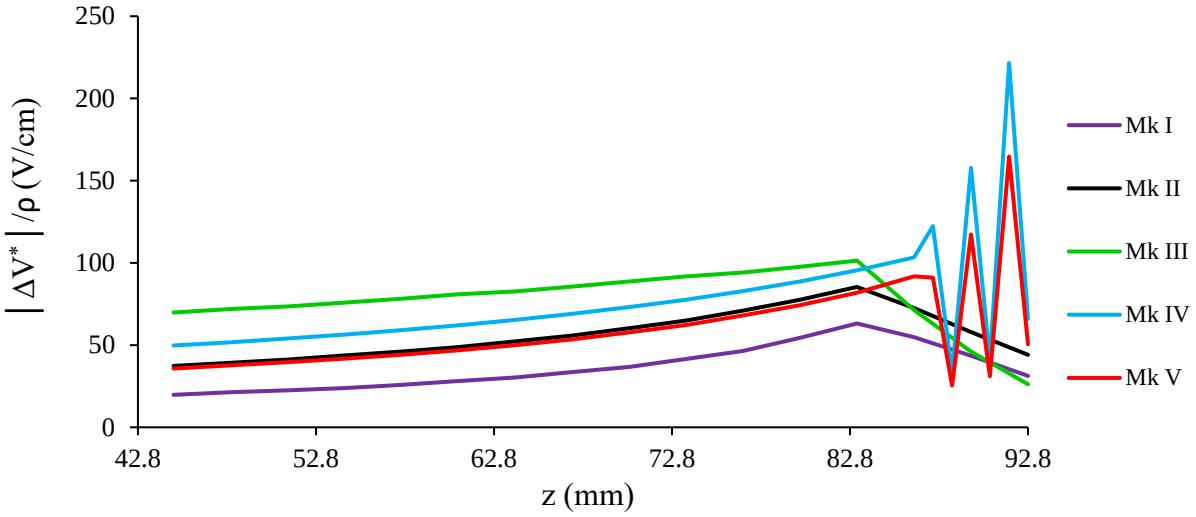

Figure 3.24: Absolute value of the difference of effective potential applied to protonated benzene in nitrogen along the radius for each z coordinate as a function of the PTR ion-funnel under RF field

Notice this is a difference of V^* across each radius but not E^* because those differences are spread along the radii through an exponential distribution and not a linear one like the DC electric field along z where it is possible to simply subtract the exit voltage to the entry voltage to divide the difference by the reactor length.

Even if Mark III presents the greatest confining effective field until P_{26} (z = 83.2 mm), it is Marks IV and V which present a clear enhancement in E* values in the last millimetres of the reactor through the use of the micro-funnel, especially through the reduction of d, the distance between adjacent electrodes This confirms the crucial role of this area in transferring the ions through the reactor exit aperture.

3.3.3.5 Central axial well – V_{trap}

Plotting V* within the RF area gives an initial idea about the influence of the RF field on the ions. Figure 3.25 represents V_{trap} for protonated benzene in nitrogen for each ion-funnel, i.e., the central axial well to override at each electrode level to be dragged across the reactor.

V_{trap} values were calculated through E 2.61.

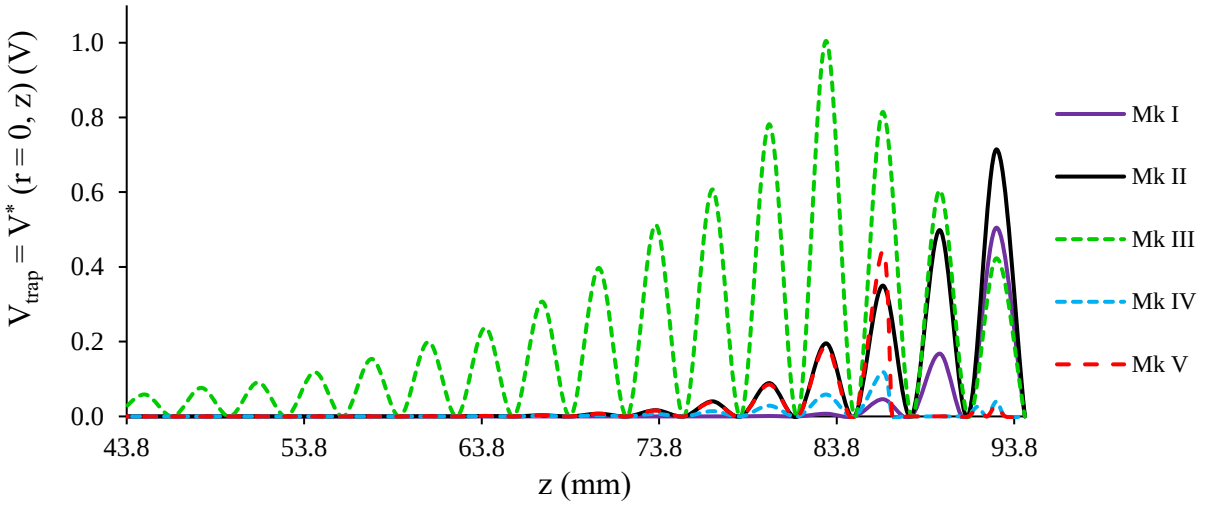

Figure 3.25: V_{trap} (central axial well) applied to protonated benzene in nitrogen as a function of the PTR ion-funnel under RF field

The plot of V_{trap} is quite revealing. Firstly, the effective potentials became greater and greater from Mark I to Mark III. However, V_{trap} also increased with the same trend, and the values for Mark III could be high enough to understand the loss of signal, compared to Mark II, where the extra ions gathered towards the centre could have been trapped in the axial wells. Secondly, the implementation of the micro-funnel has cut a huge proportion of V_{trap} in the last section of Marks IV and V, which can also explain the gain of signal compared to Marks I-III.

3.3.3.6 Overriding field – E_{over}

V_{trap} (considering γ) divided by δ (i.e. d/π) gives E_{trap}, the trapping field that needs to be exceeded by the DC electric field to have the ions transferred across the reactor along the central axis. The difference, being the overriding field E_{over} (as defined in chapter 2), is shown in Figure 3.26:

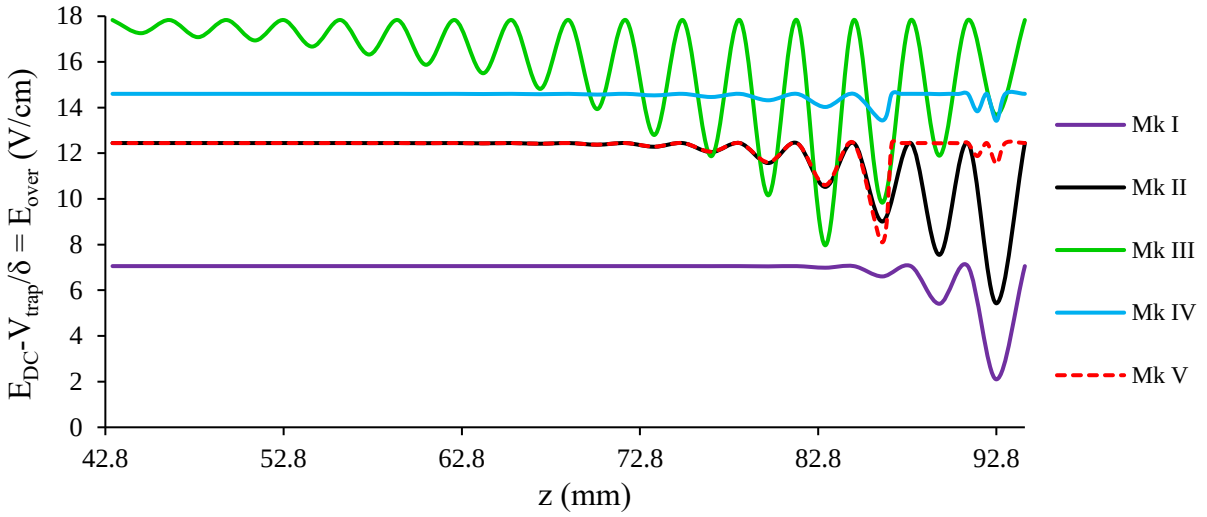

Figure 3.26: $E_{over} = E_{DC} - E_{trap}$ (overriding field along the central axis) applied to protonated benzene in nitrogen as a function of the PTR ion-funnel under RF field

Firstly, E_{over} is constantly positive for any reactor, which is consistent with the results presenting signals of protonated benzene in any experiments. Secondly, the DC electric fields have been chosen with a view to sensitivity optimization. In addition, Mark III, presenting the greatest central axial wells, needed the greatest E_{DC} value whereas Mark IV used a greater E_{DC} than Mark V and it is known that the greater E_{DC} is, the greater the DC kinetic energy and kinetic energy of centre of mass of the colliding system are.

3.3.3.7 DC kinetic energy; $E_{k,DC}$ – RF kinetic energy; $E_{k,RF}$ – Kinetic energy of centre of mass of the colliding system; E_k(CM)

For a given set of DC electric field, temperature and pressure in the reactor and a given ion in a given carrier gas, $E_{k,DC}$ and E_k(CM) remain constant, independently of the RF settings. For each ion-funnel, $E_{K,RF}$ is constant from P_{14} to P_{27} (where α is constant) and values for those three kinetic energies are expressed in Table 3.5:

Table 3.5: DC kinetic energy, RF kinetic energy and kinetic energy of centre of mass of the colliding system of protonated benzene in nitrogen as a function of the PTR ion-funnel under RF field

Parameter		**$E_{k,DC}$**	**$E_{k,RF}$**	**E_k(CM)**
Unit		**eV**	**eV**	**eV**
Application area		**P_1-P_{29}**	**P_{14}-P_{27}**	**P_1-P_{29}**
Reactor generation	**I**	0.005	0.027	0.044
	II	0.014	0.017	0.053
	III	0.025	0.006	0.065
	IV	0.029	0.028	0.070
	V	0.014	0.014	0.053

From P_{27} to P_{29}, $E_{K,RF}$ is expressed in Figure 3.27:

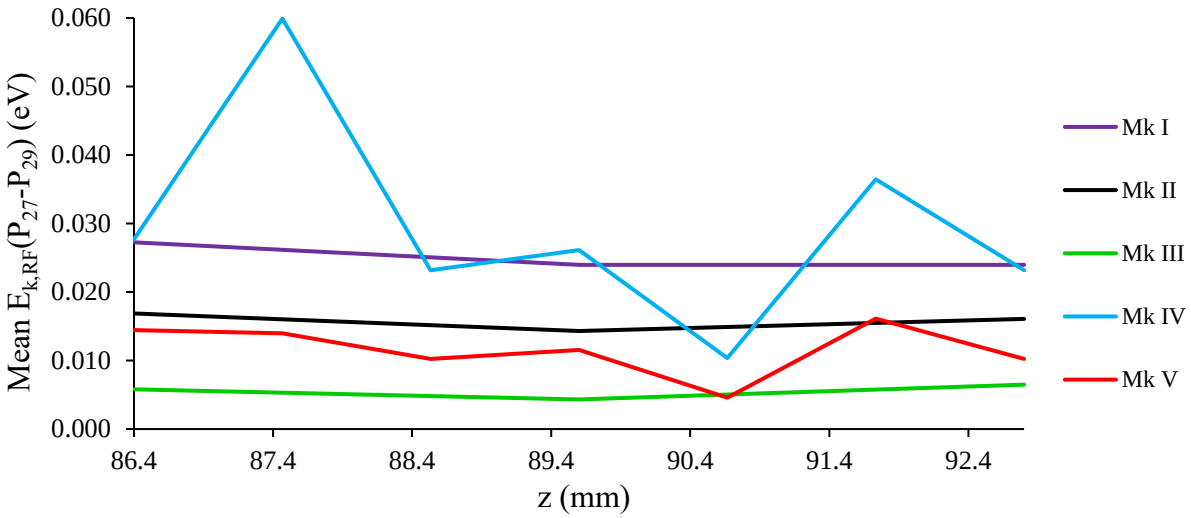

Figure 3.27: RF kinetic energy of protonated benzene in nitrogen in the last millimetres of the reactors as a function of the PTR ion-funnel under RF field

The Mark III reactor has greater values of $E_{k,DC}$ and E_k(CM) compared to the Marks I and II reactors, and this results in higher ion energies. Similarly, the values of $E_{k,DC}$, E_k(CM) and $E_{k,RF}$ are greater in Mark IV compared to Mark V. This is consistent with the observation of lower signals of protonated benzene in Mark III compared to Marks I and II, and also the lower signal in Mark IV compared to Mark V.

3.3.3.8 Product ion distribution

Considering the 5 ion-funnels with their respective conditions optimised for sensitivity, the PIDs of benzene are expressed in Figure 3.28:

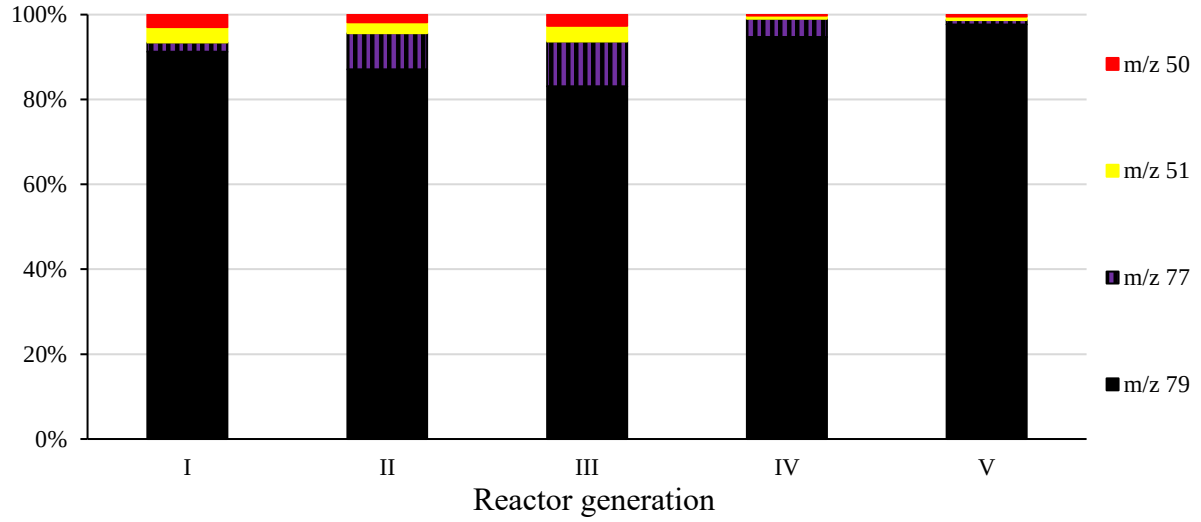

Figure 3.28: PID of benzene in nitrogen as a function of the PTR ion-funnel under RF field

Considering protonated benzene at m/z 79, Mark III presents the least soft transmission with only 83 % of MH^+ production whereas Marks IV and V present the softest transmissions with the greatest proportion by Mark V (98 % compared to 95 % by Mark IV). The ions at m/z 50, 51 are assumed to come from fragmentation of MH^+ whereas the ion at m/z 77 comes from the loss of H_2 by MH^+. However, whatever the consideration of these ions is, trends between reactors remain constant. These results are consistent with the kinetic energies interpretation. However, it must not be forgotten the reactors all operated under slightly different experimental conditions for optimised sensitivity.

The influence of ion-funnels on the reagent ion proportions can also be analysed from the data and is shown in Figure 3.29.

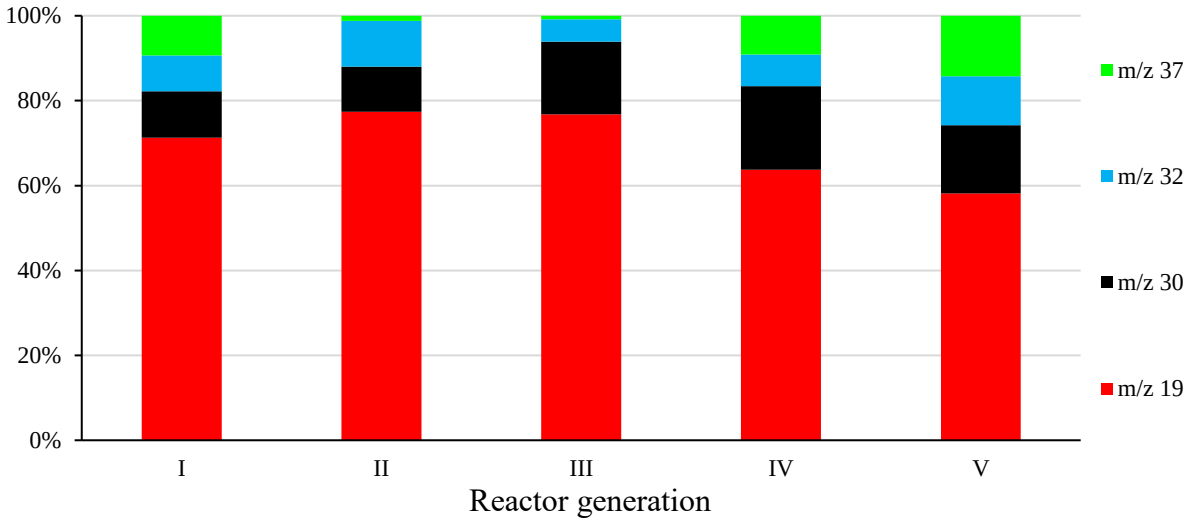

Figure 3.29: Distribution of the main reagent ions (running benzene in nitrogen) as a function of the PTR ion-funnel under RF field

The water dimer is almost non-existent in Mark III, implying a high dissociation, whereas Mark V has the highest proportion of dimer, implying the least dissociation. That confirms those reactors respectively present the hardest and the softest transmissions.

3.3.3.9 Maximum current – i_{max}

The maximum current (i_{max}) that is transmitted through the funnel sections provides more confirmation of the trends observed in the analytical data, as shown in Figure 3.30:

The reduction of i_{max} along z and until P_{27} (82.8 mm) is due to the reduction of ρ, the internal radius of each electrode. After P_{27}, the addition of the micro-funnel clearly enhanced the values for Marks IV and V. Knowing the last millimetres are the most crucial area in the reactor in transmitting the ions through the reactor exit aperture, this parameter confirms the difference of performance between Marks I, II and III and Marks IV and V.

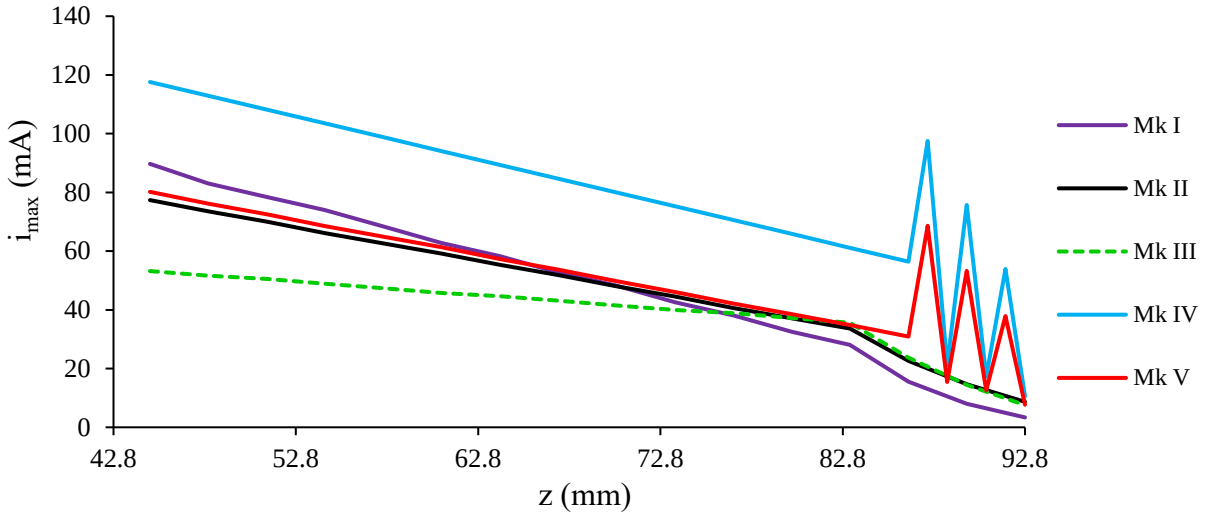

Figure 3.30: i_{max} of protonated benzene in nitrogen as a function of the PTR ion-funnel under RF field

To conclude, the sensitivity is influenced by many parameters involving the capacity of the RF field to confine the ions towards the centre of the reactor and the capacity of the RF field to provide more or less low axial wells, especially along the centre and general kinetic energies to preserve as much as possible the parent molecular ion. The best combinations come from Marks IV and V through their micro-funnels with extra signal for Mark V.

3.4 Other analyte molecules to explore softer transmission

3.4.1 Probe molecules – BTEX

Having thoroughly investigated the behaviour of benzene as the analyte of interest, more analyte molecules were studied to explore the funnels' performances and to avoid limiting observations to benzene only. However, to make fair comparisons, benzene was included in this next round of measurements. It involved different degrees of 'fragility' of the molecule through the BTEX compounds (benzene, toluene, ethylbenzene and xylenes) whose structures are shown in Figure 3.31-Figure 3.34:

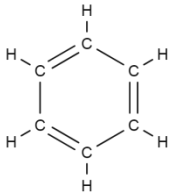

Figure 3.31: Structure of benzene

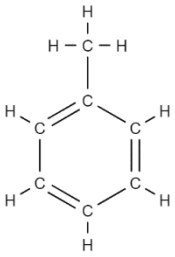

Figure 3.32: Structure of toluene

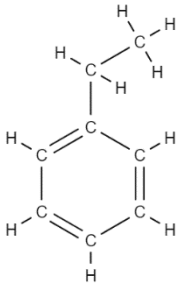

Figure 3.33: Structure of ethylbenzene

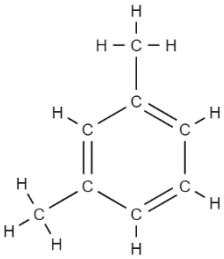

Figure 3.34: Structure of m-xylene

Notice all the xylenes behave the same in the PTR reactors and m-xylene was chosen to represent all three.

As shown in Table 3.6 [86, 90-94], the BTEX compounds are able to be protonated by hydronium and obtain a charge from oxygen inside the reactors under the experimental conditions used.

Table 3.6 Gas phase ion energetics of benzene, toluene, ethylbenzene and xylenes [86, 90-94]

Molecule	**Formula**	**Proton affinity**	**Ionisation energy**
		kJ/mol	eV
Benzene	C_6H_6	759	9.24
Toluene	C_7H_8	784	8.83
Ethylbenzene	C_8H_{10}	788	8.77
o-xylene	C_8H_8	812	8.55
m-xylene	C_8H_8	794	8.44
p-xylene	C_8H_8	796	8.56

All the ions studied in these measurements are presented in Table 3.7. The ions representing a proportion of 2 % or more in at least one reactor generation have been considered.

Table 3.7: Ions studied within the ion-funnels experiments for softer transmission involving benzene, toluene, ethylbenzene and xylenes

Group	Name	Code	Formula	m/z
Benzene ions	Butyl fragment 1	$(M\text{-}C_2H_4)^+$	$C_4H_2^+$	50
	Butyl fragment 2	$(M\text{-}C_2H_3)^+$	$C_4H_3^+$	51
	Protonated benzene – H_2	$(MH\text{-}H_2)^+$	$C_6H_5^+$	77
	Charge-exchanged benzene	M^+	$C_6H_6^+$	78
	Protonated benzene	MH^+	$C_6H_7^+$	79
Toluene ions	Butyl fragment 1	$(M\text{-}C_3H_6)^+$	$C_4H_2^+$	50
	Butyl fragment 2	$(M\text{-}C_3H_5)^+$	$C_4H_3^+$	51
	Charge-exchanged toluene – CH_3	$(M\text{-}CH_3)^+$	$C_6H_5^+$	77
	Benzene-like product ion	$(MH\text{-}CH_2)^+$	$C_6H_7^+$	79
	Protonated toluene – H_2	$(MH\text{-}H_2)^+$	$C_7H_7^+$	91
	Charge-exchanged toluene	M^+	$C_7H_8^+$	92
	Protonated toluene	MH^+	$C_7H_9^+$	93
Ethylbenzene ions	Butyl fragment 1	$(M\text{-}C_4H_8)^+$	$C_4H_2^+$	50
	Butyl fragment 2	$(M\text{-}C_4H_7)^+$	$C_4H_3^+$	51
	Charge-exchanged ethylbenzene – C_2H_5	$(M\text{-}C_2H_5)^+$	$C_6H_5^+$	77
	Benzene-like product ion	$(MH\text{-}C_2H_4)^+$	$C_6H_7^+$	79
	Charge-exchanged ethylbenzene – CH_3	$(M\text{-}CH_3)^+$	$C_7H_7^+$	91
	Toluene-like product ion	$(MH\text{-}CH_2)^+$	$C_7H_9^+$	93
	Charge-exchanged ethylbenzene	M^+	$C_8H_{10}^+$	106
	Protonated ethylbenzene	MH^+	$C_8H_{11}^+$	107
m-xylene ions	Benzene-like product ion	$(MH\text{-}C_2H_4)^+$	$C_6H_7^+$	79
	Charge-exchanged m-xylene – CH_3	$(M\text{-}CH_3)^+$	$C_7H_7^+$	91
	Toluene-like product ion	$(MH\text{-}CH_2)^+$	$C_7H_9^+$	93
	Protonated m-xylene – H_2	$(MH\text{-}H_2)^+$	$C_8H_9^+$	105
	Charge-exchanged m-xylene	M^+	$C_8H_{10}^+$	106
	Protonated m-xylene	MH^+	$C_8H_{11}^+$	107

Notice it is possible certain fragments are daughter ions from both parent molecules. Therefore, the choice has been made to remove from the results plots only the M^+ intensity, being the only ion with a 'great probability' to have been produced after charge exchange only. As for the sensitivity study, this choice does not affect the trends between ion-funnels.

3.4.2 Experimental conditions

Compared to the previous section, where the experimental parameters were optimised for sensitivity for each funnel from I to V, all parameters were fixed in this section, except for the DC entry voltage, which was scanned to produce the PIDs plots obtained with Marks I, II and V funnels only. This is because Mark III had been shown to be less effective than Mark II, and Mark V more effective than Mark IV. These experimental conditions are presented in Table 3.8:

Table 3.8 Reactor parameters during the ion-funnels experiments for softer transmission involving benzene, toluene, ethylbenzene and xylenes

Reactor generation	**Parameters <u>independent</u> on the reactor generation**		
	T	**P**	**WF in the ion source**
	ºC	**mbar**	**sccm**
	23.6	1.2	1.0
	Reactor entry	**E**	**E/n**
	V	**V/cm**	**Td**
All	23.5	2.15	7
	33.5	3.23	11
	43.5	4.30	15
	53.5	5.38	18
	63.5	6.45	22
	73.5	7.53	26
	83.5	8.60	29
	93.5	9.68	33
	103.5	10.75	37
	113.5	11.83	40
	123.5	12.90	44

	RF Ion-funnel tunings					
	P_{26}		**P_{27-28}**		**P_{29}**	
	V_{pp}	**ν**	**V_{pp}**	**ν**	**V_{pp}**	**ν**
	V	**kHz**	**V**	**kHz**	**V**	**kHz**
I	210	745	N/A	N/A	105	745
II	215	745	N/A	N/A	131.5	745
	P_{26-27}		**P_{28s}**		**P_{29s}**	
	V_{pp}	**ν**	**V_{pp}**	**ν**	**V_{pp}**	**ν**
	V	**kHz**	**V**	**kHz**	**V**	**kHz**
V	208	708	64	708	32	708

3.4.3 Results and discussions

3.4.3.1 Product ion distribution

Figure 3.35 to Figure 3.37 present the PID of benzene respectively in Mark I, II and V:

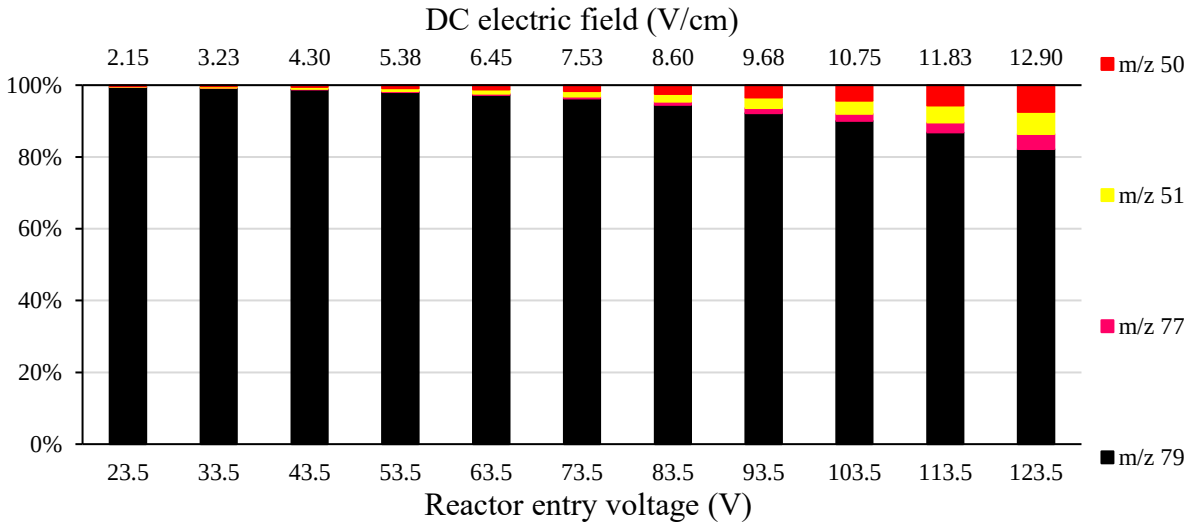

Figure 3.35: PID of benzene in nitrogen within Mark I ion-funnel under RF field and collisional damping as a function of the DC electric field

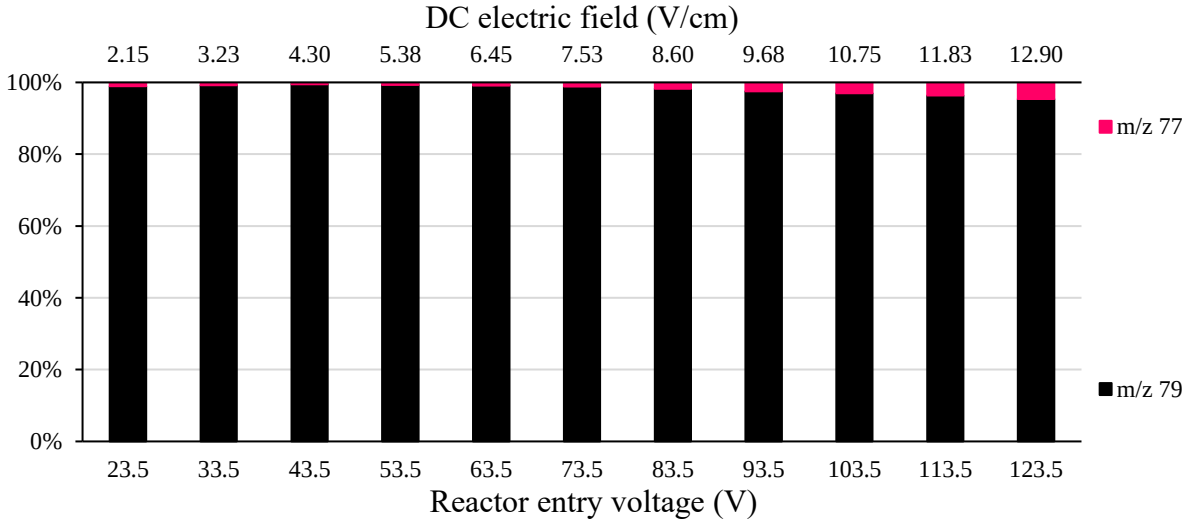

Figure 3.36: PID of benzene in nitrogen within Mark II ion-funnel under RF field and collisional damping as a function of the DC electric field

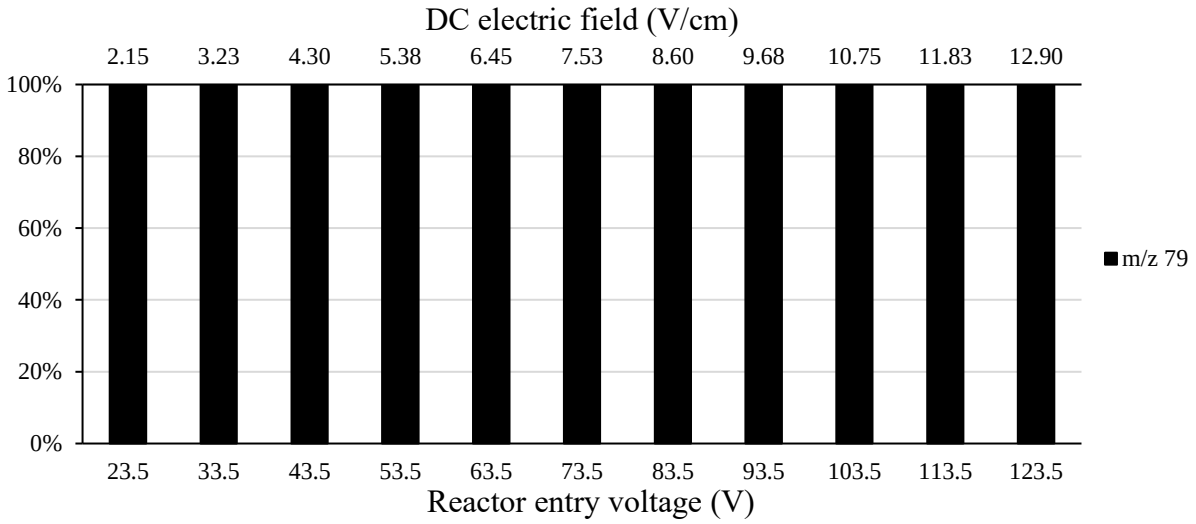

Figure 3.37: PID of benzene in nitrogen within Mark V ion-funnel under RF field and collisional damping as a function of the DC electric field

The evolution from Mark I to Mark V is characterised by an increasing softness of the benzene transmission through to the exit of the reactor.

Figure 3.38 to Figure 3.40 present the PID of toluene respectively for Marks I, II and V:

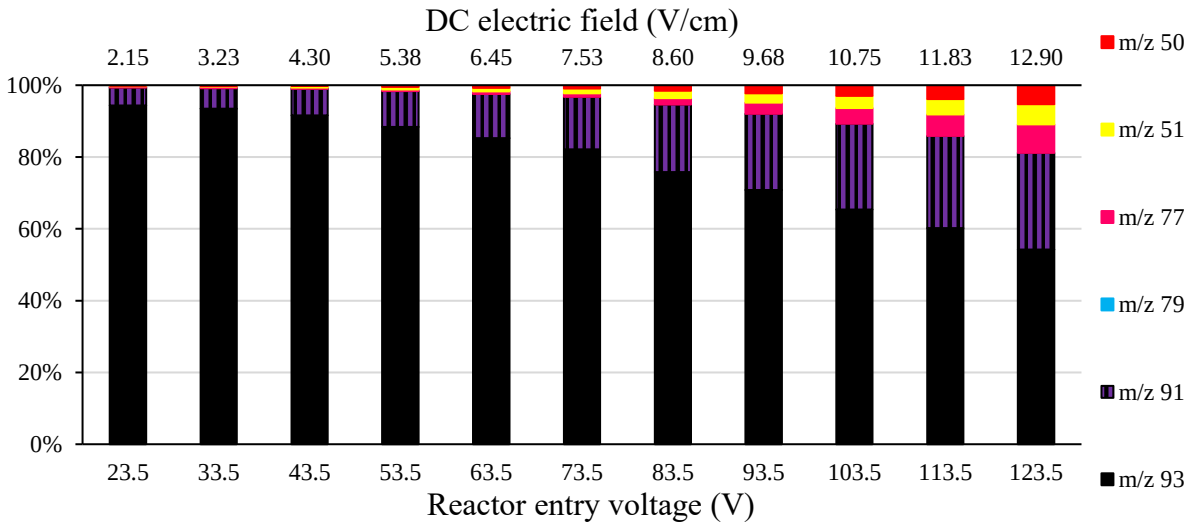

Figure 3.38: PID of toluene in nitrogen within Mark I ion-funnel under RF field and collisional damping as a function of the DC electric field

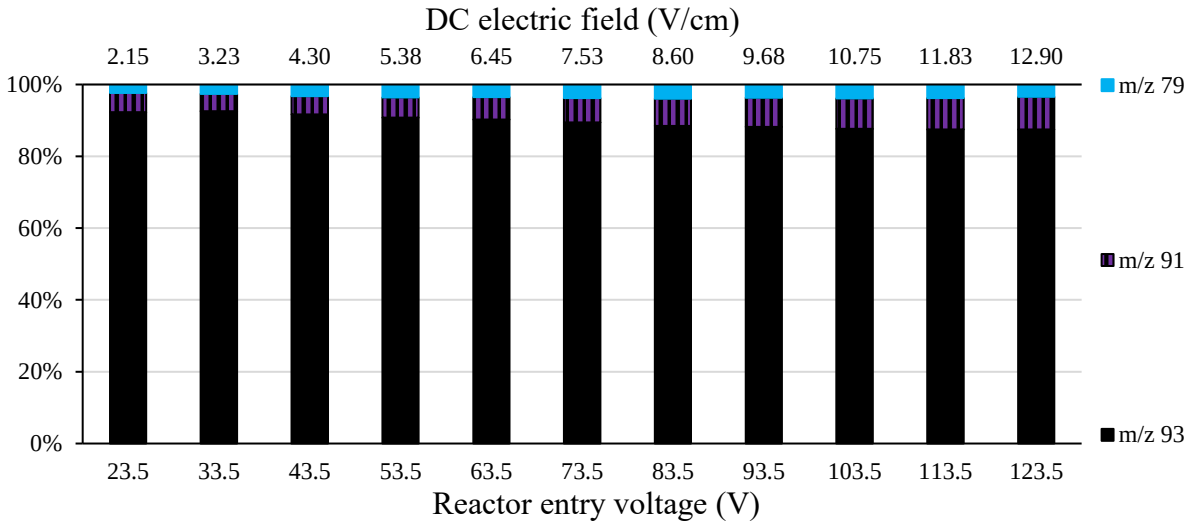

Figure 3.39: PID of toluene in nitrogen within Mark II ion-funnel under RF field and collisional damping as a function of the DC electric field

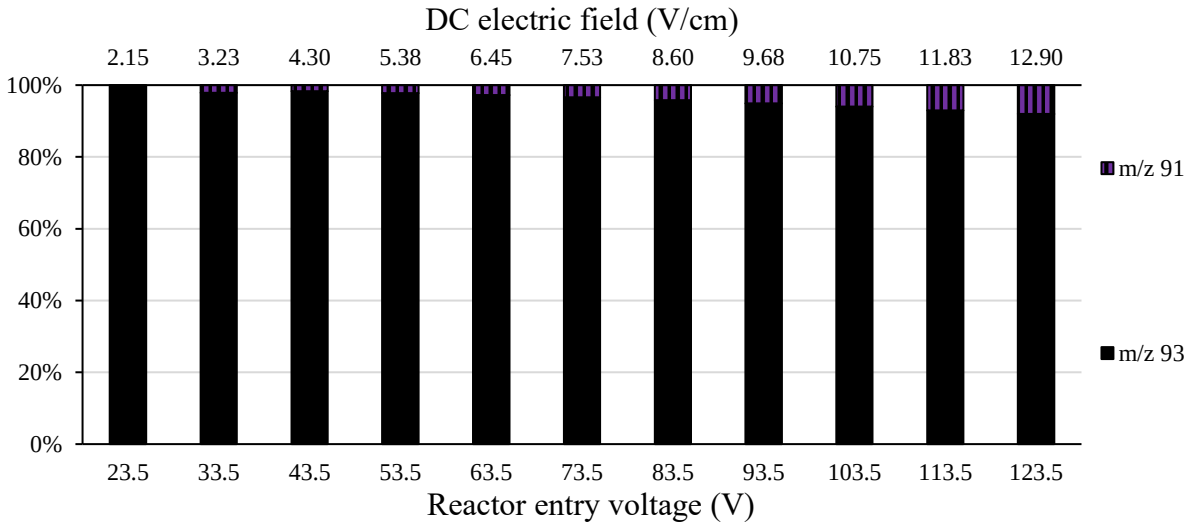

Figure 3.40: PID of toluene in nitrogen within Mark V ion-funnel under RF field and collisional damping as a function of the DC electric field

As for benzene, the behaviour of toluene from Mark I to Mark V is characterised by an increasing softness of analyte ion transmission.

Figure 3.41 to Figure 3.43 present the PID of ethylbenzene respectively for Marks I, II and V:

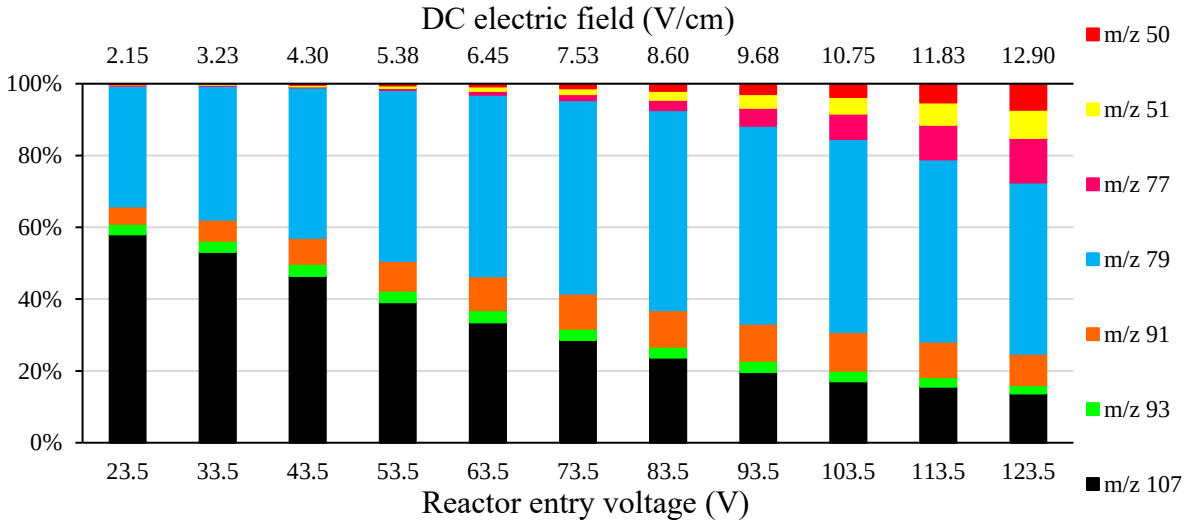

Figure 3.41: PID of ethylbenzene in nitrogen within Mark I ion-funnel under RF field and collisional damping as a function of the DC electric field

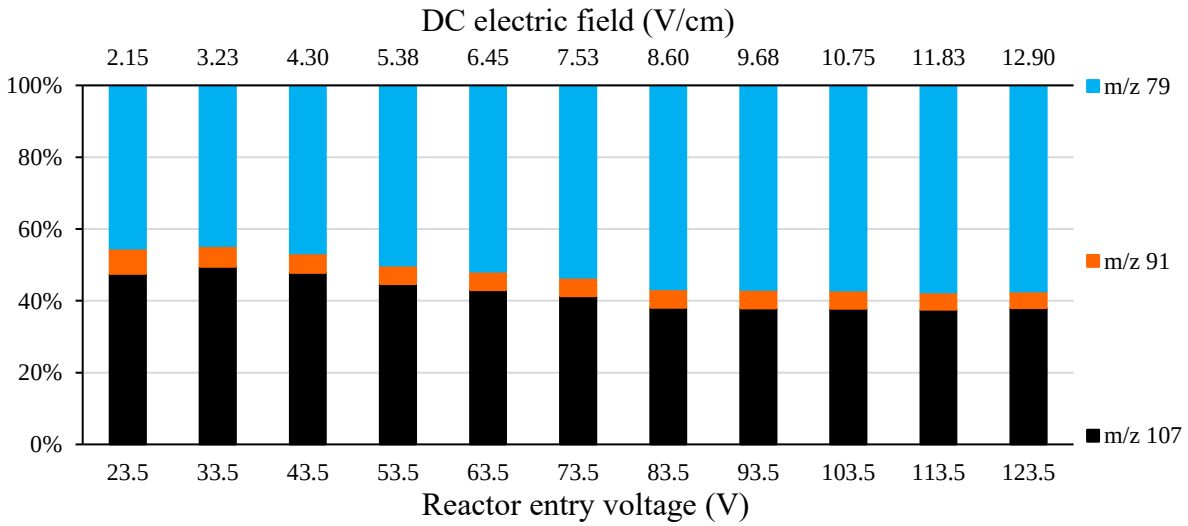

Figure 3.42: PID of ethylbenzene in nitrogen within Mark II ion-funnel under RF field and collisional damping as a function of the DC electric field

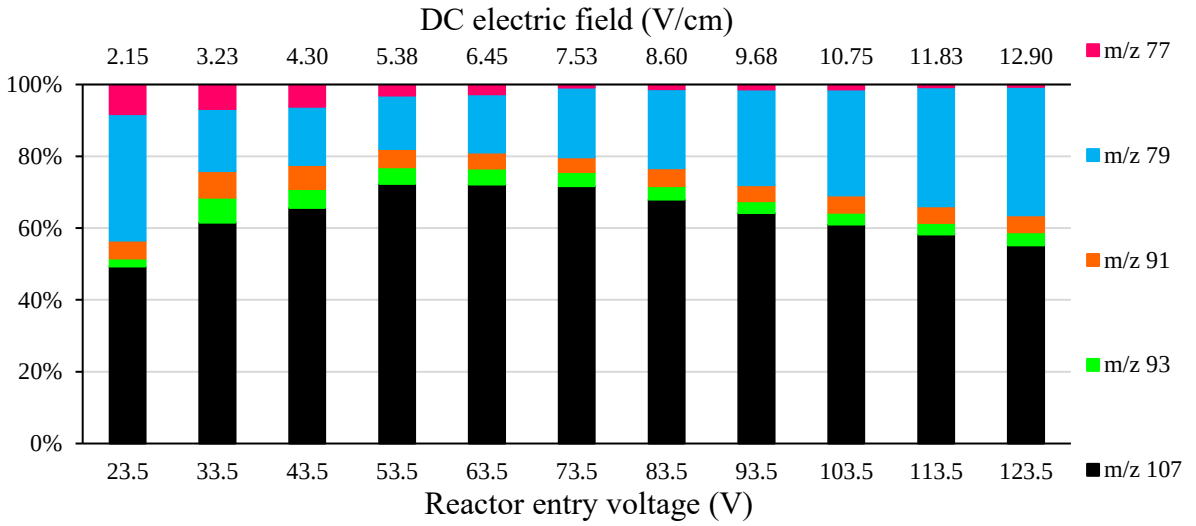

Figure 3.43: PID of ethylbenzene in nitrogen within Mark V ion-funnel under RF field and collisional damping as a function of the DC electric field

As for benzene and toluene, the behaviour of ethylbenzene from Mark I to Mark V is characterised by an increasing softness in analyte ion transmission. However, unlike them, the greatest proportion of the protonated analyte run with Mark V is met at 5-6 V/cm instead of the lowest values of E due to the fact ethylbenzene remains the most fragile BTEX chemicals with its ethyl branch.

Figure 3.44 to Figure 3.46 present the PID of m-xylene respectively for Marks I, II and V:

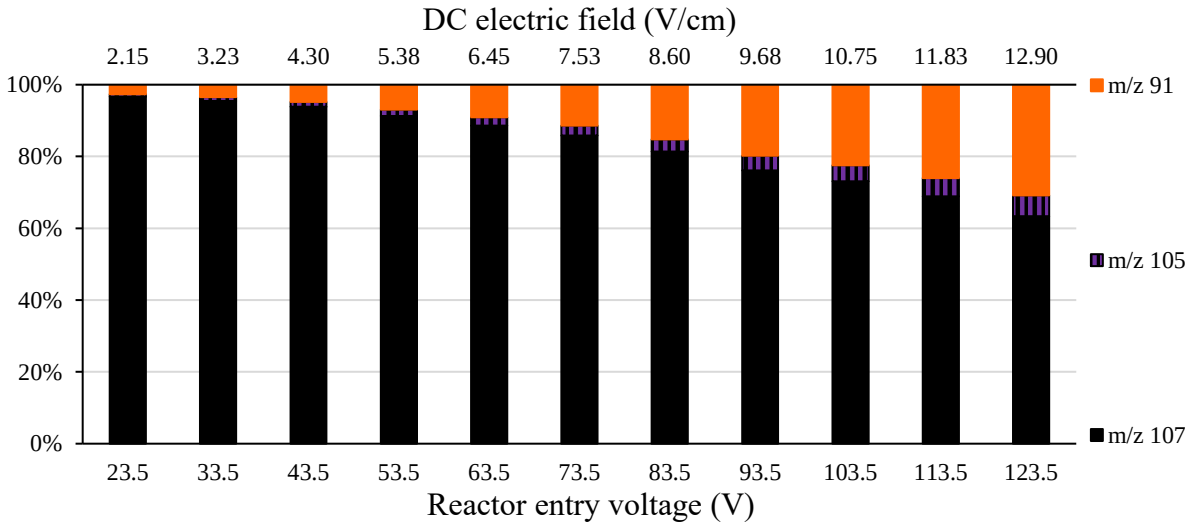

Figure 3.44: PID of m-xylene in nitrogen within Mark I ion-funnel under RF field and collisional damping as a function of the DC electric field

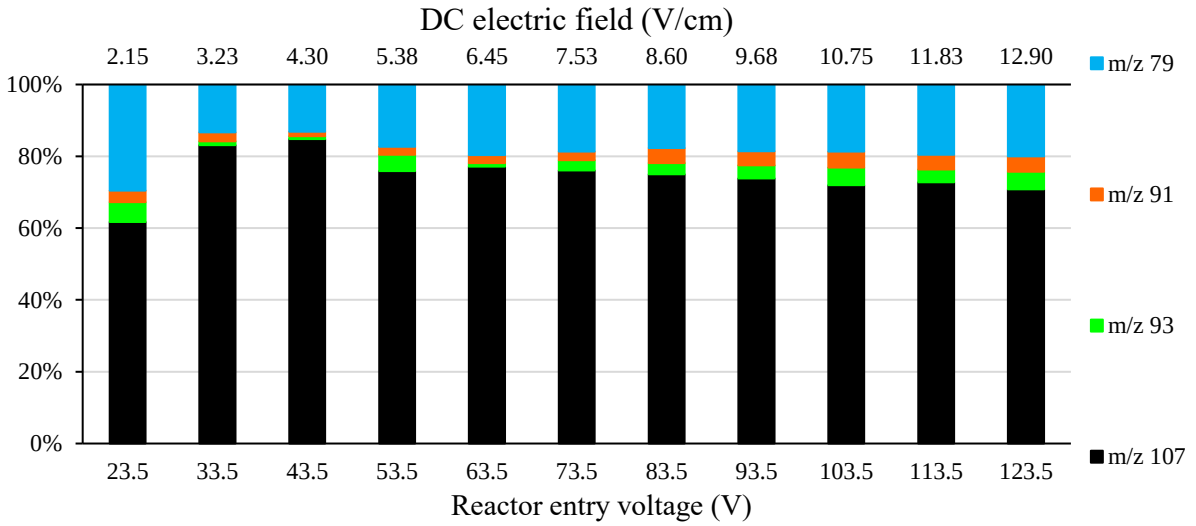

Figure 3.45: PID of m-xylene in nitrogen within Mark II ion-funnel under RF field and collisional damping as a function of the DC electric field

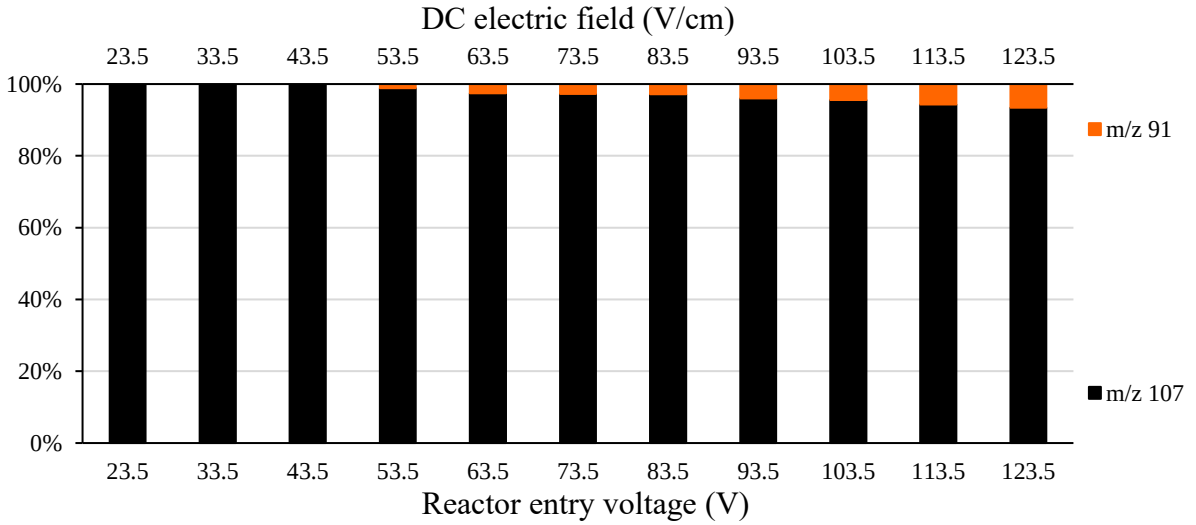

Figure 3.46: PID of m-xylene in nitrogen within Mark V ion-funnel under RF field and collisional damping as a function of the DC electric field

As for the other BTEX compounds, the behaviour of m-xylene from Mark I to Mark V is characterised by an increasing softness in analyte ion transmission.

Even for a given set of DC conditions (E_{DC}, T and P), Mark V, being the last generation of ion-funnel, offers the softest transmission of the analyte as well as the highest transmission (sensitivity).

3.4.3.2 RF kinetic energy

The confining effective field (function of the effective potential) influences how many ions are directed towards the centre of the reactor whereas the overriding field (function of the trapping field) influences how many ions are not trapped and are instead moved along the reactor towards its exit. Both parameters consequently influence the signal of a given ion, i.e. the sensitivity of the instrument for this ion, and present the same trends between ion-funnels for each BTEX compound and each DC electric field. The RF settings, specific to each geometry of the ion-funnels, were kept constant as a few percentages difference in amplitude can alter the signal. On the other hand, with E_{DC}, T and P being constant in each reactor, the DC kinetic energy and the kinetic energy in the centre of mass of the colliding system remained constant between ion-funnels, for a given DC electric field and a given BTEX single compound. For a given DC electric field, and with all other parameters held constant, the different levels of fragmentation (for each molecule and each ion-funnel) is a function only of the mean kinetic energy due to the RF-induced motion and the collisional damping in each reactor.

Figure 3.47-Figure 3.49 represent the evolution of the mean RF kinetic energy of protonated ethylbenzene, calculated through the equation E 2.68, as a function of the DC electric field within the RF area respectively for Marks I, II and V ion-funnels. Notice this compound presents the most significant change of its PID due to its fragile ethyl branch but the trends between ion-funnels remain the same for each BTEX compound.

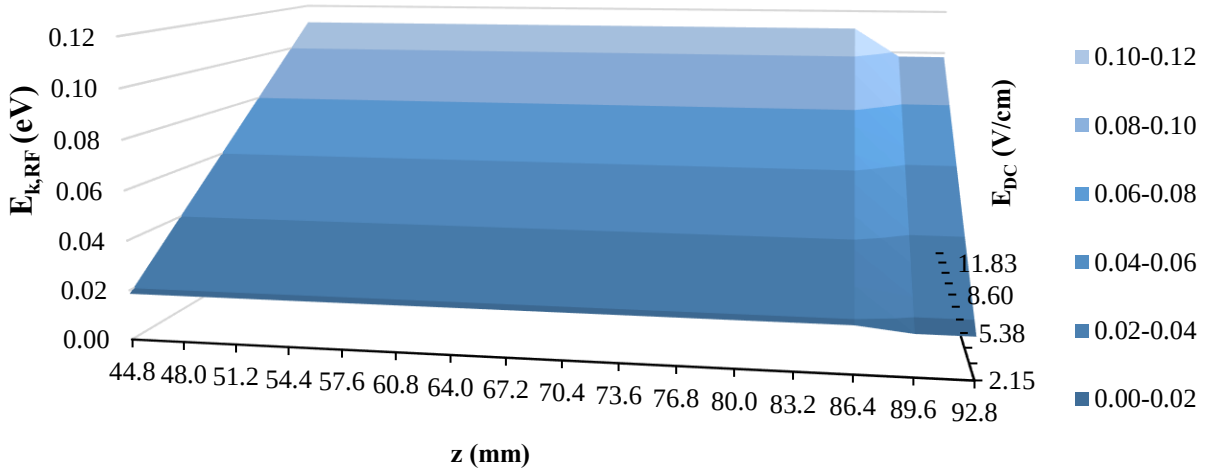

Figure 3.47: Mean kinetic energy due to the RF-induced ion motion for protonated ethylbenzene in nitrogen within Mark I ion-funnel under RF field as a function of the DC electric field

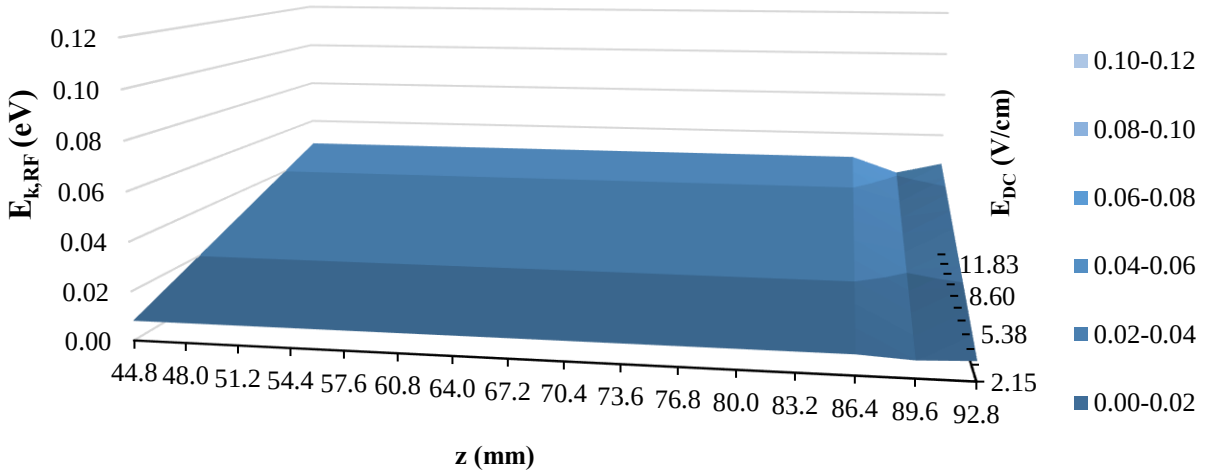

Figure 3.48: Mean kinetic energy due to the RF-induced ion motion for protonated ethylbenzene in nitrogen within Mark II ion-funnel under RF field as a function of the DC electric field

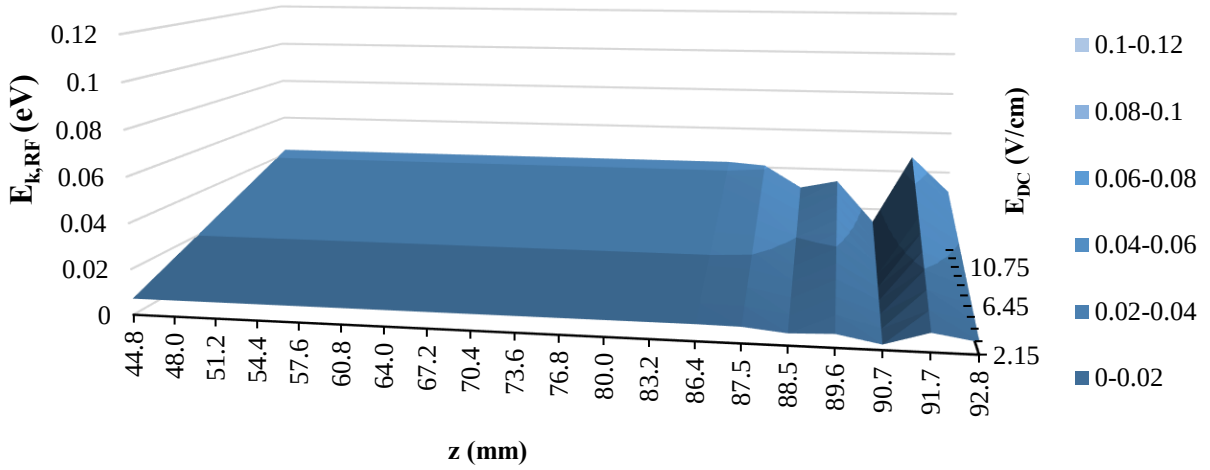

Figure 3.49: Mean kinetic energy due to the RF-induced ion motion for protonated ethylbenzene in nitrogen within Mark V ion-funnel under RF field as a function of the DC electric field

The evolution from Mark I to Mark V is characterised by a decreasing mean RF kinetic energy, in accordance with an increasing softness of the analyte transmission especially for Mark V through its micro-funnel. That is why, the analysis of PIDs as a function of the ion-funnel only confirms that the Mark V provides the softest transmission.

3.5 Conclusion

At the beginning of this project only the Mark I reactor existed, and the development and understanding of the different, subsequent funnels have been important parts of this research. The evolution of the funnels through to Mark V has resulted (in the case of Mark V) in a reproducible factor of four improvement in the sensitivity for protonated benzene compared to the original funnel.

As shown in Figure 3.35 to Figure 3.46, for a given DC field the fragmentation of BTEX compounds has been reduced significantly from the Mark I to Mark II and then to the Mark V reactor.

In the case of BTEX, the minimum fragmentation is obtained at, or close to, the lowest DC electric field. The exception to this is ethylbenzene in Mark V, where the minimum fragmentation is observed at an intermediate DC field value.

A consideration of the various expressions of the DC and RF electric fields 3D-plotted as a function of X, Y and Z in the reactor has been explored in sections 3.3.3.3 to 3.3.3.7 and has assisted in understanding the observed behaviour of the ionised analytes and, where produced, their daughter fragments.

The Mark II reactor is now standard within Kore's commercial PTR systems, and the development of the micro-funnel and its implementation is ongoing at Kore.

CHAPTER 4: EXPLORATION OF THE SPLIT OF THE DC ELECTRIC FIELD WHEN RF FIELDS ARE APPLIED IN A PTR REACTOR

4.1 Introduction

Prior to the development of the Mark I ion-funnel, measurements of ion currents made at Kore indicated that losses due to space charge occurred in the second half of the reactor, which is why the funnel was only implemented in this section. What was not explored further, possibly because the major improvements observed with the Mark I funnel were so striking, was whether this first section of the reactor could also be modified to improve sensitivity further.

Across all the reactors tested during this research it was observed that the DC electric field required to maximise the ion transmission (and thus sensitivity) was always lower by a factor of ~ 4 when the RF was applied, compared to the DC-only case. Consequently, it was proposed that space charge effects might now be far more prominent in this first section when operating the funnels and investigations were conducted into potential further sensitivity gains by raising the electric field in this first section, i.e. back to levels required for the DC-only case. Accordingly, the notion of a 'split gradient reactor (SGR)' was conceived, in which the electric field in the first section would be returned to DC-only levels, while preserving the lower DC field that is required for optimum performance of the RF funnels.

4.2 Split DC electric field – Evolution of PTR reactor

4.2.1 Description and experimental conditions

The implementation of this split gradient was achieved by the simple expedient of bringing in a separately controllable potential to P_{12} in the middle of the reactor. This permitted two DC potential gradients to be set up: a steeper one from P_1 to P_{12} and a shallower one from P_{12} to P_{29s}. After initial tests on Mark IV, it was on the Mark V ion-funnel that the experiments reported here took place. Most of the parameters were kept constant and are listed below:

- Tedlar® bags were used to prepare dilute samples of the analytes in nitrogen. The absolute concentrations were not determined, as this was not required for these comparative experiments. The length of the experiments was short and a sequence of experiments for each compound was completed within the consumption lifetime of the Tedlar bag (10 litre capacity), i.e. within a time window short enough to reliably compare signal intensities.
- Reagent ion used: H_3O^+ for proton transfer
- Frequency of ToF: ~ 14.3 kHz (70 µs ToF cycles) under RF settings of the Mark V ion-funnel described in the chapter 3.
- Data acquisition time: 14 s
- Mass species monitored: m/z 135, protonated n-butylbenzene, $C_{10}H_{15}^+$ and m/z 259, protonated hexachloro-1,3-butadiene, $C_4Cl_6H^+$ (probe molecules presented later)
- Reactor's temperature and pressure respectively kept constant at 23.6 ^oC and 1.1 mbar.

For the remainder of this chapter the terms 'LG' and 'SG' will be used to refer to the linear gradient case and the split gradient case respectively. The LG mode comprises a single and linear DC electric field across the whole reactor (c.f. Figure 4.1) whereas the SG mode splits this DC electric field into two. In both the LG and SG cases, the RF field was always applied in the second part of the reactor. $P_{1\text{-}12}$ refers to the 1st section and $P_{12\text{-}29s}$ to the 2nd section (c.f. Figure 4.2). Notice P_{12} has been maintained in the SG mode at 21 V and 25 V respectively for n-butylbenzene (nBB) and hexachloro-1,3-butadiene (HC13BD) accordingly to their best respective signal intensities.

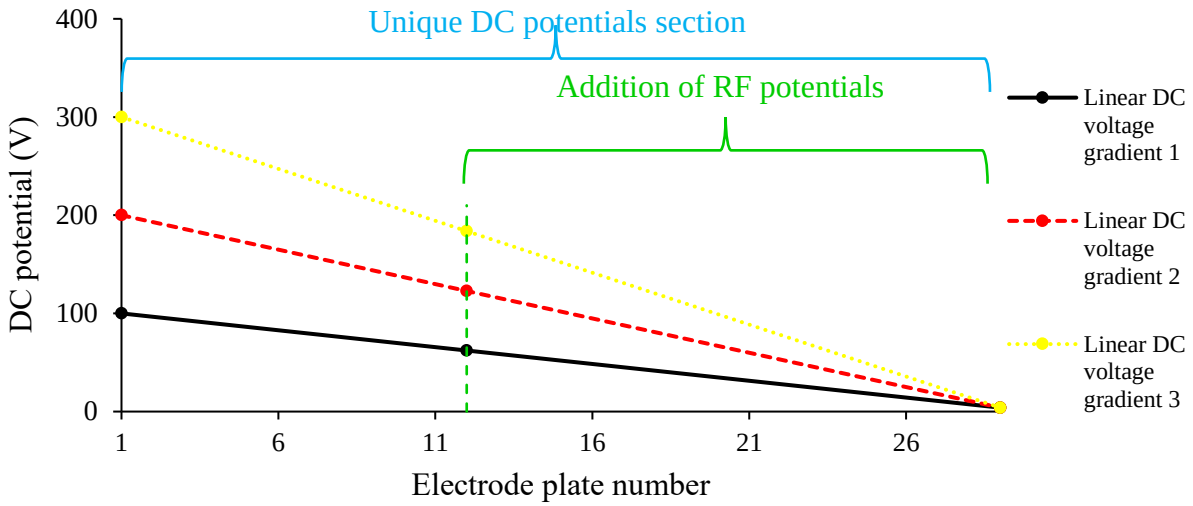

Figure 4.1: Linear DC gradients (P_1 to P_{29s}) within the PTR reactor under RF fields (P_{12} to P_{29s})

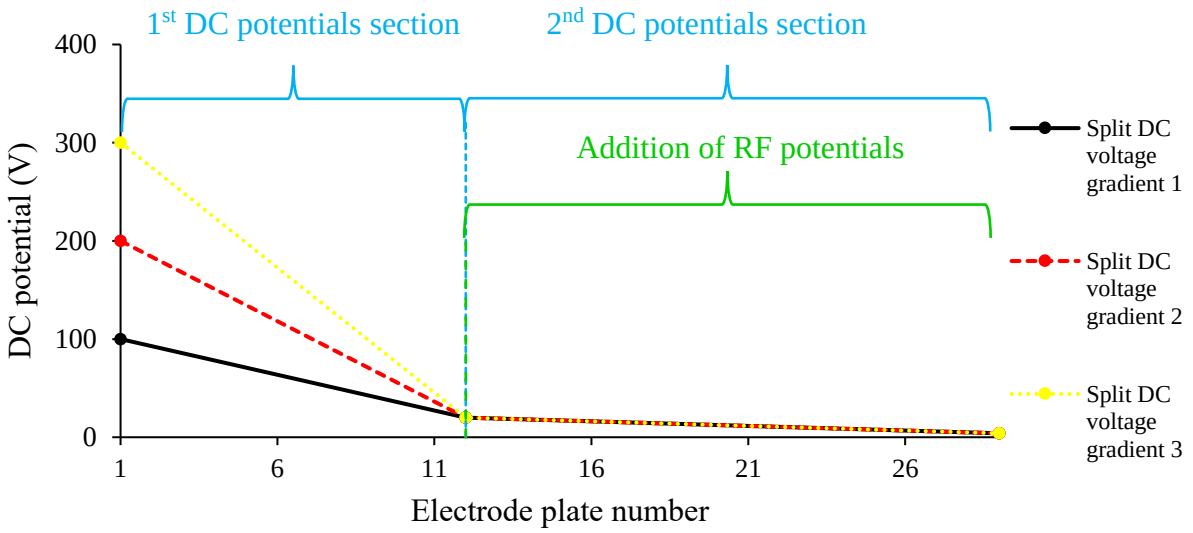

Figure 4.2: Split DC gradients (variable 1st section from P_1 to P_{12} and constant 2nd section from P_{12} to P_{29s}) within the PTR reactor under RF fields (P_{12} to P_{29s})

4.2.2 Measurements under Mark V ion-funnel using RF field

4.2.2.1 Probe molecules

- n-butylbenzene

n-butylbenzene, whose formula is $C_{10}H_{14}$ (m/z 134), is presented in Figure 4.3. This hydrocarbon is a good example of a 'fragile' molecule, being sensitive to the differences of energies brought into the reactor due to its 'weak' site at the beginning of its branch. This molecule is, under typical PTR conditions, protonated and singly charged, due to the presence of H_3O^+ and O_2^+ and NO^+, respectively. The main mass of interest is that of protonated nBB, m/z 135.

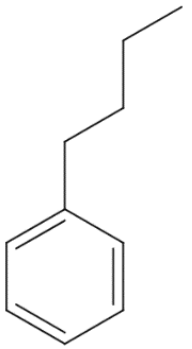

Figure 4.3: n-butylbenzene structure

- Hexachloro-1,3-butadiene

This chlorinated compound, whose formula is C_4Cl_6 (m/z 258), is presented in Figure 4.4. It is likely to be a more robust molecule in the reactor compared to nBB, owing to its symmetrical distribution of chlorine atoms resulting in a balanced electron density. No literature about its energetic properties is available. However, experiments have proven that HC13BD can be protonated and charge-exchanged under typical PTR conditions. The main mass of interest is that of protonated HC13BD, m/z 259.

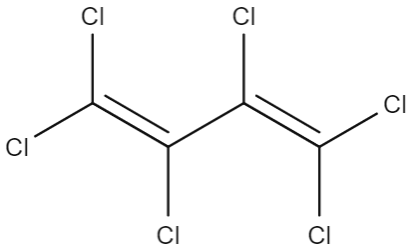

Figure 4.4: Hexachloro-1,3-butadiene structure

All the ion species studied in this chapter are presented in the Table 4.1. The ions presenting a proportion of 2 % or more in at least one reactor mode have been considered. In order to characterise the mixed ionisation, the main reagent ions have also been studied.

Table 4.1: Ions studied within the split DC electric field experiments involving n-butylbenzene and hexachloro-1,3-butadiene

Group	Name	Code	Formula	m/z
Reagent ions	Hydronium/ Protonated water	N/A	H_3O^+	19
	Nitrogen oxide	N/A	NO^+	30
	Oxygen	N/A	O_2^+	32
	Protonated water dimer	NA	$H_3O^+{\cdot}H_2O$	37
nBB ions	Propyl fragment 1	$(M\text{-}C_7H_{11})^+$	$C_3H_3^+$	39
	Propyl fragment 2	$(M\text{-}C_7H_9)^+$	$C_3H_5^+$	41
	Butyl fragment	$(M\text{-}C_6H_5)^+$	$C_4H_9^+$	57
	m/z 79 fragment – H_2	$(M\text{-}C_4H_9)^+$	$C_6H_5^+$	77
	Benzene-like product ion	$(MH\text{-}C_4H_8)^+$	$C_6H_7^+$	79
	m/z 93 fragment – H_2	$(M\text{-}C_3H_7)^+$	$C_7H_7^+$	91
	Toluene-like product ion 1	$(M\text{-}C_3H_6)^+$	$C_7H_8^+$	92
	Toluene-like product ion 2	$(MH\text{-}C_3H_6)^+$	$C_7H_9^+$	93
	Ethylbenzene-like product ion	$(M\text{-}C_2H_3)^+$	$C_8H_{11}^+$	107
	Charge-exchanged nBB	M^+	$C_{10}H_{14}^+$	134
	Protonated nBB	MH^+	$C_{10}H_{15}^+$	135
HC13BD ions	Butyl fragment 1	$(M\text{-}Cl_4)^+$	$C_4Cl_2^+$	118
	Protonated propyl fragment	$(MH\text{-}CCl_2)^+$	$C_3Cl_4H^+$	177
	Butyl fragment 2	$(M\text{-}Cl_2)^+$	$C_4Cl_4^+$	188
	Butyl fragment 3	$(M\text{-}Cl)^+$	$C_4Cl_5^+$	223
	Charge-exchanged HC13BD	M^+	$C_4Cl_6^+$	258
	Protonated HC13BD	MH^+	$C_4Cl_6H^+$	259

Any fragment ions presented in the results are assumed to come from fragmentation of MH^+. The trends between modes are not affected.

4.2.3 Results and discussions

Regarding the count rate and PID plots, two abscissa axes are displayed. In LG mode, the DC field applies throughout the whole of the reactor and is thus described in the plots as the 'Global DC electric field' and its equivalent E/n values are given whereas in SG mode the variable DC

field and its equivalent E/n values are valid until P_{12} before a fixed value for the DC field in $P_{12\text{-}29s}$.

4.2.3.1 Product ion distribution (PID)

- Linear gradient mode – n-butylbenzene (cf. Figure 4.5)

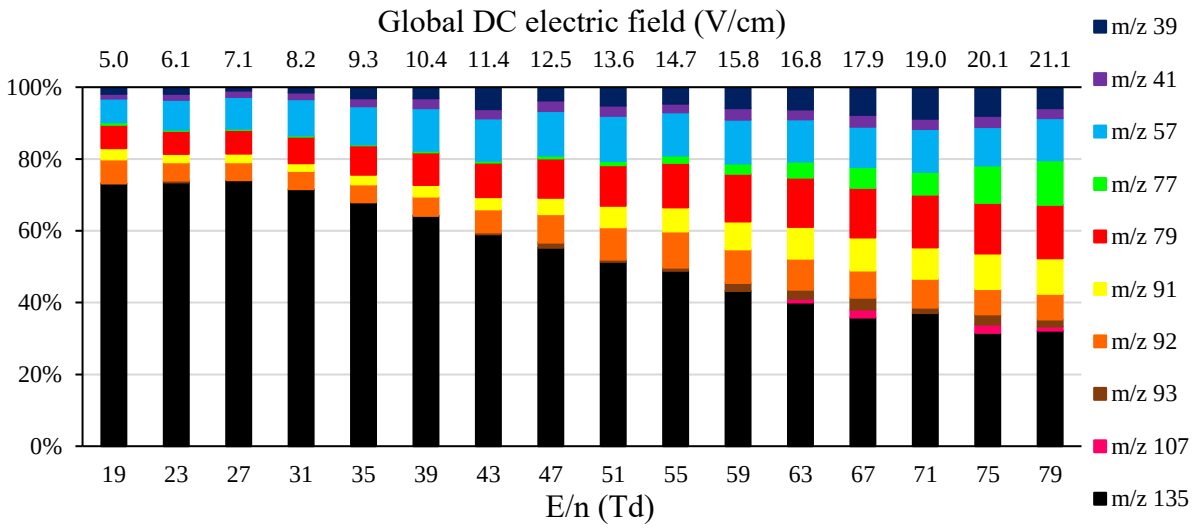

Figure 4.5: PID of nBB as a function of the linear DC electric field and E/n in RF mode

For reference, note that the typical entry voltages (P_1) that are used in the current, commercial PTR instruments from Kore (Mark II reactors) operating in RF mode with a linear DC electric field are 70-90 V, i.e. a DC electric field of ~ 7-9 V/cm across the whole reactor and E/n values of 27-35 Td in the DC-only section.

- Linear gradient mode – reagent ions running n-butylbenzene (cf. Figure 4.6)

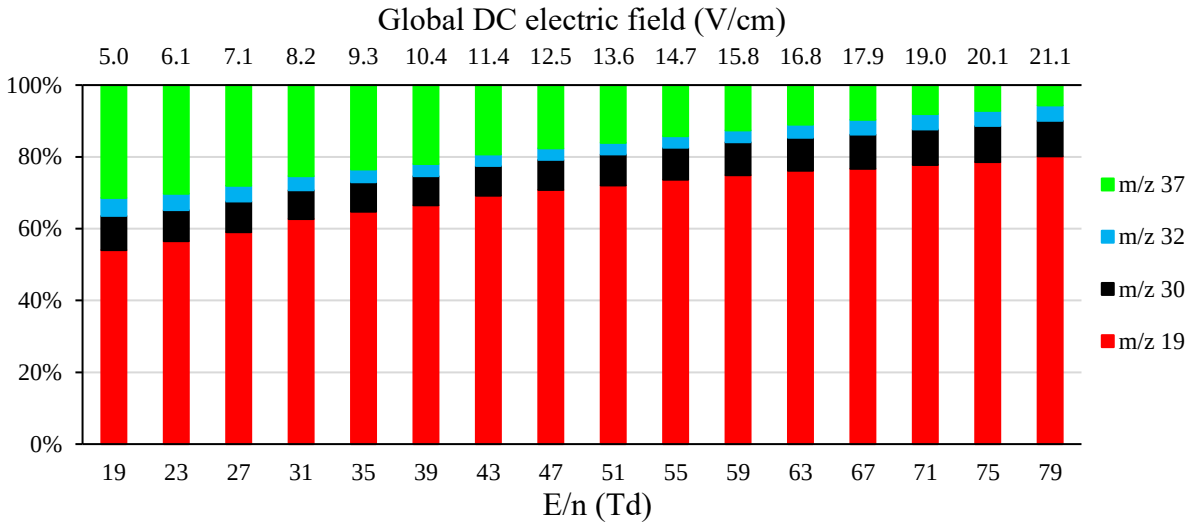

Figure 4.6: Distribution of the main reagent ions running nBB as a function of the linear DC electric field and E/n in RF mode

- Split gradient mode – n-butylbenzene (cf. Figure 4.7)

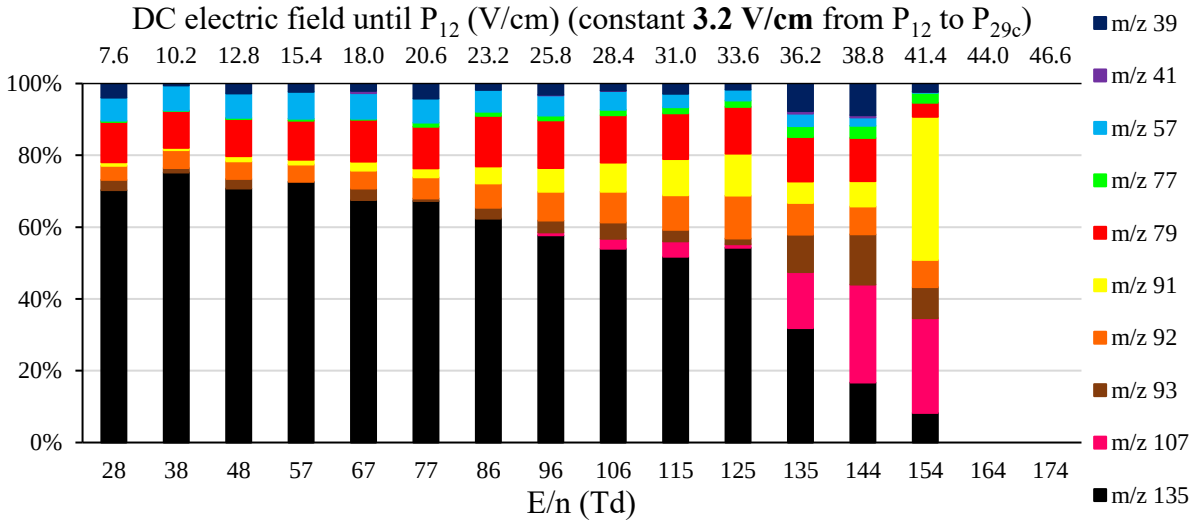

Figure 4.7: PID of nBB as a function of the split DC electric field and E/n in RF mode

Notice P_{29c} refers to the third and last plate of the electrode's group P_{29}.

Even though the proportion of the MH^+ ion is not increased by raising the electric field, the MH^+ proportion can be sustained until approximately 20 V/cm. Therefore, the DC electric field can be increased by a factor 3 over the LG case with no dramatic effect on the PIDs.

- Split gradient mode – reagent ions running n-butylbenzene (cf. Figure 4.8)

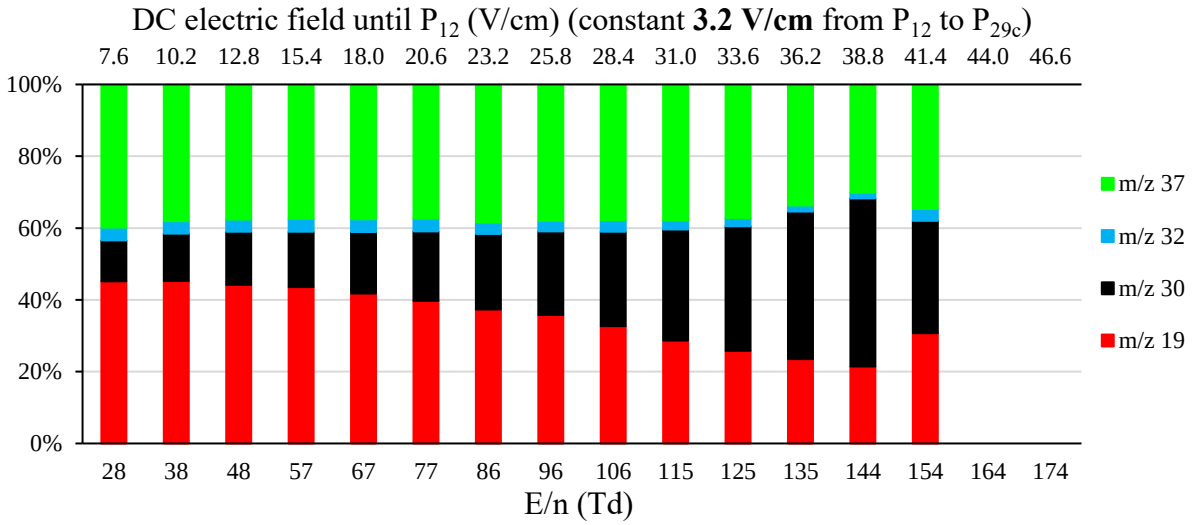

Figure 4.8: Distribution of the main reagent ions running nBB as a function of the split DC electric field and E/n in RF mode

- Linear gradient mode – Hexachloro-1,3-butadiene (cf. Figure 4.9)

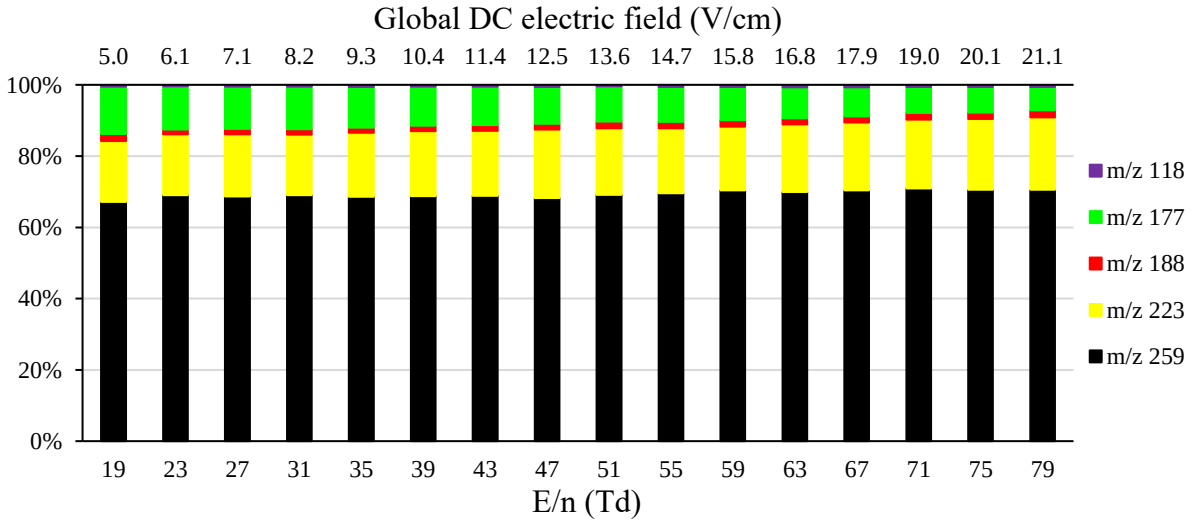

Figure 4.9: PID of HC13BD as a function of the linear DC electric field and E/n in RF mode

- Linear gradient mode – reagent ions running hexachloro-1,3-butadiene (cf. Figure 4.10)

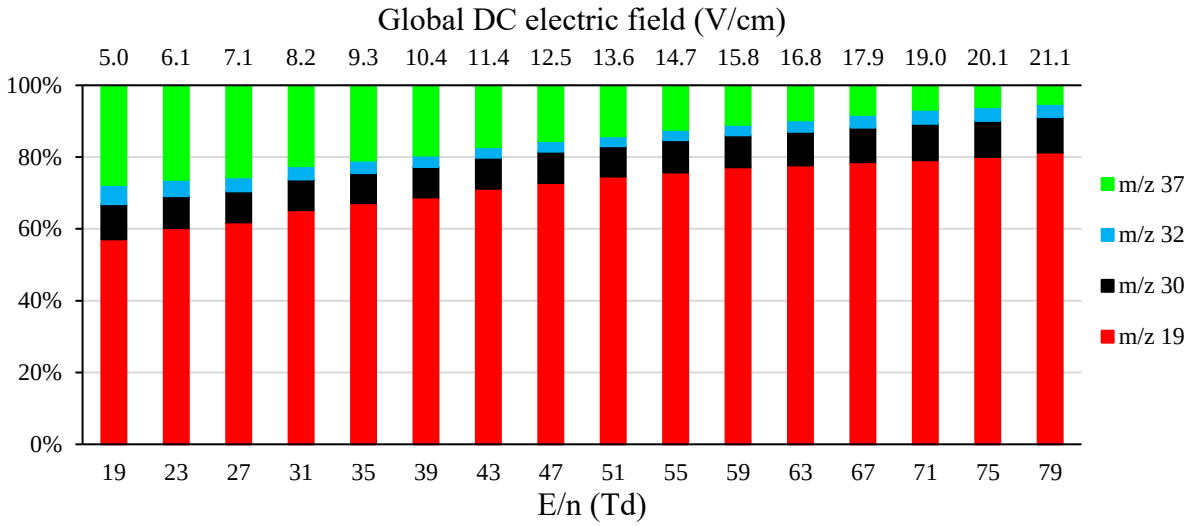

Figure 4.10: Distribution of the main reagent ions running HC13BD as a function of the linear DC electric field and E/n in RF mode

- Split gradient mode – Hexachloro-1,3-butadiene (cf. Figure 4.11)

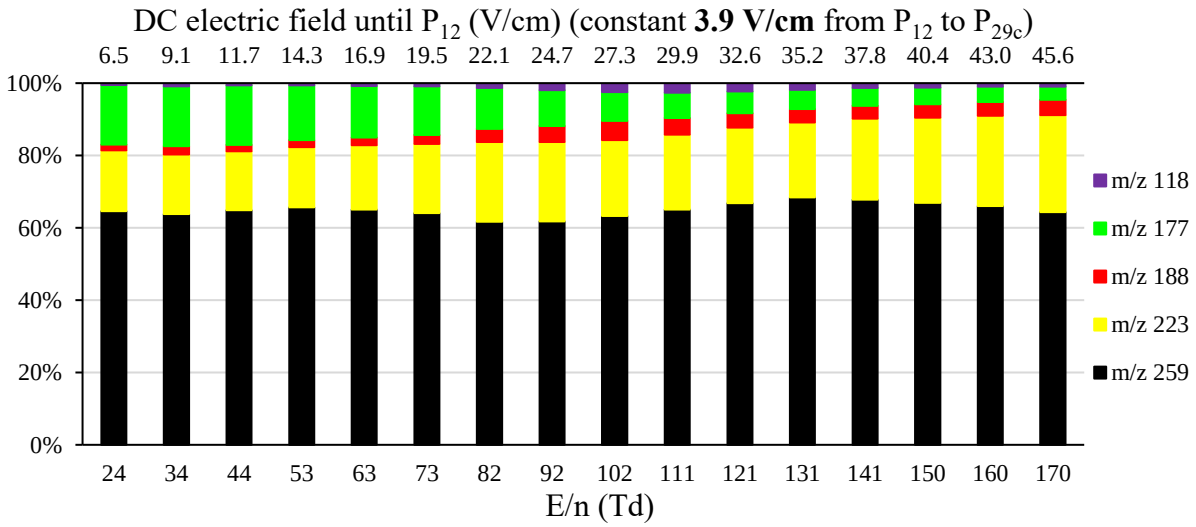

Figure 4.11: PID of HC13BD as a function of the split DC electric field and E/n in RF mode

- Split gradient mode – reagent ions running hexachloro-1,3-butadiene (cf. Figure 4.12)

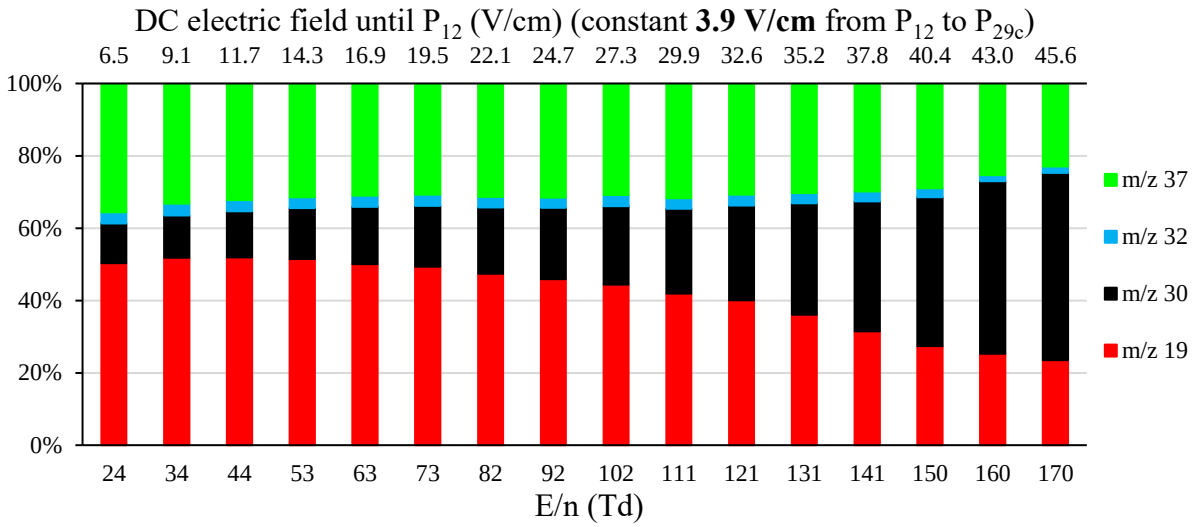

Figure 4.12: Distribution of the main reagent ions running HC13BD as a function of the split DC electric field and E/n in RF mode

From Figure 4.5 it is observed that the DC electric field must be set low in LG mode for a fragile molecule such as nBB. Otherwise, the collision energies that are experienced by ions causes fragmentation because they are pushed deeper into the RF field. For a more robust molecule such as HC13BD, this effect is not really observed over the range studied.

In SG mode, the DC electric field is kept suitably low within the funnel and can be increased in the 1st DC potential section up to 3 and 6 times, for nBB and HC13BD respectively, without observing significant losses in the MH^+ proportion.

On the other hand, the hydronium proportion is an increasing function of the DC electric field in LG mode and a decreasing one in SG mode. The split of the DC electric field clearly changed the reagent ions' distributions.

4.2.3.2 Count rate

- Linear gradient mode – n-butylbenzene (cf. Figure 4.13)

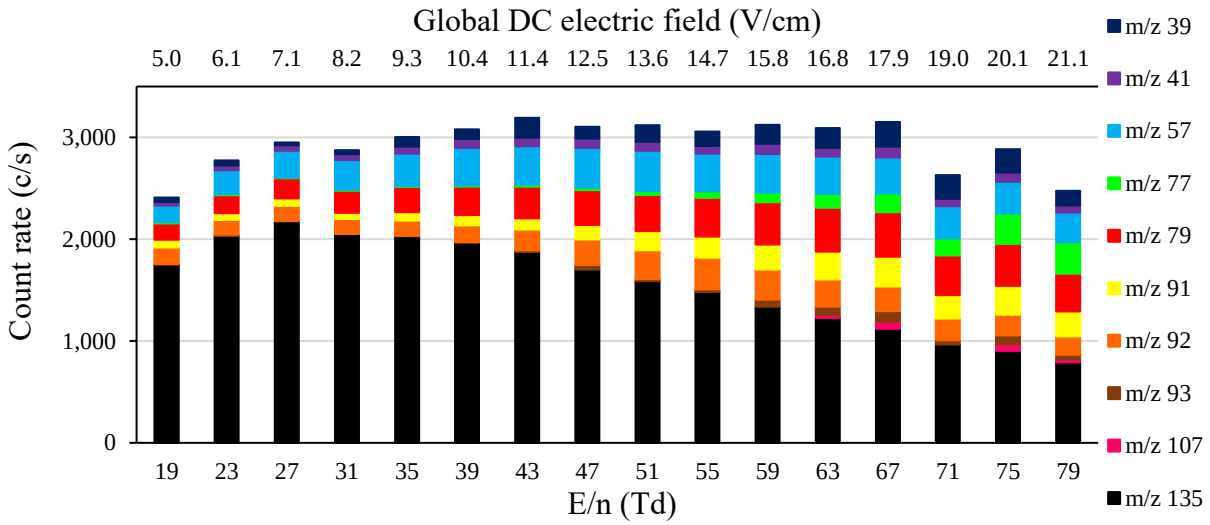

Figure 4.13: Count rate of the main nBB ions as a function of the linear DC electric field and E/n in RF mode

- Linear gradient mode – reagent ions running n-butylbenzene (cf. Figure 4.14)

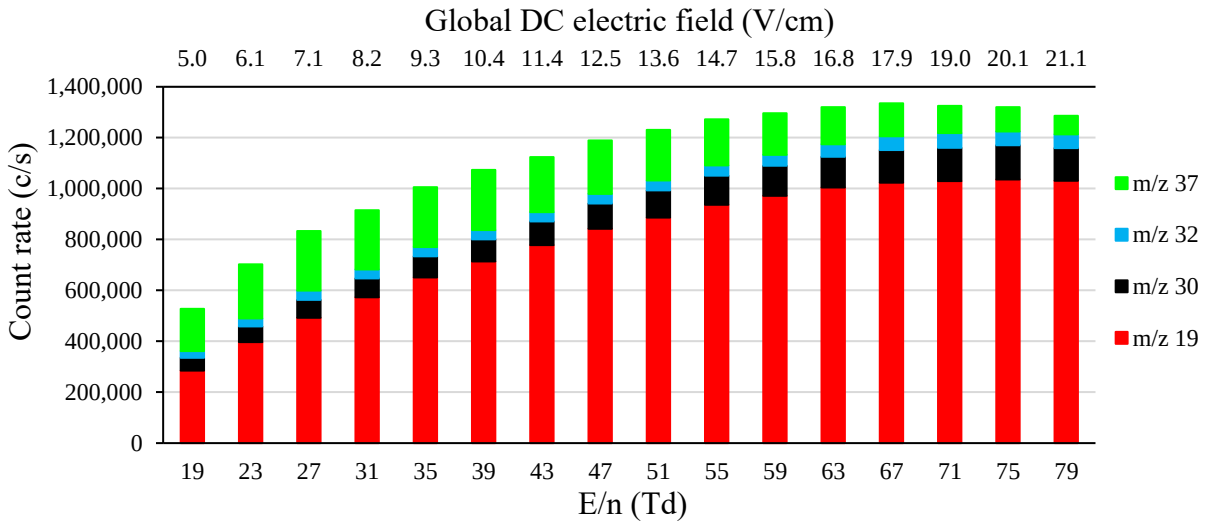

Figure 4.14: Count rate of the main reagent ions running nBB as a function of the linear DC electric field and E/n in RF mode

- Split gradient mode – n-butylbenzene (cf. Figure 4.15)

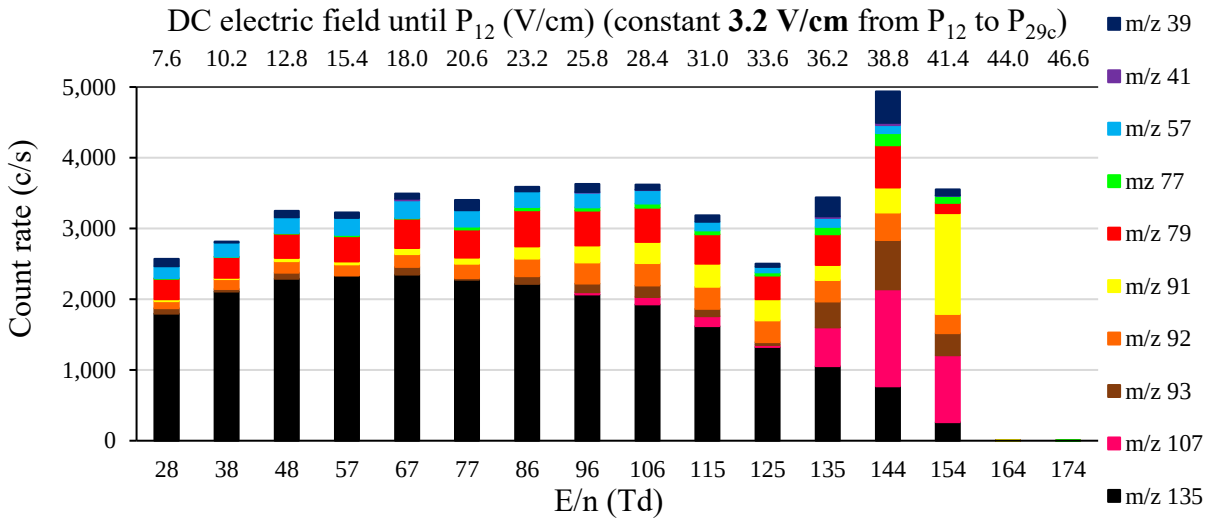

Figure 4.15: Count rate of the main nBB ions as a function of the split DC electric field and E/n in RF mode

- Split gradient mode – reagent ions running n-butylbenzene (cf. Figure 4.16)

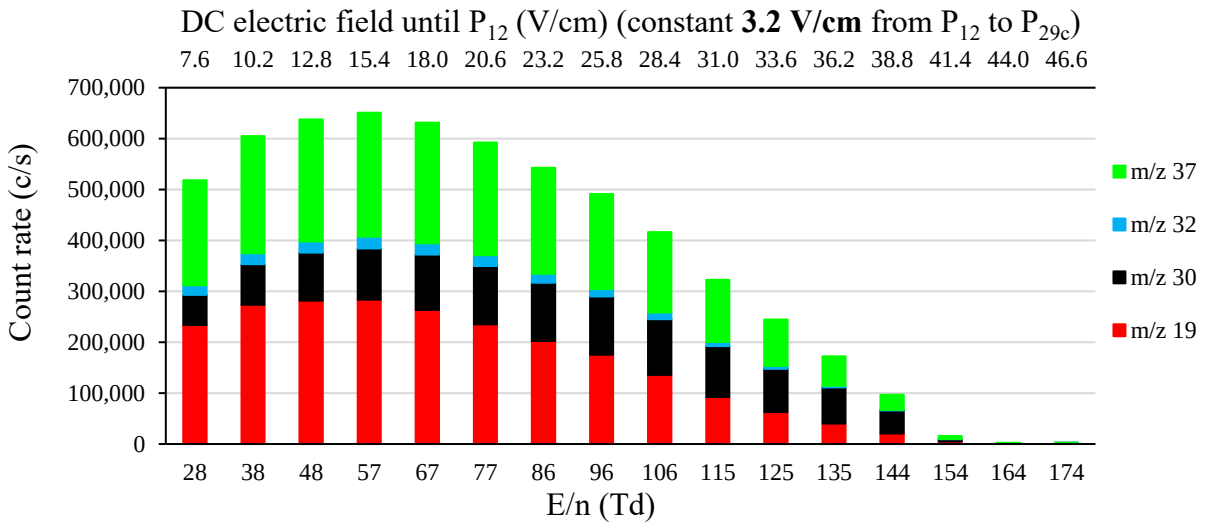

Figure 4.16: Count rate of the main reagent ions running nBB as a function of the split DC electric field and E/n in RF mode

- Linear gradient mode – Hexachloro-1,3-butadiene (cf. Figure 4.17)

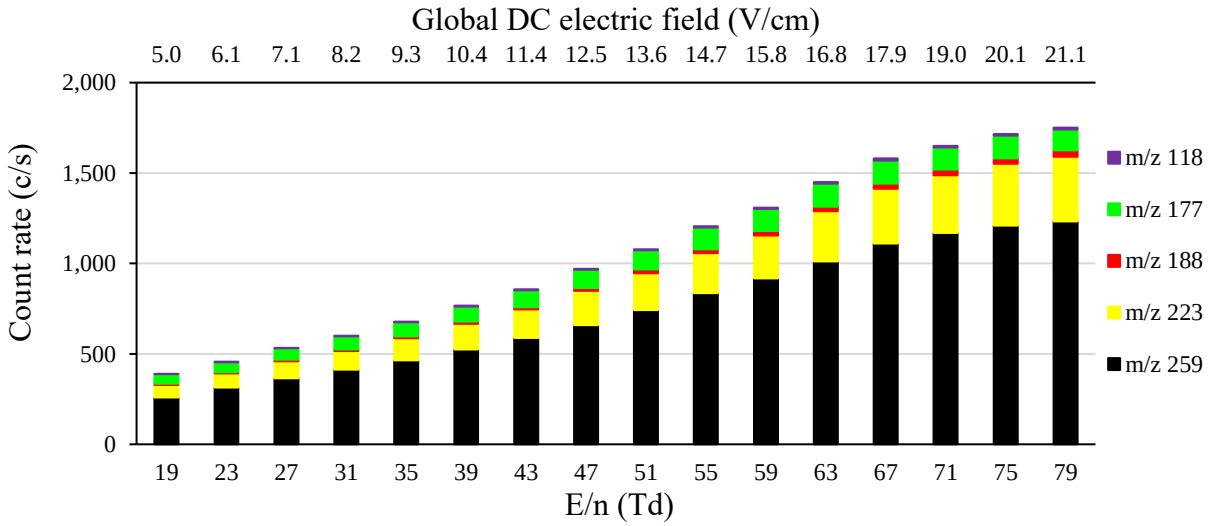

Figure 4.17: Count rate of the main HC13BD ions as a function of the linear DC electric field and E/n in RF mode

- Linear gradient mode – reagent ions running hexachloro-1,3-butadiene (cf. Figure 4.18)

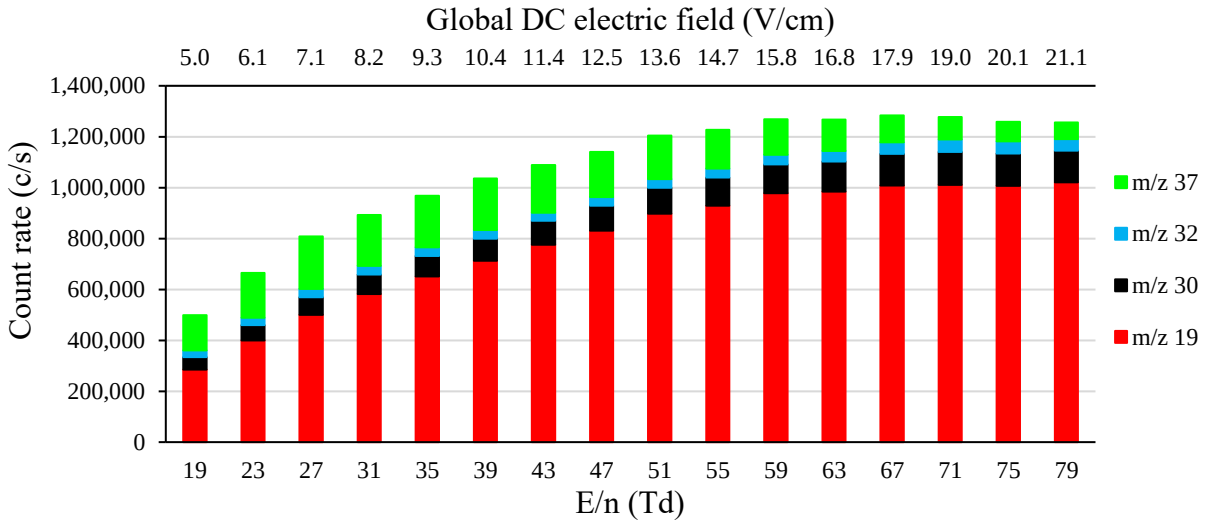

Figure 4.18: Count rate of the main reagent ions running HC13BD as a function of the linear DC electric field and E/n in RF mode

- Split gradient mode – Hexachloro-1,3-butadiene (cf. Figure 4.19)

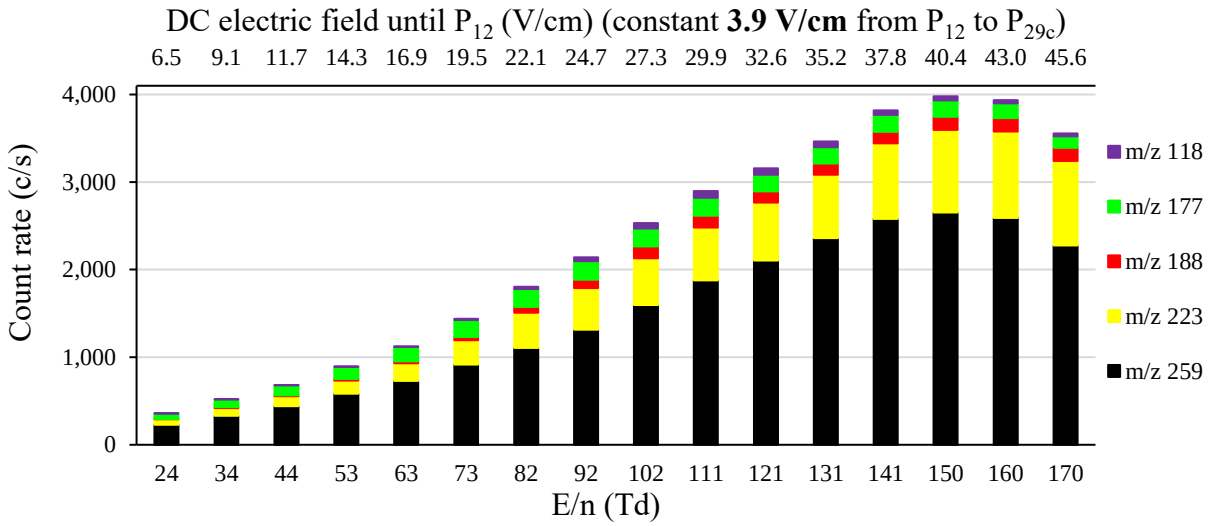

Figure 4.19: Count rate of the main HC13BD ions as a function of the split DC electric field and E/n in RF mode

- Split gradient mode – reagent ions running hexachloro-1,3-butadiene (cf. Figure 4.20)

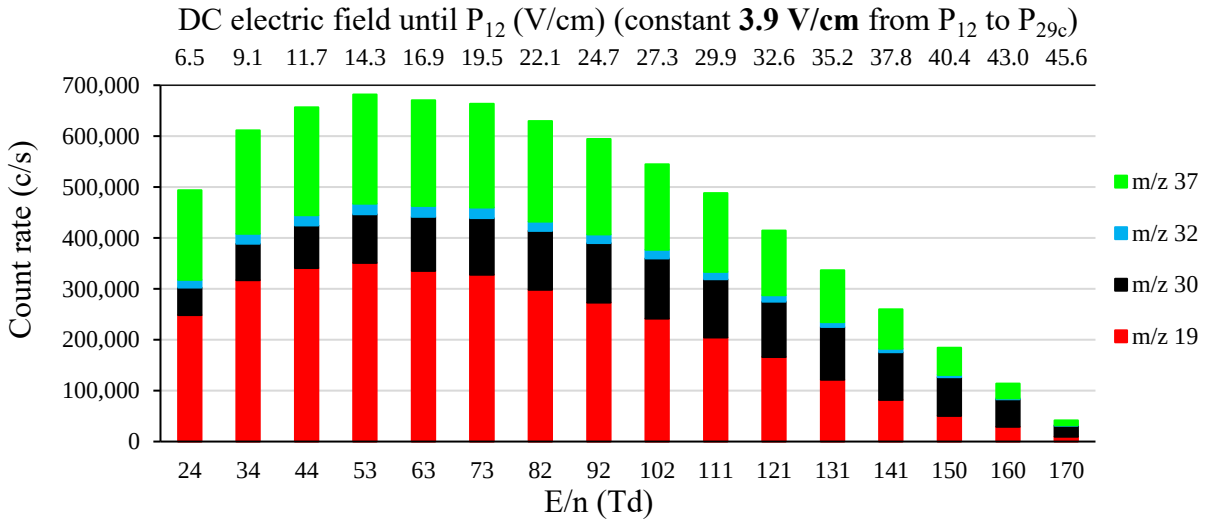

Figure 4.20: Count rate of the main reagent ions running HC13BD as a function of the split DC electric field and E/n in RF mode

Regarding n-butylbenzene, the more fragile molecule, the best performance in LG mode is observed for a DC electric field of about 7.13 V/cm (27 Td). In the SG mode it was possible to raise the DC electric field in the first half of the reactor and bring about sufficiently high collision energies to fragment the molecular ion. However, with a gradient of 15.36 V/cm (57 Td) in the first section a small yield increase of the molecular ion (~ 7 %) was achieved. A possible explanation for why this increase was not greater is offered in the next section.

Regarding hexachloro-1,3-butadiene, a more robust molecule, the best molecular ion count rate in LG mode was observed at the maximum DC electric field of 21.14 V/cm (79 Td). In the split gradient mode, despite increasing the collision energies in the first half, the molecular ion signals of HC13BD increased. Setting 40.36 V/cm (150 Td) in the first section, the yield of the molecular ion at m/z 259 was increased by ~ 115 %. This is the type of performance improvement that had been hoped for.

After analysing all the related plots, it can be seen that the reagent ions' distribution within the reactor is changed by splitting the DC electric field (c.f. Figure 4.8 and Figure 4.12). Indeed, unlike the LG mode, the SG mode causes the hydronium (m/z 19) proportion to decrease and its signal intensity to drop dramatically with increasing DC electric field. Initial thoughts to explain this phenomenon included too high collisional energies in the 1st section of the reactor. However, in SG mode, even the greatest DC electric field operating in that section (DC mode only) provides up to ~ 170 Td, which is not a range of values susceptible to reduce the hydronium signal by more than 99 % while increasing the E/n value from 79 Td.

The expectation that having a higher DC field in the first half would help to increase the analyte ion signals was definitely observed for the HC13BD and is assumed to be due to a reduction in losses due to space charge effects. The behaviour of the nBB molecule did not follow this same trend. An attempt to understand why is presented next.

4.2.3.3 Axial wells – V_{trap}

As explained in the previous chapter, the effective potential is meaningful after consideration of the collisional damping due to the RF electric field. For given ion-funnel settings (Mark V here), γ is a function of the mass and the ion mobility of the ion. This is why the following values are so different as shown in Table 4.2:

Table 4.2: average collisional damping γ due to the RF electric field as a function of the ion

Ion mass	**m/z**	**19**	**30**	**32**	**37**	**135**	**259**
γ(ion in N_2)	**N/A**	0.04	0.07	0.08	0.10	0.51	0.74

The axial well, V_{trap}, along the central axis of the reactor is a specific case of V* (effective potential) and is inversely proportional to the mass of the ion. The V_{trap} field is deepest for all ions at P_{27} (z = 86.4 mm). However, the values for the Mark V reactor being used are considerably reduced compared to the first generations of ion-funnels. This is clearly seen in Figure 4.21, which represents V_{trap} of nBB, HC13BD and their reagent ions as a function of z in the Mark V reactor.

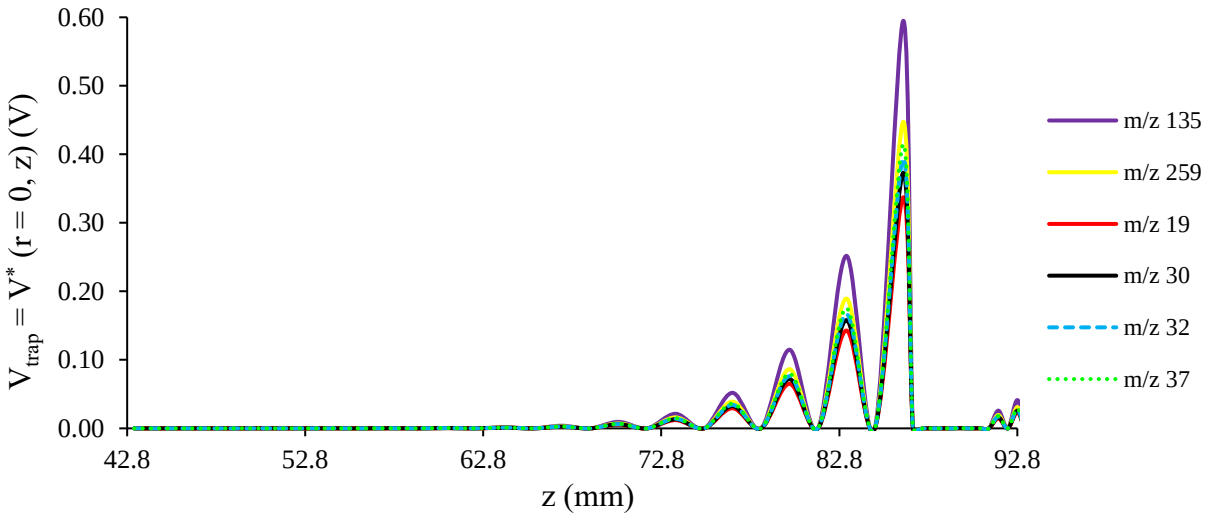

Figure 4.21: V_{trap} (central axial well) applied to both protonated nBB and HC13BD as well as to the reagent ions, all in nitrogen, under RF field

With the Mark V ion-funnel, the deepest central axial well occurs at P_{27} (86.4 mm) and is most pronounced for the heaviest ions. Despite the greater collisional damping for HC13BD (Table 4.2), the trapping is greatest for the protonated ion of nBB and may partially explain the greater enhancement of the HC13BD in the split gradient mode.

4.2.3.4 Overriding field – E_{over}

The overriding field is the difference between the DC electric field, dragging the ions across the reactor and along the centre axis, and the trapping field, susceptible to trap the ions if strong enough (derived, along the axial centre, from the central axial well previously presented).

- n-butylbenzene and reagent ions – linear gradient mode under E_{DC} = 7.13 V/cm (cf. Figure 4.22)

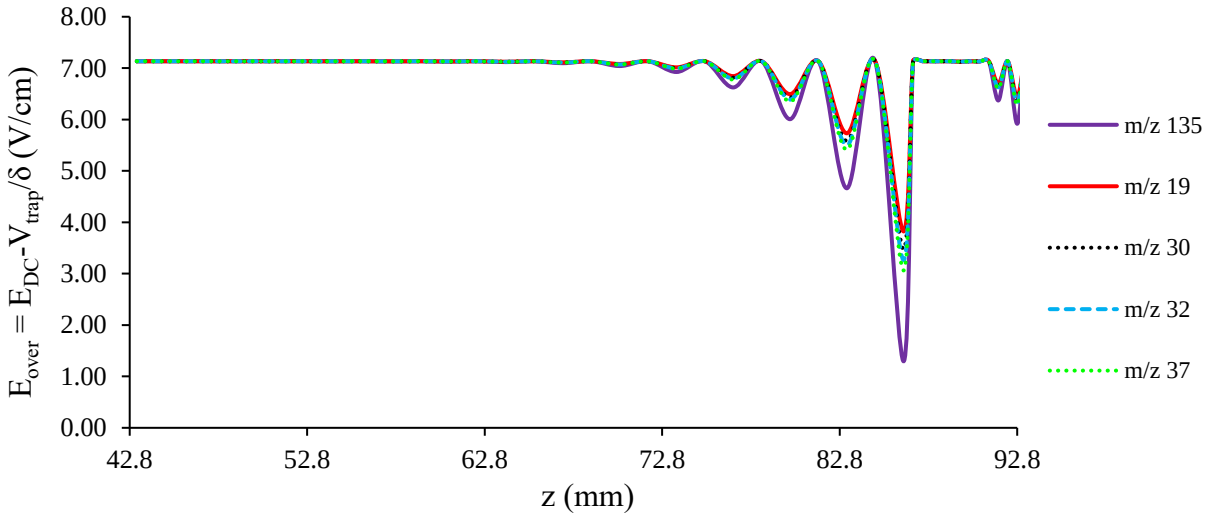

Figure 4.22: $E_{over} = E_{DC} - E_{trap}$ (overriding field along the central axis) applied to protonated nBB and the reagent ions in nitrogen under E_{DC} = 7.13 V/cm and under RF field

- n-butylbenzene and reagent ions – split gradient mode under fixed E_{DC} = 3.16 V/cm from P_{12} (cf. Figure 4.23)

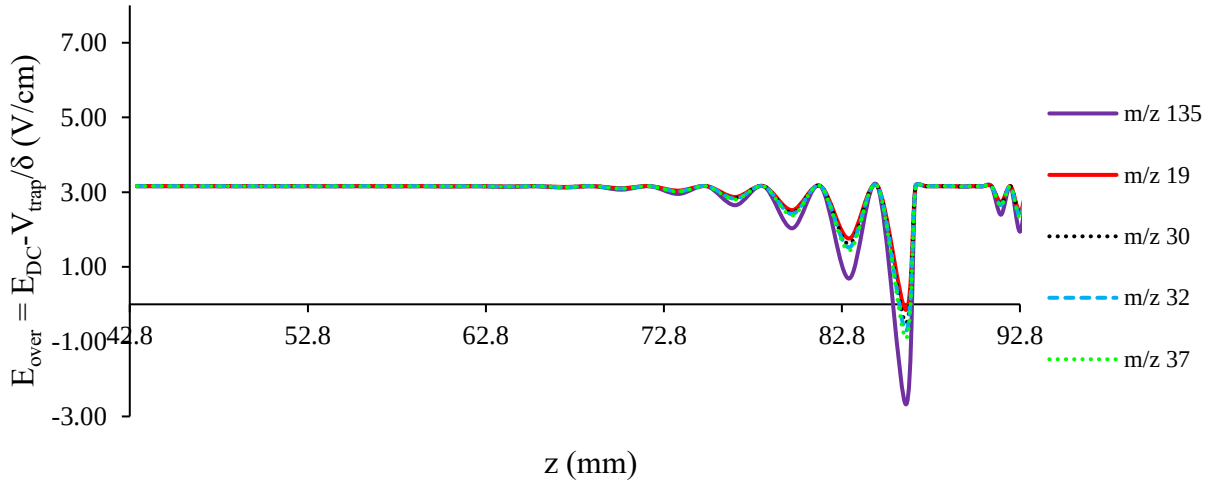

Figure 4.23: $E_{over} = E_{DC} - E_{trap}$ (overriding field along the central axis) applied to protonated nBB and the reagent ions in nitrogen under fixed E_{DC} = 3.16 V/cm in the second reactor section and under RF field

Firstly, the overriding field is clearly reduced in SG mode, making the ions, and especially protonated nBB, more likely to be trapped within the axial wells of the RF area. This increased trapping effect could offset the benefit of the reduction of the space charge effect in the first section (due to the greater DC electric field).

Secondly, it is noticeable that at P_{27}, E_{over} becomes negative at z = 86.4 mm in SG mode, i.e. theoretically insufficient to drag these ions across the reactor. However, m/z 135 was detected for those respective conditions. The main unknown parameter, compared to the ion-funnels experiments of chapter 3, is the water vapour flow inside the ion source. For the data acquired previously (chapter 3), the water flow into the glow discharge source was low (0.1 sccm), whereas for the data under discussion in this chapter it was 0.75 sccm. This will have increased the level of neutral water molecules such that the ion mobilities may have been reduced significantly [95]. Indeed, the more humid the reactor is, the lower the ion drift

velocities are and the lower the values of gamma are. This effectively reduces the intensity of the trapping fields.

The relative humidity of the reactor is not directly measurable but a reduction of 40 % of the ion mobilities, due to the relative humidity, would be enough to create a slightly positive overriding field for m/z 135.

- Hexachloro-1,3-butadiene and reagent ions – Linear mode under E_{DC} = 21.14 V/cm (cf. Figure 4.24)

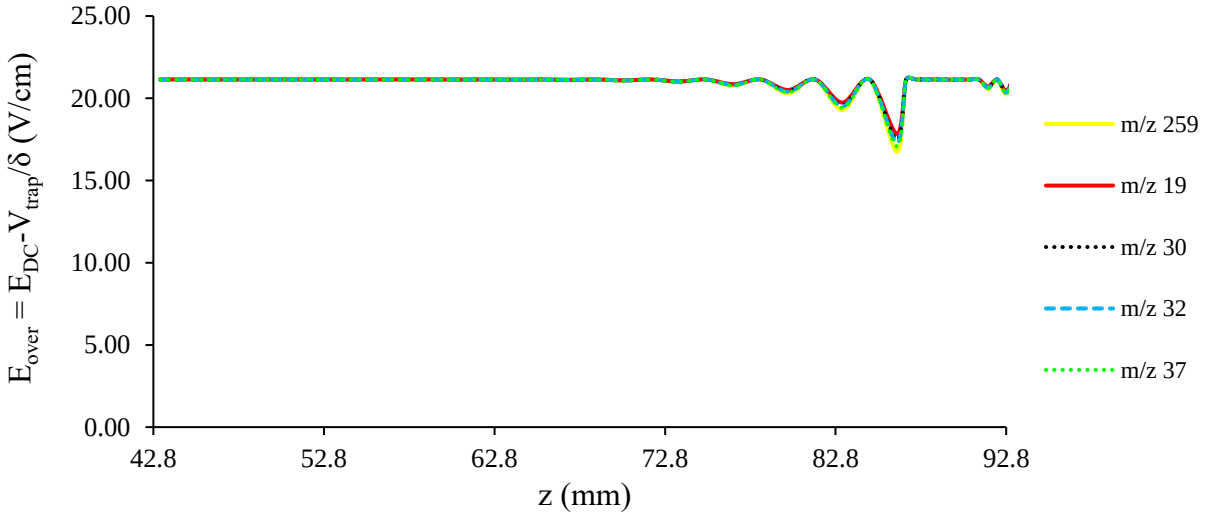

Figure 4.24: E_{over} = E_{DC} - E_{trap} (overriding field along the central axis) applied to protonated HC13BD and the reagent ions in nitrogen under E_{DC} = 21.14 V/cm and under RF field

- Hexachloro-1,3-butadiene and reagent ions – split gradient mode under fixed E_{DC} = 3.90 V/cm from P_{12} (cf. Figure 4.25)

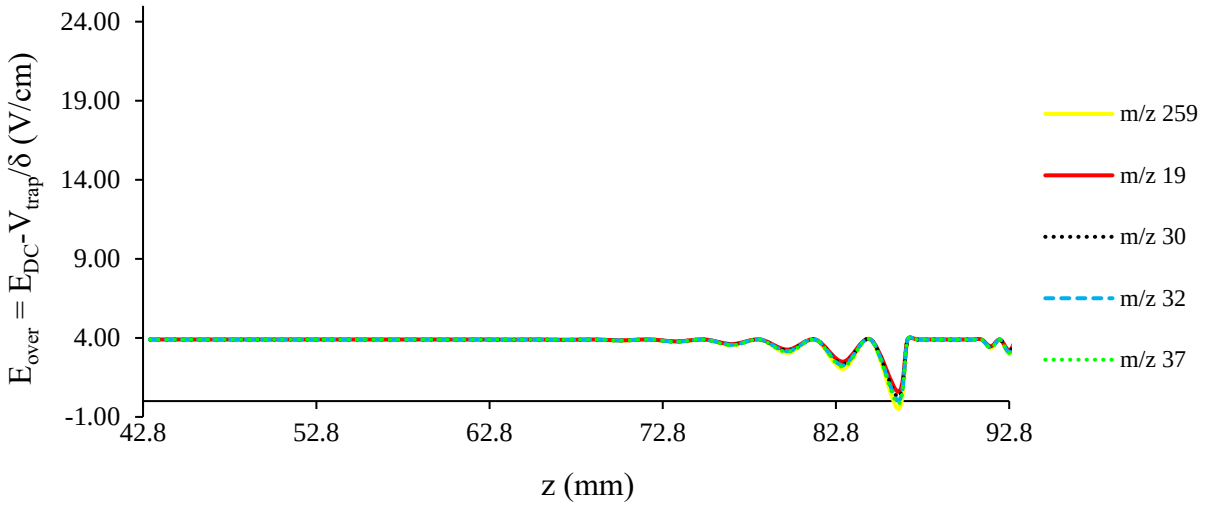

Figure 4.25: $E_{over} = E_{DC} - E_{trap}$ (overriding field along the central axis) applied to protonated HC13BD and the reagent ions in nitrogen under fixed E_{DC} = 3.90 V/cm in the second reactor section and under RF field

Having done a detailed analysis of the trapping fields for the specific conditions used for the nBB and HC13BD ions, the small difference in the value applied to P_{12} for each of the molecules appears to have had a disproportionate effect. The resulting overriding fields were sufficient to transmit the HC13BD effectively, whereas in the case of the nBB ions they were less so.

With regard to the proposal that having a higher DC field in the split gradient mode would reduce ion losses due to space-charge effects, this certainly seems true for the HC13BD, whereas for the more delicate nBB molecule there is a limit to the magnitude of the gradient in this first section before fragmentation occurs, offsetting any advantages of reducing space-charge effects. Unlike protonated nBB, protonated HC13BD, being a more robust ion, is much less affected by the greater collisional energies in the 1st section of the reactor, taking more benefits of the reduction of the space charge effect in that section.

Secondly, there is also a negative value for the deepest axial well. However, unlike for nBB, only a small reduction in the strength of the trapping field (due to humidity) would be sufficient to result in a positive value of E_{over} and thus allow for transmission of the HC13BD ions.

4.2.3.5 DC kinetic energy, RF kinetic energy, kinetic energy in the centre of mass of the colliding system

After analysing the trapping effect of the RF field and the space charge effect of the 1st section of the reactor, an energetic analysis was conducted to analyse the results around both probe molecules.

- The reduction of the space charge effect in the 1st section is realised through the increase of the DC electric field, and consequently of the DC kinetic energy ($E_{k,DC}$), in both LG and SG modes.
- The increase of the DC electric field in LG mode increases the drift velocities of ions and consequently the RF kinetic energy ($E_{k,RF}$) they undergo in the RF area.
- The kinetic energy in the centre of mass of the colliding system (E_k(CM)) is an increasing function of the ion velocities and consequently of the DC electric field.

The results of this chapter can also be considered as a function of these energies on top of the DC electric field and E/n. The following parameters are considered:

- DC electric field
- E/n
- $E_{k,DC}$-$E_{k,RF}$-E_k(CM) of the protonated analyte
- Count Rate (CR) of the protonated analyte
- The MH^+ proportion (prop.)

- The ratio of the hydronium signal divided by the molecular ion signal ($19/MH^+$)

Table 4.3 provides a colour coding to express ranges of these values and Table 4.4 and Table 4.5 display both these values and colours for nBB and HC13BD in both LG and SG modes as a function of changing the DC field. In the case of the LG mode, this is across the entire reactor, whereas for the SG mode it is only from P_1 to P_{12}. Note that there is no change in the drift velocities in the SG mode within the ion-funnel, and so the value of $E_{k,RF}$ is fixed, whereas for the LG mode it changes within the funnel with the changing DC field.

Table 4.3: Colour coding to represent the values of: Electric field E_{DC}, Reduced electric field E/n, E_{kDC}-E_{kRF}-E_k(CM), Count Rate (CR), Proportion of the ion (Prop.) and finally, the ratio of hydronium counts divided by molecular ion counts ($19/MH^+$). Data will be shown for both protonated nBB and HC13BD.

E_{DC}	**E/n**	**$E_{k,DC}$ - $E_{k,RF}$ - E_k(CM)**
V/cm	**Td**	**eV**
$0 \leq x < 10$	$0 \leq x < 40$	$0.000 \leq x < 0.050$
$10 \leq x < 20$	$40 \leq x < 80$	$0.050 \leq x < 0.100$
$20 \leq x < 30$	$80 \leq x < 120$	$0.100 \leq x < 0.200$
$30 \leq x < 40$	$120 \leq x < 160$	$0.200 \leq x < 0.300$
$40 \leq x < 50$	$160 \leq x < 200$	$0.300 \leq x < 0.400$
		$0.400 \leq x < 0.500$
CR	**Prop.**	**$19/MH^+$**
c/s	**%**	**-**
$0 \leq x < 500$	$0.00 \leq x < 20.00$	$0 \leq x < 250$
$500 \leq x < 1000$	$20.00 \leq x < 40.00$	$250 \leq x < 500$
$1000 \leq x < 1500$	$40.00 \leq x < 60.00$	$500 \leq x < 1000$
$1500 \leq x < 2000$	$60.00 \leq x < 80.00$	$1000 \leq x < 1250$
$2000 \leq x < 2500$	$80.00 \leq x < 100.00$	$1250 \leq x < 1500$
$2500 \leq x < 3000$		

- n-butylbenzene

Table 4.4: Main results of protonated nBB between linear and split E_{DC} gradient when RF fields are applied

	n-butylbenzene - m/z 135 - MH^+							
	E	**E/n**	**$E_{k,DC}$**	**$E_{k,RF}$**	**E_k(CM)**	**CR**	**Prop.**	**19/MH^+**
	V/cm	**Td**	**eV**	**eV**	**eV**	**c/s**	**%**	**-**
Area	**P_1-P_{29s}**	**P_1-P_{12}**	**P_1-P_{29s}**	**P_{13}-P_{27}**	**P_1-P_{29s}**			
LG mode	4.98	19	0.005	0.030	0.041	1753	65.01	162
	6.06	23	0.007	0.037	0.043	2032	66.50	196
	7.13	27	**0.010**	**0.044**	**0.044**	**2178**	**67.41**	**226**
	8.21	31	0.013	0.050	0.046	2051	65.84	279
	9.29	35	0.016	0.057	0.048	2029	62.51	321
	10.37	39	0.020	0.063	0.051	1969	59.73	362
	11.44	43	0.025	0.070	0.054	1875	54.64	415
	12.52	47	0.030	0.077	0.057	1703	50.61	494
	13.60	51	0.035	0.083	0.060	1589	47.18	558
	14.68	55	0.041	0.090	0.064	1481	45.03	632
	15.75	59	0.047	0.096	0.067	1338	40.30	726
	16.83	63	0.053	0.103	0.072	1227	37.65	819
	17.91	67	0.061	0.109	0.076	1121	34.02	913
	18.99	71	0.068	0.116	0.081	967	35.29	1065
	20.06	75	0.076	0.123	0.086	902	30.19	1149
	21.14	79	0.084	0.129	0.091	791	30.82	1304
Area	**P_1-P_{12}**	**P_1-P_{12}**	**P_1-P_{12}**	**N/A**	**P_1-P_{12}**			
SG mode	7.55	28	0.011		0.045	1798	63.39	130
	10.16	38	0.019		0.050	2111	67.67	130
	12.76	48	0.031		0.057	2289	63.65	123
	15.36	**57**	**0.045**		**0.066**	**2334**	**65.04**	**121**
	17.97	67	0.061		0.076	2348	60.28	112
	20.57	77	0.080		0.088	2276	59.27	103
	23.18	86	0.101		0.101	2219	54.47	91
	25.78	96	0.125		0.116	2070	49.89	85
	28.39	106	0.152		0.133	1927	46.09	71
	30.99	115	0.181		0.151	1619	42.91	57
	33.59	125	0.213		0.171	1327	42.66	48
	36.20	135	0.247		0.192	1053	26.05	38
	38.80	144	0.284		0.215	770	13.93	27
	41.41	154	0.323		0.239	262	6.81	18
	44.01	164	0.365		0.266	0	0.00	
	46.61	174	0.410		0.293	0	0.00	
	P_{12}-P_{29s}	**P_{12}-$_{29s}$**	**P_{12}-P_{29s}**	**P_{13}-P_{27}**	**P_{12}-P_{29s}**			
	3.16	N/A	0.002	0.019	0.040			

- Hexachloro-1,3-butadiene

Table 4.5: Main results of protonated HC13BD between linear and split E_{DC} gradient when RF fields are applied

	Hexachloro-1,3-butadiene - m/z 259 - MH^+							
	E	E/n	$E_{k,DC}$	$E_{k,RF}$	E_k(CM)	CR	Prop.	19/MH^+
	V/cm	Td	eV	eV	eV	c/s	%	-
Area	P_1-P_{29s}	P_1-P_{12}	P_1-P_{29s}	P_{13}-P_{27}	P_1-P_{29s}			
LG mode	4.98	19	0.007	0.063	0.040	260	47.34	1097
	6.06	23	0.010	0.077	0.041	313	52.36	1277
	7.13	27	0.013	0.091	0.043	365	54.57	1370
	8.21	31	0.018	0.104	0.044	412	56.69	1412
	9.29	35	0.023	0.118	0.046	464	57.54	1403
	10.37	39	0.028	0.132	0.048	525	57.87	1357
	11.44	43	0.034	0.145	0.050	588	57.54	1319
	12.52	47	0.041	0.159	0.052	659	56.12	1260
	13.60	51	0.049	0.173	0.054	743	56.42	1209
	14.68	55	0.057	0.186	0.057	835	57.23	1112
	15.75	59	0.065	0.200	0.060	918	58.25	1066
	16.83	63	0.075	0.214	0.063	1012	60.17	973
	17.91	67	0.084	0.227	0.066	1111	61.98	908
	18.99	71	0.095	0.241	0.069	1169	63.29	865
	20.06	75	0.106	0.255	0.073	1209	63.09	833
	21.14	**79**	**0.118**	**0.268**	**0.077**	**1232**	**63.40**	**828**
Area	P_1-P_{12}	P_1-P_{12}	P_1-P_{12}	N/A	P_1-P_{12}			
SG mode	6.51	24	0.011		0.042	229	47.43	1085
	9.11	34	0.022		0.045	330	49.26	960
	11.72	44	0.036		0.050	440	51.43	774
	14.32	53	0.054		0.056	584	53.01	601
	16.93	63	0.075		0.063	729	53.93	460
	19.53	73	0.100		0.071	917	53.67	357
	22.14	82	0.129		0.080	1107	51.95	269
	24.74	92	0.161		0.091	1314	51.73	208
	27.34	102	0.197		0.102	1595	53.23	151
	29.95	111	0.236		0.115	1878	54.95	109
	32.55	121	0.279		0.129	2103	56.68	79
	35.16	131	0.325		0.144	2362	58.35	51
	37.76	141	0.375		0.160	2581	58.07	32
	40.36	**150**	**0.429**		**0.178**	**2653**	**56.94**	**19**
	42.97	160	0.486		0.196	2591	55.68	11
	45.57	170	0.547		0.216	2277	53.18	4
	P_{12}-P_{29s}	P_{12}-$_{29s}$	P_{12}-P_{29s}	P_{13}-P_{27}	P_{12}-P_{29s}			
	3.90	N/A	0.004	0.049	0.040			

The orange boxes represent what could be regarded from an analytical point of view as the best compromise between signal intensity and minimal fragmentation of the molecule.

Comparing the LG and SG modes, the benefits of reducing the space charge effect in the 1st section (by increasing the electric field) is limited if the ions do not have a sufficiently high overriding field in the RF section where the DC field is much lower. Also, for a more fragile molecule such as nBB, it is possible that an increased electric field in the first section employed to limit the effects of space charge may be counter-productive to molecular ion detection if the collision energy in this first section is too high and causes fragmentation.

4.3 Conclusion

Splitting the DC electric field across the reactor is a compromise between reduction of the space charge effect in the 1st section, the limitation of the penetration into the RF field and the ability to override the trapping field induced by the RF field. Protonated nBB had a maximum increase of its signal intensity of just 7 %. For HC13BD however, an increase in signal intensity of 115 % was observed, with no significant change in the ion proportions. This is attributed both to its greater robustness and because, for the analytical conditions used, a greater overriding field occurred within the RF funnel section.

A final comment must be made concerning the apparently dramatic fall-off of reagent ion signals in the SG mode for both nBB and HC13BD, as seen in Figure 4.16 and Figure 4.20 and as evident in the rapidly reducing ratio of $19/MH^+$ in Table 4.4 and Table 4.5. This is, at first sight, particularly puzzling, since the analyte ions do not show the same trend.

The range of values of V/cm explored in the first half of the reactor in SG mode was more than double that which was explored in the LG mode. The maximum value in LG mode

was 21 V/cm. In SG mode up to 21 V/cm, there is little loss of the reagent ion signals, and so care must be taken in making a simple comparison.

Clearly, in SG mode, past a DC field of 21 V/cm in the first half of the reactor, the molecular ion signals of the analytes do not fall at a similar rate as the reagent ions. Therefore, it cannot be that the reagent ions are greatly reduced within the reactor, but rather that there is a mass-dependent transmission out from the reactor exit.

Given that the DC gradient and the RF conditions inside the ion-funnel were constant in SG mode, it can only be that the increased energy of the reagent ions in the first half of the reactor is responsible for the mass-dependent poor funnelling out of the reactor. The mechanism for this is not known.

CHAPTER 5: LIMITATIONS IN THE USE OF E/n FOR SPECIFYING PRODUCT ION DISTRIBUTIONS

5.1 Introduction

A key operational parameter that is quoted in the majority of studies involving PTR-MS is the reduced electric field E/n [96-98], where E is the electric field and n (directly deduced from the Ideal Gas Law) is the buffer gas number density. This is because, through the Wannier equation, it can be used to define the collisional energy of the ions. Hence, often the product ion distributions (PIDs) are given in the literature as plots of product ion percentages or relative ion intensities versus E/n. From these plots, the appropriate E/n can be selected for analytical purposes (e.g. maximum signal for highest sensitivity or product ion patterns for higher specificity). The use of E/n, however, becomes of less use when using RF ion-funnel devices, because of the combination of DC and RF electric fields contributing to the total electric field, which will have a spatial and temporal dependence; spatial because the RF amplitude decreases with increasing distance from the RF electrodes. Nevertheless, given the convenience of using E/n, it has been proposed that an effective DC reduced electric field could be assigned for DC+RF operation by comparing fragmentation behaviour between DC and DC+RF modes [77].

An aim of the PhD work was to explore the use of an effective reduced electric field by using three probe molecules, which have been specifically selected on the basis that they should have sequential fragmentation with increasing DC E/n. These are n-butylbenzene (nBB), triethylphosphate (TEP) and ethylbenzene (EB), details on the structure and thermodynamic properties are discussed later in section 5.2. The metaphor of a ‘probe’ captures the idea, analogous to a space probe, of sending out a device and receiving data back from a place where one is not able to ‘see’ directly. The criterion for choosing a probe compound was that it should be sensitive to the ion-molecule collision energy (the effective temperature of an ion-molecule collision) such that it fragments in a well-understood manner based upon its structure and bonding. By determining the E/n value at which a probe molecule generates a specific ratio of

product ions, more insight into what is happening when the same probe analyte is injected into the RF funnel should be obtained – basically attributing an effective E/n value that can be defined for RF operation.

The aim of this chapter is to report the dependence of the product ion distributions for these three probe molecules for various prototypes of the ion-funnel device, whilst operating in DC mode only for different E/n values. The goals are to determine the effects of design (and hence electric field distributions), if any, and E/n on the fragmentation behaviour, and whether an effective E/n can be used to represent the effects of RF fields on the reaction dynamics occurring in the various drift tubes.

Following proton transfer, which may be non-dissociative or dissociative, subsequent collisional induced dissociations of the initial product ions formed can occur. A key assumption in all PTR-MS studies is that provided the E/n value is constant, the product ions observed at any given E/n are the same, irrespective of how the temperature, pressure and electric field are arranged to deliver a specific E/n. However, this assumption has never been tested. Certainly, it ignores the effects of different operational temperatures, and how temperature makes a thermal contribution to the Wannier equation. However, the range of temperatures over which PTR-MS studies operate is small, and hence differences in operational temperatures to the total translational energy is small, but non-negligible, as discussed in the next section.

The Wannier equation does take into account the thermal contribution to the total translational energy of ions moving through a buffer gas under the influence of an electric field. However, what cannot be accounted for is the collisional internal excitation of H_3O^+ and of product ions in the drift tube of a PTR-MS. These increases in internal energies that lead to dissociation, result from a build-up of small increases in internal energies through multiple ion-neutral collisions. These lead to higher energy exchanges in the initial H_3O^+ reaction, or to

sequential dissociation of a molecular product ion formed by the initial proton transfer reaction. In conclusion, it is proposed that the frequency of collisions, which will be directly proportional to the pressure operating in the drift, and the drift tube temperature must play a role in determining the product ion distributions at any fixed E/n value.

A major goal of the study presented in this chapter is to determine the effects of changing temperature, pressure, electric field strength and drift tube design for a fixed E/n on the product ion distributions of the three probe molecules. It will be shown that **it is insufficient to quote simply the E/n value in PTR-MS studies operating in DC mode**, but that for a given drift tube design, E, T and P must all be provided if reproducibility of fragmentation behaviour is to be achieved, and even then, the product ion distributions will be specific to a given instrumental design.

Before presenting the results, some discussion will be provided of how temperature and pressure for a fixed E/n can have an effect on the product ion distributions. This will be a mostly qualitative discussion, because the energetic processes involved are complex, the transfer of translational energy to internal energy is inefficient, and the effects of pressure and temperature on ion mobilities are ignored.

5.1.1 Expected effects of temperature changes for fixed E/n

The Wannier equation has been described in detail in chapter 2. However, for convenience it is given below in E 5.1 [59]:

$$E_k(CM) = \frac{m_n}{m_n+m_i}\left(\frac{{v_D}^2}{2}\right)(m_i+m_c) + \frac{3}{2}k_B T_D \qquad \text{E 5.1}$$

This represents the kinetic energy in the centre of mass frame of an ion of mass m_i that is travelling through an unreactive carrier gas maintained at a temperature T_D, whose molecules have a mass m_c, and collides with a neutral reactant of mass m_n. The mean ion drift speed is v_D, being related to E/n through the following equation E 5.2 [41]:

$$v_D = K_o n_o \frac{E}{n} \qquad \text{E 5.2}$$

where K_o is the reduced ion mobility coefficient and n_o is the gas number density at STP [99].

As mentioned above, plots of product ion distributions as a function of E/n ignore the thermal contribution to fragmentation. This, as mentioned above, is perhaps reasonable given that a change in drift tube temperature by ~ 100 K will not result in a significant contribution on the collisional energy. This is illustrated below in Figure 5.1 for H_3O^+ ions colliding with N_2 at 297 K and 393 K drift tube temperatures under constant drift pressure of 0.8 mbar.

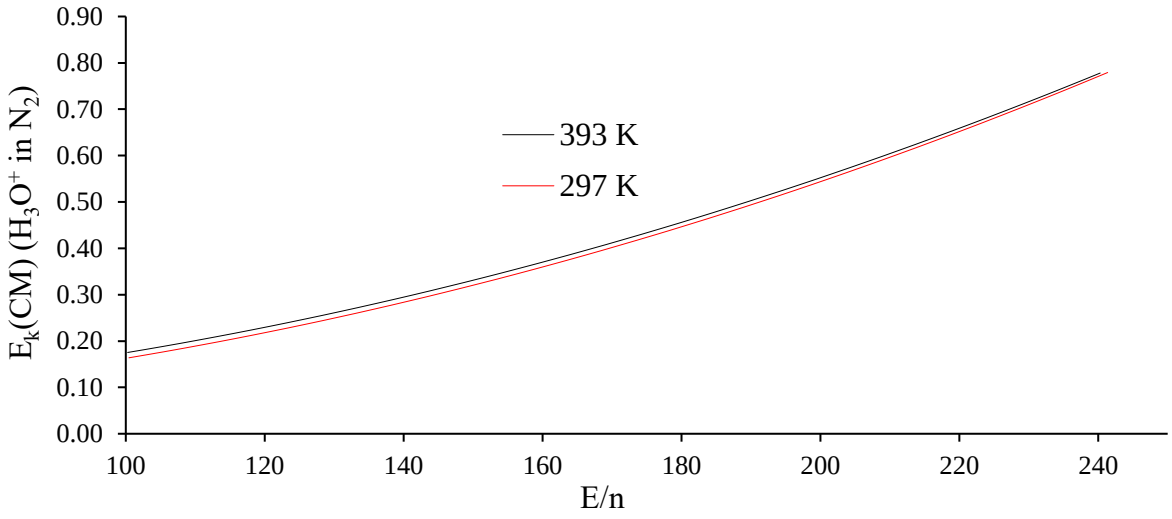

Figure 5.1: Changes in the centre of mass collisional energy as a function of E/n at two drift tube temperatures and constant pressure of 0.8 mbar. Although kinetic energy changes are small, they are not negligible.

There will also be some thermal increase of internal energy of the ions with increasing carrier gas temperature, distributed to the internal degrees of freedom according to the law of equipartition of energy, that will also contribute to the energy available for fragmentation, but that again will not significantly change over a temperature change of ~ 100 K. H_3O^+ colliding with N_2 has been used in this example, because the reduced ion mobilities are known over a large range of E/n values.

5.1.2 Expected effects of pressure changes for fixed E/n and temperature

As an ion propagates through a buffer gas under the influence of the electric field, collisions will occur with the carrier gas. The frequency of these collisions (z) is directly proportional to the number density n as given in E 5.3 [100]:

$$z = \sigma \sqrt{\frac{8k_B T_{eff}}{\pi \mu}}\, n \qquad \text{E 5.3}$$

where σ is the collision cross section and μ is the reduced mass of the colliding system. T_{eff} is the effective ion temperature given by E 5.4 [59]:

$$T_{eff} = T_D + m_n \frac{{v_D}^2}{3k_B} \qquad \text{E 5.4}$$

Once the collision frequency between an ion and a neutral is known, and to obtain the mean number of collisions for an ion across the buffer gas inside the reactor, it can be multiplied by the drift time of that ion t_D as defined in chapter 2 and given by E 5.5 for convenience:

$$t_D = \frac{l_D}{KE} = \frac{l_D}{K_o \frac{T_D P^o}{P_D T^o} E} \qquad \text{E 5.5}$$

where l_D is the drift tube length.

For fixed E/n, a lower pressure and hence a lower n, results in a lower collisional frequency. This is illustrated below in Figure 5.2 for H_3O^+ ions colliding with N_2 at 0.65 mbar and 1.2 mbar drift tube pressures and under constant drift temperature of 398 K. More collisions will build-up internal energy of H_3O^+ leading to increases in dissociative proton transfer, or for an initial product ion to fragment through collisional induced dissociation. Hence, the higher the pressure, the more fragmentation can be expected for a fixed E/n. A key objective is to test this prediction.

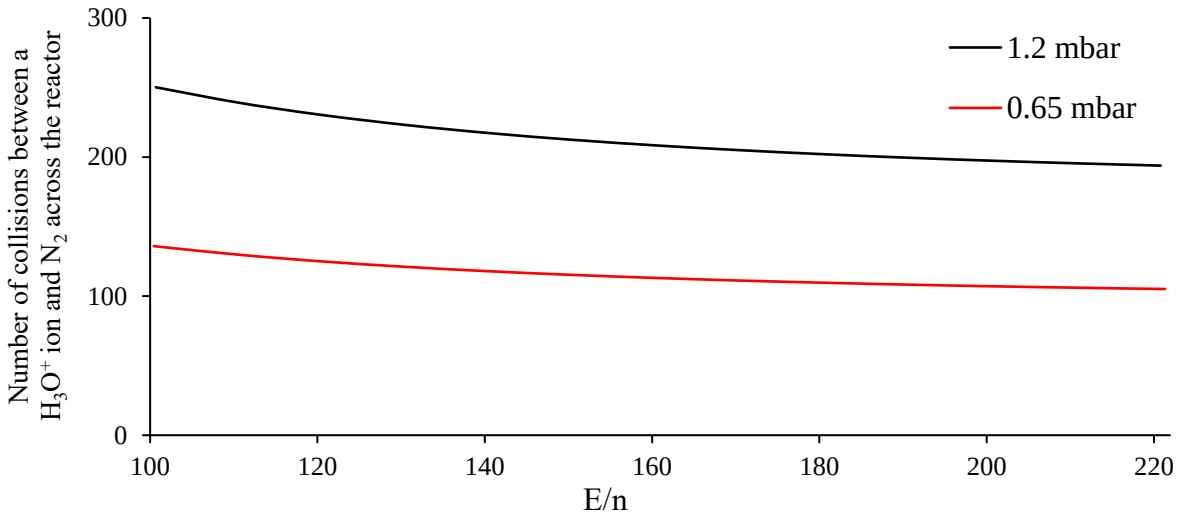

Figure 5.2 Changes in the total number of H_3O^+ + N_2 collisions as a function of E/n at two pressures whilst operating the drift tube at 398 K.

It should be noted that with PTR-MS, it is not possible to determine if a product ion derives directly from proton transfer or is a result of a secondary process caused by collisions

involving a primary product ion. However, that is not of concern here, because only the product ion distributions are of interest as a function of E/n, and not the mechanism causing them.

Another potential issue that needs to be considered is how changes in temperature and pressure in the drift tube affect the production of the protonated water clusters ($H_3O^{+\cdot}(H_2O)_n$ (n = 1, 2 and 3)) for buffer gas of fixed humidity entering the drift tube. For volatile compounds that have proton affinities greater than that of $(H_2O)_{n+1}$, proton transfer will occur at the collisional rate. Under these circumstances, if the relative amounts of H_3O^+ to $H_3O^{+\cdot}(H_2O)_n$ change for fixed E/n, as a result of different drift tube pressures and/or temperatures, then changes in the product ion distributions will occur owing to the energetically softer proton transfer from $H_3O^{+\cdot}(H_2O)_n$ to the volatile under study. The question is whether the changes in reagent ion signals are sufficient to cause noticeable modifications in the product ion distributions. Thus, it is important to have a measure of the intensities of the reagent ions present in the drift tube for fixed E/n, but under different T and P operating conditions. This has also formed part of this study. With an increase in pressure for a fixed E/n, the third body association can be expected to become more effective, resulting in an increase in $H_3O^{+\cdot}(H_2O)_n$, and hence less fragmentation being observed for those molecules that have proton affinities greater than H_2O_{n+1}, but in contrast the higher pressures will lead to more fragmentation.

In summary, there is a competition of less fragmentation with higher pressure, owing to more efficient production of protonated water clusters, and higher fragmentation owing to the more collisions involved. These two competing effects need to be considered in explaining any dependence of pressure on product ion distributions.

5.2 Characterisation of the fragmentation of probe molecules in DC mode

All the experiments with the various reactors followed a specific protocol, comparing different combinations of electric field, temperature and pressure. For a fixed value of E/n, three operational cases were followed, as summarised in Table 5.1. The aim is to compare product ion distribution plots as a function of E/n, but where the E/n value is achieved differently in each 'case'. In the following, only product ions that reached at least 3 % of the total product ion distribution for at least one E/n are considered. Each DC electric field, temperature and pressure within the reactors were specific to each reactor.

Table 5.1: Combinations of temperature (T), pressure (P) and DC electric field (E) within the PTR reactors to achieve the same E/n, in different ion-funnels

Case	T	P	E	n i.e. P/T
1	Variable	Constant	Variable	Variable
2	Constant	Variable	Variable	Variable
3	Variable	Variable	Constant	Constant

5.3 Results

5.3.1 Reagent ion signals ($H_3O^+ \cdot (H_2O)_n$) as a function of E/n

Despite the desire to have only hydronium ions in the reaction region of the drift tube, there is in practice a number of reagent ions present inside the reactor and especially for low reduced electric fields protonated water clusters ($H_3O^+ \cdot (H_2O)_n$ (n = 1, 2 or 3)) whose distributions vary as a function of E/n and its combination of E, T and P. For presentational purposes, the protonated water species are colour coded as summarised in Table 5.2.

Notice all the data points displayed in the PIDs plots of this chapter are subject to uncertainty calculations, according to derivation of equations given in Appendix A.11, and are not represented for readability purpose.

Table 5.2: Water ions considered in this study

Protonated water molecule	Code	m/z
H_3O^+	M19	19
$H_3O^+ \cdot H_2O$	M37	37
$H_3O^+ \cdot (H_2O)_2$	M55	55
$H_3O^+ \cdot (H_2O)_3$	M73	73

5.3.1.1 Reagent ion distribution ($H_3O^+ \cdot (H_2O)_n$) as a function of E/n

In this section, the results using a Mark I reactor are provided (measurements for the other reactor designs, Mark II, IV and V ion-funnels are provided in Appendix A.6). Figure 5.3-Figure 5.5 provide the distributions of water containing ions for cases 1-3, respectively. Case 1 is for when the pressure is constant but variable E and T, case 2 is when the pressure and E are variable but T is constant, and case 3 different T and P but E constant. Note the very early results using the Mark I reactor are a specific case compared to the next ion-funnel generations, because it was found later that the water vapour flow gauge was faulty and rather than 0.4 sccm being injected into the glow discharge it was in fact 8.5 sccm. However, that flow remained constant during those Mark I reactor experiments and did not change the trends described below.

Notice the curves shown in subsequent plots in this chapter are plots through all the data points collected (every 5 Td across the whole Mark I data of this chapter). Plots with data points included were deemed harder to read and thus the individual data points are not shown. Owing to factors such as statistical variations and other minor instrumental variations from experiment to experiment, the curves show departure from smooth changes in the PIDs. No significance is ascribed to these departures from perfectly smooth changes in proportions; what is important are claims about the trends in the data.

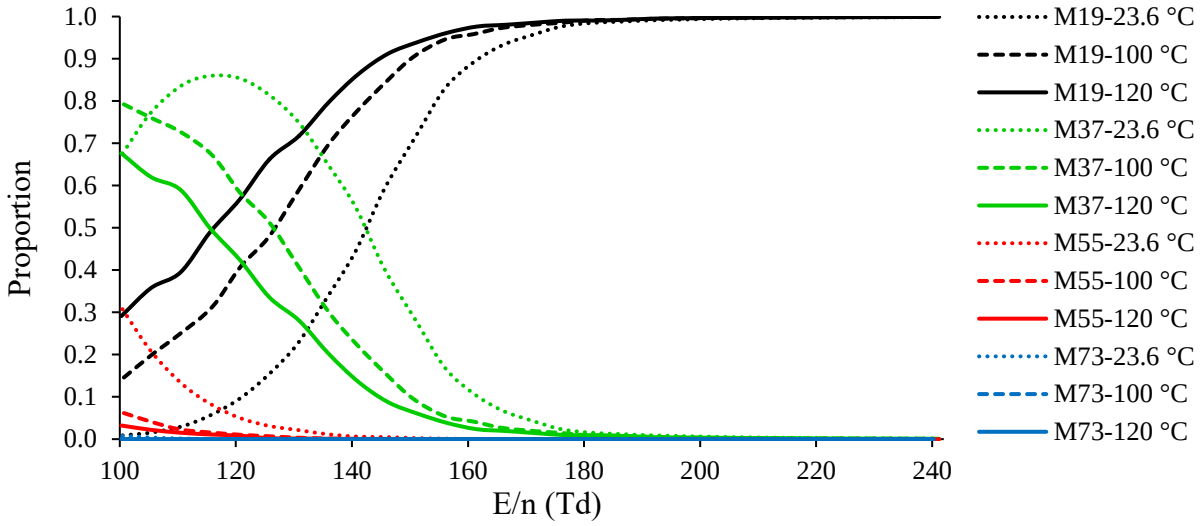

Figure 5.3: Case 1 – Distributions of water ions as a function of E/n at a constant pressure of 0.8 mbar and at three temperatures: 23.6, 100 and 120 ºC.

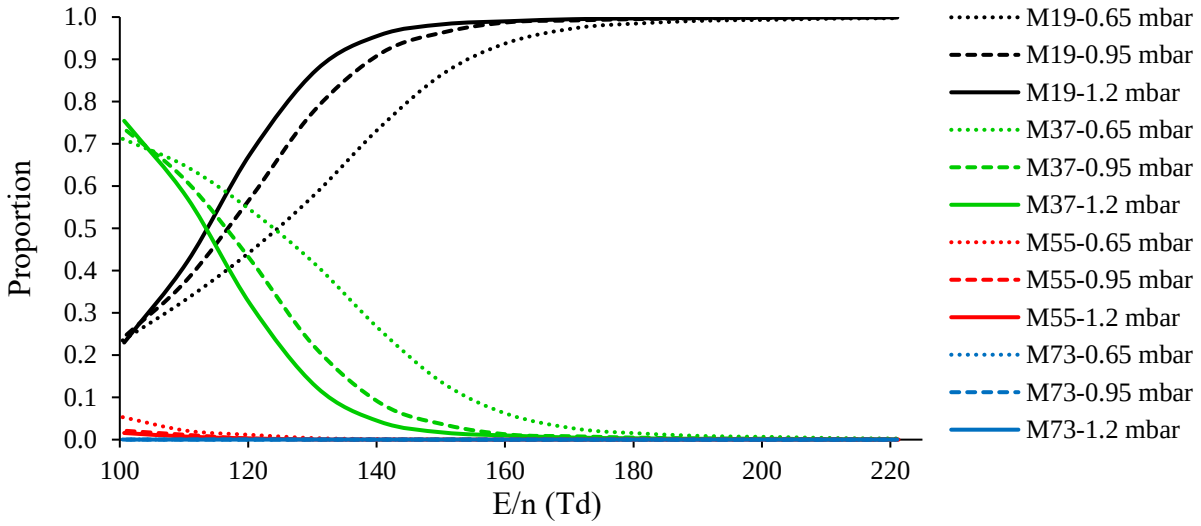

Figure 5.4: Case 2 – Distributions of water ions as a function of E/n at a constant temperature of 125 ºC and at three pressures: 0.65, 0.95 and 1.2 mbar

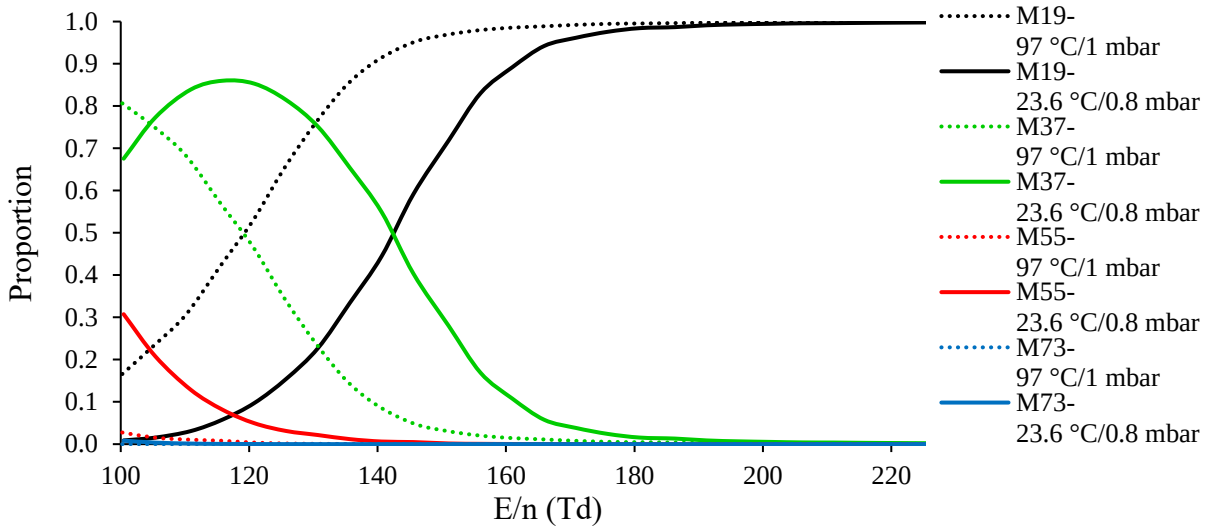

Figure 5.5: Case 3 – Distributions of water ions as a function of E/n for which the E field was kept constant and the temperature and pressure were modified to provide the same n, and hence the same E/n.

For completeness, the actual reagent ion counts are presented in the Appendix A.7. Using Cases 1 and 2, it can be seen that in general increasing the temperature for fixed P decreases the water clustering, as should be expected. However, for fixed T, increasing P resulted in less protonated water clusters. This implies that the collisional induced dissociation processes are more important than three-body association processes. The same is observed to varying degrees for the other reactor designs (see Appendix A.6). Varying combinations of T and P for a given n, creates the same trends found in Case 1, i.e., an increasing T leads to a greater hydronium proportion.

The results for the other funnel designs (see Appendix A.6) with a micro-funnel within Mark IV and V increases the 'softness' of the transmission by providing higher proportions of the largest water cluster ions at m/z 55 and 73, up to about 50 Td for Mark IV and about 80 Td for Mark V reactors.

Regarding the signal intensities (see Appendix A.7), hydronium always presents the greatest absolute signal and the general trends show the change in sensitivity and transmission

between Marks I and II and Mark IV and V. Indeed, the addition of the micro-funnel within the last generation increased the maximum hydronium signal by a factor 2 to 3.

Further data treatment related to the reagent ions distributions, not affecting the reflection about an effective E/n, was applied to the specific case of triethylphosphate, whose proton affinity does not involve only hydronium as proton giver (see Appendix A.8).

5.3.2 Product ions for the three molecules

5.3.2.1 n-butylbenzene (nBB) ($C_{10}H_{14}$)

The molecular structure of n-butylbenzene (nBB) is schematically presented in Figure 5.6, with its 4 sites of protonation (1-4) identified. Sites 2 and 3 include two locations due to chirality of the molecule. Although there are four sites for protonation only one value for the PA of nBB (792 kJ/mol) is provided in the literature [101]. Therefore, DFT calculations at 298 K were undertaken (B3LYP density functional method and the 6-31+G(d,p) basis set [102-104]) by Dr. Peter Watts (Molecular Physics Group, University of Birmingham) [105] to provide thermodynamic information involving proton transfer reactions. The calculations are summarised in Table 5.3, which also includes thermodynamic information on reaction pathways leading to some of the observed fragment product ions. DFT calculations were unable to find pathways for the other product ions, which indicates they are a result of collisional processes rather than a primary product from the reaction with a reagent ion. In comparison to 298 K, the bath gas and neutral analyte in the drift tube are thermalized to the operating temperature, but, as mentioned earlier, the reagent and product ions are at significantly higher effective translational temperatures, owing to the kinetic energy they gain

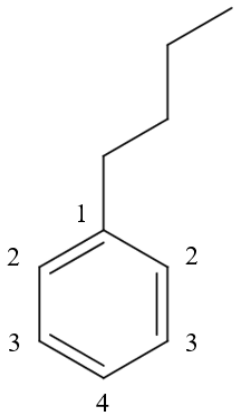

Figure 5.6: Available protonation sites of n-butylbenzene

in the applied electric field, *E*. The internal energies of the ions will thus be suprathermal and cannot be specified. Thus, the calculated energetics presented are only indicative, but can be used to determine if proton transfer is exoergic and search for plausible reaction/fragmentation pathways for the production of the observed fragment ions.

Table 5.3 Calculated 298 K enthalpy (ΔH) and free energy (ΔG) changes for the reaction pathways involving the reactions of H_3O^+ with n-butylbenzene [105]

Reactants	Protonation site	Products	$\Delta H_{298\ K}$	$\Delta G_{298\ K}$
			kJ/mol	kJ/mol
nBB + H_3O^+	1	$nBBH^+ + H_2O$	-86	-86
nBB + H_3O^+	2	$nBBH^+ + H_2O$	-121	-122
nBB + H_3O^+	3	$nBBH^+ + H_2O$	-102	-104
nBB + H_3O^+	4	$nBBH^+ + H_2O$	-127	-128
nBB + H_3O^+	1	$t\text{-}Bu^+ + C_6H_6 + H_2O$	-84	-129
nBB + H_3O^+	4	isobutene + $C_6H_7^+ + H_2O$	-20	-71
nBB + $H_3O^+ \cdot H_2O$	1	$nBBH^+ + 2H_2O$	+72	+38
nBB + $H_3O^+ \cdot H_2O$	4	$nBBH^+ + 2H_2O$	+31	-4
nBB + $H_3O^+ \cdot H_2O$	1	$t\text{-}Bu^+ + C_6H_6 + 2H_2O$	+74	-5

According to the calculated changes in free energy, protonation by H_3O^+ to all the basic sites is thermodynamically allowed. For reactions involving $H_3O^+ \cdot H_2O$, only proton transfer to site 4 is exoergic with $\Delta G_{298\ K}$ = -4 kJ/mol.

Over the range of E/n investigated, seven product ions are observed at nominal m/z values of 135, 91, 79, 77, 57, 41 and 39. $C_{10}H_{15}^+$ (m/z 135) is the protonated parent (MH^+), $C_7H_7^+$ (m/z 91) is a toluene-like ion, $C_6H_5^+$ m/z (77) and $C_6H_7^+$ (m/z 79) are benzene-like ions, $C_4H_9^+$ (m/z 57) is a butyl ion, and $C_3H_5^+$ (m/z 41) and $C_3H_3^+$ (m/z 39) are propyl ions. Two sites for fragmentation are identified on Figure 5.7. Fragmentation at site 1

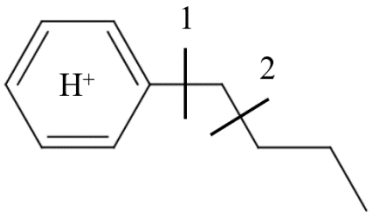

Figure 5.7: molecular structure of n-butylbenzene and fragmentation sites

leads to $C_4H_9^+$, $C_6H_5^+$ and $C_6H_7^+$. The product ions $C_7H_7^+$, $C_3H_3^+$ and $C_3H_5^+$ are a result of fragmentation from site 2. For convenience, the following colour code (cf. Table 5.4) will be used to represent the PIDs.

Table 5.4: Product ion groups of n-butylbenzene considered in this study

Group	Code	m/z
Parent molecular ion	M135	135
Toluene-like ions	Tol	91
Benzene-like ions	Ben	77 and 79
Butyl ion	M57	57
Propyl ions	Pro	39 and 41

A standard PID of nBB is as shown in Figure 5.8.

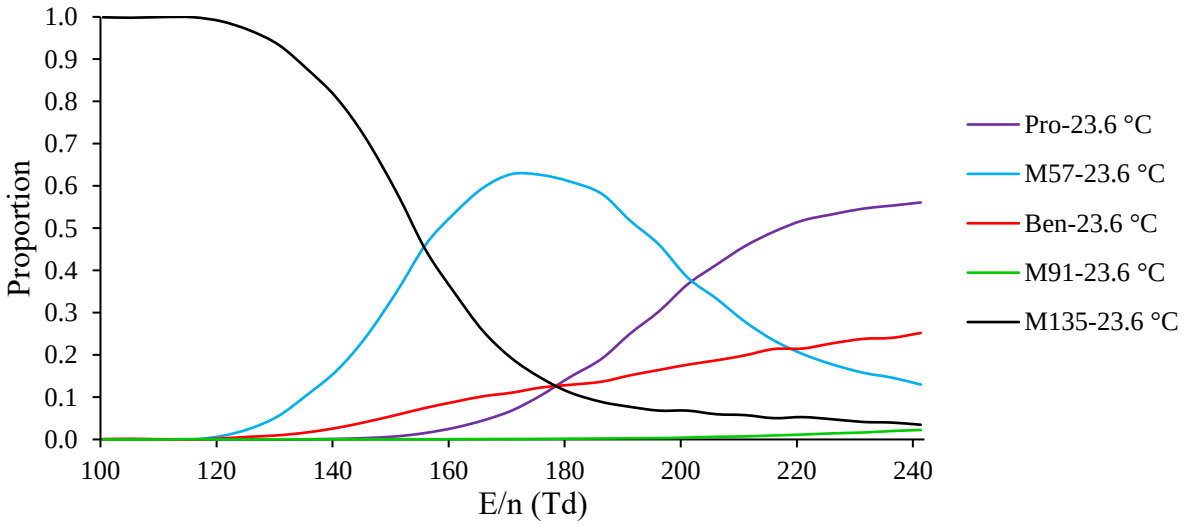

Figure 5.8: PID resulting from the reaction of H_3O^+ with n-butylbenzene as a function of E/n with the Mark V ion-funnel drift tube operating at 0.8 mbar and 23.6 °C

5.3.2.2 Triethylphosphate (TEP) ($C_6H_{15}O_4P$)

TEP has a published proton affinity of 909 kJ/mol [14], and hence proton transfer from H_3O^+ and all associated water clusters is thermodynamically allowed. DFT calculations provide details on the enthalpy and free energy changes for proton transfer, summarised in Table 5.5 [105], which also provides the energetics for loss of one ethene from the protonated parent.

Table 5.5: Triethylphosphate protonation energetics Calculated 298 K enthalpy (ΔH) and free energy (ΔG) changes for the reaction pathways involving the reactions of H_3O^+ with triethylphosphate [105]

Reactants	Products	$\Delta H_{298\ K}$	$\Delta G_{298\ K}$
		kJ/mol	kJ/mol
TEP + H_3O^+	$TEPH^+ + H_2O$	-226	-229
TEP + $H_3O^+ \cdot H_2O$	$TEPH^+ + 2H_2O$	-68	-105
TEP + $H_3O^+ \cdot 2H_2O$	$TEPH^+ + 3H_2O$	+27	-41
Transition state energy for loss of C_2H_4 above $TEPH^+$		+149	+143
$TEPH^+$	$DEPH^+ + C_2H_4$	+79	+32

Four product ions have been identified at m/z values of 183, the protonated parent ($(C_2H_5)_3O_4PH_2^+$), 155 ($(C_2H_5)_2O_4PH_2^+$), 127 ($C_2H_5O_4PH_3^+$), and 99 ($O_4PH_4^+$). $(C_2H_5)_2O_4PH_2^+$, $C_2H_5O_4PH_3^+$ and $O_4PH_4^+$ result from sequential elimination of C_2H_4 from the sites 1, 2 and 3, as illustrated in Figure 5.9. A colour code (cf. Table 5.6) is used to represent the ions in the PIDs. A standard PID of TEP is shown in Figure 5.10.

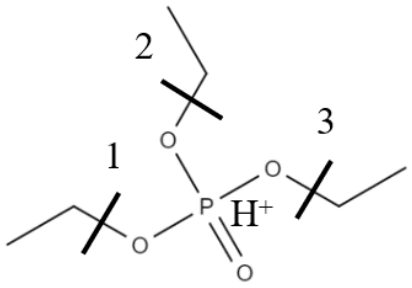

Figure 5.9: Molecular structure of triethylphosphate and fragmentation sites

Table 5.6: Product ion groups of triethylphosphate considered in this study

Group	Code	m/z
Parent molecular ion	M183	183
Elimination of 1 ethene	M155	155
Elimination of 2 ethenes	M127	127
Elimination of 3 ethenes	M99	99

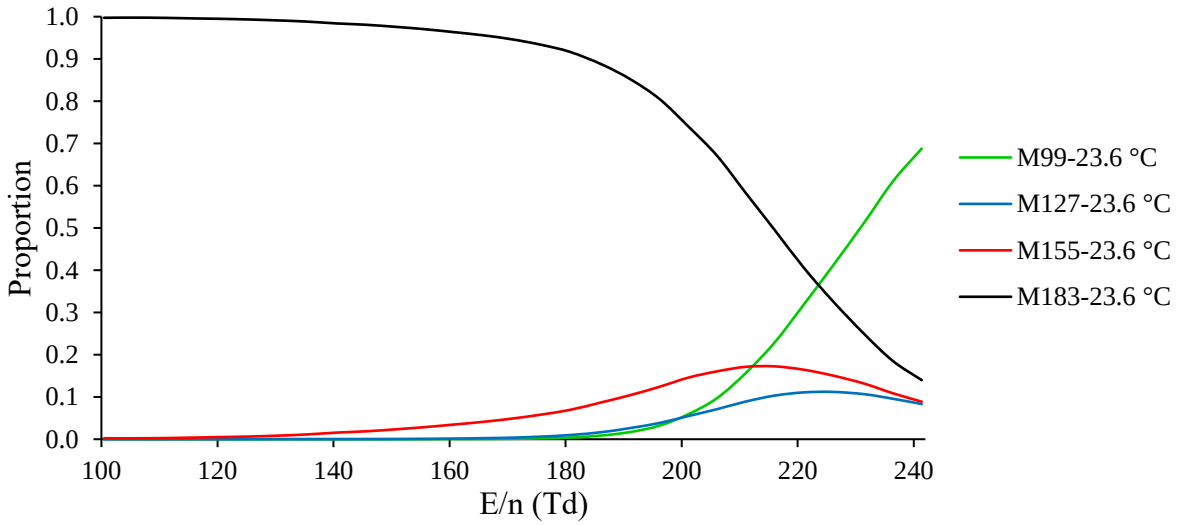

Figure 5.10: PID resulting from the reaction of H_3O^+ with triethylphosphate as a function of E/n with the Mark I ion-funnel drift tube operating at 0.8 mbar and 23.6 °C

5.3.2.3 Ethylbenzene (EB) (C_8H_{10})

This molecule has a similar structure to nBB and has a proton affinity of 788 kJ/mol [106], thus proton transfer can only occur from hydronium. Three product ions were identified: the protonated parent **(**$C_8H_{11}^+$) at m/z 107, and two fragment ions, corresponding to $C_7H_7^+$ (m/z 91), resulting from fragmentation on site 2 (cf. Figure 5.11), and $C_6H_7^+$ (m/z 79) resulting from a fragmentation on site 1. A colour code (cf. Table 5.7) will be used to represent the PIDs.

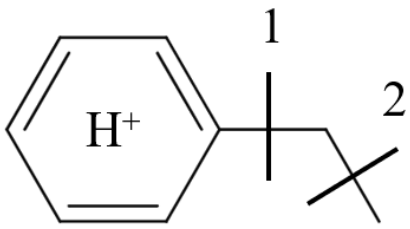

Figure 5.11: Molecular structure of ethylbenzene and fragmentation sites

Table 5.7: Product ion groups of ethylbenzene considered in this study

Group	Code	m/z
Parent molecular ion	M107	107
Toluene-like ion	M91	91
Benzene-like ion	M79	79

A standard PID of EB is shown in Figure 5.12.

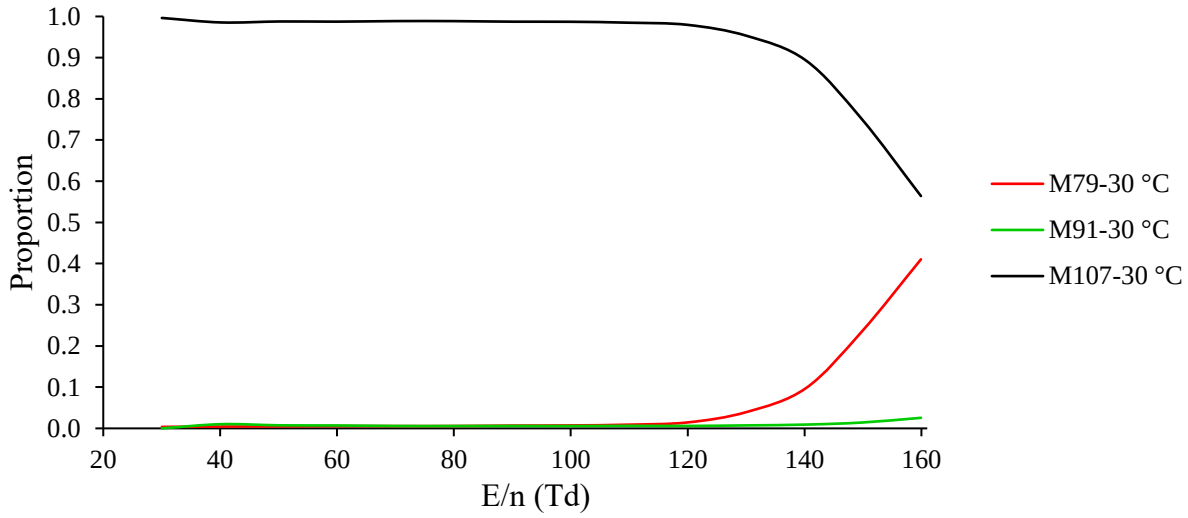

Figure 5.12: PID resulting from the reaction of H_3O^+ with ethylbenzene as a function of E/n with the Mark II ion-funnel drift tube operating at 0.9 mbar and 30 °C

5.3.3 PIDs as a function of E/n

5.3.3.1 n-butylbenzene (nBB) PIDs

In the following, the results for nBB using a Mark I reactor are provided. (Measurements for the other reactor designs, Mark IV and V ion-funnels, are provided in Appendix A.9.) Figure 5.13-Figure 5.15 provide the PIDs for nBB for case 1 pressure constant (variable E and T), case 2 pressure and E variable (T constant), and case 3 different T and P (E constant).

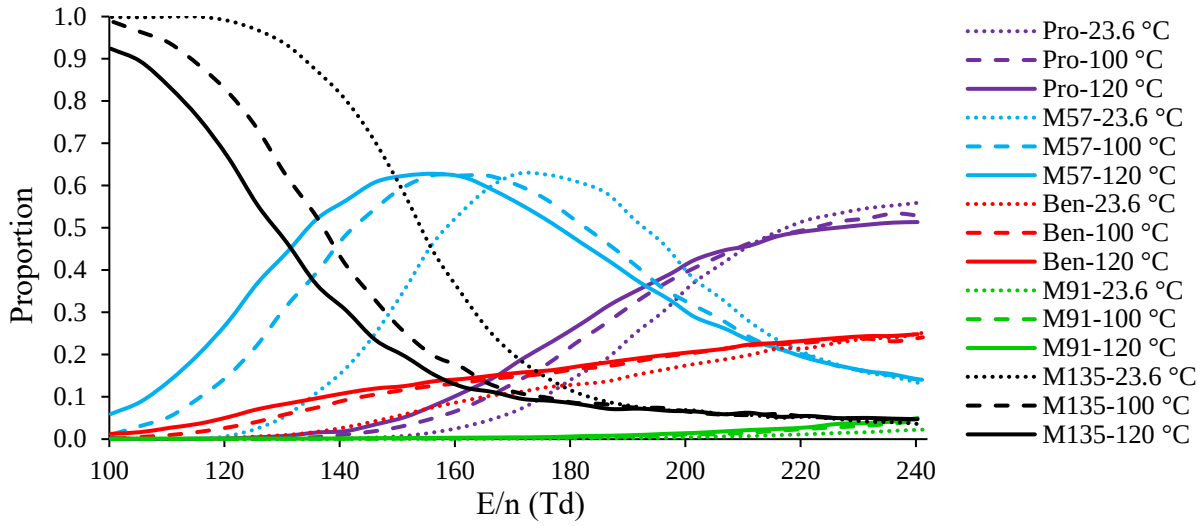

Figure 5.13: Case 1 – PIDs for n-butylbenzene as a function of E/n at a constant pressure of 0.8 mbar and at three temperatures: 23.6, 100 and 120 ºC.

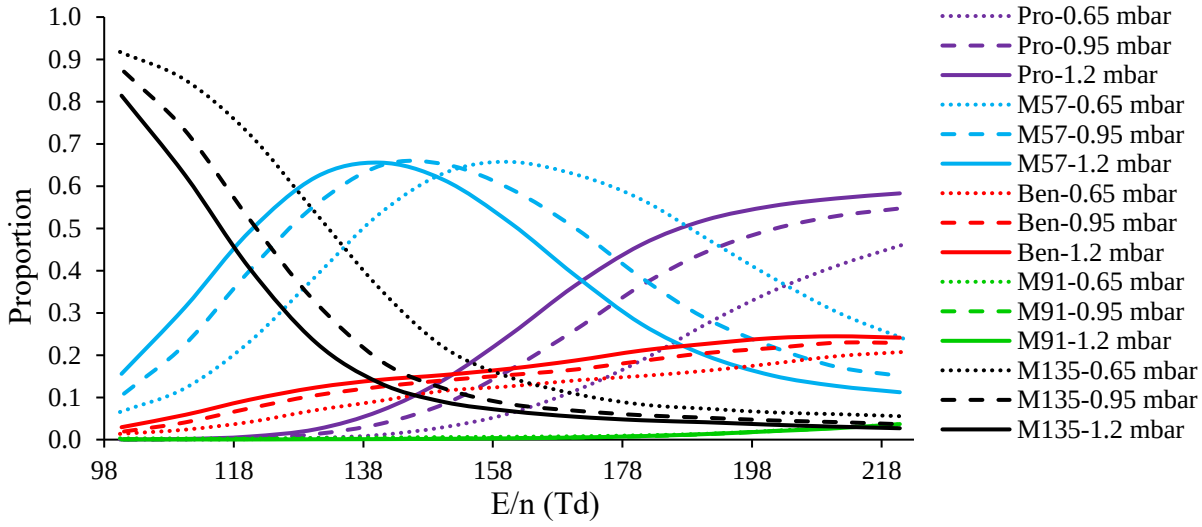

Figure 5.14: Case 2 – PIDs for n-butylbenzene as a function of E/n at a constant temperature of 125 ºC and at three pressures: 0.65, 0.95 and 1.2 mbar

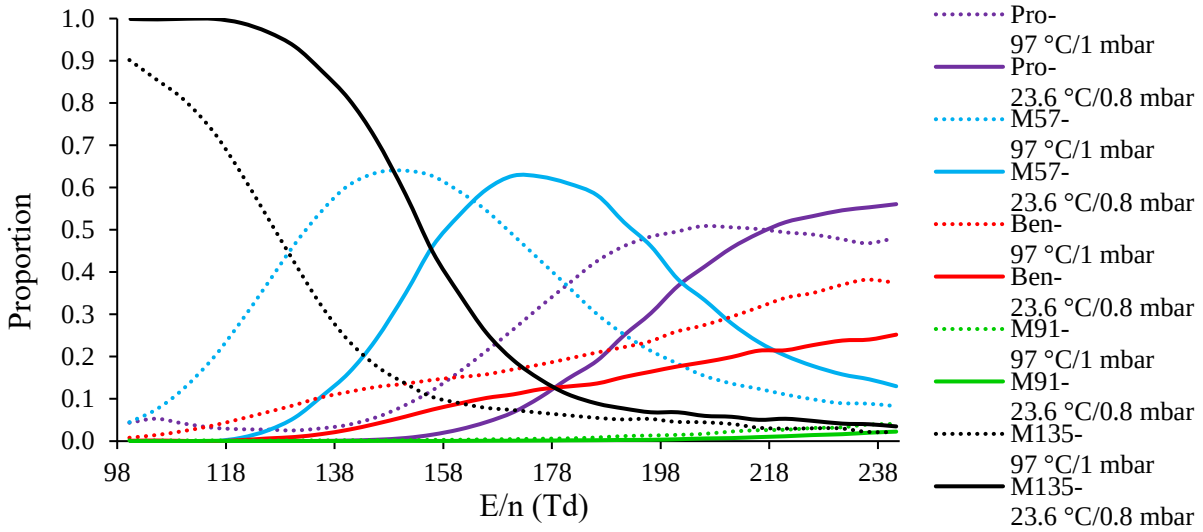

Figure 5.15: Case 3 – PIDs for n-butylbenzene as a function of E/n for which the E field was kept constant and the temperature and pressure were modified to provide the same n, and hence the same E/n.

5.3.3.2 Triethylphosphate (TEP) PIDs

In the following, the results for TEP using a Mark I reactor are provided. Figure 5.16-Figure 5.18 provide the PIDs for TEP for case 1 pressure constant (variable E and T), case 2 pressure and E variable (T constant), and case 3 different T and P (E constant).

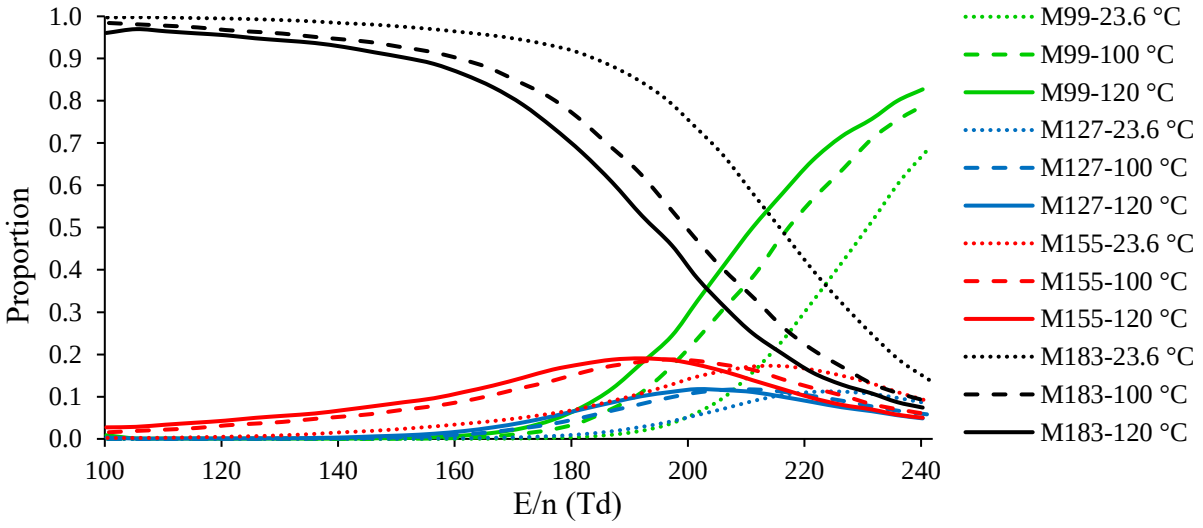

Figure 5.16: Case 1 – PIDs for TEP as a function of E/n at a constant pressure of 0.8 mbar and at three temperatures: 23.6, 100 and 120 ºC.

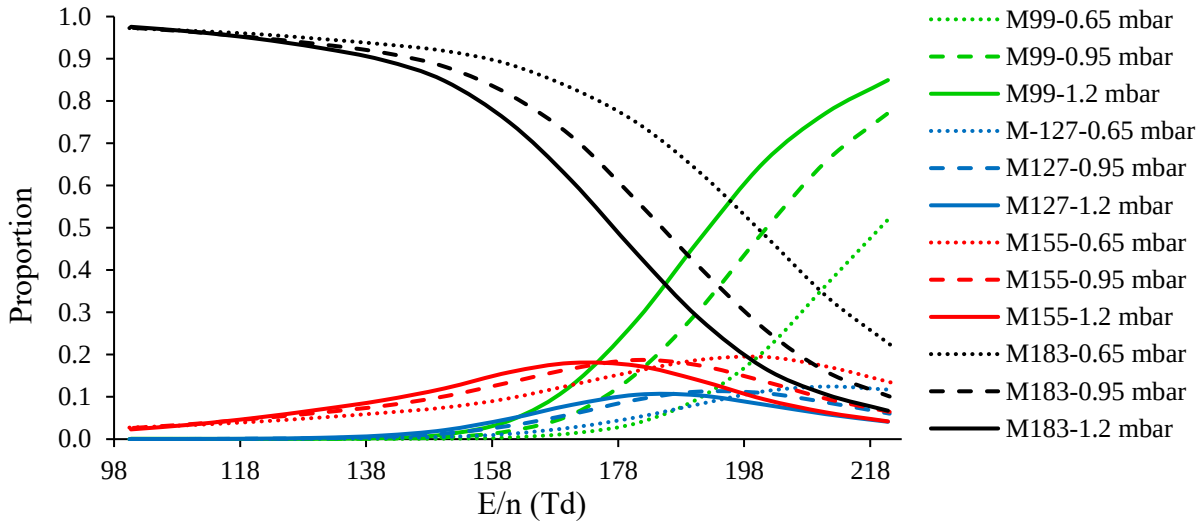

Figure 5.17: Case 2 – PIDs for TEP as a function of E/n at a constant temperature of 125 ºC and at three pressures: 0.65, 0.95 and 1.2 mbar

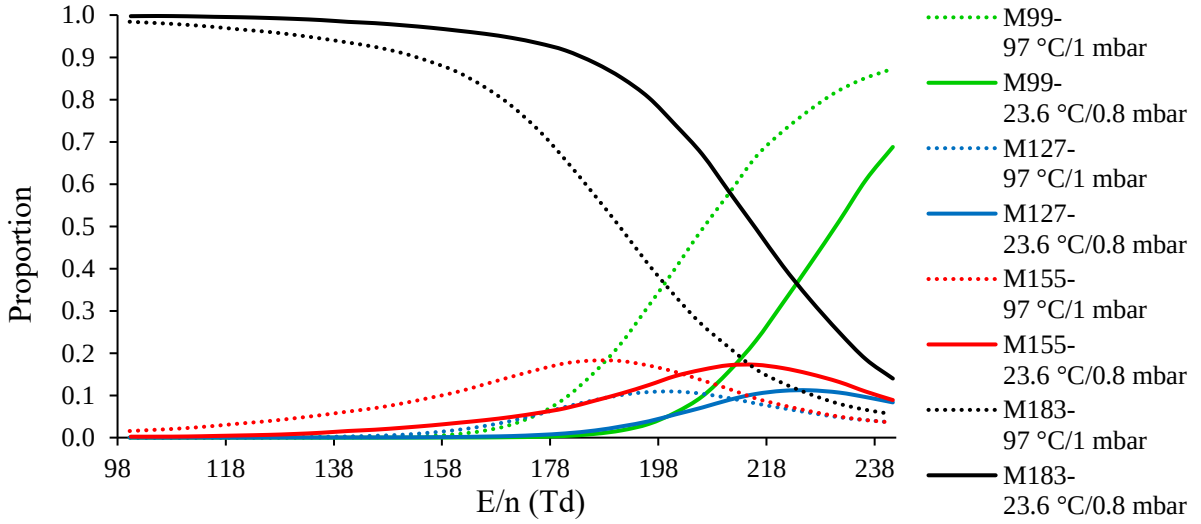

Figure 5.18: Case 3 – PIDs for TEP as a function of E/n for which the E field was kept constant and the temperature and pressure were modified to provide the same n, and hence the same E/n.

5.3.3.3 Ethylbenzene (EB) PIDs

In the following, the results for EB using a Mark II reactor are provided. Figure 5.19-Figure 5.21 provide the PIDs for EB for case 1 pressure constant (variable E and T), case 2 pressure and E variable (T constant), and case 3 different T and P (E constant).

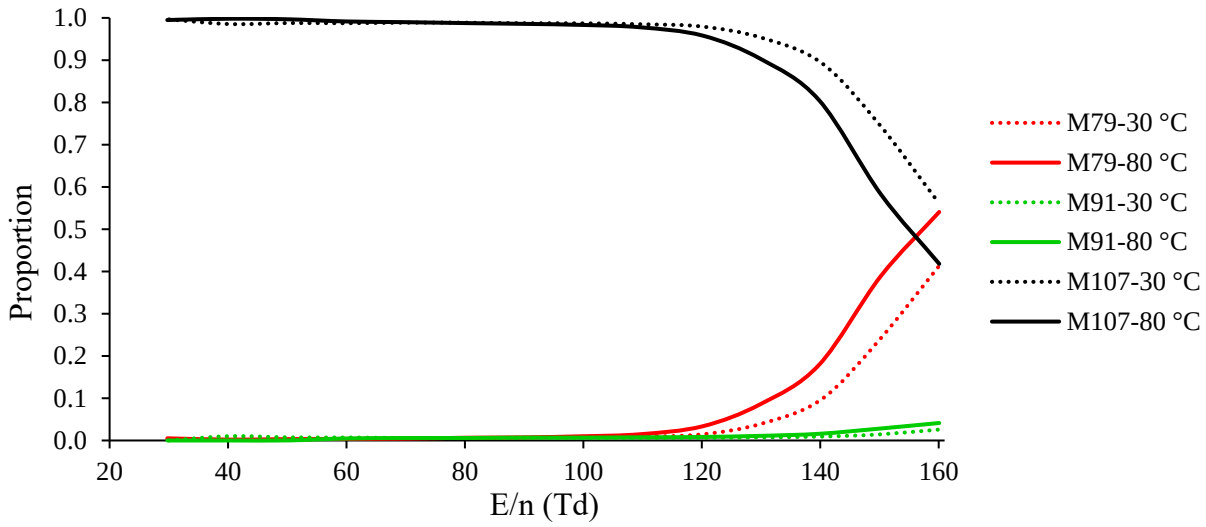

Figure 5.19: Case 1 – PIDs for EB as a function of E/n at a constant pressure of 0.8 mbar and at two temperatures: 30 and 80 ºC

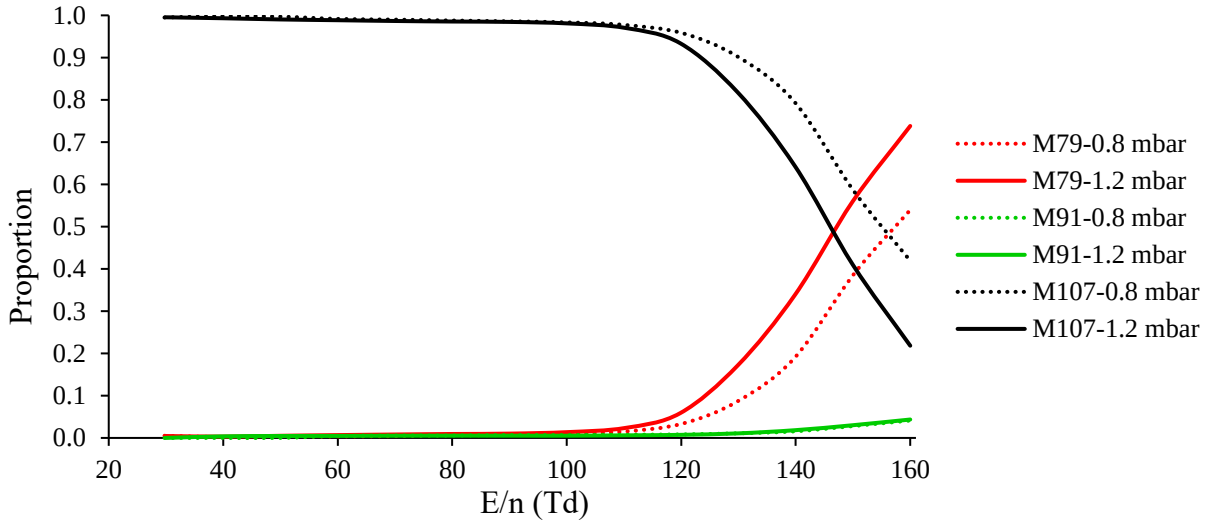

Figure 5.20: Case 2 – PIDs for EB as a function of E/n at a constant temperature of 80 ºC and at two pressures: 0.8 and 1.2 mbar

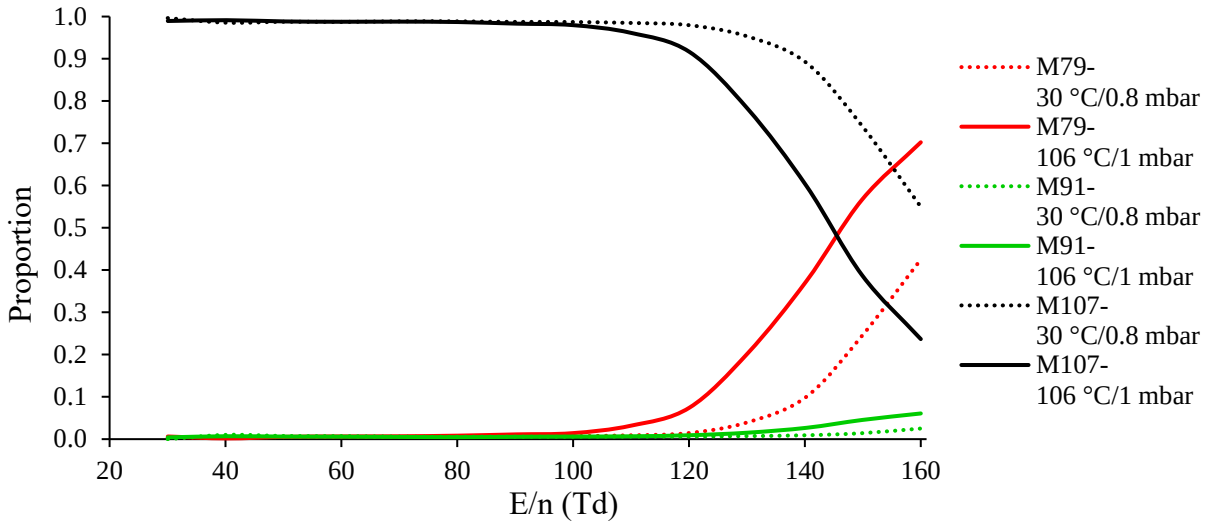

Figure 5.21: Case 3 – PIDs for EB as a function of E/n for which the E field is constant and the temperature and pressure were modified to provide the same n, and hence the same E/n.

5.3.3.4 Interpretation and discussion of the results

The results presented above serve to illustrate the effects of changes in operational parameters whilst maintaining a fixed E/n. More PID measurements, involving measurements for all the four different reactors, are available in the Appendix A.9, which show that reactor design has little to no effect on the shifts in fragmentation behaviour observed. What has been shown is that for a fixed E/n, but using a different combination of E, T and P, the PID curves are not the same, and that the fragmentation behaviour shows shifts in E/n. In order to characterise how far apart the curves are shifted for any particular ion, the difference in the observed proportions will be defined as **ΔProp**.

Consider Figure 5.21 at 150 Td, at the operating pressure of 0.8 mbar the proportion of m/z 107 is 0.74 at 30 ºC and 0.39 at 106 ºC. Thus, the Δprop is 0.35 ± 5.65 %, being also the maximum value of Δprop for m/z 107 and is thus its **ΔProp.max**. Notice that similarly to Δprop, a ΔE/n could also be defined. Increasing T brings increasing thermal translational and thermal internal energies to the ions enhancing fragmentation. Increasing P reduces the mean free path,

resulting in the ions undergoing more collisions during their transit down the reactor, and hence the distributions of their internal energies will be shifted to higher values, resulting in more fragmentation than that resulting from a lower pressure for the same E/n. Thus, PIDs plotted as a function of E/n are not definitive. Other ways have been investigated to present the PIDs to reduce the potential shifts in PIDs. The first, and most obvious, is to take into account the thermal contribution by using the Wannier equation to provide the total translational energy (thermal plus drift) in the centre-of-mass frame, E_k(CM).

5.3.4 PIDs as a function of E_k(CM)

Within the PTR reactor two types of reactions can be described. The reaction between a reagent ion and the analyte is, of course, a key step and is defined as the primary reaction (PR). However, once the analyte has been protonated, collisions between protonated analyte and nitrogen molecules are common and are consequently defined as the secondary reaction (SR). This latter reaction has the ability to change the PID of the analyte ion if the collision energy is high enough. That is why this is an important colliding system to consider as a single colliding system has to be chosen for the E_k(CM) calculation. The E_k(CM) involving the protonated water clusters with nitrogen are well known, but not those for the protonated analyte of this study. To obtain the data for the protonated parents, a secondment within the IMPACT network at the HIPC, Prague with Michal Lacko, was arranged, using a selected ion flow drift tube-mass spectrometer (SIFDT-MS). This allowed the drift times of protonated species to be determined, and hence K_o values to be calculated. As an example of such measurements, the dependence of the reduced ion mobility for $nBBH^+$ on E is presented in Figure 5.22.

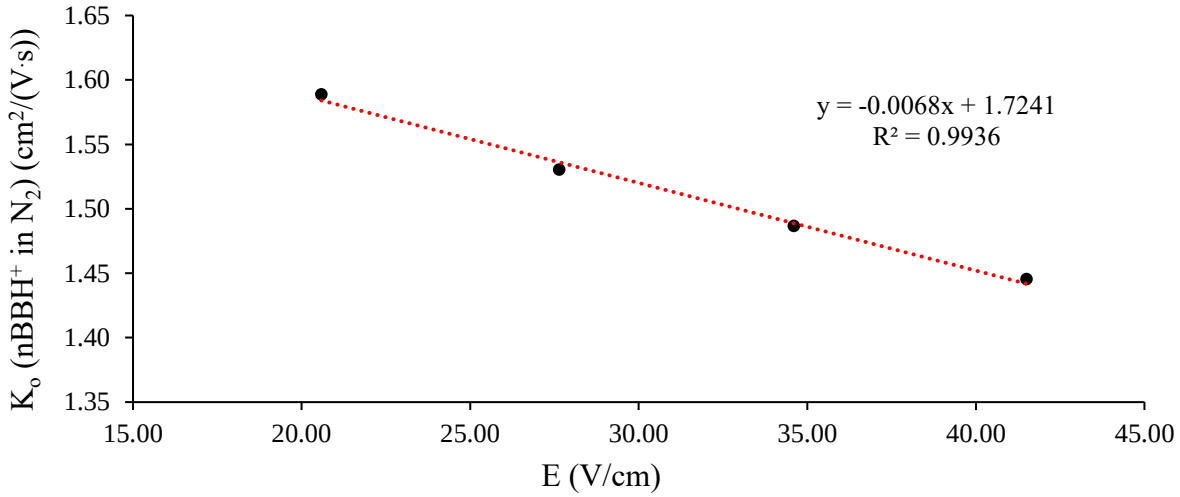

Figure 5.22: Dependence of of K_o for protonated n-butylbenzene in nitrogen on E

The measurements show that the reduced ion mobility of $nBBH^+$ decreases linearly with increasing electric field for a fixed T and P over the range of E studied. This reduction in K_o as a function of E/n was also noted over the range 10-80 Td for H_3O^+, $H_3O^+ \cdot H_2O$ and N_2H^+ [107], although the values did then rise from there up to 200 Td. Unfortunately, there was insufficient time to obtain the reduced ion mobilities of protonated TEP or EB. No K_o values have been published for TEP, and the only value available for EB (1.97 $cm^2/(V \cdot s)$) was measured in an IMS (Ion Mobility Spectrometry) instrument under very different pressure conditions [89]. Consequently, an assumption was made that these two molecules would show similar behaviour for increasing E field. The reduced ion mobilities used in the Wannier equation for EB and TEP were scaled from the K_o value for nBB based on molar mass, and are summarised in Table 5.8:

Table 5.8: Reduced ion mobilities (K_o) for protonated n-butylbenzene, ethylbenzene and triethylphosphate in nitrogen as a function of the electric field (E), in units of $cm^2V^{-1}s^{-1}$, which are used in the calculation of E_k(CM).

Compound	K_o ($cm^2/(Vs)$)
n-butylbenzene	1.72 - 0.0068E
ethylbenzene	1.80 - 0.0068E
triethylphosphate	1.59 - 0.0068E

In the following, the results for the three probe molecules come from the same data, simply replacing E/n by the E_k(CM) involving the secondary reactions, i.e. the colliding system of the protonated parent probe molecule with nitrogen. This is why the values of K_o of Table 5.8 were used to deduce the drift velocities within the E_k(CM) calculations.

5.3.4.1 n-butylbenzene (nBB) PIDs

PIDs using a Mark I reactor as a function of E/n are provided below. (Measurements for the other reactor designs, Mark IV and V ion-funnels, are provided in Appendix A.10.) Figure 5.23-Figure 5.25 provide the PIDs for nBB for case 1 pressure constant (variable E and T), case 2 pressure and E variable (T constant), and case 3 different T and P (E constant).

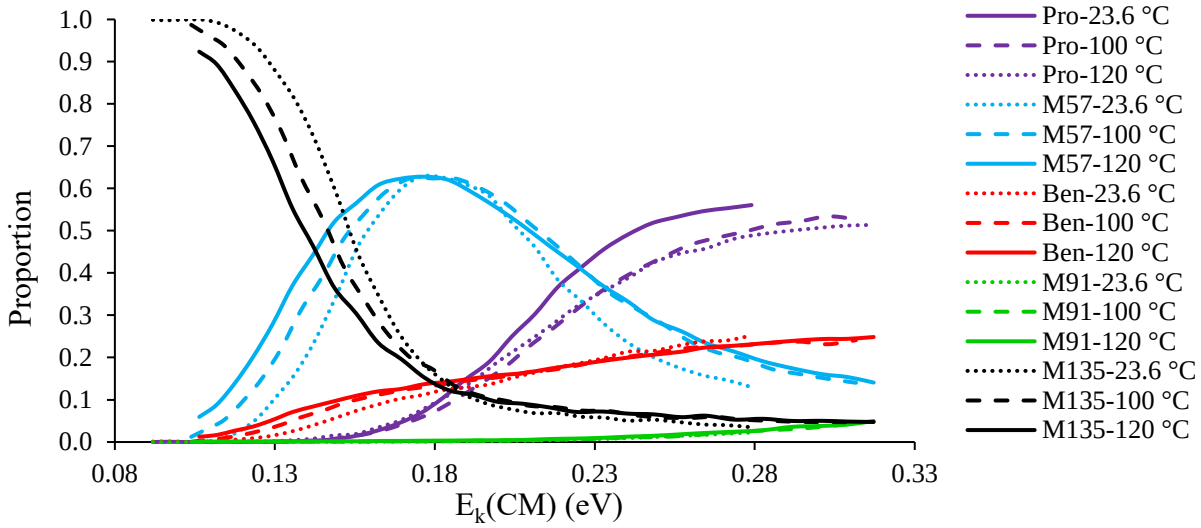

Figure 5.23: Case 1 – PID of nBB as a function of E_k(CM) at a constant drift tube pressure of 0.8 mbar and at three temperatures: 23.6, 100 and 120 °C (this plot may be compared with Figure 5.13)

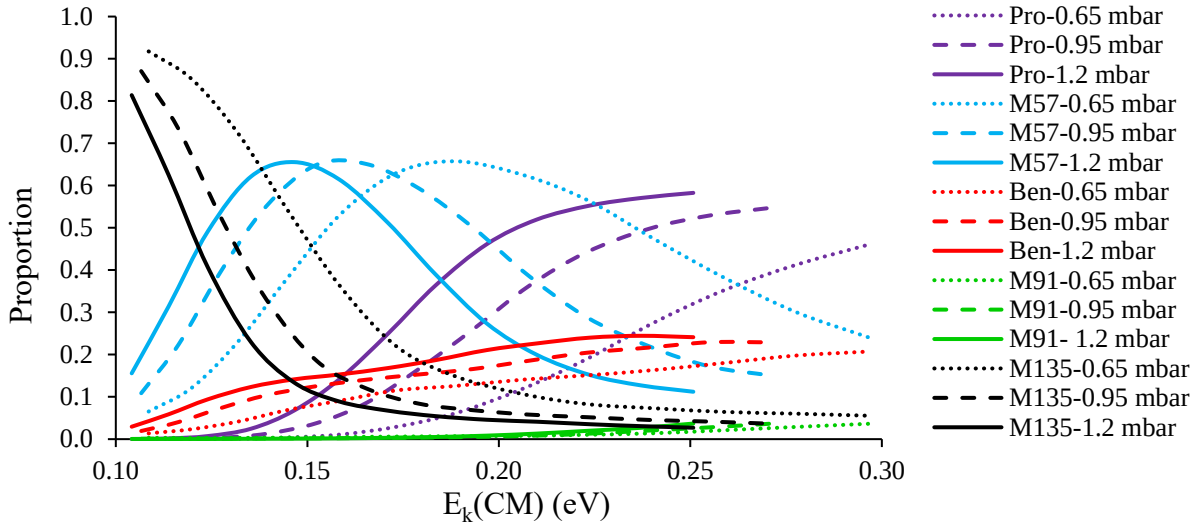

Figure 5.24: Case 2 – PID of nBB as a function of E_k(CM) at a constant drift temperature of 125 ºC and at three pressures: 0.65, 0.95 and 1.2 mbar (this plot may be compared with Figure 5.14)

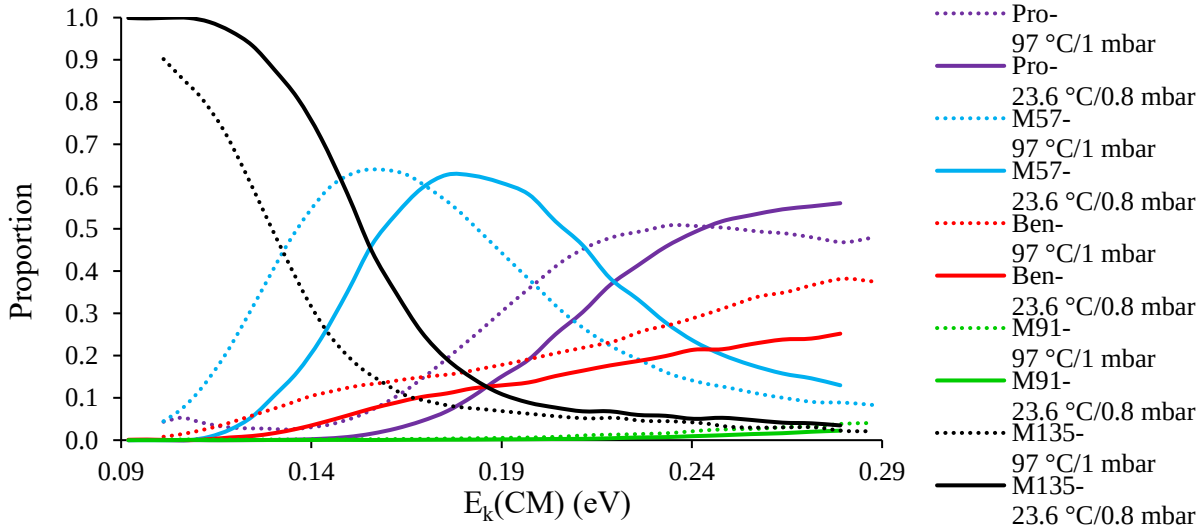

Figure 5.25: Case 3 – PIDs for nBB as a function of E_k(CM) for which the E field is constant and the temperature and pressure were modified to provide the same n, and hence the same E/n. (this plot may be compared with Figure 5.15)

5.3.4.2 Triethylphosphate (TEP) PIDs

In the following, the results for TEP using a Mark I reactor are provided. Figure 5.26-Figure 5.28 provide the PIDs for TEP for case 1 pressure constant (variable E and T), case 2 pressure and E variable (T constant), and case 3 different T and P (E constant).

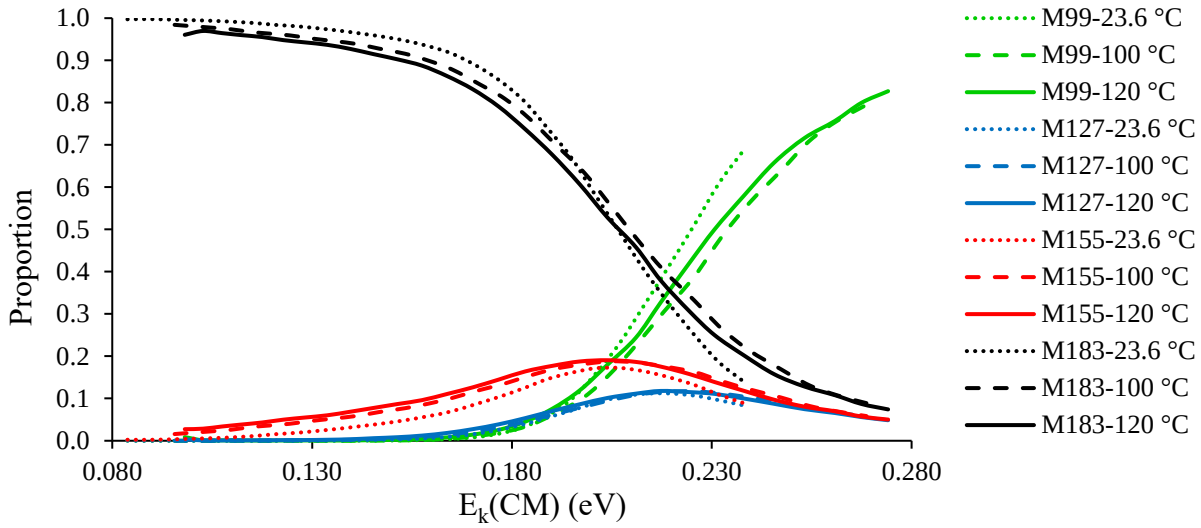

Figure 5.26: Case 1 – PID of TEP as a function of E_k(CM) at a constant drift tube pressure of 0.8 mbar and at three temperatures: 23.6, 100 and 120 °C (this plot may be compared with Figure 5.16)

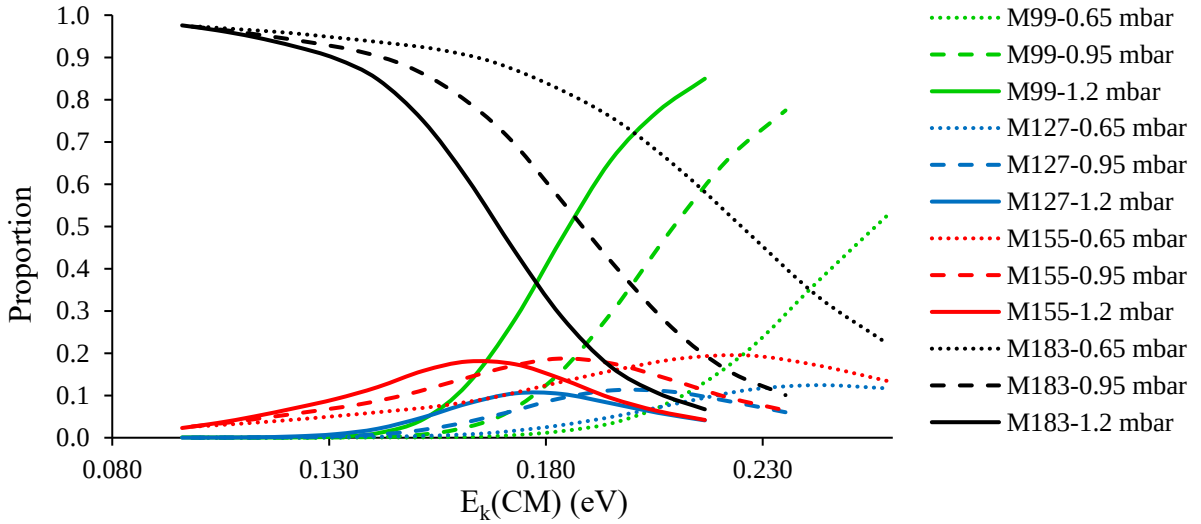

Figure 5.27: Case 2 – PID of TEP as a function of E_k(CM) at a constant drift temperature of 125 °C and at three pressures: 0.65, 0.95 and 1.2 mbar (this plot may be compared with Figure 5.17)

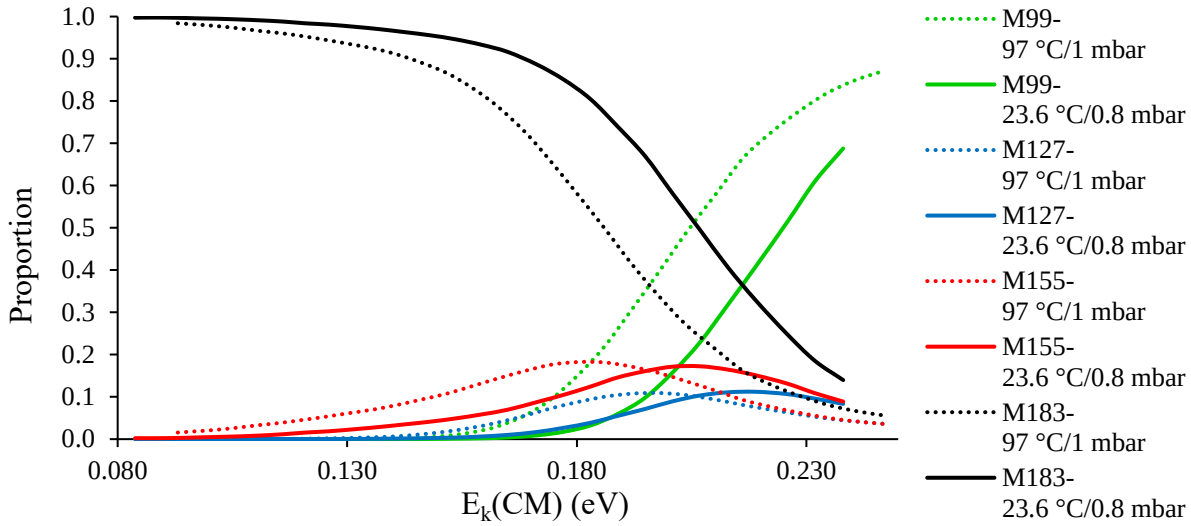

Figure 5.28: Case 3 – PIDs for TEP as a function of E_k(CM) for which the E field is constant and the temperature and pressure were modified to provide the same n, and hence the same E/n (this plot may be compared with Figure 5.18).

5.3.4.3 Ethylbenzene (EB) PIDs

In the following, the results for EB using a Mark II reactor are provided. Figure 5.29-Figure 5.31 provide the PIDs for EB for case 1 pressure constant (variable E and T), case 2 pressure and E variable (T constant), and case 3 different T and P (E constant).

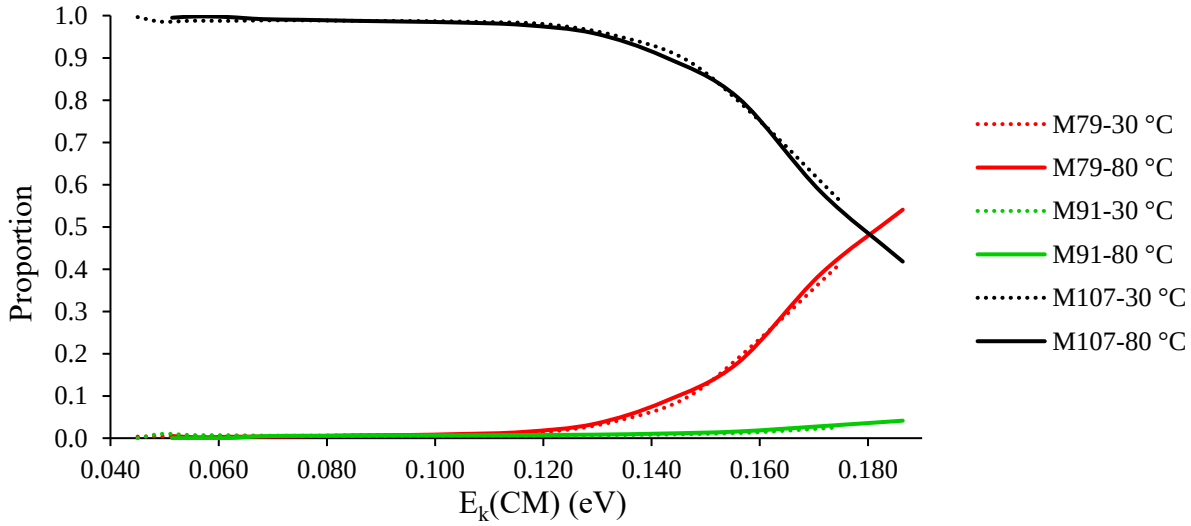

Figure 5.29: Case 1 – PID of EB as a function of E_k(CM) at a constant drift tube pressure of 0.8 mbar and at two temperatures: 30 and 80 °C (this plot may be compared with Figure 5.19)

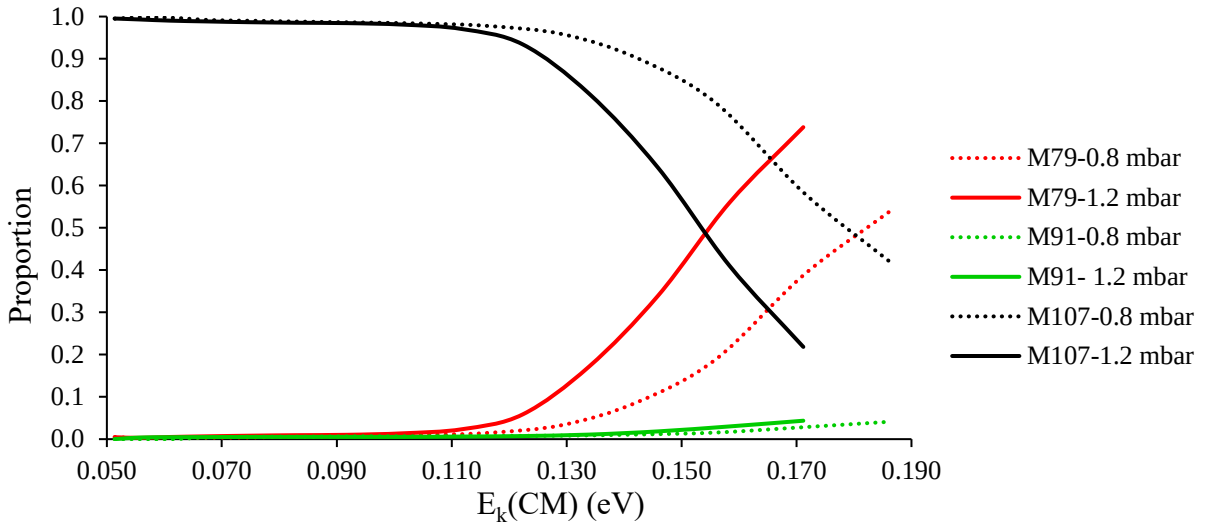

Figure 5.30 Case 2 – PID of EB as a function of E_k(CM) at a constant drift temperature of 80 ºC and at two pressures: 0.8 and 1.2 mbar (this plot may be compared with Figure 5.20)

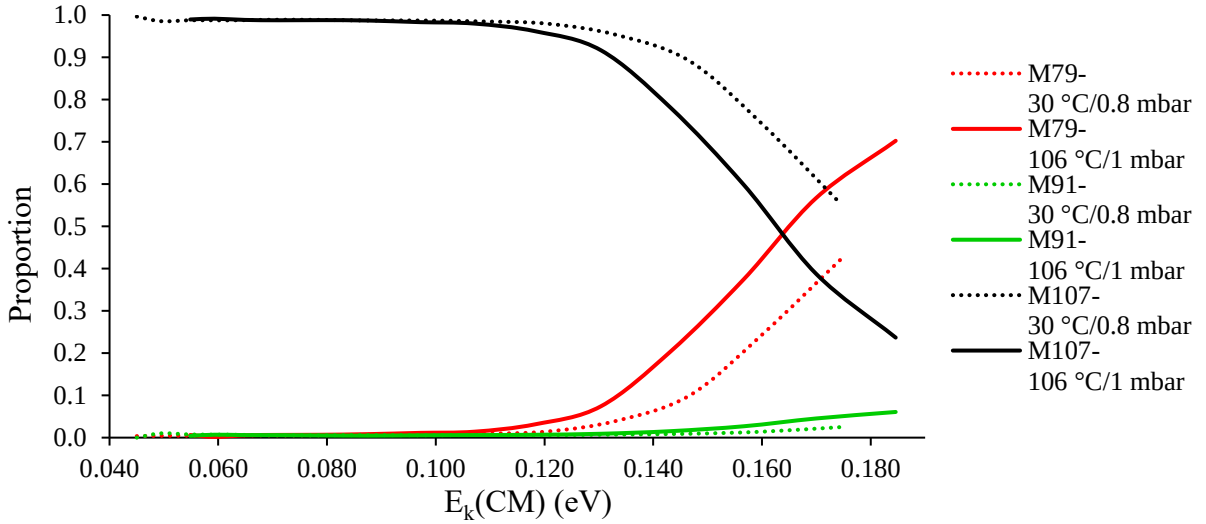

Figure 5.31 Case 3 – PIDs for EB as a function of E_k(CM) for which the E field is constant and the temperature and pressure were modified to provide the same n, and hence the same E/n (this plot may be compared with Figure 5.21).

The replacement of E/n by E_k(CM) brought the PIDs obtained closer together in the Case 1 plots. This improvement can be attributed to the fact that the contribution of the thermal energy to the collisional processes is included, and that is important for Case 1. However, in the plots for Case 2, the curves are still shifted to each other when using E_k(CM). Regarding the Case 3 plots, the shifts are less, again owing to the temperature effects being taken into account. The differences in the shifts are summarised in Table 5.9 using Δprop.max of the protonated analyte.

Table 5.9: Maximum variations of the protonated parent molecule proportion as a function of the parameter used on the x-axis and the case (either T, P or E constant)

Maximum difference of proportion (Δprop.max) of the parent molecule between the two most different curves for a given analyte and ion-funnel (green: decrease of values, red: increase of values, both from E/n)

Analyte molecule	Ion-funnel generation	Parameter used to express the PID of the analyte					
		E/n			E_k(CM)		
		Case 1	Case 2	Case 3	Case 1	Case 2	Case 3
n-butylbenzene	**I**	0.51 ± 1.66 %	0.31 ± 2.34 %	0.56 ± 0.87 %	0.26 ± 3.55 %	0.39 ± 1.72 %	0.40 ± 1.61 %
n-butylbenzene	**IV**	0.26 ± 9.47 %	0.29 ± 8.43 %	0.33 ± 5.76 %	0.03 ± 60.6 %	0.30 ± 6.87 %	0.13 ± 12.3 %
n-butylbenzene	**V**	0.19 ± 20.1 %	0.10 ± 79.9 %	0.37 ± 10.4 %	0.03 ± 128 %	0.12 ± 65.3 %	0.14 ± 22.8 %
triethylphosphate	**I**	0.36 ± 5.46 %	0.34 ± 5.04 %	0.40 ± 3.00 %	0.07 ± 32.1 %	0.55 ± 2.31 %	0.30 ± 5.80 %
ethylbenzene	**II**	0.16 ± 12.6 %	0.20 ± 9.03 %	0.35 ± 5.65 %	0.02 ± 33.4 %	0.35 ± 4.99 %	0.20 ± 13.9 %

The trend of the effect of statistical variations (RSD) of ions counts shows that the shifts in the E/n curves as represented by the difference in the proportions of MH^+ for the same E/n cannot be explained by statistical effects. Calculations have been made according to derivation of equations given in Appendix A.11.

5.4 Conclusion

The data indicate that changes in pressure is a more significant factor in determining the shifts observed, and qualitatively agree with the hypothesis that higher pressures cause greater fragmentation for a given E/n owing to increases in internal energies, and that the third body association is reduced. Simply normalising to pressure does not work to bring the curves closer together, which perhaps reflects differences in the internal energies gained by both reagent and product ions through collisions with the buffer gas as they migrate down the drift tube is too complex to model. Transferring translational energy to internal energy is inefficient, and then transferred energy will be distributed in a complex way, depending on the internal degrees of freedom available. Further work is therefore needed to reconcile the observations. That will be the subject of future studies.

These differences in fragmentation were "discovered" in the process of characterising the fragmentation of the 'probe molecules' in advance of using them to understand better the effects of adding an RF E-field. The data acquired using n-butylbenzene with use of a RF E-field (Appendix A.12) show that fragmentation is far more pronounced in RF mode, so much so that an effective reduced field cannot be assigned, at least for this molecule. This is an important finding for future use of RF funnels for analytical use. However, the most important finding of this work is that in reporting PTR-MS studies, it is insufficient to just state the E/n used, but that the temperature and pressure need to be specified if there is to be any repeatability in measurements from different groups using identical models of PTR-MS instruments.

CHAPTER 6: CHARACTERISATION OF VOCS BY CHEMICAL IONISATION: PRODUCTION OF MASS SPECTRAL LIBRARIES FOR USE IN NEW SOFTWARE FOR COMPLEX MIXTURE ANALYSIS

6.1 Introduction and aim of the new software development

The GC-MS method is a well-known 'gold standard' for analysing complex mixtures of compounds. It does this by pre-separation of the various compounds in the GC section followed by mass spectral analysis of each individual eluting peak from the GC [108, 109]. However, the GC phase is slow and GC-MS is not suitable for real-time measurements, whereas this is one of the key advantages of the PTR-MS method. The question to ask is "what information can be extracted from a complex mass spectrum where the product ions of all the compounds are present simultaneously?"

Kore Technology sought to develop software with which the mass spectral patterns of individual compounds could be identified within a complex chemical mixture. This chapter explains the basic principles of the software algorithm, and importantly the work conducted and the results obtained to (a) determine a suitable, reproducible analytical condition for data acquisition, (b) use this to characterise the mass spectral patterns from individual compounds of interest, (c) develop a commercially useful mass spectral library of compounds to be used with the PTR-MS method, and (d) test the software and provide feedback for further development of the algorithm.

The software was written by Dr Steve Mullock of Kore Technology, so no claim is made by the author on contributing to the algorithm itself. However, to put the work in this thesis into context it is necessary to explain the basic approach of the algorithm, and this follows next.

6.2 The basics of the AnalyseHR method and its two-stage process

6.2.1 Introduction

- The algorithm has been designed to make full use of some fundamental properties of ion species including:

  - The exact mass of any ion species.
  - The invariant isotopic ratios of elements (except in special cases).
  - The relative intensities from multiple isotopic peaks from any ion species.
- The algorithm has also made use of properties of the ToF spectrometers in use for this work:
  - The centroid of a mass peak determined (in this case) to 0.002 of a mass unit.
  - A mass resolution (in this case) of approximately 3,500 M/ΔM (FWHM) to identify isobaric interferences at the same mass.

A similar consideration about a deconvolution process was published by Grange et al [110].

The latter two properties are not available to quadrupole-based instruments, and from the outset the algorithm was designed to make maximum use of the information available in the ToF mass spectrum. The method proceeds in two distinct stages, and in order to understand the work conducted in this section and other chapters of this thesis involving the use of this software, they will now be described in brief.

6.2.2 Stage 1: Building a 'master ion list' and using this to determine the intensities of ion species in an empirical mass spectrum

This phase entails having a comprehensive list of ion species that may appear in the mass spectrum as a result of the presence of any compounds of interest. It is admitted that proton transfer, known as a soft ionisation, often produces fragment ions, each with their own isotopic patterns, in addition to the protonated parent ion. Far from being a hindrance, a distinct and unique pattern of multiple mass peaks from a compound is ideal for computational methods. Given this, it was decided to exploit the 'mixed mode' of ionisation that occurs when the reagent

ions are a mix of O_2^+ and H_3O^+ in a fixed ratio, since as well as making patterns more distinct, it increased the range of compounds that can be analysed in one acquisition, as there are a number of important VOCs whose proton affinities are less than that of water [111].

The master ion list that is required is simply a list of all ions that have been observed empirically at a significant level in a PTR-MS from a range of VOC compounds of interest.

Peak matching includes different steps:

- Some compound identification methods start by conducting a 'peak find', which scans across an empirical spectrum to 'find' mass peaks with an integral above a given threshold. Often a fit such as a Gaussian may be applied to determine the peak integral of each peak, as well as its centroid of mass [110, 112]. This is not the case in the AnalyseHR method. Once an analytical condition (instrument tuning) has been settled upon, a mass peak is chosen from a mass spectrum and its shape is encoded by the software as a ‘model peak’. There is no a priori reason in a ToF-MS why the mass peak should be perfectly symmetrical, since the peak shape is determined by the tuning of the reflectron analyser. For a given tuning, this shape will be reproduced on all the peaks in the mass spectrum. Secondly, by using a spectrum displayed in time, the width of several peaks across the time spectrum is determined to yield a peak width 'spreading factor' with increasing time of flight. This spreading factor is determined and entered into the software.
- The shape file and spreading factor need to be entered only once, **provided that the instrument tuning remains unchanged**. From the shape file and the spreading factor, the software can, for any ion species, now generate a peak at an exact mass and with the appropriate shape and width (mass resolution).

- The algorithm then matches, channel by channel, the intensities of the software-generated mass peaks for each ion in the master list with the empirical spectrum, using isotopic patterns to match best the empirical data. In this first phase of fitting, the software first performs an automatic adjustment of the empirical spectrum for any detector saturation effects and the approach used is given in the appendix A.5.
- If an ion is observed in the empirical spectrum that is not in the master list, it will not be fitted. In the early phase of building the master list of ions, it was necessary to look carefully at overlays of the empirical spectrum and the software-generated spectrum, looking for such omissions, so that such ions could be added to the master list.

For the peak fitting to work correctly, the empirical mass spectrum must be accurately mass calibrated. Initially this was done manually, and then later automatic mass calibration tools were incorporated into the general mass spectral acquisition program.

The output from the first phase is thus a series of peaks from ions in the master list whose intensities best match the empirical data. As mentioned above, the analyst has the opportunity to inspect the overlay of spectra by eye at this stage to check that the process has occurred as expected.

6.2.3 Stage 2: Compound identification through reference to a library of product ion distributions (PIDs) for compounds of interest

The second phase requires that there exists a library of product ion distributions (PIDs) for individual compounds of interest acquired under the set analytical conditions at given drift tube operating conditions (E/n, pressure and temperature). Producing this list of PIDs for all the

compounds in the 39-compound TO-14 mix (listed in appendix A.13 (Table A.13.1 [113])) was conducted for this thesis.

- Given the peak integrals produced by the first stage fitting, the software then attempts with a linear least squares method to find the best combination of compound PIDs that will match the peak intensities from the first stage fit. The specifics of this section of the algorithm will not be discussed here, as this author had no part in it.
- The work in this part of the thesis was therefore to undertake the following: (a) to settle upon an instrument tuning that could be used; (b) to take characteristic chemical ionisation mass spectra using a mixture of both H_3O^+ and O_2^+ reagent ions; (c) to identify the characteristic ions produced for each compound of interest, (d) to create the product ion distributions for each compound as relative ion intensities, (e) to create the master list of PIDs, and (f) to test the outputs from the software fitting for compounds.

  Quantification of the compounds involves determining 'relative sensitivity factors' (RSFs). This can be achieved after the fact by correlating the observed signal intensities with an analysis of gas standards of known concentrations. The RSF value is determined according to the equation E 6.1:

$$[X] = \frac{\text{Signal}(X)}{\text{Cycles} * \text{RSF}} \qquad \text{E 6.1}$$

  where, considering a library compound ‘X’, [X] and Signal(X) are its respective concentration and intensity. Cycles is the number of cycles run during the acquisition time. RSFs are determined by analysing single compounds with known (prepared) concentrations.

- For this work, a gas standard of EPA TO-14 was used. This is a calibration standard for GC-MS comprising a large list of anthropogenic compounds. TO-14 is strictly the method for setting up the GC-MS, and because of this, the list of compounds can vary slightly. For this work a 39-component mix was purchased and used. This does present challenges for a mass spectrum in which all the compounds appear simultaneously and at the same concentration. This is highly unlikely to be encountered in practice, but it was the most convenient way of assigning a preliminary set of RSFs to all the compounds in the library.

6.3 Experimental method and data treatment

6.3.1 Experimental conditions

The first TO-14 experiments were conducted on the research PTR-ToF-MS with the Mark I ion-funnel. The RF mode was used for sensitivity purposes with 70 V at the reactor entry and 4.5 V at the exit, providing a DC electric field of 7.04 V/cm. The reactor was maintained at room temperature (23.6 °C) and 0.8 mbar. The water vapour flow was maintained under 0.1 sccm. In order to produce library data for the algorithm development, as many of the TO-14 compounds as possible were purchased as pure compounds so that their individual PIDs could be determined. The samples were prepared by liquid injection into Tedlar® bags and each compound was run 4 times, at two different concentrations – 1 and 2 ppmv in air (a few exceptions at either lower or higher values for statistical reasons) – and two different relative humidity (RH) values, 40 % and 80 % at room temperature by mixing two flows of zero air, one dry and one saturated in water by running through a bottle filled with tap water.

6.3.2 Data treatment – Example of chloroethane

- Firstly, the acquisition of the background only (humidified air) then of the sample were run for a million ToF cycles.
- Both spectra were mass calibrated as exact masses are key information for the software.
- Both background and samples signals were normalized to hydronium (m/z 19).
- The PID, i.e. the fragmentation pattern, of the compound was then studied, noting any peak above the background that could be ascribed to the compound.
- The background was then subtracted for the considered masses of interest.
- The resulting signal underwent then, if necessary, an isotopic correction. For different ions A and B close in mass, for example separated by 1 or 2 atomic mass units, the intensity of one or many of the isotopes of ion A could interfere with ion B, and need to be subtracted from B to obtain B's true integral. A typical example is presented for benzene in Figure 3.7 where, when determining the signal intensity from protonated benzene at m/z 79, it is important to recognise and subtract the contribution from the carbon 13 isotope of $C_6H_6^+$, also at mass 79. Such corrections are important in mixed mode ionisation of complex halocarbons.
- Once the signal underwent initial treatment, the library was created with a first raw version in count as follows in Table 6.1:

Table 6.1: TO-14 Library creation process for the deconvolution software AnalyseHR using a PTR-ToF-MS – Chloroethane example – 'count' stage

Compound			**Product ions**								
Name	**m/z**	64	**m/z**	15	26	27	28	29	49	62	63
Chloroethane	**Formula**	C_2H_5Cl	**Formula**	CH_3	C_2H_2	C_2H_3	C_2H_4	C_2H_5	CH_2Cl	C_2H_3Cl	C_2H_4Cl
	Code	CE	**count**	12	514	6	994	62	65	22	954

- The next phase involved quantifying each fragment with respect to each other to highlight the significant ones as shown in Table 6.2:

Table 6.2: TO-14 Library creation process for the deconvolution software AnalyseHR using a PTR-ToF-MS – Chloroethane example – 'percentage' stage

Compound			**Product ions**								
Name	**m/z**	64	**m/z**	15	26	27	28	29	49	62	63
Chloroethane	**Formula**	C_2H_5Cl	**Formula**	CH_3	C_2H_2	C_2H_3	C_2H_4	C_2H_5	CH_2Cl	C_2H_3Cl	C_2H_4Cl
	Code	CE	**count**	1.2	51.7	0.6	100.0	6.3	6.6	2.3	96.0

Table 6.2 shows that the fragment at m/z 28 was the most intense of the chloroethane PID and was considered as 100 %. The fragment at m/z 29, for example, presented a signal whose intensity was equal to 6.3 % of that of the reference at m/z 28.

The colour code is then crucial as it helps to know instantly, across the complete library, which fragment is produced by which compound. A yellow background means the fragment has an intensity lower than 5 % of that of the reference product ion and a red background, equal or greater than 5 % of that of the reference product ion. When applicable, a black background highlights the parent molecule mass(es) and for them, the yellow/red code is applied on the figures themselves.

- The final stage was to convert the percentages into proportions that sum to 1, to be treatable by the software, as presented in Table 6.3:

Table 6.3: TO-14 Library – Chloroethane TO-14 Library creation process for the deconvolution software AnalyseHR using a PTR-ToF-MS – Chloroethane example – 'sum to 1' stage

Compound			**Fragments**								
Name	**m/z**	64	**m/z**	15	26	27	28	29	49	62	63
Chloroethane	**Formula**	C_2H_5Cl	**Formula**	CH_3	C_2H_2	C_2H_3	C_2H_4	C_2H_5	CH_2Cl	C_2H_3Cl	C_2H_4Cl
	Code	CE	**count**	0.01	0.19	0.01	0.38	0.02	0.03	0.01	0.35

The data in Table 6.3 represent the PID of chloroethane that was entered into the PID library for use with AnalyseHR software. Table 6.2 and Table 6.3 show an example of a molecule, where neither the protonated parent nor the charge-exchanged parent contributes to its PID.

6.4 Results and discussions

6.4.1 TO-14 study: The master ion list

As explained in the previous sections, the first stage of the deconvolution process constructs peaks from ions in the master ion list according to exact masses and the spreading factor inserted in the algorithm and independently of the compounds contributing to those peaks. In early phases of the TO-14 measurements, a complete fit of all the observed mass peaks in the spectrum was attempted for completeness, irrespective of whether they were related to TO-14 compounds, and one example is shown at m/z 101 in Figure 6.1, being a typical case where all the different isobaric peaks were fitted.

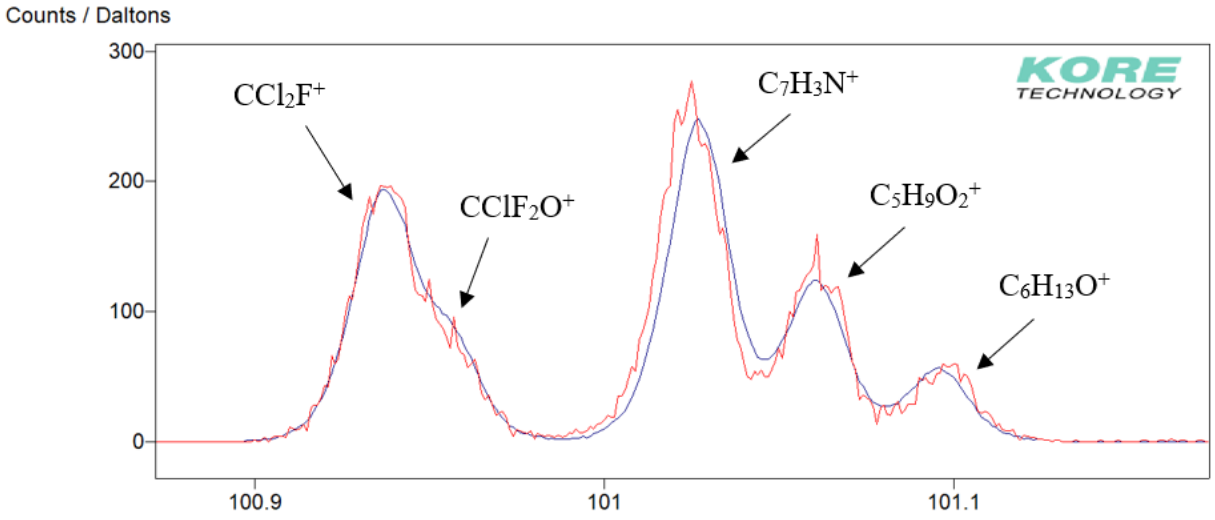

Figure 6.1: Peaks at m/z 101 from a sample of 10 ppbv of TO-14 mixture standard in zero air (red trace) run in PTR-ToF-MS and the reconstructed peaks (blue trace) after the first stage of AnalyseHR

The first version of the master ion list was a complete list of ions detected and contained many ions that did not appear in any of the TO-14 single compound library spectra, as they were part of the background spectrum according to the mass accuracy of the instrument being ~ 0.002 of a mass unit. Unless these ions overlapped to some extent with the mass peaks from the TO-14 compounds, they were excluded from the second master list in order to reduce the computational load in the second phase of compound fitting.

6.4.2 Testing with a simple, 3-component mixture and PID library

Early tests were conducted using a 3-components library involving vinyl chloride (VC), 1,1-dichloroethane (11DCE) and 1,2-dichloroethane (12DCE). Under fixed instrumental conditions within the PTR-ToF-MS, their respective PIDs were determined and are shown in Table 6.4:

Table 6.4: PID of vinyl chloride, 1,1-dichloroethane and 1,2-dichloroethane used, under reactor temperature of 23.6 °C, pressure of 0.8 mbar and DC electric field of 7.0 V/cm, for an early library of the deconvolution software AnalyseHR using a PTR-ToF-MS

Compound	Code	Formula	Product Ion Distribution (m/z)			
			49	62	63	97
			CH_2Cl	C_2H_3Cl	C_2H_4Cl	$C_2H_3Cl_2$
Vinyl chloride	**VC**	C_2H_3Cl	0.000	0.474	0.526	0.000
1,1-dichloroethane	**11DCE**	$C_2H_4Cl_2$	0.000	0.005	0.883	0.112
1,2-dichloroethane	**12DCE**	$C_2H_4Cl_2$	0.005	0.547	0.448	0.000

The AnalyseHR program automatically corrects empirical data for any detector saturation. In acquiring the data manually for the PIDs, care was taken to adjust the signals such that the c/s in any one peak was ~ 1/4 of the cycles/second, and thus did not suffer significant dead-time losses.

6.4.2.1 Stage 1

The first stage fit is only concerned with identifying which ions are detected and at what intensities. Indeed, the library, shown in Table 6.4, contains only 4 significant ions. The objective for the algorithm was to match these peaks in the mass spectra as shown in Figure 6.2 with data of 1.00 ± 0.02 ppmv of vinyl chloride in air and especially its fragment at m/z 62 where the red trace represents the signal of 1.00 ± 0.02 ppmv of vinyl chloride in air, and the second trace is the computer-generated peak that has been adjusted channel-by-channel to best match the peak integral of the empirical peak. As mentioned above, ions that do not impinge upon a mass peak from a compound of interest do not need to be in the master ion list, and in Figure 6.2, two very low intensity peaks can be seen in the empirical spectrum. The software has not attempted to fit these peaks because the ions that give rise to these peaks are not in the revised master ion list.

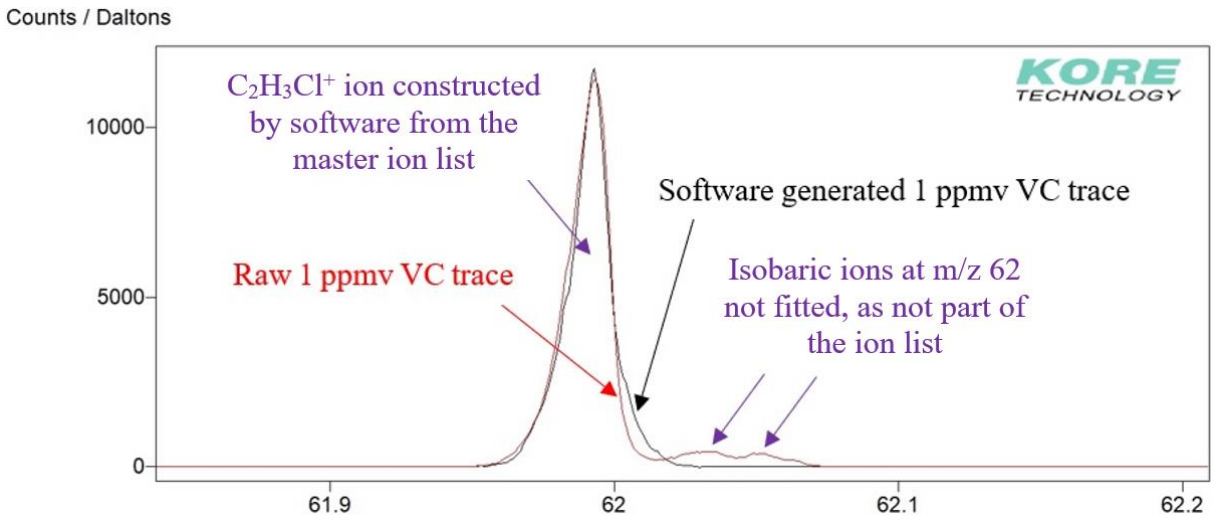

Figure 6.2: Peaks at m/z 62 from a sample of 1 ppmv of vinyl chloride in air run in PTR-ToF-MS
VC stands for vinyl chloride.

The stage 1 peak fit was deemed to be successful, as 99 % of the peak integral of $C_2H_3Cl^+$ was fitted.

6.4.2.2 Stage 2

Once the individual ions had been identified and their intensities determined, the second phase of AnalyseHR uses the PIDs in its library and finds the best compound fit to the data using a 'least squares' method. RSFs stored with PID library entries then allows each compound to be quantified.

In this study, 4 mixtures were tested:

- 1 ppmv of VC and 2 ppmv of 11DCE
- 2 ppmv of VC and 3 ppmv of 12DCE
- 1 ppmv of 11DCE and 3 ppmv of 12DCE
- 3 ppmv of VC, 1 ppmv of 11DCE and 2 ppmv of 12DCE

The results are presented in Table 6.5 where, for each compound, the prepared value and the value reported by the software are expressed, applying the uncertainty due to both the sample injection errors and the deconvolution process errors. Considering, for each mixture, the standard deviation of both total concentrations, the concentration windows match in three cases out of four. The match for the mixture of vinyl chloride and 1,1-dichloroethane presents a minimal difference of 69 ppbv. Some uncertainties can be caused by the similarity between PIDs in the library as well as certain minor ions produced (0.5 % of the relevant PID). In some cases, where a compound is not present in the mixture, the software posts a negative concentration. As there is no such thing as a negative concentration, this points out the limitations of the algorithm, and this aspect has been addressed subsequently using a 'non-negative least squares method', but does not form part of this thesis.

Table 6.5: Concentrations of vinyl chloride (VC), 1,1-dichloroethane (11DCE) and 1,2-dichloroethane (12DCE) reported by the deconvolution software AnalyseHR using an early library in the algorithm using a PTR-ToF-MS

		VC	11DCE	12DCE	TOTAL
VC 11DCE	Prepared value (ppmv)	1.000 ± 0.100	2.000 ± 0.100	0.000 N/A	3.000 ± 0.200
	Computationally determined value (ppmv)	**1.084** ± 0.009	**1.829** ± 0.005	**-0.195** N/A	**2.718** ± 0.014
		VC	**11DCE**	**12DCE**	**TOTAL**
VC 12DCE	Prepared value (ppmv)	2.000 ± 0.100	0.000 N/A	3.000 ± 0.100	5.000 ± 0.200
	Computationally determined value (ppmv)	**2.120** ± 0.012	**-0.027** N/A	**2.844** ± 0.055	**4.937** ± 0.067
		VC	**11DCE**	**12DCE**	**TOTAL**
11DCE 12DCE	Prepared value (ppmv)	0.000 N/A	1.000 ± 0.100	3.000 ± 0.100	4.000 ± 0.200
	Computationally determined value (ppmv)	**0.000** N/A	**0.991** ± 0.005	**3.257** ± 0.058	**4.248** ± 0.063
		VC	**11DCE**	**12DCE**	**TOTAL**
VC 11DCE 12DCE	Prepared value (ppmv)	3.000 ± 0.100	1.000 ± 0.100	2.000 ± 0.100	6.000 ± 0.300
	Computationally determined value (ppmv)	**3.066** ± 0.016	**0.956** ± 0.005	**2.294** ± 0.064	**6.316** ± 0.085

In general, the greater a concentration is, the lower the RSD is and the more reliable the software generated concentration is. This is due to the fact that, as the concentration becomes lower, the counts in the peaks are reduced and the standard deviations increase.

6.4.3 Effect of relative humidity and concentration

The PIDs are the 'fingerprints' of the molecules and are linked to specific analytical conditions. One of the conditions that cannot always be controlled is the humidity of any ambient air sample; indeed, it is bound to vary significantly. In order to see the effect of changing humidity on the PIDs, and particularly the changes in protonation vs charge exchange, four experiments, involving 1,2,4-trimethylbenzene (124TMB) and 1,2-dichloropropane (12DCP), were made: two at different concentrations and two at different (and realistic) humidities. The results are

shown in Figure 6.3. On the y-axis is the measured ratio of the protonated parent ion intensity divided by the charge-exchanged parent ion intensity. On the x-axis is plotted the ratio of the hydronium reagent ion signal (mass 19) divided by the oxygen reagent ion signal (mass 32). This ratio increases with humidity, possibly owing to back-diffusion of more humid air into the SD region of the ion source. As the humidity is an increasing function of the water proportion, the lowest 19/32 ratios are at 40 % relative humidity and the highest 19/32 is at 80 % relative humidity experiments.

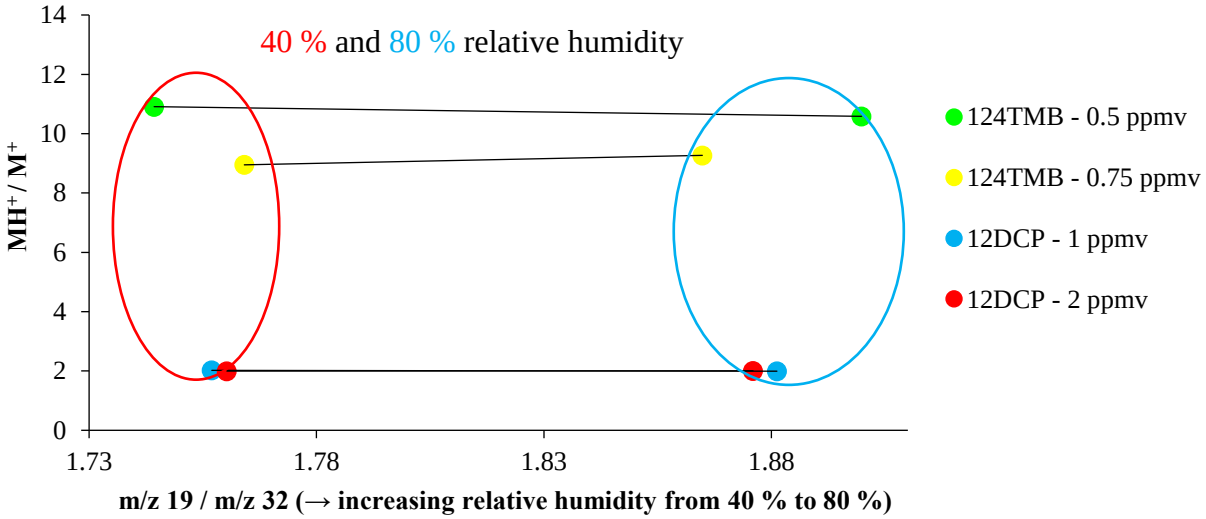

Figure 6.3: Parent compound ion ratios for 1,2,4-trimethylbenzene (124TMB) and 1,2-dichloropropane (12DCP) for both relative humidity and both ranges of concentrations

The AnalyseHR method for compound identification and quantification will clearly be most reliable when the conditions for the analysis match those under which the library PIDs were acquired. However, it is encouraging to note that over the range from 40 % to 80 % relative humidity, the MH^+/M^+ ratio only shifts by a few percent. This implies that there is little to be gained by trying to correct for day-to-day variations in ambient air humidity changes.

The MH^+/M^+ ratio variations are due to the increase of dead-time loss at higher concentration, justifying the auto saturation correction developed after these early experiments.

6.4.4 TO-14 study: the complete library and the output from AnalyseHR

The master ion list discussed previously is presented in appendix A.14 (Table A.14.1), and the TO-14 library in appendix A.15 (Table A.15.1). Those results highlight how complex a library can become when more than a few compounds of interest are considered. Using this TO-14 master ion list, the mass spectral library and the data acquired using a TO-14 standard bottle including 100 ppbv of each compound, the AnalyseHR program produced the results table presented in Table 6.6:

Table 6.6: Concentrations of the compounds involved in a TO-14 bottle standard reported by the deconvolution software AnalyseHR

Compound name	Formula	CAS-number	Concentration (ppb)	Estimated RSD (%)
VINYL CHLORIDE	**C_2H_3Cl**	**75-01-4**	70.47	1.40E+16
CHLOROETHANE	**C_2H_5Cl**	**75-00-3**	116.7	4.88
BENZENE	**C_6H_6**	**71-43-2**	91.01	1.09
DICHLOROMETHANE	**CH_2Cl_2**	**75-09-2**	171.4	0.94
TOLUENE	**C_7H_8**	**108-88-3**	135.9	0.33
1,1-DICHLOROETHENE	**$C_2H_2Cl_2$**	**75-35-4**	129.6	5.28E+15
cis-1,2-DICHLOROETHENE	**$C_2H_2Cl_2$**	**156-59-2**	80.24	5.65E+15
1,1-DICHLOROETHANE	**$C_2H_4Cl_2$**	**75-34-3**	134.1	2.21E+15
1,2-DICHLOROETHANE	**$C_2H_4Cl_2$**	**107-06-2**	70.58	9.66E+15
STYRENE	**C_8H_8**	**100-42-5**	150.5	0.38
ETHYLBENZENE	**C_8H_{10}**	**100-41-4**	181.3	0.61
o-m-p-XYLENE	**C_8H_{10}**	**108-38-3**	260.2	0.55
cis-1,3-DICHLOROPROPENE	**$C_3H_4Cl_2$**	**10061-01-5**	103.2	0.31
1,2-DICHLOROPROPANE	**$C_3H_6Cl_2$**	**78-87-5**	145.2	0.50
CHLOROBENZENE	**C_6H_5Cl**	**108-90-7**	110.6	0.45
CHLOROFORM	**$CHCl_3$**	**67-66-3**	111.5	3.29E+15
1,2,4&1-3-5-TRIMETHYLBENZENE	**C_9H_{12}**	**95-63-6**	344.1	0.26
TRICHLOROETHENE	**C_2HCl_3**	**79-01-6**	105.4	1.79
1,1,1-TRICHLOROETHANE	**$C_2H_3Cl_3$**	**71-55-6**	133.4	3.44E+15
1,1,2-TRICHLOROETHANE	**$C_2H_3Cl_3$**	**79-00-5**	116.9	3.36E+15
TRICHLOROFLUOROMETHANE	**CCl_3F**	**75-69-4**	109.1	0.52
o-m-p-DICHLOROBENZENE	**$C_6H_4Cl_2$**	**541-73-1**	316.5	0.47
CARBON TETRACHLORIDE	**CCl_4**	**56-23-5**	162.4	0.41
TETRACHLOROETHENE	**C_2Cl_4**	**127-18-4**	90.47	1.16
1,1,2,2-TETRACHLOROETHANE	**$C_2H_2Cl_4$**	**79-34-5**	123.5	-4.87
1,2-DICHLORO-1,1,2,2-TETRAFLUOROETHANE	**$C_2Cl_2F_4$**	**76-14-2**	120.4	0.73
1,2,4-TRICHLOROBENZENE	**$C_6H_3Cl_3$**	**120-82-1**	119.7	6.46
1,2-DIBROMOETHANE	**$C_2H_4Br_2$**	**106-93-4**	131.1	0.44
HEXACHLORO-1,3-BUTADIENE	**C_4Cl_6**	**87-68-3**	90.7	3.42

The unusually high values of estimated relative standard deviation (RSD) in the table are simply a mathematical consequence of the way the algorithm has calculated the uncertainties when attempting to fit compounds with extremely similar PIDs. Each compound in the gas standard was present at a concentration of 100 ppbv. The concentrations calculated for 20 of the 34 compounds in the mix were within 25 % of the known value, and 29 were within 50 %. Isomeric compounds such as the three xylene isomers produce identical PIDs and are therefore grouped together, and thus a concentration of 300 ppbv was expected. Considering the complexity of the mixture and the fact that the compounds are all present at the same concentration (thus maximising potential confusion for the algorithm), the results were regarded as encouraging. However, the results in Table 6.6 highlighted certain issues.

6.5 Limitations of the methods

- The first problem, independent of the software development, was the unavailability of certain chemicals: chloromethane, bromomethane, trans-1,3-dichloropropene, freon 12 and freon 113. They were finally removed from the library.
- As also presented in Table 6.6, certain compounds presented an unrealistically high relative standard deviation. This is described in more detail in 6.6.1 below.
- The Tedlar® bags method was not without problems. The main contaminant of these bags was dimethylacetamide (C_4H_9NO) whose protonated parent molecule was present at m/z 88. However, the hydrated molecule was present at m/z 106 and was intense enough to make the signal of the $C_8H_{10}^+$ peak untreatable. For compounds involving this mass of interest, a mixture was prepared into a canister to avoid the bag contamination.

- The algorithm was not helped by including every low intensity peak from a compound, and a decision was taken to specify a threshold intensity as a criterion for inclusion in the PID. That is why, any fragment ion whose signal was lower than 3 % of the reference ion (whose intensity represents 100 %) was not considered in the library. Notice that in the next 'informative' TO-14 libraries (i.e. with thresholds potentially different from the one used to select significant compounds in the 'software TO-14 libraries'), orange was introduced in the colour code. Any orange *background* relates to an 'intermediate' ion and represents an ion greater than 1 % but less than 5 % of the reference ion in the PID of the selected compound →Yellow *background*: less than 1 % of the reference ion in the PID of the selected compound. On the other side, any orange *figure* relates to an 'intermediate' parent molecule and represents an intermediate parent molecule with greater than 1% but less than 5% of the reference ion in the PID of the selected compound →Yellow *figure*: Negligible parent molecule(s) (less than 1 % of the reference ion) of the PID of the selected compound.

6.6 AnalyseHR software development – Further refinements

6.6.1 Statistical significance

There are some unusually high values of relative standard deviation for a few of the compounds reported in the results table in Table 6.6. This came about as a result of the way this version of the algorithm dealt with compounds having the same ions in their PIDs, but with perhaps only subtle shifts in the ion ratios. A perfect example of this would be 1,1,1-trichloroethane and 1,1,2-trichloroethane. During the first phase of peak fitting, RSD values are assigned to each ion integral. In the second phase of compound fitting, and in the case where compound PIDs are extremely similar, these RSDs can interact and 'blow up' to an extraordinary degree. Clearly

this is unhelpful, as the RSD values are intended to indicate a degree of confidence to an analyst of the compound assignment.

6.6.2 Compound groups

To solve the unrealistically high standard deviations issue, resulting from the fact there are more than one combination of single compound spectra providing the same result, a second version of the algorithm was made in which the compounds with extremely similar product ions and ion ratios were grouped together. Although this gives up the possibility of quantifying a single compound in that group, it nevertheless allows the analyst to see that at least one of the compounds in that group has been detected and the RSD could be reported more realistically. After this author had finished his residency at Kore Technology, he has been informed that the group method has been abandoned for two reasons: (1) it relies too much on human intervention in the form of an analyst deciding which compounds should be in a group, and (2) a new approach using so-called 'non-negative least squares' comparison of the PIDs has largely solved the problem described above.

6.7 Conclusions and further developments

A master ion list and PID library entries for most of the thirty-nine individual TO-14 compounds were successfully created in order to allow testing and development of the AnalyseHR algorithm. An instrument tuning was fixed in order to produce repeatable data, and the effect of ambient air humidity between 40 % and 80 % relative humidity at room temperature on protonated and charge-exchanged molecular ion ratios was shown to be less than 5 %.

The goal of being able to extract quantitative information from a complex mixture of VOCs without a pre-separation stage is a very important development in being able to preserve the power of PTR-MS as a ‘real-time’ analytical method. Owing to the success of these early trials, continuous improvements have been made in the development of the algorithm through new analytical approaches and refinements to, and additions of, the PIDs. At the time of writing there are now nearly 100 compounds in the library, covering compounds in the TO-14, TO-15 and PAMS 56 lists from the United States EPA. These lists are among the chosen compounds of interest for monitoring anthropogenic air pollution and form the basis of standard GC-MS analytical protocols [113, 114].

As well as testing and assisting in developing the algorithm using TO-14 compounds, the AnalyseHR software was also used for data reduction of the water analysis results reported in the next chapter.

Finally, as a result of the sensitivity improvements achieved through the development of the Mark II ion-funnel (reported in chapter 3), Kore took the decision to replace the Mark I funnel with the Mark II funnel in their commercial PTR-ToF-MS. Further PID data were acquired by this author with the TO-14 compounds and the PIDs were adjusted slightly for the release of AnalyseHR software supplied with commercial instruments fitted with the Mark II ion-funnel.

CHAPTER 7: DEVELOPMENT OF A NEW WATER SAMPLING DEVICE FOR VOC EXTRACTION AND SUBSEQUENT ANALYSIS BY MASS SPECTROMETRY

7.1 Introduction

Mass spectrometers are predominantly used to analyse gas phase samples. However, when it comes to environmental monitoring, liquid samples often need analysing. One important application is to determine water quality. River water in particular can be polluted. This is problematic, given that for many third world countries rivers are directly used as a supply for drinking water. It is therefore hardly surprising that water analysis has a long history. In the 1950s, spectrophotometry, involving colorimetric determination or light absorption, was commonly employed to analyse for certain metals in water samples. Although providing a high sensitivity, specialized sampling methods limited its use [115]. In the 1960s gas chromatography-mass spectrometry (GC-MS), providing the best quantitative and qualitative determinations of chemicals in water samples, became more affordable [116]. Since the late 1970s, volatile organic compounds (VOCs) and semi-volatile organic compounds (sVOCs) are commonly analysed from water samples through GC-MS [116]. In 1984, methods for GC-MS were settled in the Federal Register of the US Environmental Protection Agency becoming, through the replacement of packed columns by capillary columns, the gold standard for environmental water analysis reducing analysis run-time by half and improving resolution and lowering detection limits of organic compounds in water [116]. GC-MS remains one of the main techniques to analyse water samples for pesticides, heavy metals, hydrocarbons or polynuclear aromatic hydrocarbons (PAHs) [116, 117]. In parallel, and since its successful development in the 1980s [118], liquid chromatography in tandem with mass spectrometry (LC-MS) is also widely used in water analysis [117, 119]. Compared to GC-MS, LC-MS permits the analysis of a much wider range of analytes [120]. LC-MS commonly involves mass analysers such as quadrupole, ion trap, and even a combination of two mass analysers (LC-MS-MS) such as the triple quadrupole mass spectrometer, offering enhanced sensitivity and

selectivity [120]. LC-MS-MS have been established to assess water contaminants [119]. It has been successfully involved in detecting glyphosate and acid herbicides in water sources [117]. Nowadays, the diversity of technologies includes mass spectrometry coupled to different instruments, including inductively coupled plasma-mass spectrometry (ICP-MS), able to analyse water samples [117]. A problem, however, is that the water samples must be collected and shipped to a laboratory for analysis. This introduces delays in reporting and in real-time field measurements.

In this chapter, the analytical capabilities of using a field deployable mass spectrometric instrument to provide a suitable analytical platform to investigate water quality in real-time is explored. The key step is to get the analytes of interest in the gas phase. A novel system, which is simply called the “water sampler” has been developed, the details of which are presented in this chapter, together with proof-of-principle trials.

This is a commercial development with the vision to provide a new market area for Kore Technology Ltd. Two mass spectrometric techniques, described in full in chapter 2, will be used to test the water sampler, one is a more standard and transportable electron impact (70 eV)-time of flight-mass spectrometer (EI-ToF-MS) [121], and the other is a proton transfer reaction-time of flight-mass spectrometer (PTR-ToF-MS). The interest in using a PTR-ToF-MS is its ability to measure many compounds at once with selectivity and high sensitivity. EI-ToF-MS without compound separation leads to difficulties in assignments, and hence often gas chromatography (GC) is required, but with this comes the disadvantage that real-time measurements would not be possible. However, in techniques like PTR-ToF-MS, without pre-separation the mass peaks from complex mixtures of compounds appear together in the mass spectrum, making interpretation difficult. One approach to this challenge was discussed in the previous chapter, namely a software algorithm combined with a mass spectral library to deconvolve complex

mixtures. The AnalyseHR program discussed previously is also used in the data processing for this chapter. For these methods to work, the characteristic ions from a compound and their relative intensities under known conditions must be available to the software. For the software to work, the fragment ion mass peaks and their relative intensities that are characteristic of the compound under known condition must be available to the software.

With regard to data produced by an EI-MS, the NIST Chemistry webbook, and also the NIST mass spectral library, provide plots of EI mass spectra. However, these can only be taken as a guide owing to differences in transmission and detection sensitivities between different instruments. Hence, calibration is required. The development of a highly portable system that was easy to use, was relatively inexpensive and could be used in real-time for direct measurements of water samples in the field with high sensitivity (c/s/ppb) would be a major accomplishment.

After development of the systems described in this chapter, and during the writing of this chapter, Martinsen et al published details on a field portable membrane introduction mass spectrometer (MIMS) for real-time monitoring of volatile organic compounds in aqueous samples [122]. The issue with this instrument is the use of an ion trap MS, which is more expensive than a ToF-MS, and requires compressed helium for use in the ion trap. In this study, a much cheaper and simpler solution is aimed for, which with the algorithm for dealing with complex samples should provide the commercial edge needed for Kore Technology Ltd.

The major problem that had to be overcome was how to get the VOCs contained in water into the gas/vapour phase. A non-exhaustive list of ways to achieve this involves typical methods such as diffusion [123], evaporation [123, 124], solid phase extraction [125], liquid-liquid extraction [116], purge-and-trap [116], (ultrasonic) nebulizer [126, 127] or polymer membrane exchanger [122, 128]. Recently, Ionicon Analytik GmbH, introduced a system for

analysing liquid samples, which they called a liquid calibration unit (LCU), including a nebulizer [129]. However, this device is expensive, requires extensive training and is not portable for fieldwork. Kore's vision was to design a simpler inexpensive system preserving high performance.

The goal of this part of the PhD programme was to design, develop and test simple systems, together with software developed by Kore [121].

In the following, the Mark I model is first described. The objective of Mark I was to investigate the viability of the idea and to learn what would be required for a better engineered prototype. Both systems were designed so that they could be directly coupled to the input of either the EI-ToF-MS or the PTR-ToF-MS to analyse water samples spiked with specific compounds in trace quantities, in order to obtain details on the sensitivity, reliability and reproducibility of the system before attempting environmental monitoring of volatile organic compounds (VOCs) contained in commercial water samples.

7.2 Water sampler method – initial concepts

Before beginning the design of the Mark I model, it was considered what key features and functions were required for a new water sampler. These considerations defined the key parameters in the first prototype (Mark I model). The key features considered included the following:

- A simple method to extract the volatile organic compounds contained in water samples and introduce them into a gas flow for mass spectrometric analysis. Different approaches have been listed earlier. The solution chosen by Kore is a silicone polydimethylsiloxane (PDMS) membrane permeation module, providing reliable

permselectivity for many compounds of interest, for examples chlorinated, brominated or aromatic hydrocarbons [128]. This is called the “exchanger”.

- Once the water line is connected to the source, volatiles will diffuse through the exchanger to be carried by a carrier gas to the mass spectrometer. In the field, the carrier gas will be the ambient air, which will require purifying before use. To provide the required portability of the system, ‘passive’ purification of the carrier gas to remove water and background volatiles will be used. This can be done with hydrocarbon and moisture traps that are inserted in the gas line, to provide low levels of relative humidity (< 1 %) and hydrocarbons (< pptv). This purification prevents the need to use any pressurised high purity carrier gas, which would raise costs, limit portability and raise issues of safety.
- The water sampler needs to be inexpensive. This can be achieved, because the permeation module can be purchased for less than £150 [130]. Also, the water line is pumped by a miniature centrifugal pump, acquired for less than £100 [130]. In use, replacement of these active components permits a low maintenance cost.

7.3 Mark I water sampler – Initial development of concept

7.3.1 Description and experimental conditions

Figure 7.1 provides a schematic representation of the first design (Mark I) coupled to a mass spectrometer where the airline follows the green arrows from the air inlet to the exhaust whereas the water line follows the blue arrows from one of the bottles (either sample or background) to the waste. It is also important to specify that the pump mentioned after the hygrometer is independent of the mass spectrometer. Details are given in this section.

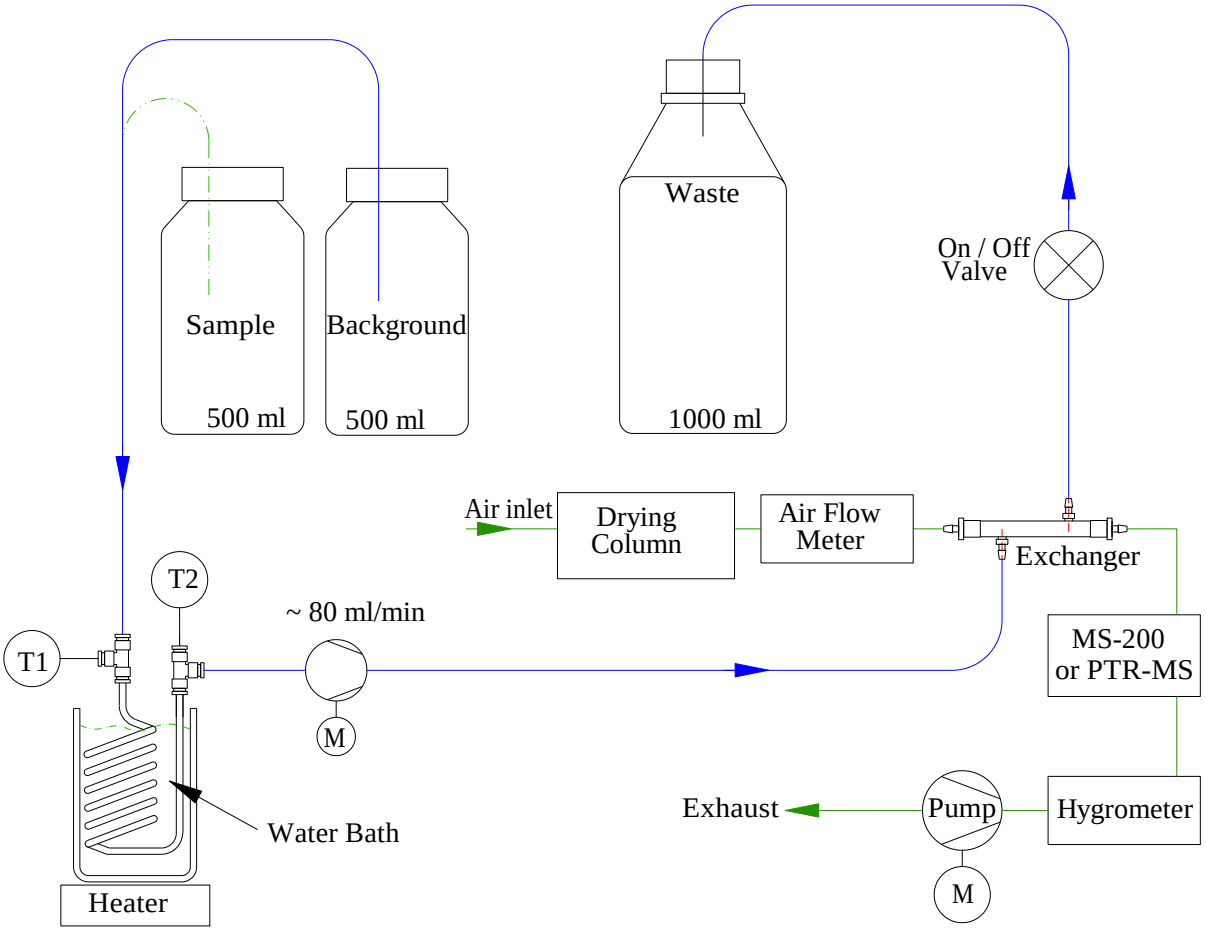

Figure 7.1: System including Mark I water sampler – global sketch
M stands for 'motor'/bench power supply. T1 and T2 are the thermometers that measure the temperatures at the entry (T1) and the exit (T2) of the heater. Exchanger represents the permeation module.

Figure 7.2 provides a photograph of the 'ad-hoc' nature of the apparatus set-up. The set-up is crude, because there was no point investing time and money in a commercial venture, before providing proof-of-concept. The exchanger, presented in both Figure 7.1 and Figure 7.2, is a 10 mm thick and 100 mm long tube enclosing 30 silicone tubes, also called 'fibres' each presenting a 0.3 mm outer diameter and a 0.19 mm inner diameter resulting in a 55 µm wall thickness. This design has been preferred to larger models since the response time of the membrane (i.e. the diffusion of the VOCs through, from the liquid phase to the gas phase) is expected to be proportional to the square of the wall thickness [130].

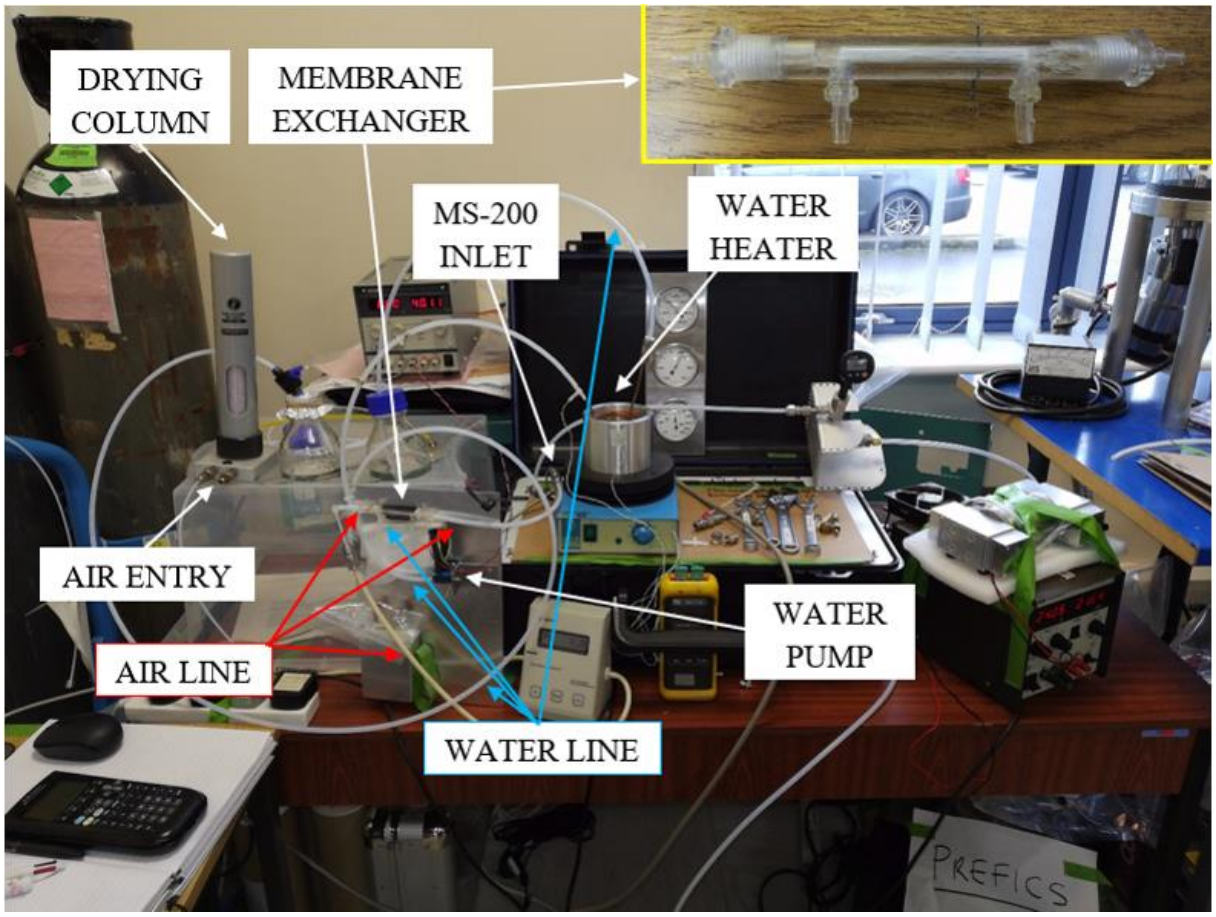

Figure 7.2: System including Mark I water sampler coupled to the MS-200 – global view

The water sample runs in an open circuit from either the sample or the background bottle to the waste bottle, being pumped through the membrane exchanger at ~ 80 mL/min by a micro centrifugal pump on the downstream side of the exchanger. This flow rate was chosen because empirically it produced the greatest VOC signals. The permeation rate of any VOC through a silicone PDMS membrane is temperature dependent [10, 11]. That is why, in order to keep the membrane temperature constant (and thus maintain a constant permeation rate), the water sample was passed through a coil of copper pipe immersed in a water bath held at 40 ºC. Unstable thermal conditions were observed at higher values. In practice, it was discovered that in order to obtain a stable temperature of 40 ºC, the water flow rate must not exceed 80 mL/ min.

Regarding the airline, the carrier gas (lab air here) passed through a drying column to remove moisture (~ 2 % relative humidity at 25 ºC) before entering the exchanger where a fraction of the volatiles that were present in the water sample permeates through the membranes into the air flow, which then was introduced to the mass spectrometric device for analysis. Notice the lab air was pumped into the airline by an external diaphragm pump at a flow of 270 sccm, which was measured with the air flow meter. This air flow (whose flow rate provided the best compromise between sensitivity and relative humidity) arrived then at the level of the MS-200, where it passed through a 'loop' where the pumping system of the mass spectrometer was used to draw air flow into the instrument. The majority of the carrier gas leaves the loop and line through the exhaust just after passing through the hygrometer. This configuration allowed the relative humidity of the sample to be determined, i.e., the mixture of the carrier gas and the VOCs from the liquid phase.

Despite a few physical issues (e.g. leaking pipes, unstable water flow, unstable temperature, air bubble formation that stopped flow), results are provided below to show that this inexpensive design worked sufficiently well to consider a more reliable, engineering prototype.

7.3.2 Initial measurements – Mark I water sampler connected to the MS-200

For testing the sampler, benzene was 'spiked' into a clean water sample. This molecule has the advantage that upon electron impact the major ion produced is M^+ at m/z 78 [131]. 1.000 ± 0.005 ppmv of benzene was prepared into normal tap water. The second test introduced 1,2,4-trichlorobenze ($C_6H_3Cl_3$) – an organochlorine compound referred to as TCB – at a level of 5.000 ± 0.025 ppmv in tap water. TCB is a common pollutant in rivers, being used as a solvent and a

dye carrier for many industrial processes [132]. It is toxic and has been found to be detrimental to fish once it enters river water [132].

Each sample analysis of the spiked tap water was alternated with a background water sample (tap water only). Each phase of analysis lasted 20 minutes. TCB is a more challenging compound owing to issues with permeation and surface adsorption.

The MS-200 is a small analyser with a resolution of only 250 (FWHM), insufficient to distinguish isobaric compounds. For this reason, mass peaks are often displayed as 'stickplot', representing the total integral at each fragment ion, identified by a *m/z* value. In the case of those measurements, EI leads to predominantly *m/z* 78 ($C_6H_6^+$) for benzene and *m/z* 180, 182 and 184 ($C_6H_3Cl_3^+$) for 1,2,4-trichlorobenzene. However, the intensity of the signal at m/z 180 was sufficiently intense that any of the other spectral peaks did not have to be included to see the response of this compound.

A portable EI-ToF-MS, the MS-200, is involved for the aim of reaching total portability. However, this instrument, working with a 2 L/s ion pump, presents a time limit of operation due to the increase of the pressure inside the mass spectrometer during long periods of analysis. That is why, in the results involving signals obtained from the MS-200, the pressure of the mass spectrometer will be discussed.

7.3.3 Results and discussions – Mark I water sampler connected to the MS-200

7.3.3.1 Benzene

Figure 7.3 represents the intensity of the signal recorded at m/z 78 (parent benzene produced by electron ionisation) in counts per acquisition (20 s). The continuous line is the sample phase whereas the dashed one is the background/flushing phase.

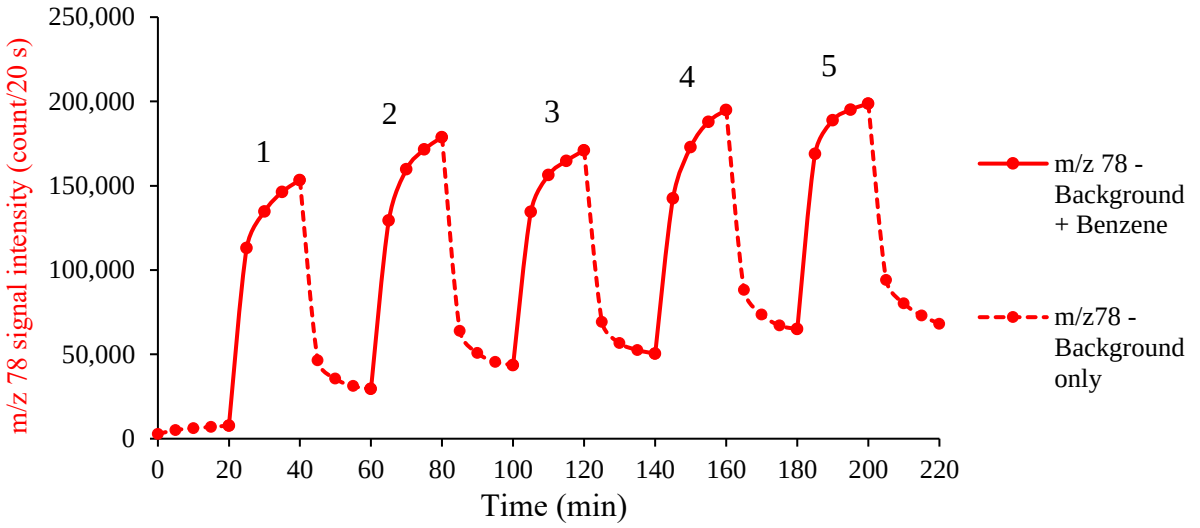

Figure 7.3: 1 ppmv benzene in water measurement – Mark I water sampler – MS-200; signal intensity recorded at m/z 78 (parent benzene produced by electron ionisation) in counts per acquisition (20 s)

In order to allow the MS-200 to be truly portable, the analyser is pumped only by a 2 l/s ion pump. After removing the sample gas, it can take many minutes for the analyte signal to fall to a level close to the level before analyte introduction. This is one of the limitations of this portable analyser. To determine a sensitivity and a limit of detection, the signal in phase 1 is compared to the instrumental background just prior to the measurement. This yields a sensitivity of 7.3 ± 0.4 c/s/ppbv and a limit of detection of 28 ± 1.4 ppbv for the charge-exchanged benzene. In subsequent phases of analysis, the span of the signal was measured with respect to the underlying signal just before benzene was re-introduced. Even though the underlying benzene signal is growing, the 'span' for each phase is consistent, as can be seen in Table 7.1:

Table 7.1: m/z 78 signal count rate above background of 1 ppmv benzene measurement with Mark I water sampler – MS-200, not being affected by the rising mass spectrometer pressure

m/z 78 response	**1**	**2**	**3**	**4**	**5**
Signal count rate above background (c/s)	7300	7500	6400	7200	6700
Mass spectrometer pressure (x 10^{-8} mbar)	28 ± 0.3	51 ± 0.5	67 ± 0.7	80 ± 0.8	86 ± 0.9

The m/z 78 count rate above the underlying signal is within 10 % variation around the average of 7000 c/s. This value is consistent despite the increase of the total background. Thus, provided regular background data can be acquired, the pumping limitation of the MS-200 does not prevent reproducible measurements.

Continuous operation of the instrument at very high analyser chamber pressures affects the lifetime of the electron multiplier. Therefore, the instrument has been fitted with an interlock that will close the inlet valve and switch off the high voltages at pressures around 10^{-6} mbar, in order to avoid damage to the detector [133]. Table 7.1 indicates that even after almost 4 h of continuous measurements the pressure in the mass spectrometer did not reach the critical value of 10^{-6} mbar. Plateaux were not reached during those measurements, that is why the data of Table 7.1 represents parameters using one measurement point for each phase (for example 80 min for sample and 60 min for background for signal 2). However, if the sample inlet to the spectrometer is closed when analysis is not required (for example in a flushing phase), the spectrometer can be operated for a full day, after which the instrument vacuum can be recovered overnight.

7.3.3.2 Trichlorobenzene (1,2,4-)

Figure 7.4 represents the intensity of the signal recorded at m/z 180 (parent TCB produced by electron ionisation) in counts per acquisition (20 s). The continuous line is the sample phase whereas the dashed one is the background/flushing phase.

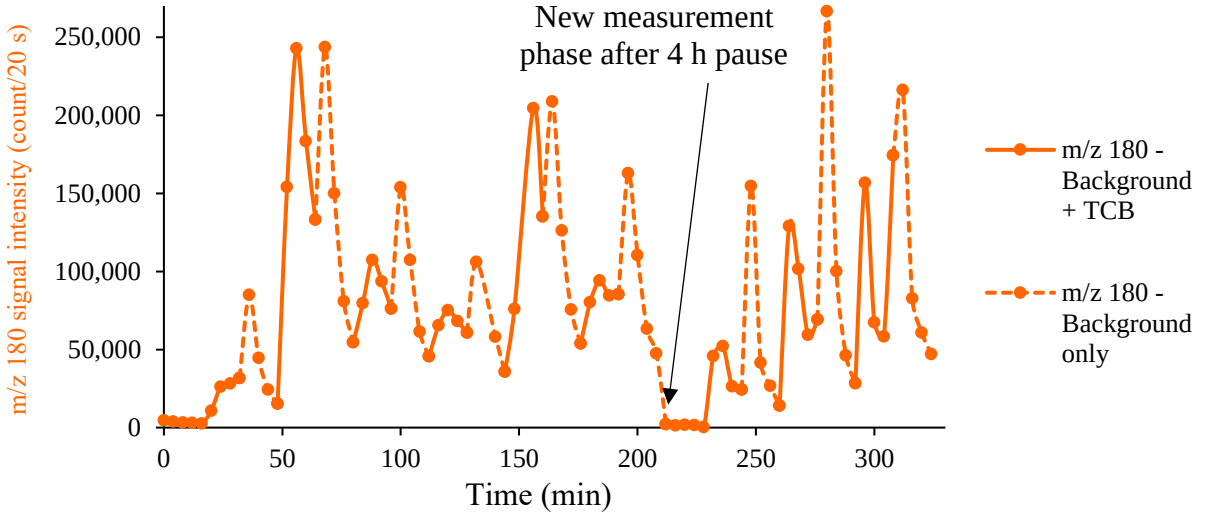

Figure 7.4: 5 ppmv TCB in water measurement – Mark I water sampler – MS-200; Signal intensity recorded at m/z 180 (parent TCB produced by electron ionisation) in counts per acquisition (20 s)

Clearly the behaviour of TCB-in-water sample is very different to the benzene-in-water sample. Following introduction of each TCB-in-water sample (continuous line), there was an expected increase in the parent molecule signal, but then an unexpected fall-off with time. Then, when the background water sample was used to flush the system (dashed line), the signal at m/z 180 immediately increased before falling to a background level. As with the benzene signal, the underlying levels of TCB slowly increased owing the limited pumping capacity of the analyser. Figure 7.4 also shows that the TCB signal is unstable. This is probably a result of TCB being 'stickier' and less volatile than benzene and, in order to keep costs down for the Mark I development, the inlet gas line was not heated.

Conclusion: Although major measurements issues were found for TCB, the consistency of the benzene signal provided confidence in the design to take the concept further. In addition, the ad-hoc design highlighted several technical issues that need to be addressed, namely leaking pipes, unstable water flow, unstable temperature, air bubble formation that stopped flow and general stabilisation. These were taken into account in the next design (Mark II water sampler).

7.4 Mark II water sampler – refinement of concept

For these experiments, a different analytical instrument was used. The second-generation water sampler, described below, was first connected to a PTR-ToF-MS where there were no pumping restrictions affecting background levels. This instrument was used in RF mode (see chapter 2, section 2.2.5) to improve sensitivity. Although the PTR-ToF-MS is a larger instrument, Kore has developed an instrument that can be operated from within a mobile van, and thus it is now not unreasonable to think that a water sampler could be part of the mobile laboratory. With this instrument, the new software, AnalyseHR, was used.

For the tests with the Mark II water sampler, a mixture of compounds, namely benzene, toluene, ethylbenzene and m-xylene (BTEX compounds) were used [134, 135]. Notice m-xylene results in the same mass spectral pattern as o- & p-xylenes, for the same experimental conditions. To undertake the tests, a number of issues had to be dealt with. Firstly, there was the need to create a library of the products ions and their branching percentages for each compound under **one specific set of conditions**. Then environmental monitoring of BTEX spiked in water (bottle, commercial water samples and river) were analysed. After the PTR-ToF-MS measurements, the Mark II water sampler was connected to the MS-200, starting with a calibration of each individual compound, i.e. respectively for benzene, toluene, ethylbenzene and m-xylene before analysing a mixture of these 4 compounds. The MS-200 software has its own version of compound deconvolution software via compound library entries. This is very similar in principle to the AnalyseHR program in which the PIDs for the compounds in the library are used, except that all mass peaks are reduced to stickplot, owing to the low mass resolution.

7.4.1 Description and experimental conditions

Figure 7.5 provides a schematic representation of the second design coupled to a mass spectrometer.

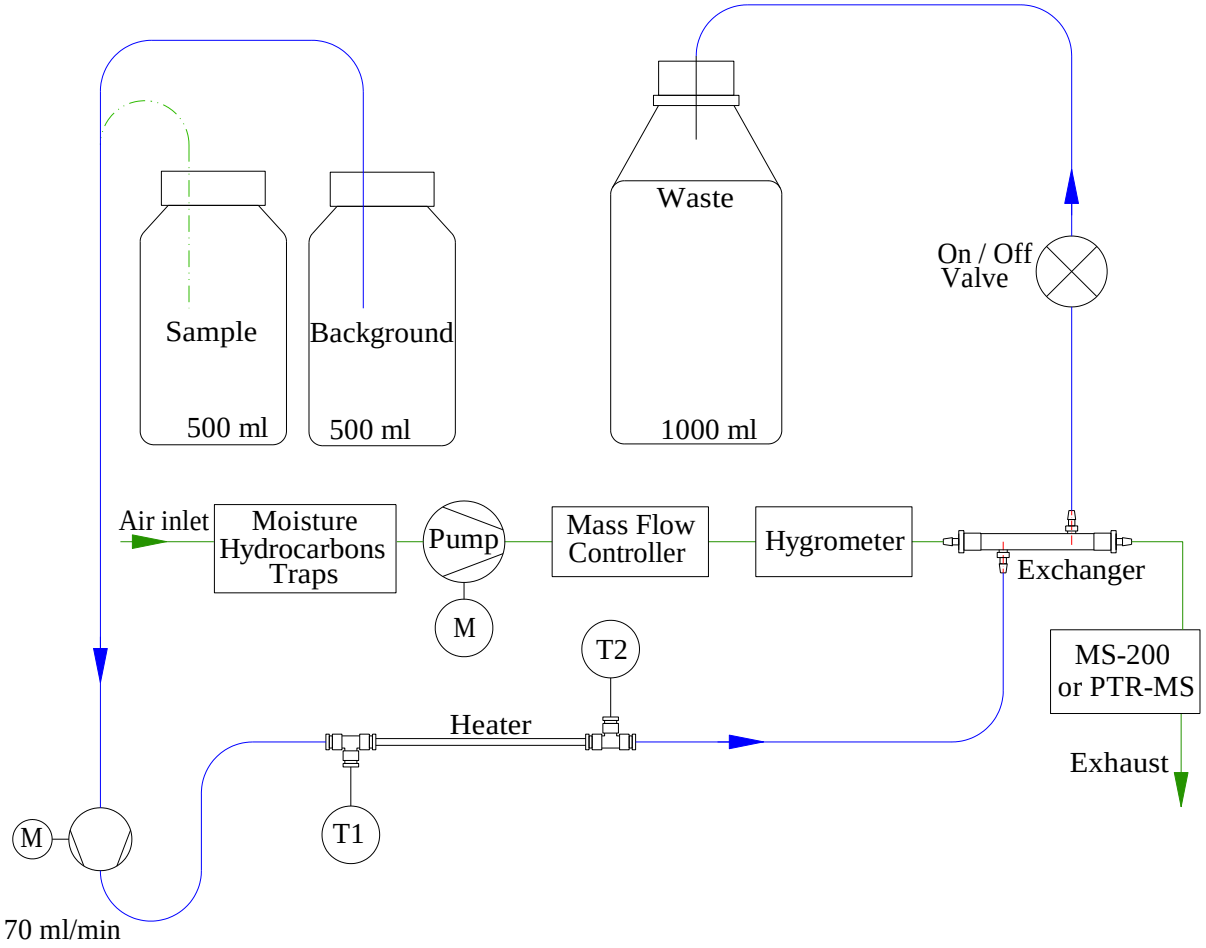

Figure 7.5: System including Mark II water sampler – global sketch
M, T1 and T2 respectively stand for 'motor'/bench power supply, the thermometers to measure temperature at the entry (T1) and the exit (T2) of the heater. Exchanger represents the permeation module.

Figure 7.6 represents a specific sketch of the second-generation water sampler itself whereas Figure 7.7 is a picture of the Mark II water sampler described in Figure 7.6.

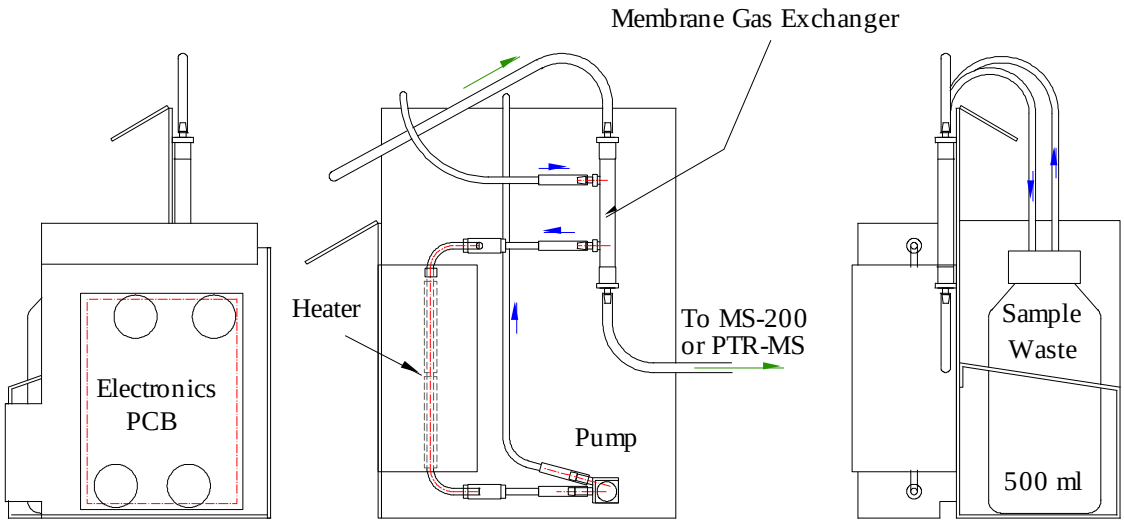

Figure 7.6: Mark II Water analyser – unit sketches (Right, Back, Left)
PCB stands for Printed Circuit Board

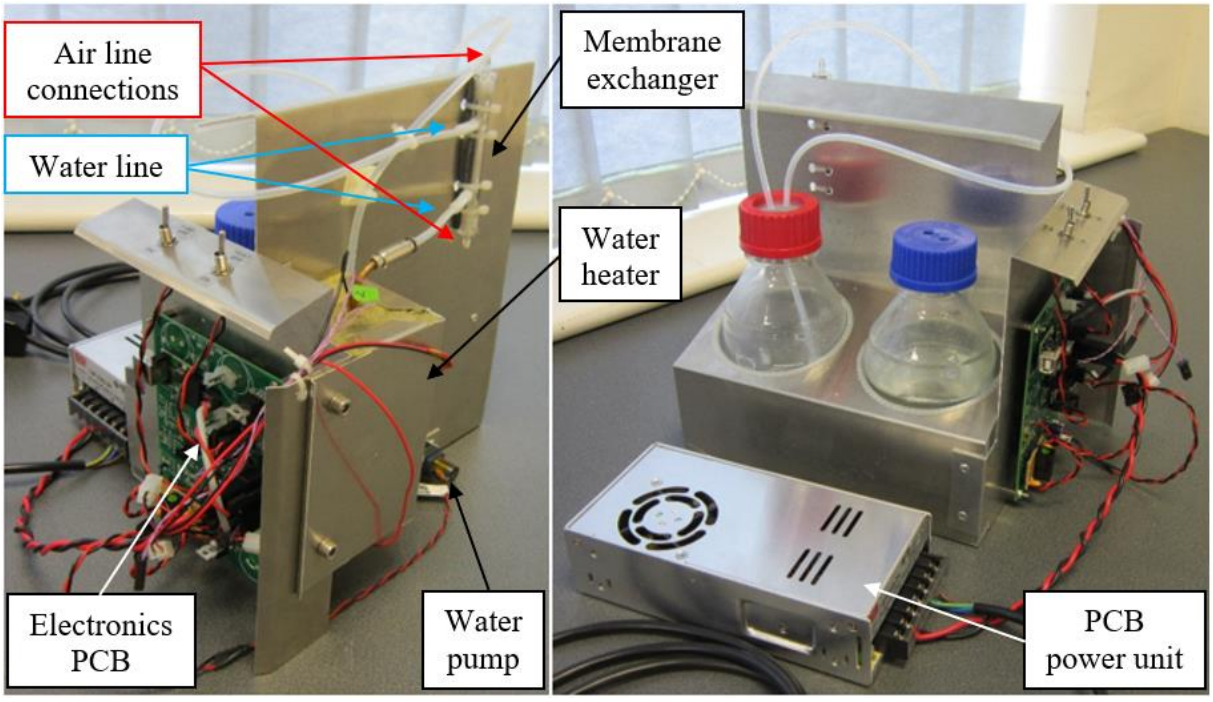

Figure 7.7: Mark II Water sampler – unit photos (Right/Back, Front/Right)
PCB stands for Printed Circuit Board

The basic principle of the Mark II water sampler is similar to that of Mark I, i.e. both water samples and background were alternatively running through a water line through the exchanger (remaining the same) where VOCs permeated into the carrier gas running in the gas line and then through to the instrument. Several changes were made to improve the reliability of the water sampler. These included:

- A new pump was installed that could be operated to produce the required water flow, with the aim of removing bubble production in the water sample. Communication was via a microprocessor using low-level hexadecimal code to set the flow, related to a specific input voltage. With this, the new water flow was more reliably maintained at 70 sccm, providing more stable experimental conditions. The pump of the Mark II sampler had a higher reliability by means of a different voltage control system. Whereas the first pump was DC power supplied, the new one was pulse width modulated (PWM) as shown in Figure 7.8:

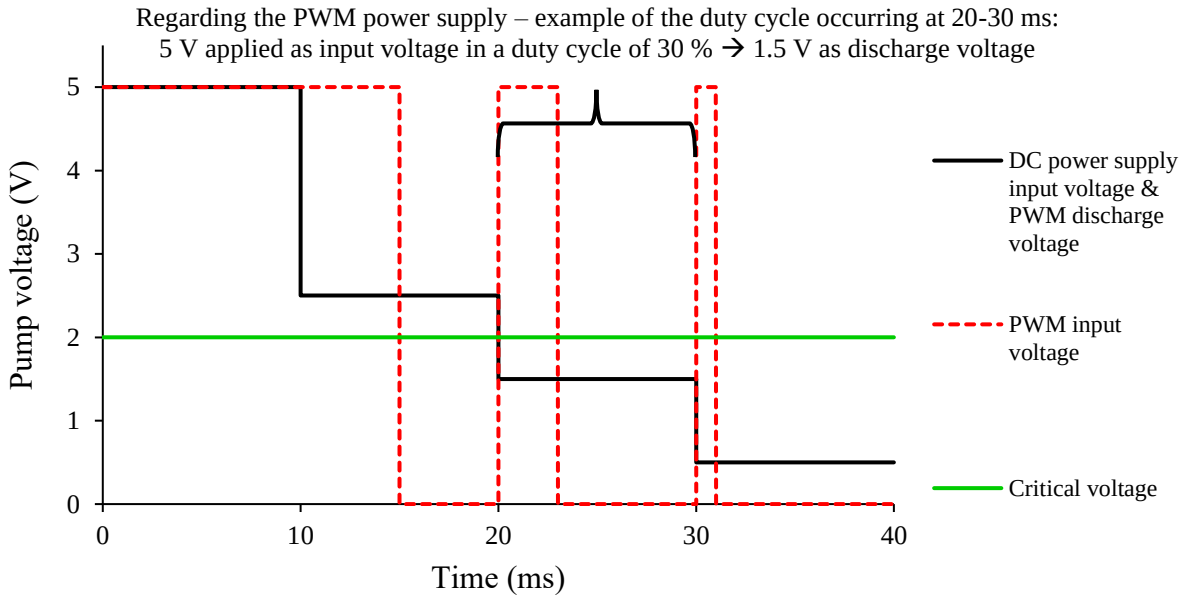

Figure 7.8: Comparison between ways of running of the DC power supply of the Mark I water sampler water pump and the pulse width modulated (PWM) power supply of the Mark II water sampler water pump

Figure 7.8 shows that there is a critical voltage (here 2 V) for the operation of the pump under which the torque transferred to the pump is insufficient to make it work. This happens using a DC power supply below a critical voltage, when, for experimental purposes, the water flow needs to be reduced. A pulse width modulated (PWM) pump is powered under a regular voltage frequency (here 100 Hz) where for each period (here 10 ms), an input voltage is provided to the pump (here 5 V) and the discharge voltage depends on what is called the duty cycle. Figure 7.8 shows the example happening between 20 and 30 ms where the input voltage is high (5 V) for 3 ms and low (0 V) for 7 ms, resulting in a duty cycle of 30 %. Once applied to the input voltage, it results in a discharge voltage of 1.5 V. However, compared to the DC power supply mode, where the discharge and the input voltages are the same (here 1.5 V), the input voltage of the PWM power supply still presents an input voltage of 5 V (> 2 V critical voltage), resulting in a constant voltage provided to the winding of the pump and consequently in the conservation of the torque sent to the pump, providing a controllable flow rate with no stall voltage. This solution has been proposed and designed by staff at Kore.

- A completely new water heater was designed. This is comprised of a Ni-Cr resistance wire tightly wound around a ~ 100 mm section of 5 mm internal diameter copper pipe (but insulated from the copper metal with a layer of Kapton polymer). The heater is enclosed in an insulated box filled with glass wool to reduce heat loss. The temperature is feedback-controlled via a dedicated microprocessor on a purpose-built electronics control board designed for this project by staff at Kore. A picture of the construction is shown in Figure 7.7. A target temperature is entered into the operating program in degrees Celsius. The challenge was to put enough power into the heater so that water at

room temperature would reach the target temperature (70 °C) by the time it exited from the short length of heated copper pipe.

- A dedicated electronics printed circuit board (PCB) was commissioned to power the new heater and control the temperature with feedback from a resistive temperature device (RTD) built into the heater. The electronics also provided power for the new water pump, with the ability to vary the flow as discussed above. The microprocessors were controlled by means of software.
- A mass flow controller was added in the carrier gas line to provide stable airflow, within 0.1 sccm variations, with the air flow set to 500 sccm (maximum value of the mass flow controller and where the best sensitivity for the compounds of interest was reached).
- Compared to the Mark I apparatus, where the lab air was only filtered by a drying column, in Mark II, moisture and hydrocarbons traps were added to the airline to reduce and maintain the initial humidity of the carrier gas to a known level (0.1 % relative humidity at 25 ºC) and the hydrocarbons background to low pptv level. This 'passive' purification, i.e. not requiring power sources or pressurized gas, was added so that water samples could be analysed in the field.
- The hygrometer was positioned before the exchanger to provide a more accurate value of the relative humidity of the carrier gas. This humidity was maintained at better than 0.1 %, independent of the water line.
- For this version, the inlet line remained at room temperature. However, its heating will be taken into consideration in any further development.

7.4.2 New measurements – Mark II water sampler connected to the PTR-ToF-MS

For each BTEX compound a background sample (tap water) and a 5.00 ± 0.45 ppbv-in-water samples were prepared, alternatively passed through the water sampler, and analysed using the PTR-ToF-MS instrument. The drift tube of the PTR-ToF-MS was maintained at a pressure of 1.4 mbar and a temperature of 25 ºC. A DC electric field of ~ 18 V/cm was provided resulting in an E/n value of 53 Td in the first half of the reactor before the RF field was superimposed to the DC field in the second half to improve sensitivity. Hydronium was used as reagent ion. However, it is important to specify that whilst using RF, the O_2^+ is substantially increased from approximately 3-5 % upon the reagent ions distribution in DC mode to about 15-20 % in RF mode. Unlike in fundamental ion-molecule research, the use of both reagent ions is not inconvenient, improving the selectivity of the instrument by identifying a more unique spectral pattern. Table 7.2 lists the product ions for each BTEX compound under this RF mode operation.

Table 7.2: ions involved in the BTEX library (including their PIDs) considered in the deconvolution software – AnalyseHR – for the Mark II water sampler – PTR-ToF-MS measurements

Neutral compound	**Product ion**			
	Code	**Formula**	**m/z**	**Proportion**
Benzene	M^+	$C_6H_6^+$	78	0.31
	MH^+	$C_6H_7^+$	79	0.69
Toluene	$(MH\text{-}H_2)^+$	$C_7H_7^+$	91	0.10
	M^+	$C_7H_8^+$	92	0.27
	MH^+	$C_7H_9^+$	93	0.63
Ethylbenzene	$(MH\text{-}C_2H_4)^+$	$C_6H_7^+$	79	0.33
	$(M\text{-}CH_3)^+$	$C_7H_7^+$	91	0.20
	M^+	$C_8H_{10}^+$	106	0.11
	MH^+	$C_8H_{11}^+$	107	0.36
Xylenes	$(M\text{-}CH_3)^+$	$C_7H_7^+$	91	0.09
	M^+	$C_8H_{10}^+$	106	0.23
	MH^+	$C_8H_{11}^+$	107	0.69

Once the library was created (including the respective relative sensitivity factors and product ion distributions), tests including the same BTEX compounds took place before initiating environmental monitoring. Once results were considered as successful enough, the Mark II water sampler was connected to the MS-200.

7.4.3 Results and discussions – Mark II water sampler connected to the research PTR-ToF-MS

7.4.3.1 BTEX library creation

From Table 7.2 can be identified the product ions from the reactions of H_3O^+ with a BTEX molecule M at m/z 79, 93 and 107 and the product ions from the reactions of O_2^+ with a BTEX molecule M at m/z 78, 92 and 106. The product ion at m/z 91 is a special case that comes from the loss of H_2 of MH^+.

The following results present, for each individual BTEX, the signal intensity of the product ions as a function of measurement time. Figure 7.9-Figure 7.12, respectively, present the data for benzene, toluene, ethylbenzene and m-xylene. Notice, as a plateau is reached and quite distinguished for both background and sample phases, a single continuous line is displayed for each ion for the purpose of clarity.

- Benzene

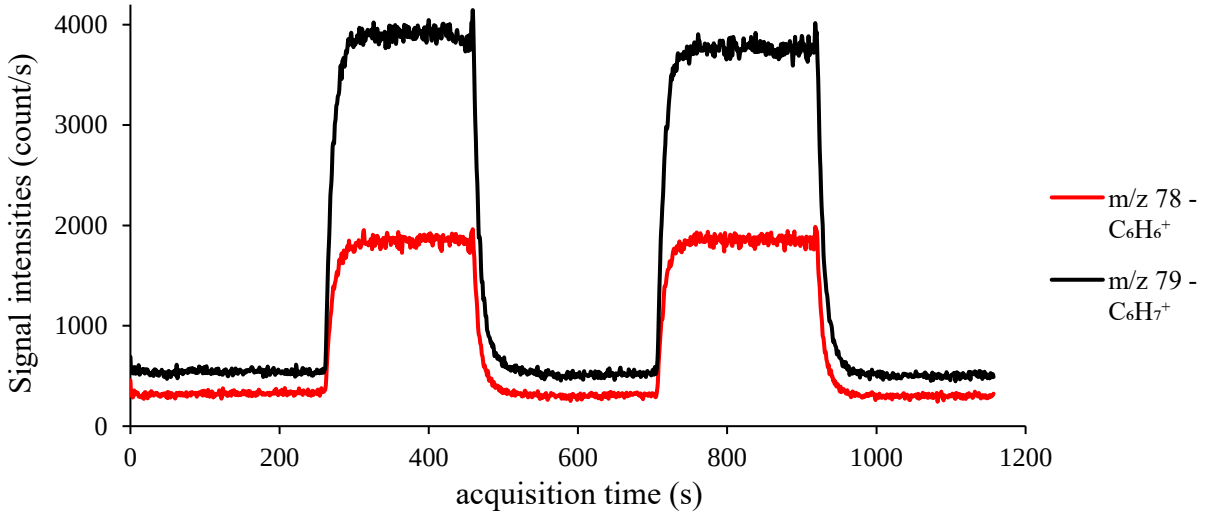

Figure 7.9: 5 ppbv benzene in water measurement using the tandem Mark II water sampler – PTR-ToF-MS; signal intensity recorded at m/z 78 (parent benzene produced by electron ionisation) and m/z 79 (parent benzene produced by proton transfer) in counts per second

- Toluene

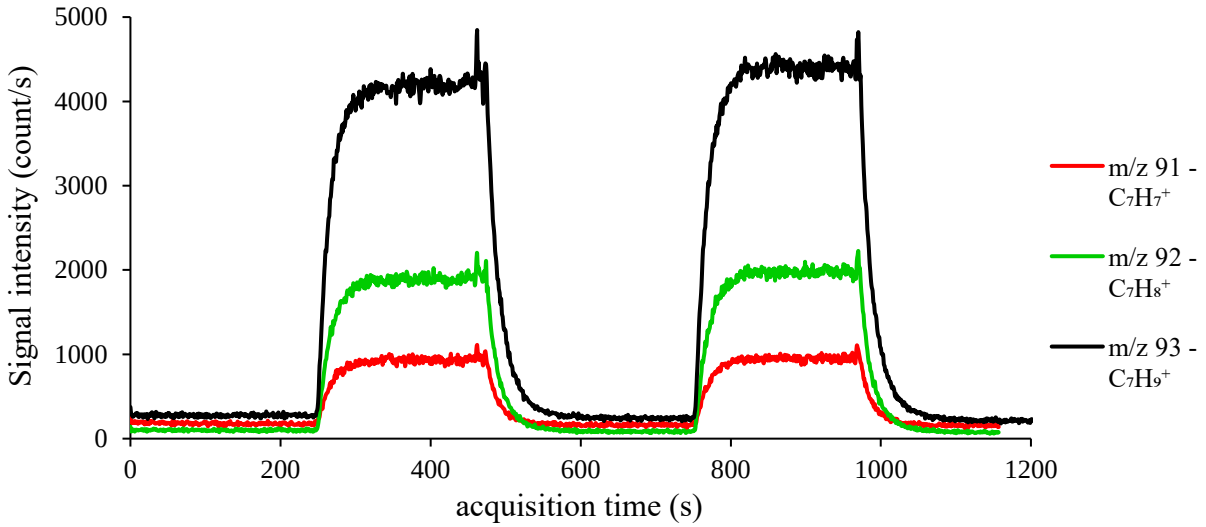

Figure 7.10: 5 ppbv toluene in water measurement using the tandem Mark II water sampler – PTR-ToF-MS; signal intensity recorded at m/z 91 (fragment ion produced by proton transfer), m/z 92 (parent toluene produced by electron ionisation) and m/z 93 (parent toluene produced by proton transfer) in counts per second

- Ethylbenzene

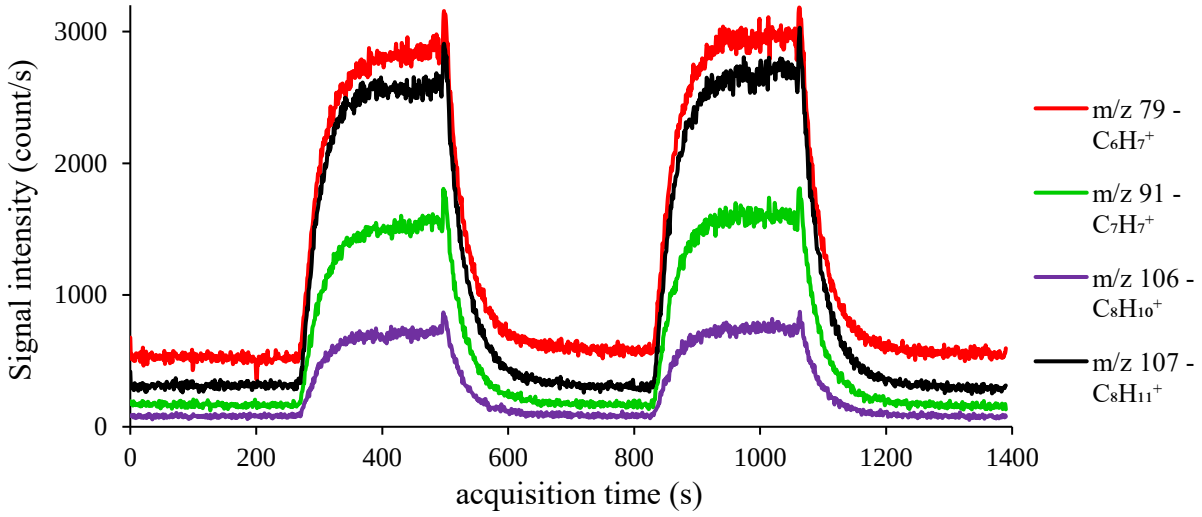

Figure 7.11: 5 ppbv ethylbenzene in water measurement using the tandem Mark II water sampler – PTR-ToF-MS; signal intensity recorded at m/z 79 (fragment ion produced by proton transfer), m/z 91 (fragment ion produced by proton transfer), m/z 106 (parent ethylbenzene produced by electron ionisation) and m/z 107 (parent ethylbenzene produced by proton transfer) in counts per second

- Xylene (m-)

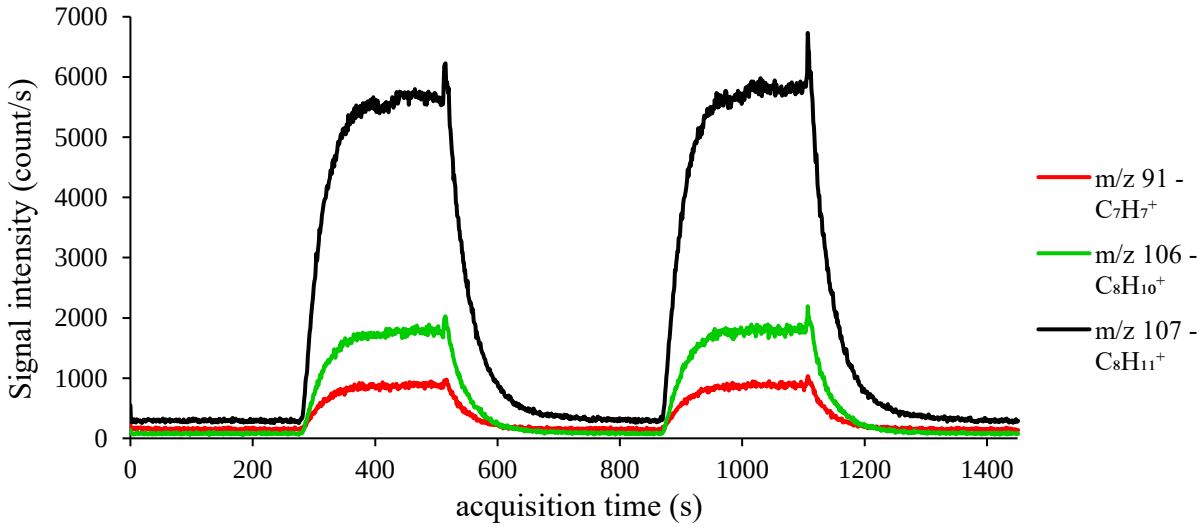

Figure 7.12: 5 ppbv m-xylene in water measurement using the tandem Mark II water sampler – PTR-ToF-MS; signal intensity recorded at m/z 91 (fragment ion produced by proton transfer), m/z 106 (parent xylenes produced by electron ionisation) and m/z 107 (parent xylenes produced by proton transfer) in counts per second

From the intensity monitoring, and for each VOC response, data were extracted from both sample and background plateaux of the same duration, and after taking an average of both signals, the product ion distributions (PID) were determined as previously summarised in Table 7.2. The data used for the BTEX library were used as reference. Details of the sensitivity using Mark II for each single compound is provided by Table 7.3:

Table 7.3: Performances of the tandem Mark II water sampler – PTR-ToF-MS for BTEX single compounds before software saturation correction

Without saturation correction	**Sensitivity**	**Limit of detection**	**FWHM**
Protonated compound	**c/s/ppbv**	**pptv**	**-**
Benzene at m/z 79	654 ± 60	15 ± 1.4	3497 ± 35
Toluene at m/z 93	1005 ± 91	9 ± 0.8	3439 ± 34
Ethylbenzene at m/z 107	567 ± 51	14 ± 1.3	3435 ± 34
Xylenes at m/z 107	1220 ± 111	7 ± 0.6	3409 ± 34

where FWHM stands for the mass resolution at Full Width Half Maximum. Notice the data in Table 7.3 are determined using the major mass peak for each single compound.

The signals of the various BTEX components were higher than anticipated, resulting in losses due to counting saturation. These have been corrected in the AnalyseHR program and are presented in Table 7.4 below. The aim of AnalyseHR is also to correct the signal integral of a peak, restoring the counts lost through dead-time losses due to saturation in pulse counting systems. The corrected data more accurately represent the performance of the Mark II water sampler when coupled to the PTR-ToF-MS.

Table 7.4: Performances of the tandem Mark II water sampler – PTR-ToF-MS for BTEX single compounds after software saturation correction

With saturation correction	Sensitivity	Detection limit	FWHM
Protonated compound	**c/s/ppbv**	**pptv**	**-**
Benzene at m/z 79	733 ± 66	14 ± 1.2	3621 ± 36
Toluene at m/z 93	1182 ± 107	7 ± 0.7	3620 ± 36
Ethylbenzene at m/z 107	622 ± 56	13 ± 1.2	3500 ± 35
Xylenes at m/z 107	1483 ± 134	6 ± 0.5	3584 ± 36

The data treatment increased the sensitivities by 10-21 %, decreased the limit of detection by 7-21 % and increased the mass resolution by 2-5 %.

The product ion distributions for each of the compounds under these instrumental conditions were entered into the AnalyseHR library, together with their concentrations. The next step was to check the accuracy of the AnalyseHR program on samples having different concentrations, and also mixtures of the BTEX compounds.

7.4.3.2 BTEX library early tests – single compounds

The next phase involved the preparation of 10 ppbv samples-in-water of each BTEX single compound separately using the Mark II water sampler connected to the PTR-ToF-MS to generate data, and then check the quantification methodology using the AnalyseHR tool. The aim was to see the accuracy and the reproducibility of the results and thus the validity of the product ion distributions and the relative sensitivity factors (both being key parameters of the deconvolution process). Results are shown in Table 7.5-Table 7.8.

Notice that water with no added compounds was also analysed to establish background signals at the m/z values of interest. In a sensitive technique such as PTR-ToF-MS, there is often a low-level background signal at every m/z and this must be taken into account. This is, in this study, the instrumental background, and it must be subtracted from the signals acquired

from the sample (as done in Table 7.5-Table 7.8) where product ion signals from the BTEX single compounds are known to appear.

For the 'prepared concentrations' an estimate has been made of the potential divergence from the target concentration due to uncertainties in the injection volumes of the 10 μL syringe (± 0.1 μL), the 1 mL syringe (± 10 μL) and the 10 mL syringe (± 100 μL). For the concentration values reported by the software, the uncertainty is expressed as ± standard deviations in the counts from which the concentrations were calculated.

Table 7.5: Benzene quantified by AnalyseHR using the tandem Mark II water sampler – PTR-ToF-MS

		Benzene	**Toluene**	**Ethylbenzene**	**Xylenes**	**Total**
Benzene only	Prepared concentration (**ppbv**)	10.00 ± 1.400	0.000 N/A	0.000 N/A	0.000 N/A	10.00 ± 1.400
	Reported concentration (**ppbv**)	**10.08** ± 0.020	**0.037** ± 0.003	**0.354** ± 0.013	**0.000** N/A	**10.47** ± 0.014

Table 7.6: Toluene quantified by AnalyseHR using the tandem Mark II water sampler – PTR-ToF-MS

		Benzene	**Toluene**	**Ethylbenzene**	**Xylenes**	**Total**
Toluene only	Prepared concentration (**ppbv**)	0.000 N/A	10.00 ± 1.400	0.000 N/A	0.000 N/A	10.00 ± 1.400
	Reported concentration (**ppbv**)	**0.212** ± 0.011	**10.87** ± 0.022	**-0.200** N/A	**0.148** ± 0.006	**11.03** ± 0.039

Table 7.7: Ethylbenzene quantified by AnalyseHR using the tandem Mark II water sampler – PTR-ToF-MS

		Benzene	**Toluene**	**Ethylbenzene**	**Xylenes**	**Total**
Ethyl-benzene only	Prepared concentration (**ppbv**)	0.000 N/A	0.000 N/A	10.00 ± 1.400	0.000 N/A	10.00 ± 1.400
	Reported concentration (**ppbv**)	**0.314** ± 0.012	**0.067** ± 0.004	**10.28** ± 0.021	**0.268** ± 0.013	**10.93** ± 0.050

Table 7.8: m-xylene quantified by AnalyseHR using the tandem Mark II water sampler – PTR-ToF-MS

		Benzene	Toluene	Ethylbenzene	Xylenes	Total
m-xylene only	Prepared concentration (**ppbv**)	0.000	0.000	0.000	10.00	10.00
		N/A	N/A	N/A	± 1.400	± 1.400
	Reported concentration (**ppbv**)	**0.223**	**0.053**	**-0.177**	**11.34**	**11.44**
		± 0.011	± 0.004	N/A	± 0.012	± 0.027

After considering the uncertainties, the concentration windows overlay in three cases out of four and for m-xylene the minimal difference is 17 pptv.

7.4.3.3 BTEX library early tests – compounds mixtures

The next tests were designed to determine how well the software could separate compounds in a mixture. Figure 7.13 shows how several of the product ions of significance in a BTEX analysis have contributions from more than one compound.

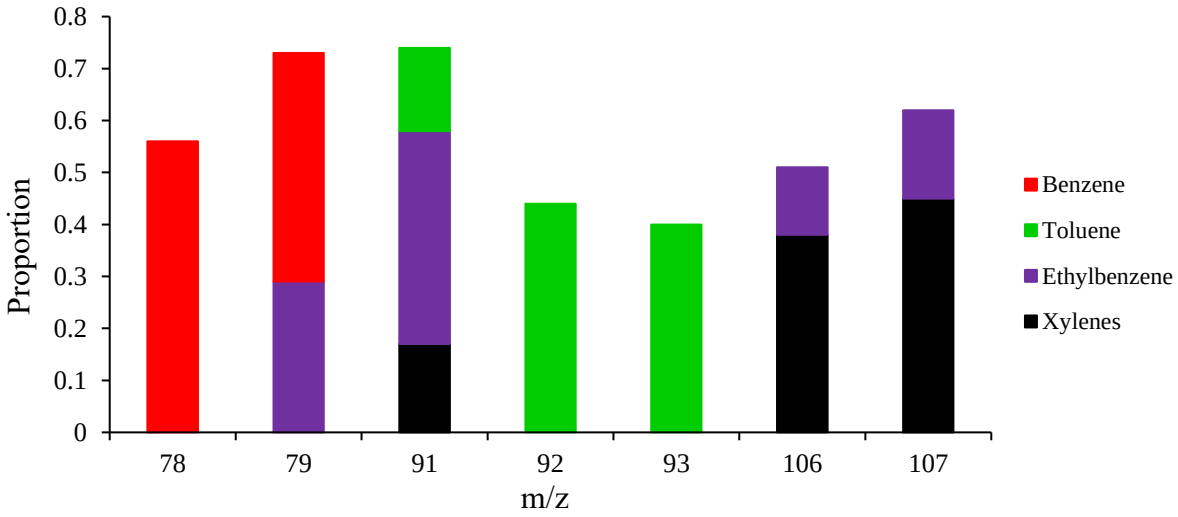

Figure 7.13: Superposition of BTEX compounds PIDs under the experimental conditions used for the Mark II water sampler – PTR-ToF-MS measurements

For example, m/z 91 has contributions from toluene, ethylbenzene and xylenes. This is the challenge for any deconvolution software, to be able to separate the different contributions and then calculate concentrations of the separate compounds. To test the deconvolution process, samples with all the BTEX compounds in water were prepared. The two mixtures prepared were mixture A: 5 ppbv of each as shown in Table 7.9 and mixture B: respectively 5, 3.75, 3.125 and 4.325 ppbv as shown in Table 7.10 (the levels for toluene, ethylbenzene and xylenes may seem rather 'unusual', but these are the calculated values when using a set injection volume that was convenient to use, still subject to errors[2]).

Table 7.9: BTEX mixture A quantified by AnalyseHR using the tandem Mark II water sampler – PTR-ToF-MS

		Benzene	**Toluene**	**Ethylbenzene**	**Xylenes**	**Total**
Mixture A	Prepared concentration (**ppbv**)	5.000 ± 0.450	5.000 ± 0.450	5.000 ± 0.450	5.000 ± 0.450	20.00 ± 1.800
	Reported concentration (**ppbv**)	**4.477** ± 0.017	**4.529** ± 0.067	**6.290** ± 0.057	**4.260** ± 0.013	**19.56** ± 0.154

Table 7.10: BTEX mixture B quantified by AnalyseHR using the tandem Mark II water sampler – PTR-ToF-MS

		Benzene	**Toluene**	**Ethylbenzene**	**Xylenes**	**Total**
Mixture B	Prepared concentration (**ppbv**)	5.000 ± 0.350	3.750 ± 0.310	3.125 ± 0.290	4.375 ± 0.330	16.25 ± 1.280
	Reported concentration (**ppbv**)	**4.644** ± 0.017	**3.408** ± 0.008	**4.262** ± 0.024	**3.980** ± 0.017	**16.30** ± 0.066

The total concentrations reported are within the expected window given the predicted errors. Most of the reported concentrations of individual compounds are close to that expected

[2]As for mixture A, mixture B has been prepared through a 2 stages dilution. For the chosen concentrations, ethylbenzene was the smallest amount to inject. Choosing 3.125 ppbv, a first injection of 1.75 µL from the pure compound into tap water was possible and then a second dilution of 285 µL of that mixture into tap water.

but tend to be on the limit of the deviations expected. The main source of error in these analyses comes from the present software algorithm, which assigned a higher concentration to ethylbenzene, overestimated by 25 to 35 %, which in turn has resulted in the other compounds being underestimated by 7 to 15 %.

The data in the previous section explored the analytical methodology, which comprised the water sampler combined with PTR-ToF-MS analysis, followed by data reduction using the AnalyseHR software to obtain quantitative results. Using this methodology, various commercial water products were analysed as first potential commercial applications of such a system. For all the subsequent analyses, the tap water at Kore Technology was used as background (incorporating the instrumental background) and, for clarity, concentrations expressed in pptv are displayed in **red** while the ones in ppbv remain displayed in **black**.

7.4.3.4 Environmental BTEX monitoring – Drinking water bottles

The first application was to use the Mark II water sampler – PTR-ToF-MS system, coupled to AnalyseHR, to analyse any potential BTEX concentrations in drinking water bottles from different brands. The results are shown in Table 7.11 and, for each sample, the results shown are an average of two measurements.

Using tap water as the reference sample, the instrumental background results in the manually estimated detection limits shown in Table 7.11. The concentrations for BTX reported by the software for the drinking water samples were all negative whereas that for ethylbenzene was positive and just above the detection limit. This would imply the presence of a small amount of this compound. However, this highlights the limitations of the algorithm in deconvolving this mixture.

Table 7.11: BTEX compounds quantified by AnalyseHR using the tandem Mark II water sampler – PTR-ToF-MS in drinking water bottles

Background: Kore Tap water		Benzene	Toluene	Ethylbenzene	Xylenes	Total
Detection limit (pptv)		**14** ± 1.2	**7.3** ± 0.7	**13** ± 1.2	**5.7** ± 0.5	**40** ± 3.6
Reported concentration (pptv)	Ashbeck	**-70** N/A	**-58** N/A	**49** ± 12	**-90** N/A	**-169** ± 12
	Buxton	**-24** N/A	**-44** N/A	**7.0** ± 11	**-48** N/A	**-109** ± 11
	Evian	**-29** N/A	**-25** N/A	**26** ± 11	**-37** N/A	**-65** ± 11
	Highland Springs	**-44** N/A	**-38** N/A	**25** ± 11	**-53** N/A	**-110** ± 11
	Volvic	**-35** N/A	**-14** N/A	**24** ± 11	**-27** N/A	**-52** ± 11

For the example of the Ashbeck case, the mass spectra of both samples and background at the masses of interest of the BTEX library are shown in Figure 7.14-Figure 7.16:

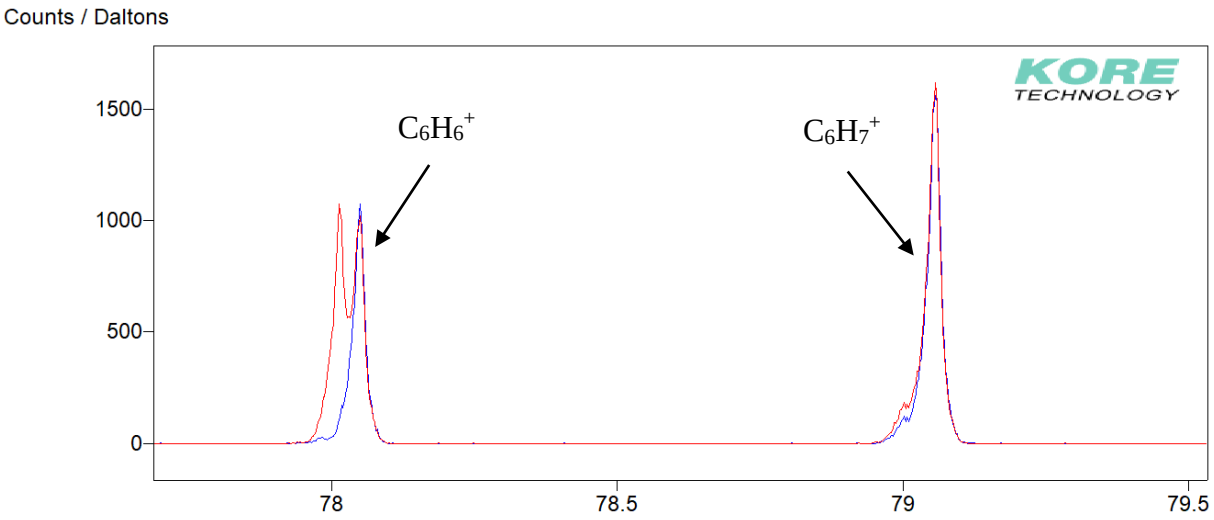

Figure 7.14: Spectra of Ashbeck drinking water (blue) overlaid on background (red) – m/z 78-79 using the tandem Mark II water sampler – PTR-ToF-MS

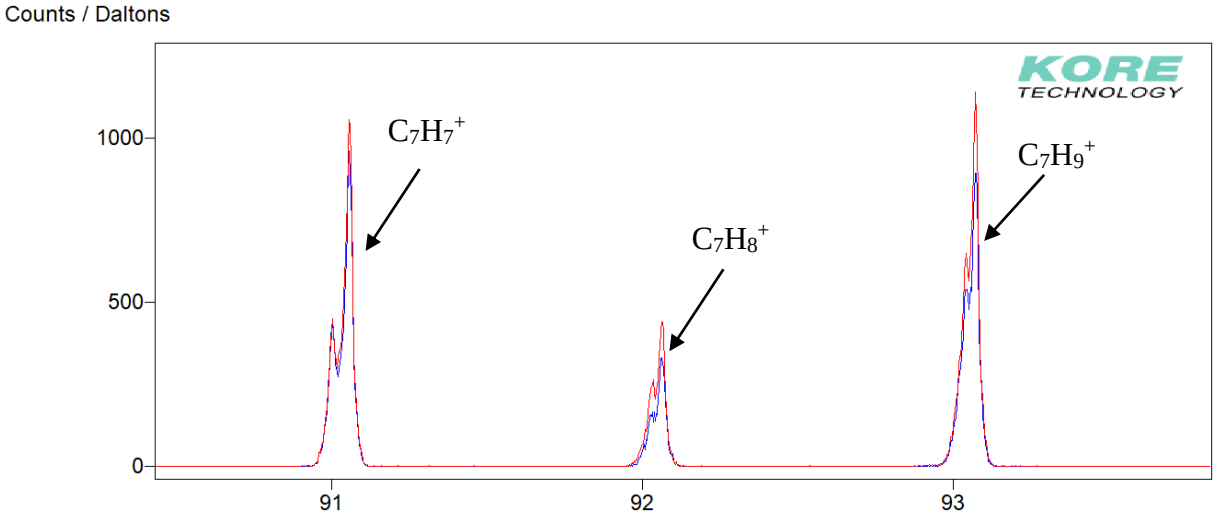

Figure 7.15: Spectra of Ashbeck drinking water (blue) overlaid on background (red) – m/z 91-93 using the tandem Mark II water sampler – PTR-ToF-MS

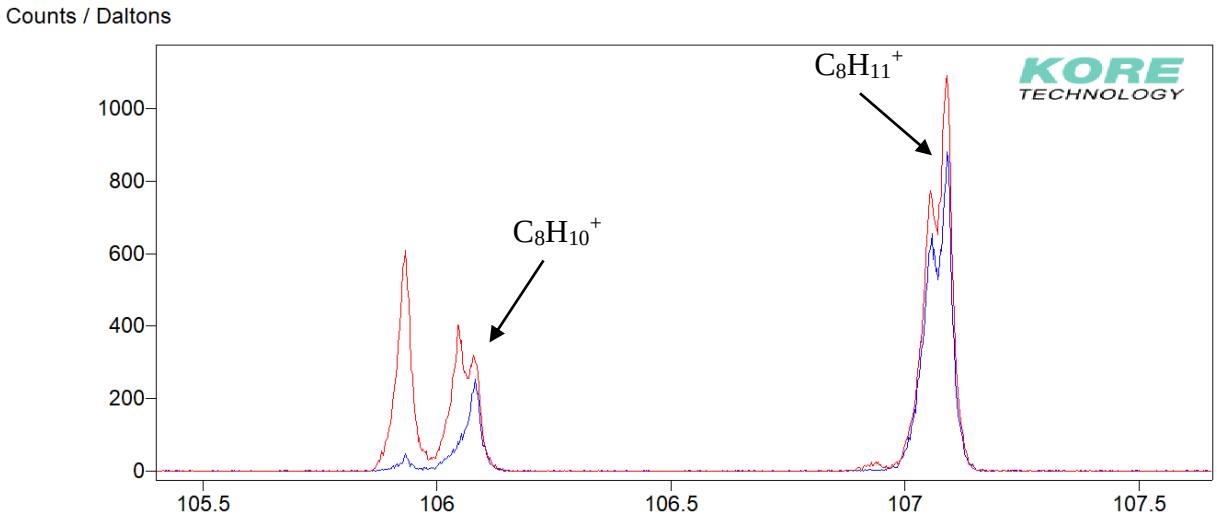

Figure 7.16: Spectra of Ashbeck drinking water (blue) overlaid on background (red) – m/z 106-107 using the tandem Mark II water sampler – PTR-ToF-MS

From Table 7.11 and Figure 7.14-Figure 7.16, no BTEX compounds were present. Indeed, the integral of the sample (in blue) minus the background (in red) was negative for all the BTEX peaks.

Figure 7.14-Figure 7.16 show isobaric compounds at each m/z of interest involved, part of the instrumental background, except at m/z 78 and m/z 106 where peaks in the tap water

were observed that were not present in the bottled water. $CHBrN^+$ was clearly identified through its isotopes at m/z (intensity) 105.93 (100 % as referential intensity), as seen in Figure 7.16, and 107.93 (97.5 %). A comment will be made about this ion later. The peaks at m/z 78.011 and the peak at m/z 106.043 were potentially $C_5H_2O^+$ and $C_7H_6O^+$ (exact m/z of lightest isotopomer 78.01056 and 106.04186 g/mol, respectively).

7.4.3.5 Environmental BTEX monitoring – De-ionised and steam ironing waters

The next applications phase involved commercial water solutions, including more complex compositions than drinking water bottles. These included de-ionised waters (one present in Kore lab and a commercial one) and commercial steam ironing waters involving special scents through molecules like monoterpenes. The quantification of BTEX compounds has been monitored and results are shown in Table 7.12.

Note that four samples out of five were diluted due to severe saturations of the signals of at least one mass of interest considered in the BTEX library of AnalyseHR. That is why a dilution factor was applied, if relevant, on the software-generated concentrations expressed in pptv to provide then the real concentration, in ppbv.

Table 7.12 shows that the total BTEX concentration was, in each case, reported as greater than the total detection limit, meaning the total BTEX signal was not negligible.
The de-ionised water from Kore was stored in a large 50-litre capacity plastic reservoir and clearly shows an unexpected benzene contamination.

Unexpectedly, the water products that are sold for steam irons appeared to have high levels of BTEX. Tesco steam iron water had levels 6 times greater than the Tesco de-ionised water, and the ‘Spring Fresh’ and ‘Spring Petals’ products appeared to have even higher levels.

Table 7.12: BTEX compounds quantified by AnalyseHR using the tandem Mark II water sampler – PTR-ToF-MS in de-ionised and steam ironing waters

Background: Kore Tap water			Benzene	Toluene	Ethylbenzene	Xylenes	Total
	Dilution factor	**Detection limit (pptv)**	**14** ± 1.2	**7.3** ± 0.7	**13** ± 1.2	**5.7** ± 0.5	**40** ± 3.6
Software-reported concentration before (pptv) and after (ppbv) application of dilution factor when relevant	**100**	De-ionised water – Kore	**7214** ± 17	**-0.5** N/A	**433** ± 13	**-82** N/A	**7565** ± 30
			721	**-0.1**	**43**	**-8.2**	**756**
	1	De-ionised water – Tesco	**130** ± 8.0	**1173** ± 5.6	**781** ± 13	**176** ± 6.1	**2260** ± 33
			0.1	**1.2**	**0.8**	**0.2**	**2.3**
	4	Steam Iron Water – Tesco	**75** ± 8.2	**1139** ± 6.2	**3076** ± 31	**-50** N/A	**4240** ± 45
			0.3	**4.6**	**12**	**-0.2**	**17**
	100	Ironing water 'spring fresh' – Tesco	**257** ± 8.7	**2510** ± 7.9	**5057** ± 20	**-36** N/A	**7788** ± 38
			26	**251**	**506**	**-4**	**779**
	100	Ironing water 'spring petals' – Tesco	**-106** N/A	**659** ± 5.1	**3053** ± 19	**0.0** N/A	**3606** ± 24
			-11	**66**	**305**	**0.0**	**361**

The example of the Spring Fresh data, whose apparent BTEX signals were the most intense, is seen in the overlay of mass spectra of the sample and background in Figure 7.17-Figure 7.19:

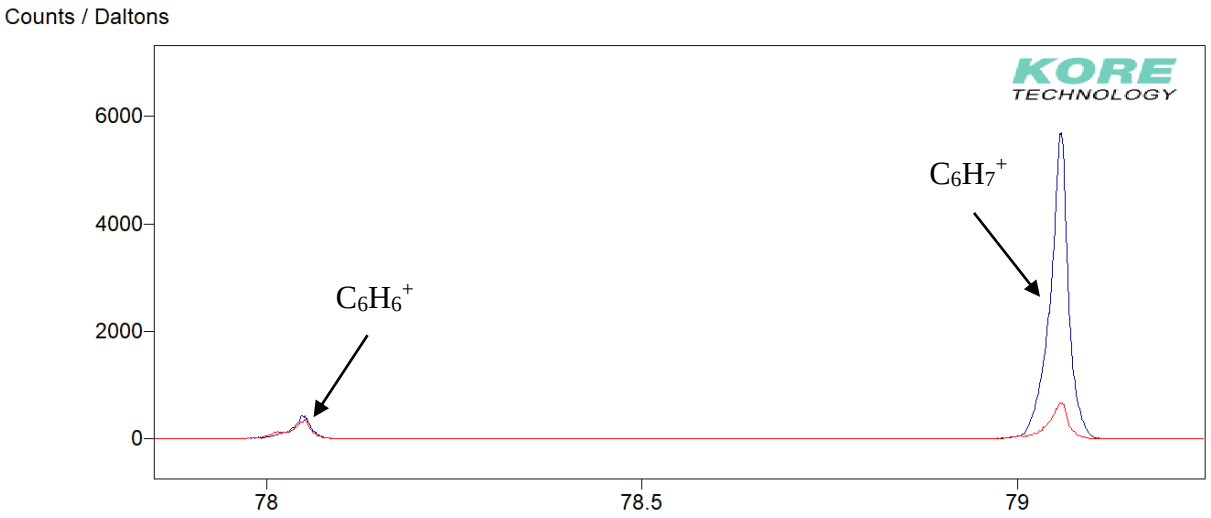

Figure 7.17: Spectra of Spring Fresh ironing water response (blue) overlaid on background (red) (m/z 78-79) using the tandem Mark II water sampler – PTR-ToF-MS

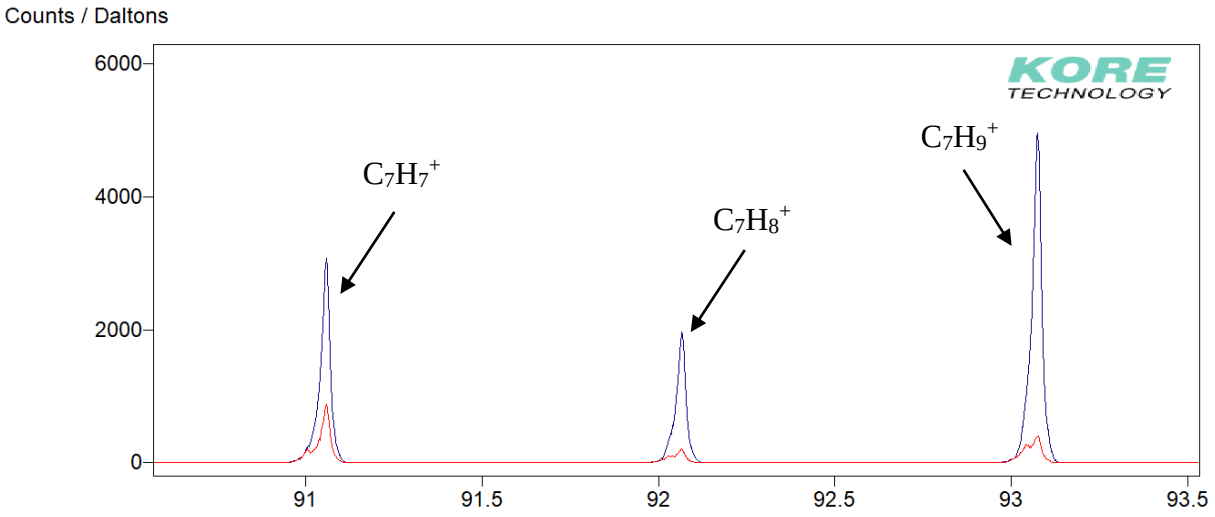

Figure 7.18: Spectra of Spring Fresh ironing water response (blue) overlaid on background (red) (m/z 91-93) using the tandem Mark II water sampler – PTR-ToF-MS

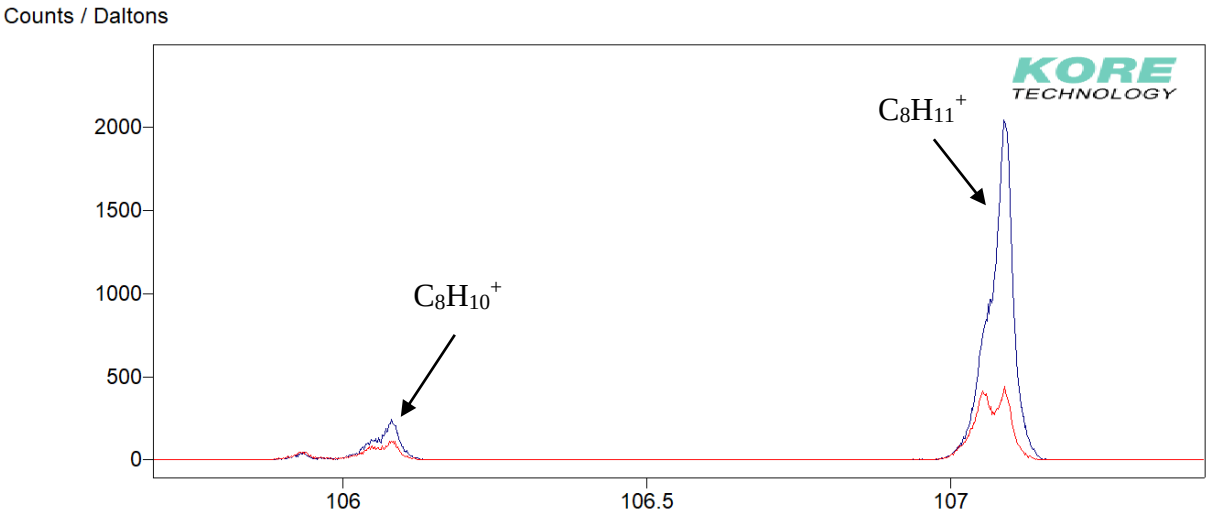

Figure 7.19: Spectra of Spring Fresh ironing water response (blue) overlaid on background (red) (m/z 106-107) using the tandem Mark II water sampler – PTR-ToF-MS

The implication from the data is that the commercial water products contained unusual high levels of BTEX. However, since this was highly unlikely, another explanation was sought. The clue came from the high m/z region of the PTR-ToF-MS mass spectrum from ironing water Spring Fresh presented in Figure 7.20:

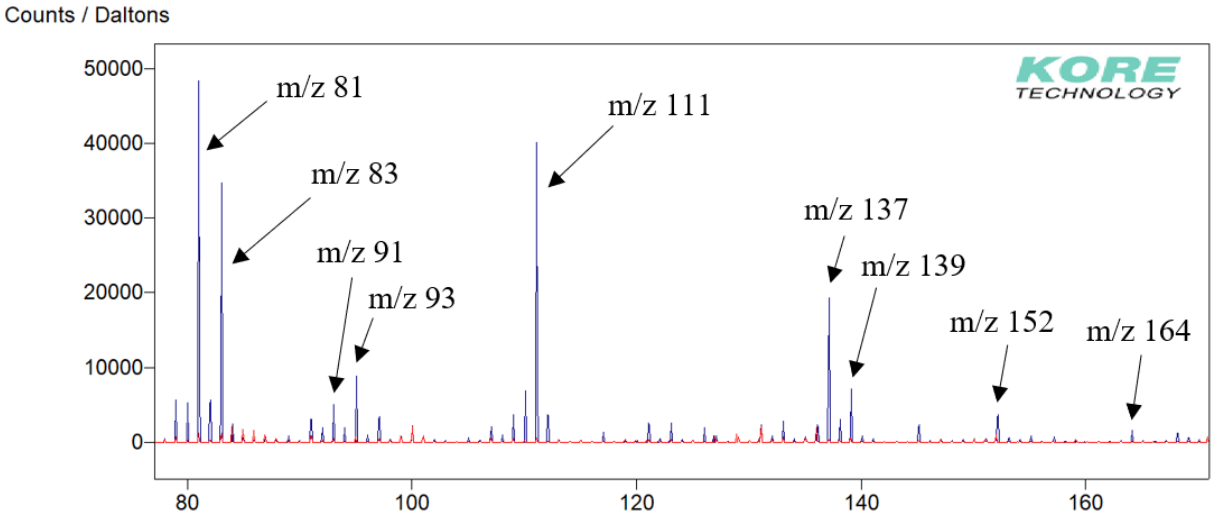

Figure 7.20: Spectra of Spring Fresh ironing water response (blue) above background (red) (m/z 78-171) using the tandem Mark II water sampler – PTR-ToF-MS

In Figure 7.20, numerous high mass peaks were observed above the background, indicating that some other compound(s) were present in this product. It is well known in mass spectrometry that high mass molecules can produce lower mass fragments. It is less well-known, but not secret, that many of these domestic products marketed with terms such as Spring Fresh contain monoterpenes (and particularly limonene) to provide a pleasant scent [136].

To determine if such compounds were present in these commercial products, samples of two common additives, S-limonene (orange scent) and α-pinene (pine scent), were run under the same instrumental conditions used for the water analysis. Both monoterpenes have molecular ions of m/z ratio of 136 and were protonated to provide the main parent molecule at m/z 137 (exact molar mass of 137.13302 g/mol). The reactor conditions, especially through the activation of the RF field, were such that many product ions were generated, like the most intense ion produced at m/z 81 [136, 137], whose mass spectral data in the high mass region results of S-limonene and α-pinene are respectively presented in Figure 7.21 and Figure 7.22:

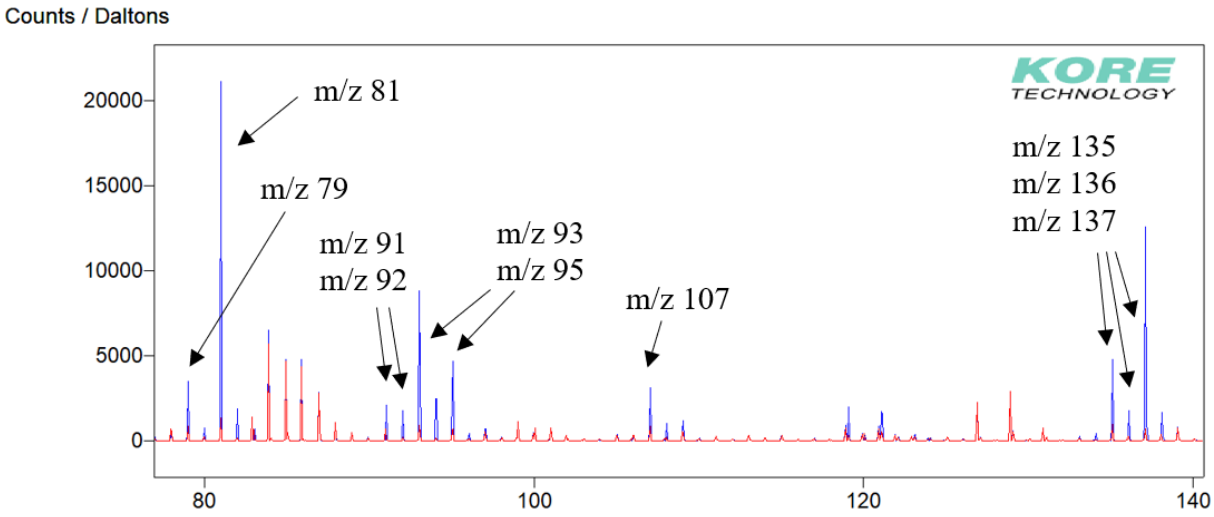

Figure 7.21: Spectra of S-limonene response (blue) above background (red) (m/z 78-140) using the tandem Mark II water sampler – PTR-ToF-MS

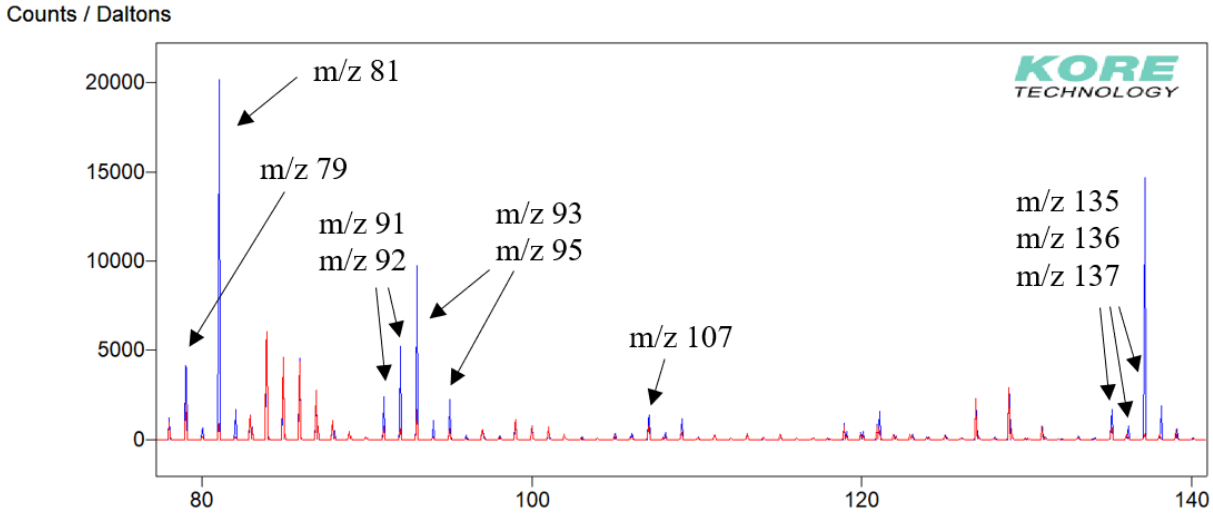

Figure 7.22: Spectra of α-pinene response (blue) above background (red) (m/z 78-140) using the tandem Mark II water sampler – PTR-ToF-MS

The spectra indicate that these monoterpenes produce fragment ions, which were being mistaken for mass peaks from BTEX. In order to account for these compounds, it was necessary to determine their product ion distributions and then add these compounds and their PIDs into the analysis library. From an intensity at m/z 137, a PID indicated to the software what proportion of the signal at m/z 79, 91, 92, 93, 106 or 107 is due to the monoterpene, and thus can effectively be stripped out to give the residual that is potentially due to BTEX compounds.

Three more versions of the software library were then created and the data were re-analysed with these libraries for the following four cases:

- Case 1: benzene, toluene, ethylbenzene, xylenes considered (used so far)
- Case 2: benzene, toluene, ethylbenzene, xylenes, S-limonene considered
- Case 3: benzene, toluene, ethylbenzene, xylenes, α-pinene considered
- Case 4: benzene, toluene, ethylbenzene, xylenes, S-limonene, α-pinene considered

The results are presented for the de-ionised water from Tesco in Table 7.13 (where 'Y' and 'N' stand for Yes and No about the presence of each compound) and Figure 7.23 and Figure 7.24:

Table 7.13: BTEX concentrations in de-ionised water from Tesco as a function of the library used (cases 1 to 4 including different chemicals) in the deconvolution software AnalyseHR

Compounds present in library (Y/N) → / Sample analysed ↓	Case	BTEX	S-LIMONENE	α-PINENE	Concentration of the library compounds generated by the AnalyseHR Software						Sum	
					Benzene	Toluene	Ethyl-benzene	Xylenes	S-Limonene	α-Pinene	BTEX	Total
	Detection limit (ppbv)				0.014 ± 0.001	0.007 ± 0.001	0.013 ± 0.001	0.006 ± 0.001	0.709 ± 0.059	0.951 ± 0.079	0.040 ± 0.004	1.700 ± 0.142
Reported concentrations of de-ionised water – Tesco (ppbv)	1	Y	N	N	0.130 ± 0.008	1.173 ± 0.006	0.781 ± 0.013	0.176 ± 0.006	0.000 N/A	0.000 N/A	2.260 ± 0.033	2.260 ± 0.033
	2	Y	Y	N	-0.212 N/A	0.052 ± 0.003	-0.086 N/A	0.184 ± 0.005	1048 ± 1.048	0.000 N/A	-0.062 ± 0.008	1048 ± 1.056
	3	Y	N	Y	-0.175 N/A	-0.148 N/A	1.922 ± 0.016	-0.107 N/A	0.000 N/A	1105 ± 1.380	1.492 ± 0.016	1106 ± 1.396
	4	Y	Y	Y	-0.246 N/A	-0.210 N/A	0.745 ± 0.017	0.038 ± 0.008	695.0 ± 1.984	709.8 ± 1.494	0.327 ± 0.025	1405 ± 3.503

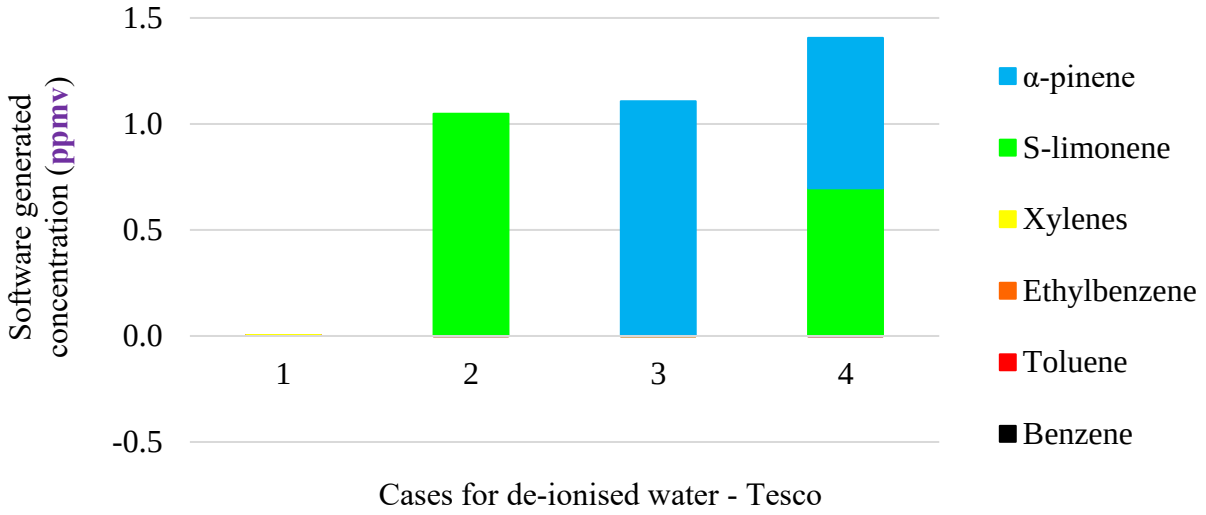

Figure 7.23: BTEX and monoterpenes concentrations generated by AnalyseHR in de-ionised water from Tesco as a function of the deconvolution library considered using the tandem Mark II water sampler – PTR-ToF-MS

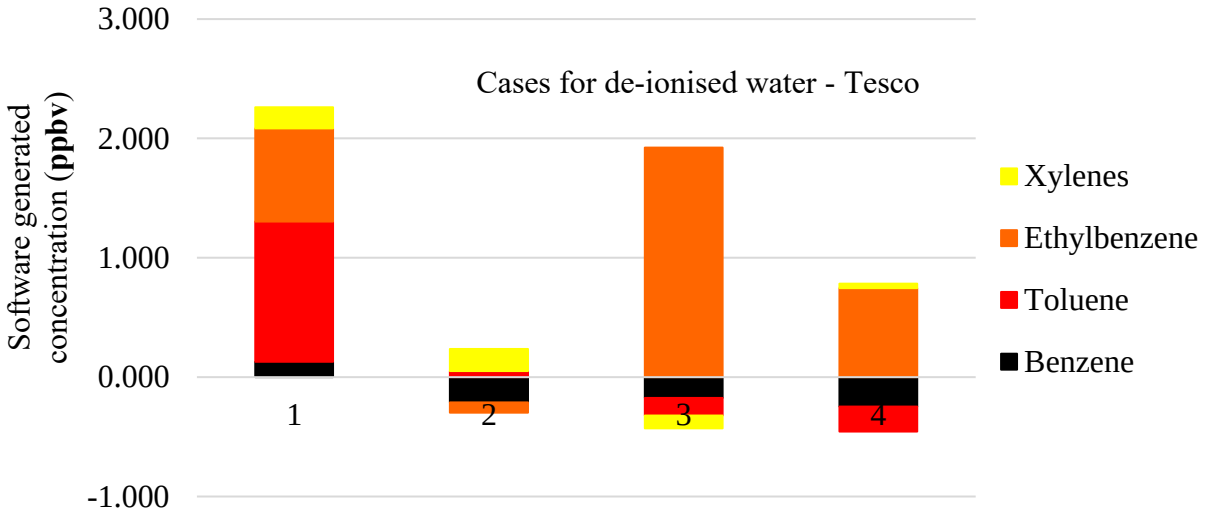

Figure 7.24: BTEX concentrations generated by AnalyseHR in de-ionised water from Tesco as a function of the deconvolution library considered using the tandem Mark II water sampler – PTR-ToF-MS

Figure 7.23 shows the calculated concentrations of BTEX and both monoterpenes (positive and negative) using the four different libraries associated with the four cases described. S-Limonene and α-pinene concentrations were then removed in Figure 7.24 for clarity purpose. Once the PIDs from those monoterpenes were included in the analysis library,

a different picture emerges. For libraries 2, 3 and 4, the benzene, toluene and xylenes concentrations fell to values less than 250 pptv, with uncertainty in the ion counts giving either positive or negative values.

Figure 7.24 is the most illuminating one with presence of high concentrations of monoterpenes in the water (above 1 ppmv) to give it a pleasant scent when in use. This highlights one of the challenges in developing this type of deconvolution software: if a compound is not in the analysis library and has coincident mass peaks with ions being part of it, then the signal in those former compounds is assigned, **erroneously**, to those that are in the library.

The results from using an analysis library with both monoterpenes still indicated an ethylbenzene level of ~ 750 pptv. It is possible that other compounds were present in this water product and that their PIDs contained mass peaks common with ethylbenzene Indeed, considering the results using library 2. i.e. adding only S-limonene to the BTEX compounds, the total concentration of these last ones becomes slightly negative, which could result in a very high probability to have S-limonene in that water product. M/z 91 is a common fragment product ion from many high mass organics and is, under the current experimental conditions, the major ion in the PID of ethylbenzene (cf. Figure 7.13). That is why the main ongoing challenge about AnalyseHR is to extend the library with different sets of common pollutants to increase the probability to spot instantly real pollutant when present in samples.

7.4.3.6 Environmental BTEX monitoring – River waters

The final stage of BTEX monitoring using the Mark II water sampler – PTR-ToF-MS system was to collect water samples in the field. River water samples were gathered from the local environment in and around Ely, Cambridgeshire, as shown in Figure 7.25:

Figure 7.25:Collection spots of river waters
Background modified from Google Earth

The collection areas included boatyards and proximity to different industries and a wastewater treatment plant. The near river industry refers to an area along the bank of the river, including an asphalt plant, a mechanical products industry and a surfacing and flooring company. Table 7.14 presents the results of one sample, taken near to the water treatment plant, but whose values are representative of all the samples taken and run during the set of experiments.

Table 7.14: BTEX compounds quantified by AnalyseHR using the tandem Mark II water sampler – PTR-ToF-MS in river water

Background: Tap water Kore		Benzene	Toluene	Ethylbenzene	Xylenes	Total
Detection limit (pptv)		**14** ± 1.2	**7.3** ± 0.7	**13** ± 1.2	**5.7** ± 0.5	**40** ± 3.6
Reported concentration (pptv)	**Great Ouse river water – Ely area**	**-27** N/A	**17** ± 3.2	**16** ± 11	**-20** N/A	**-14** ± 14

Results from Table 7.14 come from mass spectral data whose river water sample and the background are both shown at the different masses of interest in Figure 7.26-Figure 7.28:

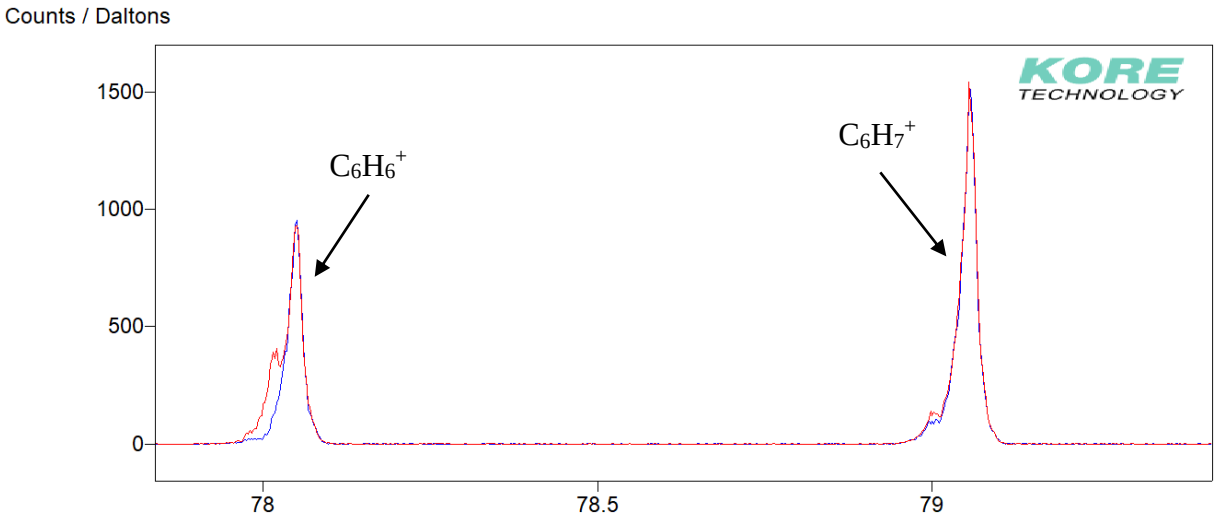

Figure 7.26: Spectra of river water (blue) overlaid on background (red) (m/z 78-79) using the tandem Mark II water sampler – PTR-ToF-MS

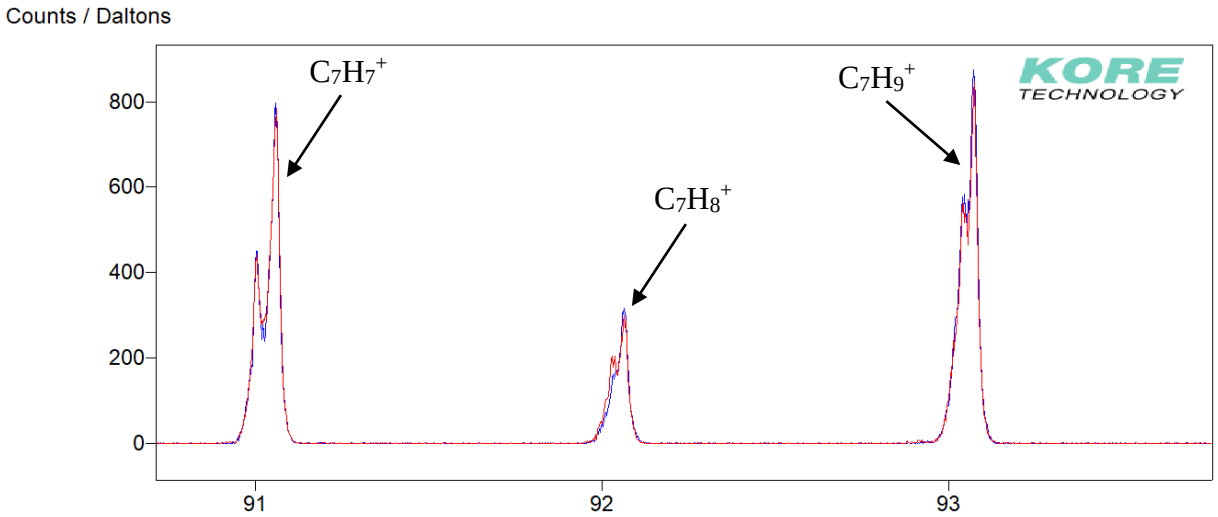

Figure 7.27: Spectra of river water (blue) overlaid on background (red) (m/z 91-93) using the tandem Mark II water sampler – PTR-ToF-MS

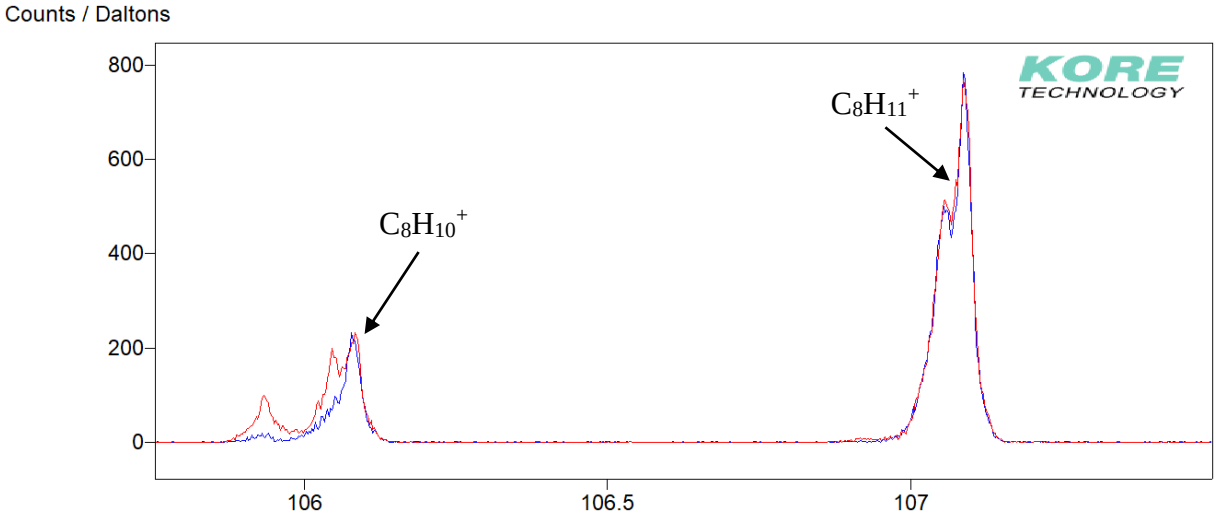

Figure 7.28: Spectra of river water (blue) overlaid on background (red) (m/z 106-107) using the tandem Mark II water sampler – PTR-ToF-MS

Figure 7.26-Figure 7.28 and Table 7.14 all show that, for all river water, the BTEX signals were not detected above the background levels and that BTEX compounds were consequently absent from the samples. Indeed, even if toluene and ethylbenzene were above their respective detection limit, the total BTEX concentration was under the detection limit, and even negative. Toluene and ethylbenzene were reported as present, whereas benzene and the xylenes concentrations were 'negative'. Again, the limit of the algorithm is observed; the sum is below the detection limit, however.

After BTEX monitoring, the river waters in and around Ely appeared as clean as Kore tap water in terms of those 4 pollutant's concentrations. However, on closer examination of the data, some mass peaks present in tap water samples were not observed in river water samples. After consideration of the exact masses of the extra peaks, an assignment of dibromochloromethane was made. The mass spectra indicated the presence of its protonated parent molecular ion after loss of H_2 i.e. $CClBr_2^+$ $(MH\text{-}H_2)^+$ at m/z 205 (exact molar mass of 204.8055 g/mol) as well as fragments like $CHBr_2^+$ at m/z 171, Br_2^+ at m/z 158 and $CHBrCl^+$ at m/z 127. Notice those fragments presented many detectable isotopes involving ^{37}Cl and ^{81}Br.

This chemical is a common addition to drinking water that is chlorinated to kill bacteria and viruses that could cause serious waterborne infectious diseases [138].

At a lower intensity, there were also signals due to nitrogen trichloride. The charge-exchanged molecule i.e. NCl_3^+ (M^+) at m/z 119 (exact molar mass of 118.9096 g/mol) and its isotope at m/z 121 were identified and its presence in drinking water can be explained through different chemical reactions. The mixed mode of ionisation that has been used was useful in making these identifications.

Chlorine is the most common water treatment product. However, when chlorine dissolves in water, it creates the weak acid, HClO which, reacting with ammonia (NH_3^+, detected at m/z 17), forms NH_2Cl whose NCl^+, fragment after the loss of H_2, has been measured at m/z 49. NH_2Cl reacts then with water, HClO and itself to form nitrogen trichloride (NCl_3^+, detected at m/z 119) and $NHCl_2$ ($NHCl_2^+$, detected at m/z 85 and NCl_2^+ at m/z 84) [139]. As for dibromochloromethane, ion fragments involving ^{37}Cl were also detected.

The most intense above-named ions are shown in Figure 7.29 and this spectrum shows that these chlorinated compounds were absent in river water (red trace).

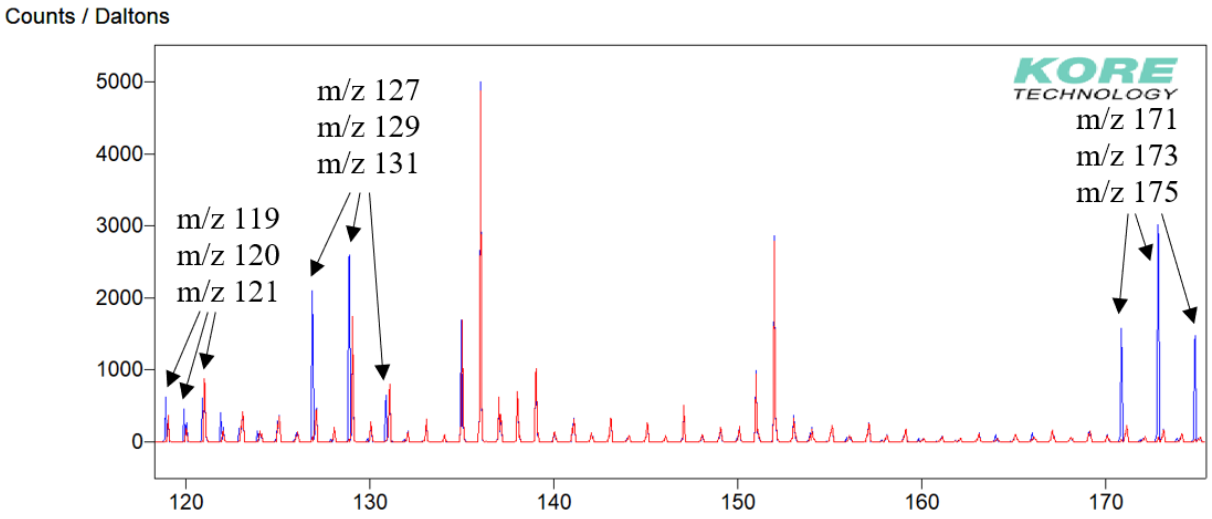

Figure 7.29: Spectra of tap water from Kore (blue) above river water (red) (m/z 119-175) using the tandem Mark II water sampler – PTR-ToF-MS highlighting the presence of halogenated compounds

Using the data from the Kore tap water as the instrumental background combined both the ‘true’ instrumental background (residual signal permanently present within a given instrument) and anything in the Kore tap water (like dibromochloromethane or nitrogen trichloride). Therefore, if, in a different study, the two above-named chlorinated compounds were the object of the study, either river or **commercial** drinking water could be used as background to highlight their signals at mass ranges such as 119-123, 127-131 or 171-175. This means, in this hypothesis, either river or **commercial** drinking waters could provide a useful indication of the instrumental background, i.e. as ‘zero signal’ and the chlorinated compounds, present in tap water, would appear this time, ‘clearly’ above the background.

Notice the contribution of heavier protonated hydrocarbons (like those of S-limonene and α-pinene) to the benzene peak at m/z 79 explain why the ratio $C_6H_6^+/C_6H_7^+$ is not necessarily about ¼ (respectively to the O_2^+/H_3O^+ ratio).

7.4.3.7 Presentation of the complete data set analysed by PTR-ToF-MS and discussion

The mass spectral results of all the water samples are presented in Table 7.15 including all the significant detected ions for (a) BTEX, (b) the chlorinated compounds found in tap water and (c) monoterpenes used as fragrance additives in non-drinking waters. Also listed are ions that were detected at levels above that of the instrumental background which are not yet assigned to a specific compound.

The instrumental background, being always present, is included in the signal of Kore tap water (declared as 'zero' signal) which was used as background and subtracted from any sample signal. As explained earlier, the chlorinated compounds were present in this tap water but not part of the instrumental background. As they do not coincide with the compounds being analysed, they were effectively ignored.

Table 7.15: Signal intensity of BTEX and other considered peaks in the water samples studied using the tandem Mark II water sampler – PTR-ToF-MS

Colour	Signal intensity per acquisition (c/10 s)
W (white)	Intensity < 1000
Y (yellow)	1000 ≤ Intensity < 5000
O (orange)	5000 ≤ Intensity < 20000
R (red)	20000 ≤ Intensity < 50000
G (green)	50000 ≤ Intensity < 100000
B (blue)	100000 ≤ Intensity < 200000
P (purple)	200000 ≤ Intensity < 300000
K (black)	300000 ≤ Intensity

BTEX and Cl-compounds:

Sample	Origin	77 (C_6H_5)	78 (C_6H_6)	79 (C_6H_7)	91 (C_7H_7)	92 (C_7H_8)	93 (C_7H_9)	105 (C_8H_9)	106 (C_8H_{10})	107 (C_8H_{11})	49 (NCl)	84 (NCl_2)	85 (NCl_2H)	119 (NCl_3)	127 ($CHBrCl$)	171 ($CHBr_2$)	205 (CBr_2Cl)
Instrumental background	Instrument	Y	O	R	R	O	R	Y	O	R	Y	R	R	Y	B	R	W
Tap water (background)	Kore	W	W	W	W	W	W	W	W	W	W	W	W	W	W	W	W
River water	Great Ouse	W	W	W	W	W	Y	W	W	W	W	W	W	W	W	W	W
Drinking water	Tesco	W	W	W	W	W	W	W	W	W	W	W	W	W	W	W	W
De-ionised water	Kore	Y	B	P	W	W	W	W	W	W	W	W	W	W	W	W	W
De-ionised water	Tesco	Y	W	R	O	O	G	O	O	R	W	W	O	W	G	W	W
Steam Iron Water	Tesco	Y	W	G	G	R	G	O	Y	R	W	W	W	W	R	W	W
Ironing water spring petals	Tesco	Y	W	R	P	R	R	G	O	R	W	W	W	W	R	W	W
Ironing water spring fresh	Tesco	O	Y	B	G	G	B	O	O	G	W	W	W	W	R	W	W

Monoterpenes:

Sample	Origin	133 ($C_{10}H_{13}$)	135 ($C_{10}H_{15}$)	136 ($C_{10}H_{16}$)	137 ($C_{10}H_{17}$)	139 ($C_{10}H_{19}$)	153 ($C_{10}H_{15}H_2O$)	154 ($C_{10}H_{16}H_2O$)	155 ($C_{10}H_{17}H_2O$)
Instrumental background	Instrument	O	O	Y	O	Y	O	Y	O
Tap water (background)	Kore	W	W	W	W	W	W	W	W
River water	Great Ouse	W	W	W	Y	W	W	W	W
Drinking water	Tesco	W	W	W	Y	W	W	W	W
De-ionised water	Kore	W	W	W	W	W	W	W	W
De-ionised water	Tesco	O	G	G	K	O	B	G	R
Steam Iron Water	Tesco	G	R	O	B	P	O	O	R
Ironing water spring petals	Tesco	R	O	O	B	B	O	O	O
Ironing water spring fresh	Tesco	G	R	G	K	P	R	O	R

Masses above background levels that are as yet unassigned to a compound:

Sample	Origin	39 (C_3H_3)	41 (C_3H_5)	53 (C_4H_5)	55 (C_4H_7)	57 (C_4H_9)	61 ($C_2H_5O_2$)	67 (C_5H_7)	69 (C_5H_9)	80 (C_6H_8)	81 (C_6H_9)	83 ($CHCl_2$)	95 (C_7H_{11})	97 (C_7H_{13})	105 (C_8H_9)	109 (C_8H_{13})	110 (C_8H_{14})	111 (C_8H_{15})
Instrumental background	Instrument	R	O	Y	R	O	G	R	G	O	R	O	R	O	O	O	O	O
Tap water (background)	Kore	W	W	W	W	W	W	W	W	W	W	W	W	W	W	W	W	W
River water	Great Ouse	Y	W	W	O	W	Y	W	Y	W	Y	W	W	W	W	W	W	W
Drinking water	Tesco	W	W	W	W	W	W	W	W	W	Y	W	W	W	W	W	W	W
De-ionised water	Kore	W	W	Y	W	W	W	W	W	O	W	W	O	W	W	W	W	W
De-ionised water	Tesco	R	R	O	O	R	Y	R	G	O	P	G	B	O	R	R	O	R
Steam Iron Water	Tesco	B	B	R	P	B	K	B	K	B	K	R	G	G	O	R	G	K
Ironing water spring petals	Tesco	B	G	O	B	B	K	B	P	R	P	W	G	G	G	R	R	B
Ironing water spring fresh	Tesco	P	B	R	P	B	G	P	K	B	K	W	P	G	R	B	P	K

Sample	Origin	121 (C_9H_{13})	123 (C_9H_{15})	126	145	152	158	159	164	168	171	174	183	193	200	207	228
Instrumental background	Instrument	O	O	O	O	Y	Y	O	O	Y	O	Y	O	O	Y	G	Y
Tap water (background)	Kore	W	W	W	W	W	W	W	W	W	W	W	W	W	W	W	W
River water	Great Ouse	W	W	W	W	W	W	W	W	W	W	W	W	W	W	Y	W
Drinking water	Tesco	W	W	W	W	W	W	W	W	W	W	W	W	W	W	W	W
De-ionised water	Kore	W	W	W	W	W	W	W	W	W	W	W	W	W	W	W	W
De-ionised water	Tesco	R	O	Y	O	B	W	Y	O	W	Y	W	W	W	W	W	Y
Steam Iron Water	Tesco	O	G	R	G	O	G	B	O	G	R	R	R	R	Y	R	O
Ironing water spring petals	Tesco	R	B	O	B	O	R	B	Y	R	Y	G	O	O	Y	G	W
Ironing water spring fresh	Tesco	G	G	G	B	B	Y	W	G	G	G	W	O	R	O	O	O

- River water and, unsurprisingly, commercial drinking waters presented levels of BTEX peaks below the detection limits of the method.
- Dibromochloromethane and nitrogen trichloride were absent in river and commercial drinking waters. However, tap water contained these compounds.
- De-ionised and ironing waters appeared to have similar fragrance additives.
- Without incorporating PIDs for monoterpenes like S-limonene and α-pinene, the analysis of the AnalyseHR program incorrectly assigned some of the fragment ion masses to BTEX compounds. In the case of the addition of S-limonene only, no positive total BTEX concentration was assigned anymore.
- There was a clear difference between both de-ionised waters. The spectrum from the Tesco product resembled those of the steam ironing waters, whereas the Kore de-ionised water one resembled that from tap water plus a significant benzene contamination.
- The unidentified masses above the background level could help in the identification of compounds present in those samples, for example as fragments from heavier molecules.

7.4.4 Mark II water sampler connected to the MS-200

One of the goals of developing a compact water sampler for use with a mass spectrometer is the possibility of coupling it to a portable analyser. This makes possible real-time measurements in the field without the need to send samples back to a laboratory. This type of 'in-situ' analysis is very attractive because of the immediacy of the result, and it avoids any contamination or VOC losses due to sample storage and transportation.

Thus, once it was evident that the Mark II water sampler was producing reliable and reproducible results with the PTR-ToF-MS, it was decided to return to the MS-200 portable mass spectrometer.

7.4.4.1 BTEX library creation

In the following data, in order to generate the BTEX library for this instrument with its own deconvolution tool, water samples with individual BTEX compounds were prepared, sampled by the water analyser, and passed to the inlet of the MS-200 permeating through both its inlet membranes. The responses in terms of sensitivity and limit of detection for the charge-exchanged VOC and reproducibility for the m/z of interest for 500 ± 41 ppbv samples are shown in Figure 7.30-Figure 7.33 and Table 7.16-Table 7.19.

- Benzene

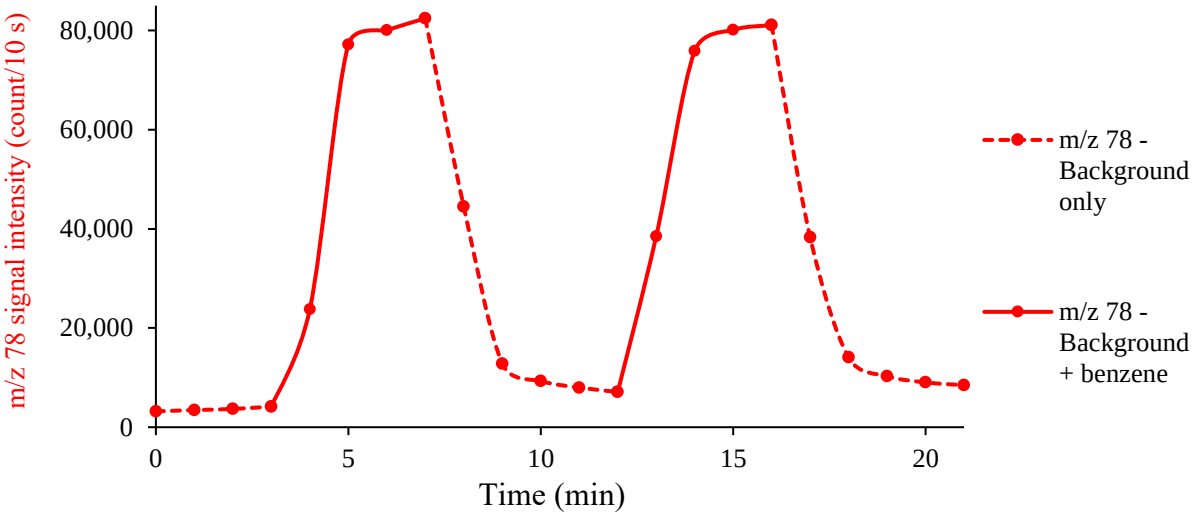

Figure 7.30: 500 ppbv benzene in water measurement using the tandem Mark II water sampler – MS-200

Table 7.16: Performances of the tandem Mark II water sampler – MS-200 for benzene

Parent benzene ion produced by electron ionisation: $C_6H_6^+$		
Sensitivity (c/s/ppbv)	**Limit of detection (ppbv)**	
16 ± 1.3	1,24 ± 0.10	
m/z 78 response	**1**	**2**
Signal count rate above background (c/s)	7825	7395
Mass spectrometer pressure (x 10^{-8} mbar)	16 ± 0.2	17 ± 0.2

The benzene response (m/z 78, M^+ parent molecule) can be compared with that of Mark I (7.3 ± 0.4 c/s/ppbv). The sensitivity was enhanced by a factor greater than 2, whereas for the same amount of time considered, the detection limit and the mass spectrometer pressure are lower. Indeed, the Mark II water analyser was a more controllable device across all control parameters.

- Toluene

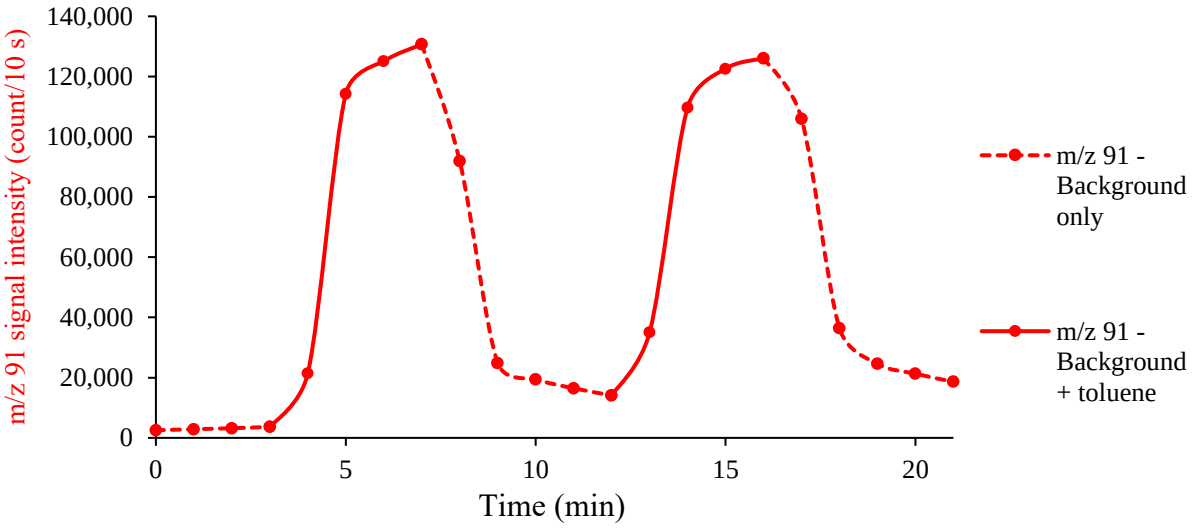

Figure 7.31: 500 ppbv toluene in water measurement using the tandem Mark II water sampler – MS-200

Table 7.17: Performances of the tandem Mark II water sampler – MS-200 for toluene

Parent toluene ion produced by electron ionisation: $C_7H_7^+$		
Sensitivity (c/s/ppbv)	**Limit of detection (ppbv)**	
25 ± 2.1	0.71 ± 0.06	
m/z 91 response	**1**	**2**
Signal count rate above background (c/s)	12705	11190
Mass spectrometer pressure (x 10^{-8} mbar)	22 ± 0.2	25 ± 0.3

The toluene response was measured using m/z 91 ($(M-H)^+$ parent molecule after loss of H). The MS-200 presented a greater sensitivity and a lower detection limit for toluene than for benzene.

- Ethylbenzene

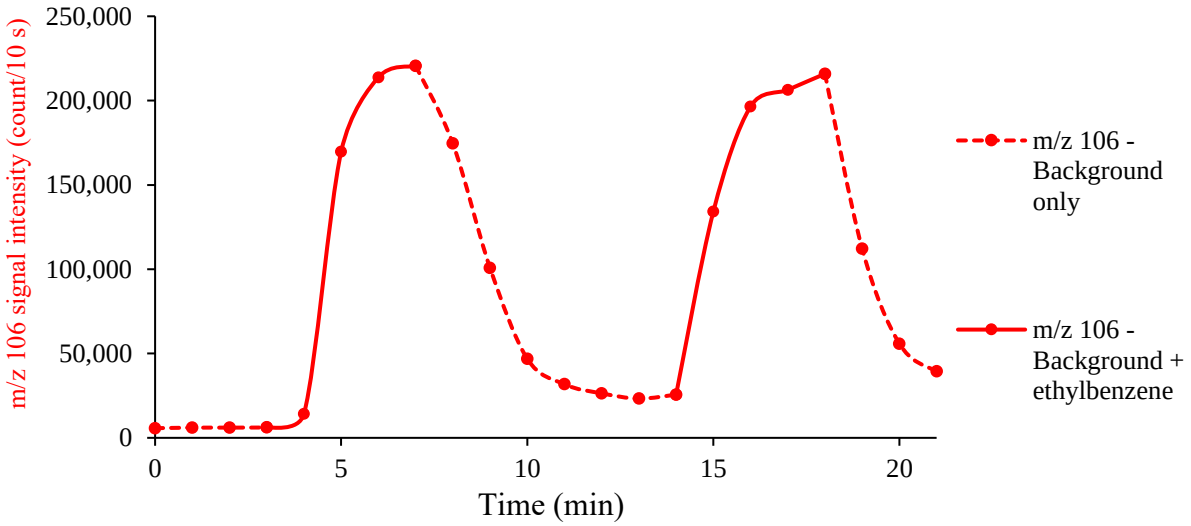

Figure 7.32: 500 ppbv ethylbenzene in water measurement using the tandem Mark II water sampler – MS-200

Table 7.18: Performances of the tandem Mark II water sampler – MS-200 for ethylbenzene

Parent ethylbenzene ion produced by electron ionisation: $C_8H_{10}^+$		
Sensitivity (c/s/ppbv)	**Limit of detection (ppbv)**	
43 ± 3.6	0.55 ± 0.05	
m/z 106 response	**1**	**2**
Signal count rate above background (c/s)	21441	19086
Mass spectrometer pressure (x 10^{-8} mbar)	30 ± 0.3	37 ± 0.4

The ethylbenzene response was measured using mass 106 (M^+ parent molecule). The MS-200 presented a greater sensitivity and a lower detection limit for ethylbenzene than for toluene.

- Xylene (m-)

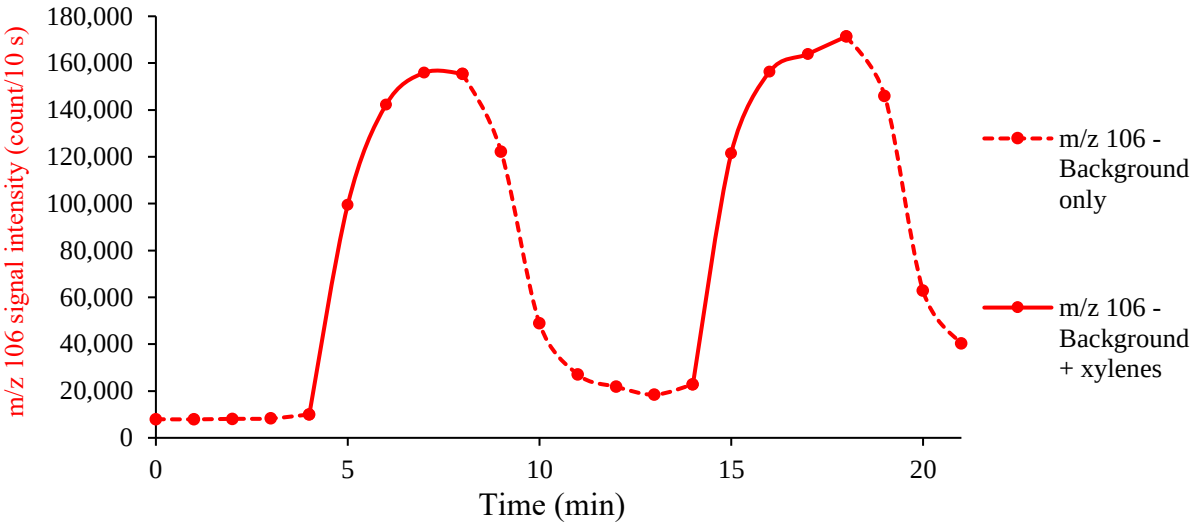

Figure 7.33: 500 ppbv m-xylene in water measurement using the tandem Mark II water sampler – MS-200

Table 7.19: Performances of the tandem Mark II water sampler – MS-200 for m-xylene

Parent m-xylene ions produced by electron ionisation: $C_8H_{10}^+$		
Sensitivity (c/s/ppbv)	**Limit of detection (ppbv)**	
30 ± 2.5	0.96 ± 0.08	
m/z 106 response	**1**	**2**
Signal count rate above background (c/s)	14595	14857
Mass spectrometer pressure (x 10^{-8} mbar)	37 ± 0.4	42 ± 0.4

The m-xylene response was measured using mass 106 (M^+ parent molecule). The MS-200 presented for xylenes the second greatest sensitivity and the second lowest detection limit.

This second water sampler presented greater performance while connected to the MS-200 enabling more realistic sensitivity and limit of detection through a greater signal. Regarding benzene, both sample and background phases were closer to a plateau than with the first prototype sampler and the MS-200 provided a lower detection limit whereas the other BTEX compounds presented greater ionisation yields and lower limits of detection than benzene.

7.4.4.2 BTEX library early tests – Compounds mixture

As with the PTR-ToF-MS, the MS-200 was challenged with mixtures of BTEX passed through the more reliable Mark II water sampler. The MS-200 software has its own version of compound deconvolution software via compound library entries. This is very similar in principle to the AnalyseHR program in which the product ion distributions for the compounds in the library are used, except that all mass peaks are reduced to stickplots (unit mass resolution due to the low mass resolution of the MS-200).

For this BTEX mixture, 200 ± 22 ppbv of each compound were prepared in tap water. As only m-xylene was used, the total VOC concentration was 800 ± 88 ppbv. Figure 7.34 shows the signal at the m/z of the charge-exchanged parent molecule for benzene i.e. at m/z 78, for ethylbenzene and m-xylene i.e. at m/z 106 but after loss of H for toluene i.e. at m/z 91.

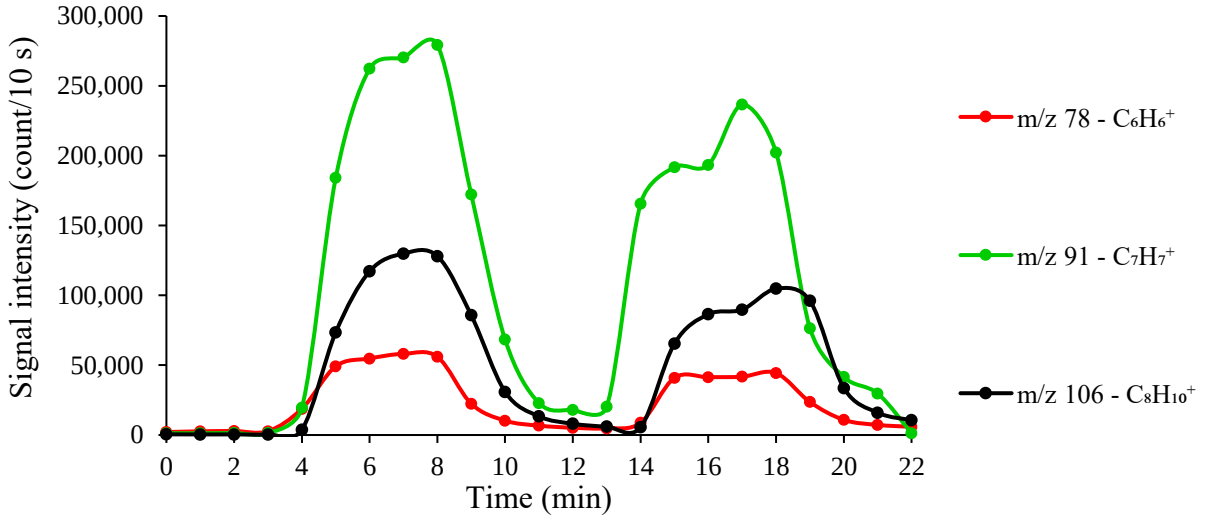

Figure 7.34: Mixture of 200 ppbv in water of each BTEX compound using the tandem Mark II water sampler – MS-200

The signals at m/z 91 were more intense because toluene, ethylbenzene and xylenes all produced ions at this mass. The next most intense is m/z 106, with contributions from

ethylbenzene and xylenes. M/z 78 signal from benzene had the lowest response at equal BTEX concentrations. In parallel the mass spectrometer pressure rose from 14 to 16 x 10^{-8} mbar.

The sequence of measurements involved tap water – BTEX in tap water – tap water – BTEX in tap water again – tap water. Unlike with the individual compounds, the second BTEX in water sample produced signal intensities that were reduced by 24 %. The reason for this is not known.

Signal intensities for the individual compounds at known concentrations were used to generate the relative sensitivity factors that were subsequently used in the mixture analysis software to generate the evolution of the concentration of the BTEX compounds as shown in Figure 7.35 and Figure 7.36 respectively presenting the evolutions of the total BTEX concentration and of the individual BTEX concentrations.

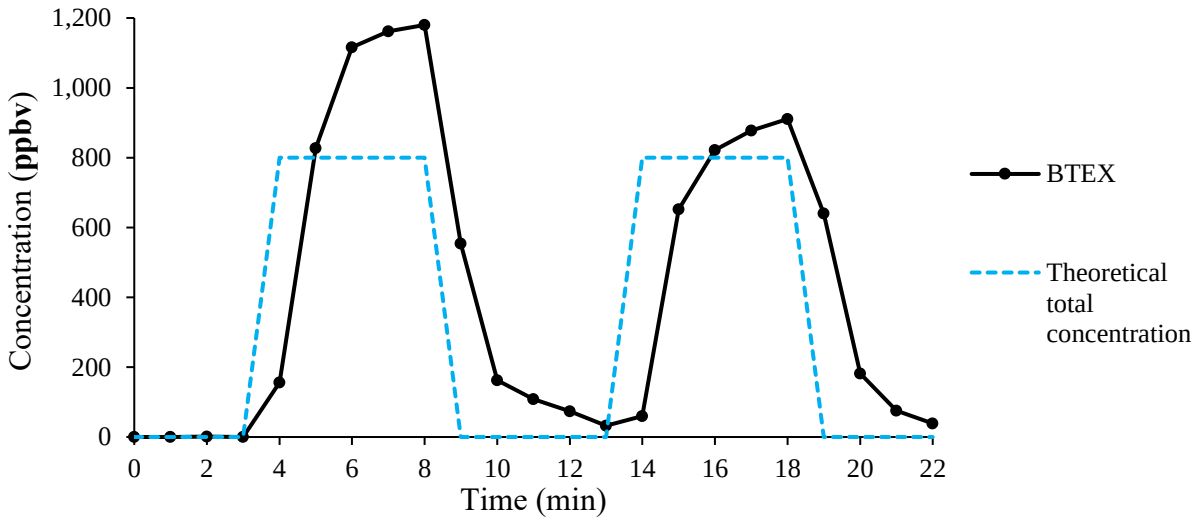

Figure 7.35: BTEX response in total concentration (mixture of 200 ppbv in water of each BTEX compound; 800 ppbv cumulated) generated by the deconvolution tool as a function of the time (10 s acquisition) using the tandem Mark II water sampler – MS-200

The calculated concentrations were 200 ± 22 ppbv for each compound and consequently 800 ± 88 ppbv whereas the relative standard deviations of the software generated concentrations

were within 3 %. Considering standard deviations, windows of both total concentrations (theoretical and software generated) overlay for three points out of four in the second response.

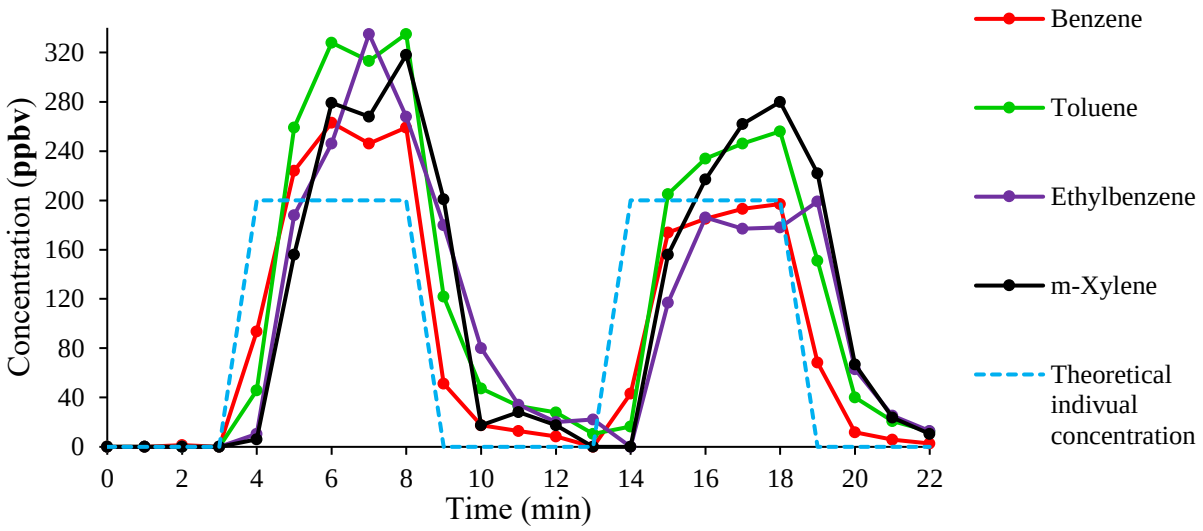

Figure 7.36: BTEX response in individual concentrations (mixture of 200 ppbv in water of each BTEX compound) generated by the deconvolution tool as a function of the time (10 s acquisition) using the tandem Mark II water sampler – MS-200

Figure 7.36 shows that, although the concentrations from the analysis software were higher than expected for most of the points, the distribution of the individual compounds indicated that the mixture analysis was successful in deconvolution of the mixture.

Figure 7.36 also shows the permeation rates of benzene and toluene through PDMS membranes were greater than those of ethylbenzene and m-xylene. Each time a BTEX-in-water sample was introduced, the ethylbenzene and m-xylene signals lagged behind the benzene and toluene signals [140, 141].

7.5 Conclusion

The purpose of the mixture analysis, for both AnalyseHR and the MS-200 deconvolution tool, is to use the PIDs and the sensitivity factors from the individual compounds to determine the

combination of BTEX signals that best fits the mass spectral data from the mixture and in this sense, these early results were considered as promising and further developments of the Mark II water sampler are ongoing. On the other side the coupling of the inexpensive Mark II water sampler coupled to the MS-200 offers total portability of the system with sensitivity and limit of detection of the instrument, analysing BTEX compounds, of respectively count/s/ppbv levels and pptv levels. When total portability and instant quantification are not required and the Mark II water sampler is connected to the research PTR-ToF-MS either in lab or in a van, the respective sensitivities present values in the c/s/ppbv-pptv levels and respective limit of detections at even lower ppbv levels. The extra signals were also the result of the use of the RF field, enhancing the ion transmission and the richness of the spectra due to the mixed mode of ionisation. However, as long as, the experimental conditions are kept strictly constant, providing a constant reagent ion ratio, the data are reliably treated by the deconvolution software and the analytical systems.

CHAPTER 8: TOTAL OH REACTIVITY MEASUREMENT BY MEANS OF A TRANSPORTABLE ELECTRON IMPACT IONISATION-TIME OF FLIGHT-MASS SPECTROMETER

8.1 Introduction

For more than fifty years the field of atmospheric chemistry has studied the speciation, concentrations and environmental impacts of diverse volatile organic compounds (VOCs) in the troposphere [142]. These volatiles are emitted into the lower atmosphere from both natural and anthropogenic sources. OH radicals play a key role in the troposphere, oxidising many of the VOCs, thereby producing secondary pollutants like ozone and secondary organic aerosol [142]. Exceptions are highly unreactive molecules such as halocarbons [143]. Given that OH radicals are the principal sinks of VOCs in the troposphere, many studies have focused on investigating the reactions of volatiles with hydroxyl radical (OH) and determining total atmospheric OH reactivity [142-146].

There are two general processes to measure the total OH reactivity, the Laser-Induced Fluorescence (LIF) and the Comparative Reactivity Method (CRM). In both cases, the OH radicals are created by photolysis of another molecule, typically O_3, H_2O or H_2O_2 [142-144]. The LIF method directly measures the decay rate of the OH radicals. Once the OH radicals are created, they are collected into the LIF cell where, subject to a specific laser wavelength, the fluorescence signal is then detected by a photomultiplier tube and counted by a photon counting method [143, 144]. The CRM method, which has been adopted by many groups, [142, 146-149], employs PTR-MS. Unlike the LIF method which presents a greater time resolution, a lower uncertainty and a direct measurement of OH decay [142], the CRM method involves relatively low cost [142] using a small sampling flow rate (range of hundreds sccm), which makes it possible to extend the experiments to smaller reaction chambers for field campaigns [149]. For the CRM method, a reactive compound normally absent in the air, pyrrole (C_4H_5N) is most commonly used and is injected into a glass reactor (called here the ‘OH reactor’). The OH radicals are introduced into the reactor at a constant rate to react with pyrrole, firstly in zero

air and then in ambient air containing other OH reactive species. PTR-MS measurements determine the concentration of pyrrole leaving the reactor under the following conditions: (i) zero air with no OH present in the reactor (concentration C1), (ii) with OH in the reactor (concentration C2, under conditions for which [OH] < [pyrrole]), and (iii) in air containing reactive VOCs with OH (concentration C_3). [143-145]. The reactivity, R_{air}, of the ambient air sample is determined using E 8.1 [142, 145]:

$$R_{air} = \frac{C3 - C2}{C1 - C3} k_p C1 \qquad \text{E 8.1}$$

where k_p is the reaction rate coefficient for pyrrole reacting with OH. Notice the concentrations entered into the equation must be expressed in molecules per unit volume and not in ppbv.

The analytical technique that has been used successfully in tandem with the CRM method is PTR-MS, however this then takes a low-cost apparatus (CRM) and increases the cost of the final measurement. The aim of the work presented in this chapter was to explore the use of the Kore field deployable mass spectrometric Electron Impact-Time of Flight-Mass Spectrometer (EI-ToF-MS), called INFORMS (cf. Figure 8.1), to determine if this relatively inexpensive analytical technique could be used to monitor the pyrrole concentration, using the CRM method, during field

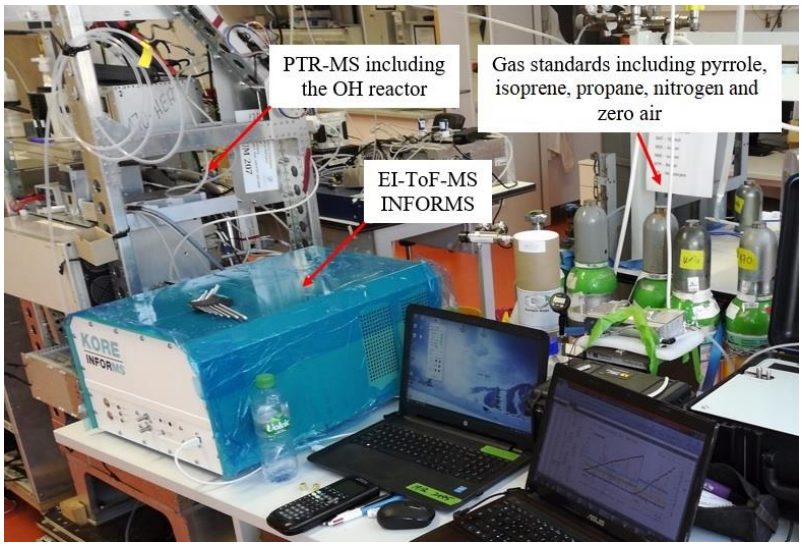

Figure 8.1: The OH reactivity apparatus at the ORSUM lab, Mainz. The CRM was monitored with either the PTR-MS (leftmost equipment) or the EI-ToF-MS (blue cover)

campaigns. The main challenge was to determine if this instrument was able to measure those pyrrole concentrations accurately enough through CRM to determine the total OH reactivity of given ambient air comparing its results with those of a PTR-MS. This project took place during an IMPACT secondment at the Max Planck Institute of Chemistry of Mainz, Germany, in collaboration with Nijing Wang within the 'ORSUM' group (Organic Reactive Species Understanding & Measurement) led by Professor Jonathan Williams.

8.2 Methods

8.2.1 Protocol and experimental conditions

The CRM method presented in the introduction and used during this project is described in details through the system displayed in Figure 8.2, adapted from [145], where the PTR-MS from the ORSUM group has been replaced by the Kore instrument.

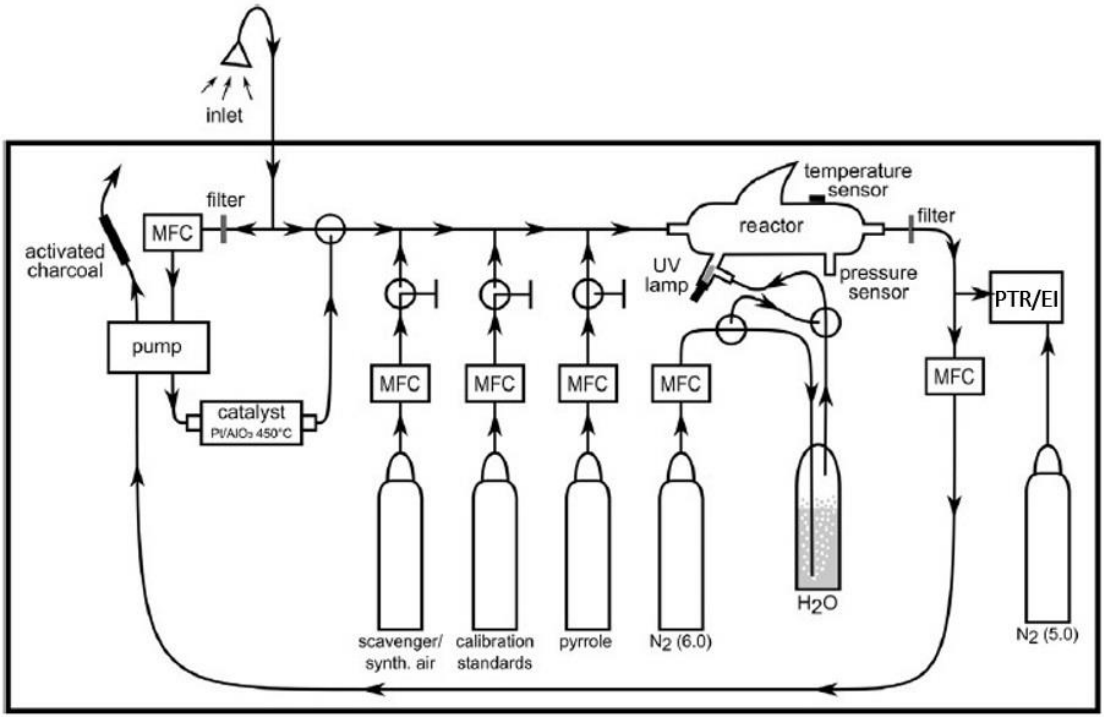

Figure 8.2: Scheme of the Comparative Reactivity Method in order to determine the total OH reactivity of ambient air replacing a PTR-MS by a transportable EI-ToF-MS (adapted from [145])
'MFC' and 'synth. air' respectively stand for mass flow controller and synthetic air (i.e. zero air).

Unlike the PTR-MS usually used, the EI-MS presents, due to its compact design, a lower mass resolution (maximum 1100 M/ΔM FWHM at m/z 40), a lower sensitivity and a higher detection limit. The subsequent results highlighted these limitations.

The sequence of the evolution of the pyrrole concentration is typically monitored as shown in Figure 8.3.

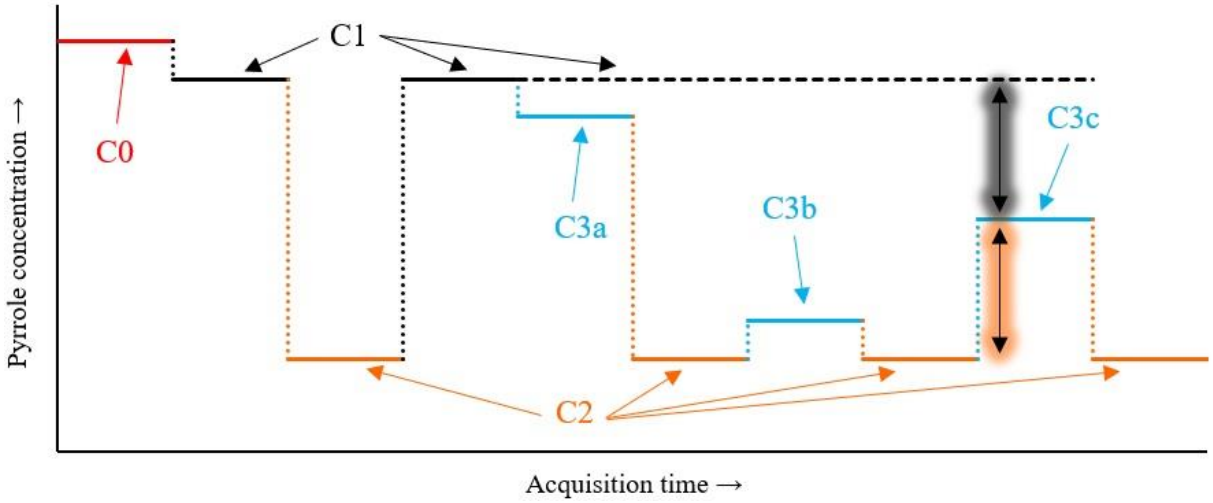

Figure 8.3: Pyrrole concentration evolution in the Comparative Reactivity Method in order to determine the total OH reactivity of an air sample. Pyrrole presents a concentration C0 in dry conditions in the absence of UV light, C1 after photolysis through UV rays, C2 after reaction with the OH radicals without competition and C3 competing with other VOC(s) to react with the OH radicals. This competition (represented by the bolded arrows) can lead to a preservation of most of pyrrole (C3a), a consumption of most of pyrrole (C3b) or an equilibrate competition (C3c). Notice C1 can be reached through two different methods.

The different steps (with reference to both Figure 8.2 and Figure 8.3) are as follow:

- Step 1: A constant flow of pyrrole in zero air was set and run into the reactor; another flow of dry nitrogen was also run into the reactor. The UV lamp is kept off as well as the flow of a given VOC (able to react with OH).

  → There is no OH radical in the reactor and the maximum concentration of pyrrole detectable under the given setting is measured, this is C0.

- Step 2: The UV lamp is turned on and two methods are available.

- Step 2-a: The 'dry nitrogen method' – The flow of nitrogen remains dry and there are still no OH radicals in the system.

  → The UV rays consume a proportion of pyrrole through photolysis, so that the starting concentration of the pyrrole for reaction is C1. Results from INFORMS have shown C1 represents on average a loss of pyrrole of 10-30 % from C0.

- Step 2-b: The 'scavenger method' – The flow of nitrogen is saturated with water molecules, creating OH radicals and a 'OH scavenger' VOC is then introduced into the reactor in excess.

  → The OH scavenger completely reacts with the OH radicals, preserving pyrrole, whose concentration returns to C1. This enables C1 to be reached in 'ready conditions', i.e. in the presence of OH radicals. This method presents the advantage to reach C1 more quickly between each environmental air sample measurement than the dry nitrogen one where the reduction of the humidity to dry conditions in the reactor is more time-consuming [149]. Notice this OH scavenger is only used to *preserve* pyrrole during the intermediate C1 measurements and is different from the VOC, which will *compete* with pyrrole to react with OH radicals later in the method.

- Step 3: Once C1 level is ensured, independently of the method used in Step 2, there are only OH radicals in presence of pyrrole running wet nitrogen.

  → The OH radicals created by the UV rays react with pyrrole. After all the OH radicals are consumed, pyrrole is still left at a concentration C2.

- Step 4: Ambient air or test gas is introduced into the reactor.

  → Due to other VOCs competing with pyrrole to react with OH radicals, the pyrrole concentration increases compared to C2 level (as shown in Figure 8.3). Pyrrole is still

present at a concentration C3 and as a function of the OH reactivity of the air sample, the competition between pyrrole and the test gas could lead to either preservation of most of the pyrrole, consumption of most of the pyrrole or an equilibrium between the consumption of pyrrole and the test gas, represented by C3a, C3b and C3c respectively in Figure 8.3. Notice that due to varying humidity of ambient air, PTR calibrations should be realised under different relative humidity rates for more accurate quantitative analysis [150].

Between each ambient air measurement (C3), C2 is reached again. For any atmospheric measurement, this is a competition between pyrrole and the ambient VOCs to react with the OH radicals as expressed through the glowing arrows in Figure 8.3 where the concentrations of ambient VOCs will influence the concentration of pyrrole left.

Once the concentrations are determined, i.e. C1, C2 and C3, the total OH reactivity of the ambient air, R_{air}, can be calculated as expressed previously in the equation E 8.1 [142, 145].

Concerning the total OH reactivity measurements at the MPIC, the flows of pyrrole, zero air and ambient air were set to 4, 200 and 200 sccm, respectively. The OH scavenger VOC (i.e. C1 using the scavenger method) was, in this project, propane (m/z 44) and was, when applicable, injected sufficiently in excess into the OH reactor to preserve the concentration C1 of pyrrole. In all measurements, the atmospheric pressure and a temperature of 30 ^{o}C were kept constant within the reactor of both the PTR-MS used at the MPIC and INFORMS.

8.2.2 Probe molecule – Pyrrole – Calibration measurements

Pyrrole (C_4H_5N), whose molecular structure is presented in Figure 8.4, has, under electron ionisation impact, its main product ion at m/z 67 [151]. However, that ion $C_4H_5N^+$ (m/z 67.042)

can be predicted to have interference with isoprene (C_5H_8) whose main product ion after electron ionisation impact appears at m/z 67.055. The separation of both ions, using INFORMS, was expected to be challenging due to its limited mass resolution, since tens of ppbv of isoprene are usually injected as test gas at the ORSUM lab. However, measurements involving isoprene were conducted as this VOC is naturally present in the atmosphere but at tens of pptv levels [143], which could lead to less intense interferences than the present results show.

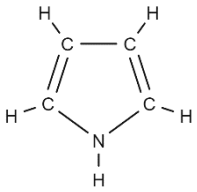

Figure 8.4: Molecular structure of pyrrole

8.2.2.1 Detection limit of INFORMS for pyrrole

In order to relate detected signals from pyrrole in the mass spectrometer to concentration, and due to the unavailability of a commercial standard, it was necessary to prepare a pyrrole standard. This was done preparing a solution of 1.28 ± 0.025 ppmv of pyrrole in dry nitrogen in a 5-litre stainless steel canister. The signal of pyrrole at m/z 67.04, with a peak integral of 6,389, is shown in Figure 8.5.

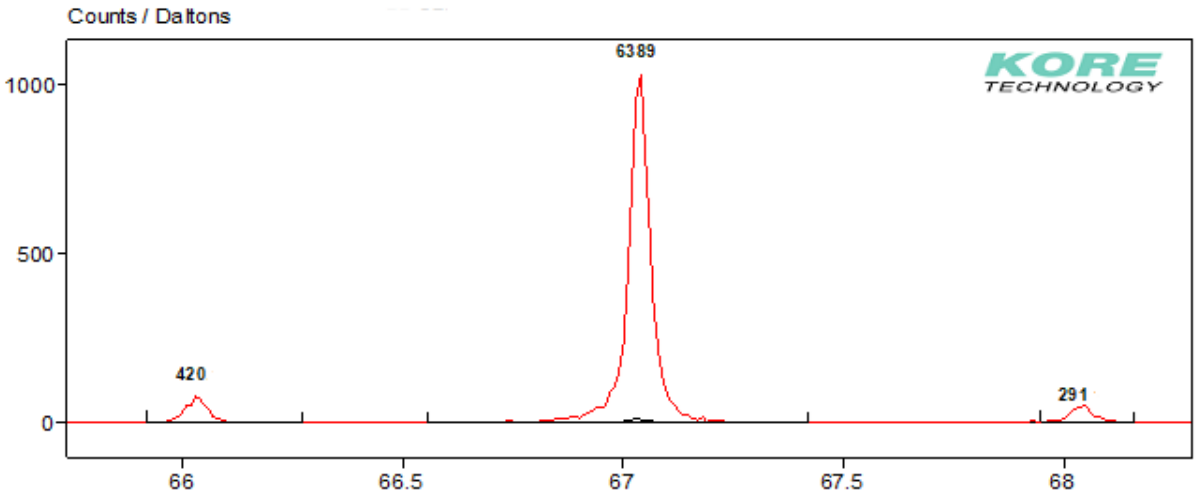

Figure 8.5: Signal of the main pyrrole product ion (M^+) at m/z 67 running 1.28 ppmv of pyrrole within the transportable EI-ToF-MS INFORMS during 10 s acquisition

The limit of detection is defined as follows in the equation E 8.2.

$$\text{Limit of detection} = \frac{3 * \sqrt{\int \text{background signal}} * \text{pyrrole concentration}}{\int \text{pyrrole signal}} \qquad \text{E 8.2}$$

A value of 5.07 ppbv is obtained. However, prior experience had shown that there are losses of low concentration VOCs to the internal walls of the canister. Therefore, this value can reliably be considered as even lower for experiments involving a commercial pyrrole standard.

Even considering the detection limit of ~ 5 ppbv was acceptable and, having established the sensitivity, work could then be started with the OH reactor in Mainz.

Figure 8.5 also provides data to deduce INFORMS presents a sensitivity to pyrrole at m/z 67 of 4850 ± 170 c/ppmv in 10 seconds, (± 100 from injection errors and ± 70 from the standard deviation in the counting statistics).

8.2.2.2 Calibration of pyrrole response using INFORMS

Using the INFORMS instrument connected to the OH reactor, the main parameters to analyse are calibration and linearity of response to pyrrole. Small changes (SD of ~ 5 %) in the instrument sensitivity were noted by variations in the $^{40}Ar^{+}$ signal (which has a constant concentration in air), and thus, to account for any instrumental variation, the pyrrole signals were normalised to the $^{40}Ar^{+}$ signal, the main ion consistently presenting a signal not saturated and above the noise using INFORMS. Different concentrations were run as shown in Figure 8.6 where each point presents a relative standard deviation (RSD) within 3 %.

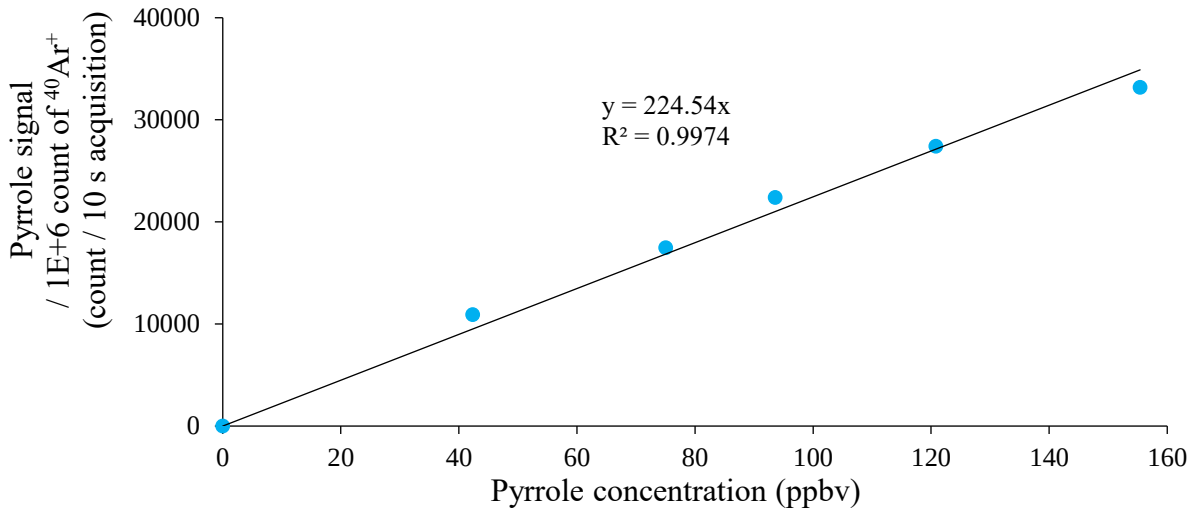

Figure 8.6: Pyrrole response linearity using INFORMS connected to the OH reactor

The linearity of the pyrrole calibration means that the EI-ToF-MS can be used for measurements over a large pyrrole concentration range to conduct the OH reactivity measurement.

Once the choice of pyrrole was confirmed, propane (C_3H_8) was used as the OH scavenger, leaving pyrrole *preserved* during C1 measurements whereas isoprene (C_5H_8) then propene (C_3H_6) were used as test gases to *compete* with pyrrole during C3 measurements. Notice, propene does present a fragment ion at m/z 40, interfering with argon, even if the mass resolution of INFORMS made possible to present a better separation for these isobaric compounds at m/z 40 than for pyrrole and isoprene at m/z 67.

8.3 Results and discussions

Unlike the preliminary tests realised at Kore, the longer experiments conducted at the MPIC revealed an unexpected issue with the INFORMS detector whose gain needed to be increased by ~ 40 V per hour of continuous experiment, representing an increase of 1.4-1.7 % of the gain depending on its starting value. In order to measure the low VOC concentration, the INFORMS instrument was operated at its highest sensitivity for long periods during these experiments.

Unfortunately, this meant that the total ion currents reaching the detector due to ionised matrix gas species were extremely high (and no mass gating was available for blanking the intense matrix peaks). This resulted in more rapid ageing of the detector than was expected. Consequently, in order to operate within the remaining life of the detector, data acquisition times were restricted for the period of the secondment.

Pyrrole concentration was monitored under the comparative reactivity method, using propane as OH scavenger and initially isoprene as test gas. After numerous attempts, due to the expected interferences at m/z 67, the most reliable measurements led to the results shown in Figure 8.7 after conversion of the pyrrole signal into concentration through the calibration shown in Figure 8.6. Notice no RSDs are displayed for clarity purposes and all the uncertainties were considered into the final OH reactivity calculation. For each range of concentration, an average was considered, which is also represented in Figure 8.7.

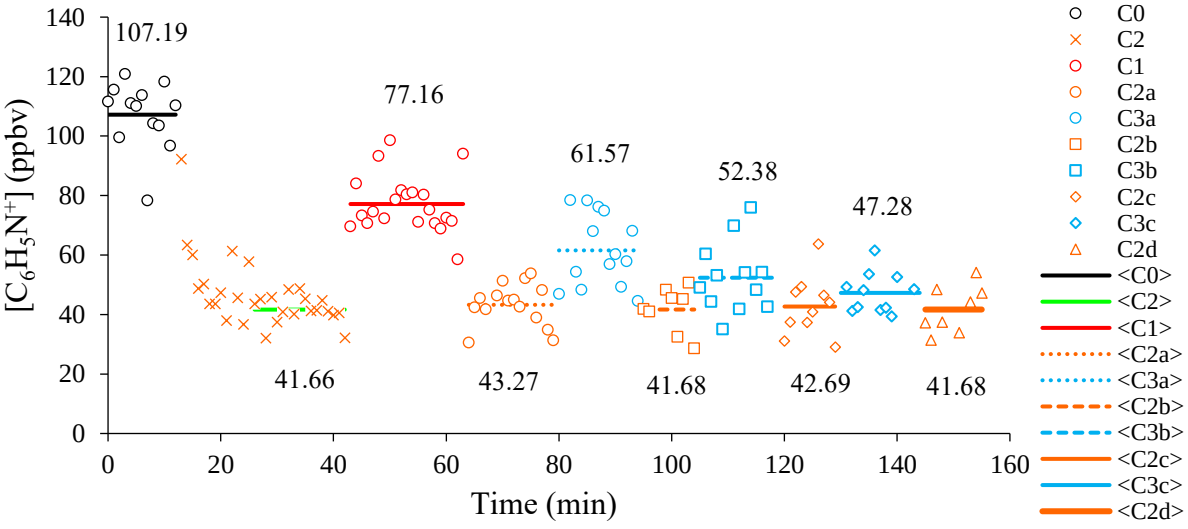

Figure 8.7: Pyrrole concentration monitored under the comparative reactivity method with the use of isoprene using INFORMS connected to the OH reactor

Using the concentrations from Figure 8.7 as well as the value of 1.28 x 10^{-16} m^3/(molecules·s) for k_p [144] provides the results as follows in Table 8.1.

Table 8.1: Total OH reactivity measured with isoprene as test gas using the portable EI-ToF-MS and the PTR

Isoprene introduction modifying C3 (ppbv)	**OH reactivity (R_{air}) of the air sample using isoprene**						
	EI data			**PTR data**			**Ratio $R_{air,EI}/R_{air,PTR}$**
	(s^{-1})	**SD (s^{-1})**	**RSD (%)**	**(s^{-1})**	**SD (s^{-1})**	**RSD (%)**	
33.84	289	133	46.02	34	3.4	10.04	**8.53**
17.15	97	255	262.65	19	1.9	10.00	**5.11**
8.79	40	167	415.03	8	0.79	10.09	**5.14**

Except for the greatest concentration of isoprene injected, the RSD is greater than 100 %, demonstrating the difficulty of making these measurements with INFORMS, on top of providing a reactivity with a factor 5 to 8 times greater than that obtained from the PTR measurements. This is simply because the pyrrole signal at m/z 67 has a contribution of the fragment ion of isoprene (loss of H following electron ionisation impact) as mentioned previously. That is why isoprene was then replaced by propene providing the following results in Figure 8.8.

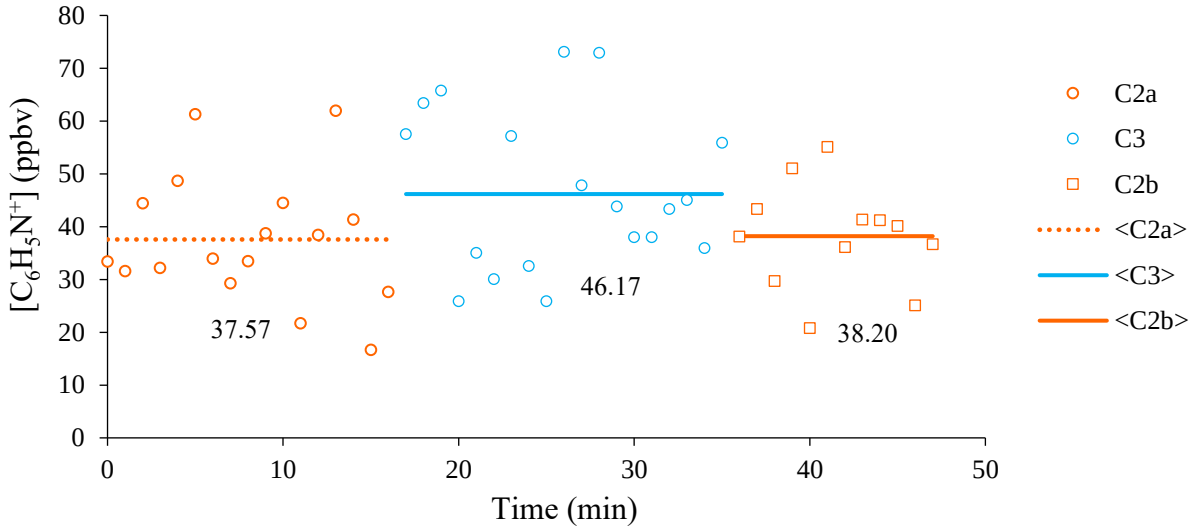

Figure 8.8: Pyrrole concentration monitored under the comparative reactivity method with the use of propene using INFORMS connected to the OH reactor

To limit the effect of loss of sensitivity of the INFORMS detector, only C2s and C3 were measured. The value of C1 (expected to be stable under the same reactor working condition) determined during the experiments using isoprene were used providing a new OH reactivity value using INFORMS of 63 ± 247 s^{-1} whereas in parallel, the measurements using the PTR provided a value of 39 ± 3.9 s^{-1}.

Measuring, through the use of propene, a more realistic integral of pyrrole provided a more accurate measurement of its concentration, improving the ratio of OH reactivity values ($R_{air,EI}/R_{air,PTR}$) by a factor of 3.2 to 5.2 compared to the measurement using isoprene, leaving OH reactivity 'only' greater than the PTR results by 63 %. However, the RSD of the reactivity obtained from the INFORMS experiment is greater than 100 %. Further reflections were held to conduct further tests in order to find the most reliable conditions for the total OH reactivity measurement using the INFORMS instrument, changing certain parameters one by one. This study highlighted some limits in the current design of the system.

8.4 Conclusion

The main objective of this study was to determine if CRM could be undertaken using a lower-cost analytical instrument. However, after a month of attempts, it became clear that several problems need to be overcome to be able to use an EI-MS instead of a PTR-MS. The lack of a high enough mass resolution to separate isobaric interferences made it difficult to deduce count rates for key ions of interest with certainty. Further issues remained. These include the following:

- With the INFORMS instrument, the most reliable normalization comes from the natural abundance of argon in air. However, this element was in competition with an isobaric compound at m/z 40: a fragment ion coming from propene.

→ Even though, using propene was much better than isoprene, the ideal solution would be to replace propene with another test VOC, not having any fragmentation at m/z 40.

- Isoprene is a commonly found VOC in ambient air. Without high mass resolution to separate $C_5H_7^+$ at m/z 67.055 from $C_4H_5N^+$ at m/z 67.042, determining the signal intensity for pyrrole at mass 67 in the presence of isoprene is challenging.

  → In preparation for potential further tests with this instrument, pyrrole would need to be replaced by another VOC that does not contain fragment ions in its EI (70 eV) mass spectrum that are the same as those for isoprene and argon.

- The least expected issue with the compact EI mass spectrometer was the need to adjust the detector gain more frequently than expected, even over the course of the one-month secondment.

  → For this instrument, and to address this issue, the detector has now been switched by Kore from a discrete dynode detector to a small diameter DMCP detector.

CHAPTER 9: SUMMARY, CORE CONTRIBUTIONS AND FUTURE WORK

9.1 Development and implementation of new ion-funnels into a PTR reactor

Sensitivity improvement was the principal goal of the ion-funnel developments in this research. Furthermore, a design constraint was to see how much could be achieved by modifications to the existing arrangement of stacked electrodes within the reactor, thus aiming for significant improvements with minimal impact on the cost of implementation; an important consideration for a commercial product.

A core contribution has been an improvement in sensitivity by a factor of two with the Mark II funnel, and this contribution is evidenced by this funnel becoming standard within the current commercial offering from Kore. Further developments led to the Mark V arrangement, in which the last two electrodes of a Mark II reactor were replaced by six electrodes to form what is termed as the 'micro-funnel'. A minor modification of the existing RF power supply allowed this arrangement to double the signal intensity of the ions at the detector of the mass spectrometer by another factor of two.

To obtain further gains in sensitivity and overall operational performance, the following future work could be pursued:

1) Develop the RF power supply to control better the six electrodes in the micro-funnel. It is clear that optimising the RF field in this last part of the funnel is critical, as the electrodes have the smallest apertures and all ions pass through the RF field at this point before exiting the reactor.
2) Develop a new RF power supply to operate at higher frequency and voltages to explore the interaction of frequency and amplitude on the transmission of the funnel. This is now being tested at Kore at the time of writing.
3) Dispense with a section of the reactor having only a DC electric field, and instead either extend the funnel across the existing length of the reactor, or remove the first section

and halve the length of the reactor, but increasing the pressure to maintain the same number of collisions.

9.2 Exploration of the split of the DC electric field when RF fields are applied in a PTR reactor

Within the existing reactor arrangement, the first half of the electrode stack is not a funnel and has no RF field applied. Reducing the DC voltage gradient in the first half is required to optimise the funnelling, but this leaves the first half of the reactor with a very low E/n value, which led to significant ion losses, possibly due to space charge effects.

The reactor was separated electrically into two sections with no design changes and thus no cost implications. The E/n value in the first half could then be set to resemble that used in the DC (only) mode when no RF field was applied. In the second section, the low electric field required to optimise the funnelling was preserved. With this arrangement, a core contribution has been to double the sensitivity again, thus giving an eightfold increase in sensitivity when used in the Mark V reactor, compared to the original Mark I reactor. However, differences were noted in the enhancement of molecular ion signals for some ions, such as protonated n-butylbenzene and protonated hexachloro-1,3-butadiene. In the latter case, a doubling of signal was achieved, whereas in the former case it was only 7 %. Through application of the RF theory developed in chapter 2 it was realised that if the DC electric field is set too low in the funnel section, then it is possible to trap ions by having too low an 'overriding field'.

To further this work the following future work could be pursued:

If the existing reactor structure is maintained, namely a first half with no funnelling, and a split gradient is seen as beneficial for further enhancements in sensitivity, then more work is required

to understand how to set the gradient in the second one, i.e. the funnel section, to avoid accidentally trapping ions.

9.3 Limitations in the use of E/n for specifying product ion distributions

The discovery of shifts in the product ion distributions when deriving the same E/n value but with different combinations of E, T and P, was completely unexpected, especially given how widely quoted are optimum E/n values and ranges for the study of different analytes. This is the first time this discrepancy has been explored systematically and proven to be repeatable and is thus a core contribution. For PTR-MS instrumentation where E, T and P are always set to the same values, it is legitimate to compare the product ion distributions of different analytes across different instruments. However, when E/n is nominally the same but derived using different values of E, T and P, it is not legitimate, and care must be taken when comparing data.

After collaboration with Dr Michal Lacko of the HIPC of Prague, who at the time was also an Early Stage Researcher within IMPACT, to determine an ion mobility value for protonated n-butylbenzene using a SIFDT-MS, the parameter E/n was replaced by the kinetic energy in the centre of mass of the colliding system. This greatly reduced the shifts observed when varying the temperature for a given E/n. Effects of varying pressure have not been well understood, however it was hoped that information gathered by characterising the product ion distribution of certain 'probe' analytes in the DC (only) mode would allow for knowledge of the effective E/n values to be deduced when applying the RF field. This proved to be rather optimistic; the product ion distribution curves in RF mode are complex.

Further work:

1) If the shifts in the E/n curves due to pressure changes are to be understood, more work must be done to explore what phenomena cause greater fragmentation as the pressure increases for the same nominal E/n.
2) To assess how any new ion-funnel developments affect the transmission of ions, and particularly more fragile ions, the behaviour of well-characterised 'probe' molecules is still thought to be a valid way to proceed and should be explored further.

9.4 Characterisation of VOCs by chemical ionisation: Production of mass spectral libraries for use in new software for complex mixture analysis

The question was posed: “Without resorting to a pre-separation technique, how much information can be extracted from a mass spectrum when mass peaks from a complex mixture of compounds appear simultaneously?” In parallel with software developments done by staff at Kore, it was necessary to settle upon a measurement protocol that could be used to generate the product ion distributions for individual compounds, thus building a mass spectral library for the PTR-ToF-MS. Having created individual library entries for most of the 39 VOC compounds in the gas mix known as TO-14, the algorithm could be tested against the hardest of all challenges: 39 compounds of the same concentration in a gas standard appearing in the mass spectrum simultaneously.

As a result of this core contribution at this stage of software development, and after work in this thesis was complete, the following work was undertaken at Kore and is now complete:

1) Removal of a 'group' approach to cope with compounds that produce very similar product ion distributions by placing them in a single, reported group (this is not referring to isomers).

2) Development of a non-negative least squares algorithm for the second stage of compound fitting for greater compound matching.
3) Use and refinement of the analytical measurement protocol to increase the size of the library to over 90 VOCs.
4) Offering the mass spectral library and the deconvolution software as part of the commercial instrument package.
5) Demonstration of the use of the library method to produce real-time quantitative analysis at the rate of one result per second while transporting the PTR-ToF-MS in a van, i.e., taking data 'on the move'.

9.5 Development of a new water sampling device for VOC extraction and subsequent analysis by mass spectrometry

The desire to be able to perform on-site testing for VOCs in rivers or other sources of water led to a prototype water sampler, with the prototype coupled to the portable mass spectrometer, the MS-200 EI-ToF-MS. A core contribution has been the development of a new, more reliable and compact version of the water sampler. This was characterised first in tandem with the PTR-ToF-MS, after which it was used with the MS-200 portable instrument once again.

After creating a small mass spectral library of individual compounds using the MS-200, mixtures of BTEX in water were analysed by the MS-200 and the new deconvolution software reported good matches with the prepared concentrations. Various bottled waters have also been analysed, as well as river water in the Ely area.

Further work:

1) Packaging the water sampler in a robust housing so that it can be transported into the field along with the portable and transportable mass spectrometers (EI-ToF-MS and PTR-ToF-MS).
2) Enabling the unit to be powered without mains electricity to achieve true field-portability.

9.6 Total OH reactivity measurement by means of a transportable electron impact ionisation-time of flight-mass spectrometer

By taking a Kore EI-ToF-MS to Germany, an attempt was made to replace the existing PTR-MS used at the MPIC in Mainz for their 'total OH reactivity' measurements. This was conducted in collaboration with Dr Nijing Wang, who at the time was also an Early Stage Researcher within IMPACT.

Given the limited resolution of the small EI-ToF-MS and its much lower sensitivity for VOCs compared to a high performance PTR-MS, it was not possible to obtain sufficient VOC specificity in the data to achieve the desired goal.

Future work:

Repeat the project with an EI-ToF-MS having a longer flight length to achieve sufficient mass resolution to avoid the isobaric interferences experienced with the small spectrometer.

REFERENCES

1. European Commission - Research Executive Agency Director. GRANT AGREEMENT NUMBER — 674911 — IMPACT. 2015.

2. KORE TECHNOLOGY Limited. Products 2014 (Accessed on the: [updated 20th September 2017. Available from: http://www.kore.co.uk/prodgall.htm.

3. Change i-IPoC. Climate Change 2022 - Impacts, Adaptation and Vulnerability - Summary for Poloicymakers. 2022.

4. Altiner M, Yildirim M. Production and characterization of synthetic aragonite prepared from dolomite by eco-friendly leaching–carbonation process. Advanced Powder Technology. 2017;28(2):553-564.

5. Honarmand M, Givzad M. An efficient and eco-friendly process for the Knoevenagel reaction using nano organosalt catalyst. International Journal of Environmental Science and Technology. 2017;15(7):1551-1560.

6. Reverberi AP, Varbanov PS, Lauciello S, Salerno M, Fabiano B. An eco-friendly process for zerovalent bismuth nanoparticles synthesis. Journal of Cleaner Production. 2018;198:37-45.

7. United States Environmental Protection Agency. Basics of Green Chemistry 2017 (Accessed on the: 10/03/2019) [updated 21st March 2017. Available from: https://www.epa.gov/greenchemistry/basics-green-chemistry.

8. United States Environmental Protection Agency. Remediation 2018 (Accessed on the: 10/03/2019) [updated 20th November 2018. Available from: https://search.epa.gov/epasearch/epasearch?querytext=remediation&areaname=&areacontacts=&areasearchurl=&typeofsearch=epa&result_template=2col.ftl.

9. United States Environmental Protection Agency. What is Superfund? 2018 (Accessed on the: 10/03/2019) [updated 4th June 2018. Available from: https://www.epa.gov/superfund/what-superfund.

10. Shimadzu. Analysis of Volatile Organic Compounds in the Environment Using the Restore Function of TD-GC/MS 2020 (Accessed on the: 16/03/2022) [updated 2020. Available from: https://www.shimadzu.com/an/literature/gcms/jpo219008.html.

11. Jarvis GK, Kennedy RA, Mayhew CA, Tuckett RP. Charge transfer from neutral perfluorocarbons to various cations: long-range versus short-range reaction mechanisms. International Journal of Mass Spectrometry. 2000;202:21.

12. Mayhew CA. Reactions of Ne+ and Ne2+ ions with several molecular species at 300 K: the importance of energy resonance, Franck-Condon factors and electron correlation effects on reaction efficiencies. J Phys B: At Mol Opt Phys. 1992;25:18.

13. KORE TECHNOLOGY Limited - Internal data. Proton affinities and ionization energies of common chemicals. 2019.

14. NIST. NIST20: Updates to the NIST Tandem and Electron Ionization Spectral Libraries 2020 (Accessed on the: 16/03/2022) [updated 2020. Available from: https://www.nist.gov/programs-projects/nist20-updates-nist-tandem-and-electron-ionization-spectral-libraries.

15. American Chemical Society. Areas of Chemistry 2021 (Accessed on the: 10/03/2019) [Available from: https://www.acs.org/content/acs/en/careers/college-to-career/areas-of-chemistry.html.

16. Guidance Corner. Different Branches of Chemistry and Their Examples 2021 (Accessed on the: 10/03/2019) [Available from: https://guidancecorner.com/branches-of-chemistry/.

17. University of Wisconsin La Crosse. Different types of Chemistry 2021 (Accessed on the: 10/03/2019) [Available from: https://www.uwlax.edu/chemistry-and-biochemistry/student-resources/different-types-of-chemistry/.

18. Paracelsus. Die dritte Defension wegen des Schreibens der neuen Rezepte. Das Buch Paragranum - Septem Defensiones. 21538. p. 508-513.

19. Torres C, Reyes PG, Castillo F, Martínez H. Paschen law for argon glow discharge. Journal of Physics: Conference Series. 2012;370.

20. Lieberman MA, Lichtenberg AJ. Principles of plasma discharges and materials processing. 2nd ed: Wiley; 2005.

21. Ellis AM, Mayhew CA. Ion-Molecule Chemistry Leading to H_3O^+ Production. Proton transfer reaction mass spectrometry: principles and applications: Wiley; 2014. p. 59-61.

22. Gross JH. Creating a Beam of Ions. Mass Spectrometry : A Textbook: Springer; 2004. p. 112.

23. National Institute of Standards and Technology CW, SRD 69,,. Water 2018 (Accessed on the: 23/07/2021) [updated 2018. Available from: https://webbook.nist.gov/cgi/cbook.cgi?ID=C7732185&Units=SI&Mask=20#Ion-Energetics.

24. NASA. Equation of State (Ideal Gas) 2021 (Accessed on the: 22/07/2021) [updated 2021. Available from: https://www.grc.nasa.gov/www/k-12/airplane/eqstat.html.

25. Romano A, Hanna GB. Identification and quantification of VOCs by proton transfer reaction time of flight mass spectrometry: An experimental workflow for the optimization of specificity, sensitivity, and accuracy. J Mass Spectrom. 2018;53(4):287-295.

26. Guo T, Peng Z, Zhu H, Xu L, Dong J-G, Huang Z-X, et al. Research Progress and Application of Ion Funnel Technique. Chinese Journal of Analytical Chemistry. 2019;47(1):13-22.

27. Gross JH. Formation of Ions in Chemical Ionization. Mass Spectrometry : A Textbook: Springer; 2004. p. 331-332.

28. Ellis AM, Mayhew CA. Introduction. Proton transfer reaction mass spectrometry: principles and applications: Wiley; 2014. p. 25-27.

29. Mallet AI, Down S. Proton transfer. Dictionary of Mass Spectrometry: Wiley; 2010. p. 128.

30. Blake RS, Monks PS, Ellis AM. Proton transfer reaction mass spectrometry. Spectroscopy Europe. 2012;24.

31. Tomoda S, Kimura K. IONIZATION ENERGIES AND HYDROGEN-BOND STRENGTH OF THE WATER CLUSTERS. Chemical Physics Letter. 1983;102:560-564.

32. Kawai Y, Yamaguchi S, Okada Y, Takeuchi K, Yamauchi Y, Ozawa S, et al. Reactions of protonated water clusters H+(H2O)n (n=1–6) with dimethylsulfoxide in a guided ion beam apparatus. Chemical Physics Letters. 2003;377(1-2):69-73.

33. Goebbert DJ, Wentold PG. Water dimer proton affinity from the kinetic method: dissociation energy of the water dimer. Eur J Mass Spectrom (Chichester). 2004;10(6):837-846.

34. Gross JH. Gas Phase Basicity and Proton Affinity. Mass Spectrometry : A Textbook: Springer; 2004. p. 50.

35. Ellis AM, Mayhew CA. Thermodynamics of Proton Transfer. Proton transfer reaction mass spectrometry: principles and applications: Wiley; 2014. p. 27-31.

36. Ellis AM, Mayhew CA. The Flowing Afterglow Technique. Proton transfer reaction mass spectrometry: principles and applications: Wiley; 2014. p. 11-14.

37. Gross JH. Detectors. Mass Spectrometry : A Textbook: Springer; 2004. p. 175-180.

38. Mallet AI, Down S. Charge exchange. Dictionary of Mass Spectrometry: Wiley; 2010. p. 23.

39. PFEIFFER VACUUM. Mean free path 2019 (Accessed on the: 10/05/2019) [updated 2019. Available from: https://www.pfeiffer-vacuum.com/en/know-how/introduction-to-vacuum-technology/fundamentals/mean-free-path/.

40. Mallet AI, Down S. scanning analyser. Dictionary of Mass Spectrometry: Wiley; 2010. p. 142.

41. Ellis AM, Mayhew CA. Drift Tubes : Ion Mobility and Transit Times. Proton transfer reaction mass spectrometry: principles and applications: Wiley; 2014. p. 69-71.

42. Fort KL, Silveira JA, Russell DH. The periodic focusing ion funnel: theory, design, and experimental characterization by high-resolution ion mobility-mass spectrometry. Anal Chem. 2013;85(20):9543-9548.

43. Kelly RT, Tolmachev AV, Page JS, Tang K, Smith RD. The ion funnel: theory, implementations, and applications. Mass Spectrom Rev. 2010;29(2):294-312.

44. Shaffer SA, Tolmachev AV, Prior DC, Anderson GA, Udseth HR, Smith RD. Characterization of an Improved Electrodynamic Ion Funnel Interface for Electrospray Ionization Mass Spectrometry. Analytical Chemistry. 1999;71:2957-2964.

45. Tolmachev AV, Kim T, Udseth HR, Smith RD, Bailey TH, Futrell JH. Simulation-based optimization of the electrodynamic ion funnel
for high sensitivity electrospray ionization mass spectrometry. International Journal of Mass Spectrometry. 2000;203:31-47.

46. Tolmachev AV, Vilkov AN, Bogdanov B, Pasa-Tolic L, Masselon CD, Smith RD. Collisional activation of ions in RF ion traps and ion guides: the effective ion temperature treatment. J Am Soc Mass Spectrom. 2004;15(11):1616-1628.

47. Albrecht S, Afchine A, Barthel J, Dick M, Rongen H, Stroh F, et al. An efficient ion funnel operating at 100 mbar background pressure 2014 (Accessed on the: 22/05/2020) [Available from: https://www.ptc.uni-wuppertal.de/fileadmin/_migrated/content_uploads/TP736_S.Albrecht_01.pdf.

48. Ibrahim Y, Tang K, Tolmachev AV, Shvartsburg AA, Smith RD. Improving mass spectrometer sensitivity using a high-pressure electrodynamic ion funnel interface. J Am Soc Mass Spectrom. 2006;17(9):1299-1305.

49. Schlottmann F, Allers M, Kirk AT, Bohnhorst A, Zimmermann S. A Simple Printed Circuit Board-Based Ion Funnel for Focusing Low m/z Ratio Ions with High Kinetic Energies at Elevated Pressure. J Am Soc Mass Spectrom. 2019;30(9):1813-1823.

50. de Brito JF. A Lightweight High-sensitivity Chemical Mass Spectrometer for Organic Compounds: Karlsruhe Institute of Technology; 2011.

51. Tolmachev AV, Chernushevich IV, Dodonov AF, Standing KG. A collisional focusing ion guide for coupling an atmospheric pressure ion source to a mass spectrometer. Nuclear Instruments and Methods in Physics Research. 1997;B 124:112-119.

52. Ellis AM, Mullock SJ. Theoretical treatment of RF excitation of ions and effective temperature (Unpublished internal technical discussion document at Kore Technology Ltd). 2012.

53. Smith D, Spanel P. Selected ion flow tube mass spectrometry (SIFT-MS) for on-line trace gas analysis. Mass Spectrom Rev. 2005;24(5):661-700.

54. de Gouw J, Warneke C, Karl T, Eerdekensc G, van der Veen C, Fall R. Sensitivity and specificity of atmospheric trace gas detection
by proton-transfer-reaction mass spectrometry. International Journal of Mass Spectrometry. 2003;223-224:365-382.

55. Wannier GH. On the Motion of Gaseous Ions in a Strong Electric Field. I. Physical Review. 1951;83(2):281-289.

56. Wannier GH. Motion of Gaseous Ions in Strong Electric Fields. Bell System Technical Journal. 1953;32(1):170-254.

57. Ellis AM, Mayhew CA. Drift Tubes : Ion-Molecule Collision Energies. Proton transfer reaction mass spectrometry: principles and applications: Wiley; 2014. p. 71-73.

58. Valance C, Department of Chemistry, University of Oxford. Treating collisions in the lab and centre of mass frames (Accessed on the: 21/02/2021) [Available from: http://vallance.chem.ox.ac.uk/pdfs/Collisions.pdf.

59. Geiger F. Fast-response measurements of organic trace species in the Earth‘s atmosphere. KIT Scientific Publishing2014.

60. Ellis AM, Mayhew CA. Time-of-flight Mass Spectrometry. Proton transfer reaction mass spectrometry: principles and applications: Wiley; 2014. p. 90-97.

61. Gross JH. Time-of-Flight Instruments. Mass Spectrometry : A Textbook: Springer; 2004. p. 113-130.

62. Bolton PR, Borghesi M, Brenner C, Carroll DC, De Martinis C, Fiorini F, et al. Instrumentation for diagnostics and control of laser-accelerated proton (ion) beams. Phys Med. 2014;30(3):255-270.

63. Ladislas Wiza J. MICROCHANNEL PLATE DETECTORS. Nuclear Instruments and Methods. 1621979. p. 587-601.

64. Cody RB, editor Introduction to DART MS. Technology Transition Workshop; National Institute of Justice.

65. de Hoffmann E, Stroobant V. Detectors and Computers. Mass Spectrometry : Principles and Applications. 3rd ed: Wiley; 2007. p. 175-187.

66. Gross JH. Layout of an Electron Ionization Source. Mass Spectrometry : A Textbook: Springer; 2004. p. 200-201.

67. Gross JH. Generation of Primary Electrons. Mass Spectrometry : A Textbook: Springer; 2004. p. 202-203.

68. Kore Technology - Internal data. MS-200s User Manual. 2008.

69. Gross JH. Electron Ionization. Mass Spectrometry : A Textbook: Springer; 2004. p. 15-16.

70. Gross JH. Formations of Ions. Mass Spectrometry : A Textbook: Springer; 2004. p. 193-194.

71. Gross JH. Writing Conventions For Molecular Ions. Mass Spectrometry : A Textbook: Springer; 2004. p. 223-225.

72. Gross JH. Ionization Energy. Mass Spectrometry : A Textbook: Springer; 2004. p. 16-18.

73. Gross JH. Efficiency of Electron Ionization. Mass Spectrometry : A Textbook: Springer; 2004. p. 196-197.

74. Gross JH. Low-Energy Electron Ionization Mass Spectra. Mass Spectrometry : A Textbook: Springer; 2004. p. 198-200.

75. Shimadzu. Structure of Electron Multiplier (Discrete-Dynode Type) 2020 (Accessed on the: 24/09/2020) [updated 2020. Available from: https://www.shimadzu.com/an/structure_electron.html.

76. Ellis AM, Mayhew CA. Discrete Dynode Detector. Proton transfer reaction mass spectrometry: principles and applications: Wiley; 2014. p. 98-100.

77. Barber S, Blake RS, White IR, Monks PS, Reich F, Mullock S, et al. Increased sensitivity in proton transfer reaction mass spectrometry by incorporation of a radio frequency ion funnel. Anal Chem. 2012;84(12):5387-5391.

78. Ellis AM, Mayhew CA. Preface. Proton transfer reaction mass spectrometry: principles and applications: Wiley; 2014. p. XIII-XV.

79. Fiches G, Déléris I, Saint-Eve A, Pollet B, Brunerie P, Souchon I. Modifying PTR-MS operating conditions for quantitative headspace analysis of hydro-alcoholic beverages. 1. Variation of the mean collision energy to control ionization processes occurring during PTR-MS analyses of 10–40% (v/v) ethanol–water solutions. International Journal of Mass Spectrometry. 2013;356:41-45.

80. Pagonis D, Sekimoto K, de Gouw J. A Library of Proton-Transfer Reactions of H3O(+) Ions Used for Trace Gas Detection. J Am Soc Mass Spectrom. 2019;30(7):1330-1335.

81. Steeghs MML, Sikkens C, Crespo E, Cristescu SM, Harren FJM. Development of a proton-transfer reaction ion trap mass spectrometer: Online detection and analysis of volatile organic compounds. International Journal of Mass Spectrometry. 2007;262(1-2):16-24.

82. Zhang X, Huo X, Tang F, Zha Z, Yang F, Ni Y, et al. Characterisation and optimisation of ion discrimination in a mini ion funnel for a miniature mass spectrometer. Analytical Methods. 2019;11(19):2551-2558.

83. Brunner T, Fudenberg D, Varentsov V, Sabourov A, Gratta G, Dilling J, et al. An RF-only ion-funnel for extraction from high-pressure gases. International Journal of Mass Spectrometry. 2015;379:110-120.

84. Zhu H, Zhao G-S, Xu L, Peng Z, Feng B, Dong J-G, et al. Development of a SIMION-Simulated Ion Funnel Tube for Proton Transfer Reaction Mass Spectrometry. Chinese Journal of Analytical Chemistry. 2018;46(8):e1868-e1873.

85. Brown PA, Cristescu SM, Mullock SJ, Reich DF, Lamont-Smith CS, Harren FJM. Implementation and characterization of an RF ion funnel ion guide as a proton transfer reaction chamber. International Journal of Mass Spectrometry. 2017;414:31-38.

86. National Institute of Standards and Technology CW, SRD 69,,. Benzene 2018 (Accessed on the: 11/03/2020) [updated 2018. Available from: https://webbook.nist.gov/cgi/cbook.cgi?ID=C71432&Units=SI&Mask=20#Ion-Energetics.

87. National Institute of Standards and Technology P, ,. Atomic Weights and Isotopic Compositions for All Elements 2018 (Accessed on the: 20/02/2020) [Available from: https://physics.nist.gov/cgi-bin/Compositions/stand_alone.pl.

88. National Institute of Standards and Technology CW, SRD 69,,. Nitrogen 2018 (Accessed on the: 11/03/2020) [updated 2018. Available from: https://webbook.nist.gov/cgi/cbook.cgi?ID=C7727379&Units=SI&Mask=20#Ion-Energetics.

89. Agbonkonkon N, Dennis Tolley H, Asplund MC, Lee ED, Lee ML. Prediction of Gas-Phase Reduced Ion Mobility Constants (Ko). Analytical Chemistry. 2004;76:52235229.

90. National Institute of Standards and Technology CW, SRD 69,,. Toluene 2018 (Accessed on the: 12/05/2021) [updated 2018. Available from: https://webbook.nist.gov/cgi/cbook.cgi?ID=C108883&Units=SI&Mask=20#Ion-Energetics.

91. National Institute of Standards and Technology CW, SRD 69,,. Ethylbenzene 2018 (Accessed on the: 12/05/2021) [updated 2018. Available from: https://webbook.nist.gov/cgi/cbook.cgi?ID=C100414&Units=SI&Mask=20#Ion-Energetics.

92. National Institute of Standards and Technology CW, SRD 69,,. o-xylene 2018 (Accessed on the: 12/05/2021) [updated 2018. Available from: https://webbook.nist.gov/cgi/cbook.cgi?ID=C95476&Units=SI&Mask=20#Ion-Energetics.

93. National Institute of Standards and Technology CW, SRD 69,,. m-xylene 2018 (Accessed on the: 12/05/2021) [updated 2018. Available from: https://webbook.nist.gov/cgi/cbook.cgi?ID=C108383&Units=SI&Mask=20#Ion-Energetics.

94. National Institute of Standards and Technology CW, SRD 69,,. p-xylene 2018 (Accessed on the: 12/05/2021) [updated 2018. Available from: https://webbook.nist.gov/cgi/cbook.cgi?ID=C106423&Units=SI&Mask=20#Ion-Energetics.

95. Warneke C, van der Veen C, Luxembourg S, de Gouw JA, Kok A. Measurements of benzene and toluene in ambient air using proton-transfer-reaction mass spectrometry: calibration, humidity dependence, and field intercomparison. International Journal of Mass Spectrometry. 2001;207:167-182.

96. Hewitt CN, Hayward S, Tani A. The application of proton transfer reaction-mass spectrometry (PTR-MS) to the monitoring and analysis of volatile organic compounds in the atmosphere. J Environ Monit. 2003;5(1):1-7.

97. TOFWERK. What is Proton Transfer Reaction Mass Spectrometry (PTR-MS)? 2021 (Accessed on the: 25/05/2021) [updated 2021. Available from: https://www.tofwerk.com/proton-transfer-reaction-mass-spectrometry/.

98. Ionicon. PTR-MS 2021 (Accessed on the: 25/05/2021) [updated 2021. Available from: https://www.ionicon.com/technologies/details/ptr-ms.

99. Allers M, Kirk AT, Schaefer C, Erdogdu D, Wissdorf W, Benter T, et al. Field-Dependent Reduced Ion Mobilities of Positive and Negative Ions in Air and Nitrogen in High Kinetic Energy Ion Mobility Spectrometry (HiKE-IMS). J Am Soc Mass Spectrom. 2020;31(10):2191-2201.

100. Ellis AM, Mayhew CA. Ion Cluster Distributions. Proton transfer reaction mass spectrometry: principles and applications: Wiley; 2014. p. 73-76.

101. National Institute of Standards and Technology CW, SRD 69,,. Benzene, n-butyl- 2018 (Accessed on the: 11/03/2020) [updated 2018. Available from: https://webbook.nist.gov/cgi/cbook.cgi?ID=C104518&Units=SI&Mask=20#Ion-Energetics.

102. Nguyen TT. (1)H/(13)C chemical shift calculations for biaryls: DFT approaches to geometry optimization. R Soc Open Sci. 2021;8(9):210954.

103. Tirado-Rives J, Jorgensen WL. Performance of B3LYP Density Functional Methods for a Large Set of Organic Molecules. Journal of Chemical Theory and Computation. 2008;4:297-306.

104. Duwage CP, Jayendran CR. Exchange Functionals and Basis Set Comparisons for Theoretical Studies of ZnO nonoclusters. 2021.

105. Watts P. Thermodynamic interpretations of n-butylbenzene and triethylphosphate protonations. 2017.

106. National Institute of Standards and Technology CW, SRD 69,,. Ethylbenzene 2021 (Accessed on the: 13/02/2022) [updated 2021. Available from: https://webbook.nist.gov/cgi/cbook.cgi?ID=C100414&Units=SI&Mask=20#Ion-Energetics.

107. Dotan I, Albritton DL, Lindinger W, Pahl M. Mobilities of CO2+, N2H+, H3O+, H3O+·H2O, and H3O+· (H2O)2 ions in N2. The Journal of Chemical Physics. 1976;65(11):5028-5030.

108. American Chemical Society. Gas Chromatography-Mass Spectrometry 2021 (Accessed on the: 13/06/2021) [Available from: https://www.acs.org/content/acs/en/education/whatischemistry/landmarks/gas-chromatography-mass-spectrometry.html.

109. Restek. The GC Separation Process 2021 (Accessed on the: 13/06/2021) [Available from: https://www.restek.com/en/technical-literature-library/articles/the-GC-separation-process/.

110. Grange AH, Sovocool GW. Automated determination of precursor ion, product ion, and neutral loss compositions and deconvolution of composite mass spectra using ion correlation based on exact masses and relative isotopic abundances. Rapid Commun Mass Spectrom. 2008;22(15):2375-2390.

111. Amador-Muñoz O, Misztal PK, Weber R, Worton DR, Zhang H, Drozd G, et al. Sensitive detection of n-alkanes using a mixed ionization mode proton-transfer-reaction mass spectrometer. Atmospheric Measurement Techniques. 2016;9(11):5315-5329.

112. Lu J, Trnka MJ, Roh SH, Robinson PJ, Shiau C, Fujimori DG, et al. Improved Peak Detection and Deconvolution of Native Electrospray Mass Spectra from Large Protein Complexes. J Am Soc Mass Spectrom. 2015;26(12):2141-2151.

113. United States Environmental Protection Agency. Compendium Method TO-14A. 1999.

114. Chromatotec group. airmOzone : Ozone precursors (PAMS 56) and Toxics monitoring 2006 (Accessed on the: 07/03/2022) [updated 2006. Available from: http://www.chromatotec.com/Ozone,precursors,PAMS,56,Toxics,monitoring,with,airmOzone-Article-2558-VOCsArray-Product-43.html.

115. Rainwater FH, Thatcher LL. Methods for Collection and Analysis of Water Samples. UNITED STATES DEPARTMENT OF THE INTERIOR,
GEOLOGICAL SURVEY; 1960 1960.

116. Nowicki H. Carbon Testing: Mass Spectrometry is King in Water Analysis WCPonline,,2001 (Accessed on the: 27/03/2021) [updated 2021. Available from: http://wcponline.com/2001/01/15/carbon-testing-mass-spectrometry-king-water-analysis/.

117. Biswas S. LC-MS-MS and GC-MS for Water Quality Monitoring. In: Manager L, editor. Lab Manager2017.

118. Karst U. Wilfried M.A. Niessen: Liquid chromatography–mass spectrometry (Third edition). Analytical and Bioanalytical Chemistry. 3892007. p. 1303-1304.

119. Mattern DJ, Edler S, Becker T, Garaguso I. Analysis of Challenging Polar Contaminants in Water by LC-MS-MS with Direct Injection Perkin Elmer2020 (Accessed on the: 28/03/2021) [Available from: https://www.perkinelmer.com/lab-solutions/resources/docs/app_70124-polarcontaminants-in-water.pdf.

120. Merck. Water for LC-MS 2021 (Accessed on the: 27/03/2021) [updated 2021. Available from: https://www.merckmillipore.com/GB/en/water-purification/learning-centers/applications/organic-analysis/lc-ms/lWib.qB.vb4AAAFA5fIBvVBh,nav?ReferrerURL=https%3A%2F%2Fwww.google.co.uk%2F&bd=1.

121. White AJ, Blamire MG, Corlett CA, Griffiths BW, Martin DM, Spencer SB, et al. Development of a portable time-of-flight membrane inlet mass spectrometer for environmental analysis. Review of scientific instruments. 1998;69.

122. Martinsen MR, Davey NG, Bell RJ, Krogh ET, Gill CG, Mikkelsen Ø, et al. A field portable membrane introduction mass spectrometer with in-line standard infusion and sample heat exchanger for real-time monitoring of volatile organic compounds in aqueous samples. Environmental Chemistry and Ecotoxicology. 2020;2:168-174.

123. Owlstone. Top 5 Methods for Generating Calibration Gas Standards 2021 (Accessed on the: 20/03/2021) [updated 2021. Available from: https://www.owlstoneinc.com/top-5-methods-generating-calibration-gas-standards/.

124. Tarasov A. Introduction to quantitative gas analysis. Practical aspects of

mass-spectrometry (Theory, Manual/Tutorial, Examples)*. Fritz-Haber-Institut Max Planck Gesellschaft - Department of Inorganic Chemistry.

125. Hyland KC, Heffeman A. Two Nontargeted Screening Approaches for Examination of Drinking Water Before and After Treatment SCIEX2019 (Accessed on the: 08/04/2021) [updated 2019. Available from: https://sciex.com/content/dam/SCIEX/pdf/tech-notes/all/Examination-of-Waters-During-Treatment-with-Nontargeted-Screening.pdf.

126. Wuilloud RG, Acevedo HA, Vazquez FA, Martinez LD. Determination of Lead in Drinking Water by Icp-Aes with Ultrasonic Nebulization and Flow-Injection on-Line Preconcentration Using an Amberlite Xad-16 Resin. Analytical Letters. 2002;35(10):1649-1665.

127. Suddendorf RF, Boyer KW. Nebulizer for analysis of high salt content samples with inductively coupled plasma emission spectrometry. Analytical Chemistry. 2002;50(13):1769-1771.

128. LaPack MA, Tou JC, McGuffin VL, Enke CG. The correlation of membrane permselectivity with Hildebrand solubility parameters. Journal of Membrane Science. 1994;86:263-280.

129. Ionicon Analytik. Liquid Calibration Unit (LCU) 2021 (Accessed on the: 20/03/2021) [updated 2021. Available from: https://www.ionicon.com/accessories/details/liquid-calibration-unit-lcu.

130. Kore Technology - Internal data. Water Analysis using the MS200. 2016.

131. CHEMDATA.NIST.GOV. NIST EI Library 2020 (Accessed on the: 04/05/2021) [updated 2020. Available from: https://chemdata.nist.gov/dokuwiki/doku.php?id=chemdata:start.

132. Euro Chlor. 1,2,4-Trichlorobenzene 2002 (Accessed on the: 20/03/2021) [updated April 2002. Available from: https://www.eurochlor.org/wp-content/uploads/2019/04/8-11-4-19_marine_ra_124_trichlorobenzene.pdf.

133. Kore Technology - internal data. MS-200 User Manual. 2008.

134. Liu K, Zhang C, Cheng Y, Liu C, Zhang H, Zhang G, et al. Serious BTEX pollution in rural area of the North China Plain during winter season. J Environ Sci (China). 2015;30:186-190.

135. Asadi M, Mirmohammadi M. Experimental study of benzene, toluene, ethylbenzene, and xylene (BTEX) contributions in the air pollution of Tehran, Iran. Environmental Quality Management. 2017;27(1):83-93.

136. Materić D, Lanza M, Sulzer P, Herbig J, Bruhn D, Gauci V, et al. Selective reagent ion-time of flight-mass spectrometry study of six common monoterpenes. International Journal of Mass Spectrometry. 2017;421:40-50.

137. Misztal PK, Heal MR, Nemitz E, Cape JN. Development of PTR-MS selectivity for structural isomers: Monoterpenes as a case study. International Journal of Mass Spectrometry. 2012;310:10-19.

138. Epic Water Filters. Dibromochloromethane 2019 (Accessed on the: 20/02/2020) [updated 2019. Available from: https://epicwaterfilters.co.uk/pages/dibromochloromethane.

139. Gérardin F, Cloteaux A, Midoux N. Modeling of variations in nitrogen trichloride concentration over time in swimming pool water. Process Safety and Environmental Protection. 2015;94:452-462.

140. Bramston-Cook R. Kovats Indices for C2-C13 Hydrocarbons and Selected Oxygenates/Halocarbons with 100% Dimethylpolysiloxane Columns 2010 (Accessed on the: 21/05/2020) [updated 2010. Available from: http://www.lotusinstruments.com/wp/wp-content/uploads/List-of-Kovats-Indices-for-C2-C13-Hydrocarbons.pdf.

141. Zabiegala B, Partyka M, Gorecki T, Namiesnik J. Application of the chromatographic retention index system for the estimation of the calibration constants of permeation passive samplers with polydimethylsiloxane membranes. J Chromatogr A. 2006;1117(1):19-30.

142. Yang Y, Shao M, Wang X, Nölscher AC, Kessel S, Guenther A, et al. Towards a quantitative understanding of total OH reactivity: A review. Atmospheric Environment. 2016;134:147-161.

143. Nakashima Y, Kato S, Greenberg J, Harley P, Karl T, Turnipseed A, et al. Total OH reactivity measurements in ambient air in a southern Rocky mountain ponderosa pine forest during BEACHON-SRM08 summer campaign. Atmospheric Environment. 2014;85:1-8.

144. Dillon TJ, Tucceri ME, Dulitz K, Horowitz A, Vereecken L, Crowley JN. Reaction of hydroxyl radicals with C4H5N (pyrrole): temperature and pressure dependent rate coefficients. J Phys Chem A. 2012;116(24):6051-6058.

145. Praplan AP, Pfannerstill EY, Williams J, Hellén H. OH reactivity of the urban air in Helsinki, Finland, during winter. Atmospheric Environment. 2017;169:150-161.

146. Williams J, Keßel SU, Nölscher AC, Yang Y, Lee Y, Yáñez-Serrano AM, et al. Opposite OH reactivity and ozone cycles in the Amazon rainforest and megacity Beijing: Subversion of biospheric oxidant control by anthropogenic emissions. Atmospheric Environment. 2016;125:112-118.

147. Dolgorouky C, Gros V, Sarda-Esteve R, Sinha V, Williams J, Marchand N, et al. Total OH reactivity measurements in Paris during the 2010 MEGAPOLI winter campaign. Atmospheric Chemistry and Physics. 2012;12(20):9593-9612.

148. Kim S, Guenther A, Karl T, Greenberg J. Contributions of primary and secondary biogenic VOC tototal OH reactivity during the CABINEX (Community Atmosphere-Biosphere INteractions Experiments)-09 field campaign. Atmospheric Chemistry and Physics. 2011;11(16):8613-8623.

149. Michoud V, Hansen RF, Locoge N, Stevens PS, Dusanter S. Detailed characterizations of the new Mines Douai comparative reactivity method instrument via laboratory experiments and modeling. Atmospheric Measurement Techniques. 2015;8(8):3537-3553.

150. Wang N. Carbonyl compounds and their OH reactivities in outdoor and indoor environments: Johannes Gutenberg, Mainz; 2020.

151. National Institute of Standards and Technology CW, SRD 69,,. Pyrrole 2021 (Accessed on the: 14/03/2022) [updated 2021. Available from: https://webbook.nist.gov/cgi/cbook.cgi?ID=C109977&Units=SI&Mask=200#Mass-Spec.

152. KORE TECHNOLOGY Limited. 4GHz time-to-digital converter (TDC) 2014 (Accessed on the: [updated 12th March 2014. Available from: http://www.kore.co.uk/tdc4g.htm.

153. Wròblewski T, Ziemczonek L, Karwasz GP. Proton transfer reactions for ionized water clusters. 2004.

154. Ku HH. Notes on the Use of Propagation of Error Formulas. JOURNAL OF RESEARCH of the National Bureau of Standards. 1966;70C:263-273.

APPENDICES

A.1 Location of the ESRs within the IMPACT network

Figure A.1.1: Location of the ESRs within the IMPACT network
Used from ESR 2: Michal Lacko

Each position was funded by the European Commission through the grant agreement 674911 – IMPACT.

A.2 Beneficiary groups, hosted ESRs and their respective countries

Table A.2.1: Beneficiary groups, hosted ESRs and their respective countries

Organisation	Country	Early Stage Researcher	Country
WP1 – Fundamental science			
Molecular Physics, University of Birmingham	UK	1 – David Olivenza León	ES
J. Heyrovsky Institute of Physical Chemistry, Academy of Sciences of the Czech Republic Research Institute	CZ	2 – Michal Lacko	SK
WP3 – Instrumental and software development			
Ionicon Analytik GmbH	AUT	3 – Felix Piel	DEU
Kore Technology Ltd.	UK	4 – Renaud Dassonville	FRA
WP2 – Applications			
Department of Experimental Physics, Comenius University	SK	5 – Bartosz Michalczuk	POL
Laboratoire des Sciences du Climat et de l'Environnement, Centre National de la Recherche Scientifique	FRA	6 – Sandy Bsaibes	LB
Max Planck Institut für Chemie	DEU	7 – Nijing Wang	CN
Molecular and Laser Physics, Radboud Universiteit Nijmegen	NL	8 – Ben Henderson	UK
Universitätsmedizin Rostock	DEU	9 – Giovanni Pugliese	IT
Institute for Breath Research, Universität Innsbruck	AUT	10 – Michaela Malásková	SK

A.3 Proton affinities and ionisation energies of typical chemicals

Table A.3.1: Proton affinities and ionisation energies of important compounds. ND means no data available.

Base	Formula	Proton affinity	Ionisation energy
Neutral molecules		**(kJ/mol)**	**(eV)**
Helium	He	178	24.59
Neon	Ne	199	21.54
Argon	Ar	369	15.76
Oxygen	O_2	421	12.07
Hydrogen	H2	422	15.43
Krypton	Kr	425	13.99
Nitrogen	N_2	493	15.58
Xenon	Xe	500	12.13
Chlorine atom	Cl	514	12.96
Carbon tetrafluoride	CF_4	529	14.7
Nitric Oxide	NO	532	9.26
Carbon Dioxide	CO_2	541	13.78
Methane	CH_4	543	12.61
Nitrous Oxide	N_2O	550	12.89
Hydrochloric Acid	HCl	557	12.74
Sulphur Hexafluoride	SF_6	575	15.32
Nitrogen Dioxide	NO_2	591	9.59
Carbon Monoxide	CO	594	14.01
Ethane	C_2H_6	596	11.52
Zinc	Zn	608	9.39
Ozone	O_3	625	12.53
n-Propane	C_3H_8	626	10.94
Carbonyl Sulphide	COS	628	11.18
Silane	SiH_4	640	11
Butane	C_4H_{10}	661	10.53
Bromomethane	CH_3Br	664	10.54
Sulphur Dioxide	SO_2	672	12.35
n-Pentane	C_5H_{12}	673	10.28
iso-Butane	C_4H_{10}	677	10.68/10.94
Heptane	C_7H_{16}	678/710	9.93
Ethylene	C_2H_4	681	10.51
Carbon Disulphide	CS_2	682	10.07
Octane	C_8H_{18}	684/730	9.8
Nonane	C_9H_{20}	686	9.71
Cyclohexane	C_6H_{12}	687	9.88
Hexane	C_6H_{14}	690/691	10.13
Decane	$C_{10}H_{22}$	691	9.65
Water	H_2O	691	12.62

Undecane	$C_{11}H_{24}$	692	9.56
Dodecane	$C_{12}H_{26}$	692	9.48
Ethylene Chloride	C_2H_5Cl	693	11.07
Hydrogen Sulphide	H_2S	709	10.45
Hydrogen Cyanide	HCN	712	13.6
Formaldehyde	CH_2O	713	10.88
Benzene	C_6H_6	750	9.25
Propene	C_3H_6	752	9.73
Chlorobenzene	C_6H_5Cl	753	9.07
Methanol	CH_3OH	754	10.84
Acetaldehyde	C_2H_4O	768.5	10.23
Methanethiol	CH_4S	773.4	9.44
Ethanol	C_2H_5OH	776	10.48
1,3-Butadiene	C_4H_6	783	9.07
Toluene	C_7H_8	784	8.82
Phosphine	PH_3	785	9.87
Propanol	C_3H_7OH	786	10.22
Ethylbenzene	C_8H_{10}	788	8.77
n-Butylbenzene	$C_{10}H_{14}$	792	8.7
p-Xylene	C_8H_{10}	794	8.56
Pentanal	$C_5H_{10}O$	797	9.74
1,4-Dioxane	$C_4H_8O_2$	797	9.19
2-propenal	C_3H_4O	797	10.1
Naphthalene	$C_{10}H_8$	803	8.14
Water Dimer	H_4O_2	808	ND
Acetone	C_3H_6O	812	9.7
Chloroethene	C_2H_3Cl	815	10
Dimethyl disulphide	$C_2H_6S_2$	815.3	7.4
Dimethyl sulphide	C_2H_6S	831	8.7
Ethyl Acetate	$C_4H_8O_2$	836	10.01
Styrene	C_8H_8	839.5	8.46
MTBE	$C_5H_{12}O$	841.6	ND
Ammonia	NH_3	854	10.07
Triethyl Phosphate	$C_6H_{15}O_4P$	909	10.5
Indole	C_8H_7N	933.4	7.76
Trimethylamine	C_3H_9N	949	7.85
Silver	Ag	ND	7.57
1,2,4-Trichlorobenzene	$C_6H_3Cl_3$	ND	9.04
Gold	Au	ND	9.22
Tridecane	$C_{13}H_{28}$	ND	9.42
iso-Pentane	C_5H_{12}	ND	10.32
Mercury	Hg	ND	10.44
Chlorine	Cl_2	ND	11.48

A.4 Schematic of the SCI-ToF-MS

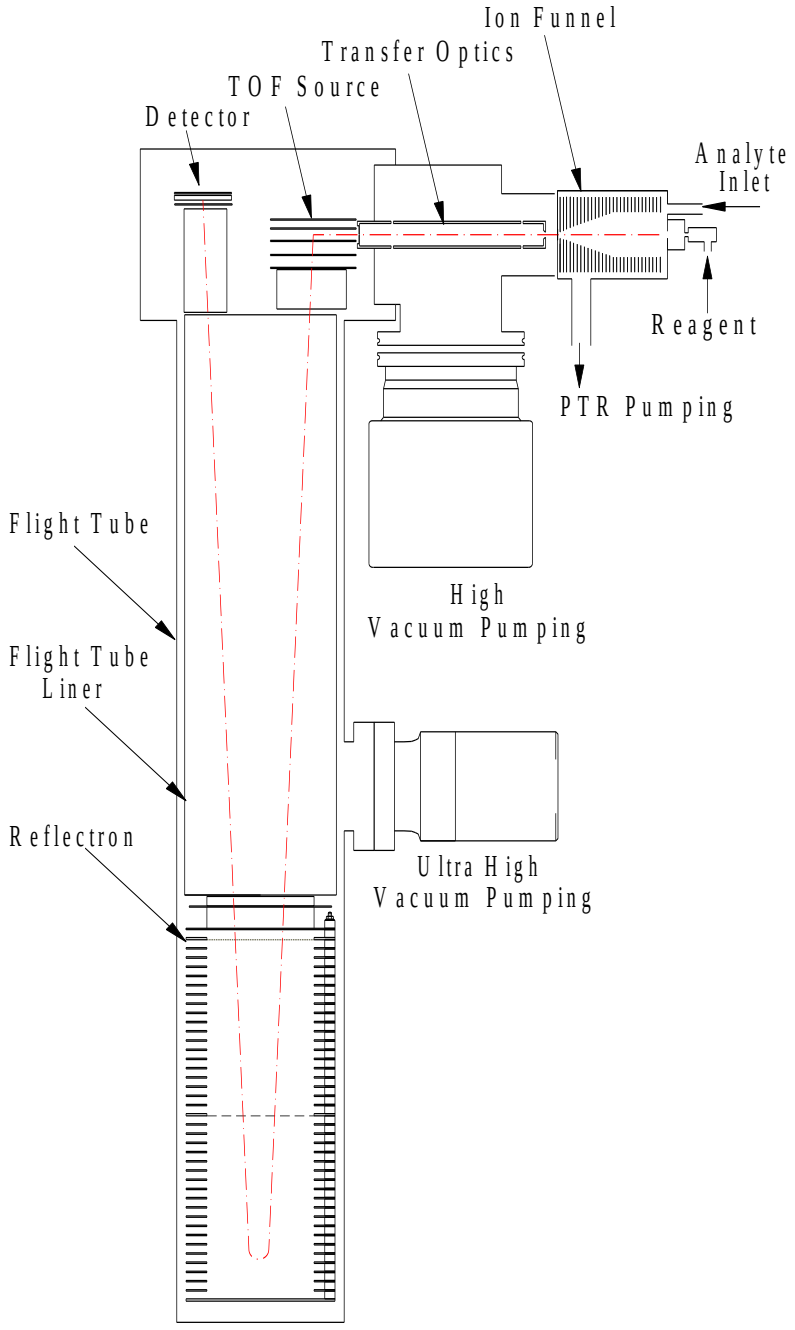

Figure A.4.1: General schematic of the SCI-ToF-MS

A.5 Presentation of detectors and TDC technologies and methodology

The simplest ion detector is a Faraday cup, i.e. a single electrode where the ions deposit their charge and the generated electric current flows through a high impedance resistor creating the voltage which is used to measure the ion flux [37]. Such detectors are suitable for high ion currents of several picoamperes or more, but are not suitable for the ToF experiment where, as a result of the 'duty cycle' of pulsing, the ion currents are much lower. With the emergence of scanning mass spectrometers such as quadrupole mass analysers (meaning the analyser is regularly cycled to permit transmission and detection of ions of certain m/z values [40]), secondary electron multipliers (SEM) became common [37] to make single ion detection possible. SEM's process is based on the high probability that the impact of ions on a solid surface leads to emission of electrons, called secondary electrons, which under an accelerating potential strike further surfaces releasing yet more electrons until sufficient amplification has been achieved to enable an output current to be measured [37]. There are typically 15-25 stages of amplification in such a detector with typically 100 V potential difference at each stage, resulting in a detector gain of approximately 2 kV across the whole of the detector. The ion-to-electrons conversion process requires (a) that the impact energy of the ion is greater than a few hundred eV. In the research PTR, the impact energy is approximately 2 keV, and (b) that the secondary electron coefficient of the material in the detector surfaces is greater than 1 to permit the electron cascade to occur.

The electron amplification process is achieved in the research PTR instrument using a dual micro channel plate detector (DMCP). This detector was composed of a million 10 μm channels separated by 12 μm to each other providing an active circular area with a diameter of 25 mm. Commercial DMCPs provide characteristics within the same ranges [65].

The gain of a single plate is 10^3-10^4 which is lower than other SEMs, that is why 2 plates are sandwiched together to provide gains of 10^6-10^7. To make the cascade effect possible, the channels need to have a certain angle compared to the surface of the front plate with an opposite inclination of the channels of the 2nd plate. This configuration is called a Chevron plate. It is also possible to assemble 3 plates with the channels of a 3rd plate parallel to those of the 1st one. This is called a z stack [37]. MCP channels are coated with a high secondary electron coefficient semiconductor substance to maximise the cascade effect, typically lead oxide [65]. Notice this coefficient must be greater than 1 to generate secondary electrons. As well as presenting a larger surface area for the ions compared to other detectors, the MCP has also the advantage to be relatively thin. Unlike other SEM devices, the MCP should be kept under vacuum so as to limit the ingress of water molecules into the channels. If left unchecked, a MCP is so hygroscopic that even in normal laboratory air it can absorb enough water in a week or two to 'self-crack'. Also (D)MCP must be kept perpendicular to the incoming ions trajectories to avoid extending the ToF of certain ions, which would result in mass resolution losses. The performance of a detector is described through its gain G.

At Kore and since 2010, 4 GHz TDCs have been in use for ToF-MS, offering a time resolution of 250 ps, which is, compared to the previous 0.5 GHz TDC (i.e. 2 ns resolution), a resolution enhancement of 8 [152]. Any signal, converted by a TDC, can also be impacted by the condition of the surface within the detector. One of the principal ageing mechanisms of these detectors is the slow degradation in the secondary electron coefficient of the channel surfaces, mainly due to deposition of carbon. For this reason, the life of a DMCP detector is influenced by the level of vacuum that can be maintained at the detector. Nevertheless, ageing will take place, requiring that the detector gain be increased from time to time, until the maximum value of gain is reached (usually limited by voltage breakdown at values such as 3.3

kV) [63]. Once this gain's plateau is reached, the performances of the detector can only decrease with time and the detector should be replaced.

To maximize the lifetime of the MCP, the "60 % rule" is usually followed at Kore. For a given ion at a given setting, the signal is measured. The voltage across the MCP is then increased by 60 V. If the signal increases by more than 60 %, the gain is too low and by less than 60 %, the gain is too high. The typical evolution of the signal as a function of the gain voltage is presented in Figure A.5.1:

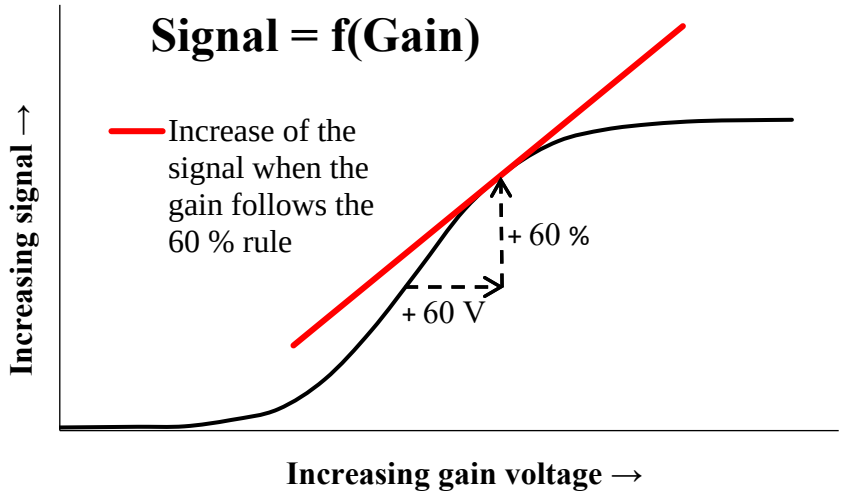

Figure A.5.1: Signal of a single peak as a function of the gain voltage – 60 % rule

The other aspect affecting the reliability of a measurement is counting saturation. Indeed, the time taken from ion arrival at the detector front surface to the event being recorded by the TDC is the 'dead time' of the system and is typically on the order of 20-25 ns. During this time, if another ion arrives at the detector, it cannot be counted because the signal from the previous ion has not yet been processed. This situation only occurs if two ions in a single ToF cycle are separated in their time of flight by less than 20 ns, such as when two ions of the same m/z arrive at the detector in the same ToF cycle. In such a case, the ion counting process suffers a 'dead time loss'. As the count rate increases there is an increasing chance that ions arrive during the

dead time of a detection event. This is most pronounced when there are ‘particularly intense’ peaks in the spectrum. Thus, for example, if the pulsing frequency of the ToF experiment is 20 kHz, then if the measured count rate on a single mass peak is 20 kc/s (i.e. one ion is recorded every ToF cycle at a given m/z), then there is significant dead-time losses because the ions of that m/z do not arrive in a perfect sequence of 1 ion per ToF cycle, but in a sequence such as: 0, 1, 1, 2, 0, 3, 1 ,1, 0. This situation is addressed by Poisson statistics, and the dead-time losses are predictable for large numbers of ion counts.

The graphical representation of dead-time losses due to Poisson statistics in a pulse counting system is presented in Figure A.5.2 and Figure A.5.3, and comes from internal data at Kore. It indicates that even at small fractions of the ToF cycle repetition rate, dead-time losses occur, and do so with greater magnitude as the measured count rate for a single m/z rises toward the ToF cycle repetition rate.

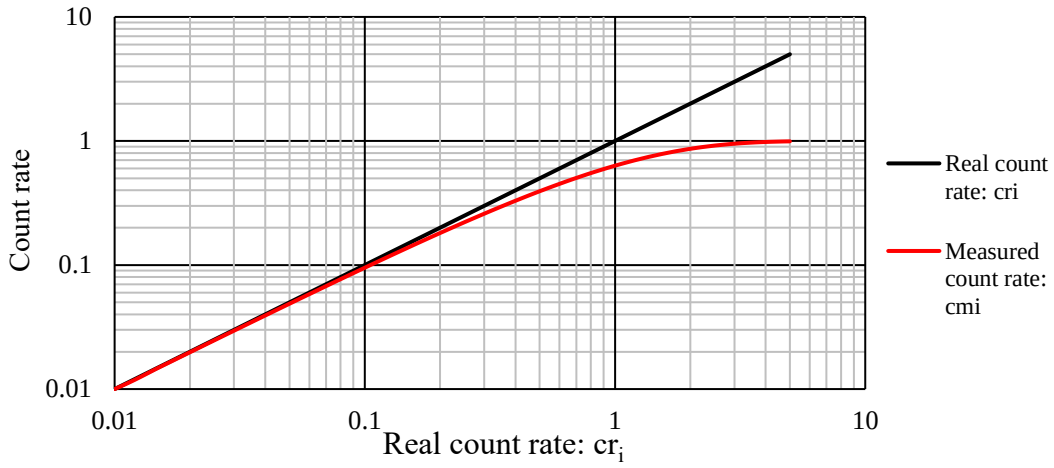

Figure A.5.2: Link between real and measured count rates through dead-time losses in counting saturation

In a pulse counting system any comparison of peak integrals for the purpose of comparison or quantification must take this phenomenon into account. In the deconvolution software designed

in parallel with this thesis and presented later, the first step in the data treatment is a dead-time correction (saturation correction) of the mass spectral data using Poisson statistics.

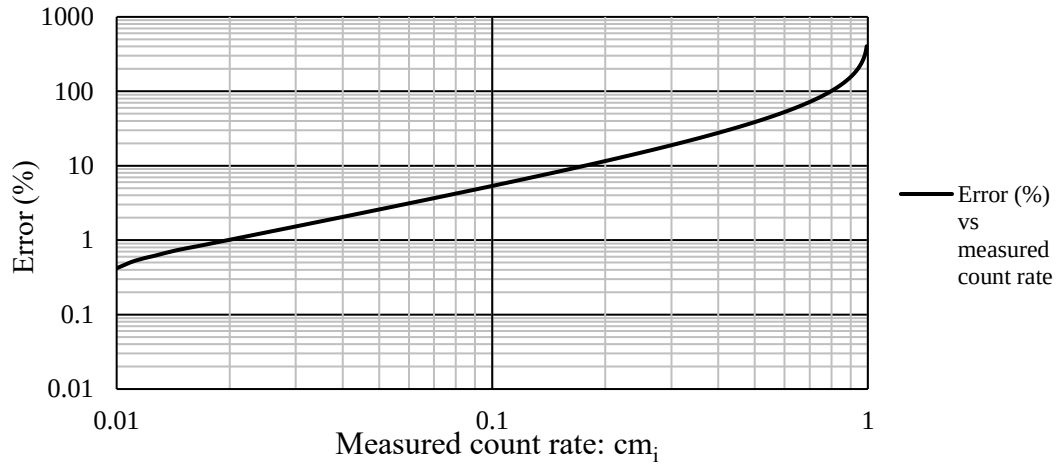

Figure A.5.3: Error between real and measured count rates through dead-time losses in counting saturation

A.6 Water ions distributions as a function of E/n using Mark II, IV and V ion-funnels

Figure A.6.1-Figure A.6.3 provide data using a Mark II ion-funnel for the three cases.

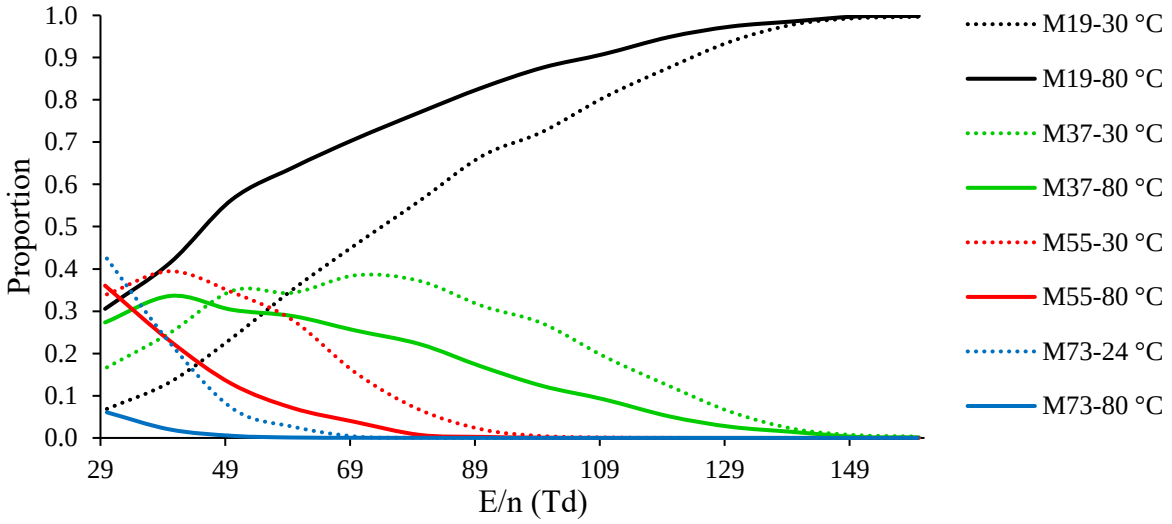

Figure A.6.1: Case 1 – Distributions of water ions as a function of E/n using a **Mark II ion-funnel drift tube** operating at a constant pressure of 0.8 mbar and at two temperatures: 30 and 80 ºC

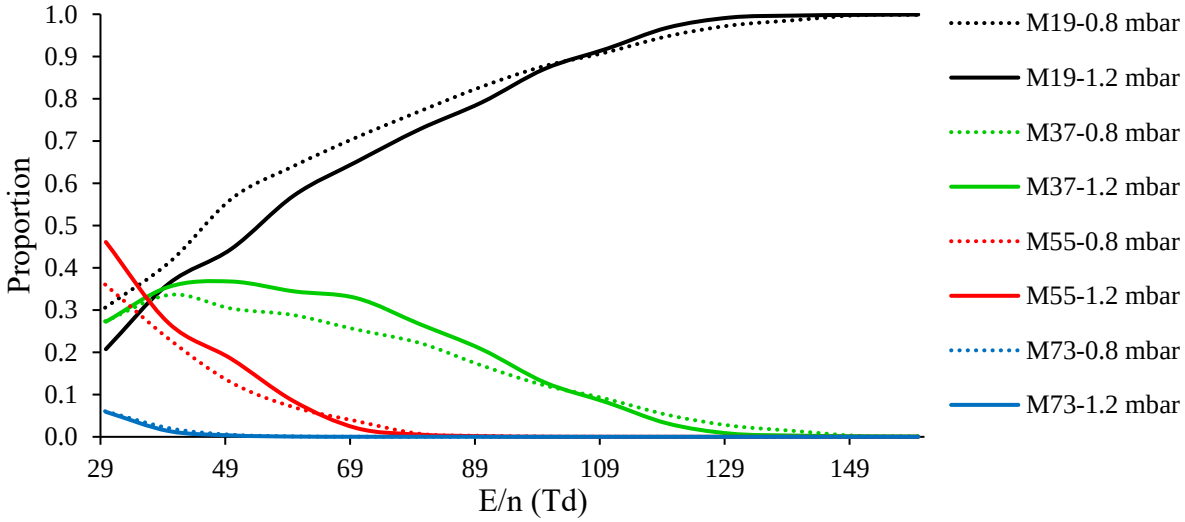

Figure A.6.2: Case 2 – Distributions of water ions as a function of E/n using a **Mark II ion-funnel drift tube** operating at a constant temperature of 80 ºC and at two pressures: 0.8 and 1.2 mbar

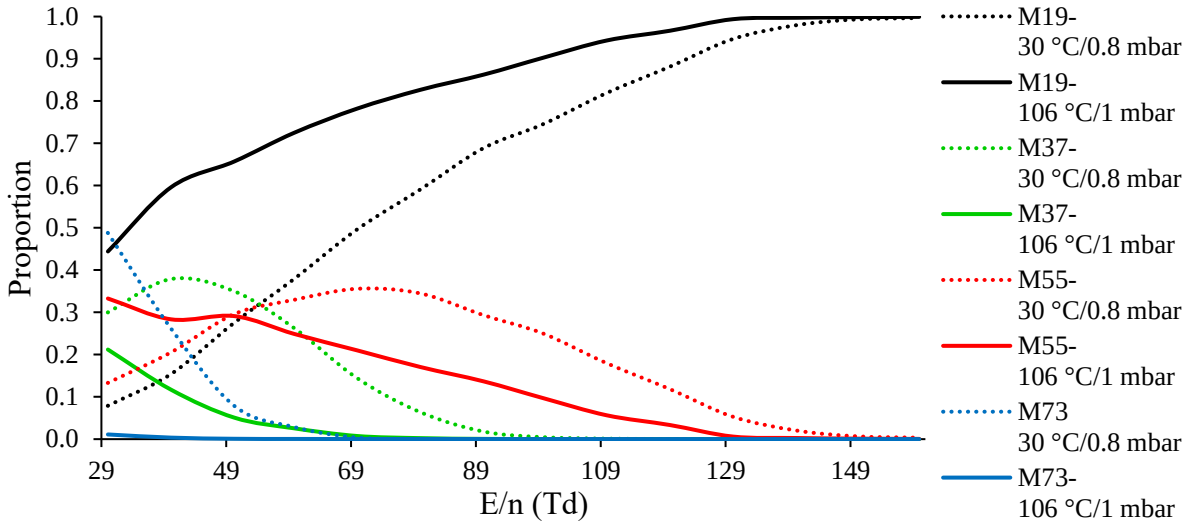

Figure A.6.3: Case 3 – Distributions of water ions as a function of E/n using a **Mark II ion-funnel drift tube** for which the E field was kept constant and the temperature and pressure were modified to provide the same n, and hence the same E/n.

Figure A.6.4-Figure A.6.6 provide data using a Mark IV ion-funnel for the three cases.

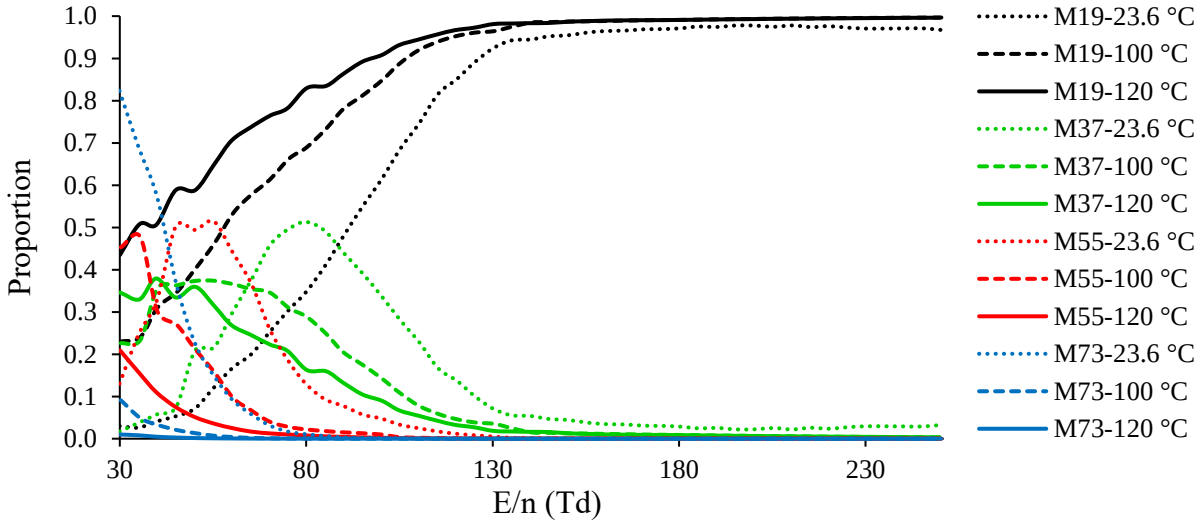

Figure A.6.4: Case 1 – Distributions of water ions as a function of E/n using a **Mark IV ion-funnel drift tube** operating at a constant pressure of 0.8 mbar and at three temperatures: 23.6, 100 and 120 ºC

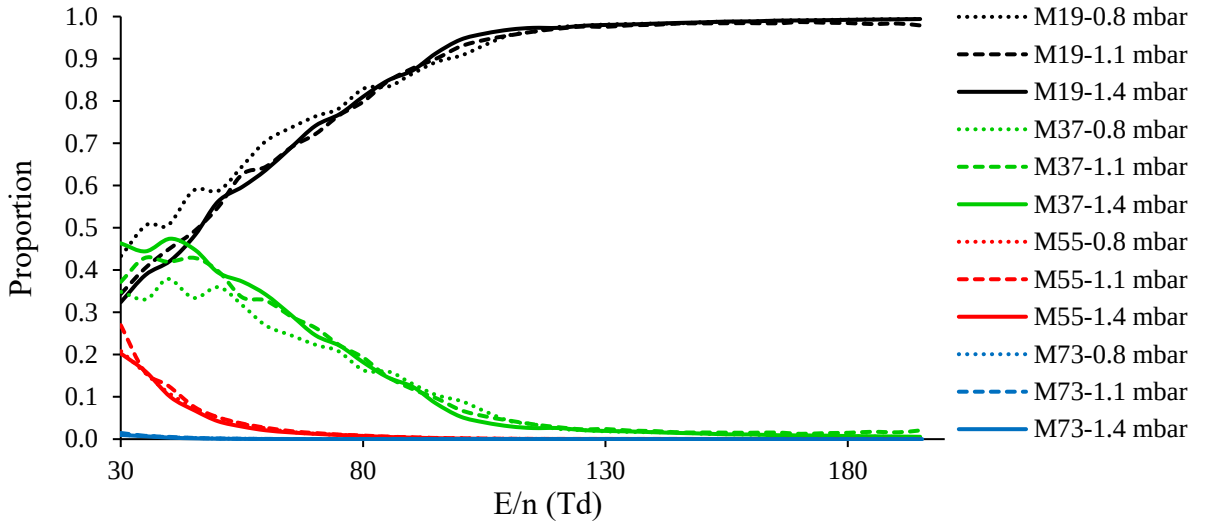

Figure A.6.5: Case 2 – Distributions of water ions as a function of E/n using a **Mark IV ion-funnel drift tube** operating at a constant temperature of 130 ºC and at three pressures: 0.8 and 1.1 and 1.4 mbar

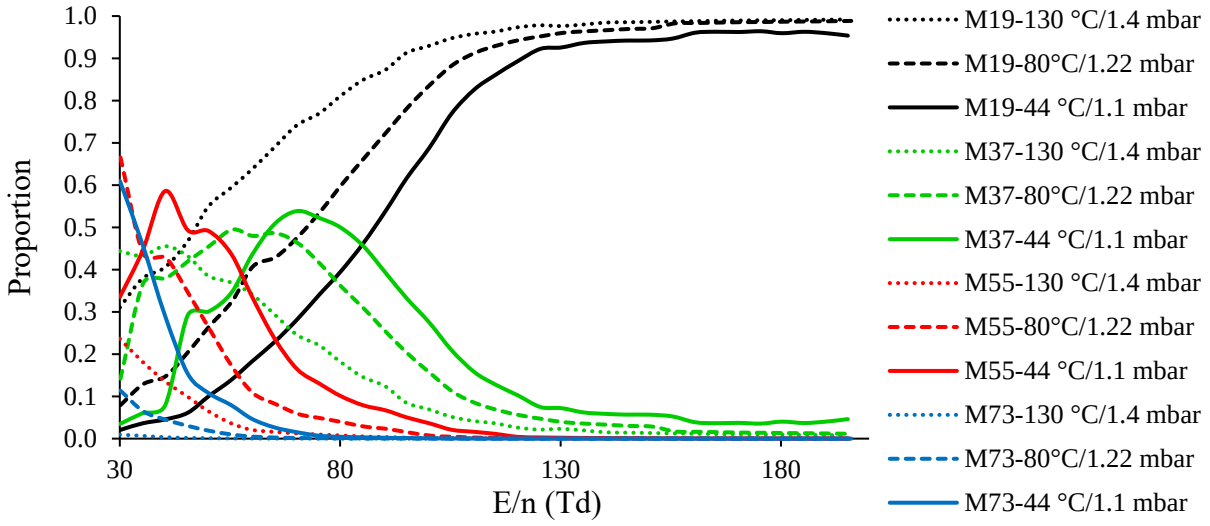

Figure A.6.6: Case 3 – Distributions of water ions as a function of E/n using a **Mark IV ion-funnel drift tube** for which the E field was kept constant and the temperature and pressure were modified to provide the same n, and hence the same E/n.

Figure A.6.7-Figure A.6.9 provide data using a Mark V ion-funnel for the three cases.

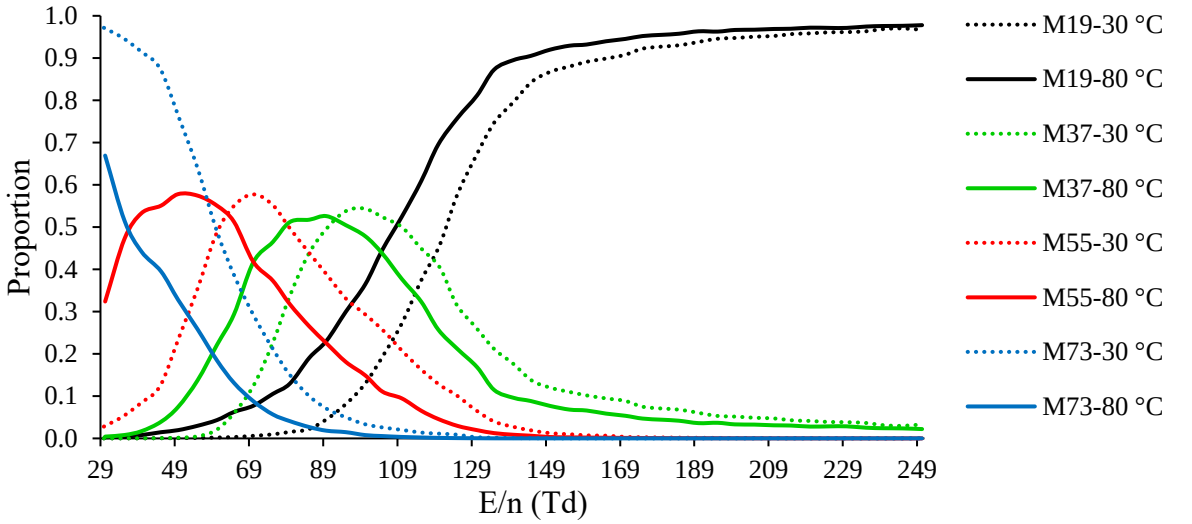

Figure A.6.7: Case 1 – Distributions of water ions as a function of E/n using a **Mark V ion-funnel drift tube** operating at a constant pressure of 0.8 mbar and at two temperatures: 30 and 80 ºC

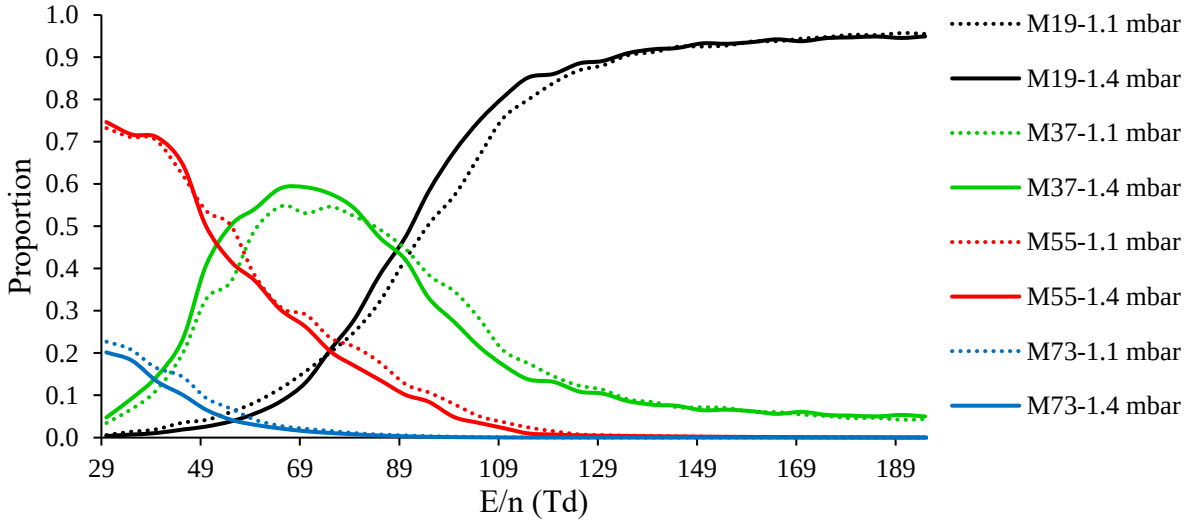

Figure A.6.8: Case 2 – Distributions of water ions as a function of E/n using a **Mark V ion-funnel drift tube** operating at a constant temperature of 130 ºC and at two pressures: 1.1 and 1.4 mbar

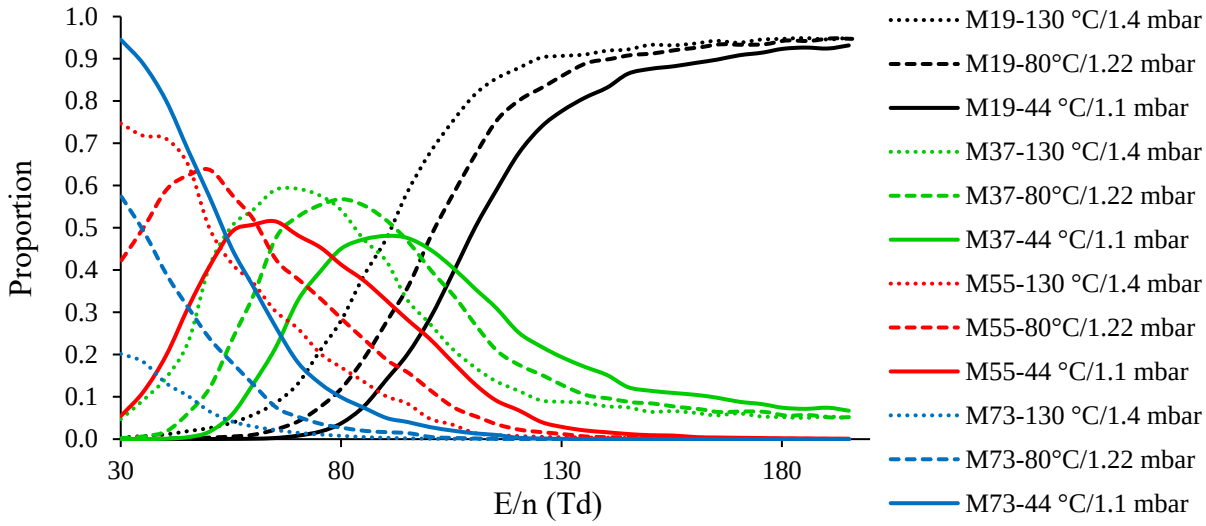

Figure A.6.9: Case 3 – Distributions of water ions as a function of E/n using a **Mark V ion-funnel drift tube** for which the E field was kept constant and the temperature and pressure were modified to provide the same n, and hence the same E/n.

A.7 Water ions signal intensities as a function of E/n using Mark I, II, IV and V ion-funnels

Figure A.7.1-Figure A.7.3 provide data using a Mark I ion-funnel for the three cases.

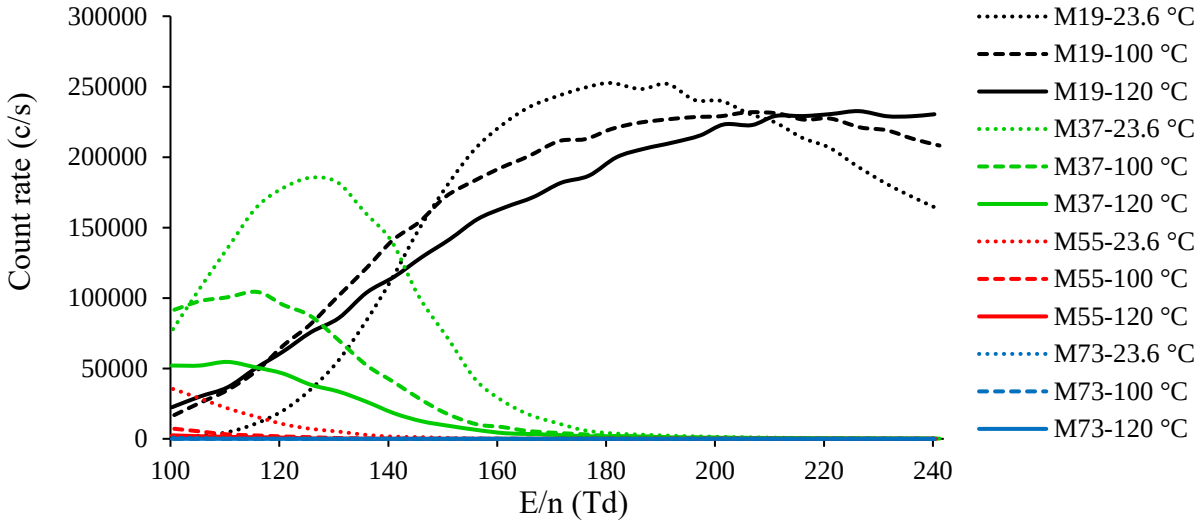

Figure A.7.1: Case 1 – Signal intensities of water ions as a function of E/n using a **Mark I ion-funnel drift tube** operating at a constant pressure of 0.8 mbar and at three temperatures: 23.6, 100 and 120 ºC.

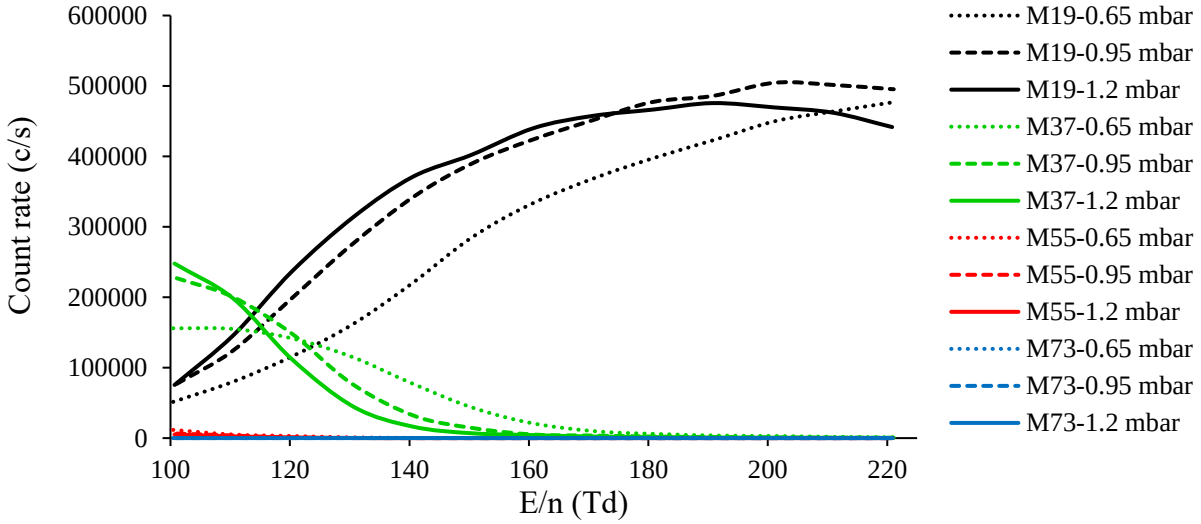

Figure A.7.2: Case 2 – Signal intensities of water ions as a function of E/n using a **Mark I ion-funnel drift tube** operating at a constant temperature of 125 ºC and at three pressures: 0.65, 0.95 and 1.2 mbar

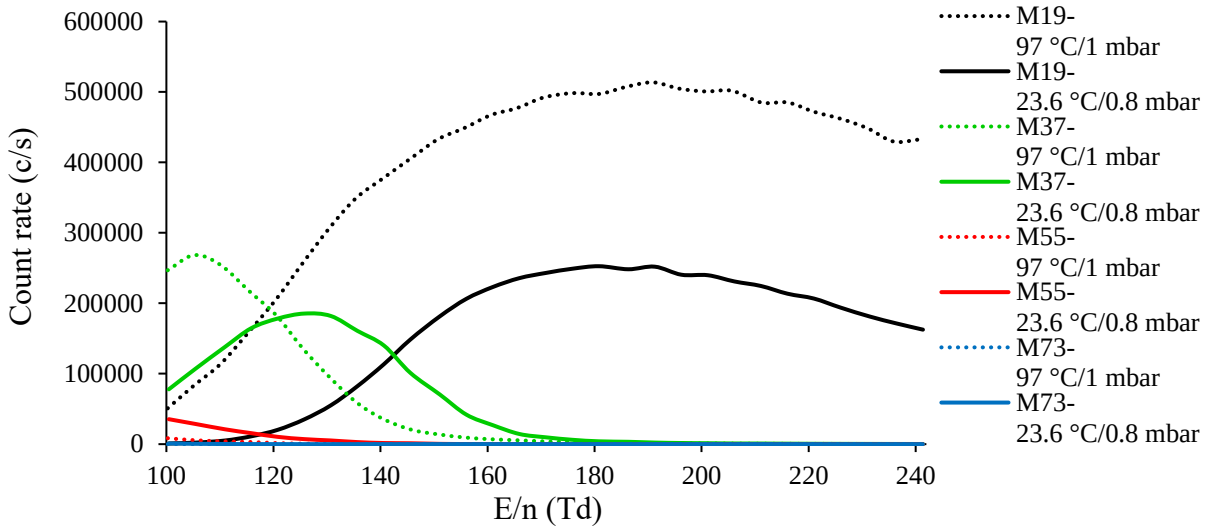

Figure A.7.3: Case 3 – Distributions of water ions as a function of E/n **Mark I ion-funnel drift tube** for which the E field was kept constant and the temperature and pressure were modified to provide the same n, and hence the same E/n.

Figure A.7.4-Figure A.7.6 provide data using a Mark II ion-funnel for the three cases.

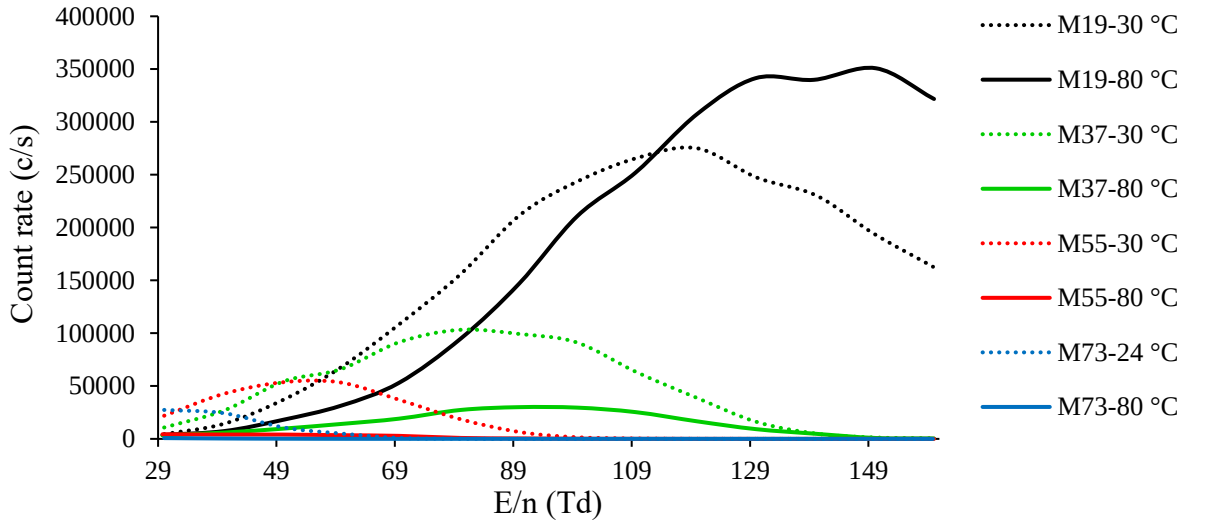

Figure A.7.4: Case 1 – Signal intensities of water ions as a function of E/n using a **Mark II ion-funnel drift tube** operating at a constant pressure of 0.8 mbar and at two temperatures: 30 and 80 ºC

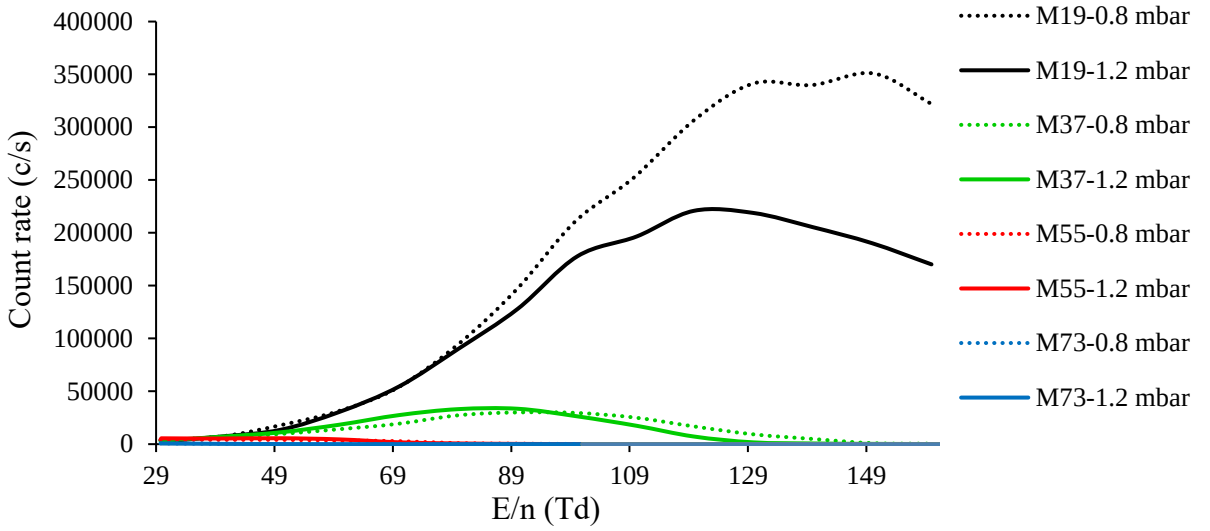

Figure A.7.5: Case 2 – Signal intensities of water ions as a function of E/n using a **Mark II ion-funnel drift tube** operating at a constant temperature of 80 ºC and at two pressures: 0.8 and 1.2 mbar

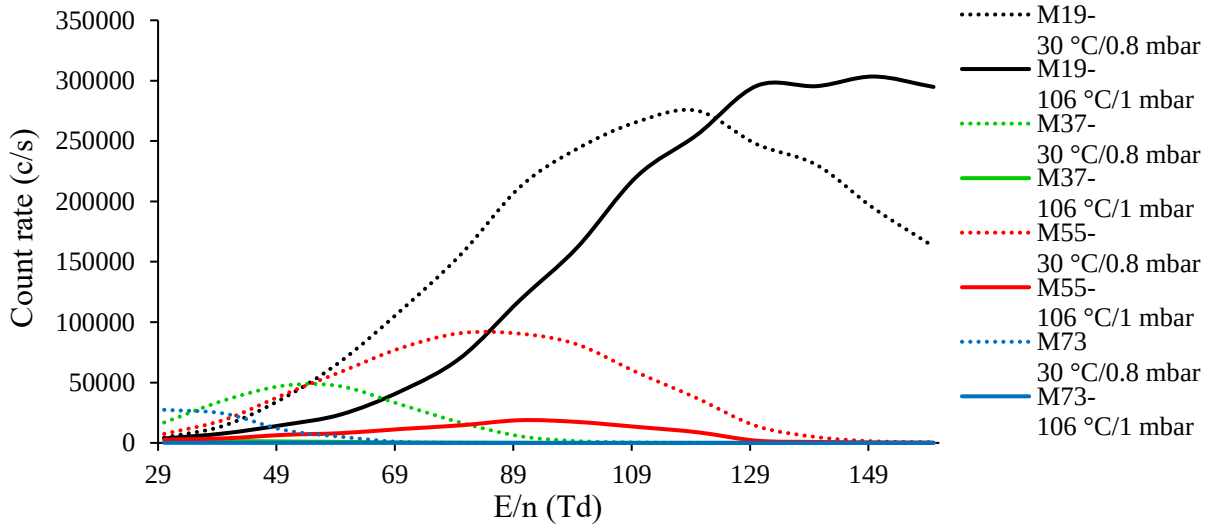

Figure A.7.6: Case 3 – Signal intensities of water ions as a function of E/n using a **Mark II ion-funnel drift tube** for which the E field was kept constant and the temperature and pressure were modified to provide the same n, and hence the same E/n.

Figure A.7.7-Figure A.7.9 provide data using a Mark IV ion-funnel for the three cases.

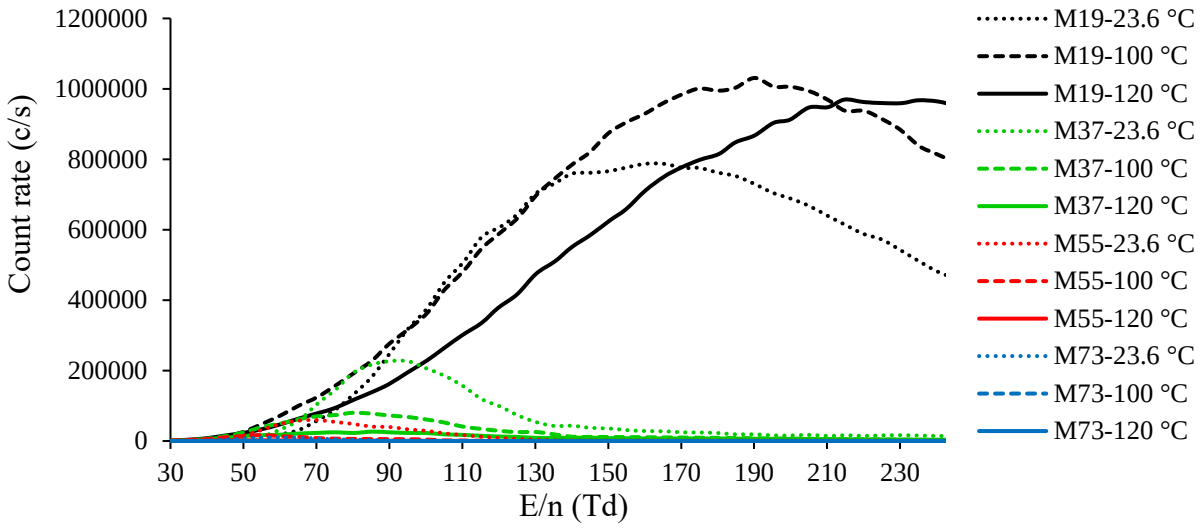

Figure A.7.7: Case 1 – Signal intensities of water ions as a function of E/n using a **Mark IV ion-funnel drift tube** operating at a constant pressure of 0.8 mbar and at three temperatures: 23.6, 100 and 120 ºC

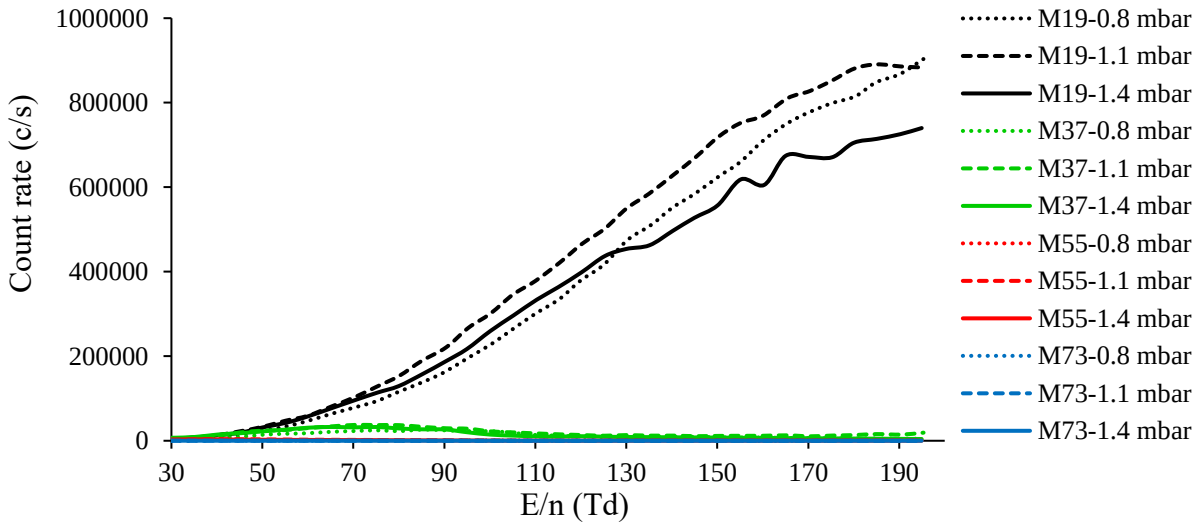

Figure A.7.8: Case 2 – Signal intensities of water ions as a function of E/n using a **Mark IV ion-funnel drift tube** operating at a constant temperature of 130 ºC and at three pressures: 0.8 and 1.1 and 1.4 mbar

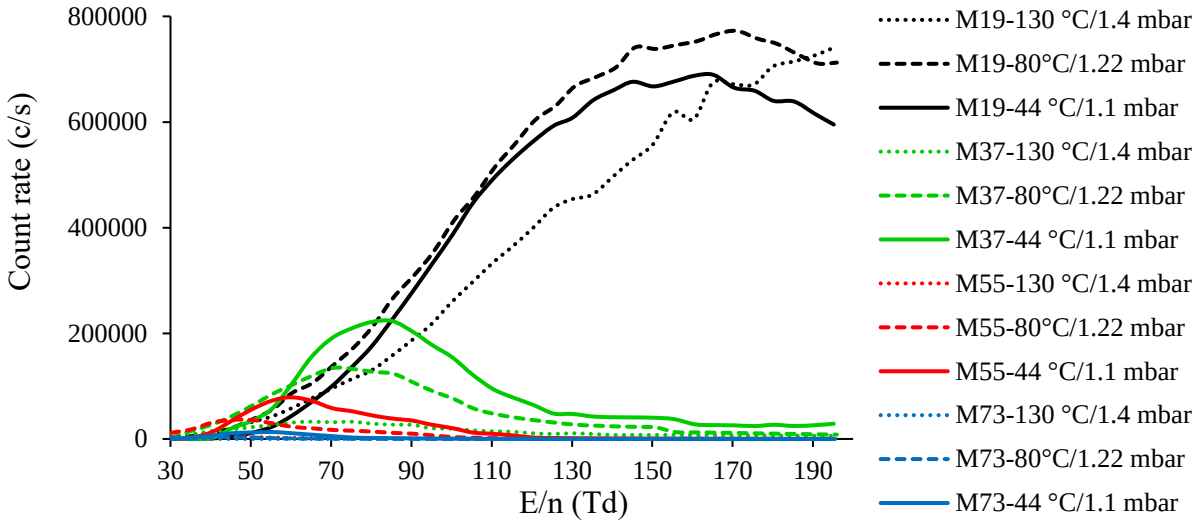

Figure A.7.9: Case 3 – Signal intensities of water ions as a function of E/n using a **Mark IV ion-funnel drift tube** for which the E field was kept constant and the temperature and pressure were modified to provide the same n, and hence the same E/n.

Figure A.7.10-Figure A.7.12 provide data using a Mark V ion-funnel for the three cases.

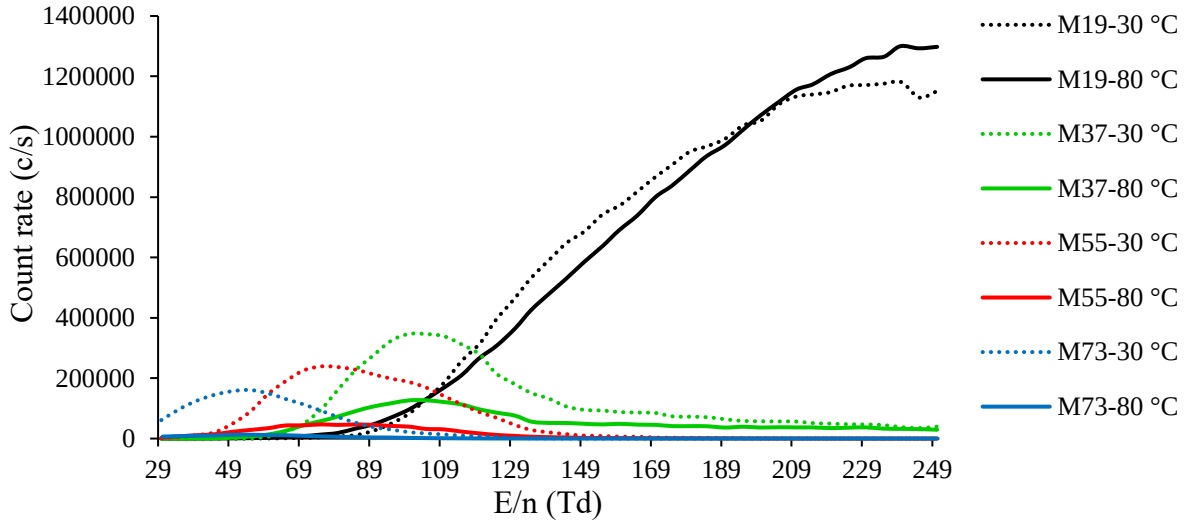

Figure A.7.10: Case 1 – Signal intensities of water ions as a function of E/n using a **Mark V ion-funnel drift tube** operating at a constant pressure of 0.8 mbar and at two temperatures: 30 and 80 ºC

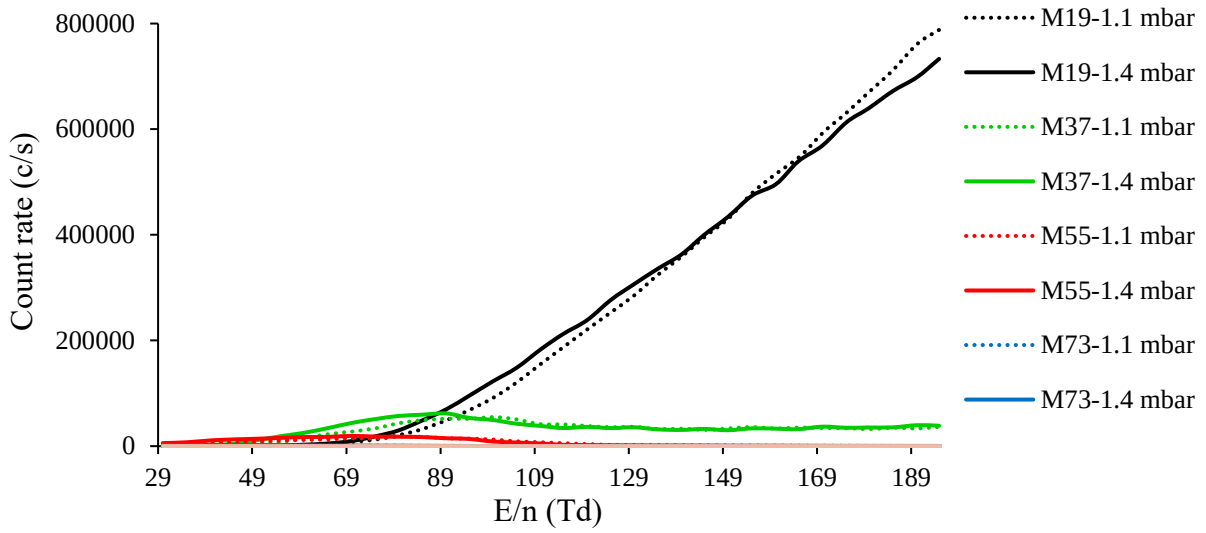

Figure A.7.11: Case 2 – Signal intensities of water ions as a function of E/n using a **Mark V ion-funnel drift tube** operating at a constant temperature of 130 ºC and at two pressures: 1.1 and 1.4 mbar

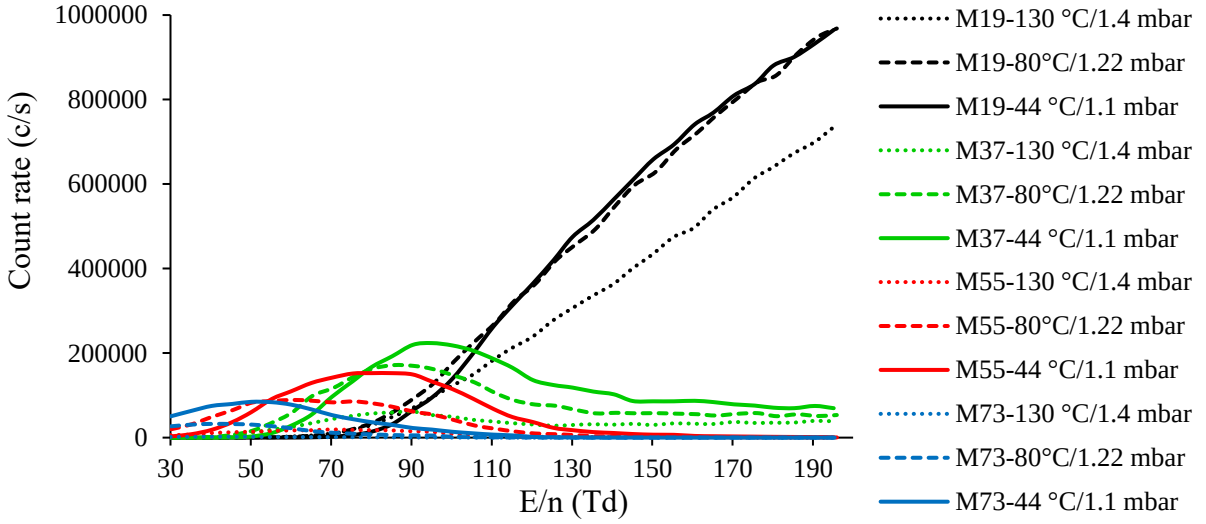

Figure A.7.12: Case 3 – Signal intensities of water ions as a function of E/n using a **Mark V ion-funnel drift tube** for which the E field was kept constant and the temperature and pressure were modified to provide the same n, and hence the same E/n.

A.8 A discussion on how the ionisation and fragmentation of analytes with high proton affinities can be affected when water ions other than hydronium are involved.

A.8.1 Water reagent ions

Attempts to find an analytical alternative to E/n using the E_k(CM) parameter have been partially successful in reducing the observed shifts in these curves. The E_k(CM) approach sought to accommodate both primary (water ions with neutral analyte) and secondary reactions (protonated analyte with nitrogen) and their associated collisional energies. It focused mainly on including the secondary reactions.

The ion energetics of TEP add yet another complexity to any attempt to understand changes in the PIDs as a function of E/n. TEP has a proton affinity of 909 kJ/mol. At high energies in the reactor, H_3O^+ dominates, but as the collision energy decreases through (any combination of) E, T and P, the proportions of dimer, trimer and quaternary water ions increase. An analyte molecule such as TEP can be protonated by a water dimer ion (PA($(H_2O)_2$) = 808 kJ/mol), and if it is, the excess energy in that collision will be much less than with H_3O^+ (PA(H_2O) = 691 kJ/mol), resulting in a softer ionisation. Calculated values for the proton affinity of the water trimer show only a relatively small increase in proton affinity compared to the dimer [153], and so it is quite possible that the water trimer ion can also protonate TEP, with presumably an even softer ionisation. As the proportions of the water reagent ions change with E/n, so will the fragmentation patterns for a molecule such as TEP. In this approach therefore, an effort has been put in to characterising more fully the effects of the changing proportions of these water ions on the ionisation and fragmentation of the TEP molecule.

To express the changing proportions of these water ions as the collision energy changes, a simple parameter is defined. The parameter '1 divided by 1 minus the hydronium ion proportion', called the water ions parameter (WIP), ranges from 1 at low E/n values to >1500

as the hydronium proportion moves closer to 1 at high E/n values. This WIP is expressed in E A.8.1:

$$\text{WIP} = \left(1 - \frac{\text{Intensity}(H_3O^+)}{\text{Intensity}(H_3O^+ + H_3O^+.H_2O + H_3O^+.(H_2O)_2 + H_3O^+.(H_2O)_3)}\right)^{-1} \quad \text{E A.8.1}$$

This is the parameter that is used on the x-axis in the upcoming graphs. The form of these plots has a very different appearance to the previously plotted curves, but nevertheless, the purpose is to see if the curves for each ion overlay, irrespective of the E, T and P conditions that gave the ratio of these water ions.

Once the new plots have been presented, a comparison will be made of the ΔProp. parameter across the three methods of data plotting.

A.8.2 Results – Triethylphosphate – Mark I reactor: DC-only mode

A.8.2.1 Case 1 – Pressure constant at 0.8 mbar and three temperatures: 23.6, 100 and 120 ºC

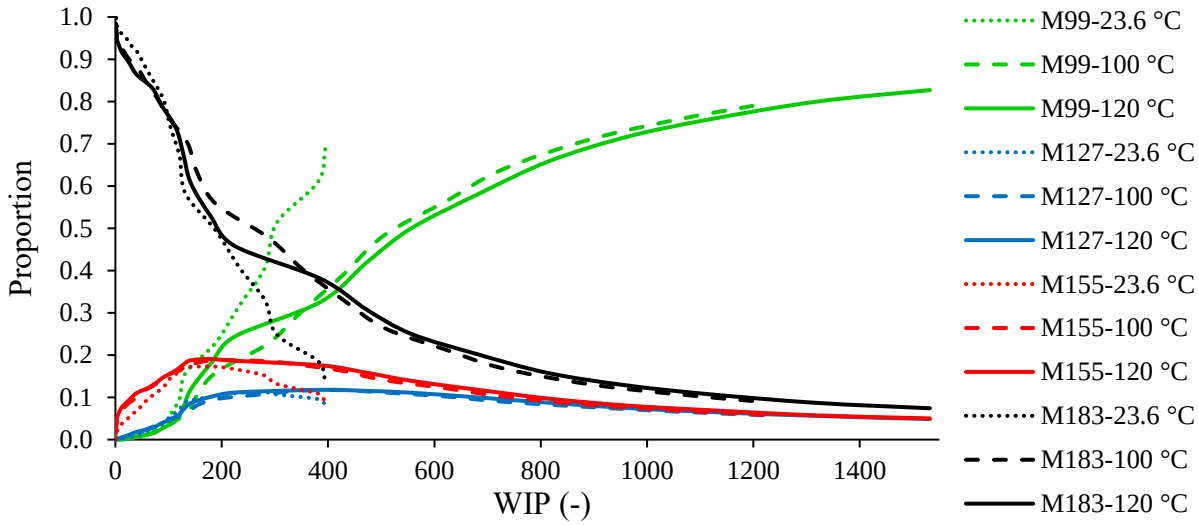

Figure A.8.1: Mark I ion-funnel – PID for triethylphosphate as a function of the water ions parameter, pressure constant (this plot may be compared with Figure 5.16)

A.8.2.2 Case 2 – Temperature constant at 125 ºC and three pressures: 0.65, 0.95 and 1.2 mbar

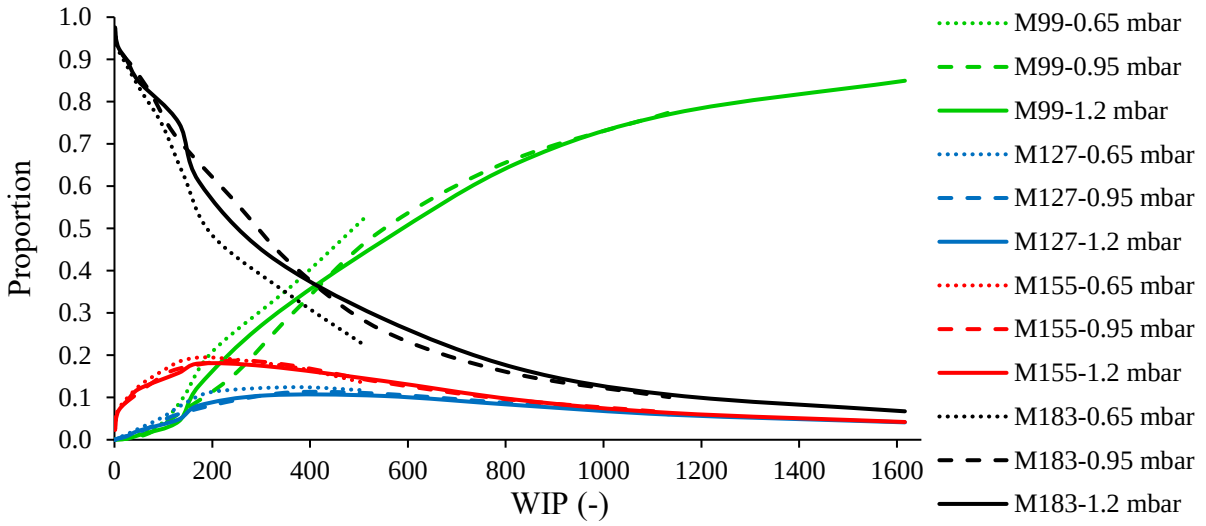

Figure A.8.2: Mark I ion-funnel – PID for triethylphosphate as a function of the water ions parameter, temperature constant (this plot may be compared with Figure 5.17)

A.8.2.3 Case 3 – At each E/n value: Electric field constant and two different combinations of temperature and pressure to achieve the same n and E/n

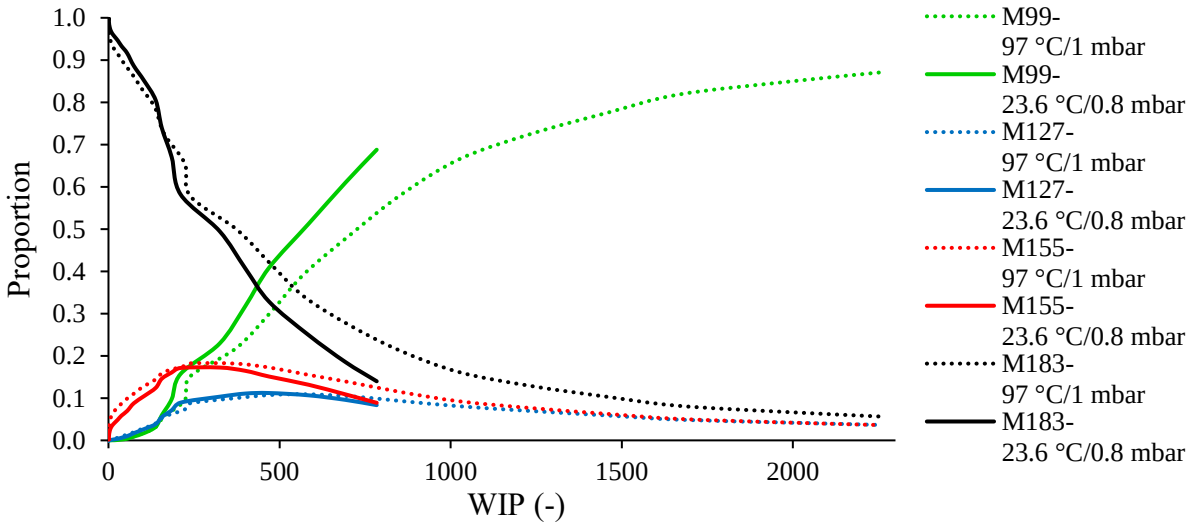

Figure A.8.3: Mark I ion-funnel – PID for triethylphosphate as a function of the water ions parameter, number density and E/n constant (this plot may be compared with Figure 5.18)

The data plotted with the water ions parameter on the x-axis showed further correction compared to the E_k(CM) correction. In order to make a more quantitative comparison between the different methods used to correct the shifts in the PID curves, it is informative to compare the Δprop.max regarding the protonated analyte for the experiments as shown in Table A.8.1:

Table A.8.1: Maximum variations of the protonated triethylphosphate proportion as a function of the parameter used on the x-axis

Maximum difference of proportion (Δprop.max) of the protonated parent molecule for a given analyte and reactor (green: decrease of values, red: increase of values, both from E/n)				
Analyte molecule	**Reactor generation (DC-only mode)**	**Parameter used to express the PID of the analyte**		
		E/n	**E_k(CM)**	**Water ions parameter**
triethylphosphate	**I**	0.60 ± 2.38 %	0.55 ± 2.31 %	0.30 ± 5.72 %

The water ions parameter presents the smallest Δprop.max of the TEP protonated analyte (0.30 ± 5.72 %) and is even equal to 0.15 ± 14.9 % comparing 8 curves out of the 9 ones presented. Notice the RSDs are calculated according to the method presented in Appendix A.11. In the case of TEP the form of the PID curves will be greatly affected by the reagent ion proportions, for reasons given above. Thus, in the case of an analyte such as TEP with a high proton affinity, i.e. greater than 900 kJ/mol, accounting for changes in the reagent ion proportions is important in understanding the form of the PID.

It is not suggested that this approach has fundamental explanatory power, since the reason why water ion proportions should vary at all for the same calculated E/n is not explained.

A.9 Plotting n-butylbenzene PIDs as a function of E/n (Marks IV and V reactors)

In this appendix, the full data set that was collected in the E/n studies is shown as evidence to support the claims that PIDs plotted as a function of E/n do not overlay when the E/n value is produced using different values of E, T and P. As in the body text, the curves are fits to data points recorded every 10 Td (and not 5 Td like for Mark I anymore). These have been removed for convenience of comparison. This applies to all plots shown subsequently.

Figure A.9.1-Figure A.9.3 provide data for the Mark IV ion-funnel.

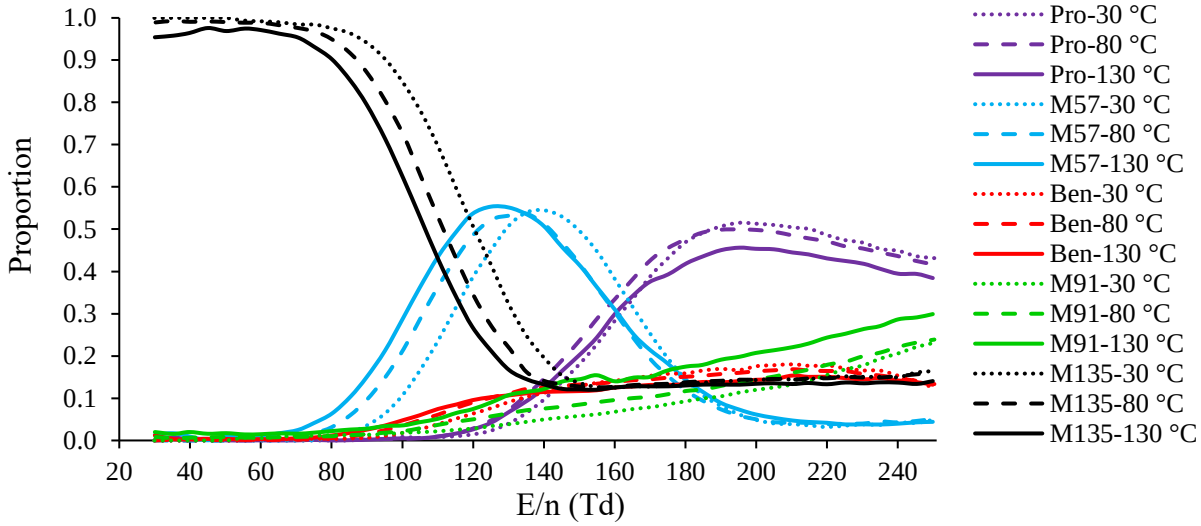

Figure A.9.1: Case 1 – PIDs for n-butylbenzene as a function of E/n with the **Mark IV ion-funnel drift tube** operating at a constant pressure of 0.8 mbar and at three temperatures: 30, 80 and 130 ºC.

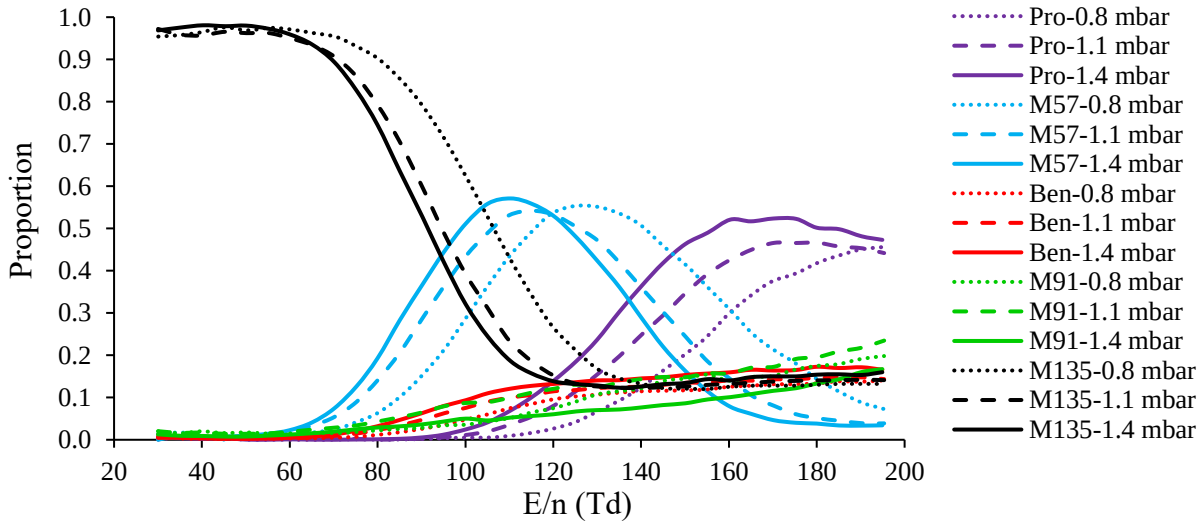

Figure A.9.2: Case 2 – PIDs for n-butylbenzene as a function of E/n using the **Mark IV ion-funnel drift tube** operating at a constant temperature of 125 ºC and at three pressures: 0.65, 0.95 and 1.2 mbar

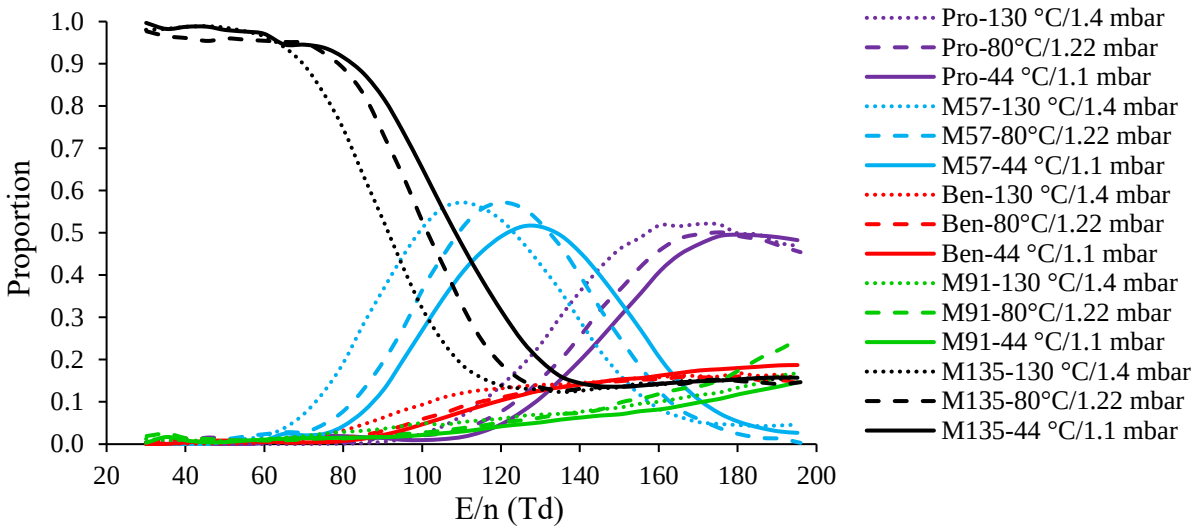

Figure A.9.3: Case 3 – PIDs for n-butylbenzene as a function of E/n using the **Mark IV ion-funnel drift tube** for which the E field was kept constant and the temperature and pressure were modified to provide the same n, and hence the same E/n.

Figure A.9.4-Figure A.9.6 provide data for the Mark V ion-funnel.

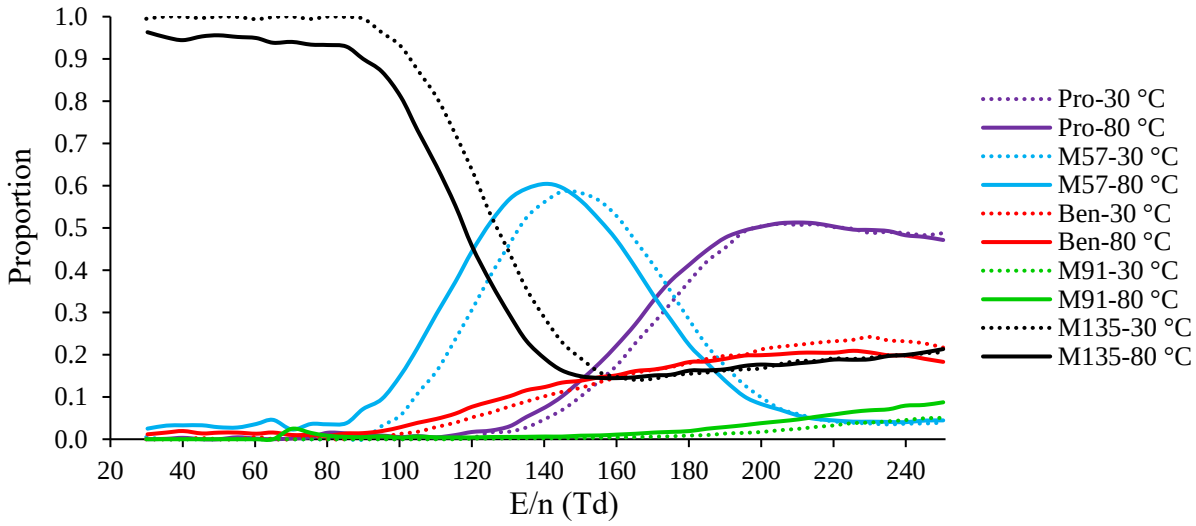

Figure A.9.4: Case 1 – PIDs for n-butylbenzene as a function of E/n with the **Mark V ion-funnel drift tube** operating at a constant pressure of 0.8 mbar and at two temperatures: 30 and 80 ºC.

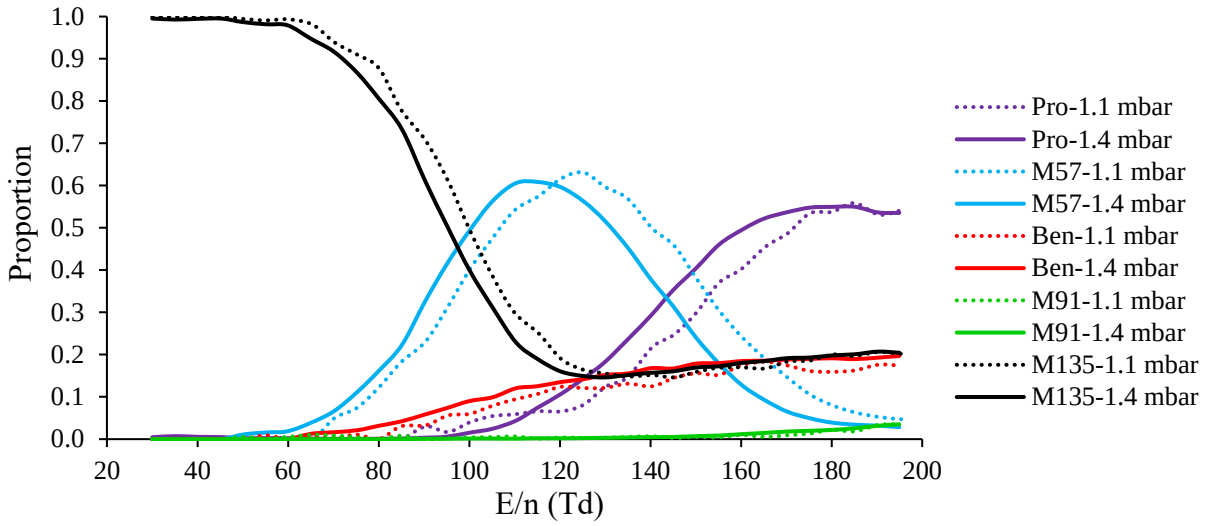

Figure A.9.5: Case 2 – PIDs for n-butylbenzene as a function of E/n using the **Mark V ion-funnel drift tube** operating at a constant temperature of 130 ºC and at two pressures: 1.1 and 1.4 mbar

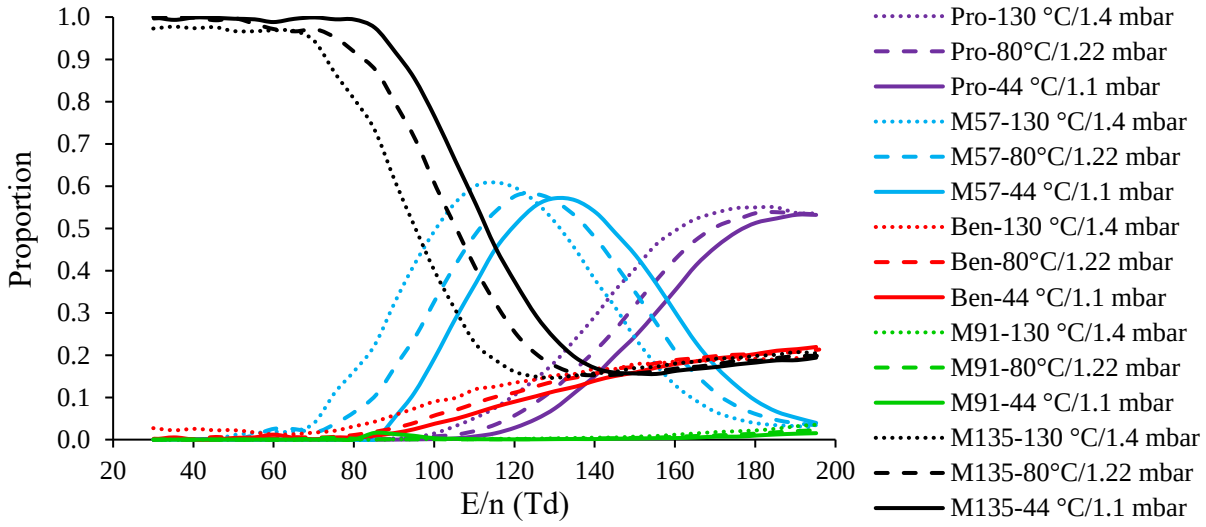

Figure A.9.6: Case 3 – PIDs for n-butylbenzene as a function of E/n using the **Mark V ion-funnel drift tube** for which the E field was kept constant and the temperature and pressure were modified to provide the same n, and hence the same E/n.

A.10 Plotting n-butylbenzene PIDs as a function of E_k(CM) (Marks IV and V reactors)

This appendix shows the full data set associated with attempts to reconcile the shifts in the PID plots using the E_k(CM) method of plotting the data.

Figure A.10.1-Figure A.10.3 provide data for the Mark IV ion-funnel.

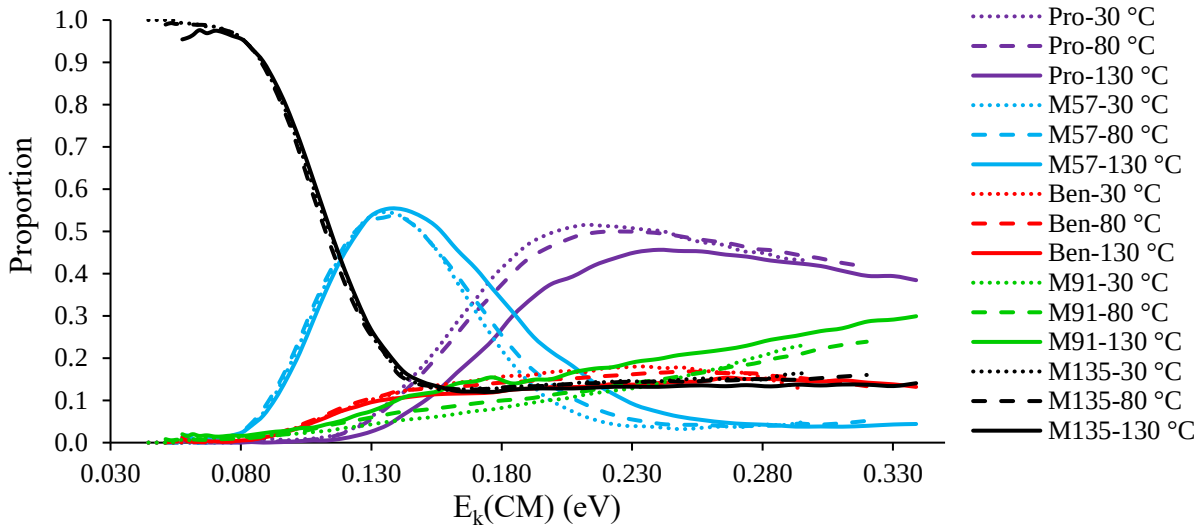

Figure A.10.1: Case 1 – PID of nBB as a function of E_k(CM) using the **Mark IV ion-funnel drift tube** operating at a constant drift tube pressure of 0.8 mbar and at three temperatures: 30, 80 and 130 °C (this plot may be compared with Figure A.9.1)

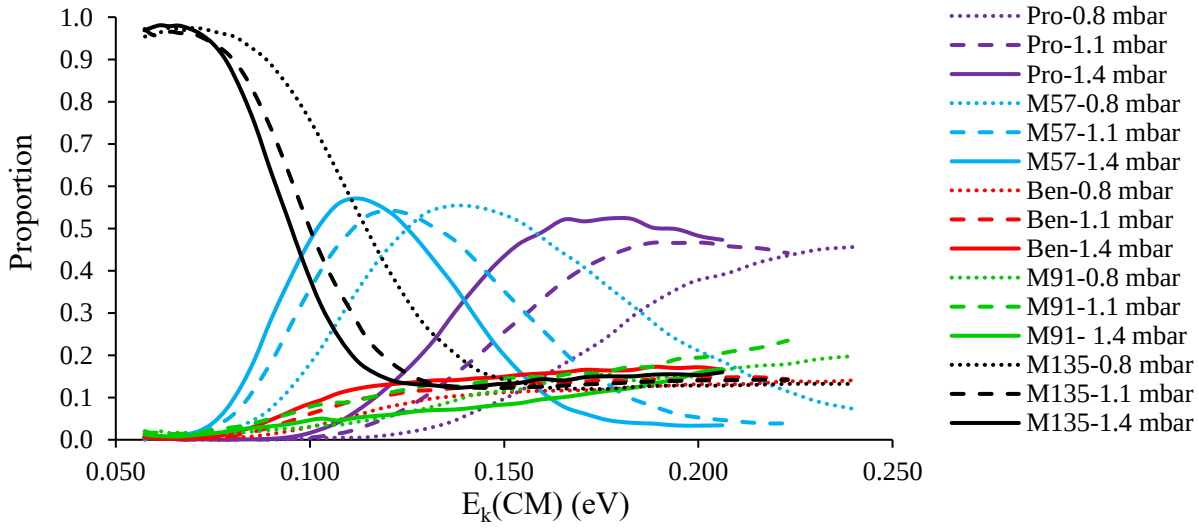

Figure A.10.2: Case 2 – PID for n-butylbenzene as a function of E_k(CM) n using the **Mark IV ion-funnel drift tube** operating at a constant temperature of 125 °C and at three pressures: 0.65, 0.95 and 1.2 mbar (this plot may be compared with Figure A.9.2)

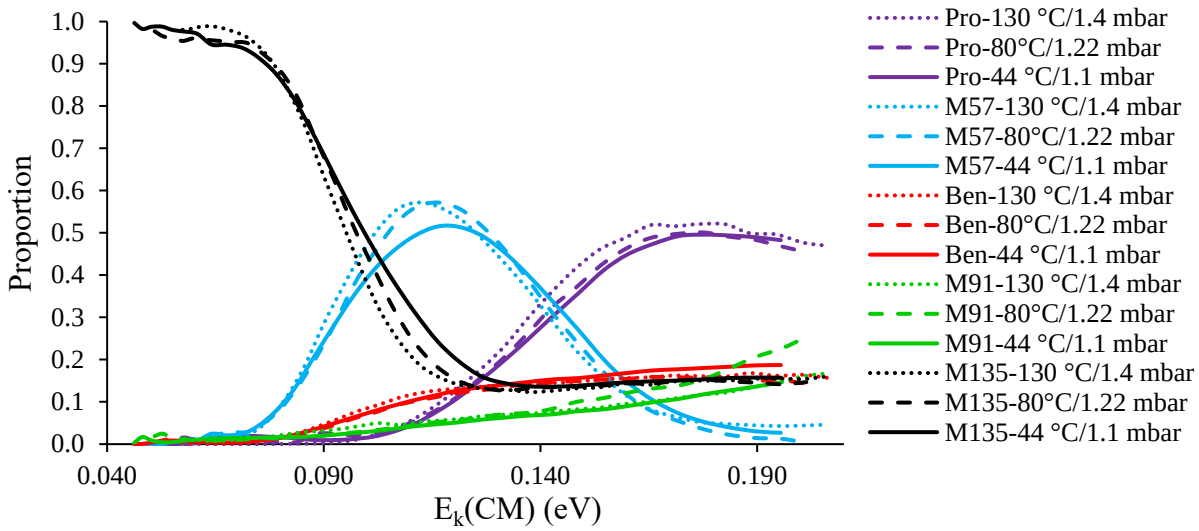

Figure A.10.3: Case 3 – PIDs for n-butylbenzene as a function of E_k(CM) using the **Mark IV ion-funnel drift tube** for which the E field was kept constant and the temperature and pressure were modified to provide the same n, and hence the same E/n. (this plot may be compared with Figure A.9.3)

Figure A.10.4-Figure A.10.6 provide data for the Mark V ion-funnel.

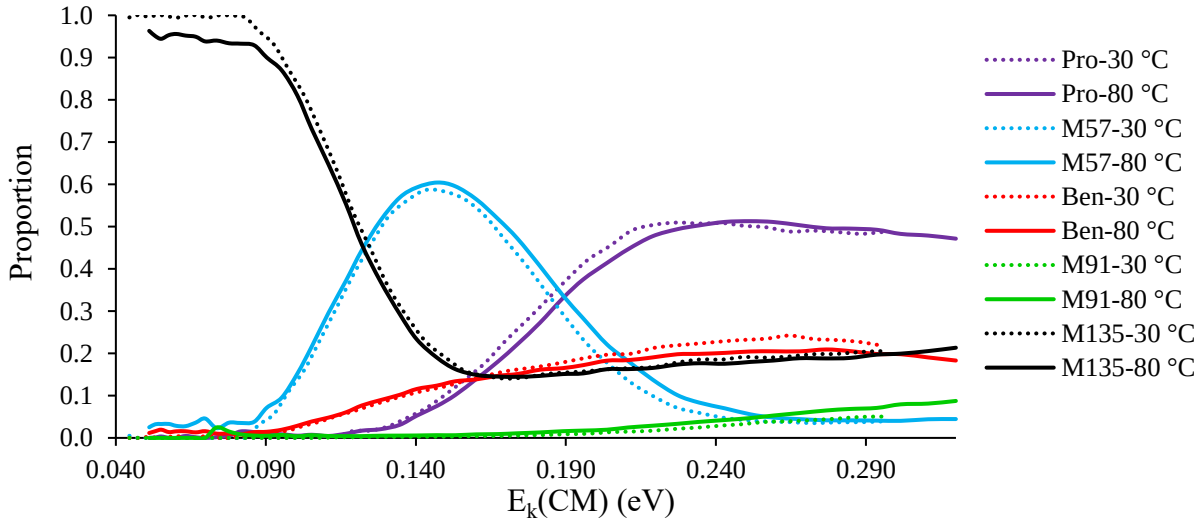

Figure A.10.4: Case 1 – PID of nBB as a function of E_k(CM) using the **Mark V ion-funnel drift tube** operating at a constant drift tube pressure of 0.8 mbar and at two temperatures: 30 and 80 ºC (this plot may be compared with Figure A.9.4)

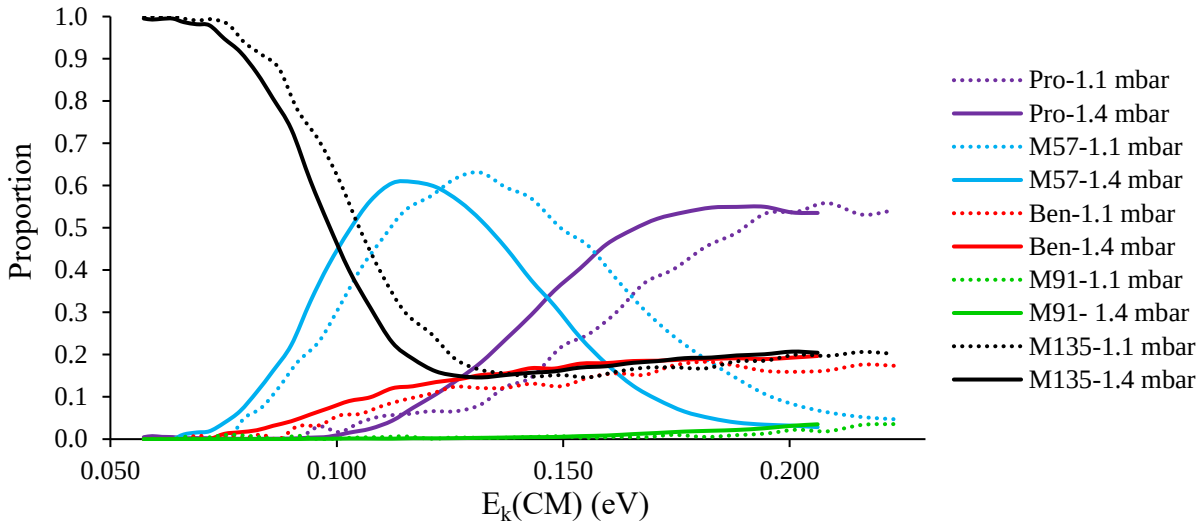

Figure A.10.5: Case 2 – PID for n-butylbenzene as a function of E_k(CM) n using the **Mark V ion-funnel drift tube** operating at a constant temperature of 130 ºC and at two pressures:1.1 and 1.4 mbar (this plot may be compared with Figure A.9.5)

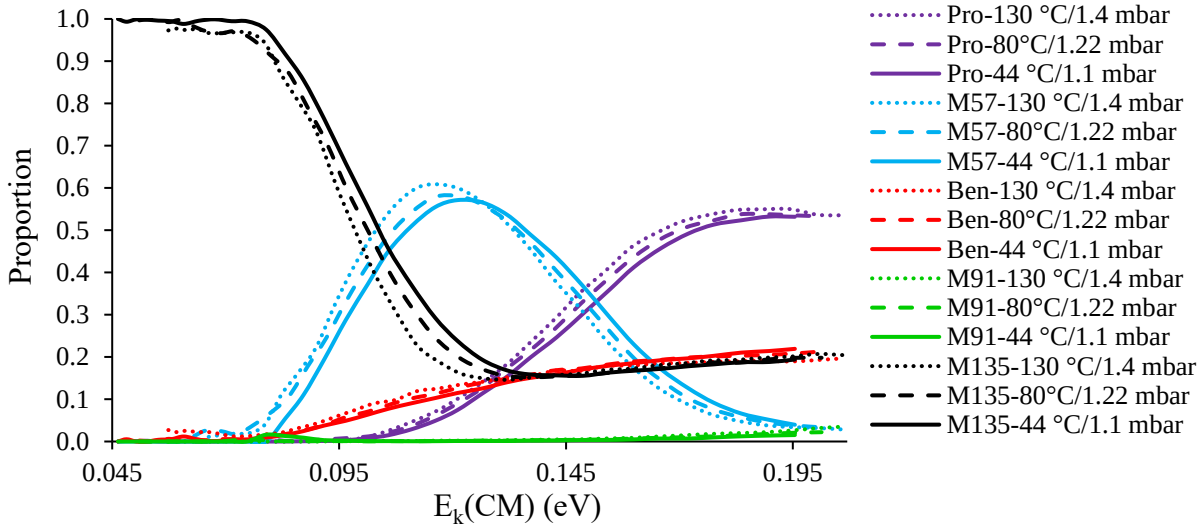

Figure A.10.6: Case 3 – PIDs for n-butylbenzene as a function of E_k(CM) using the **Mark V ion-funnel drift tube** for which the E field was kept constant and the temperature and pressure were modified to provide the same n, and hence the same E/n. (this plot may be compared with Figure A.9.6)

A.11 Determination of the uncertainties relative to the Δprop.max values

In the current approach and for two parameters A and B, the following assumptions are considered:

1) $\sigma(A) = \sqrt{A} \leftrightarrow (\sigma(A)/A)^2 = 1/A$

   This assumption is made because the charge transfer is a statistical process, with each transfer being independent of any other. These are the conditions for Poisson statistics to hold, which gives the relationship between the uncertainty and measured value.

2) A, σ(A)
   B, σ(B)
   } Have independent variation

When considering A and B integrals, the standard deviation of A and B combinations is presented in the equations E.A.11.1, E.A.11.2 and E.A.11.3 [154]:

$$\sigma(A+B) = \sqrt{\sigma(A)^2 + \sigma(B)^2} \qquad \text{E A.11.1}$$

$$\sigma(A-B) = \sqrt{\sigma(A)^2 + \sigma(B)^2} \qquad \text{E A.11.2}$$

$$\sigma\left(\frac{A}{B}\right) = \frac{A}{B}\sqrt{\left(\frac{\sigma(A)}{A}\right)^2 + \left(\frac{\sigma(B)}{B}\right)^2} \qquad \text{E A.11.3}$$

E.A.11.1 and E.A.11.3 respectively give specific cases presented in E.A.11.4 and E.A.11.5:

$$\sigma(1+A) = \sigma(A) \qquad \text{E A.11.4}$$

$$\sigma\left(\frac{1}{A}\right) = \frac{1}{A}\frac{\sigma(A)}{A} = \frac{\sigma(A)}{A^2} \qquad \text{E A.11.5}$$

Where E.A.11.5 is rearranged in E.A.11.6:

$$\sigma(A) = A^2\sigma\left(\frac{1}{A}\right) \qquad \text{E A.11.6}$$

According to the calculations, the different proportions of MH^+ must consider only two ions. This is why, for each probe molecule and each reactor mode, a single ion (or ions group) is considered additionally to MH^+ such that **the assumption** that the sum of the two ions signals be sufficiently representative of the sum of all the product ions initially present in the respective

PIDs for each Δprop.max conditions is considered. The different selected ions are listed in Table A.11.1.

Table A.11.1: Ions considered on top of MH^+ in the Δprop.max uncertainties calculations

Δprop.max uncertainties			
Analyte molecule	**Ion-funnel generation**	**Mode**	**Ion (m/z) considered on top of MH^+ in the uncertainty calculation**
n-butylbenzene	**I**	**DC**	57 (butyl ion)
n-butylbenzene	**II**		57 (butyl ion)
n-butylbenzene	**V**		57 (butyl ion)
triethylphosphate	**I**		99 (elimination of 3 ethenes)
ethylbenzene	**II**		79 (benzene-like ion)
n-butylbenzene	**I**	**RF**	39+41 (propyl group)
n-butylbenzene	**II**		39+41 (propyl group)
n-butylbenzene	**V**		39+41 (propyl group)

Noticing the new MH^+ proportions is noted S = A/(A+B) with A and B respectively the signal integrals of MH^+ and the other considered ion, the uncertainty of S is expressed, using E.A.11.3, E.A.11.4 and E.A.11.6, and after rearrangement by E.A.11.7:

$$\sigma(S) = \frac{AB}{(A+B)^2}\sqrt{\left(\frac{\sigma(A)}{A}\right)^2 + \left(\frac{\sigma(B)}{B}\right)^2} \qquad \text{E A.11.7}$$

Considering then that Δprop.max = $S_1 - S_2$ with S_1 and S_2 the two most different MH^+ proportions (for the case(s) considered), its uncertainty is, using E.A.11.2, given by E.A.11.8:

$$\sigma(S_1 - S_2) = \sqrt{\sigma(S_1)^2 + \sigma(S_2)^2} \qquad \text{E A.11.8}$$

3σ is then applied to all the Δprop.max calculated.

A.12 Characterisation of the fragmentation of a probe molecule in RF mode

Clearly the measurements made in the DC-only mode needed to be understood before even attempting to understand the behaviour observed when the RF field is applied. This was done by highlighting the unreliability of E/n to characterise fully the fragmentation of a given analyte.

A.12.1 Description and experimental conditions

The only difference from the DC-only mode was the addition of the RF field in the second half of each reactor considered. In each case, the parameters used were the same as those used for optimum funnelling performance, and as discussed in chapter 3. They are summarised now in Table A.12.1 (settings involving all the ion-funnels are presented in chapter 3 subpart 3.3.2).

Table A.12.1: Reactors parameters during the E/n experiments related to RF mode
Vpp stands for the peak-to-peak voltage amplitude

Reactor generation	**RF Ion-funnel tunings**					
	$P_{26\text{-}28}$				**P_{29}**	
	V_{pp}		**ν**		**V_{pp}**	**ν**
	V		**kHz**		**V**	**kHz**
I	210		745		105	745
II	215		745		131.5	745
	$P_{26\text{-}27}$		**P_{28s}**		**P_{29s}**	
	V_{pp}	**ν**	**V_{pp}**	**ν**	**V_{pp}**	**ν**
	V	**kHz**	**V**	**kHz**	**V**	**kHz**
V	208	708	64	708	32	708

With the application of the RF field, it is not possible to give a single E/n value for the reactor. Nevertheless, the DC field down the reactor is known, and so E/n in the following plots is given from the DC component. In the RF mode, the transmission of molecular ions out of the reactor

is optimised by having a reduced DC field, and thus the yield of molecular ions is greatest at what appear to be extremely low values of E/n.

A.12.2 Results – Plotting n-butylbenzene PIDs as a function of E/n in RF mode

A.12.2.1 Mark I reactor in RF mode

Figure A.12.1 provides the results using a Mark I reactor in RF mode for Case 1 pressure constant (variable E and T).

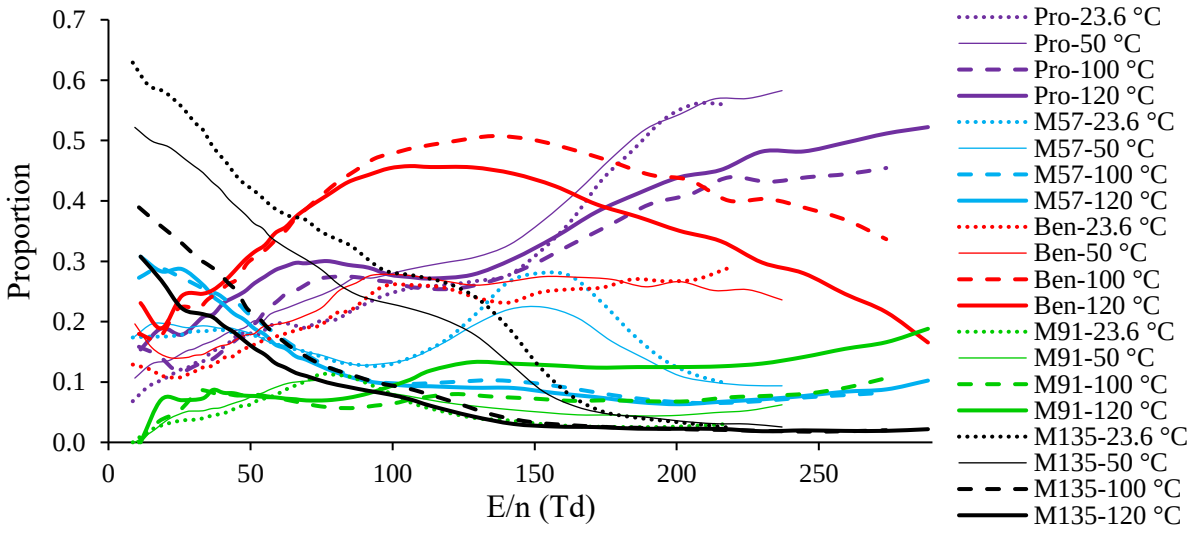

Figure A.12.1: Case 1 – PIDs for n-butylbenzene as a function of E/n using the Mark I ion-funnel drift tube operating at a constant pressure of 0.8 mbar and at four different temperatures: 23.6, 50, 100 and 120 °C in RF mode

During the time that the PTR instrument was configured with the Mark I funnel, only different temperatures were explored in RF mode.

A.12.2.2 Mark II reactor in RF mode

Figure A.12.2-Figure A.12.4 provide the results using a Mark II reactor in RF mode for the three Cases

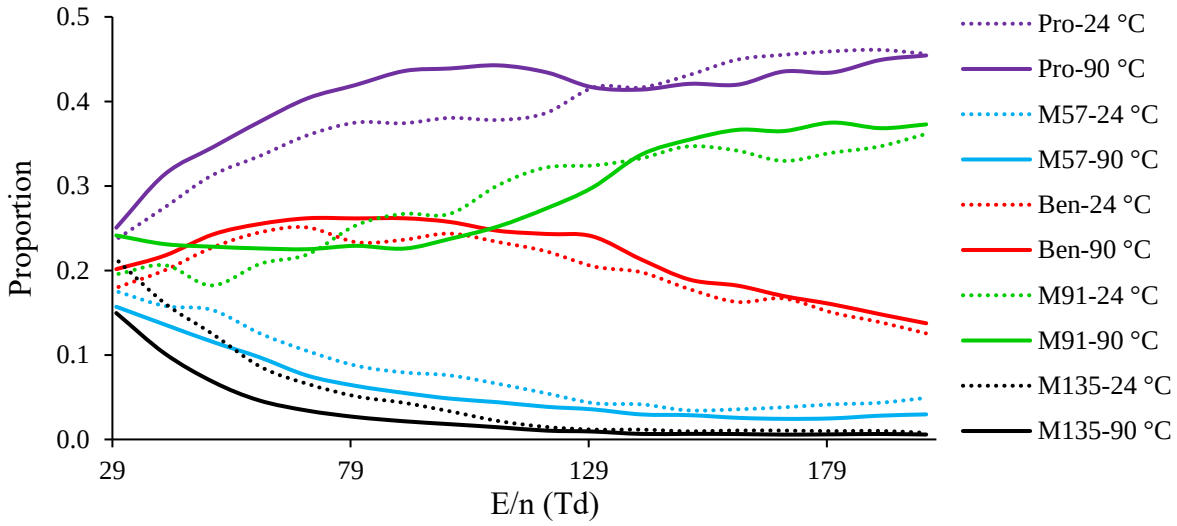

Figure A.12.2: Case 1 – PIDs for n-butylbenzene as a function of E/n using the Mark II ion-funnel drift tube operating at a constant pressure of 0.9 mbar and at two different temperatures: 24 and 90 ºC in RF mode

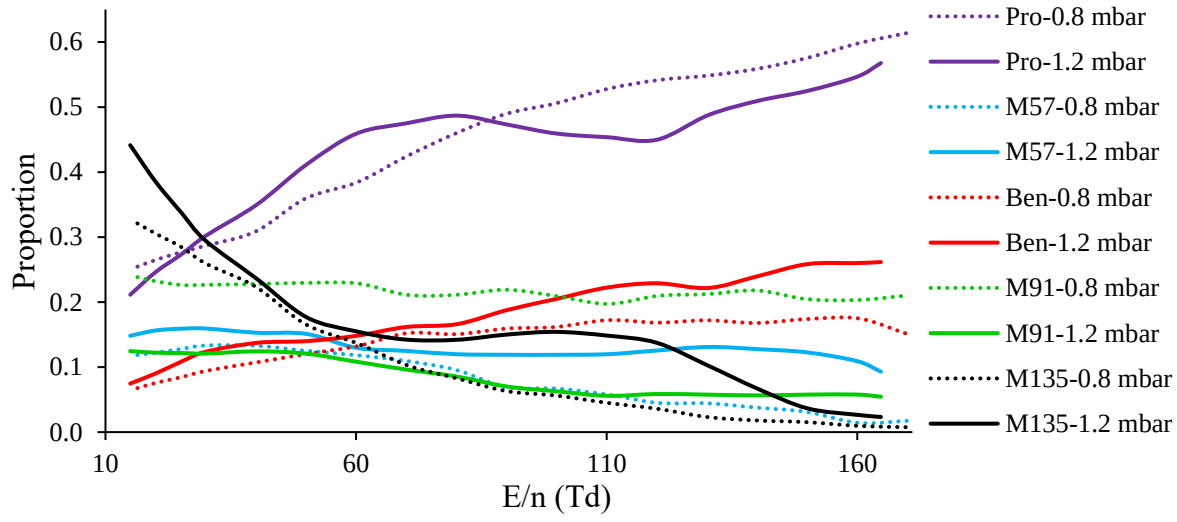

Figure A.12.3: Case 2 – PIDs for n-butylbenzene as a function of E/n using the Mark II ion-funnel drift tube operating at a constant temperature of 23 ºC and at two different pressures: 0.8 and 1.2 mbar in RF mode

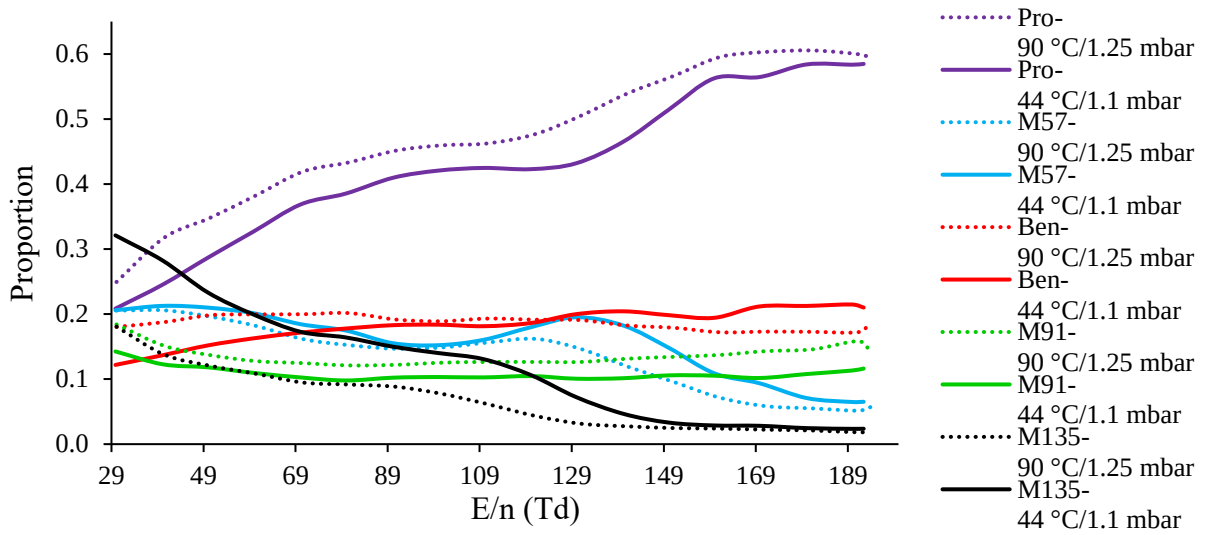

Figure A.12.4: Case 3 – PIDs for n-butylbenzene as a function of E/n using the Mark II ion-funnel drift tube for which the E field was kept constant and the temperature and pressure were modified to provide the same n, and hence the same E/n. in RF mode

A.12.2.3 Mark V reactor in RF mode

Figure A.12.5-Figure A.12.7 provide the results using a Mark V reactor in RF mode for the three Cases

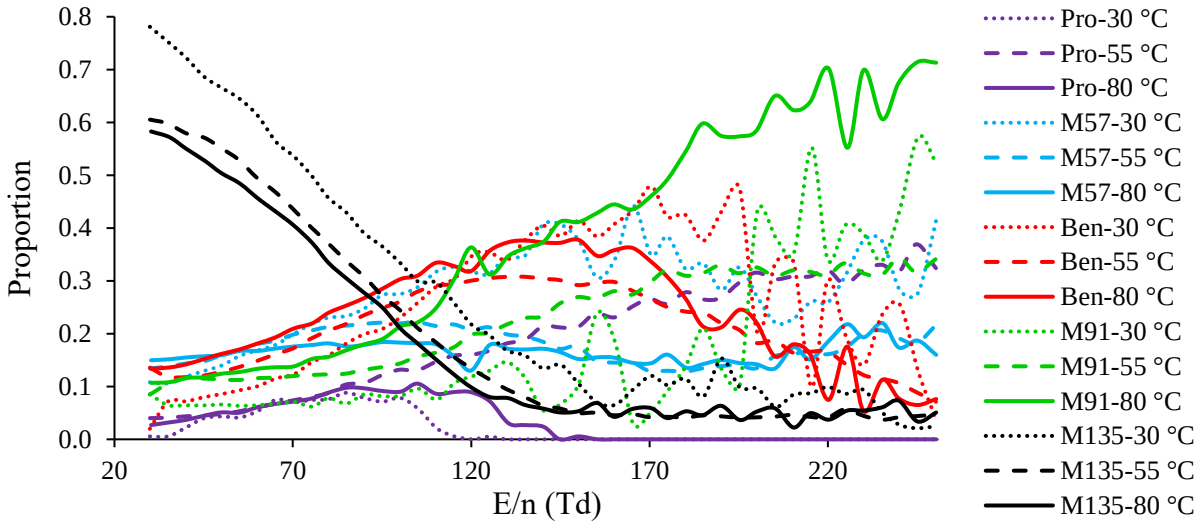

Figure A.12.5: Case 1 – PIDs for n-butylbenzene as a function of E/n using the Mark V ion-funnel drift tube operating at a constant pressure of 0.8 mbar and at three different temperatures: 30, 55 and 80 °C in RF mode

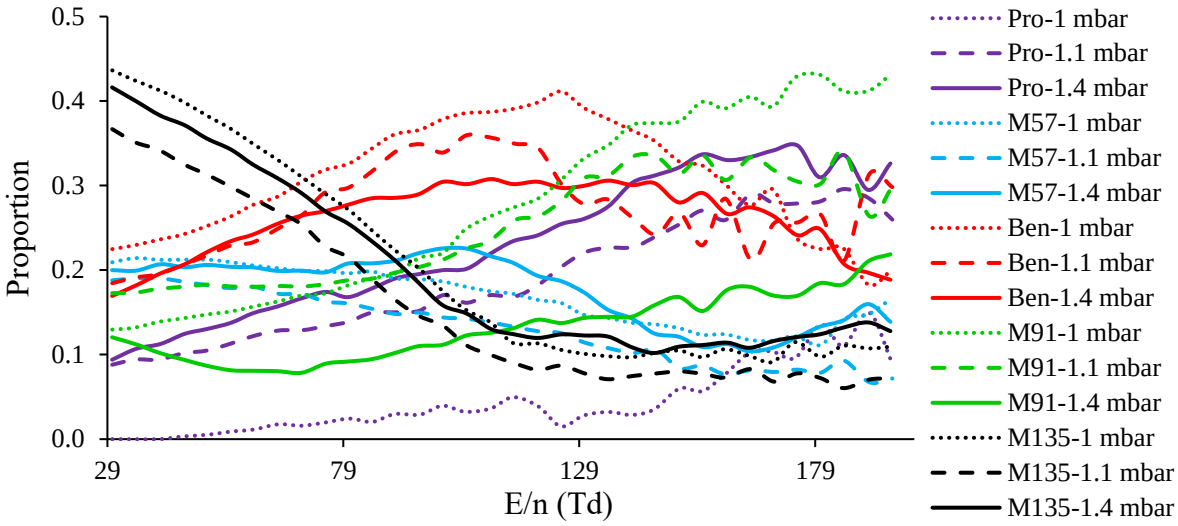

Figure A.12.6: Case 2 – PIDs for n-butylbenzene as a function of E/n using the Mark V ion-funnel drift tube operating at a constant temperature of 130 ºC and at three different pressures: 1, 1.1 and 1,4 mbar in RF mode

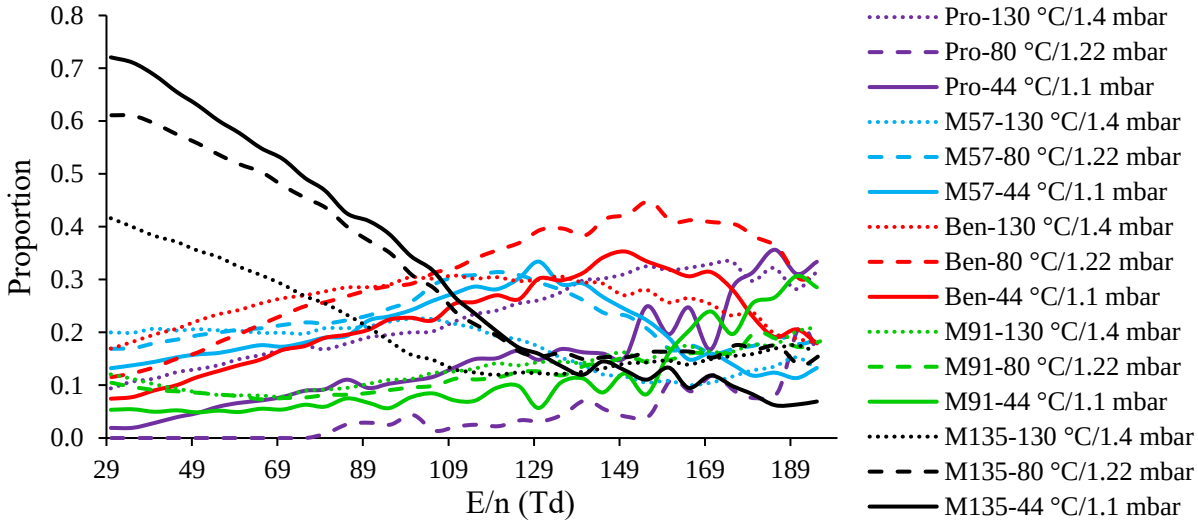

Figure A.12.7: Case 3 – PIDs for n-butylbenzene as a function of E/n using the Mark V ion-funnel drift tube for which the E field was kept constant and the temperature and pressure were modified to provide the same n, and hence the same E/n. in RF mode

The first remark to make about the data in RF mode is that the different curves still show significant shifts. Compared to the DC mode, the protonated parent molecule occurred at lower proportions. This is due to the effect of the RF, which enhances the collisional energy available

in the reactor. Therefore, m/z 57 is never dominant in the RF data plots. The conditions inside the reactor are energetic enough to make protonated nBB undergo collisional activation, consequently making the fragments from bond fissions dominant (m/z 39, 79 and 91) providing extra energy that increased the rate of H_2 losses from m/z 41 giving rise of m/z 39 (the propyl group) and favoured the bond fission of protonated nBB leading to m/z 91 to the rearrangement leading to m/z 92.

It is interesting to note the difference in behaviour in RF mode between the Marks I and II reactors and the Mark V reactor. The proportion of protonated molecular ions is greater for the Mark V funnel and is closer to the DC-only conditions. This is because in the case of all reactors except Mark V, only the last electrode in the reactor has a reduced amplitude as shown in Table A.12.1, whereas in the Mark V reactor the amplitude of the RF field is lower in the last section of the funnel. All ions must pass through this final section of the funnel and will inevitably experience the RF field, but since it is of lower amplitude, less energy is available to drive any collisional activation.

A.12.3 A new data treatment – Replacement of E/n by E_k(CM) in RF mode

Despite the added complexity of the RF mode, there is still an aspiration to see if the shifts could be at least partially corrected. Since it is thought that the fragmentation processes are dominated by the RF field, the more energy-based approach of the E_k(CM) method was employed once again.

A.12.4 Results – Plotting n-butylbenzene PIDs as a function of E_k(CM) in RF mode

A.12.4.1 Mark I reactor in RF mode

Figure A.12.8 provides the results using a Mark I reactor in RF mode for Case 1 pressure constant (variable E and T).

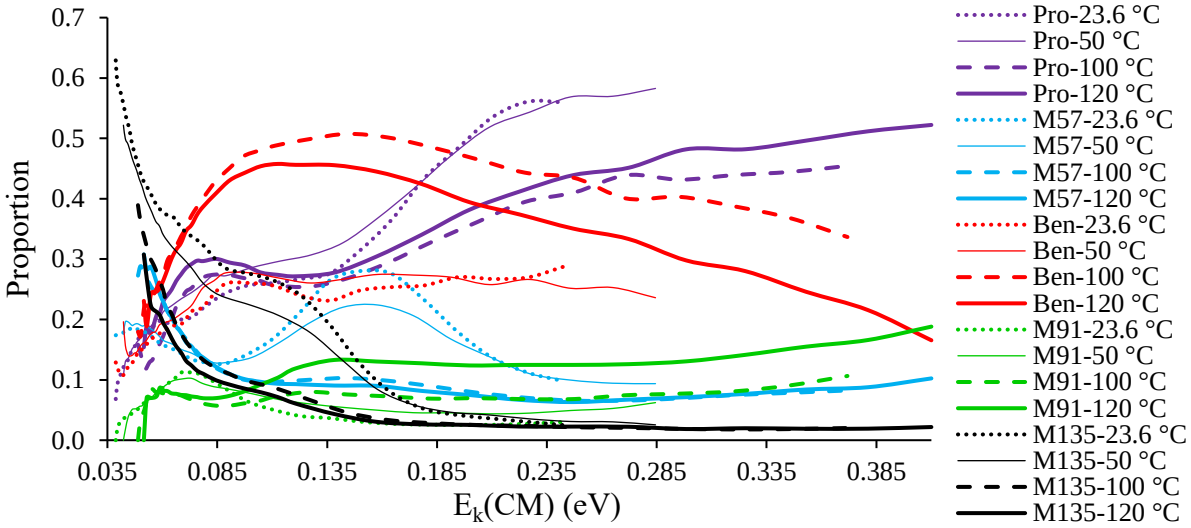

Figure A.12.8: Case 1 – PIDs for n-butylbenzene as a function of E_k(CM) using the Mark I ion-funnel drift tube operating at a constant pressure of 0.8 mbar and at four different temperatures: 23.6, 50, 100 and 120 ºC in RF mode (this plot may be compared with Figure A.12.1)

A.12.4.2 Mark II reactor in RF mode

Figure A.12.9-Figure A.12.11 provide the results using a Mark II reactor in RF mode for the three Cases.

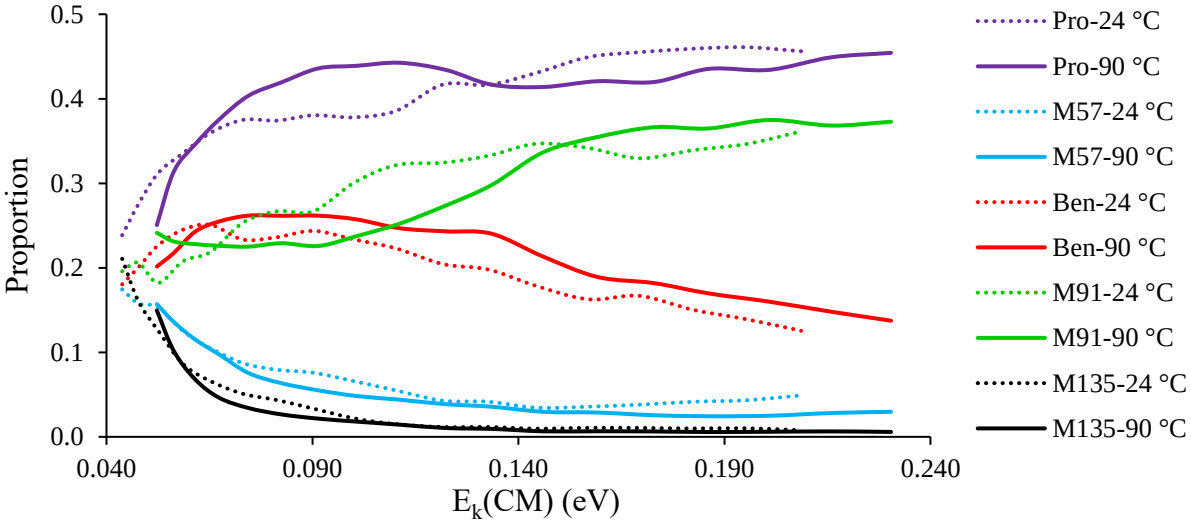

Figure A.12.9: Case 1 – PIDs for n-butylbenzene as a function of E_k(CM) using the Mark II ion-funnel drift tube operating at a constant pressure of 0.9 mbar and at two different temperatures: 24 and 90 ºC in RF mode (this plot may be compared with Figure A.12.2)

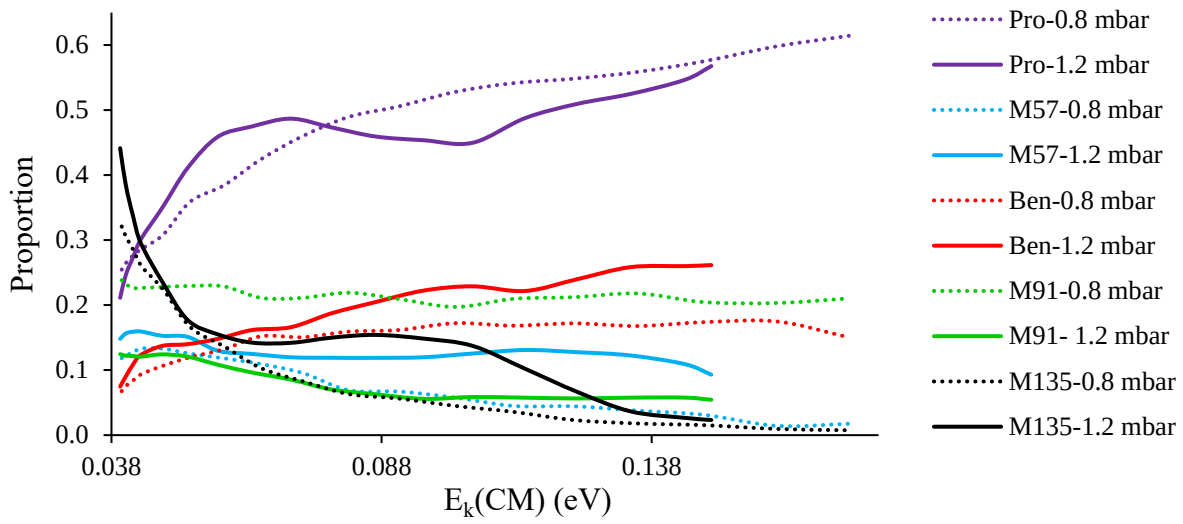

Figure A.12.10: Case 2 – PIDs for n-butylbenzene as a function of E_k(CM) using the Mark II ion-funnel drift tube operating at a constant temperature of 23 ºC and at two different pressures: 0.8 and 1.2 mbar in RF mode (this plot may be compared with Figure A.12.3)

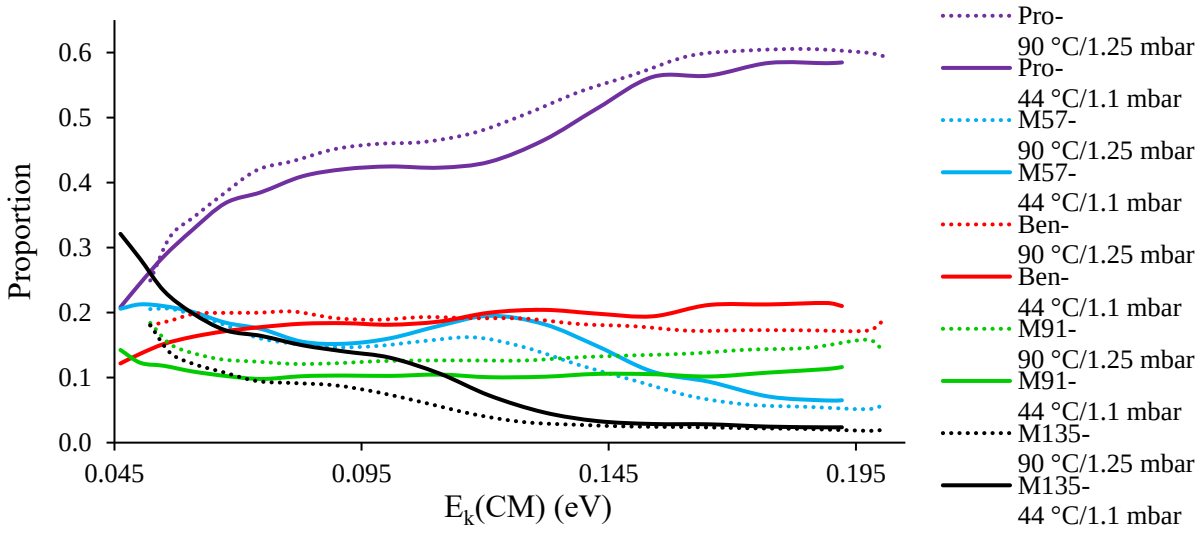

Figure A.12.11: Case 3 – PIDs for n-butylbenzene as a function of E/n using the Mark II ion-funnel drift tube for which the E field was kept constant and the temperature and pressure were modified to provide the same n, and hence the same E/n. in RF mode (this plot may be compared with Figure A.12.4)

A.12.4.3 n-butylbenzene – Mark V reactor in RF mode

Figure A.12.12-Figure A.12.14 provide the results using a Mark V reactor in RF mode for the three Cases

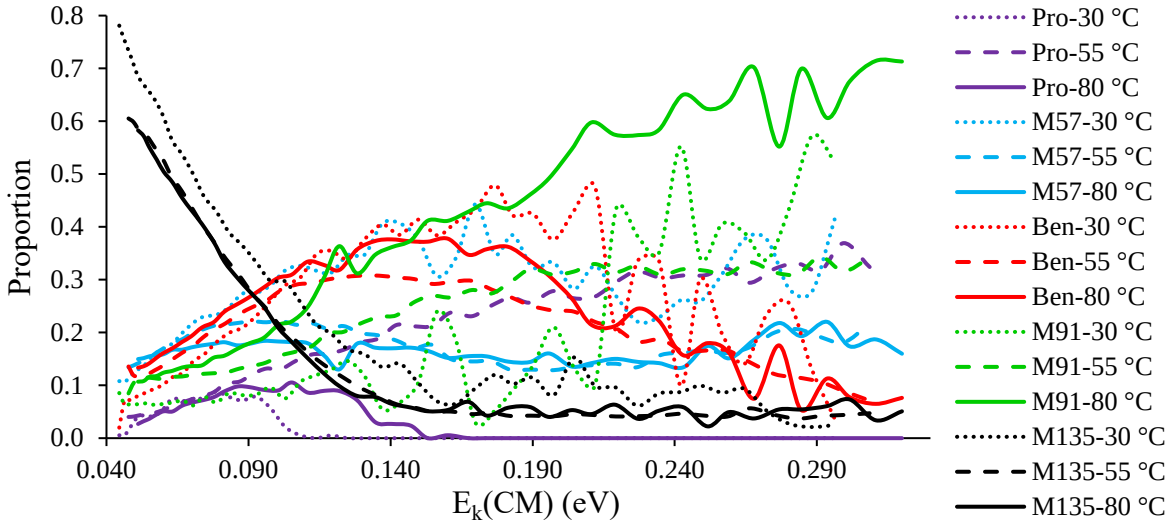

Figure A.12.12: Case 1 – PIDs for n-butylbenzene as a function of E_k(CM) using the Mark V ion-funnel drift tube operating at a constant pressure of 0.8 mbar and at three different temperatures: 30, 55 and 80 ºC in RF mode (this plot may be compared with Figure A.12.5)

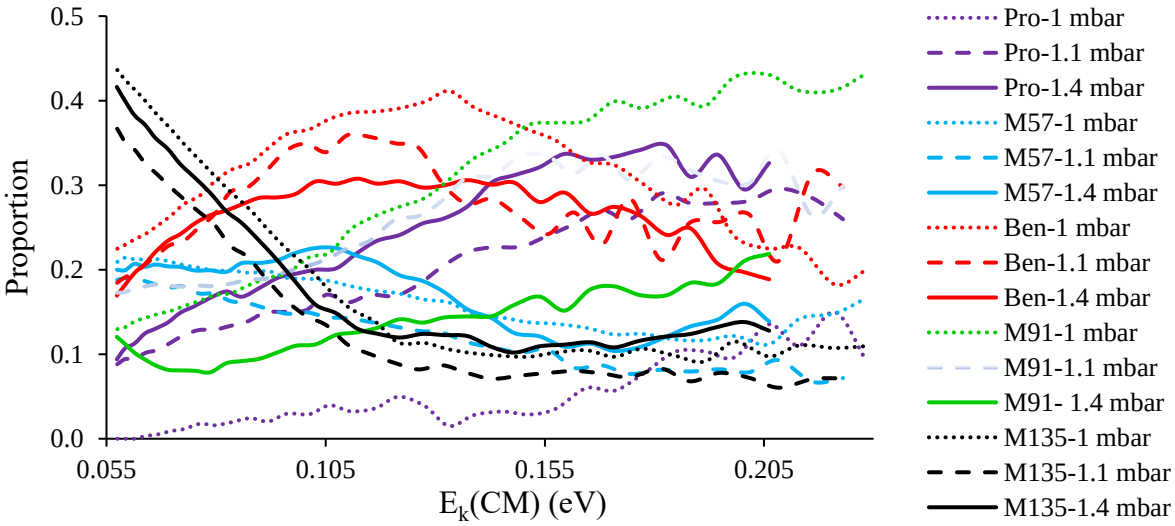

Figure A.12.13: Case 2 – PIDs for n-butylbenzene as a function of E_k(CM) using the Mark V ion-funnel drift tube operating at a constant temperature of 130 ºC and at three different pressures: 1, 1.1 and 1,4 mbar in RF mode (this plot may be compared with Figure A.12.6)

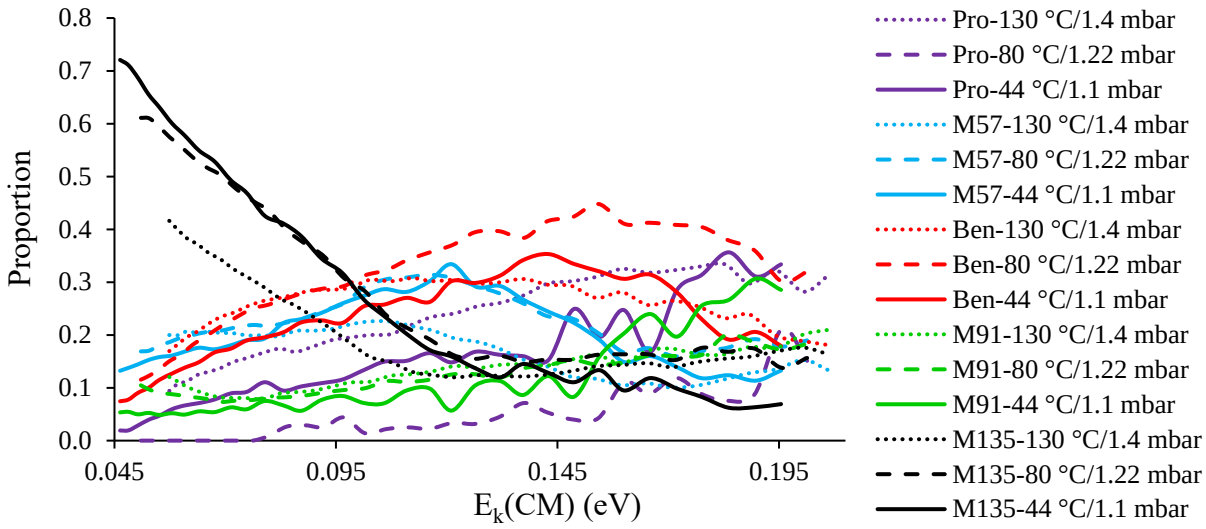

Figure A.12.14: Case 3 – PIDs for n-butylbenzene as a function of E_k(CM) using the Mark V ion-funnel drift tube for which the E field was kept constant and the temperature and pressure were modified to provide the same n, and hence the same E/n. in RF mode (this plot may be compared with Figure A.12.7)

The improvement in the display of the data as a function of E_k(CM) was not as clear as in DC mode – proof of the greater complexity of the RF mode. However, the initial RF mode data and their E_k(CM) correction suggest that the greater fragmentation is more collisional activation-related. Δprop.max regarding the protonated analyte for the RF mode experiments are shown in Table A.12.2.

Table A.12.2: Maximum variations of the protonated parent molecule as a function of the parameter used on the x-axis (RF mode)

Maximum difference of proportion (Δprop.max) of the protonated parent molecule for a given analyte and reactor (green: decrease of values, red: increase of values, both from E/n)			
Analyte molecule	**Reactor generation (RF mode)**	**Parameter used to express the PID of the analyte**	
		E/n	**E_k(CM)**
n-butylbenzene	**I (Case 1 only)**	0.30 ± 2.52 %	0.20 ± 1.06 %
n-butylbenzene	**II**	0.25 ± 1.95 %	0.15 ± 2.35 %
n-butylbenzene	**V**	0.40 ± 2.15 %	0.25 ± 4.18 %

Notice the RSDs are still calculated according to the method developed in the Appendix A.11.

A.12.5 Conclusion of the study in RF mode

The main analytical goal of the RF funnel development was to improve sensitivity. On top of achieving this goal with a reproducible factor 4 in terms of signal intensity compared to the Mark I ion-funnel, the Mark V design results in product ion distributions, which clearly demonstrate that the Mark V ion-funnel causes less fragmentation, probably due to reduction of the RF amplitudes in the final section through which all ions pass.

On the other hand, and perhaps more importantly, a better understanding of the fragmentation of molecules in the PTR reactor has been achieved. In DC mode, after replacing E/n by E_k(CM), i.e. considering the secondary reaction energy of the colliding system, improvements were made in the overlay of the different sets of E/n plots but certain cases remained uncorrected.

In RF mode, the E_k(CM) correction partially corrected the plots. Clearly there is much more work to be done to understand more fully the effects of applying RF fields within a PTR reactor.

A.13 Compounds following the compendium method TO-14A

Table A.13.1: Compounds following the compendium method TO-14A

Name(s)	Code	Formula	m/z	CAS-number
1,1,1-trichloroethane	111TCE	$C_2H_3Cl_3$	132	71-55-6
1,1,2,2-tetrachloroethane	TeCE	$C_2H_2Cl_4$	166	79-34-5
1,1,2-trichloroethane	112TCE	$C_2H_3Cl_3$	132	79-00-5
1,1-dichloroethane	11DCE	$C_2H_4Cl_2$	98	75-34-3
1,1-dichloroethene 1,1-dichloroethylene	11DCEy	$C_2H_2Cl_2$	96	75-35-4
1,2,4-trichlorobenzene	124TCB	$C_6H_3Cl_3$	180	120-82-1
1,2,4-trymethylbenzene	124TMB	C_9H_{12}	120	95-63-6
1,2-dibromoethane	12DBE	$C_2H_4Br_2$	186	106-93-4
1,2-dichloroethane	12DCE	$C_2H_4Cl_2$	98	107-06-2
1,2-dichloropropane	12DCP	$C_3H_6Cl_2$	112	78-87-5
1,3,5-trymethylbenzene mesitylene	135TMB	C_9H_{12}	120	108-67-8
benzene	B	C_6H_6	78	71-43-2
bromomethane	BM	CH_3Br	94	74-83-9
cis-1,2-dichloroethene cis-1,2-dichloroethylene	c12DCEy	$C_2H_2Cl_2$	96	156-59-2
cis-1,3-dichloropropene cis-1,3-dichloropropylene	c13DCPy	$C_3H_4Cl_2$	110	10061-01-5
chlorobenzene	CB	C_6H_5Cl	112	108-90-7
chloroethane	CE	C_2H_5Cl	64	75-00-3
chloroform trichloromethane	CF	$CHCl_3$	118	67-66-3
chloromethane	CM	CH_3Cl	50	74-87-3
carbon tetrachloride tetrachloromethane	CTC	CCl_4	152	56-23-5
dichloromethane	DCM	CH_2Cl_2	84	75-09-2
ethylbenzene	EB	C_8H_{10}	106	100-41-4
trichlorofluoromethane freon-11 halocarbon 11	F11	CCl_3F	136	75-69-4
1,1,2-trichloro-1,2,2-trifluoroethane freon-113 halocarbon 113	F113	$C_2Cl_3F_3$	186	75-69-5
1,2-dichloro-1,1,2,2-tetrafluoroethane freon-114 halocarbon 114	F114	$C_2Cl_2F_4$	170	76-14-2
dichlorodifluoromethane freon-12 halocarbon 12	F12	CCl_2F_2	120	75-71-8

hexachloro-1,3-butadiene	**HC13BD**	**C_4Cl_6**	**258**	**87-68-3**
1,3-dichlorobenzene **meta-dichlorobenzene** **m-dichlorobenzene**	**mDCB**	**$C_6H_4Cl_2$**	**146**	**541-73-1**
1,3-dimethylbenzene **meta-xylene** **m-xylene**	**mX**	**C_8H_{10}**	**106**	**108-38-3**
1,2-dichlorobenze **ortho-dichlorobenzene** **o-dichlorobenzene**	**oDCB**	**$C_6H_4Cl_2$**	**146**	**95-50-1**
1,2-dimethylbenzene **ortho-xylene** **o-xylene**	**oX**	**C_8H_{10}**	**106**	**95-47-6**
1,4-dichlorobenzene **para-dichlorobenzene** **p-dichlorobenzene**	**pDCB**	**$C_6H_4Cl_2$**	**146**	**106-46-7**
1,4-dimethylbenzene **para-xylene** **p-xylene**	**pX**	**C_8H_{10}**	**106**	**106-42-3**
ethenylbenzene **vinylbenzene** **styrene**	**S**	**C_8H_8**	**104**	**100-42-5**
methylbenzene **toluene**	**T**	**C_7H_8**	**92**	**108-88-3**
trans-1,3-dichloropropene **trans-1,3-dichloropropylene**	**t13DCPy**	**$C_3H_4Cl_2$**	**110**	**10061-02-6**
trichloroethene **trichloroethylene**	**TCEy**	**C_2HCl_3**	**130**	**79-01-6**
tetrachloroehtene **tetrachloroethylene**	**TeCEy**	**C_2Cl_4**	**164**	**127-18-4**
chloroethene **chloroethylene** **vinyl chloride**	**VC**	**C_2H_3Cl**	**62**	**75-01-4**

A.14 TO-14 master ions list – 40 % RH, low concentration, Mark I ion-funnel

Table A.14.1: TO-14 master ions list – 40 % RH, low concentration, Mark I ion-funnel

TO-14 ions involved in the library												
Mass			Formula	Mass			Formula	Mass			Formula
m/z		g/mol		m/z		g/mol		m/z		g/mol	
15	15	15.0235	CH_3	78	78	78.0470	C_6H_6	110	110	109.9690	$C_3H_4Cl_2$
26	26	26.0157	C_2H_2		78	78.0555	$C_2H_8NO_2$		(x+1)109	110.0323	$C_5{}^{13}CH_5O_2$
27	27	27.0235	C_2H_3	79	79	79.0395	$C_2H_7O_3$	111	111	111.0446	$C_6H_7O_2$
28	28	28.0187	CH_2N		79	79.0548	C_6H_7	112	112	111.9847	$C_3H_6Cl_2$
	28	28.0313	C_2H_4	82	82	81.9377	CCl_2		112*	112.0080	C_6H_5Cl
29	29	29.0140	HN_2		82	82.0055	$C_4H_2O_2$		(x+1)111	112.0480	$C_5{}^{13}CH_7O_2$
	29	29.0391	C_2H_5	83	83	82.9455	$CHCl_2$	113	113	113.0158	C_6H_6Cl
37	37	37.0290	H_5O_2		83	83.0109	$C_2H_2F_3$		113	113.0250	$C_2H_6FO_4$
39	39	39.0235	C_3H_3		83*	83.0497	C_5H_7O		113*	113.0603	$C_6H_9O_2$
	(x+2)37	39.0332	$H_5O^{18}O$	85	85	84.9657	$CClF_2$	117	117	116.9066	CCl_3
41	41	41.0391	C_3H_5		85	85.0290	$C_4H_5O_2$		117	117.0188	$C_4H_5O_4$
47	47	46.9689	CCl	91	91	91.0395	$C_3H_7O_3$	118	118	117.9377	C_4Cl_2
	47	47.0133	CH_3O_2		91	91.0548	C_7H_7	120	120	120.0661	$C_4H_{10}NO_3$
48	48	48.0086	NH_2O_2		91*	91.0759	$C_4H_{11}O_2$		120	120.0939	C_9H_{12}
49	49	48.9845	CH_2Cl	92	92	92.0348	$C_2H_6NO_3$	121	(x+1)120	121.0694	$C_3{}^{13}CH_{10}NO_3$
	(x+1)48	49.0056	$^{15}NH_2O_2$		92	92.0626	C_7H_8		121	121.1017	C_9H_{13}
50	50	50.0004	H_2O_3		92*	92.0712	$C_3H_{10}NO_2$	129	129	129.0578	C_9H_7N
	50	50.0157	C_4H_2	93	93	93.0400	C_6H_5O	130	130	129.9144	C_2HCl_3
51	(x+1)50	51.0046	$H_2O_2{}^{17}O$		93*	93.0552	$C_3H_9O_3$		(x+1)129	130.0612	$C_8{}^{13}CH_7N$
	51	51.0235	C_4H_3		93	93.0704	C_7H_9	131	131	130.9222	$C_2H_2Cl_3$
	51	51.0446	CH_7O_2	94	94	93.9377	C_2Cl_2		131	131.0371	C_8H_5NO
52	52	51.9949	C_3O		94*	93.9418	CH_3Br	132	132	131.9300	$C_2H_3Cl_3$
	52*	52.0187	C_2H_3N	95	95	95.0497	C_6H_7O	133	133	132.9379	$C_2H_4Cl_3$
	52	52.0313	C_4H_4	96	96	95.9534	$C_2H_2Cl_2$		133	133.0280	$AlO(H_2O)_5$
	52**	52.0399	NH_6O_2		(x+1)95	96.0530	$C_5{}^{13}CH_7O$	135	135	134.9625	C_2ClF_4
53	53	53.0027	C_3HO	97	97	96.9612	$C_2H_3Cl_2$		135	135.0293	$C_4H_7O_5$
	53	53.0391	C_4H_5		97	97.0078	$AlO(H_2O)_3$	137	137	136.9128	$CHCl_3F$
60	60	59.9767	C_2HCl	98	98	97.9690	$C_2H_4Cl_2$		137	137.0239	$C_7H_5O_3$
	60	60.0449	C_2H_6NO		98	98.0242	$C_4H_4NO_2$	141	141	140.9066	C_3Cl_3
61	61	60.9845	C_2H_2Cl	101	101	100.9361	CCl_2F		141	141.0538	$C_5H_7N_3O_2$
	61	61.0290	$C_2H_5O_2$		101	101.0265	C_7H_3N	146	146	145.9690	$C_6H_4Cl_2$
62	62	61.9923	C_2H_3Cl	103	103	103.0422	C_7H_5N		146	146.0368	$C_9H_6O_2$
	(x+1)61	62.0323	$C^{13}CH_5O_2$		103	103.0548	C_8H_7	147	147	146.9768	$C_6H_5Cl_2$
63	63	63.0002	C_2H_4Cl		103*	103.0759	$C_5H_{11}O_2$		147	147.0657	$C_6H_{11}O_4$
	63	63.0082	CH_3O_3	104	104	104.0374	$C_6H_4N_2$	151	151	150.9329	$C_2Cl_2F_3$
	63*	63.0446	$C_2H_7O_2$		104	104.0626	C_8H_8		151	151.0395	$C_8H_7O_3$
65	65	65.0239	CH_5O_3		104*	104.0712	$C_4H_{10}NO_2$	153	153	152.9066	C_4Cl_3
	65	65.0391	C_5H_5	105	105	104.9340	C_2H_2Br	164	164	163.8754	C_2Cl_4
	65*	65.0603	$C_2H_9O_2$		105	105.0578	C_7H_7N	165	165	164.8832	C_2HCl_4
71	71	70.9689	C_3Cl		105*	105.0704	C_8H_9	166	166	165.8911	$C_2H_2Cl_4$
	71	71.0133	$C_3H_3O_2$	106	106	105.9377	C_3Cl_2	170	170	169.9313	$C_2Cl_2F_4$
75	75	75.0002	C_3H_4Cl		106*	105.9418	C_2H_3Br	177	177	176.8832	C_3HCl_4
	75*	75.0235	C_6H_3		106**	106.0783	C_8H_{10}	180	180	179.9300	$C_6H_3Cl_3$
	75	75.0446	$C_3H_7O_2$	107	107	106.9051	Ag	181	181	180.9379	$C_6H_4Cl_3$
76	76	76.0080	C_3H_5Cl		107	106.9455	C_3HCl_2	186	186	185.8680	$C_2H_4Br_2$
	76	76.0399	$C_2H_6NO_2$		107*	106.9496	C_2H_4Br	188	188	187.8754	C_4Cl_4
77	77	77.0158	C_3H_6Cl		107*	107.0344	$C_3H_7O_4$	223	223	222.8443	C_4Cl_5
	77*	77.0391	C_6H_5		107**	107.0861	C_8H_{11}	258	258	257.8131	C_4Cl_6
	77	77.0603	$C_3H_9O_2$	109	109	108.9612	$C_3H_3Cl_2$	259	259	258.8209	C_4HCl_6
					109	109.0290	$C_6H_5O_2$				

A.15 TO-14 library – 40 % RH, low concentration, Mark I ion-funnel

This appendix presents the first complete matrix (library) of product ions for the TO-14 compounds. Here is the coding to interpret it:

- *Background* colour:
    - White: Any ion not being part of the PID of the selected compound.
    - Yellow: Negligible ion (less than 5 % of the reference ion) of the PID of the selected compound.
    - Red: Consequent ion (at least 5 % of the reference ion) of the PID of the selected compound.
    - Black: Parent molecule(s) (if detected) of the selected compound.
    - Green: Any ion of the PID of the selected compound but based on assumption due to the impossibility to run the compound.
- *Figure* colour:
    - Yellow: Negligible parent molecule(s) (less than 5 % of the reference ion) of the PID of the selected compound
    - Red: * If black background: Consequent parent molecule(s) (at least 5 % of the reference ion) of the PID of the selected compound.

      * If white background: independent isobaric compound of one of the fragments of the library
    - Purple: Column of one of the isotopes of one of the peaks of the library
    - Green: Column of one of the assumed ions of the selected compound not run during the experiments
    - Grey: Colum of one of the ions involved in certain PID but judged as too intense to be reliably considered

- Column head:
    - (x+1)mass: Isotope of the ion from m/z x, based at one extra amu, i.e. x+1
    - (x+2)mass: Isotope of the ion from m/z x, based at two extra amu, i.e. x+2
    - $^{\text{neutron number}}$element: Isotope of an element, different from the most abundant one, i.e. different number of neutrons.
    - Number*/number**: To distinguish isobaric compounds once there are at least two ions from the library and sometimes independent ions as well
    - ?: Unidentified ion of the library

To make the results of the deconvolution more reliable (at least in the early versions of the software) it is essential to identify any isobaric compounds of an ion of the library. Most of them are the red columns, i.e. independent ions but also the purple columns, i.e. isotopes of ions of the library (not needed to be inserted into the library used by the software as the natural isotopic abundances of the elements have been entered into the coding) and a few green columns, i.e. assumed ions of the library.

The fact to assume certain PIDs is to get results as realistic as possible. Indeed, any molecules introduced in the library need to present a pattern to be treated by AnalyseHR.

For readability reasons only the code of the TO-14 compounds and their m/z and formula have been specified. More details can be found in the appendix A.13 (Table A.13.1).

Table A.15.1: TO-14 library – 40 % RH, low concentration, Mark I ion-funnel (18 pages)

TO-14 compound Code	m/z	m/z	15	26	27	28		29		37
			15	26	27	28	28	29	29	37
		g/mol	15.0235	26.0157	27.0235	28.0187	28.0313	29.0140	29.0391	37.0290
		Formula	CH_3	C_2H_2	C_2H_3	CH_2N	C_2H_4	HN_2	C_2H_5	H_5O_2
CM	50	CH_3Cl	1.00	0.00	0.00	0.00	0.00	0.00	0.00	0.00
VC	62	C_2H_3Cl	0.00	0.00	0.00	0.00	0.00	0.00	0.00	0.00
CE	64	C_2H_5Cl	0.01	0.20	0.00	0.00	0.38	0.00	0.02	0.00
B	78	C_6H_6	0.00	0.00	0.00	0.00	0.00	0.00	0.00	0.00
DCM	84	CH_2Cl_2	0.00	0.00	0.00	0.00	0.00	0.00	0.00	0.00
T	92	C_7H_8	0.00	0.00	0.00	0.00	0.00	0.00	0.00	0.00
BM	94	CH_3Br	0.00	0.00	0.00	0.00	0.00	0.00	0.00	0.00
11DCEy	96	$C_2H_2Cl_2$	0.00	0.00	0.00	0.00	0.00	0.00	0.00	0.00
c12DCEy	96	$C_2H_2Cl_2$	0.00	0.00	0.00	0.00	0.00	0.00	0.00	0.00
11DCE	98	$C_2H_4Cl_2$	0.00	0.00	0.00	0.00	0.00	0.00	0.00	0.00
12DCE	98	$C_2H_4Cl_2$	0.00	0.00	0.00	0.00	0.00	0.00	0.00	0.00
S	104	C_8H_8	0.00	0.00	0.00	0.00	0.00	0.00	0.00	0.00
EB	106	C_8H_{10}	0.00	0.00	0.00	0.00	0.00	0.00	0.00	0.00
mX	106	C_8H_{10}	0.00	0.00	0.00	0.00	0.00	0.00	0.00	0.00
oX	106	C_8H_{10}	0.00	0.00	0.00	0.00	0.00	0.00	0.00	0.00
pX	106	C_8H_{10}	0.00	0.00	0.00	0.00	0.00	0.00	0.00	0.00
c13DCPy	110	$C_3H_4Cl_2$	0.00	0.00	0.00	0.00	0.00	0.00	0.00	0.00
t13DCPy	110	$C_3H_4Cl_2$	0.00	0.00	0.00	0.00	0.00	0.00	0.00	0.00
12DCP	112	$C_3H_6Cl_2$	0.00	0.00	0.00	0.00	0.00	0.00	0.00	0.00
CB	112	C_6H_5Cl	0.00	0.00	0.00	0.00	0.00	0.00	0.00	0.00
CF	118	$CHCl_3$	0.00	0.00	0.00	0.00	0.00	0.00	0.00	0.00
124TMB	120	C_9H_{12}	0.00	0.00	0.00	0.00	0.00	0.00	0.00	0.00
135TMB	120	C_9H_{12}	0.00	0.00	0.00	0.00	0.00	0.00	0.00	0.00
F12	120	CCl_2F_2	0.00	0.00	0.00	0.00	0.00	0.00	0.00	0.00
TCEy	130	C_2HCl_3	0.00	0.00	0.00	0.00	0.00	0.00	0.00	0.00
111TCE	132	$C_2H_3Cl_3$	0.00	0.00	0.00	0.00	0.00	0.00	0.00	0.00
112TCE	132	$C_2H_3Cl_3$	0.00	0.01	0.00	0.00	0.00	0.00	0.00	0.00
F11	136	CCl_3F	0.00	0.00	0.00	0.00	0.00	0.00	0.00	0.00
mDCB	146	$C_6H_4Cl_2$	0.00	0.00	0.00	0.00	0.00	0.00	0.00	0.00
oDCB	146	$C_6H_4Cl_2$	0.00	0.00	0.00	0.00	0.00	0.00	0.00	0.00
pDCB	146	$C_6H_4Cl_2$	0.00	0.00	0.00	0.00	0.00	0.00	0.00	0.00
CTC	152	CCl_4	0.00	0.00	0.00	0.00	0.00	0.00	0.00	0.00
TeCEy	164	C_2Cl_4	0.00	0.00	0.00	0.00	0.00	0.00	0.00	0.00
TeCE	166	$C_2H_2Cl_4$	0.00	0.00	0.00	0.00	0.00	0.00	0.00	0.00
F114	170	$C_2Cl_2F_4$	0.00	0.00	0.00	0.00	0.00	0.00	0.00	0.00
124TCB	180	$C_6H_3Cl_3$	0.00	0.00	0.00	0.00	0.00	0.00	0.00	0.00
12DBE	186	$C_2H_4Br_2$	0.00	0.00	0.00	0.00	0.00	0.00	0.00	0.00
F113	186	$C_2Cl_3F_3$	0.00	0.00	0.00	0.00	0.00	0.00	0.00	0.00
HC13BD	258	C_4Cl_6	0.00	0.00	0.00	0.00	0.00	0.00	0.00	0.00

TO-14 compound Code	m/z	m/z	39		41	47		48	49	
			39	(x+2)37	41	47	47	48	49	(x+1)48
		g/mol	39.0235	39.0332	41.0391	46.9689	47.0133	48.0086	48.9845	49.0056
		Formula	C_3H_3	$H_5O^{18}O$	C_3H_5	CCl	CH_3O_2	NH_2O_2	CH_2Cl	$^{15}NH_2O_2$
CM	50	CH_3Cl	0.00	0.00	0.00	0.00	0.00	0.00	0.00	0.00
VC	62	C_2H_3Cl	0.00	0.00	0.00	0.00	0.00	0.00	0.00	0.00
CE	64	C_2H_5Cl	0.00	0.00	0.00	0.00	0.00	0.00	0.03	0.00
B	78	C_6H_6	0.01	0.00	0.00	0.00	0.00	0.00	0.00	0.00
DCM	84	CH_2Cl_2	0.00	0.00	0.00	0.04	0.00	0.00	0.55	0.00
T	92	C_7H_8	0.00	0.00	0.00	0.00	0.00	0.00	0.00	0.00
BM	94	CH_3Br	0.00	0.00	0.00	0.00	0.00	0.00	0.00	0.00
11DCEy	96	$C_2H_2Cl_2$	0.00	0.00	0.00	0.00	0.00	0.00	0.00	0.00
c12DCEy	96	$C_2H_2Cl_2$	0.00	0.00	0.00	0.00	0.00	0.00	0.00	0.00
11DCE	98	$C_2H_4Cl_2$	0.00	0.00	0.00	0.00	0.00	0.00	0.00	0.00
12DCE	98	$C_2H_4Cl_2$	0.00	0.00	0.00	0.00	0.00	0.00	0.01	0.00
S	104	C_8H_8	0.00	0.00	0.00	0.00	0.00	0.00	0.00	0.00
EB	106	C_8H_{10}	0.01	0.00	0.00	0.00	0.00	0.00	0.00	0.00
mX	106	C_8H_{10}	0.00	0.00	0.00	0.00	0.00	0.00	0.00	0.00
oX	106	C_8H_{10}	0.02	0.00	0.00	0.00	0.00	0.00	0.00	0.00
pX	106	C_8H_{10}	0.02	0.00	0.00	0.00	0.00	0.00	0.00	0.00
c13DCPy	110	$C_3H_4Cl_2$	0.00	0.00	0.00	0.00	0.00	0.00	0.03	0.00
t13DCPy	110	$C_3H_4Cl_2$	0.00	0.00	0.00	0.00	0.00	0.00	0.03	0.00
12DCP	112	$C_3H_6Cl_2$	0.43	0.00	0.26	0.00	0.00	0.00	0.00	0.00
CB	112	C_6H_5Cl	0.00	0.00	0.00	0.00	0.00	0.00	0.00	0.00
CF	118	$CHCl_3$	0.00	0.00	0.00	0.00	0.00	0.00	0.00	0.00
124TMB	120	C_9H_{12}	0.00	0.00	0.00	0.00	0.00	0.00	0.00	0.00
135TMB	120	C_9H_{12}	0.00	0.00	0.00	0.00	0.00	0.00	0.00	0.00
F12	120	CCl_2F_2	0.00	0.00	0.00	0.00	0.00	0.00	0.00	0.00
TCEy	130	C_2HCl_3	0.00	0.00	0.00	0.00	0.00	0.00	0.00	0.00
111TCE	132	$C_2H_3Cl_3$	0.00	0.00	0.00	0.00	0.00	0.00	0.00	0.00
112TCE	132	$C_2H_3Cl_3$	0.00	0.00	0.00	0.00	0.00	0.00	0.00	0.00
F11	136	CCl_3F	0.00	0.00	0.00	0.00	0.00	0.00	0.00	0.00
mDCB	146	$C_6H_4Cl_2$	0.00	0.00	0.00	0.00	0.00	0.00	0.00	0.00
oDCB	146	$C_6H_4Cl_2$	0.00	0.00	0.00	0.00	0.00	0.00	0.00	0.00
pDCB	146	$C_6H_4Cl_2$	0.00	0.00	0.00	0.00	0.00	0.00	0.00	0.00
CTC	152	CCl_4	0.00	0.00	0.00	0.00	0.00	0.00	0.00	0.00
TeCEy	164	C_2Cl_4	0.00	0.00	0.00	0.00	0.00	0.00	0.00	0.00
TeCE	166	$C_2H_2Cl_4$	0.00	0.00	0.00	0.00	0.00	0.00	0.00	0.00
F114	170	$C_2Cl_2F_4$	0.00	0.00	0.00	0.00	0.00	0.00	0.00	0.00
124TCB	180	$C_6H_3Cl_3$	0.00	0.00	0.00	0.00	0.00	0.00	0.00	0.00
12DBE	186	$C_2H_4Br_2$	0.00	0.00	0.00	0.00	0.00	0.00	0.00	0.00
F113	186	$C_2Cl_3F_3$	0.00	0.00	0.00	0.00	0.00	0.00	0.00	0.00
HC13BD	258	C_4Cl_6	0.00	0.00	0.00	0.00	0.00	0.00	0.00	0.00

TO-14 compound Code	m/z	m/z	50		51			52			
			50	50	(x+1)50	51	51	52	52*	52	52**
		g/mol	50.0004	50.0157	51.0046	51.0235	51.0446	51.9949	52.0187	52.0313	52.0400
		Formula	H_2O_3	C_4H_2	$H_2O_2{}^{17}O$	C_4H_3	CH_7O_2	C_3O	C_2H_3N	C_4H_4	?
CM	50	CH_3Cl	0.00	0.00	0.00	0.00	0.00	0.00	0.00	0.00	0.00
VC	62	C_2H_3Cl	0.00	0.00	0.00	0.00	0.00	0.00	0.00	0.00	0.00
CE	64	C_2H_5Cl	0.00	0.00	0.00	0.00	0.00	0.00	0.00	0.00	0.00
B	78	C_6H_6	0.00	0.00	0.00	0.01	0.00	0.00	0.00	0.00	0.00
DCM	84	CH_2Cl_2	0.00	0.00	0.00	0.00	0.00	0.00	0.00	0.00	0.00
T	92	C_7H_8	0.00	0.00	0.00	0.01	0.00	0.00	0.00	0.00	0.00
BM	94	CH_3Br	0.00	0.00	0.00	0.00	0.00	0.00	0.00	0.00	0.00
11DCEy	96	$C_2H_2Cl_2$	0.00	0.00	0.00	0.00	0.00	0.00	0.00	0.00	0.00
c12DCEy	96	$C_2H_2Cl_2$	0.00	0.00	0.00	0.00	0.00	0.00	0.00	0.00	0.00
11DCE	98	$C_2H_4Cl_2$	0.00	0.00	0.00	0.00	0.00	0.00	0.00	0.00	0.00
12DCE	98	$C_2H_4Cl_2$	0.00	0.00	0.00	0.00	0.00	0.00	0.00	0.00	0.00
S	104	C_8H_8	0.00	0.00	0.00	0.00	0.00	0.00	0.00	0.00	0.00
EB	106	C_8H_{10}	0.00	0.00	0.00	0.00	0.00	0.00	0.00	0.00	0.00
mX	106	C_8H_{10}	0.00	0.00	0.00	0.00	0.00	0.00	0.00	0.00	0.00
oX	106	C_8H_{10}	0.00	0.00	0.00	0.00	0.00	0.00	0.00	0.00	0.00
pX	106	C_8H_{10}	0.00	0.00	0.00	0.00	0.00	0.00	0.00	0.00	0.00
c13DCPy	110	$C_3H_4Cl_2$	0.00	0.00	0.00	0.00	0.00	0.00	0.00	0.00	0.00
t13DCPy	110	$C_3H_4Cl_2$	0.00	0.00	0.00	0.00	0.00	0.00	0.00	0.00	0.00
12DCP	112	$C_3H_6Cl_2$	0.00	0.00	0.00	0.00	0.00	0.00	0.00	0.00	0.00
CB	112	C_6H_5Cl	0.00	0.00	0.00	0.01	0.00	0.00	0.00	0.00	0.00
CF	118	$CHCl_3$	0.00	0.00	0.00	0.00	0.00	0.00	0.00	0.00	0.00
124TMB	120	C_9H_{12}	0.00	0.00	0.00	0.00	0.00	0.00	0.00	0.00	0.00
135TMB	120	C_9H_{12}	0.00	0.00	0.00	0.00	0.00	0.00	0.00	0.00	0.00
F12	120	CCl_2F_2	0.00	0.00	0.00	0.00	0.00	0.00	0.00	0.00	0.00
TCEy	130	C_2HCl_3	0.00	0.00	0.00	0.00	0.00	0.00	0.00	0.00	0.00
111TCE	132	$C_2H_3Cl_3$	0.00	0.00	0.00	0.00	0.00	0.00	0.00	0.00	0.00
112TCE	132	$C_2H_3Cl_3$	0.00	0.00	0.00	0.00	0.00	0.00	0.00	0.00	0.00
F11	136	CCl_3F	0.00	0.00	0.00	0.00	0.00	0.00	0.00	0.00	0.00
mDCB	146	$C_6H_4Cl_2$	0.00	0.00	0.00	0.00	0.00	0.00	0.00	0.00	0.00
oDCB	146	$C_6H_4Cl_2$	0.00	0.00	0.00	0.00	0.00	0.00	0.00	0.00	0.00
pDCB	146	$C_6H_4Cl_2$	0.00	0.00	0.00	0.00	0.00	0.00	0.00	0.00	0.00
CTC	152	CCl_4	0.00	0.00	0.00	0.00	0.00	0.00	0.00	0.00	0.00
TeCEy	164	C_2Cl_4	0.00	0.00	0.00	0.00	0.00	0.00	0.00	0.00	0.00
TeCE	166	$C_2H_2Cl_4$	0.00	0.00	0.00	0.00	0.00	0.00	0.00	0.00	0.00
F114	170	$C_2Cl_2F_4$	0.00	0.00	0.00	0.00	0.00	0.00	0.00	0.00	0.00
124TCB	180	$C_6H_3Cl_3$	0.00	0.00	0.00	0.00	0.00	0.00	0.00	0.00	0.00
12DBE	186	$C_2H_4Br_2$	0.00	0.00	0.00	0.00	0.00	0.00	0.00	0.00	0.00
F113	186	$C_2Cl_3F_3$	0.00	0.00	0.00	0.00	0.00	0.00	0.00	0.00	0.00
HC13BD	258	C_4Cl_6	0.00	0.00	0.00	0.00	0.00	0.00	0.00	0.00	0.00

TO-14 compound Code	m/z	m/z	53		60		61		62	
			53	53	60	60	61	61	62	(x+1)61
		g/mol	53.0027	53.0391	59.9767	60.0449	60.9845	61.0290	61.9923	62.0323
		Formula	C_3HO	C_4H_5	C_2HCl	C_2H_6NO	C_2H_2Cl	$C_2H_5O_2$	C_2H_3Cl	$C^{13}CH_5O_2$
CM	50	CH_3Cl	0.00	0.00	0.00	0.00	0.00	0.00	0.00	0.00
VC	62	C_2H_3Cl	0.00	0.00	0.00	0.00	0.00	0.00	0.48	0.00
CE	64	C_2H_5Cl	0.00	0.00	0.00	0.00	0.00	0.00	0.01	0.00
B	78	C_6H_6	0.00	0.01	0.00	0.00	0.00	0.00	0.00	0.00
DCM	84	CH_2Cl_2	0.00	0.00	0.00	0.00	0.00	0.00	0.00	0.00
T	92	C_7H_8	0.00	0.00	0.00	0.00	0.00	0.00	0.00	0.00
BM	94	CH_3Br	0.00	0.00	0.00	0.00	0.00	0.00	0.00	0.00
11DCEy	96	$C_2H_2Cl_2$	0.00	0.00	0.00	0.00	0.00	0.00	0.00	0.00
c12DCEy	96	$C_2H_2Cl_2$	0.00	0.00	0.00	0.00	0.02	0.00	0.00	0.00
11DCE	98	$C_2H_4Cl_2$	0.00	0.00	0.00	0.00	0.00	0.00	0.00	0.00
12DCE	98	$C_2H_4Cl_2$	0.00	0.00	0.00	0.00	0.00	0.00	0.57	0.00
S	104	C_8H_8	0.00	0.00	0.00	0.00	0.00	0.00	0.00	0.00
EB	106	C_8H_{10}	0.00	0.00	0.00	0.00	0.00	0.00	0.00	0.00
mX	106	C_8H_{10}	0.00	0.00	0.00	0.00	0.00	0.00	0.00	0.00
oX	106	C_8H_{10}	0.00	0.00	0.00	0.00	0.00	0.00	0.00	0.00
pX	106	C_8H_{10}	0.00	0.00	0.00	0.00	0.00	0.00	0.00	0.00
c13DCPy	110	$C_3H_4Cl_2$	0.00	0.00	0.00	0.00	0.00	0.00	0.00	0.00
t13DCPy	110	$C_3H_4Cl_2$	0.00	0.00	0.00	0.00	0.00	0.00	0.00	0.00
12DCP	112	$C_3H_6Cl_2$	0.00	0.00	0.00	0.00	0.00	0.00	0.08	0.00
CB	112	C_6H_5Cl	0.00	0.00	0.00	0.00	0.00	0.00	0.00	0.00
CF	118	$CHCl_3$	0.00	0.00	0.00	0.00	0.00	0.00	0.00	0.00
124TMB	120	C_9H_{12}	0.00	0.00	0.00	0.00	0.00	0.00	0.00	0.00
135TMB	120	C_9H_{12}	0.00	0.00	0.00	0.00	0.00	0.00	0.00	0.00
F12	120	CCl_2F_2	0.00	0.00	0.00	0.00	0.00	0.00	0.00	0.00
TCEy	130	C_2HCl_3	0.00	0.00	0.01	0.00	0.00	0.00	0.00	0.00
111TCE	132	$C_2H_3Cl_3$	0.00	0.00	0.00	0.00	0.01	0.00	0.00	0.00
112TCE	132	$C_2H_3Cl_3$	0.00	0.00	0.00	0.00	0.04	0.00	0.00	0.00
F11	136	CCl_3F	0.00	0.00	0.00	0.00	0.00	0.00	0.00	0.00
mDCB	146	$C_6H_4Cl_2$	0.00	0.00	0.00	0.00	0.00	0.00	0.00	0.00
oDCB	146	$C_6H_4Cl_2$	0.00	0.00	0.00	0.00	0.00	0.00	0.00	0.00
pDCB	146	$C_6H_4Cl_2$	0.00	0.00	0.00	0.00	0.00	0.00	0.00	0.00
CTC	152	CCl_4	0.00	0.00	0.00	0.00	0.00	0.00	0.00	0.00
TeCEy	164	C_2Cl_4	0.00	0.00	0.00	0.00	0.00	0.00	0.00	0.00
TeCE	166	$C_2H_2Cl_4$	0.00	0.00	0.00	0.00	0.00	0.00	0.00	0.00
F114	170	$C_2Cl_2F_4$	0.00	0.00	0.00	0.00	0.00	0.00	0.00	0.00
124TCB	180	$C_6H_3Cl_3$	0.00	0.00	0.00	0.00	0.00	0.00	0.00	0.00
12DBE	186	$C_2H_4Br_2$	0.00	0.00	0.00	0.00	0.00	0.00	0.00	0.00
F113	186	$C_2Cl_3F_3$	0.00	0.00	0.00	0.00	0.00	0.00	0.00	0.00
HC13BD	258	C_4Cl_6	0.00	0.00	0.00	0.00	0.00	0.00	0.00	0.00

TO-14 compound Code	m/z	m/z	63			65			71	
			63	63	63*	65	65	65*	71	71
		g/mol	63.0002	63.0082	63.0446	65.0239	65.0391	65.0603	70.9689	71.0133
		Formula	C_2H_4Cl	CH_3O_3	$C_2H_7O_2$	CH_5O_3	C_5H_5	$C_2H_9O_2$	C_3Cl	$C_3H_3O_2$
CM	50	CH_3Cl	0.00	0.00	0.00	0.00	0.00	0.00	0.00	0.00
VC	62	C_2H_3Cl	0.52	0.00	0.00	0.00	0.00	0.00	0.00	0.00
CE	64	C_2H_5Cl	0.35	0.00	0.00	0.00	0.00	0.00	0.00	0.00
B	78	C_6H_6	0.00	0.00	0.00	0.00	0.00	0.00	0.00	0.00
DCM	84	CH_2Cl_2	0.00	0.00	0.00	0.00	0.00	0.00	0.00	0.00
T	92	C_7H_8	0.00	0.00	0.00	0.00	0.00	0.00	0.00	0.00
BM	94	CH_3Br	0.00	0.00	0.00	0.00	0.00	0.00	0.00	0.00
11DCEy	96	$C_2H_2Cl_2$	0.91	0.00	0.00	0.00	0.00	0.00	0.00	0.00
c12DCEy	96	$C_2H_2Cl_2$	0.00	0.00	0.00	0.00	0.00	0.00	0.00	0.00
11DCE	98	$C_2H_4Cl_2$	0.91	0.00	0.00	0.00	0.00	0.00	0.00	0.00
12DCE	98	$C_2H_4Cl_2$	0.42	0.00	0.00	0.00	0.00	0.00	0.00	0.00
S	104	C_8H_8	0.00	0.00	0.00	0.00	0.00	0.00	0.00	0.00
EB	106	C_8H_{10}	0.00	0.00	0.00	0.00	0.00	0.00	0.00	0.00
mX	106	C_8H_{10}	0.00	0.00	0.00	0.00	0.00	0.00	0.00	0.00
oX	106	C_8H_{10}	0.00	0.00	0.00	0.00	0.00	0.00	0.00	0.00
pX	106	C_8H_{10}	0.00	0.00	0.00	0.00	0.00	0.00	0.00	0.00
c13DCPy	110	$C_3H_4Cl_2$	0.00	0.00	0.00	0.00	0.00	0.00	0.00	0.00
t13DCPy	110	$C_3H_4Cl_2$	0.00	0.00	0.00	0.00	0.00	0.00	0.00	0.00
12DCP	112	$C_3H_6Cl_2$	0.03	0.00	0.00	0.00	0.00	0.00	0.00	0.00
CB	112	C_6H_5Cl	0.00	0.00	0.00	0.00	0.00	0.00	0.00	0.00
CF	118	$CHCl_3$	0.00	0.00	0.00	0.00	0.00	0.00	0.00	0.00
124TMB	120	C_9H_{12}	0.00	0.00	0.00	0.00	0.00	0.00	0.00	0.00
135TMB	120	C_9H_{12}	0.00	0.00	0.00	0.00	0.00	0.00	0.00	0.00
F12	120	CCl_2F_2	0.00	0.00	0.00	0.00	0.00	0.00	0.00	0.00
TCEy	130	C_2HCl_3	0.00	0.00	0.00	0.00	0.00	0.00	0.00	0.00
111TCE	132	$C_2H_3Cl_3$	0.00	0.00	0.00	0.00	0.00	0.00	0.00	0.00
112TCE	132	$C_2H_3Cl_3$	0.00	0.00	0.00	0.00	0.00	0.00	0.00	0.00
F11	136	CCl_3F	0.00	0.00	0.00	0.00	0.00	0.00	0.00	0.00
mDCB	146	$C_6H_4Cl_2$	0.00	0.00	0.00	0.00	0.00	0.00	0.00	0.00
oDCB	146	$C_6H_4Cl_2$	0.00	0.00	0.00	0.00	0.00	0.00	0.00	0.00
pDCB	146	$C_6H_4Cl_2$	0.00	0.00	0.00	0.00	0.00	0.00	0.00	0.00
CTC	152	CCl_4	0.00	0.00	0.00	0.00	0.00	0.00	0.00	0.00
TeCEy	164	C_2Cl_4	0.00	0.00	0.00	0.00	0.00	0.00	0.00	0.00
TeCE	166	$C_2H_2Cl_4$	0.00	0.00	0.00	0.00	0.00	0.00	0.00	0.00
F114	170	$C_2Cl_2F_4$	0.00	0.00	0.00	0.00	0.00	0.00	0.00	0.00
124TCB	180	$C_6H_3Cl_3$	0.00	0.00	0.00	0.00	0.00	0.00	0.00	0.00
12DBE	186	$C_2H_4Br_2$	0.00	0.00	0.00	0.00	0.00	0.00	0.00	0.00
F113	186	$C_2Cl_3F_3$	0.00	0.00	0.00	0.00	0.00	0.00	0.00	0.00
HC13BD	258	C_4Cl_6	0.00	0.00	0.00	0.00	0.00	0.00	0.00	0.00

TO-14 compound Code	m/z	m/z	75			76		77		
			75	75*	75	76	76	77	77*	77
		g/mol	75.0002	75.0235	75.0446	76.0080	76.0399	77.0158	77.0391	77.0603
		Formula	C_3H_4Cl	C_6H_3	$C_3H_7O_2$	C_3H_5Cl	$C_2H_6NO_2$	C_3H_6Cl	C_6H_5	$C_3H_9O_2$
CM	50	CH_3Cl	0.00	0.00	0.00	0.00	0.00	0.00	0.00	0.00
VC	62	C_2H_3Cl	0.00	0.00	0.00	0.00	0.00	0.00	0.00	0.00
CE	64	C_2H_5Cl	0.00	0.00	0.00	0.00	0.00	0.00	0.00	0.00
B	78	C_6H_6	0.00	0.00	0.00	0.00	0.00	0.00	0.01	0.00
DCM	84	CH_2Cl_2	0.00	0.00	0.00	0.00	0.00	0.00	0.00	0.00
T	92	C_7H_8	0.00	0.00	0.00	0.00	0.00	0.00	0.00	0.00
BM	94	CH_3Br	0.00	0.00	0.00	0.00	0.00	0.00	0.00	0.00
11DCEy	96	$C_2H_2Cl_2$	0.00	0.00	0.00	0.00	0.00	0.00	0.00	0.00
c12DCEy	96	$C_2H_2Cl_2$	0.00	0.00	0.00	0.00	0.00	0.00	0.00	0.00
11DCE	98	$C_2H_4Cl_2$	0.00	0.00	0.00	0.00	0.00	0.00	0.00	0.00
12DCE	98	$C_2H_4Cl_2$	0.00	0.00	0.00	0.00	0.00	0.00	0.00	0.00
S	104	C_8H_8	0.00	0.00	0.00	0.00	0.00	0.00	0.00	0.00
EB	106	C_8H_{10}	0.00	0.00	0.00	0.00	0.00	0.00	0.00	0.00
mX	106	C_8H_{10}	0.00	0.00	0.00	0.00	0.00	0.00	0.00	0.00
oX	106	C_8H_{10}	0.00	0.00	0.00	0.00	0.00	0.00	0.00	0.00
pX	106	C_8H_{10}	0.00	0.00	0.00	0.00	0.00	0.00	0.00	0.00
c13DCPy	110	$C_3H_4Cl_2$	0.96	0.00	0.00	0.00	0.00	0.00	0.00	0.00
t13DCPy	110	$C_3H_4Cl_2$	0.96	0.00	0.00	0.00	0.00	0.00	0.00	0.00
12DCP	112	$C_3H_6Cl_2$	0.00	0.00	0.00	0.07	0.00	0.13	0.00	0.00
CB	112	C_6H_5Cl	0.00	0.00	0.00	0.00	0.00	0.00	0.01	0.00
CF	118	$CHCl_3$	0.00	0.00	0.00	0.00	0.00	0.00	0.00	0.00
124TMB	120	C_9H_{12}	0.00	0.00	0.00	0.00	0.00	0.00	0.00	0.00
135TMB	120	C_9H_{12}	0.00	0.00	0.00	0.00	0.00	0.00	0.00	0.00
F12	120	CCl_2F_2	0.00	0.00	0.00	0.00	0.00	0.00	0.00	0.00
TCEy	130	C_2HCl_3	0.00	0.00	0.00	0.00	0.00	0.00	0.00	0.00
111TCE	132	$C_2H_3Cl_3$	0.00	0.00	0.00	0.00	0.00	0.00	0.00	0.00
112TCE	132	$C_2H_3Cl_3$	0.00	0.00	0.00	0.00	0.00	0.00	0.00	0.00
F11	136	CCl_3F	0.00	0.00	0.00	0.00	0.00	0.00	0.00	0.00
mDCB	146	$C_6H_4Cl_2$	0.00	0.01	0.00	0.00	0.00	0.00	0.00	0.00
oDCB	146	$C_6H_4Cl_2$	0.00	0.01	0.00	0.00	0.00	0.00	0.00	0.00
pDCB	146	$C_6H_4Cl_2$	0.00	0.01	0.00	0.00	0.00	0.00	0.00	0.00
CTC	152	CCl_4	0.00	0.00	0.00	0.00	0.00	0.00	0.00	0.00
TeCEy	164	C_2Cl_4	0.00	0.00	0.00	0.00	0.00	0.00	0.00	0.00
TeCE	166	$C_2H_2Cl_4$	0.00	0.00	0.00	0.00	0.00	0.00	0.00	0.00
F114	170	$C_2Cl_2F_4$	0.00	0.00	0.00	0.00	0.00	0.00	0.00	0.00
124TCB	180	$C_6H_3Cl_3$	0.00	0.00	0.00	0.00	0.00	0.00	0.00	0.00
12DBE	186	$C_2H_4Br_2$	0.00	0.00	0.00	0.00	0.00	0.00	0.00	0.00
F113	186	$C_2Cl_3F_3$	0.00	0.00	0.00	0.00	0.00	0.00	0.00	0.00
HC13BD	258	C_4Cl_6	0.00	0.00	0.00	0.00	0.00	0.00	0.00	0.00

TO-14 compound Code	m/z	m/z	78		79		82		83		
			78	78	79	79	82	82	83	83	83*
		g/mol	78.0470	78.0560	79.0400	79.0548	81.9377	82.0055	82.9455	83.0180	83.0516
		Formula	C_6H_6	?	$C_2H_5O_2(H_2O)$	C_6H_7	CCl_2	$C_4H_2O_2$	$CHCl_2$	?	?
CM	50	CH_3Cl	0.00	0.00	0.00	0.00	0.00	0.00	0.00	0.00	0.00
VC	62	C_2H_3Cl	0.00	0.00	0.00	0.00	0.00	0.00	0.00	0.00	0.00
CE	64	C_2H_5Cl	0.00	0.00	0.00	0.00	0.00	0.00	0.00	0.00	0.00
B	78	C_6H_6	0.20	0.00	0.00	0.76	0.00	0.00	0.00	0.00	0.00
DCM	84	CH_2Cl_2	0.00	0.00	0.00	0.00	0.00	0.00	0.41	0.00	0.00
T	92	C_7H_8	0.00	0.00	0.00	0.00	0.00	0.00	0.00	0.00	0.00
BM	94	CH_3Br	0.00	0.00	0.00	0.00	0.00	0.00	0.00	0.00	0.00
11DCEy	96	$C_2H_2Cl_2$	0.00	0.00	0.00	0.00	0.00	0.00	0.01	0.00	0.00
c12DCEy	96	$C_2H_2Cl_2$	0.00	0.00	0.00	0.00	0.00	0.00	0.00	0.00	0.00
11DCE	98	$C_2H_4Cl_2$	0.00	0.00	0.00	0.00	0.00	0.00	0.01	0.00	0.00
12DCE	98	$C_2H_4Cl_2$	0.00	0.00	0.00	0.00	0.00	0.00	0.00	0.00	0.00
S	104	C_8H_8	0.00	0.00	0.00	0.01	0.00	0.00	0.00	0.00	0.00
EB	106	C_8H_{10}	0.01	0.00	0.00	0.41	0.00	0.00	0.00	0.00	0.00
mX	106	C_8H_{10}	0.00	0.00	0.00	0.00	0.00	0.00	0.00	0.00	0.00
oX	106	C_8H_{10}	0.00	0.00	0.00	0.00	0.00	0.00	0.00	0.00	0.00
pX	106	C_8H_{10}	0.00	0.00	0.00	0.00	0.00	0.00	0.00	0.00	0.00
c13DCPy	110	$C_3H_4Cl_2$	0.00	0.00	0.00	0.00	0.00	0.00	0.00	0.00	0.00
t13DCPy	110	$C_3H_4Cl_2$	0.00	0.00	0.00	0.00	0.00	0.00	0.00	0.00	0.00
12DCP	112	$C_3H_6Cl_2$	0.00	0.00	0.00	0.00	0.00	0.00	0.00	0.00	0.00
CB	112	C_6H_5Cl	0.00	0.00	0.00	0.00	0.00	0.00	0.00	0.00	0.00
CF	118	$CHCl_3$	0.00	0.00	0.00	0.00	0.00	0.00	0.99	0.00	0.00
124TMB	120	C_9H_{12}	0.00	0.00	0.00	0.00	0.00	0.00	0.00	0.00	0.00
135TMB	120	C_9H_{12}	0.00	0.00	0.00	0.00	0.00	0.00	0.00	0.00	0.00
F12	120	CCl_2F_2	0.00	0.00	0.00	0.00	0.00	0.00	0.00	0.00	0.00
TCEy	130	C_2HCl_3	0.00	0.00	0.00	0.00	0.00	0.00	0.00	0.00	0.00
111TCE	132	$C_2H_3Cl_3$	0.00	0.00	0.00	0.00	0.00	0.00	0.00	0.00	0.00
112TCE	132	$C_2H_3Cl_3$	0.00	0.00	0.00	0.00	0.00	0.00	0.78	0.00	0.00
F11	136	CCl_3F	0.00	0.00	0.00	0.00	0.00	0.00	0.00	0.00	0.00
mDCB	146	$C_6H_4Cl_2$	0.00	0.00	0.00	0.00	0.00	0.00	0.00	0.00	0.00
oDCB	146	$C_6H_4Cl_2$	0.00	0.00	0.00	0.00	0.00	0.00	0.00	0.00	0.00
pDCB	146	$C_6H_4Cl_2$	0.00	0.00	0.00	0.00	0.00	0.00	0.00	0.00	0.00
CTC	152	CCl_4	0.00	0.00	0.00	0.00	0.01	0.00	0.00	0.00	0.00
TeCEy	164	C_2Cl_4	0.00	0.00	0.00	0.00	0.00	0.00	0.10	0.00	0.00
TeCE	166	$C_2H_2Cl_4$	0.00	0.00	0.00	0.00	0.00	0.00	0.84	0.00	0.00
F114	170	$C_2Cl_2F_4$	0.00	0.00	0.00	0.00	0.00	0.00	0.00	0.00	0.00
124TCB	180	$C_6H_3Cl_3$	0.00	0.00	0.00	0.00	0.00	0.00	0.00	0.00	0.00
12DBE	186	$C_2H_4Br_2$	0.00	0.00	0.00	0.00	0.00	0.00	0.00	0.00	0.00
F113	186	$C_2Cl_3F_3$	0.00	0.00	0.00	0.00	0.00	0.00	0.00	0.00	0.00
HC13BD	258	C_4Cl_6	0.00	0.00	0.00	0.00	0.00	0.00	0.00	0.00	0.00

TO-14 compound Code	m/z	m/z	85		91			92		
			85	85	91	91	91*	92	92	92*
		g/mol	84.9657	85.0290	91.0395	91.0548	91.0759	92.0348	92.0626	92.0712
		Formula	$CClF_2$	$C_4H_5O_2$	C_3H_7O	C_7H_7	$C_4H_{11}O_2$	$C_2H_6NO_3$	C_7H_8	$C_3H_{10}NO_2$
CM	50	CH_3Cl	0.00	0.00	0.00	0.00	0.00	0.00	0.00	0.00
VC	62	C_2H_3Cl	0.00	0.00	0.00	0.00	0.00	0.00	0.00	0.00
CE	64	C_2H_5Cl	0.00	0.00	0.00	0.00	0.00	0.00	0.00	0.00
B	78	C_6H_6	0.00	0.00	0.00	0.00	0.00	0.00	0.00	0.00
DCM	84	CH_2Cl_2	0.00	0.00	0.00	0.00	0.00	0.00	0.00	0.00
T	92	C_7H_8	0.00	0.00	0.00	0.09	0.00	0.00	0.14	0.00
BM	94	CH_3Br	0.00	0.00	0.00	0.00	0.00	0.00	0.00	0.00
11DCEy	96	$C_2H_2Cl_2$	0.00	0.00	0.00	0.00	0.00	0.00	0.00	0.00
c12DCEy	96	$C_2H_2Cl_2$	0.00	0.00	0.00	0.00	0.00	0.00	0.00	0.00
11DCE	98	$C_2H_4Cl_2$	0.00	0.00	0.00	0.00	0.00	0.00	0.00	0.00
12DCE	98	$C_2H_4Cl_2$	0.00	0.00	0.00	0.00	0.00	0.00	0.00	0.00
S	104	C_8H_8	0.00	0.00	0.00	0.00	0.00	0.00	0.00	0.00
EB	106	C_8H_{10}	0.00	0.00	0.00	0.12	0.00	0.00	0.00	0.00
mX	106	C_8H_{10}	0.00	0.00	0.00	0.07	0.00	0.00	0.00	0.00
oX	106	C_8H_{10}	0.00	0.00	0.00	0.06	0.00	0.00	0.00	0.00
pX	106	C_8H_{10}	0.00	0.00	0.00	0.07	0.00	0.00	0.00	0.00
c13DCPy	110	$C_3H_4Cl_2$	0.00	0.00	0.00	0.00	0.00	0.00	0.00	0.00
t13DCPy	110	$C_3H_4Cl_2$	0.00	0.00	0.00	0.00	0.00	0.00	0.00	0.00
12DCP	112	$C_3H_6Cl_2$	0.00	0.00	0.00	0.00	0.00	0.00	0.00	0.00
CB	112	C_6H_5Cl	0.00	0.00	0.00	0.00	0.00	0.00	0.00	0.00
CF	118	$CHCl_3$	0.00	0.00	0.00	0.00	0.00	0.00	0.00	0.00
124TMB	120	C_9H_{12}	0.00	0.00	0.00	0.01	0.00	0.00	0.00	0.00
135TMB	120	C_9H_{12}	0.00	0.00	0.00	0.01	0.00	0.00	0.00	0.00
F12	120	CCl_2F_2	1.00	0.00	0.00	0.00	0.00	0.00	0.00	0.00
TCEy	130	C_2HCl_3	0.00	0.00	0.00	0.00	0.00	0.00	0.00	0.00
111TCE	132	$C_2H_3Cl_3$	0.00	0.00	0.00	0.00	0.00	0.00	0.00	0.00
112TCE	132	$C_2H_3Cl_3$	0.00	0.00	0.00	0.00	0.00	0.00	0.00	0.00
F11	136	CCl_3F	0.00	0.00	0.00	0.00	0.00	0.00	0.00	0.00
mDCB	146	$C_6H_4Cl_2$	0.00	0.00	0.00	0.00	0.00	0.00	0.00	0.00
oDCB	146	$C_6H_4Cl_2$	0.00	0.00	0.00	0.00	0.00	0.00	0.00	0.00
pDCB	146	$C_6H_4Cl_2$	0.00	0.00	0.00	0.00	0.00	0.00	0.00	0.00
CTC	152	CCl_4	0.00	0.00	0.00	0.00	0.00	0.00	0.00	0.00
TeCEy	164	C_2Cl_4	0.00	0.00	0.00	0.00	0.00	0.00	0.00	0.00
TeCE	166	$C_2H_2Cl_4$	0.00	0.00	0.00	0.00	0.00	0.00	0.00	0.00
F114	170	$C_2Cl_2F_4$	0.79	0.00	0.00	0.00	0.00	0.00	0.00	0.00
124TCB	180	$C_6H_3Cl_3$	0.00	0.00	0.00	0.00	0.00	0.00	0.00	0.00
12DBE	186	$C_2H_4Br_2$	0.00	0.00	0.00	0.00	0.00	0.00	0.00	0.00
F113	186	$C_2Cl_3F_3$	0.00	0.00	0.00	0.00	0.00	0.00	0.00	0.00
HC13BD	258	C_4Cl_6	0.00	0.00	0.00	0.00	0.00	0.00	0.00	0.00

TO-14 compound Code	m/z	m/z	93			94		95	96	
			93	93*	93	94	94*	95	96	(x+1)95
		g/mol	93.0400	93.0552	93.0704	93.9377	93.9418	95.0497	95.9534	96.0530
		Formula	?	$C_3H_9O_3$	C_7H_9	C_2Cl_2	CH_3Br	C_6H_7O	$C_2H_2Cl_2$	$C_5{}^{13}CH_7O$
CM	50	CH_3Cl	0.00	0.00	0.00	0.00	0.00	0.00	0.00	0.00
VC	62	C_2H_3Cl	0.00	0.00	0.00	0.00	0.00	0.00	0.00	0.00
CE	64	C_2H_5Cl	0.00	0.00	0.00	0.00	0.00	0.00	0.00	0.00
B	78	C_6H_6	0.00	0.00	0.00	0.00	0.00	0.00	0.00	0.00
DCM	84	CH_2Cl_2	0.00	0.00	0.00	0.00	0.00	0.00	0.00	0.00
T	92	C_7H_8	0.00	0.00	0.76	0.00	0.00	0.00	0.00	0.00
BM	94	CH_3Br	0.00	0.00	0.00	0.00	1.00	0.00	0.00	0.00
11DCEy	96	$C_2H_2Cl_2$	0.00	0.00	0.00	0.00	0.00	0.00	0.00	0.00
c12DCEy	96	$C_2H_2Cl_2$	0.00	0.00	0.00	0.00	0.00	0.00	0.96	0.00
11DCE	98	$C_2H_4Cl_2$	0.00	0.00	0.00	0.00	0.00	0.00	0.00	0.00
12DCE	98	$C_2H_4Cl_2$	0.00	0.00	0.00	0.00	0.00	0.00	0.00	0.00
S	104	C_8H_8	0.00	0.00	0.00	0.00	0.00	0.00	0.00	0.00
EB	106	C_8H_{10}	0.00	0.00	0.00	0.00	0.00	0.00	0.00	0.00
mX	106	C_8H_{10}	0.00	0.00	0.00	0.00	0.00	0.00	0.00	0.00
oX	106	C_8H_{10}	0.00	0.00	0.00	0.00	0.00	0.00	0.00	0.00
pX	106	C_8H_{10}	0.00	0.00	0.00	0.00	0.00	0.00	0.00	0.00
c13DCPy	110	$C_3H_4Cl_2$	0.00	0.00	0.00	0.00	0.00	0.00	0.00	0.00
t13DCPy	110	$C_3H_4Cl_2$	0.00	0.00	0.00	0.00	0.00	0.00	0.00	0.00
12DCP	112	$C_3H_6Cl_2$	0.00	0.00	0.00	0.00	0.00	0.00	0.00	0.00
CB	112	C_6H_5Cl	0.00	0.00	0.00	0.00	0.00	0.00	0.00	0.00
CF	118	$CHCl_3$	0.00	0.00	0.00	0.00	0.00	0.00	0.00	0.00
124TMB	120	C_9H_{12}	0.00	0.00	0.00	0.00	0.00	0.00	0.00	0.00
135TMB	120	C_9H_{12}	0.00	0.00	0.00	0.00	0.00	0.00	0.00	0.00
F12	120	CCl_2F_2	0.00	0.00	0.00	0.00	0.00	0.00	0.00	0.00
TCEy	130	C_2HCl_3	0.00	0.00	0.00	0.00	0.00	0.00	0.00	0.00
111TCE	132	$C_2H_3Cl_3$	0.00	0.00	0.00	0.00	0.00	0.00	0.00	0.00
112TCE	132	$C_2H_3Cl_3$	0.00	0.00	0.00	0.00	0.00	0.00	0.00	0.00
F11	136	CCl_3F	0.00	0.00	0.00	0.00	0.00	0.00	0.00	0.00
mDCB	146	$C_6H_4Cl_2$	0.00	0.00	0.00	0.00	0.00	0.00	0.00	0.00
oDCB	146	$C_6H_4Cl_2$	0.00	0.00	0.00	0.00	0.00	0.00	0.00	0.00
pDCB	146	$C_6H_4Cl_2$	0.00	0.00	0.00	0.00	0.00	0.00	0.00	0.00
CTC	152	CCl_4	0.00	0.00	0.00	0.00	0.00	0.00	0.00	0.00
TeCEy	164	C_2Cl_4	0.00	0.00	0.00	0.07	0.00	0.00	0.00	0.00
TeCE	166	$C_2H_2Cl_4$	0.00	0.00	0.00	0.00	0.00	0.00	0.00	0.00
F114	170	$C_2Cl_2F_4$	0.00	0.00	0.00	0.00	0.00	0.00	0.00	0.00
124TCB	180	$C_6H_3Cl_3$	0.00	0.00	0.00	0.00	0.00	0.00	0.00	0.00
12DBE	186	$C_2H_4Br_2$	0.00	0.00	0.00	0.00	0.00	0.00	0.00	0.00
F113	186	$C_2Cl_3F_3$	0.00	0.00	0.00	0.00	0.00	0.00	0.00	0.00
HC13BD	258	C_4Cl_6	0.00	0.00	0.00	0.00	0.00	0.00	0.00	0.00

TO-14 compound Code	m/z	m/z	97		98		101		103		
			97	97	98	98	101	101	103	103	103*
		g/mol	96.9612	97.0078	97.9690	98.0242	100.9361	101.0265	103.0422	103.0548	103.0759
		Formula	$C_2H_3Cl_2$	$AlO(H_2O)_3$	$C_2H_4Cl_2$	$C_4H_4NO_2$	CCl_2F	C_7H_3N	C_7H_5N	C_8H_7	$C_5H_{11}O_2$
CM	50	CH_3Cl	0.00	0.00	0.00	0.00	0.00	0.00	0.00	0.00	0.00
VC	62	C_2H_3Cl	0.00	0.00	0.00	0.00	0.00	0.00	0.00	0.00	0.00
CE	64	C_2H_5Cl	0.00	0.00	0.00	0.00	0.00	0.00	0.00	0.00	0.00
B	78	C_6H_6	0.00	0.00	0.00	0.00	0.00	0.00	0.00	0.00	0.00
DCM	84	CH_2Cl_2	0.00	0.00	0.00	0.00	0.00	0.00	0.00	0.00	0.00
T	92	C_7H_8	0.00	0.00	0.00	0.00	0.00	0.00	0.00	0.00	0.00
BM	94	CH_3Br	0.00	0.00	0.00	0.00	0.00	0.00	0.00	0.00	0.00
11DCEy	96	$C_2H_2Cl_2$	0.08	0.00	0.00	0.00	0.00	0.00	0.00	0.00	0.00
c12DCEy	96	$C_2H_2Cl_2$	0.02	0.00	0.00	0.00	0.00	0.00	0.00	0.00	0.00
11DCE	98	$C_2H_4Cl_2$	0.08	0.00	0.00	0.00	0.00	0.00	0.00	0.00	0.00
12DCE	98	$C_2H_4Cl_2$	0.00	0.00	0.00	0.00	0.00	0.00	0.00	0.00	0.00
S	104	C_8H_8	0.00	0.00	0.00	0.00	0.00	0.00	0.00	0.01	0.00
EB	106	C_8H_{10}	0.00	0.00	0.00	0.00	0.00	0.00	0.00	0.00	0.00
mX	106	C_8H_{10}	0.00	0.00	0.00	0.00	0.00	0.00	0.00	0.00	0.00
oX	106	C_8H_{10}	0.00	0.00	0.00	0.00	0.00	0.00	0.00	0.00	0.00
pX	106	C_8H_{10}	0.00	0.00	0.00	0.00	0.00	0.00	0.00	0.00	0.00
c13DCPy	110	$C_3H_4Cl_2$	0.00	0.00	0.00	0.00	0.00	0.00	0.00	0.00	0.00
t13DCPy	110	$C_3H_4Cl_2$	0.00	0.00	0.00	0.00	0.00	0.00	0.00	0.00	0.00
12DCP	112	$C_3H_6Cl_2$	0.00	0.00	0.00	0.00	0.00	0.00	0.00	0.00	0.00
CB	112	C_6H_5Cl	0.00	0.00	0.00	0.00	0.00	0.00	0.00	0.00	0.00
CF	118	$CHCl_3$	0.00	0.00	0.00	0.00	0.00	0.00	0.00	0.00	0.00
124TMB	120	C_9H_{12}	0.00	0.00	0.00	0.00	0.00	0.00	0.00	0.00	0.00
135TMB	120	C_9H_{12}	0.00	0.00	0.00	0.00	0.00	0.00	0.00	0.00	0.00
F12	120	CCl_2F_2	0.00	0.00	0.00	0.00	0.00	0.00	0.00	0.00	0.00
TCEy	130	C_2HCl_3	0.00	0.00	0.00	0.00	0.00	0.00	0.00	0.00	0.00
111TCE	132	$C_2H_3Cl_3$	0.99	0.00	0.00	0.00	0.00	0.00	0.00	0.00	0.00
112TCE	132	$C_2H_3Cl_3$	0.15	0.00	0.00	0.00	0.00	0.00	0.00	0.00	0.00
F11	136	CCl_3F	0.00	0.00	0.00	0.00	0.50	0.00	0.00	0.00	0.00
mDCB	146	$C_6H_4Cl_2$	0.00	0.00	0.00	0.00	0.00	0.00	0.00	0.00	0.00
oDCB	146	$C_6H_4Cl_2$	0.00	0.00	0.00	0.00	0.00	0.00	0.00	0.00	0.00
pDCB	146	$C_6H_4Cl_2$	0.00	0.00	0.00	0.00	0.00	0.00	0.00	0.00	0.00
CTC	152	CCl_4	0.00	0.00	0.00	0.00	0.00	0.00	0.00	0.00	0.00
TeCEy	164	C_2Cl_4	0.00	0.00	0.00	0.00	0.00	0.00	0.00	0.00	0.00
TeCE	166	$C_2H_2Cl_4$	0.00	0.00	0.00	0.00	0.00	0.00	0.00	0.00	0.00
F114	170	$C_2Cl_2F_4$	0.00	0.00	0.00	0.00	0.16	0.00	0.00	0.00	0.00
124TCB	180	$C_6H_3Cl_3$	0.00	0.00	0.00	0.00	0.00	0.00	0.00	0.00	0.00
12DBE	186	$C_2H_4Br_2$	0.00	0.00	0.00	0.00	0.00	0.00	0.00	0.00	0.00
F113	186	$C_2Cl_3F_3$	0.00	0.00	0.00	0.00	0.25	0.00	0.00	0.00	0.00
HC13BD	258	C_4Cl_6	0.00	0.00	0.00	0.00	0.00	0.00	0.00	0.00	0.00

TO-14 compound Code	m/z	m/z	104			105			106		
			104	104	104*	105	105	105*	106	106*	106**
		g/mol	104.0374	104.0626	104.0712	104.9340	105.0578	105.0704	105.9377	105.9418	106.0783
		Formula	$C_6H_4N_2$	C_8H_8	$C_4H_{10}NO_2$	C_2H_2Br	C_7H_7N	C_8H_9	C_3Cl_2	C_2H_3Br	C_8H_{10}
CM	50	CH_3Cl	0.00	0.00	0.00	0.00	0.00	0.00	0.00	0.00	0.00
VC	62	C_2H_3Cl	0.00	0.00	0.00	0.00	0.00	0.00	0.00	0.00	0.00
CE	64	C_2H_5Cl	0.00	0.00	0.00	0.00	0.00	0.00	0.00	0.00	0.00
B	78	C_6H_6	0.00	0.00	0.00	0.00	0.00	0.00	0.00	0.00	0.00
DCM	84	CH_2Cl_2	0.00	0.00	0.00	0.00	0.00	0.00	0.00	0.00	0.00
T	92	C_7H_8	0.00	0.00	0.00	0.00	0.00	0.00	0.00	0.00	0.00
BM	94	CH_3Br	0.00	0.00	0.00	0.00	0.00	0.00	0.00	0.00	0.00
11DCEy	96	$C_2H_2Cl_2$	0.00	0.00	0.00	0.00	0.00	0.00	0.00	0.00	0.00
c12DCEy	96	$C_2H_2Cl_2$	0.00	0.00	0.00	0.00	0.00	0.00	0.00	0.00	0.00
11DCE	98	$C_2H_4Cl_2$	0.00	0.00	0.00	0.00	0.00	0.00	0.00	0.00	0.00
12DCE	98	$C_2H_4Cl_2$	0.00	0.00	0.00	0.00	0.00	0.00	0.00	0.00	0.00
S	104	C_8H_8	0.00	0.13	0.00	0.00	0.00	0.85	0.00	0.00	0.00
EB	106	C_8H_{10}	0.00	0.00	0.00	0.00	0.00	0.01	0.00	0.00	0.04
mX	106	C_8H_{10}	0.00	0.00	0.00	0.00	0.00	0.02	0.00	0.00	0.12
oX	106	C_8H_{10}	0.00	0.00	0.00	0.00	0.00	0.01	0.00	0.00	0.23
pX	106	C_8H_{10}	0.00	0.00	0.00	0.00	0.00	0.01	0.00	0.00	0.23
c13DCPy	110	$C_3H_4Cl_2$	0.00	0.00	0.00	0.00	0.00	0.00	0.00	0.00	0.00
t13DCPy	110	$C_3H_4Cl_2$	0.00	0.00	0.00	0.00	0.00	0.00	0.00	0.00	0.00
12DCP	112	$C_3H_6Cl_2$	0.00	0.00	0.00	0.00	0.00	0.00	0.00	0.00	0.00
CB	112	C_6H_5Cl	0.00	0.00	0.00	0.00	0.00	0.00	0.00	0.00	0.00
CF	118	$CHCl_3$	0.00	0.00	0.00	0.00	0.00	0.00	0.00	0.00	0.00
124TMB	120	C_9H_{12}	0.00	0.00	0.00	0.00	0.00	0.05	0.00	0.00	0.00
135TMB	120	C_9H_{12}	0.00	0.00	0.00	0.00	0.00	0.05	0.00	0.00	0.00
F12	120	CCl_2F_2	0.00	0.00	0.00	0.00	0.00	0.00	0.00	0.00	0.00
TCEy	130	C_2HCl_3	0.00	0.00	0.00	0.00	0.00	0.00	0.00	0.00	0.00
111TCE	132	$C_2H_3Cl_3$	0.00	0.00	0.00	0.00	0.00	0.00	0.00	0.00	0.00
112TCE	132	$C_2H_3Cl_3$	0.00	0.00	0.00	0.00	0.00	0.00	0.00	0.00	0.00
F11	136	CCl_3F	0.00	0.00	0.00	0.00	0.00	0.00	0.00	0.00	0.00
mDCB	146	$C_6H_4Cl_2$	0.00	0.00	0.00	0.00	0.00	0.00	0.00	0.00	0.00
oDCB	146	$C_6H_4Cl_2$	0.00	0.00	0.00	0.00	0.00	0.00	0.00	0.00	0.00
pDCB	146	$C_6H_4Cl_2$	0.00	0.00	0.00	0.00	0.00	0.00	0.00	0.00	0.00
CTC	152	CCl_4	0.00	0.00	0.00	0.00	0.00	0.00	0.00	0.00	0.00
TeCEy	164	C_2Cl_4	0.00	0.00	0.00	0.00	0.00	0.00	0.00	0.00	0.00
TeCE	166	$C_2H_2Cl_4$	0.00	0.00	0.00	0.00	0.00	0.00	0.00	0.00	0.00
F114	170	$C_2Cl_2F_4$	0.00	0.00	0.00	0.00	0.00	0.00	0.00	0.00	0.00
124TCB	180	$C_6H_3Cl_3$	0.00	0.00	0.00	0.00	0.00	0.00	0.00	0.00	0.00
12DBE	186	$C_2H_4Br_2$	0.00	0.00	0.00	0.00	0.00	0.00	0.00	0.00	0.00
F113	186	$C_2Cl_3F_3$	0.00	0.00	0.00	0.00	0.00	0.00	0.00	0.00	0.00
HC13BD	258	C_4Cl_6	0.00	0.00	0.00	0.00	0.00	0.00	0.00	0.00	0.00

TO-14 compound Code	m/z	m/z	107					109		110	
			107	107	107*	107*	107**	109	109	110	(x+1)109
		g/mol	106.9051	106.9455	106.9496	107.0344	107.0861	108.9612	108.9612	109.9690	110.0323
		Formula	Ag	C_3HCl_2	C_2H_4Br	$C_3H_7O_4$	C_8H_{11}	$C_3H_3Cl_2$	$C_6H_5O_2$	$C_3H_4Cl_2$	$C_5{}^{13}CH_5O_2$
CM	50	CH_3Cl	0.00	0.00	0.00	0.00	0.00	0.00	0.00	0.00	0.00
VC	62	C_2H_3Cl	0.00	0.00	0.00	0.00	0.00	0.00	0.00	0.00	0.00
CE	64	C_2H_5Cl	0.00	0.00	0.00	0.00	0.00	0.00	0.00	0.00	0.00
B	78	C_6H_6	0.00	0.00	0.00	0.00	0.00	0.00	0.00	0.00	0.00
DCM	84	CH_2Cl_2	0.00	0.00	0.00	0.00	0.00	0.00	0.00	0.00	0.00
T	92	C_7H_8	0.00	0.00	0.00	0.00	0.00	0.00	0.00	0.00	0.00
BM	94	CH_3Br	0.00	0.00	0.00	0.00	0.00	0.00	0.00	0.00	0.00
11DCEy	96	$C_2H_2Cl_2$	0.00	0.00	0.00	0.00	0.00	0.00	0.00	0.00	0.00
c12DCEy	96	$C_2H_2Cl_2$	0.00	0.00	0.00	0.00	0.00	0.00	0.00	0.00	0.00
11DCE	98	$C_2H_4Cl_2$	0.00	0.00	0.00	0.00	0.00	0.00	0.00	0.00	0.00
12DCE	98	$C_2H_4Cl_2$	0.00	0.00	0.00	0.00	0.00	0.00	0.00	0.00	0.00
S	104	C_8H_8	0.00	0.00	0.00	0.00	0.00	0.00	0.00	0.00	0.00
EB	106	C_8H_{10}	0.00	0.00	0.00	0.00	0.40	0.00	0.00	0.00	0.00
mX	106	C_8H_{10}	0.00	0.00	0.00	0.00	0.79	0.00	0.00	0.00	0.00
oX	106	C_8H_{10}	0.00	0.00	0.00	0.00	0.68	0.00	0.00	0.00	0.00
pX	106	C_8H_{10}	0.00	0.00	0.00	0.00	0.67	0.00	0.00	0.00	0.00
c13DCPy	110	$C_3H_4Cl_2$	0.00	0.00	0.00	0.00	0.00	0.00	0.00	0.01	0.00
t13DCPy	110	$C_3H_4Cl_2$	0.00	0.00	0.00	0.00	0.00	0.00	0.00	0.01	0.00
12DCP	112	$C_3H_6Cl_2$	0.00	0.00	0.00	0.00	0.00	0.00	0.00	0.00	0.00
CB	112	C_6H_5Cl	0.00	0.00	0.00	0.00	0.00	0.00	0.00	0.00	0.00
CF	118	$CHCl_3$	0.00	0.00	0.00	0.00	0.00	0.00	0.00	0.00	0.00
124TMB	120	C_9H_{12}	0.00	0.00	0.00	0.00	0.00	0.00	0.00	0.00	0.00
135TMB	120	C_9H_{12}	0.00	0.00	0.00	0.00	0.00	0.00	0.00	0.00	0.00
F12	120	CCl_2F_2	0.00	0.00	0.00	0.00	0.00	0.00	0.00	0.00	0.00
TCEy	130	C_2HCl_3	0.00	0.00	0.00	0.00	0.00	0.00	0.00	0.00	0.00
111TCE	132	$C_2H_3Cl_3$	0.00	0.00	0.00	0.00	0.00	0.00	0.00	0.00	0.00
112TCE	132	$C_2H_3Cl_3$	0.00	0.00	0.00	0.00	0.00	0.00	0.00	0.00	0.00
F11	136	CCl_3F	0.00	0.00	0.00	0.00	0.00	0.00	0.00	0.00	0.00
mDCB	146	$C_6H_4Cl_2$	0.00	0.00	0.00	0.00	0.00	0.00	0.00	0.00	0.00
oDCB	146	$C_6H_4Cl_2$	0.00	0.00	0.00	0.00	0.00	0.00	0.00	0.00	0.00
pDCB	146	$C_6H_4Cl_2$	0.00	0.00	0.00	0.00	0.00	0.00	0.00	0.00	0.00
CTC	152	CCl_4	0.00	0.00	0.00	0.00	0.00	0.00	0.00	0.00	0.00
TeCEy	164	C_2Cl_4	0.00	0.00	0.00	0.00	0.00	0.00	0.00	0.00	0.00
TeCE	166	$C_2H_2Cl_4$	0.00	0.00	0.00	0.00	0.00	0.00	0.00	0.00	0.00
F114	170	$C_2Cl_2F_4$	0.00	0.00	0.00	0.00	0.00	0.00	0.00	0.00	0.00
124TCB	180	$C_6H_3Cl_3$	0.00	0.00	0.00	0.00	0.00	0.00	0.00	0.00	0.00
12DBE	186	$C_2H_4Br_2$	0.00	0.00	1.00	0.00	0.00	0.00	0.00	0.00	0.00
F113	186	$C_2Cl_3F_3$	0.00	0.00	0.00	0.00	0.00	0.00	0.00	0.00	0.00
HC13BD	258	C_4Cl_6	0.00	0.01	0.00	0.00	0.00	0.00	0.00	0.00	0.00

TO-14 compound Code	m/z	m/z	111	112			113			117	
			111	112	112*	(x+1)111	113	113	113*	117	117
		g/mol	111.0446	111.9847	112.0080	112.0480	113.0158	113.0280	113.0603	116.9066	117.0188
		Formula	$C_6H_7O_2$	$C_3H_6Cl_2$	C_6H_5Cl	$C_5{}^{13}CH_7O_2$	C_6H_6Cl	?	$C_6H_9O_2$	CCl_3	$C_4H_5O_4$
CM	50	CH_3Cl	0.00	0.00	0.00	0.00	0.00	0.00	0.00	0.00	0.00
VC	62	C_2H_3Cl	0.00	0.00	0.00	0.00	0.00	0.00	0.00	0.00	0.00
CE	64	C_2H_5Cl	0.00	0.00	0.00	0.00	0.00	0.00	0.00	0.00	0.00
B	78	C_6H_6	0.00	0.00	0.00	0.00	0.00	0.00	0.00	0.00	0.00
DCM	84	CH_2Cl_2	0.00	0.00	0.00	0.00	0.00	0.00	0.00	0.00	0.00
T	92	C_7H_8	0.00	0.00	0.00	0.00	0.00	0.00	0.00	0.00	0.00
BM	94	CH_3Br	0.00	0.00	0.00	0.00	0.00	0.00	0.00	0.00	0.00
11DCEy	96	$C_2H_2Cl_2$	0.00	0.00	0.00	0.00	0.00	0.00	0.00	0.00	0.00
c12DCEy	96	$C_2H_2Cl_2$	0.00	0.00	0.00	0.00	0.00	0.00	0.00	0.00	0.00
11DCE	98	$C_2H_4Cl_2$	0.00	0.00	0.00	0.00	0.00	0.00	0.00	0.00	0.00
12DCE	98	$C_2H_4Cl_2$	0.00	0.00	0.00	0.00	0.00	0.00	0.00	0.00	0.00
S	104	C_8H_8	0.00	0.00	0.00	0.00	0.00	0.00	0.00	0.00	0.00
EB	106	C_8H_{10}	0.00	0.00	0.00	0.00	0.00	0.00	0.00	0.00	0.00
mX	106	C_8H_{10}	0.00	0.00	0.00	0.00	0.00	0.00	0.00	0.00	0.00
oX	106	C_8H_{10}	0.00	0.00	0.00	0.00	0.00	0.00	0.00	0.00	0.00
pX	106	C_8H_{10}	0.00	0.00	0.00	0.00	0.00	0.00	0.00	0.00	0.00
c13DCPy	110	$C_3H_4Cl_2$	0.00	0.00	0.00	0.00	0.00	0.00	0.00	0.00	0.00
t13DCPy	110	$C_3H_4Cl_2$	0.00	0.00	0.00	0.00	0.00	0.00	0.00	0.00	0.00
12DCP	112	$C_3H_6Cl_2$	0.00	0.00	0.00	0.00	0.00	0.00	0.00	0.00	0.00
CB	112	C_6H_5Cl	0.00	0.00	0.20	0.00	0.78	0.00	0.00	0.00	0.00
CF	118	$CHCl_3$	0.00	0.00	0.00	0.00	0.00	0.00	0.00	0.01	0.00
124TMB	120	C_9H_{12}	0.00	0.00	0.00	0.00	0.00	0.00	0.00	0.00	0.00
135TMB	120	C_9H_{12}	0.00	0.00	0.00	0.00	0.00	0.00	0.00	0.00	0.00
F12	120	CCl_2F_2	0.00	0.00	0.00	0.00	0.00	0.00	0.00	0.00	0.00
TCEy	130	C_2HCl_3	0.00	0.00	0.00	0.00	0.00	0.00	0.00	0.00	0.00
111TCE	132	$C_2H_3Cl_3$	0.00	0.00	0.00	0.00	0.00	0.00	0.00	0.00	0.00
112TCE	132	$C_2H_3Cl_3$	0.00	0.00	0.00	0.00	0.00	0.00	0.00	0.01	0.00
F11	136	CCl_3F	0.00	0.00	0.00	0.00	0.00	0.00	0.00	0.50	0.00
mDCB	146	$C_6H_4Cl_2$	0.00	0.00	0.00	0.00	0.00	0.00	0.00	0.00	0.00
oDCB	146	$C_6H_4Cl_2$	0.00	0.00	0.00	0.00	0.00	0.00	0.00	0.00	0.00
pDCB	146	$C_6H_4Cl_2$	0.00	0.00	0.00	0.00	0.00	0.00	0.00	0.00	0.00
CTC	152	CCl_4	0.00	0.00	0.00	0.00	0.00	0.00	0.00	0.99	0.00
TeCEy	164	C_2Cl_4	0.00	0.00	0.00	0.00	0.00	0.00	0.00	0.00	0.00
TeCE	166	$C_2H_2Cl_4$	0.00	0.00	0.00	0.00	0.00	0.00	0.00	0.00	0.00
F114	170	$C_2Cl_2F_4$	0.00	0.00	0.00	0.00	0.00	0.00	0.00	0.00	0.00
124TCB	180	$C_6H_3Cl_3$	0.00	0.00	0.00	0.00	0.00	0.00	0.00	0.00	0.00
12DBE	186	$C_2H_4Br_2$	0.00	0.00	0.00	0.00	0.00	0.00	0.00	0.00	0.00
F113	186	$C_2Cl_3F_3$	0.00	0.00	0.00	0.00	0.00	0.00	0.00	0.00	0.00
HC13BD	258	C_4Cl_6	0.00	0.00	0.00	0.00	0.00	0.00	0.00	0.03	0.00

TO-14 compound Code	m/z	m/z	118	120		121		129	130	
			118	120	120	(x+1)120	121	129	130	(x+1)129
		g/mol	117.9377	120.0661	120.0939	120.0694	121.1017	129.0578	129.9144	130.0612
		Formula	C_4Cl_2	$C_4H_{10}NO_3$	C_9H_{12}	$C_3{}^{13}CH_{10}NO_3$	C_9H_{13}	C_9H_7N	C_2HCl_3	$C_8{}^{13}CH_7N$
CM	50	CH_3Cl	0.00	0.00	0.00	0.00	0.00	0.00	0.00	0.00
VC	62	C_2H_3Cl	0.00	0.00	0.00	0.00	0.00	0.00	0.00	0.00
CE	64	C_2H_5Cl	0.00	0.00	0.00	0.00	0.00	0.00	0.00	0.00
B	78	C_6H_6	0.00	0.00	0.00	0.00	0.00	0.00	0.00	0.00
DCM	84	CH_2Cl_2	0.00	0.00	0.00	0.00	0.00	0.00	0.00	0.00
T	92	C_7H_8	0.00	0.00	0.00	0.00	0.00	0.00	0.00	0.00
BM	94	CH_3Br	0.00	0.00	0.00	0.00	0.00	0.00	0.00	0.00
11DCEy	96	$C_2H_2Cl_2$	0.00	0.00	0.00	0.00	0.00	0.00	0.00	0.00
c12DCEy	96	$C_2H_2Cl_2$	0.00	0.00	0.00	0.00	0.00	0.00	0.00	0.00
11DCE	98	$C_2H_4Cl_2$	0.00	0.00	0.00	0.00	0.00	0.00	0.00	0.00
12DCE	98	$C_2H_4Cl_2$	0.00	0.00	0.00	0.00	0.00	0.00	0.00	0.00
S	104	C_8H_8	0.00	0.00	0.00	0.00	0.00	0.00	0.00	0.00
EB	106	C_8H_{10}	0.00	0.00	0.00	0.00	0.00	0.00	0.00	0.00
mX	106	C_8H_{10}	0.00	0.00	0.00	0.00	0.00	0.00	0.00	0.00
oX	106	C_8H_{10}	0.00	0.00	0.00	0.00	0.00	0.00	0.00	0.00
pX	106	C_8H_{10}	0.00	0.00	0.00	0.00	0.00	0.00	0.00	0.00
c13DCPy	110	$C_3H_4Cl_2$	0.00	0.00	0.00	0.00	0.00	0.00	0.00	0.00
t13DCPy	110	$C_3H_4Cl_2$	0.00	0.00	0.00	0.00	0.00	0.00	0.00	0.00
12DCP	112	$C_3H_6Cl_2$	0.00	0.00	0.00	0.00	0.00	0.00	0.00	0.00
CB	112	C_6H_5Cl	0.00	0.00	0.00	0.00	0.00	0.00	0.00	0.00
CF	118	$CHCl_3$	0.00	0.00	0.00	0.00	0.00	0.00	0.00	0.00
124TMB	120	C_9H_{12}	0.00	0.00	0.08	0.00	0.86	0.00	0.00	0.00
135TMB	120	C_9H_{12}	0.00	0.00	0.08	0.00	0.86	0.00	0.00	0.00
F12	120	CCl_2F_2	0.00	0.00	0.00	0.00	0.00	0.00	0.00	0.00
TCEy	130	C_2HCl_3	0.00	0.00	0.00	0.00	0.00	0.00	0.51	0.00
111TCE	132	$C_2H_3Cl_3$	0.00	0.00	0.00	0.00	0.00	0.00	0.00	0.00
112TCE	132	$C_2H_3Cl_3$	0.00	0.00	0.00	0.00	0.00	0.00	0.00	0.00
F11	136	CCl_3F	0.00	0.00	0.00	0.00	0.00	0.00	0.00	0.00
mDCB	146	$C_6H_4Cl_2$	0.00	0.00	0.00	0.00	0.00	0.00	0.00	0.00
oDCB	146	$C_6H_4Cl_2$	0.00	0.00	0.00	0.00	0.00	0.00	0.00	0.00
pDCB	146	$C_6H_4Cl_2$	0.00	0.00	0.00	0.00	0.00	0.00	0.00	0.00
CTC	152	CCl_4	0.00	0.00	0.00	0.00	0.00	0.00	0.00	0.00
TeCEy	164	C_2Cl_4	0.00	0.00	0.00	0.00	0.00	0.00	0.01	0.00
TeCE	166	$C_2H_2Cl_4$	0.00	0.00	0.00	0.00	0.00	0.00	0.06	0.00
F114	170	$C_2Cl_2F_4$	0.00	0.00	0.00	0.00	0.00	0.00	0.00	0.00
124TCB	180	$C_6H_3Cl_3$	0.00	0.00	0.00	0.00	0.00	0.00	0.00	0.00
12DBE	186	$C_2H_4Br_2$	0.00	0.00	0.00	0.00	0.00	0.00	0.00	0.00
F113	186	$C_2Cl_3F_3$	0.00	0.00	0.00	0.00	0.00	0.00	0.00	0.00
HC13BD	258	C_4Cl_6	0.02	0.00	0.00	0.00	0.00	0.00	0.00	0.00

TO-14 compound Code	m/z	m/z	131		132	133		135		137	
			131	131	132	133	133	135	135	137	137
		g/mol	130.9222	131.0371	131.9300	132.9379	133.0280	134.9625	135.0293	136.9128	136.9128
		Formula	$C_2H_2Cl_3$	C_8H_5NO	$C_2H_3Cl_3$	$C_2H_4Cl_3$	$AlO(H_2O)_5$	C_2ClF_4	$C_4H_7O_5$	$CHCl_3F$	$C_7H_5O_3$
CM	50	CH_3Cl	0.00	0.00	0.00	0.00	0.00	0.00	0.00	0.00	0.00
VC	62	C_2H_3Cl	0.00	0.00	0.00	0.00	0.00	0.00	0.00	0.00	0.00
CE	64	C_2H_5Cl	0.00	0.00	0.00	0.00	0.00	0.00	0.00	0.00	0.00
B	78	C_6H_6	0.00	0.00	0.00	0.00	0.00	0.00	0.00	0.00	0.00
DCM	84	CH_2Cl_2	0.00	0.00	0.00	0.00	0.00	0.00	0.00	0.00	0.00
T	92	C_7H_8	0.00	0.00	0.00	0.00	0.00	0.00	0.00	0.00	0.00
BM	94	CH_3Br	0.00	0.00	0.00	0.00	0.00	0.00	0.00	0.00	0.00
11DCEy	96	$C_2H_2Cl_2$	0.00	0.00	0.00	0.00	0.00	0.00	0.00	0.00	0.00
c12DCEy	96	$C_2H_2Cl_2$	0.00	0.00	0.00	0.00	0.00	0.00	0.00	0.00	0.00
11DCE	98	$C_2H_4Cl_2$	0.00	0.00	0.00	0.00	0.00	0.00	0.00	0.00	0.00
12DCE	98	$C_2H_4Cl_2$	0.00	0.00	0.00	0.00	0.00	0.00	0.00	0.00	0.00
S	104	C_8H_8	0.00	0.00	0.00	0.00	0.00	0.00	0.00	0.00	0.00
EB	106	C_8H_{10}	0.00	0.00	0.00	0.00	0.00	0.00	0.00	0.00	0.00
mX	106	C_8H_{10}	0.00	0.00	0.00	0.00	0.00	0.00	0.00	0.00	0.00
oX	106	C_8H_{10}	0.00	0.00	0.00	0.00	0.00	0.00	0.00	0.00	0.00
pX	106	C_8H_{10}	0.00	0.00	0.00	0.00	0.00	0.00	0.00	0.00	0.00
c13DCPy	110	$C_3H_4Cl_2$	0.00	0.00	0.00	0.00	0.00	0.00	0.00	0.00	0.00
t13DCPy	110	$C_3H_4Cl_2$	0.00	0.00	0.00	0.00	0.00	0.00	0.00	0.00	0.00
12DCP	112	$C_3H_6Cl_2$	0.00	0.00	0.00	0.00	0.00	0.00	0.00	0.00	0.00
CB	112	C_6H_5Cl	0.00	0.00	0.00	0.00	0.00	0.00	0.00	0.00	0.00
CF	118	$CHCl_3$	0.00	0.00	0.00	0.00	0.00	0.00	0.00	0.00	0.00
124TMB	120	C_9H_{12}	0.00	0.00	0.00	0.00	0.00	0.00	0.00	0.00	0.00
135TMB	120	C_9H_{12}	0.00	0.00	0.00	0.00	0.00	0.00	0.00	0.00	0.00
F12	120	CCl_2F_2	0.00	0.00	0.00	0.00	0.00	0.00	0.00	0.00	0.00
TCEy	130	C_2HCl_3	0.48	0.00	0.00	0.00	0.00	0.00	0.00	0.00	0.00
111TCE	132	$C_2H_3Cl_3$	0.00	0.00	0.00	0.00	0.00	0.00	0.00	0.00	0.00
112TCE	132	$C_2H_3Cl_3$	0.00	0.00	0.00	0.01	0.00	0.00	0.00	0.00	0.00
F11	136	CCl_3F	0.00	0.00	0.00	0.00	0.00	0.00	0.00	0.00	0.00
mDCB	146	$C_6H_4Cl_2$	0.00	0.00	0.00	0.00	0.00	0.00	0.00	0.00	0.00
oDCB	146	$C_6H_4Cl_2$	0.00	0.00	0.00	0.00	0.00	0.00	0.00	0.00	0.00
pDCB	146	$C_6H_4Cl_2$	0.00	0.00	0.00	0.00	0.00	0.00	0.00	0.00	0.00
CTC	152	CCl_4	0.00	0.00	0.00	0.00	0.00	0.00	0.00	0.00	0.00
TeCEy	164	C_2Cl_4	0.00	0.00	0.00	0.00	0.00	0.00	0.00	0.00	0.00
TeCE	166	$C_2H_2Cl_4$	0.10	0.00	0.00	0.00	0.00	0.00	0.00	0.00	0.00
F114	170	$C_2Cl_2F_4$	0.00	0.00	0.00	0.00	0.00	0.00	0.00	0.00	0.00
124TCB	180	$C_6H_3Cl_3$	0.00	0.00	0.00	0.00	0.00	0.00	0.00	0.00	0.00
12DBE	186	$C_2H_4Br_2$	0.00	0.00	0.00	0.00	0.00	0.00	0.00	0.00	0.00
F113	186	$C_2Cl_3F_3$	0.00	0.00	0.00	0.00	0.00	0.00	0.00	0.00	0.00
HC13BD	258	C_4Cl_6	0.00	0.00	0.00	0.00	0.00	0.00	0.00	0.00	0.00

TO-14 compound Code	m/z	m/z	141		146		147		151	
			141	141	146	146	147	147	151	151
		g/mol	140.9066	141.0538	145.9690	146.0368	146.9768	147.0657	150.9329	151.0395
		Formula	C_3Cl_3	$C_5H_7N_3O_2$	$C_6H_4Cl_2$	$C_9H_6O_2$	$C_6H_5Cl_2$	$C_6H_{11}O_4$	$C_2Cl_2F_3$	$C_8H_7O_3$
CM	50	CH_3Cl	0.00	0.00	0.00	0.00	0.00	0.00	0.00	0.00
VC	62	C_2H_3Cl	0.00	0.00	0.00	0.00	0.00	0.00	0.00	0.00
CE	64	C_2H_5Cl	0.00	0.00	0.00	0.00	0.00	0.00	0.00	0.00
B	78	C_6H_6	0.00	0.00	0.00	0.00	0.00	0.00	0.00	0.00
DCM	84	CH_2Cl_2	0.00	0.00	0.00	0.00	0.00	0.00	0.00	0.00
T	92	C_7H_8	0.00	0.00	0.00	0.00	0.00	0.00	0.00	0.00
BM	94	CH_3Br	0.00	0.00	0.00	0.00	0.00	0.00	0.00	0.00
11DCEy	96	$C_2H_2Cl_2$	0.00	0.00	0.00	0.00	0.00	0.00	0.00	0.00
c12DCEy	96	$C_2H_2Cl_2$	0.00	0.00	0.00	0.00	0.00	0.00	0.00	0.00
11DCE	98	$C_2H_4Cl_2$	0.00	0.00	0.00	0.00	0.00	0.00	0.00	0.00
12DCE	98	$C_2H_4Cl_2$	0.00	0.00	0.00	0.00	0.00	0.00	0.00	0.00
S	104	C_8H_8	0.00	0.00	0.00	0.00	0.00	0.00	0.00	0.00
EB	106	C_8H_{10}	0.00	0.00	0.00	0.00	0.00	0.00	0.00	0.00
mX	106	C_8H_{10}	0.00	0.00	0.00	0.00	0.00	0.00	0.00	0.00
oX	106	C_8H_{10}	0.00	0.00	0.00	0.00	0.00	0.00	0.00	0.00
pX	106	C_8H_{10}	0.00	0.00	0.00	0.00	0.00	0.00	0.00	0.00
c13DCPy	110	$C_3H_4Cl_2$	0.00	0.00	0.00	0.00	0.00	0.00	0.00	0.00
t13DCPy	110	$C_3H_4Cl_2$	0.00	0.00	0.00	0.00	0.00	0.00	0.00	0.00
12DCP	112	$C_3H_6Cl_2$	0.00	0.00	0.00	0.00	0.00	0.00	0.00	0.00
CB	112	C_6H_5Cl	0.00	0.00	0.00	0.00	0.00	0.00	0.00	0.00
CF	118	$CHCl_3$	0.00	0.00	0.00	0.00	0.00	0.00	0.00	0.00
124TMB	120	C_9H_{12}	0.00	0.00	0.00	0.00	0.00	0.00	0.00	0.00
135TMB	120	C_9H_{12}	0.00	0.00	0.00	0.00	0.00	0.00	0.00	0.00
F12	120	CCl_2F_2	0.00	0.00	0.00	0.00	0.00	0.00	0.00	0.00
TCEy	130	C_2HCl_3	0.00	0.00	0.00	0.00	0.00	0.00	0.00	0.00
111TCE	132	$C_2H_3Cl_3$	0.00	0.00	0.00	0.00	0.00	0.00	0.00	0.00
112TCE	132	$C_2H_3Cl_3$	0.00	0.00	0.00	0.00	0.00	0.00	0.00	0.00
F11	136	CCl_3F	0.00	0.00	0.00	0.00	0.00	0.00	0.00	0.00
mDCB	146	$C_6H_4Cl_2$	0.00	0.00	0.18	0.00	0.81	0.00	0.00	0.00
oDCB	146	$C_6H_4Cl_2$	0.00	0.00	0.23	0.00	0.76	0.00	0.00	0.00
pDCB	146	$C_6H_4Cl_2$	0.00	0.00	0.22	0.00	0.77	0.00	0.00	0.00
CTC	152	CCl_4	0.00	0.00	0.00	0.00	0.00	0.00	0.00	0.00
TeCEy	164	C_2Cl_4	0.00	0.00	0.00	0.00	0.00	0.00	0.00	0.00
TeCE	166	$C_2H_2Cl_4$	0.00	0.00	0.00	0.00	0.00	0.00	0.00	0.00
F114	170	$C_2Cl_2F_4$	0.00	0.00	0.00	0.00	0.00	0.00	0.04	0.00
124TCB	180	$C_6H_3Cl_3$	0.00	0.00	0.03	0.00	0.00	0.00	0.00	0.00
12DBE	186	$C_2H_4Br_2$	0.00	0.00	0.00	0.00	0.00	0.00	0.00	0.00
F113	186	$C_2Cl_3F_3$	0.00	0.00	0.00	0.00	0.00	0.00	0.75	0.00
HC13BD	258	C_4Cl_6	0.01	0.00	0.00	0.00	0.00	0.00	0.00	0.00

TO-14 compound Code	m/z	m/z	153	164	165	166	170	177	180
			153	164	165	166	170	177	180
		g/mol	152.9066	163.8754	164.8832	165.8911	169.9313	176.8832	179.9300
		Formula	C_4Cl_3	C_2Cl_4	C_2HCl_4	$C_2H_2Cl_4$	$C_2Cl_2F_4$	C_3HCl_4	$C_6H_3Cl_3$
CM	50	CH_3Cl	0.00	0.00	0.00	0.00	0.00	0.00	0.00
VC	62	C_2H_3Cl	0.00	0.00	0.00	0.00	0.00	0.00	0.00
CE	64	C_2H_5Cl	0.00	0.00	0.00	0.00	0.00	0.00	0.00
B	78	C_6H_6	0.00	0.00	0.00	0.00	0.00	0.00	0.00
DCM	84	CH_2Cl_2	0.00	0.00	0.00	0.00	0.00	0.00	0.00
T	92	C_7H_8	0.00	0.00	0.00	0.00	0.00	0.00	0.00
BM	94	CH_3Br	0.00	0.00	0.00	0.00	0.00	0.00	0.00
11DCEy	96	$C_2H_2Cl_2$	0.00	0.00	0.00	0.00	0.00	0.00	0.00
c12DCEy	96	$C_2H_2Cl_2$	0.00	0.00	0.00	0.00	0.00	0.00	0.00
11DCE	98	$C_2H_4Cl_2$	0.00	0.00	0.00	0.00	0.00	0.00	0.00
12DCE	98	$C_2H_4Cl_2$	0.00	0.00	0.00	0.00	0.00	0.00	0.00
S	104	C_8H_8	0.00	0.00	0.00	0.00	0.00	0.00	0.00
EB	106	C_8H_{10}	0.00	0.00	0.00	0.00	0.00	0.00	0.00
mX	106	C_8H_{10}	0.00	0.00	0.00	0.00	0.00	0.00	0.00
oX	106	C_8H_{10}	0.00	0.00	0.00	0.00	0.00	0.00	0.00
pX	106	C_8H_{10}	0.00	0.00	0.00	0.00	0.00	0.00	0.00
c13DCPy	110	$C_3H_4Cl_2$	0.00	0.00	0.00	0.00	0.00	0.00	0.00
t13DCPy	110	$C_3H_4Cl_2$	0.00	0.00	0.00	0.00	0.00	0.00	0.00
12DCP	112	$C_3H_6Cl_2$	0.00	0.00	0.00	0.00	0.00	0.00	0.00
CB	112	C_6H_5Cl	0.00	0.00	0.00	0.00	0.00	0.00	0.00
CF	118	$CHCl_3$	0.00	0.00	0.00	0.00	0.00	0.00	0.00
124TMB	120	C_9H_{12}	0.00	0.00	0.00	0.00	0.00	0.00	0.00
135TMB	120	C_9H_{12}	0.00	0.00	0.00	0.00	0.00	0.00	0.00
F12	120	CCl_2F_2	0.00	0.00	0.00	0.00	0.00	0.00	0.00
TCEy	130	C_2HCl_3	0.00	0.00	0.00	0.00	0.00	0.00	0.00
111TCE	132	$C_2H_3Cl_3$	0.00	0.00	0.00	0.00	0.00	0.00	0.00
112TCE	132	$C_2H_3Cl_3$	0.00	0.00	0.00	0.00	0.00	0.00	0.00
F11	136	CCl_3F	0.00	0.00	0.00	0.00	0.00	0.00	0.00
mDCB	146	$C_6H_4Cl_2$	0.00	0.00	0.00	0.00	0.00	0.00	0.00
oDCB	146	$C_6H_4Cl_2$	0.00	0.00	0.00	0.00	0.00	0.00	0.00
pDCB	146	$C_6H_4Cl_2$	0.00	0.00	0.00	0.00	0.00	0.00	0.00
CTC	152	CCl_4	0.00	0.00	0.00	0.00	0.00	0.00	0.00
TeCEy	164	C_2Cl_4	0.00	0.77	0.05	0.00	0.00	0.00	0.00
TeCE	166	$C_2H_2Cl_4$	0.00	0.00	0.00	0.00	0.00	0.00	0.00
F114	170	$C_2Cl_2F_4$	0.00	0.00	0.00	0.00	0.01	0.00	0.00
124TCB	180	$C_6H_3Cl_3$	0.00	0.00	0.00	0.00	0.00	0.00	0.24
12DBE	186	$C_2H_4Br_2$	0.00	0.00	0.00	0.00	0.00	0.00	0.00
F113	186	$C_2Cl_3F_3$	0.00	0.00	0.00	0.00	0.00	0.00	0.00
HC13BD	258	C_4Cl_6	0.01	0.01	0.00	0.00	0.00	0.14	0.00

TO-14 compound Code	m/z	m/z	181	186	188	223	258	259
			181	186	188	223	258	259
		g/mol	180.9379	185.8680	187.8754	222.8443	257.8131	258.8209
		Formula	$C_6H_4Cl_3$	$C_2H_4Br_2$	C_4Cl_4	C_4Cl_5	C_4Cl_6	C_4HCl_6
CM	50	CH_3Cl	0.00	0.00	0.00	0.00	0.00	0.00
VC	62	C_2H_3Cl	0.00	0.00	0.00	0.00	0.00	0.00
CE	64	C_2H_5Cl	0.00	0.00	0.00	0.00	0.00	0.00
B	78	C_6H_6	0.00	0.00	0.00	0.00	0.00	0.00
DCM	84	CH_2Cl_2	0.00	0.00	0.00	0.00	0.00	0.00
T	92	C_7H_8	0.00	0.00	0.00	0.00	0.00	0.00
BM	94	CH_3Br	0.00	0.00	0.00	0.00	0.00	0.00
11DCEy	96	$C_2H_2Cl_2$	0.00	0.00	0.00	0.00	0.00	0.00
c12DCEy	96	$C_2H_2Cl_2$	0.00	0.00	0.00	0.00	0.00	0.00
11DCE	98	$C_2H_4Cl_2$	0.00	0.00	0.00	0.00	0.00	0.00
12DCE	98	$C_2H_4Cl_2$	0.00	0.00	0.00	0.00	0.00	0.00
S	104	C_8H_8	0.00	0.00	0.00	0.00	0.00	0.00
EB	106	C_8H_{10}	0.00	0.00	0.00	0.00	0.00	0.00
mX	106	C_8H_{10}	0.00	0.00	0.00	0.00	0.00	0.00
oX	106	C_8H_{10}	0.00	0.00	0.00	0.00	0.00	0.00
pX	106	C_8H_{10}	0.00	0.00	0.00	0.00	0.00	0.00
c13DCPy	110	$C_3H_4Cl_2$	0.00	0.00	0.00	0.00	0.00	0.00
t13DCPy	110	$C_3H_4Cl_2$	0.00	0.00	0.00	0.00	0.00	0.00
12DCP	112	$C_3H_6Cl_2$	0.00	0.00	0.00	0.00	0.00	0.00
CB	112	C_6H_5Cl	0.00	0.00	0.00	0.00	0.00	0.00
CF	118	$CHCl_3$	0.00	0.00	0.00	0.00	0.00	0.00
124TMB	120	C_9H_{12}	0.00	0.00	0.00	0.00	0.00	0.00
135TMB	120	C_9H_{12}	0.00	0.00	0.00	0.00	0.00	0.00
F12	120	CCl_2F_2	0.00	0.00	0.00	0.00	0.00	0.00
TCEy	130	C_2HCl_3	0.00	0.00	0.00	0.00	0.00	0.00
111TCE	132	$C_2H_3Cl_3$	0.00	0.00	0.00	0.00	0.00	0.00
112TCE	132	$C_2H_3Cl_3$	0.00	0.00	0.00	0.00	0.00	0.00
F11	136	CCl_3F	0.00	0.00	0.00	0.00	0.00	0.00
mDCB	146	$C_6H_4Cl_2$	0.00	0.00	0.00	0.00	0.00	0.00
oDCB	146	$C_6H_4Cl_2$	0.00	0.00	0.00	0.00	0.00	0.00
pDCB	146	$C_6H_4Cl_2$	0.00	0.00	0.00	0.00	0.00	0.00
CTC	152	CCl_4	0.00	0.00	0.00	0.00	0.00	0.00
TeCEy	164	C_2Cl_4	0.00	0.00	0.00	0.00	0.00	0.00
TeCE	166	$C_2H_2Cl_4$	0.00	0.00	0.00	0.00	0.00	0.00
F114	170	$C_2Cl_2F_4$	0.00	0.00	0.00	0.00	0.00	0.00
124TCB	180	$C_6H_3Cl_3$	0.73	0.00	0.00	0.00	0.00	0.00
12DBE	186	$C_2H_4Br_2$	0.00	0.00	0.00	0.00	0.00	0.00
F113	186	$C_2Cl_3F_3$	0.00	0.00	0.00	0.00	0.00	0.00
HC13BD	258	C_4Cl_6	0.00	0.00	0.03	0.17	0.24	0.33